CMS Draft Analysis Note

The content of this note is intended for CMS internal use and distribution only

2015/11/18
Head Id: 310950
Archive Id: Unversioned directory
Archive Date: 2015/11/17
Archive Tag: trunk

Search for new physics in final states with jets and missing transverse momentum in $\sqrt{s}$ = 13 TeV pp collisions with the α_T variable

M. Baber[2], R. Bainbridge[2], F. Blekman[3], O. Buchmüller[2], J. Brooke[1], S. Casasso[2], M. Citron[2], A. Elwood[2], H. Flächer[1], A. Garcia-Bellido[4], C. Laner[2], K.H. Lo[4], S.A. Malik[2], B. Penning[2], T. Sakuma[1], D. Smith[1,3], and A. Tapper[2]

[1] University of Bristol, Bristol, UK
[2] Imperial College, London, UK
[3] Vrije Universiteit Brussel, Brussel, BE
[4] University of Rochester, NY, US

DRAFT

Abstract

This note summarises an inclusive search for new physics processes that produce final states with jets and missing transverse energy in pp collisions at a centre-of-mass energy of $\sqrt{s}$ = 13 TeV. In this search, a dimensionless kinematic variable, α_T, provides powerful discriminating power between events with genuine and misreconstructed missing transverse energy, which allows the use of soft final-state objects in the definition of the trigger and candidate signal event selections. The search is based on the total number of jets per event, the number of jets originating from bottom quarks per event and the scalar and vector sum of transverse momenta of these jets. We analyse 1.3 fb^{-1} of data and provide interpretations for gluino-mediated simplified models.

This box is only visible in draft mode. Please make sure the values below make sense.

PDFAuthor:	Robin Aggleton, Mark Baber, Robert Bainbridge, Freya Blekman, Oliver Buchmueller, Jim Brooke, Stefano Casasso, Matthew Citron, Adam Elwood, Henning Flaecher, Aran Garcia-Bellido, Christian Laner, Kin Ho Lo, Chris Lucas, Sarah Alam Malik, Bjoern Penning, Tai Sakuma, Dominic Smith, Alex Tapper.
PDFTitle:	Search for new physics in final states with jets and missing transverse momentum in 13 TeV pp collisions with the AlphaT variable: the Early Analysis exercise
PDFSubject:	CMS, jets, missing transverse momentum, supersymmetry, dark matter, AlphaT
PDFKeywords:	CMS, jets, missing transverse momentum, supersymmetry, dark matter, AlphaT

Please also verify that the abstract does not use any user defined symbols

DRAFT

Contents

1 Introduction . . . 3
2 Analysis strategy . . . 5
2.1 The analysis during Run 1 . . . 5
2.2 Developments for Run 2 . . . 7
3 Definition of α_{T} . . . 10
4 Data sets . . . 12
4.1 Data . . . 12
4.2 Simulation . . . 13
4.3 Pileup reweighting . . . 25
4.4 Cross sections for SM samples . . . 26
5 Trigger strategy . . . 28
5.1 Hadronic signal region . . . 28
5.2 Control samples . . . 31
6 Physics objects . . . 34
6.1 Jets . . . 34
6.2 b-tagged jets . . . 34
6.3 Muons . . . 34
6.4 Photons . . . 35
6.5 Electrons . . . 35
6.6 Single isolated tracks . . . 35
6.7 Missing transverse momentum . . . 36
7 Event selection for signal and control regions . . . 37
7.1 Pre-selection . . . 37
7.2 Lepton and photon vetoes . . . 39
7.3 The hadronic signal region . . . 39
7.4 Adding the $H_{\mathrm{T}}^{\mathrm{miss}}$ dimension . . . 43
7.5 The hadronic control region . . . 44
7.6 Commonalities between the data control regions . . . 44
7.7 The μ + jets control sample . . . 44
7.8 The $\mu\mu$ + jets control sample . . . 44
7.9 The e + jets control sample . . . 45
7.10 The ee + jets control sample . . . 45
7.11 The γ + jets control sample . . . 45
8 Corrections to cross section for SM samples . . . 46
8.1 Correction to the γ+jets sample . . . 46
8.2 Correction to the W+jets, $t\bar{t}$+jets and Z+jets samples . . . 47
9 Characterisation of the signal and control regions . . . 49
9.1 Yields and distributions for the μ + jets control sample . . . 50
9.2 Yields and distributions for the $\mu\mu$ + jets control sample . . . 54
9.3 Yields and distributions for the photon + jets control sample . . . 58
9.4 Expected yields and distributions in the signal region . . . 62
10 Estimation for QCD multijet events . . . 69

DRAFT

11 Background estimation for processes with genuine $E_{\mathrm{T}}^{\mathrm{miss}}$ . . . 73
11.1 Overview of SM background processes . . . 73
11.2 The "transfer factor" method . . . 73
11.3 Adding the $H_{\mathrm{T}}^{\mathrm{miss}}$ dimension . . . 79
11.4 Data control samples used in the method . . . 79
12 Systematic uncertainties in the transfer factors . . . 81
12.1 Definition of a closure test . . . 81
12.2 Definition of the "core" closure tests . . . 82
12.3 Systematic uncertainties from ensembles of closure tests . . . 83
12.4 Closure test ensembles for specific backgrounds . . . 84
12.5 Closure tests based on 1.28 fb^{-1} . . . 84
12.6 Normalisation systematic uncertainties based on 1.28 fb^{-1} . . . 92
12.7 Dedicated closure test ensemble and systematic for α_{T} modelling . . . 93
12.8 Additional ensembles as cross checks . . . 94
12.9 Simulation-based studies of normalisation systematic uncertainties . . . 94
13 Systematic uncertainties in the $H_{\mathrm{T}}^{\mathrm{miss}}$ dimension . . . 98
13.1 Validation with 8 TeV Data . . . 98
13.2 Deriving systematics on the $H_{\mathrm{T}}^{\mathrm{miss}}$ imension . . . 99
13.3 Validation with 13 TeV ata . . . 101
13.4 Bias injection test . . . 102
13.5 Expected systematic uncertainties for the 13 TeV nalysis . . . 102
14 Likelihood model . . . 110
15 Results . . . 112
16 Interpretation in Simplified SUSY models . . . 150
16.1 Signal models . . . 150
16.2 Signal acceptance and contamination . . . 150
16.3 Systematic uncertainties on signal efficiency times acceptance . . . 151
16.4 Expected exclusion limits and discovery significance . . . 152
17 Interpretation in Dark Matter models . . . 154
17.1 Light flavour models . . . 154
17.2 Heavy flavour models . . . 166
18 Summary . . . 172
A Kinematic distributions for the signal region . . . 176
B Trigger efficiency measurements of signal models . . . 191
C Trigger efficiency measurements of α_{T} triggers . . . 193
D Low-H_{T} Level-1 seeds . . . 194
E Nuisance Parameters Fit . . . 196
F Control of Z_{inv} background . . . 197
G $H_{\mathrm{T}}^{\mathrm{miss}}$ templates . . . 198
H Yields for 3fb^{-1} . . . 206
I Signal acceptance from asymmetric jet p_{T} thresholds . . . 213

DRAFT

1 Introduction

In this note we summarise the α_T analysis, which searches for signatures of physics beyond the standard model in events with jets and missing transverse momentum (E_T^{miss}). This analysis uses the kinematic variable α_T to efficiently select candidate signal events with genuine missing transverse momentum while providing robust rejection against QCD multijet background events. With the α_T variable, CMS has been searching for supersymmetry (SUSY) in proton-proton collisions data collected during LHC Run 1. With data at a centre-of-mass energy of 7 TeV collected in 2010 and 2011, the α_T analysis has excluded a large parameter space of the constrained minimal supersymmetric extension of the standard model (CMSSM) [1–3] and a parameter space of simplified models [3]. With data at a centre-of-mass energy of 8 TeV collected and promptly reconstructed in 2012, the α_T analysis further excluded a parameter space of simplified models [4]. Additional sets of data which were collected in 2012 but were reconstructed later during the LHC Long Shutdown 1 (LS1) are called the "parked data", which contain data for events triggered with lower energy thresholds [5]. The search strategy in this note is an extension of that in Ref. [5].

After two years of the LS1, in June 2015, the LHC started its Run 2 and is delivering proton-proton collisions to CMS at a higher centre-of-mass energy of 13 TeV. The higher energy collision considerably increases the production cross sections of heavy particles, providing a strong motivation to continue the search for supersymmetry. The α_T analysis is particularly suited for this search and has potential for discovery in early data. The reconstruction of missing transverse momentum in different collider environment or at new collider energy is typically very challenging and often requires an extended period of development. However, the α_T variable is designed to provide robust discriminating power between sources of genuine and "fake" (e.g. instrumental) E_T^{miss}, as well as using an estimator of E_T^{miss} that relies solely on the vector sum of jet transverse momenta (H_T^{miss}).

The nature of dark matter (DM) is one of the outstanding problems in particle physics and a massive weakly interactive particle (WIMP) is highly motivated. A WIMP is not a specific elementary particle, but rather a broad class of possible particles. The most highly scrutinized thermal relic DM candidate is the lightest neutralino particle of supersymmetric (SUSY) theories. The neutralino is particularly well-motivated since, in addition to solving the DM problem, SUSY extensions of the SM contain a number of other attractive features both for particle physics and in early Universe cosmology. Most prominently known, is that SUSY does not only provide an excellent DM candidate but also solves the fine-tuning problem. However, not only SUSY but also non-supersymmetric models of physics beyond the standard model predict the production of DM at LHC Run 2.

The α_T variable efficiently selects events that potentially contain DM candidates produced in the collisions. In Run 2, we extend the α_T analysis to significantly improve the acceptance to dark matter production at the LHC.

The study in this note started as part of the PHYS14 exercise [6] which focused on preparation of the Run 2 physics analyses.

Section 2 discusses changes in the search methods made since Run 1. Sec. 3 defines the α_T variable. Section 4 lists the data sets used in this note. Section 5 describes the preparation of the triggers for Run 2. Section 6 defines the physics objects used in this note. Section 7 describes how events are selected. Section 9 shows the expected event yields in the signal and control regions. While Section 10 discusses how multijet background events are controlled, Section 11 estimates background from other processes. Then, Sec. 12 discusses systematic uncertainties

DRAFT

in the estimates. With likelihood models introduced in Section 14, we interpret the results in simplified SUSY models in Sec. 16 and Dark Matter models in 17. Finally Sec. 18 summarises this exercise.

DRAFT

2 Analysis strategy

2.1 The analysis during Run 1

While the analysis strategy has evolved significantly since the beginning of Run 1, certain design features have remained central to the RA1 analysis throughout Run 1 and will continue to do so during Run 2. These features, along with some of the more important recent developments, are outlined below.

Model-independent search for new physics:

The analysis is designed to be sensitive to a range of beyond standard model (BSM) physics scenarios with signatures that are characterised by jets and significant $E_{\mathrm{T}}^{\mathrm{miss}}$ in the final state. The search is one of the original Reference Analyses (RAs) that formed the basis of the CMS SUSY search program at the beginning of Run 1. The program was designed to be inclusive, model-independent (as much as possible), and topology-based.

The current incarnation of the RA1 search still retains its generic, inclusive nature. A binned signal region, defined by a set of inclusive selection criteria, is employed to provide sensitivity to a range of new physics models. By the end of Run 1, three discriminating variables were used to categorise signal event candidates: H_{T}, n_{jet}, and n_{b}. In the case of SUSY, this choice of variables provides sensitivity to the direct pair-production of all flavours of squarks (including the third generation), as well as pair-produced gluinos and their decays via all favours of quarks. The large dynamic range in H_{T} provides sensitivity to a large range of mass splittings between the parent sparticle and the LSP.

Robust performance under Start-Up conditions:

The search relies on the α_{T} variable, which strongly suppresses the dominant background of multijet production from QCD, while maintaining acceptance to new physics signatures with genuine $E_{\mathrm{T}}^{\mathrm{miss}}$ in the final state. At the beginning of Run 1, the α_{T} variable was chosen because it was shown to be extremely effective at operating under Start-Up conditions, when the beam conditions and detector performance were poorly understood. For example, multijet events with significant $E_{\mathrm{T}}^{\mathrm{miss}}$ from jet mismeasurements due to instrumental effects are penalised to lower values of α_{T}, hence the variable exhibits an intrinsic robustness against potential sources of "fake" $E_{\mathrm{T}}^{\mathrm{miss}}$.

While the Collaboration now has a good understanding of the detector performance under Run 1 conditions, the strategy we employ is still very relevant when exploring the new high-energy, high-luminosity frontier in Run 2.

Inclusive trigger strategy with low thresholds:

The trigger strategy has made use of the α_{T} variable at the HLT since 2011. Given the rejection power of α_{T} for multijet events, we employ this variable (crossed with H_{T}) at the trigger level, which allows to push to lower thresholds for a given trigger rate with respect to other discriminating variables typically used in jets + $E_{\mathrm{T}}^{\mathrm{miss}}$ searches (e.g. $E_{\mathrm{T}}^{\mathrm{miss}}$, $H_{\mathrm{T}}^{\mathrm{miss}}$, etc). A suite of H_{T}-α_{T} cross triggers allowed the RA1 search to push as low as $H_{\mathrm{T}} > 200\,\mathrm{GeV}$ and (effectively) $H_{\mathrm{T}}^{\mathrm{miss}} \gtrsim 100\,\mathrm{GeV}$ at the trigger, and as low as $H_{\mathrm{T}} > 200\,\mathrm{GeV}$ and (effectively) $H_{\mathrm{T}}^{\mathrm{miss}} \gtrsim 130\,\mathrm{GeV}$ in the signal region definition, with near-maximum signal efficiency at the cost of ~ 25 Hz (of which $\sim$15 was "parked").

Multijet-free signal region.

As the analysis has evolved, the event selection has been tailored to provide a multijet-free

sample of signal event candidates. This is achieved by applying a H_T-dependent α_T threshold, tuned to suppress the multijet contribution to the sub-percent level with respect to the total background counts per signal region bin. This is extremely important for the lowest H_T bins, which provide a significant contribution to the overall sensitivity to compressed SUSY or Dark Matter models. Additional studies of the "parked data" led to the addition of another powerful variable to further discriminate against heavy flavour decays in QCD multijet events, known as $\Delta\phi^*_{\mathrm{min}}$, which inspects the azimuthal separation of jets and E_T^{miss}.

Access to new physics via initial state radiation:

The analysis acceptance to compressed SUSY models relies not on the detection of very soft objects (often failing acceptance cuts) produced in the decay of the sparticles, but instead on the presence of jets from initial state radiation. The signal acceptance times efficiency for this mechanism is typically at the sub-percent level. Further, the signal is characterised by a very broad shape in H_T, with significant counts at low H_T, as well low values of n_{jet}, n_b, and H_T^{miss}. Hence, the highest signal counts are typically found in the bins with the highest background counts, typically populated by events from W + jets and Z$\rightarrow \nu\nu$ + jets, which results in a poor S/B. Hence, the signal shape over many bins has to be considered in order to achieve reasonable sensitivity to such signatures. One distinguishing feature with respect to the SM backgrounds, which is most pronounced for (near-)degenerate spectra, is that while the values of H_T and H_T^{miss} are typically small, the ratio H_T^{miss}/H_T is large with respect to SM backgrounds.

This mechanism of signal acceptance was the focus of the "parked analysis" in Ref [5]. While the interpretations of this result focused on strongly-produced compressed SUSY models, the same mechanism can be used to access the direct production of a Dark Matter candidate. Sensitivity to this class of models relies heavily on tight background control and low thresholds. This is the motivation for the strategies of developing high-performance triggers with low thresholds, tuning the event selection to provide a multijet-free signal region, and relying on a large ensemble of closure tests in data to demonstrate excellent control of the non-multijet backgrounds in the signal region.

Data-driven background estimation methods and closure tests:

The analysis relies on multiple data control samples to predict the non-multijet backgrounds. The control samples have a composition similar to the signal region, cover a similar kinematic phase space, have a large acceptance, and are signal-depleted. The analysis relies on transfer factors constructed from MC to extrapolate from the control regions to the signal region. The extrapolation is minimised by using identical binning in all samples. Potential residual biases in the transfer factors, e.g. from MC mismodelling, are probed though a large ensemble of closure tests performed between numerous data control sub-samples. Several hundred statistically independent tests are performed, which cover a wide range of potential biases.

These closure tests are one of the most crucial components of this analysis, as they provide an understanding of the reliance on MC (in the form of ratios, i.e. transfer factors) that is *founded on comparison with data*. Any potential biases or dependencies on the discriminating variables used to categorise the signal events must be understood prior to unblinding the signal region. There are concrete examples in the past when the closure tests have revealed problems, which had to be understood and solved prior to continuing with the analysis.

In the absence of any significant biases, the closure tests are then used to determine systematic uncertainties on the transfer factors, which are propagated through to the analysis result via the likelihood model. These systematic uncertainties are therefore motivated through comparisons with control data and are, ultimately, statistically limited by the data counts in the control

DRAFT

samples. With increasing integrated luminosity, we expect the closure tests to be increasingly statistically-significant probes of potential biases and, in the absence of bias, the systematic uncertainties will correspondingly reduce.

2.2 Developments for Run 2

Building on the experience gained during Run 1, we developed the analysis to provide improved sensitivity to a range of new physics models. These developments fall broadly under three categories:

- general optimisations concerning trigger, event reconstruction and selection;
- improvements concerning simplifed Dark Matter models and compressed SUSY models.
- improvements in the sensitivity to heavy objects, such as gluinos

Some of these changes have already been studied and/or implemented during supplementary studies to the Run 1 "parked analysis", as described in Ref. [5]. Others, like an extensive addition of new jet categories are presented for the first time. These addtitions consitute a significant effort and aim to achieve very good sensitivity for DM signatures recommended by the ATLAS-CMS DM Forum [7]. The status will be noted at appropriate points in this document. A summary of these changes are listed below. This list is not exhaustive and some developments are still subject to (minor) change.

Particle Flow event reconstruction:

The analysis switched from relying on jets reconstructed solely from calorimeter information to the use of jets from the Particle Flow (PF) reconstruction algorithm. This change provides performance improvements for jet-based variables (including H_{T}, $H_{\mathrm{T}}^{\mathrm{miss}}$, and α_{T}) and, in particular, better mitigate any effects relating to pileup.

General event selection optimisation:

In addition to the switch to PF, all event selection criteria for the signal region and control samples have been reviewed. The jet p_{T} threshold is no longer scaled at low H_{T} as during Run 1, and the binning in H_{T} has been simplified. Also binning choice in the signal region had evolved to consider the anticipated integrated luminosity and data taking conditions. We also plan to investigate developments concerning e.g. boosted objects.

Trigger strategy:

The trigger strategy is similar to that of Run 1, and continues to rely on a suite of H_{T}-α_{T} cross triggers at the HLT. The trigger decision is now based on PF jets, rather than calorimeter-based jets as during Run 1. The H_{T} and α_{T} thresholds used at the end of Run 1 have been maintained, which fall in the range of $200 < H_{\mathrm{T}} < 400\,\mathrm{GeV}$ and $0.57 > \alpha_{\mathrm{T}} > 0.51$. The p_{T} requirements on the lead two jets have been raised, in order to help control rate, while maintaining acceptance to events with soft second jets.

The highest H_{T} bins in the analysis is seeded by the lowest unprescaled H_{T} trigger, which currently has a threshold of $H_{\mathrm{T}} > 800\,\mathrm{GeV}$.

Single object muon, electron, photon, and (prescaled) H_{T} triggers are used to seed the control samples.

There have also been developments of novel L1 seeds to improve efficiencies at low H_{T}. The performance of the L1 cross triggers based on these seeds provides very high efficiency down

DRAFT

to $H_T > 200\,\text{GeV}$.

H_T-dependent α_T thresholds:

During Run-1, the α_T thresholds were raised as high as $\alpha_T > 0.65$ for the lowest H_T bins to suppress potential contamination from multijet events to the sub-percent level with respect to the total background counts. A constant threshold of $\alpha_T > 0.55$ was used for all bins satisfying $H_T > 325\,\text{GeV}$. However, α_T is a relative quantity that relates H_T and H_T^{miss} (and ΔH_T) such that there is an effective lower bound on H_T^{miss} that increases linearly with H_T. In order to maximise signal acceptance, while maintaining at least the same level of multijet rejection as in the lowest H_T bins, the α_T threshold is lowered as a function of H_T in line with the thresholds for the suite of HLT triggers. This approach allows an α_T threshold as low as 0.52 for the region $H_T > 400\,\text{GeV}$, which corresponds to a lower bound on H_T^{miss} of $\sim 110\,\text{GeV}$. This (approximate) requirement on H_T^{miss} is (indirectly) imposed on all bins in the low H_T region through an appropriate choice of α_T threshold.

This dependence on H_T of the α_T thresholds allows improve acceptance, particularly to "jetty" signatures which are a characteristic of gluino pair-production and decay. The approach allows to maintain an approximately constant H_T^{miss} requirement of $\sim 130\,\text{GeV}$ through the full range of $H_T > 200\,\text{GeV}$.

For the region $H_T > 800\,\text{GeV}$, events are collected with the lowest unprescaled H_T trigger in the HLT menu. As there is no α_T requirement in the trigger, we choose to drop the α_T requirement in the event selection and instead employ only a requirement on the variable $\Delta\phi^*_{min}$ to control any potential multijet contamination, in conjunction with a loose baseline requirement of $H_T^{miss} > 130\,\text{GeV}$ (which corresponds to an α_T threshold of ~ 0.507). While the use of α_T is necessary to push to low values of H_T and H_T^{miss}, we opt for only the $\Delta\phi^*_{min}$ and H_T^{miss} requirements at high H_T, as this approach improves the signal efficiency in the high jet multiplicity environment while still controlling multijet contamination.

Adding the H_T^{miss} dimension:

During Run 1, events in the signal region were categorised according to three discriminating variables: H_T, n_{jet}, and n_b. While H_T has historically been used in many searches for new physics at the LHC as an estimator for the mass scale of new physics, another characteristic signature for (R-parity conserving) SUSY and other models involving the direct production of a Dark Matter candidate is the presence of significant E_T^{miss}.

Early in the `PHYS14` exercise, we explored the options for an additional discriminating variable that improves the analysis sensitivity to both the strong production of heavy objects such as gluinos and squarks as well as compressed SUSY models and Dark Matter candidates. The variable H_T^{miss} was chosen, given its generally good performance with respect to the other variables that were investigated, plus this variable fits naturally with the current "robust" analysis strategy of relying solely on jets as input (rather than e.g. E_T^{miss}). Events are binned according to this variable, which supersedes the "effective" single bin approach employed in Run 1 via the α_T requirement that, depending on the H_T scale, translated into an "effective" minimum H_T^{miss} requirement of $\sim$130–500 GeV.

Additional n_{jet} categories:

We adopted a more granular jet multiplicity binning in Run 2, in which events are categorised according to whether they contain exactly one, two, three, four, or at least five jets. This compares with the two categories of $n_{jet} = 2 - 3$ and $n_{jet} \geq 4$ used during Run 1. Events are also categorised according to the number of jets that are tagged as originating from b-quarks, with

DRAFT

up to as many as four b-tags (as during Run 1). This improved granularity in the number of jets helps to improve the sensitivity to a wide range of models, including compressed SUSY scenarios, collider production of Dark Matter, and gluino-mediated models.

"Asymmetric" jet p_{T} thresholds:

The nominal event selection criteria for the signal region include an increased threshold of 100 GeV for the two hardest jets in the event. This raised threshold is aimed at reducing the V + jets backgrounds while maintaining acceptance to SUSY models due to the assumed pair-production of sparticles. (The decay of each sparticle is assumed to result in at least one hard jet.)

However, for compressed SUSY and Dark Matter models, signal acceptance is largely due to the presence of jets from initial state radiation. Under this scenario, it is beneficial to relax the requirements on the second leading jet in the event in order to maximise acceptance. Hence, in addition to each "nominal" n_{jet} category, there is now a new orthogonal "asymmetric" n_{jet} category that still requires a hard leading jet but also requires a soft second jet. The "asymmetric" dijet category is therefore comparable to the dijet bin of the monojet analysis [8–10]. Given that a minimum of two jets are still required, the method of using α_{T} to suppress multijet contamination is still applicable.

"Monojet" selection:

In order to achieve a complete coverage of the jet multiplicity phase space, and further improve acceptance to low WIMP and mediator masses in simplified SUSY and DM models, we also lowered the jet multiplicity requirement of the analysis to include the "monojet" category, in which exactly one jet above the 100 GeV is required. In this case, a requirement on $\Delta\phi^{*}_{\mathrm{min}}$ alone, and not α_{T}, is sufficient to suppress the multijet background to a negligible level.

Additional electron data control samples:

Preliminary studies have been performed to add the e + jets and ee + jets data control samples. These two samples closely mirror their μ + jets and $\mu\mu$ + jets counterparts. Further, we mirrored the H_{T}-dependent α_{T} thresholds of the signal region in the γ + jets sample. The overall aim is to maximise the data counts in multiple control samples to allow better control of the predictions made in the analysis. Primarily, the additional samples provide additional redundancy and potential cross checks via the "RA1-style" closure tests. Further, the additional control samples will help to reduce the statistical uncertainties associated with the predictions in the signal region. While the electron selections are fully implemented they are not yet considered in the final analysis to further validate multijet background predictions in these final states.

Developments concerning closure tests:

As in Run 1, closure tests are performed in bins of n_{jet} and H_{T}. These tests allow to identify any biases or dependencies in the predictions. Two new closure test have been developed to test the estimations of the $Z \to \nu\nu$ background and the W charge asymmetry. Also the addition of two electron control samples will allow for additional closure tests, further improving the understanding of the transfer factors constructed from MC, with the ultimate aim of reducing their associated systematic uncertainties.

DRAFT

3 Definition of α_T

The α_T [11–13] variable is used to efficiently reject multijet events without significant E_T^{miss} or with transverse energy mismeasurements, while retaining a large sensitivity to new physics with final-state signatures containing significant E_T^{miss}.

The measurement of E_T^{miss} typically relies on independent sources of information from each of the calorimeter, tracking, and muon subdetectors. Relative to other physics objects, this measurement is particularly sensitive to the beam conditions and detector performance. This difficulty is compounded by the high-energy, high-luminosity hadron collider environment at the LHC and the lack of precise theoretical predictions for the kinematic properties and cross sections of multijet events. Hence it is very challenging to control and model accurately the multijet background in the high-E_T^{miss} phase space that is typical of SUSY searches.

Given these difficulties, the variable α_T was developed to avoid direct reliance on a measurement of E_T^{miss}, instead depending solely on the measurements of the transverse energies and (relative) azimuthal angles of jets. The variable is intrinsically robust against the presence of jet energy mismeasurements in multijet systems.
For dijet events, the α_T variable is defined as:

$$\alpha_T = \frac{{E_T}^{j_2}}{M_T}, \tag{1}$$

where ${E_T}^{j_2}$ is the transverse energy of the less energetic jet and M_T is the transverse mass of the dijet system, defined as

$$M_T = \sqrt{\left(\sum_{i=1}^{2} {E_T}^{j_i}\right)^2 - \left(\sum_{i=1}^{2} p_x^{j_i}\right)^2 - \left(\sum_{i=1}^{2} p_y^{j_i}\right)^2}. \tag{2}$$

where ${E_T}^{j_i}$, $p_x^{j_i}$, and $p_y^{j_i}$ are, respectively, the transverse energy and x or y components of the transverse momentum of jet j_i.

For a perfectly measured dijet event with ${E_T}^{j_1} = {E_T}^{j_2}$ and jets back-to-back in ϕ, and in the limit in which the momentum of each jet is large compared with its mass, the value of α_T is 0.5. For the case of an imbalance in the measured transverse energies of back-to-back jets, α_T is reduced to a value smaller than 0.5, which gives the variable its intrinsic robustness with respect to jet energy mismeasurements. Values significantly greater than 0.5 are observed when the two jets are not back-to-back and are recoiling against significant, genuine E_T^{miss}.

The definition of the α_T variable can be generalised for events with two or more jets as follows. The mass scale of the physics processes being probed is characterised by the scalar sum of the transverse energy E_T of jets considered in the analysis, defined as $H_T = \sum_{i=1}^{n_{jet}} {E_T}^{j_i}$, where n_{jet} is the number of jets with E_T above a predefined threshold. The estimator for E_T^{miss} is given by the magnitude of the transverse momenta $\vec{p_T}$ vectorial sum over these jets, defined as $H_T^{miss} = |\sum_{i=1}^{N_{jet}} \vec{p_T}^{j_i}|$.

For events with three or more jets, a pseudo-dijet system is formed by combining the jets in the event into two pseudo-jets. The total E_T for each of the two pseudo-jets is calculated as the scalar sum of the measured E_T of the contributing jets. The combination chosen is the one that minimises the absolute E_T difference between the two pseudo-jets, ΔH_T. This simple clustering

DRAFT

criterion provides the best separation between multijet events and events with genuine $E_{\mathrm{T}}^{\mathrm{miss}}$. Eq. 1 can therefore be generalised as:

$$\alpha_{\mathrm{T}} = \frac{1}{2} \times \frac{H_{\mathrm{T}} - \Delta H_{\mathrm{T}}}{\sqrt{{H_{\mathrm{T}}}^2 - {H_{\mathrm{T}}^{\mathrm{miss}}}^2}} = \frac{1}{2} \times \frac{1 - (\Delta H_{\mathrm{T}}/H_{\mathrm{T}})}{\sqrt{1 - (H_{\mathrm{T}}^{\mathrm{miss}}/H_{\mathrm{T}})^2}} \,. \tag{3}$$

In the presence of jet energy mismeasurements, the direction and magnitude of the apparent missing transverse energy, $H_{\mathrm{T}}^{\mathrm{miss}}$, and energy imbalance of the pseudo-dijet system, ΔH_{T}, are highly correlated. This correlation is much weaker for R-parity-conserving SUSY with each of the two decay chains producing the LSP.

It is useful to consider the limiting case $\Delta H_{\mathrm{T}} \to 0$ to understand the relationship between α_{T} and the ratio $H_{\mathrm{T}}^{\mathrm{miss}}/H_{\mathrm{T}}$:

$$\frac{H_{\mathrm{T}}^{\mathrm{miss}}}{H_{\mathrm{T}}} = \sqrt{1 - \frac{1}{4 \cdot \alpha_{\mathrm{T}}^2}} \tag{4}$$

For reference, under the assumption of $\Delta H_{\mathrm{T}} = 0$, the values of $\alpha_{\mathrm{T}} = 0.55$, 0.60, and 0.65 map onto values of the ratio $H_{\mathrm{T}}^{\mathrm{miss}}/H_{\mathrm{T}} = 0.42$, 0.55, and 0.64.

DRAFT

4 Data sets

4.1 Data

In this note, we use proton-proton collision data at $\sqrt{s} = 13$ TeV collected in 2015. This version of the note uses 1.3 fb^{-1} of data certified by the physics validation group. The JSON file listed in Table 1 specifies the periods of the time in which these certified data are collected. Table 2 lists the names of the data sets relevant for the analysis, along with the integrated luminosities for each data set. Since the certification of the data collected in 2015 is ongoing, we will use more data in the final version of the note.

We perform a blind analysis. In the previous version of the note, the data in the signal region is blinded with the exception of 149.48 pb^{-1} of the certified data specified by the JSON file in Table 3. Data in the control regions is never blinded. These bliding policies are agree in the SUS PAG.

In the review of the previous version of the note and related presentations in the SUS PAG, it becomes clear that we understand the data in the control regions and a small fraction of the unblinded data in the signal region well enough to predict the backgrounds in the signal region. As a result, no data in the signal region is blinded in this version of the note.

Table 1: The JSON file that specifies the periods of the time in which 1.2 fb^{-1} of the certified data are collected

`Cert_246908-258750_13TeV_PromptReco_Collisions15_25ns_JSON.txt`

Table 2: Data sets

Data set	$\int \mathcal{L} dt [\text{pb}^{-1}]$
`/HTMHT/Run2015D-05Oct2015-v1/MINIAOD`	551.60
`/HTMHT/Run2015D-PromptReco-v4/MINIAOD`	711.21
`/JetHT/Run2015D-05Oct2015-v1/MINIAOD`	552.67
`/JetHT/Run2015D-PromptReco-v4/MINIAOD`	711.21
`/MET/Run2015D-05Oct2015-v1/MINIAOD`	552.67
`/MET/Run2015D-PromptReco-v4/MINIAOD`	711.21
`/SingleElectron/Run2015D-05Oct2015-v1/MINIAOD`	552.63
`/SingleElectron/Run2015D-PromptReco-v4/MINIAOD`	710.98
`/SingleMuon/Run2015D-05Oct2015-v1/MINIAOD`	552.67
`/SingleMuon/Run2015D-PromptReco-v4/MINIAOD`	711.21
`/SinglePhoton/Run2015D-05Oct2015-v1/MINIAOD`	552.67
`/SinglePhoton/Run2015D-PromptReco-v4/MINIAOD`	711.21
`/ZeroBias/Run2015D-05Oct2015-v1/MINIAOD`	552.67
`/ZeroBias/Run2015D-PromptReco-v4/MINIAOD`	279.43

Table 3: The JSON file specifying the 149.48 pb^{-1} of the certified data that we never blind

`Cert_246908-257599_13TeV_PromptReco_Collisions15_25ns_JSON_v3.txt`

DRAFT

4.2 Simulation

Table 4 lists the data sets of simulated events of the standard model background processes used in this note. Tables from 5 to 15 lists those of the signal processes. In these data sets, in addition to the main interaction, each event contains on average 20 minimum bias interactions which simulate multiple interactions per bunch-crossing (in-time pileup). The expected detector signal from previous or following bunch crossings (out-of-time pileup) with 25ns bunch spacing is overlapped.

DRAFT

Table 4: Simulated background samples

Data set	Cross section [pb]
/DYJetsToLL_M-50_HT-100to200_TuneCUETP8M1_13TeV-madgraphMLM-pythia8/RunIISpring15DR74-Asympt25ns_MCRUN2_74_V9-v2/MINIAODSIM	$1.715 \times 10^{+02}$
/DYJetsToLL_M-50_HT-200to400_TuneCUETP8M1_13TeV-madgraphMLM-pythia8/RunIISpring15DR74-Asympt25ns_MCRUN2_74_V9-v2/MINIAODSIM	$5.258 \times 10^{+01}$
/DYJetsToLL_M-50_HT-400to600_TuneCUETP8M1_13TeV-madgraphMLM-pythia8/RunIISpring15DR74-Asympt25ns_MCRUN2_74_V9-v2/MINIAODSIM	$6.761 \times 10^{+00}$
/DYJetsToLL_M-50_HT-600toInf_TuneCUETP8M1_13TeV-madgraphMLM-pythia8/RunIISpring15DR74-Asympt25ns_MCRUN2_74_V9-v2/MINIAODSIM	$2.718 \times 10^{+00}$
/GJets_HT-40To100_TuneCUETP8M1_13TeV-madgraphMLM-pythia8/RunIISpring15DR74-Asympt25ns_MCRUN2_74_V9-v2/MINIAODSIM	$2.308 \times 10^{+04}$
/GJets_HT-100To200_TuneCUETP8M1_13TeV-madgraphMLM-pythia8/RunIISpring15DR74-Asympt25ns_MCRUN2_74_V9-v2/MINIAODSIM	$9.110 \times 10^{+03}$
/GJets_HT-200To400_TuneCUETP8M1_13TeV-madgraphMLM-pythia8/RunIISpring15DR74-Asympt25ns_MCRUN2_74_V9-v2/MINIAODSIM	$2.298 \times 10^{+03}$
/GJets_HT-400To600_TuneCUETP8M1_13TeV-madgraphMLM-pythia8/RunIISpring15DR74-Asympt25ns_MCRUN2_74_V9-v1/MINIAODSIM	$2.730 \times 10^{+02}$
/GJets_HT-600ToInf_TuneCUETP8M1_13TeV-madgraphMLM-pythia8/RunIISpring15DR74-Asympt25ns_MCRUN2_74_V9-v1/MINIAODSIM	$9.450 \times 10^{+01}$
/QCD_HT100to200_TuneCUETP8M1_13TeV-madgraphMLM-pythia8/RunIISpring15DR74-Asympt25ns_MCRUN2_74_V9-v2/MINIAODSIM	$2.754 \times 10^{+07}$
/QCD_HT200to300_TuneCUETP8M1_13TeV-madgraphMLM-pythia8/RunIISpring15DR74-Asympt25ns_MCRUN2_74_V9-v2/MINIAODSIM	$1.735 \times 10^{+06}$
/QCD_HT300to500_TuneCUETP8M1_13TeV-madgraphMLM-pythia8/RunIISpring15DR74-Asympt25ns_MCRUN2_74_V9-v2/MINIAODSIM	$3.670 \times 10^{+05}$
/QCD_HT500to700_TuneCUETP8M1_13TeV-madgraphMLM-pythia8/RunIISpring15DR74-Asympt25ns_MCRUN2_74_V9-v1/MINIAODSIM	$2.940 \times 10^{+04}$
/QCD_HT700to1000_TuneCUETP8M1_13TeV-madgraphMLM-pythia8/RunIISpring15DR74-Asympt25ns_MCRUN2_74_V9-v1/MINIAODSIM	$6.524 \times 10^{+03}$
/QCD_HT1000to1500_TuneCUETP8M1_13TeV-madgraphMLM-pythia8/RunIISpring15DR74-Asympt25ns_MCRUN2_74_V9-v2/MINIAODSIM	$1.064 \times 10^{+03}$
/QCD_HT1500to2000_TuneCUETP8M1_13TeV-madgraphMLM-pythia8/RunIISpring15DR74-Asympt25ns_MCRUN2_74_V9-v1/MINIAODSIM	$1.215 \times 10^{+02}$
/QCD_HT2000toInf_TuneCUETP8M1_13TeV-madgraphMLM-pythia8/RunIISpring15DR74-Asympt25ns_MCRUN2_74_V9-v1/MINIAODSIM	$2.542 \times 10^{+01}$
/TTJets_TuneCUETP8M1_13TeV-madgraphMLM-pythia8/RunIISpring15DR74-Asympt25ns_MCRUN2_74_V9-v2/MINIAODSIM	$8.318 \times 10^{+02}$
/TTJets_DiLept_TuneCUETP8M1_13TeV-madgraphMLM-pythia8/RunIISpring15DR74-Asympt25ns_MCRUN2_74_V9-v2/MINIAODSIM	$8.829 \times 10^{+01}$
/TTJets_DiLept_TuneCUETP8M1_13TeV-madgraphMLM-pythia8/RunIISpring15DR74-Asympt25ns_MCRUN2_74_V9_ext1-v1/MINIAODSIM	$8.829 \times 10^{+01}$
/TTJets_HT-600to800_TuneCUETP8M1_13TeV-madgraphMLM-pythia8/RunIISpring15DR74-Asympt25ns_MCRUN2_74_V9-v1/MINIAODSIM	$2.667 \times 10^{+00}$
/TTJets_HT-800to1200_TuneCUETP8M1_13TeV-madgraphMLM-pythia8/RunIISpring15DR74-Asympt25ns_MCRUN2_74_V9-v1/MINIAODSIM	$1.098 \times 10^{+00}$
/TTJets_HT-1200to2500_TuneCUETP8M1_13TeV-madgraphMLM-pythia8/RunIISpring15DR74-Asympt25ns_MCRUN2_74_V9-v1/MINIAODSIM	1.987×10^{-01}
/TTJets_HT-2500toInf_TuneCUETP8M1_13TeV-madgraphMLM-pythia8/RunIISpring15DR74-Asympt25ns_MCRUN2_74_V9-v1/MINIAODSIM	2.368×10^{-03}
/TTJets_SingleLeptFromT_TuneCUETP8M1_13TeV-madgraphMLM-pythia8/RunIISpring15DR74-Asympt25ns_MCRUN2_74_V9-v1/MINIAODSIM	$1.827 \times 10^{+02}$
/TTJets_SingleLeptFromT_TuneCUETP8M1_13TeV-madgraphMLM-pythia8/RunIISpring15DR74-Asympt25ns_MCRUN2_74_V9_ext1-v1/MINIAODSIM	$1.827 \times 10^{+02}$
/TTJets_SingleLeptFromTbar_TuneCUETP8M1_13TeV-madgraphMLM-pythia8/RunIISpring15DR74-Asympt25ns_MCRUN2_74_V9-v2/MINIAODSIM	$1.827 \times 10^{+02}$
/TTJets_SingleLeptFromTbar_TuneCUETP8M1_13TeV-madgraphMLM-pythia8/RunIISpring15DR74-Asympt25ns_MCRUN2_74_V9_ext1-v1/MINIAODSIM	$1.827 \times 10^{+02}$
/TT_TuneCUETP8M1_13TeV-powheg-pythia8/RunIISpring15DR74-Asympt25ns_MCRUN2_74_V9-v2/MINIAODSIM	$8.318 \times 10^{+02}$
/ST_s-channel_4f_leptonDecays_13TeV-amcatnlo-pythia8_TuneCUETP8M1/RunIISpring15DR74-Asympt25ns_MCRUN2_74_V9-v1/MINIAODSIM	$3.681 \times 10^{+00}$
/ST_t-channel_4f_leptonDecays_13TeV-amcatnlo-pythia8_TuneCUETP8M1/RunIISpring15DR74-Asympt25ns_MCRUN2_74_V9-v1/MINIAODSIM	$7.031 \times 10^{+01}$
/ST_tW_top_5f_inclusiveDecays_13TeV-powheg-pythia8_TuneCUETP8M1/RunIISpring15DR74-Asympt25ns_MCRUN2_74_V9-v1/MINIAODSIM	$3.560 \times 10^{+01}$
/ST_tW_antitop_5f_inclusiveDecays_13TeV-powheg-pythia8_TuneCUETP8M1/RunIISpring15DR74-Asympt25ns_MCRUN2_74_V9-v1/MINIAODSIM	$3.560 \times 10^{+01}$
/WJetsToLNu_HT-100To200_TuneCUETP8M1_13TeV-madgraphMLM-pythia8/RunIISpring15DR74-Asympt25ns_MCRUN2_74_V9-v1/MINIAODSIM	$1.630 \times 10^{+03}$
/WJetsToLNu_HT-200To400_TuneCUETP8M1_13TeV-madgraphMLM-pythia8/RunIISpring15DR74-Asympt25ns_MCRUN2_74_V9-v1/MINIAODSIM	$4.356 \times 10^{+02}$
/WJetsToLNu_HT-400To600_TuneCUETP8M1_13TeV-madgraphMLM-pythia8/RunIISpring15DR74-Asympt25ns_MCRUN2_74_V9-v3/MINIAODSIM	$5.917 \times 10^{+01}$
/WJetsToLNu_HT-600To800_TuneCUETP8M1_13TeV-madgraphMLM-pythia8/RunIISpring15DR74-Asympt25ns_MCRUN2_74_V9-v2/MINIAODSIM	$1.549 \times 10^{+01}$
/WJetsToLNu_HT-800To1200_TuneCUETP8M1_13TeV-madgraphMLM-pythia8/RunIISpring15DR74-Asympt25ns_MCRUN2_74_V9-v1/MINIAODSIM	$6.365 \times 10^{+00}$
/WJetsToLNu_HT-1200To2500_TuneCUETP8M1_13TeV-madgraphMLM-pythia8/RunIISpring15DR74-Asympt25ns_MCRUN2_74_V9-v1/MINIAODSIM	$1.609 \times 10^{+00}$
/WJetsToLNu_HT-2500ToInf_TuneCUETP8M1_13TeV-madgraphMLM-pythia8/RunIISpring15DR74-Asympt25ns_MCRUN2_74_V9-v2/MINIAODSIM	3.738×10^{-02}
/WWTo2L2Nu_13TeV-powheg/RunIISpring15DR74-Asympt25ns_MCRUN2_74_V9-v1/MINIAODSIM	$1.246 \times 10^{+01}$
/WZ_TuneCUETP8M1_13TeV-pythia8/RunIISpring15DR74-Asympt25ns_MCRUN2_74_V9-v1/MINIAODSIM	$6.610 \times 10^{+01}$
/ZJetsToNuNu_HT-100To200_13TeV-madgraph/RunIISpring15DR74-Asympt25ns_MCRUN2_74_V9-v1/MINIAODSIM	$3.450 \times 10^{+02}$
/ZJetsToNuNu_HT-200To400_13TeV-madgraph/RunIISpring15DR74-Asympt25ns_MCRUN2_74_V9-v1/MINIAODSIM	$9.638 \times 10^{+01}$
/ZJetsToNuNu_HT-400To600_13TeV-madgraph/RunIISpring15DR74-Asympt25ns_MCRUN2_74_V9-v1/MINIAODSIM	$1.346 \times 10^{+01}$
/ZJetsToNuNu_HT-600ToInf_13TeV-madgraph/RunIISpring15DR74-Asympt25ns_MCRUN2_74_V9-v1/MINIAODSIM	$5.170 \times 10^{+00}$
/ZZ_TuneCUETP8M1_13TeV-pythia8/RunIISpring15DR74-Asympt25ns_MCRUN2_74_V9-v3/MINIAODSIM	$3.180 \times 10^{+01}$

DRAFT

Table 5: Simulated signal samples: SMS T1qqqq

Data set
/SMS-T1qqqq_mGluino-600_mLSP-1to300_TuneCUETP8M1_13TeV-madgraphMLM-pythia8/RunIISpring15FSPremix-MCRUN2_74_V9-v1/MINIAODSIM
/SMS-T1qqqq_mGluino-600_mLSP-400to475_TuneCUETP8M1_13TeV-madgraphMLM-pythia8/RunIISpring15FSPremix-MCRUN2_74_V9-v1/MINIAODSIM
/SMS-T1qqqq_mGluino-600_mLSP-500to575_TuneCUETP8M1_13TeV-madgraphMLM-pythia8/RunIISpring15FSPremix-MCRUN2_74_V9-v1/MINIAODSIM
/SMS-T1qqqq_mGluino-625_mLSP-425to525_TuneCUETP8M1_13TeV-madgraphMLM-pythia8/RunIISpring15FSPremix-MCRUN2_74_V9-v1/MINIAODSIM
/SMS-T1qqqq_mGluino-625to650_mLSP-475to550_TuneCUETP8M1_13TeV-madgraphMLM-pythia8/RunIISpring15FSPremix-MCRUN2_74_V9-v1/MINIAODSIM
/SMS-T1qqqq_mGluino-675_mLSP-500to650_TuneCUETP8M1_13TeV-madgraphMLM-pythia8/RunIISpring15FSPremix-MCRUN2_74_V9-v1/MINIAODSIM
/SMS-T1qqqq_mGluino-750to775_mLSP-450to750_TuneCUETP8M1_13TeV-madgraphMLM-pythia8/RunIISpring15FSPremix-MCRUN2_74_V9-v1/MINIAODSIM
/SMS-T1qqqq_mGluino-800to825_mLSP-1to750_TuneCUETP8M1_13TeV-madgraphMLM-pythia8/RunIISpring15FSPremix-MCRUN2_74_V9-v1/MINIAODSIM
/SMS-T1qqqq_mGluino-825to875_mLSP-400to825_TuneCUETP8M1_13TeV-madgraphMLM-pythia8/RunIISpring15FSPremix-MCRUN2_74_V9-v1/MINIAODSIM
/SMS-T1qqqq_mGluino-1000to1025_mLSP-1to1000_TuneCUETP8M1_13TeV-madgraphMLM-pythia8/RunIISpring15FSPremix-MCRUN2_74_V9-v1/MINIAODSIM
/SMS-T1qqqq_mGluino-1025to1075_mLSP-400to1050_TuneCUETP8M1_13TeV-madgraphMLM-pythia8/RunIISpring15FSPremix-MCRUN2_74_V9-v1/MINIAODSIM
/SMS-T1qqqq_mGluino-1075_mLSP-925to975_TuneCUETP8M1_13TeV-madgraphMLM-pythia8/RunIISpring15FSPremix-MCRUN2_74_V9-v1/MINIAODSIM
/SMS-T1qqqq_mGluino-1100to1125_mLSP-1to1100_TuneCUETP8M1_13TeV-madgraphMLM-pythia8/RunIISpring15FSPremix-MCRUN2_74_V9-v1/MINIAODSIM
/SMS-T1qqqq_mGluino-1125to1175_mLSP-925to1125_TuneCUETP8M1_13TeV-madgraphMLM-pythia8/RunIISpring15FSPremix-MCRUN2_74_V9-v1/MINIAODSIM
/SMS-T1qqqq_mGluino-1225to1250_mLSP-1to1225_TuneCUETP8M1_13TeV-madgraphMLM-pythia8/RunIISpring15FSPremix-MCRUN2_74_V9-v1/MINIAODSIM
/SMS-T1qqqq_mGluino-1250to1275_mLSP-550to1250_TuneCUETP8M1_13TeV-madgraphMLM-pythia8/RunIISpring15FSPremix-MCRUN2_74_V9-v1/MINIAODSIM
/SMS-T1qqqq_mGluino-1300to1325_mLSP-1to1275_TuneCUETP8M1_13TeV-madgraphMLM-pythia8/RunIISpring15FSPremix-MCRUN2_74_V9-v1/MINIAODSIM
/SMS-T1qqqq_mGluino-1325to1350_mLSP-1to1275_TuneCUETP8M1_13TeV-madgraphMLM-pythia8/RunIISpring15FSPremix-MCRUN2_74_V9-v1/MINIAODSIM
/SMS-T1qqqq_mGluino-1400to1450_mLSP-1to1275_TuneCUETP8M1_13TeV-madgraphMLM-pythia8/RunIISpring15FSPremix-MCRUN2_74_V9-v1/MINIAODSIM
/SMS-T1qqqq_mGluino-1450to1500_mLSP-1to1275_TuneCUETP8M1_13TeV-madgraphMLM-pythia8/RunIISpring15FSPremix-MCRUN2_74_V9-v1/MINIAODSIM
/SMS-T1qqqq_mGluino-1500to1550_mLSP-1to1250_TuneCUETP8M1_13TeV-madgraphMLM-pythia8/RunIISpring15FSPremix-MCRUN2_74_V9-v1/MINIAODSIM
/SMS-T1qqqq_mGluino-1550_mLSP-950_TuneCUETP8M1_13TeV-madgraphMLM-pythia8/RunIISpring15FSPremix-MCRUN2_74_V9-v1/MINIAODSIM
/SMS-T1qqqq_mGluino-1600to1650_mLSP-1to1250_TuneCUETP8M1_13TeV-madgraphMLM-pythia8/RunIISpring15FSPremix-MCRUN2_74_V9-v1/MINIAODSIM
/SMS-T1qqqq_mGluino-1650to1750_mLSP-1to1250_TuneCUETP8M1_13TeV-madgraphMLM-pythia8/RunIISpring15FSPremix-MCRUN2_74_V9-v1/MINIAODSIM
/SMS-T1qqqq_mGluino-1750_mLSP-50to1250_TuneCUETP8M1_13TeV-madgraphMLM-pythia8/RunIISpring15FSPremix-MCRUN2_74_V9-v1/MINIAODSIM
/SMS-T1qqqq_mGluino-1850to1950_mLSP-1to1250_TuneCUETP8M1_13TeV-madgraphMLM-pythia8/RunIISpring15FSPremix-MCRUN2_74_V9-v1/MINIAODSIM
/SMS-T1qqqq_mGluino-1950to2000_mLSP-1to1250_TuneCUETP8M1_13TeV-madgraphMLM-pythia8/RunIISpring15FSPremix-MCRUN2_74_V9-v1/MINIAODSIM
/SMS-T1qqqq_mGluino-2000_mLSP-50to950_TuneCUETP8M1_13TeV-madgraphMLM-pythia8/RunIISpring15FSPremix-MCRUN2_74_V9-v1/MINIAODSIM

DRAFT

Table 6: Simulated signal samples: SMS T1tttt

Data set
/SMS-T1tttt_mGluino-600_mLSP-250to325_TuneCUETP8M1_13TeV-madgraphMLM-pythia8/RunIISpring15FSPremix-MCRUN2_74_V9-v1/MINIAODSIM
/SMS-T1tttt_mGluino-625_mLSP-275to375_TuneCUETP8M1_13TeV-madgraphMLM-pythia8/RunIISpring15FSPremix-MCRUN2_74_V9-v1/MINIAODSIM
/SMS-T1tttt_mGluino-625to650_mLSP-200to400_TuneCUETP8M1_13TeV-madgraphMLM-pythia8/RunIISpring15FSPremix-MCRUN2_74_V9-v1/MINIAODSIM
/SMS-T1tttt_mGluino-650to675_mLSP-250to425_TuneCUETP8M1_13TeV-madgraphMLM-pythia8/RunIISpring15FSPremix-MCRUN2_74_V9-v1/MINIAODSIM
/SMS-T1tttt_mGluino-675_mLSP-325to450_TuneCUETP8M1_13TeV-madgraphMLM-pythia8/RunIISpring15FSPremix-MCRUN2_74_V9-v1/MINIAODSIM
/SMS-T1tttt_mGluino-700_mLSP-1to450_TuneCUETP8M1_13TeV-madgraphMLM-pythia8/RunIISpring15FSPremix-MCRUN2_74_V9-v1/MINIAODSIM
/SMS-T1tttt_mGluino-700to750_mLSP-200to500_TuneCUETP8M1_13TeV-madgraphMLM-pythia8/RunIISpring15FSPremix-MCRUN2_74_V9-v1/MINIAODSIM
/SMS-T1tttt_mGluino-750to775_mLSP-350to525_TuneCUETP8M1_13TeV-madgraphMLM-pythia8/RunIISpring15FSPremix-MCRUN2_74_V9-v1/MINIAODSIM
/SMS-T1tttt_mGluino-775_mLSP-475to550_TuneCUETP8M1_13TeV-madgraphMLM-pythia8/RunIISpring15FSPremix-MCRUN2_74_V9-v1/MINIAODSIM
/SMS-T1tttt_mGluino-800to825_mLSP-1to575_TuneCUETP8M1_13TeV-madgraphMLM-pythia8/RunIISpring15FSPremix-MCRUN2_74_V9-v1/MINIAODSIM
/SMS-T1tttt_mGluino-825to850_mLSP-200to600_TuneCUETP8M1_13TeV-madgraphMLM-pythia8/RunIISpring15FSPremix-MCRUN2_74_V9-v1/MINIAODSIM
/SMS-T1tttt_mGluino-850to875_mLSP-450to625_TuneCUETP8M1_13TeV-madgraphMLM-pythia8/RunIISpring15FSPremix-MCRUN2_74_V9-v1/MINIAODSIM
/SMS-T1tttt_mGluino-875to900_mLSP-1to650_TuneCUETP8M1_13TeV-madgraphMLM-pythia8/RunIISpring15FSPremix-MCRUN2_74_V9-v1/MINIAODSIM
/SMS-T1tttt_mGluino-950to975_mLSP-350to725_TuneCUETP8M1_13TeV-madgraphMLM-pythia8/RunIISpring15FSPremix-MCRUN2_74_V9-v1/MINIAODSIM
/SMS-T1tttt_mGluino-975_mLSP-600to750_TuneCUETP8M1_13TeV-madgraphMLM-pythia8/RunIISpring15FSPremix-MCRUN2_74_V9-v1/MINIAODSIM
/SMS-T1tttt_mGluino-1000to1050_mLSP-1to800_TuneCUETP8M1_13TeV-madgraphMLM-pythia8/RunIISpring15FSPremix-MCRUN2_74_V9-v1/MINIAODSIM
/SMS-T1tttt_mGluino-1050_mLSP-50to775_TuneCUETP8M1_13TeV-madgraphMLM-pythia8/RunIISpring15FSPremix-MCRUN2_74_V9-v1/MINIAODSIM
/SMS-T1tttt_mGluino-1100_mLSP-1to775_TuneCUETP8M1_13TeV-madgraphMLM-pythia8/RunIISpring15FSPremix-MCRUN2_74_V9-v1/MINIAODSIM
/SMS-T1tttt_mGluino-1100to1125_mLSP-700to900_TuneCUETP8M1_13TeV-madgraphMLM-pythia8/RunIISpring15FSPremix-MCRUN2_74_V9-v1/MINIAODSIM
/SMS-T1tttt_mGluino-1150_mLSP-1to800_TuneCUETP8M1_13TeV-madgraphMLM-pythia8/RunIISpring15FSPremix-MCRUN2_74_V9-v1/MINIAODSIM
/SMS-T1tttt_mGluino-1150to1175_mLSP-750to925_TuneCUETP8M1_13TeV-madgraphMLM-pythia8/RunIISpring15FSPremix-MCRUN2_74_V9-v1/MINIAODSIM
/SMS-T1tttt_mGluino-1175_mLSP-950_TuneCUETP8M1_13TeV-madgraphMLM-pythia8/RunIISpring15FSPremix-MCRUN2_74_V9-v1/MINIAODSIM
/SMS-T1tttt_mGluino-1200_mLSP-1to825_TuneCUETP8M1_13TeV-madgraphMLM-pythia8/RunIISpring15FSPremix-MCRUN2_74_V9-v1/MINIAODSIM
/SMS-T1tttt_mGluino-1200to1225_mLSP-800to1000_TuneCUETP8M1_13TeV-madgraphMLM-pythia8/RunIISpring15FSPremix-MCRUN2_74_V9-v1/MINIAODSIM
/SMS-T1tttt_mGluino-1250to1275_mLSP-700to1050_TuneCUETP8M1_13TeV-madgraphMLM-pythia8/RunIISpring15FSPremix-MCRUN2_74_V9-v1/MINIAODSIM
/SMS-T1tttt_mGluino-1275_mLSP-900to975_TuneCUETP8M1_13TeV-madgraphMLM-pythia8/RunIISpring15FSPremix-MCRUN2_74_V9-v1/MINIAODSIM
/SMS-T1tttt_mGluino-1300_mLSP-1to1075_TuneCUETP8M1_13TeV-madgraphMLM-pythia8/RunIISpring15FSPremix-MCRUN2_74_V9-v1/MINIAODSIM
/SMS-T1tttt_mGluino-1300to1325_mLSP-700to1100_TuneCUETP8M1_13TeV-madgraphMLM-pythia8/RunIISpring15FSPremix-MCRUN2_74_V9-v1/MINIAODSIM
/SMS-T1tttt_mGluino-1350to1375_mLSP-50to1025_TuneCUETP8M1_13TeV-madgraphMLM-pythia8/RunIISpring15FSPremix-MCRUN2_74_V9-v1/MINIAODSIM
/SMS-T1tttt_mGluino-1400_mLSP-1to1175_TuneCUETP8M1_13TeV-madgraphMLM-pythia8/RunIISpring15FSPremix-MCRUN2_74_V9-v1/MINIAODSIM
/SMS-T1tttt_mGluino-1400to1425_mLSP-50to1100_TuneCUETP8M1_13TeV-madgraphMLM-pythia8/RunIISpring15FSPremix-MCRUN2_74_V9-v1/MINIAODSIM
/SMS-T1tttt_mGluino-1425to1450_mLSP-1to1200_TuneCUETP8M1_13TeV-madgraphMLM-pythia8/RunIISpring15FSPremix-MCRUN2_74_V9-v1/MINIAODSIM
/SMS-T1tttt_mGluino-1450to1475_mLSP-50to1075_TuneCUETP8M1_13TeV-madgraphMLM-pythia8/RunIISpring15FSPremix-MCRUN2_74_V9-v1/MINIAODSIM
/SMS-T1tttt_mGluino-1475to1500_mLSP-1to1250_TuneCUETP8M1_13TeV-madgraphMLM-pythia8/RunIISpring15FSPremix-MCRUN2_74_V9-v1/MINIAODSIM
/SMS-T1tttt_mGluino-1500to1525_mLSP-50to1125_TuneCUETP8M1_13TeV-madgraphMLM-pythia8/RunIISpring15FSPremix-MCRUN2_74_V9-v1/MINIAODSIM
/SMS-T1tttt_mGluino-1525to1550_mLSP-1to1300_TuneCUETP8M1_13TeV-madgraphMLM-pythia8/RunIISpring15FSPremix-MCRUN2_74_V9-v1/MINIAODSIM
/SMS-T1tttt_mGluino-1600to1650_mLSP-1to1350_TuneCUETP8M1_13TeV-madgraphMLM-pythia8/RunIISpring15FSPremix-MCRUN2_74_V9-v1/MINIAODSIM
/SMS-T1tttt_mGluino-1650to1700_mLSP-1to1400_TuneCUETP8M1_13TeV-madgraphMLM-pythia8/RunIISpring15FSPremix-MCRUN2_74_V9-v1/MINIAODSIM
/SMS-T1tttt_mGluino-1700to1750_mLSP-1to1450_TuneCUETP8M1_13TeV-madgraphMLM-pythia8/RunIISpring15FSPremix-MCRUN2_74_V9-v1/MINIAODSIM
/SMS-T1tttt_mGluino-1800to1850_mLSP-1to1450_TuneCUETP8M1_13TeV-madgraphMLM-pythia8/RunIISpring15FSPremix-MCRUN2_74_V9-v1/MINIAODSIM
/SMS-T1tttt_mGluino-1850to1900_mLSP-1to1450_TuneCUETP8M1_13TeV-madgraphMLM-pythia8/RunIISpring15FSPremix-MCRUN2_74_V9-v1/MINIAODSIM
/SMS-T1tttt_mGluino-1900to1950_mLSP-0to1450_TuneCUETP8M1_13TeV-madgraphMLM-pythia8/RunIISpring15FSPremix-MCRUN2_74_V9-v1/MINIAODSIM
/SMS-T1tttt_mGluino-1950_mLSP-700to950_TuneCUETP8M1_13TeV-madgraphMLM-pythia8/RunIISpring15FSPremix-MCRUN2_74_V9-v1/MINIAODSIM

DRAFT

Table 7: Simulated signal samples: SMS T1bbbb

Data set
/SMS-T1bbbb_mGlu-1050-1075_mLSP-850to975-850to925-1000to1050_TuneCUETP8M1_13TeV-madgraph-pythia8/RunIISpring15FSPremix-MCRUN2_74_V9-v1/MINIAODSIM
/SMS-T1bbbb_mGlu-1250-1275_mLSP-400to950-1175to1200-1050to1175_TuneCUETP8M1_13TeV-madgraph-pythia8/RunIISpring15FSPremix-MCRUN2_74_V9-v1/MINIAODSIM
/SMS-T1bbbb_mGluino-600_mLSP-1to300_TuneCUETP8M1_13TeV-madgraphMLM-pythia8/RunIISpring15FSPremix-MCRUN2_74_V9-v1/MINIAODSIM
/SMS-T1bbbb_mGluino-600_mLSP-400to475_TuneCUETP8M1_13TeV-madgraphMLM-pythia8/RunIISpring15FSPremix-MCRUN2_74_V9-v1/MINIAODSIM
/SMS-T1bbbb_mGluino-600_mLSP-500to575_TuneCUETP8M1_13TeV-madgraphMLM-pythia8/RunIISpring15FSPremix-MCRUN2_74_V9-v1/MINIAODSIM
/SMS-T1bbbb_mGluino-625-650_mLSP-525to600-400to450_TuneCUETP8M1_13TeV-madgraphMLM-pythia8/RunIISpring15FSPremix-MCRUN2_74_V9-v1/MINIAODSIM
/SMS-T1bbbb_mGluino-625_mLSP-400to500_TuneCUETP8M1_13TeV-madgraphMLM-pythia8/RunIISpring15FSPremix-MCRUN2_74_V9-v1/MINIAODSIM
/SMS-T1bbbb_mGluino-650_mLSP-475to625_TuneCUETP8M1_13TeV-madgraphMLM-pythia8/RunIISpring15FSPremix-MCRUN2_74_V9-v1/MINIAODSIM
/SMS-T1bbbb_mGluino-675_mLSP-450to650_TuneCUETP8M1_13TeV-madgraphMLM-pythia8/RunIISpring15FSPremix-MCRUN2_74_V9-v1/MINIAODSIM
/SMS-T1bbbb_mGluino-700-725-750_mLSP-625to675-500to700-400_TuneCUETP8M1_13TeV-madgraphMLM-pythia8/RunIISpring15FSPremix-MCRUN2_74_V9-v1/MINIAODSIM
/SMS-T1bbbb_mGluino-700_mLSP-1to600_TuneCUETP8M1_13TeV-madgraphMLM-pythia8/RunIISpring15FSPremix-MCRUN2_74_V9-v1/MINIAODSIM
/SMS-T1bbbb_mGluino-750-775_mLSP-400to725-550to600_TuneCUETP8M1_13TeV-madgraphMLM-pythia8/RunIISpring15FSPremix-MCRUN2_74_V9-v1/MINIAODSIM
/SMS-T1bbbb_mGluino-775_mLSP-625to750_TuneCUETP8M1_13TeV-madgraphMLM-pythia8/RunIISpring15FSPremix-MCRUN2_74_V9-v1/MINIAODSIM
/SMS-T1bbbb_mGluino-800-825_mLSP-1to775-600_TuneCUETP8M1_13TeV-madgraphMLM-pythia8/RunIISpring15FSPremix-MCRUN2_74_V9-v1/MINIAODSIM
/SMS-T1bbbb_mGluino-825-850_mLSP-625to800-400to700_TuneCUETP8M1_13TeV-madgraphMLM-pythia8/RunIISpring15FSPremix-MCRUN2_74_V9-v1/MINIAODSIM
/SMS-T1bbbb_mGluino-850-875_mLSP-725to825-650to825_TuneCUETP8M1_13TeV-madgraphMLM-pythia8/RunIISpring15FSPremix-MCRUN2_74_V9-v1/MINIAODSIM
/SMS-T1bbbb_mGluino-875-900-925_mLSP-850-1to875-700_TuneCUETP8M1_13TeV-madgraphMLM-pythia8/RunIISpring15FSPremix-MCRUN2_74_V9-v1/MINIAODSIM
/SMS-T1bbbb_mGluino-925-950_mLSP-725to900-400to800_TuneCUETP8M1_13TeV-madgraphMLM-pythia8/RunIISpring15FSPremix-MCRUN2_74_V9-v3/MINIAODSIM
/SMS-T1bbbb_mGluino-950-975_mLSP-825to925-750to925_TuneCUETP8M1_13TeV-madgraphMLM-pythia8/RunIISpring15FSPremix-MCRUN2_74_V9-v1/MINIAODSIM
/SMS-T1bbbb_mGluino-975_mLSP-950_TuneCUETP8M1_13TeV-madgraphMLM-pythia8/RunIISpring15FSPremix-MCRUN2_74_V9-v1/MINIAODSIM
/SMS-T1bbbb_mGluino-1000-1025_mLSP-1to975-1000_TuneCUETP8M1_13TeV-madgraphMLM-pythia8/RunIISpring15FSPremix-MCRUN2_74_V9-v1/MINIAODSIM
/SMS-T1bbbb_mGluino-1075_mLSP-950to975_TuneCUETP8M1_13TeV-madgraphMLM-pythia8/RunIISpring15FSPremix-MCRUN2_74_V9-v1/MINIAODSIM
/SMS-T1bbbb_mGluino-1100_mLSP-1to1075_TuneCUETP8M1_13TeV-madgraphMLM-pythia8/RunIISpring15FSPremix-MCRUN2_74_V9-v1/MINIAODSIM
/SMS-T1bbbb_mGluino-1125-1150_mLSP-900to1100-1000to1075_TuneCUETP8M1_13TeV-madgraphMLM-pythia8/RunIISpring15FSPremix-MCRUN2_74_V9-v1/MINIAODSIM
/SMS-T1bbbb_mGluino-1150_mLSP-400to975-1100to1125_TuneCUETP8M1_13TeV-madgraphMLM-pythia8/RunIISpring15FSPremix-MCRUN2_74_V9-v1/MINIAODSIM
/SMS-T1bbbb_mGluino-1175_mLSP-950to1150_TuneCUETP8M1_13TeV-madgraphMLM-pythia8/RunIISpring15FSPremix-MCRUN2_74_V9-v1/MINIAODSIM
/SMS-T1bbbb_mGluino-1200_mLSP-1to1175_TuneCUETP8M1_13TeV-madgraphMLM-pythia8/RunIISpring15FSPremix-MCRUN2_74_V9-v1/MINIAODSIM
/SMS-T1bbbb_mGluino-1225-1250_mLSP-1000to1175-1000to1150_TuneCUETP8M1_13TeV-madgraphMLM-pythia8/RunIISpring15FSPremix-MCRUN2_74_V9-v1/MINIAODSIM
/SMS-T1bbbb_mGluino-1300_mLSP-1to1250_TuneCUETP8M1_13TeV-madgraphMLM-pythia8/RunIISpring15FSPremix-MCRUN2_74_V9-v1/MINIAODSIM
/SMS-T1bbbb_mGluino-1325-1350_mLSP-1100to1175-1000to1300_TuneCUETP8M1_13TeV-madgraphMLM-pythia8/RunIISpring15FSPremix-MCRUN2_74_V9-v1/MINIAODSIM
/SMS-T1bbbb_mGluino-1350-1375_mLSP-1to950-1150to1175_TuneCUETP8M1_13TeV-madgraphMLM-pythia8/RunIISpring15FSPremix-MCRUN2_74_V9-v1/MINIAODSIM
/SMS-T1bbbb_mGluino-1400-1450_mLSP-1to1350-1to200_TuneCUETP8M1_13TeV-madgraphMLM-pythia8/RunIISpring15FSPremix-MCRUN2_74_V9-v1/MINIAODSIM
/SMS-T1bbbb_mGluino-1450-1500_mLSP-250to1400-1350to1450_TuneCUETP8M1_13TeV-madgraphMLM-pythia8/RunIISpring15FSPremix-MCRUN2_74_V9-v1/MINIAODSIM
/SMS-T1bbbb_mGluino-1500-1550_mLSP-1to1300-1000to1300_TuneCUETP8M1_13TeV-madgraphMLM-pythia8/RunIISpring15FSPremix-MCRUN2_74_V9-v1/MINIAODSIM
/SMS-T1bbbb_mGluino-1550_mLSP-1to950-1350to1450_TuneCUETP8M1_13TeV-madgraphMLM-pythia8/RunIISpring15FSPremix-MCRUN2_74_V9-v1/MINIAODSIM
/SMS-T1bbbb_mGluino-1600_mLSP-1to1450_TuneCUETP8M1_13TeV-madgraphMLM-pythia8/RunIISpring15FSPremix-MCRUN2_74_V9-v1/MINIAODSIM
/SMS-T1bbbb_mGluino-1650-1700_mLSP-350to1450-1to650_TuneCUETP8M1_13TeV-madgraphMLM-pythia8/RunIISpring15FSPremix-MCRUN2_74_V9-v2/MINIAODSIM
/SMS-T1bbbb_mGluino-1700-1750_mLSP-700to1450-1to650_TuneCUETP8M1_13TeV-madgraphMLM-pythia8/RunIISpring15FSPremix-MCRUN2_74_V9-v1/MINIAODSIM
/SMS-T1bbbb_mGluino-1750_mLSP-700to1450_TuneCUETP8M1_13TeV-madgraphMLM-pythia8/RunIISpring15FSPremix-MCRUN2_74_V9-v1/MINIAODSIM
/SMS-T1bbbb_mGluino-1800-1850_mLSP-1to1450-1to450_TuneCUETP8M1_13TeV-madgraphMLM-pythia8/RunIISpring15FSPremix-MCRUN2_74_V9-v1/MINIAODSIM
/SMS-T1bbbb_mGluino-1850-1900_mLSP-500to1450-1to950_TuneCUETP8M1_13TeV-madgraphMLM-pythia8/RunIISpring15FSPremix-MCRUN2_74_V9-v1/MINIAODSIM
/SMS-T1bbbb_mGluino-1900-1950_mLSP-1000to1450-1to1450_TuneCUETP8M1_13TeV-madgraphMLM-pythia8/RunIISpring15FSPremix-MCRUN2_74_V9-v1/MINIAODSIM
/SMS-T1bbbb_mGluino-2000_mLSP-1to1450_TuneCUETP8M1_13TeV-madgraphMLM-pythia8/RunIISpring15FSPremix-MCRUN2_74_V9-v1/MINIAODSIM

DRAFT

Table 8: Simulated signal samples: DM Vector

Data set
/DMV_NNPDF30_Vector_Mchi-10_Mchi-1_gSM-0p25_gDM-1p0_13TeV-powheg/RunIISpring15DR74-Asympt25ns_MCRUN2_74_V9-v1/MINIAODSIM
/DMV_NNPDF30_Vector_Mphi-10_Mchi-1_gSM-1p0_gDM-1p0_13TeV-powheg/RunIISpring15DR74-Asympt25ns_MCRUN2_74_V9-v1/MINIAODSIM
/DMV_NNPDF30_Vector_Mchi-10_Mchi-10_gSM-0p25_gDM-1p0_13TeV-powheg/RunIISpring15DR74-Asympt25ns_MCRUN2_74_V9-v1/MINIAODSIM
/DMV_NNPDF30_Vector_Mphi-10_Mchi-10_gSM-1p0_gDM-1p0_13TeV-powheg/RunIISpring15DR74-Asympt25ns_MCRUN2_74_V9-v1/MINIAODSIM
/DMV_NNPDF30_Vector_Mchi-10_Mchi-50_gSM-0p25_gDM-1p0_13TeV-powheg/RunIISpring15DR74-Asympt25ns_MCRUN2_74_V9-v1/MINIAODSIM
/DMV_NNPDF30_Vector_Mchi-10_Mchi-100_gSM-0p25_gDM-1p0_13TeV-powheg/RunIISpring15DR74-Asympt25ns_MCRUN2_74_V9-v1/MINIAODSIM
/DMV_NNPDF30_Vector_Mchi-10_Mchi-150_gSM-0p25_gDM-1p0_13TeV-powheg/RunIISpring15DR74-Asympt25ns_MCRUN2_74_V9-v1/MINIAODSIM
/DMV_NNPDF30_Vector_Mchi-10_Mchi-500_gSM-0p25_gDM-1p0_13TeV-powheg/RunIISpring15DR74-Asympt25ns_MCRUN2_74_V9-v1/MINIAODSIM
/DMV_NNPDF30_Vector_Mchi-20_Mchi-1_gSM-0p25_gDM-1p0_13TeV-powheg/RunIISpring15DR74-Asympt25ns_MCRUN2_74_V9-v1/MINIAODSIM
/DMV_NNPDF30_Vector_Mphi-20_Mchi-1_gSM-1p0_gDM-1p0_13TeV-powheg/RunIISpring15DR74-Asympt25ns_MCRUN2_74_V9-v1/MINIAODSIM
/DMV_NNPDF30_Vector_Mphi-50_Mchi-1_gSM-1p0_gDM-1p0_13TeV-powheg/RunIISpring15DR74-Asympt25ns_MCRUN2_74_V9-v1/MINIAODSIM
/DMV_NNPDF30_Vector_Mphi-50_Mchi-10_gSM-1p0_gDM-1p0_13TeV-powheg/RunIISpring15DR74-Asympt25ns_MCRUN2_74_V9-v1/MINIAODSIM
/DMV_NNPDF30_Vector_Mchi-50_Mchi-50_gSM-0p25_gDM-1p0_13TeV-powheg/RunIISpring15DR74-Asympt25ns_MCRUN2_74_V9-v1/MINIAODSIM
/DMV_NNPDF30_Vector_Mphi-100_Mchi-1_gSM-0p25_gDM-1p0_13TeV-powheg/RunIISpring15DR74-Asympt25ns_MCRUN2_74_V9-v1/MINIAODSIM
/DMV_NNPDF30_Vector_Mphi-100_Mchi-10_gSM-0p25_gDM-1p0_13TeV-powheg/RunIISpring15DR74-Asympt25ns_MCRUN2_74_V9-v1/MINIAODSIM
/DMV_NNPDF30_Vector_Mphi-100_Mchi-10_gSM-1p0_gDM-1p0_13TeV-powheg/RunIISpring15DR74-Asympt25ns_MCRUN2_74_V9-v1/MINIAODSIM
/DMV_NNPDF30_Vector_Mphi-100_Mchi-100_gSM-0p25_gDM-1p0_13TeV-powheg/RunIISpring15DR74-Asympt25ns_MCRUN2_74_V9-v1/MINIAODSIM
/DMV_NNPDF30_Vector_Mphi-100_Mchi-100_gSM-1p0_gDM-1p0_13TeV-powheg/RunIISpring15DR74-Asympt25ns_MCRUN2_74_V9-v1/MINIAODSIM
/DMV_NNPDF30_Vector_Mphi-200_Mchi-1_gSM-0p25_gDM-1p0_13TeV-powheg/RunIISpring15DR74-Asympt25ns_MCRUN2_74_V9-v1/MINIAODSIM
/DMV_NNPDF30_Vector_Mphi-200_Mchi-1_gSM-1p0_gDM-1p0_13TeV-powheg/RunIISpring15DR74-Asympt25ns_MCRUN2_74_V9-v1/MINIAODSIM
/DMV_NNPDF30_Vector_Mphi-200_Mchi-10_gSM-0p25_gDM-1p0_13TeV-powheg/RunIISpring15DR74-Asympt25ns_MCRUN2_74_V9-v1/MINIAODSIM
/DMV_NNPDF30_Vector_Mphi-200_Mchi-10_gSM-1p0_gDM-1p0_13TeV-powheg/RunIISpring15DR74-Asympt25ns_MCRUN2_74_V9-v1/MINIAODSIM
/DMV_NNPDF30_Vector_Mphi-200_Mchi-50_gSM-0p25_gDM-1p0_13TeV-powheg/RunIISpring15DR74-Asympt25ns_MCRUN2_74_V9-v1/MINIAODSIM
/DMV_NNPDF30_Vector_Mphi-200_Mchi-50_gSM-1p0_gDM-1p0_13TeV-powheg/RunIISpring15DR74-Asympt25ns_MCRUN2_74_V9-v1/MINIAODSIM
/DMV_NNPDF30_Vector_Mphi-200_Mchi-100_gSM-1p0_gDM-1p0_13TeV-powheg/RunIISpring15DR74-Asympt25ns_MCRUN2_74_V9-v1/MINIAODSIM
/DMV_NNPDF30_Vector_Mphi-200_Mchi-150_gSM-0p25_gDM-1p0_13TeV-powheg/RunIISpring15DR74-Asympt25ns_MCRUN2_74_V9-v1/MINIAODSIM
/DMV_NNPDF30_Vector_Mphi-200_Mchi-150_gSM-1p0_gDM-1p0_13TeV-powheg/RunIISpring15DR74-Asympt25ns_MCRUN2_74_V9-v1/MINIAODSIM
/DMV_NNPDF30_Vector_Mphi-300_Mchi-1_gSM-0p25_gDM-1p0_13TeV-powheg/RunIISpring15DR74-Asympt25ns_MCRUN2_74_V9-v1/MINIAODSIM
/DMV_NNPDF30_Vector_Mphi-300_Mchi-10_gSM-1p0_gDM-1p0_13TeV-powheg/RunIISpring15DR74-Asympt25ns_MCRUN2_74_V9-v1/MINIAODSIM
/DMV_NNPDF30_Vector_Mphi-300_Mchi-50_gSM-0p25_gDM-1p0_13TeV-powheg/RunIISpring15DR74-Asympt25ns_MCRUN2_74_V9-v1/MINIAODSIM
/DMV_NNPDF30_Vector_Mphi-300_Mchi-50_gSM-1p0_gDM-1p0_13TeV-powheg/RunIISpring15DR74-Asympt25ns_MCRUN2_74_V9-v1/MINIAODSIM
/DMV_NNPDF30_Vector_Mphi-300_Mchi-100_gSM-0p25_gDM-1p0_13TeV-powheg/RunIISpring15DR74-Asympt25ns_MCRUN2_74_V9-v1/MINIAODSIM
/DMV_NNPDF30_Vector_Mphi-300_Mchi-100_gSM-1p0_gDM-1p0_13TeV-powheg/RunIISpring15DR74-Asympt25ns_MCRUN2_74_V9-v1/MINIAODSIM
/DMV_NNPDF30_Vector_Mphi-300_Mchi-150_gSM-0p25_gDM-1p0_13TeV-powheg/RunIISpring15DR74-Asympt25ns_MCRUN2_74_V9-v1/MINIAODSIM
/DMV_NNPDF30_Vector_Mphi-300_Mchi-150_gSM-1p0_gDM-1p0_13TeV-powheg/RunIISpring15DR74-Asympt25ns_MCRUN2_74_V9-v1/MINIAODSIM
/DMV_NNPDF30_Vector_Mphi-500_Mchi-1_gSM-0p25_gDM-1p0_13TeV-powheg/RunIISpring15DR74-Asympt25ns_MCRUN2_74_V9-v1/MINIAODSIM
/DMV_NNPDF30_Vector_Mphi-500_Mchi-1_gSM-1p0_gDM-1p0_13TeV-powheg/RunIISpring15DR74-Asympt25ns_MCRUN2_74_V9-v1/MINIAODSIM
/DMV_NNPDF30_Vector_Mphi-500_Mchi-10_gSM-0p25_gDM-1p0_13TeV-powheg/RunIISpring15DR74-Asympt25ns_MCRUN2_74_V9-v1/MINIAODSIM
/DMV_NNPDF30_Vector_Mphi-500_Mchi-10_gSM-1p0_gDM-1p0_13TeV-powheg/RunIISpring15DR74-Asympt25ns_MCRUN2_74_V9-v1/MINIAODSIM
/DMV_NNPDF30_Vector_Mphi-500_Mchi-50_gSM-1p0_gDM-1p0_13TeV-powheg/RunIISpring15DR74-Asympt25ns_MCRUN2_74_V9-v1/MINIAODSIM
/DMV_NNPDF30_Vector_Mphi-500_Mchi-100_gSM-0p25_gDM-1p0_13TeV-powheg/RunIISpring15DR74-Asympt25ns_MCRUN2_74_V9-v1/MINIAODSIM
/DMV_NNPDF30_Vector_Mphi-500_Mchi-100_gSM-1p0_gDM-1p0_13TeV-powheg/RunIISpring15DR74-Asympt25ns_MCRUN2_74_V9-v1/MINIAODSIM
/DMV_NNPDF30_Vector_Mphi-500_Mchi-150_gSM-1p0_gDM-1p0_13TeV-powheg/RunIISpring15DR74-Asympt25ns_MCRUN2_74_V9-v1/MINIAODSIM
/DMV_NNPDF30_Vector_Mphi-500_Mchi-500_gSM-1p0_gDM-1p0_13TeV-powheg/RunIISpring15DR74-Asympt25ns_MCRUN2_74_V9-v1/MINIAODSIM
/DMV_NNPDF30_Vector_Mphi-1000_Mchi-50_gSM-0p25_gDM-1p0_13TeV-powheg/RunIISpring15DR74-Asympt25ns_MCRUN2_74_V9-v1/MINIAODSIM
/DMV_NNPDF30_Vector_Mphi-1000_Mchi-100_gSM-1p0_gDM-1p0_13TeV-powheg/RunIISpring15DR74-Asympt25ns_MCRUN2_74_V9-v1/MINIAODSIM
/DMV_NNPDF30_Vector_Mphi-1000_Mchi-150_gSM-1p0_gDM-1p0_13TeV-powheg/RunIISpring15DR74-Asympt25ns_MCRUN2_74_V9-v1/MINIAODSIM
/DMV_NNPDF30_Vector_Mphi-1000_Mchi-500_gSM-0p25_gDM-1p0_13TeV-powheg/RunIISpring15DR74-Asympt25ns_MCRUN2_74_V9-v1/MINIAODSIM
/DMV_NNPDF30_Vector_Mphi-1000_Mchi-1000_gSM-0p25_gDM-1p0_13TeV-powheg/RunIISpring15DR74-Asympt25ns_MCRUN2_74_V9-v1/MINIAODSIM
/DMV_NNPDF30_Vector_Mphi-1000_Mchi-1000_gSM-1p0_gDM-1p0_13TeV-powheg/RunIISpring15DR74-Asympt25ns_MCRUN2_74_V9-v1/MINIAODSIM
/DMV_NNPDF30_Vector_Mphi-2000_Mchi-1_gSM-0p25_gDM-1p0_13TeV-powheg/RunIISpring15DR74-Asympt25ns_MCRUN2_74_V9-v1/MINIAODSIM
/DMV_NNPDF30_Vector_Mphi-2000_Mchi-10_gSM-0p25_gDM-1p0_13TeV-powheg/RunIISpring15DR74-Asympt25ns_MCRUN2_74_V9-v1/MINIAODSIM
/DMV_NNPDF30_Vector_Mphi-2000_Mchi-100_gSM-1p0_gDM-1p0_13TeV-powheg/RunIISpring15DR74-Asympt25ns_MCRUN2_74_V9-v1/MINIAODSIM
/DMV_NNPDF30_Vector_Mphi-10000_Mchi-50_gSM-0p25_gDM-1p0_13TeV-powheg/RunIISpring15DR74-Asympt25ns_MCRUN2_74_V9-v1/MINIAODSIM
/DMV_NNPDF30_Vector_Mphi-10000_Mchi-50_gSM-1p0_gDM-1p0_13TeV-powheg/RunIISpring15DR74-Asympt25ns_MCRUN2_74_V9-v1/MINIAODSIM
/DMV_NNPDF30_Vector_Mphi-10000_Mchi-100_gSM-1p0_gDM-1p0_13TeV-powheg/RunIISpring15DR74-Asympt25ns_MCRUN2_74_V9-v1/MINIAODSIM
/DMV_NNPDF30_Vector_Mphi-10000_Mchi-150_gSM-1p0_gDM-1p0_13TeV-powheg/RunIISpring15DR74-Asympt25ns_MCRUN2_74_V9-v1/MINIAODSIM
/DMV_NNPDF30_Vector_Mphi-10000_Mchi-500_gSM-1p0_gDM-1p0_13TeV-powheg/RunIISpring15DR74-Asympt25ns_MCRUN2_74_V9-v1/MINIAODSIM

Table 9: Simulated signal samples: DM Axial

Data set
/DMV_NNPDF30_Axial_Mchi-10_Mchi-1_gSM-0p25_gDM-1p0_13TeV-powheg/RunIISpring15DR74-Asympt25ns_MCRUN2_74_V9-v1/MINIAODSIM
/DMV_NNPDF30_Axial_Mphi-10_Mchi-1_gSM-1p0_gDM-1p0_13TeV-powheg/RunIISpring15DR74-Asympt25ns_MCRUN2_74_V9-v1/MINIAODSIM
/DMV_NNPDF30_Axial_Mchi-10_Mchi-10_gSM-0p25_gDM-1p0_13TeV-powheg/RunIISpring15DR74-Asympt25ns_MCRUN2_74_V9-v1/MINIAODSIM
/DMV_NNPDF30_Axial_Mphi-10_Mchi-10_gSM-1p0_gDM-1p0_13TeV-powheg/RunIISpring15DR74-Asympt25ns_MCRUN2_74_V9-v1/MINIAODSIM
/DMV_NNPDF30_Axial_Mchi-10_Mchi-50_gSM-0p25_gDM-1p0_13TeV-powheg/RunIISpring15DR74-Asympt25ns_MCRUN2_74_V9-v1/MINIAODSIM
/DMV_NNPDF30_Axial_Mchi-10_Mchi-100_gSM-0p25_gDM-1p0_13TeV-powheg/RunIISpring15DR74-Asympt25ns_MCRUN2_74_V9-v1/MINIAODSIM
/DMV_NNPDF30_Axial_Mchi-10_Mchi-500_gSM-0p25_gDM-1p0_13TeV-powheg/RunIISpring15DR74-Asympt25ns_MCRUN2_74_V9-v1/MINIAODSIM
/DMV_NNPDF30_Axial_Mphi-20_Mchi-1_gSM-1p0_gDM-1p0_13TeV-powheg/RunIISpring15DR74-Asympt25ns_MCRUN2_74_V9-v1/MINIAODSIM
/DMV_NNPDF30_Axial_Mchi-20_Mchi-10_gSM-0p25_gDM-1p0_13TeV-powheg/RunIISpring15DR74-Asympt25ns_MCRUN2_74_V9-v1/MINIAODSIM
/DMV_NNPDF30_Axial_Mphi-20_Mchi-10_gSM-1p0_gDM-1p0_13TeV-powheg/RunIISpring15DR74-Asympt25ns_MCRUN2_74_V9-v1/MINIAODSIM
/DMV_NNPDF30_Axial_Mchi-50_Mchi-1_gSM-0p25_gDM-1p0_13TeV-powheg/RunIISpring15DR74-Asympt25ns_MCRUN2_74_V9-v1/MINIAODSIM
/DMV_NNPDF30_Axial_Mchi-50_Mchi-10_gSM-0p25_gDM-1p0_13TeV-powheg/RunIISpring15DR74-Asympt25ns_MCRUN2_74_V9-v1/MINIAODSIM
/DMV_NNPDF30_Axial_Mphi-50_Mchi-10_gSM-1p0_gDM-1p0_13TeV-powheg/RunIISpring15DR74-Asympt25ns_MCRUN2_74_V9-v1/MINIAODSIM
/DMV_NNPDF30_Axial_Mphi-50_Mchi-50_gSM-1p0_gDM-1p0_13TeV-powheg/RunIISpring15DR74-Asympt25ns_MCRUN2_74_V9-v1/MINIAODSIM
/DMV_NNPDF30_Axial_Mphi-100_Mchi-1_gSM-0p25_gDM-1p0_13TeV-powheg/RunIISpring15DR74-Asympt25ns_MCRUN2_74_V9-v1/MINIAODSIM
/DMV_NNPDF30_Axial_Mphi-100_Mchi-1_gSM-1p0_gDM-1p0_13TeV-powheg/RunIISpring15DR74-Asympt25ns_MCRUN2_74_V9-v1/MINIAODSIM
/DMV_NNPDF30_Axial_Mphi-100_Mchi-10_gSM-0p25_gDM-1p0_13TeV-powheg/RunIISpring15DR74-Asympt25ns_MCRUN2_74_V9-v1/MINIAODSIM
/DMV_NNPDF30_Axial_Mphi-100_Mchi-100_gSM-0p25_gDM-1p0_13TeV-powheg/RunIISpring15DR74-Asympt25ns_MCRUN2_74_V9-v1/MINIAODSIM
/DMV_NNPDF30_Axial_Mphi-100_Mchi-100_gSM-1p0_gDM-1p0_13TeV-powheg/RunIISpring15DR74-Asympt25ns_MCRUN2_74_V9-v1/MINIAODSIM
/DMV_NNPDF30_Axial_Mphi-200_Mchi-1_gSM-0p25_gDM-1p0_13TeV-powheg/RunIISpring15DR74-Asympt25ns_MCRUN2_74_V9-v1/MINIAODSIM
/DMV_NNPDF30_Axial_Mphi-200_Mchi-1_gSM-1p0_gDM-1p0_13TeV-powheg/RunIISpring15DR74-Asympt25ns_MCRUN2_74_V9-v1/MINIAODSIM
/DMV_NNPDF30_Axial_Mphi-200_Mchi-10_gSM-0p25_gDM-1p0_13TeV-powheg/RunIISpring15DR74-Asympt25ns_MCRUN2_74_V9-v1/MINIAODSIM
/DMV_NNPDF30_Axial_Mphi-200_Mchi-10_gSM-1p0_gDM-1p0_13TeV-powheg/RunIISpring15DR74-Asympt25ns_MCRUN2_74_V9-v1/MINIAODSIM
/DMV_NNPDF30_Axial_Mphi-200_Mchi-50_gSM-1p0_gDM-1p0_13TeV-powheg/RunIISpring15DR74-Asympt25ns_MCRUN2_74_V9-v1/MINIAODSIM
/DMV_NNPDF30_Axial_Mphi-200_Mchi-150_gSM-0p25_gDM-1p0_13TeV-powheg/RunIISpring15DR74-Asympt25ns_MCRUN2_74_V9-v1/MINIAODSIM
/DMV_NNPDF30_Axial_Mphi-300_Mchi-1_gSM-0p25_gDM-1p0_13TeV-powheg/RunIISpring15DR74-Asympt25ns_MCRUN2_74_V9-v1/MINIAODSIM
/DMV_NNPDF30_Axial_Mphi-300_Mchi-1_gSM-1p0_gDM-1p0_13TeV-powheg/RunIISpring15DR74-Asympt25ns_MCRUN2_74_V9-v1/MINIAODSIM
/DMV_NNPDF30_Axial_Mphi-300_Mchi-10_gSM-1p0_gDM-1p0_13TeV-powheg/RunIISpring15DR74-Asympt25ns_MCRUN2_74_V9-v1/MINIAODSIM
/DMV_NNPDF30_Axial_Mphi-300_Mchi-50_gSM-1p0_gDM-1p0_13TeV-powheg/RunIISpring15DR74-Asympt25ns_MCRUN2_74_V9-v1/MINIAODSIM
/DMV_NNPDF30_Axial_Mphi-300_Mchi-100_gSM-1p0_gDM-1p0_13TeV-powheg/RunIISpring15DR74-Asympt25ns_MCRUN2_74_V9-v1/MINIAODSIM
/DMV_NNPDF30_Axial_Mphi-300_Mchi-150_gSM-0p25_gDM-1p0_13TeV-powheg/RunIISpring15DR74-Asympt25ns_MCRUN2_74_V9-v1/MINIAODSIM
/DMV_NNPDF30_Axial_Mphi-300_Mchi-150_gSM-1p0_gDM-1p0_13TeV-powheg/RunIISpring15DR74-Asympt25ns_MCRUN2_74_V9-v1/MINIAODSIM
/DMV_NNPDF30_Axial_Mphi-500_Mchi-1_gSM-0p25_gDM-1p0_13TeV-powheg/RunIISpring15DR74-Asympt25ns_MCRUN2_74_V9-v1/MINIAODSIM
/DMV_NNPDF30_Axial_Mphi-500_Mchi-1_gSM-1p0_gDM-1p0_13TeV-powheg/RunIISpring15DR74-Asympt25ns_MCRUN2_74_V9-v1/MINIAODSIM
/DMV_NNPDF30_Axial_Mphi-500_Mchi-10_gSM-1p0_gDM-1p0_13TeV-powheg/RunIISpring15DR74-Asympt25ns_MCRUN2_74_V9-v1/MINIAODSIM
/DMV_NNPDF30_Axial_Mphi-500_Mchi-50_gSM-0p25_gDM-1p0_13TeV-powheg/RunIISpring15DR74-Asympt25ns_MCRUN2_74_V9-v1/MINIAODSIM
/DMV_NNPDF30_Axial_Mphi-500_Mchi-50_gSM-1p0_gDM-1p0_13TeV-powheg/RunIISpring15DR74-Asympt25ns_MCRUN2_74_V9-v1/MINIAODSIM
/DMV_NNPDF30_Axial_Mphi-500_Mchi-100_gSM-0p25_gDM-1p0_13TeV-powheg/RunIISpring15DR74-Asympt25ns_MCRUN2_74_V9-v1/MINIAODSIM
/DMV_NNPDF30_Axial_Mphi-500_Mchi-100_gSM-1p0_gDM-1p0_13TeV-powheg/RunIISpring15DR74-Asympt25ns_MCRUN2_74_V9-v1/MINIAODSIM
/DMV_NNPDF30_Axial_Mphi-500_Mchi-150_gSM-1p0_gDM-1p0_13TeV-powheg/RunIISpring15DR74-Asympt25ns_MCRUN2_74_V9-v1/MINIAODSIM
/DMV_NNPDF30_Axial_Mphi-500_Mchi-500_gSM-0p25_gDM-1p0_13TeV-powheg/RunIISpring15DR74-Asympt25ns_MCRUN2_74_V9-v1/MINIAODSIM
/DMV_NNPDF30_Axial_Mphi-500_Mchi-500_gSM-1p0_gDM-1p0_13TeV-powheg/RunIISpring15DR74-Asympt25ns_MCRUN2_74_V9-v1/MINIAODSIM
/DMV_NNPDF30_Axial_Mphi-1000_Mchi-1_gSM-1p0_gDM-1p0_13TeV-powheg/RunIISpring15DR74-Asympt25ns_MCRUN2_74_V9-v1/MINIAODSIM
/DMV_NNPDF30_Axial_Mphi-1000_Mchi-10_gSM-1p0_gDM-1p0_13TeV-powheg/RunIISpring15DR74-Asympt25ns_MCRUN2_74_V9-v1/MINIAODSIM
/DMV_NNPDF30_Axial_Mphi-1000_Mchi-50_gSM-0p25_gDM-1p0_13TeV-powheg/RunIISpring15DR74-Asympt25ns_MCRUN2_74_V9-v1/MINIAODSIM
/DMV_NNPDF30_Axial_Mphi-1000_Mchi-50_gSM-1p0_gDM-1p0_13TeV-powheg/RunIISpring15DR74-Asympt25ns_MCRUN2_74_V9-v1/MINIAODSIM
/DMV_NNPDF30_Axial_Mphi-1000_Mchi-150_gSM-0p25_gDM-1p0_13TeV-powheg/RunIISpring15DR74-Asympt25ns_MCRUN2_74_V9-v1/MINIAODSIM
/DMV_NNPDF30_Axial_Mphi-1000_Mchi-500_gSM-0p25_gDM-1p0_13TeV-powheg/RunIISpring15DR74-Asympt25ns_MCRUN2_74_V9-v1/MINIAODSIM
/DMV_NNPDF30_Axial_Mphi-2000_Mchi-1_gSM-0p25_gDM-1p0_13TeV-powheg/RunIISpring15DR74-Asympt25ns_MCRUN2_74_V9-v1/MINIAODSIM
/DMV_NNPDF30_Axial_Mphi-2000_Mchi-1_gSM-1p0_gDM-1p0_13TeV-powheg/RunIISpring15DR74-Asympt25ns_MCRUN2_74_V9-v1/MINIAODSIM
/DMV_NNPDF30_Axial_Mphi-2000_Mchi-50_gSM-0p25_gDM-1p0_13TeV-powheg/RunIISpring15DR74-Asympt25ns_MCRUN2_74_V9-v1/MINIAODSIM
/DMV_NNPDF30_Axial_Mphi-2000_Mchi-100_gSM-1p0_gDM-1p0_13TeV-powheg/RunIISpring15DR74-Asympt25ns_MCRUN2_74_V9-v1/MINIAODSIM
/DMV_NNPDF30_Axial_Mphi-2000_Mchi-150_gSM-1p0_gDM-1p0_13TeV-powheg/RunIISpring15DR74-Asympt25ns_MCRUN2_74_V9-v1/MINIAODSIM
/DMV_NNPDF30_Axial_Mphi-5000_Mchi-1_gSM-1p0_gDM-1p0_13TeV-powheg/RunIISpring15DR74-Asympt25ns_MCRUN2_74_V9-v1/MINIAODSIM
/DMV_NNPDF30_Axial_Mphi-5000_Mchi-10_gSM-1p0_gDM-1p0_13TeV-powheg/RunIISpring15DR74-Asympt25ns_MCRUN2_74_V9-v1/MINIAODSIM
/DMV_NNPDF30_Axial_Mphi-5000_Mchi-50_gSM-1p0_gDM-1p0_13TeV-powheg/RunIISpring15DR74-Asympt25ns_MCRUN2_74_V9-v1/MINIAODSIM
/DMV_NNPDF30_Axial_Mphi-5000_Mchi-100_gSM-1p0_gDM-1p0_13TeV-powheg/RunIISpring15DR74-Asympt25ns_MCRUN2_74_V9-v1/MINIAODSIM
/DMV_NNPDF30_Axial_Mphi-5000_Mchi-150_gSM-1p0_gDM-1p0_13TeV-powheg/RunIISpring15DR74-Asympt25ns_MCRUN2_74_V9-v1/MINIAODSIM
/DMV_NNPDF30_Axial_Mphi-5000_Mchi-500_gSM-1p0_gDM-1p0_13TeV-powheg/RunIISpring15DR74-Asympt25ns_MCRUN2_74_V9-v1/MINIAODSIM
/DMV_NNPDF30_Axial_Mphi-10000_Mchi-1_gSM-0p25_gDM-1p0_13TeV-powheg/RunIISpring15DR74-Asympt25ns_MCRUN2_74_V9-v1/MINIAODSIM
/DMV_NNPDF30_Axial_Mphi-10000_Mchi-1_gSM-1p0_gDM-1p0_13TeV-powheg/RunIISpring15DR74-Asympt25ns_MCRUN2_74_V9-v1/MINIAODSIM
/DMV_NNPDF30_Axial_Mphi-10000_Mchi-10_gSM-1p0_gDM-1p0_13TeV-powheg/RunIISpring15DR74-Asympt25ns_MCRUN2_74_V9-v1/MINIAODSIM
/DMV_NNPDF30_Axial_Mphi-10000_Mchi-100_gSM-0p25_gDM-1p0_13TeV-powheg/RunIISpring15DR74-Asympt25ns_MCRUN2_74_V9-v1/MINIAODSIM
/DMV_NNPDF30_Axial_Mphi-10000_Mchi-150_gSM-0p25_gDM-1p0_13TeV-powheg/RunIISpring15DR74-Asympt25ns_MCRUN2_74_V9-v1/MINIAODSIM

Table 10: Simulated signal samples: DM Scalar

Data set
/DMS_NNPDF30_Scalar_Mphi-10_Mchi-1_gSM-1p0_gDM-1p0_13TeV-powheg/RunIISpring15DR74-Asympt25ns_MCRUN2_74_V9-v1/MINIAODSIM
/DMS_NNPDF30_Scalar_Mphi-10_Mchi-10_gSM-1p0_gDM-1p0_13TeV-powheg/RunIISpring15DR74-Asympt25ns_MCRUN2_74_V9-v1/MINIAODSIM
/DMS_NNPDF30_Scalar_Mphi-20_Mchi-1_gSM-1p0_gDM-1p0_13TeV-powheg/RunIISpring15DR74-Asympt25ns_MCRUN2_74_V9-v1/MINIAODSIM
/DMS_NNPDF30_Scalar_Mphi-20_Mchi-10_gSM-1p0_gDM-1p0_13TeV-powheg/RunIISpring15DR74-Asympt25ns_MCRUN2_74_V9-v1/MINIAODSIM
/DMS_NNPDF30_Scalar_Mphi-50_Mchi-10_gSM-1p0_gDM-1p0_13TeV-powheg/RunIISpring15DR74-Asympt25ns_MCRUN2_74_V9-v1/MINIAODSIM
/DMS_NNPDF30_Scalar_Mphi-100_Mchi-1_gSM-1p0_gDM-1p0_13TeV-powheg/RunIISpring15DR74-Asympt25ns_MCRUN2_74_V9-v1/MINIAODSIM
/DMS_NNPDF30_Scalar_Mphi-100_Mchi-10_gSM-1p0_gDM-1p0_13TeV-powheg/RunIISpring15DR74-Asympt25ns_MCRUN2_74_V9-v1/MINIAODSIM
/DMS_NNPDF30_Scalar_Mphi-100_Mchi-50_gSM-1p0_gDM-1p0_13TeV-powheg/RunIISpring15DR74-Asympt25ns_MCRUN2_74_V9-v1/MINIAODSIM
/DMS_NNPDF30_Scalar_Mphi-100_Mchi-100_gSM-1p0_gDM-1p0_13TeV-powheg/RunIISpring15DR74-Asympt25ns_MCRUN2_74_V9-v1/MINIAODSIM
/DMS_NNPDF30_Scalar_Mphi-200_Mchi-1_gSM-1p0_gDM-1p0_13TeV-powheg/RunIISpring15DR74-Asympt25ns_MCRUN2_74_V9-v1/MINIAODSIM
/DMS_NNPDF30_Scalar_Mphi-200_Mchi-10_gSM-1p0_gDM-1p0_13TeV-powheg/RunIISpring15DR74-Asympt25ns_MCRUN2_74_V9-v1/MINIAODSIM
/DMS_NNPDF30_Scalar_Mphi-200_Mchi-50_gSM-1p0_gDM-1p0_13TeV-powheg/RunIISpring15DR74-Asympt25ns_MCRUN2_74_V9-v1/MINIAODSIM
/DMS_NNPDF30_Scalar_Mphi-200_Mchi-100_gSM-1p0_gDM-1p0_13TeV-powheg/RunIISpring15DR74-Asympt25ns_MCRUN2_74_V9-v1/MINIAODSIM
/DMS_NNPDF30_Scalar_Mphi-200_Mchi-150_gSM-1p0_gDM-1p0_13TeV-powheg/RunIISpring15DR74-Asympt25ns_MCRUN2_74_V9-v1/MINIAODSIM
/DMS_NNPDF30_Scalar_Mphi-300_Mchi-1_gSM-1p0_gDM-1p0_13TeV-powheg/RunIISpring15DR74-Asympt25ns_MCRUN2_74_V9-v1/MINIAODSIM
/DMS_NNPDF30_Scalar_Mphi-300_Mchi-10_gSM-1p0_gDM-1p0_13TeV-powheg/RunIISpring15DR74-Asympt25ns_MCRUN2_74_V9-v1/MINIAODSIM
/DMS_NNPDF30_Scalar_Mphi-300_Mchi-100_gSM-1p0_gDM-1p0_13TeV-powheg/RunIISpring15DR74-Asympt25ns_MCRUN2_74_V9-v1/MINIAODSIM
/DMS_NNPDF30_Scalar_Mphi-300_Mchi-150_gSM-1p0_gDM-1p0_13TeV-powheg/RunIISpring15DR74-Asympt25ns_MCRUN2_74_V9-v1/MINIAODSIM
/DMS_NNPDF30_Scalar_Mphi-500_Mchi-1_gSM-1p0_gDM-1p0_13TeV-powheg/RunIISpring15DR74-Asympt25ns_MCRUN2_74_V9-v1/MINIAODSIM
/DMS_NNPDF30_Scalar_Mphi-500_Mchi-10_gSM-1p0_gDM-1p0_13TeV-powheg/RunIISpring15DR74-Asympt25ns_MCRUN2_74_V9-v1/MINIAODSIM
/DMS_NNPDF30_Scalar_Mphi-500_Mchi-50_gSM-1p0_gDM-1p0_13TeV-powheg/RunIISpring15DR74-Asympt25ns_MCRUN2_74_V9-v1/MINIAODSIM
/DMS_NNPDF30_Scalar_Mphi-500_Mchi-150_gSM-1p0_gDM-1p0_13TeV-powheg/RunIISpring15DR74-Asympt25ns_MCRUN2_74_V9-v1/MINIAODSIM
/DMS_NNPDF30_Scalar_Mphi-500_Mchi-500_gSM-1p0_gDM-1p0_13TeV-powheg/RunIISpring15DR74-Asympt25ns_MCRUN2_74_V9-v1/MINIAODSIM
/DMS_NNPDF30_Scalar_Mphi-1000_Mchi-1_gSM-1p0_gDM-1p0_13TeV-powheg/RunIISpring15DR74-Asympt25ns_MCRUN2_74_V9-v1/MINIAODSIM
/DMS_NNPDF30_Scalar_Mphi-1000_Mchi-10_gSM-1p0_gDM-1p0_13TeV-powheg/RunIISpring15DR74-Asympt25ns_MCRUN2_74_V9-v1/MINIAODSIM
/DMS_NNPDF30_Scalar_Mphi-1000_Mchi-100_gSM-1p0_gDM-1p0_13TeV-powheg/RunIISpring15DR74-Asympt25ns_MCRUN2_74_V9-v1/MINIAODSIM
/DMS_NNPDF30_Scalar_Mphi-1000_Mchi-500_gSM-1p0_gDM-1p0_13TeV-powheg/RunIISpring15DR74-Asympt25ns_MCRUN2_74_V9-v1/MINIAODSIM
/DMS_NNPDF30_Scalar_Mphi-2000_Mchi-1_gSM-1p0_gDM-1p0_13TeV-powheg/RunIISpring15DR74-Asympt25ns_MCRUN2_74_V9-v1/MINIAODSIM
/DMS_NNPDF30_Scalar_Mphi-2000_Mchi-100_gSM-1p0_gDM-1p0_13TeV-powheg/RunIISpring15DR74-Asympt25ns_MCRUN2_74_V9-v1/MINIAODSIM
/DMS_NNPDF30_Scalar_Mphi-2000_Mchi-150_gSM-1p0_gDM-1p0_13TeV-powheg/RunIISpring15DR74-Asympt25ns_MCRUN2_74_V9-v1/MINIAODSIM
/DMS_NNPDF30_Scalar_Mphi-2000_Mchi-1000_gSM-1p0_gDM-1p0_13TeV-powheg/RunIISpring15DR74-Asympt25ns_MCRUN2_74_V9-v1/MINIAODSIM
/DMS_NNPDF30_Scalar_Mphi-5000_Mchi-10_gSM-1p0_gDM-1p0_13TeV-powheg/RunIISpring15DR74-Asympt25ns_MCRUN2_74_V9-v1/MINIAODSIM
/DMS_NNPDF30_Scalar_Mphi-5000_Mchi-50_gSM-1p0_gDM-1p0_13TeV-powheg/RunIISpring15DR74-Asympt25ns_MCRUN2_74_V9-v1/MINIAODSIM
/DMS_NNPDF30_Scalar_Mphi-5000_Mchi-100_gSM-1p0_gDM-1p0_13TeV-powheg/RunIISpring15DR74-Asympt25ns_MCRUN2_74_V9-v1/MINIAODSIM
/DMS_NNPDF30_Scalar_Mphi-5000_Mchi-150_gSM-1p0_gDM-1p0_13TeV-powheg/RunIISpring15DR74-Asympt25ns_MCRUN2_74_V9-v1/MINIAODSIM
/DMS_NNPDF30_Scalar_Mphi-5000_Mchi-500_gSM-1p0_gDM-1p0_13TeV-powheg/RunIISpring15DR74-Asympt25ns_MCRUN2_74_V9-v1/MINIAODSIM
/DMS_NNPDF30_Scalar_Mphi-5000_Mchi-1000_gSM-1p0_gDM-1p0_13TeV-powheg/RunIISpring15DR74-Asympt25ns_MCRUN2_74_V9-v1/MINIAODSIM
/DMS_NNPDF30_Scalar_Mphi-10000_Mchi-1_gSM-1p0_gDM-1p0_13TeV-powheg/RunIISpring15DR74-Asympt25ns_MCRUN2_74_V9-v1/MINIAODSIM
/DMS_NNPDF30_Scalar_Mphi-10000_Mchi-10_gSM-1p0_gDM-1p0_13TeV-powheg/RunIISpring15DR74-Asympt25ns_MCRUN2_74_V9-v1/MINIAODSIM
/DMS_NNPDF30_Scalar_Mphi-10000_Mchi-500_gSM-1p0_gDM-1p0_13TeV-powheg/RunIISpring15DR74-Asympt25ns_MCRUN2_74_V9-v1/MINIAODSIM
/DMS_NNPDF30_Scalar_Mphi-10000_Mchi-1000_gSM-1p0_gDM-1p0_13TeV-powheg/RunIISpring15DR74-Asympt25ns_MCRUN2_74_V9-v1/MINIAODSIM

DRAFT

Table 11: Simulated signal samples: DM Pseudoscalar

Data set
/DMS_NNPDF30_Pseudoscalar_Mphi-10_Mchi-1_gSM-1p0_gDM-1p0_13TeV-powheg/RunIISpring15DR74-Asympt25ns_MCRUN2_74_V9-v1/MINIAODSIM
/DMS_NNPDF30_Pseudoscalar_Mphi-10_Mchi-10_gSM-1p0_gDM-1p0_13TeV-powheg/RunIISpring15DR74-Asympt25ns_MCRUN2_74_V9-v1/MINIAODSIM
/DMS_NNPDF30_Pseudoscalar_Mphi-20_Mchi-1_gSM-1p0_gDM-1p0_13TeV-powheg/RunIISpring15DR74-Asympt25ns_MCRUN2_74_V9-v1/MINIAODSIM
/DMS_NNPDF30_Pseudoscalar_Mphi-20_Mchi-10_gSM-1p0_gDM-1p0_13TeV-powheg/RunIISpring15DR74-Asympt25ns_MCRUN2_74_V9-v1/MINIAODSIM
/DMS_NNPDF30_Pseudoscalar_Mphi-50_Mchi-10_gSM-1p0_gDM-1p0_13TeV-powheg/RunIISpring15DR74-Asympt25ns_MCRUN2_74_V9-v1/MINIAODSIM
/DMS_NNPDF30_Pseudoscalar_Mphi-50_Mchi-50_gSM-1p0_gDM-1p0_13TeV-powheg/RunIISpring15DR74-Asympt25ns_MCRUN2_74_V9-v1/MINIAODSIM
/DMS_NNPDF30_Pseudoscalar_Mphi-100_Mchi-10_gSM-1p0_gDM-1p0_13TeV-powheg/RunIISpring15DR74-Asympt25ns_MCRUN2_74_V9-v1/MINIAODSIM
/DMS_NNPDF30_Pseudoscalar_Mphi-100_Mchi-100_gSM-1p0_gDM-1p0_13TeV-powheg/RunIISpring15DR74-Asympt25ns_MCRUN2_74_V9-v1/MINIAODSIM
/DMS_NNPDF30_Pseudoscalar_Mphi-200_Mchi-1_gSM-1p0_gDM-1p0_13TeV-powheg/RunIISpring15DR74-Asympt25ns_MCRUN2_74_V9-v1/MINIAODSIM
/DMS_NNPDF30_Pseudoscalar_Mphi-200_Mchi-10_gSM-1p0_gDM-1p0_13TeV-powheg/RunIISpring15DR74-Asympt25ns_MCRUN2_74_V9-v1/MINIAODSIM
/DMS_NNPDF30_Pseudoscalar_Mphi-200_Mchi-100_gSM-1p0_gDM-1p0_13TeV-powheg/RunIISpring15DR74-Asympt25ns_MCRUN2_74_V9-v1/MINIAODSIM
/DMS_NNPDF30_Pseudoscalar_Mphi-200_Mchi-150_gSM-1p0_gDM-1p0_13TeV-powheg/RunIISpring15DR74-Asympt25ns_MCRUN2_74_V9-v1/MINIAODSIM
/DMS_NNPDF30_Pseudoscalar_Mphi-300_Mchi-10_gSM-1p0_gDM-1p0_13TeV-powheg/RunIISpring15DR74-Asympt25ns_MCRUN2_74_V9-v1/MINIAODSIM
/DMS_NNPDF30_Pseudoscalar_Mphi-300_Mchi-50_gSM-1p0_gDM-1p0_13TeV-powheg/RunIISpring15DR74-Asympt25ns_MCRUN2_74_V9-v1/MINIAODSIM
/DMS_NNPDF30_Pseudoscalar_Mphi-300_Mchi-100_gSM-1p0_gDM-1p0_13TeV-powheg/RunIISpring15DR74-Asympt25ns_MCRUN2_74_V9-v1/MINIAODSIM
/DMS_NNPDF30_Pseudoscalar_Mphi-300_Mchi-150_gSM-1p0_gDM-1p0_13TeV-powheg/RunIISpring15DR74-Asympt25ns_MCRUN2_74_V9-v1/MINIAODSIM
/DMS_NNPDF30_Pseudoscalar_Mphi-500_Mchi-1_gSM-1p0_gDM-1p0_13TeV-powheg/RunIISpring15DR74-Asympt25ns_MCRUN2_74_V9-v1/MINIAODSIM
/DMS_NNPDF30_Pseudoscalar_Mphi-500_Mchi-50_gSM-1p0_gDM-1p0_13TeV-powheg/RunIISpring15DR74-Asympt25ns_MCRUN2_74_V9-v1/MINIAODSIM
/DMS_NNPDF30_Pseudoscalar_Mphi-500_Mchi-100_gSM-1p0_gDM-1p0_13TeV-powheg/RunIISpring15DR74-Asympt25ns_MCRUN2_74_V9-v1/MINIAODSIM
/DMS_NNPDF30_Pseudoscalar_Mphi-500_Mchi-150_gSM-1p0_gDM-1p0_13TeV-powheg/RunIISpring15DR74-Asympt25ns_MCRUN2_74_V9-v1/MINIAODSIM
/DMS_NNPDF30_Pseudoscalar_Mphi-500_Mchi-500_gSM-1p0_gDM-1p0_13TeV-powheg/RunIISpring15DR74-Asympt25ns_MCRUN2_74_V9-v1/MINIAODSIM
/DMS_NNPDF30_Pseudoscalar_Mphi-1000_Mchi-1_gSM-1p0_gDM-1p0_13TeV-powheg/RunIISpring15DR74-Asympt25ns_MCRUN2_74_V9-v1/MINIAODSIM
/DMS_NNPDF30_Pseudoscalar_Mphi-1000_Mchi-10_gSM-1p0_gDM-1p0_13TeV-powheg/RunIISpring15DR74-Asympt25ns_MCRUN2_74_V9-v1/MINIAODSIM
/DMS_NNPDF30_Pseudoscalar_Mphi-1000_Mchi-100_gSM-1p0_gDM-1p0_13TeV-powheg/RunIISpring15DR74-Asympt25ns_MCRUN2_74_V9-v1/MINIAODSIM
/DMS_NNPDF30_Pseudoscalar_Mphi-1000_Mchi-150_gSM-1p0_gDM-1p0_13TeV-powheg/RunIISpring15DR74-Asympt25ns_MCRUN2_74_V9-v1/MINIAODSIM
/DMS_NNPDF30_Pseudoscalar_Mphi-1000_Mchi-1000_gSM-1p0_gDM-1p0_13TeV-powheg/RunIISpring15DR74-Asympt25ns_MCRUN2_74_V9-v1/MINIAODSIM
/DMS_NNPDF30_Pseudoscalar_Mphi-2000_Mchi-1_gSM-1p0_gDM-1p0_13TeV-powheg/RunIISpring15DR74-Asympt25ns_MCRUN2_74_V9-v1/MINIAODSIM
/DMS_NNPDF30_Pseudoscalar_Mphi-2000_Mchi-10_gSM-1p0_gDM-1p0_13TeV-powheg/RunIISpring15DR74-Asympt25ns_MCRUN2_74_V9-v1/MINIAODSIM
/DMS_NNPDF30_Pseudoscalar_Mphi-2000_Mchi-50_gSM-1p0_gDM-1p0_13TeV-powheg/RunIISpring15DR74-Asympt25ns_MCRUN2_74_V9-v1/MINIAODSIM
/DMS_NNPDF30_Pseudoscalar_Mphi-2000_Mchi-150_gSM-1p0_gDM-1p0_13TeV-powheg/RunIISpring15DR74-Asympt25ns_MCRUN2_74_V9-v1/MINIAODSIM
/DMS_NNPDF30_Pseudoscalar_Mphi-2000_Mchi-500_gSM-1p0_gDM-1p0_13TeV-powheg/RunIISpring15DR74-Asympt25ns_MCRUN2_74_V9-v1/MINIAODSIM
/DMS_NNPDF30_Pseudoscalar_Mphi-2000_Mchi-1000_gSM-1p0_gDM-1p0_13TeV-powheg/RunIISpring15DR74-Asympt25ns_MCRUN2_74_V9-v1/MINIAODSIM
/DMS_NNPDF30_Pseudoscalar_Mphi-5000_Mchi-1_gSM-1p0_gDM-1p0_13TeV-powheg/RunIISpring15DR74-Asympt25ns_MCRUN2_74_V9-v1/MINIAODSIM
/DMS_NNPDF30_Pseudoscalar_Mphi-5000_Mchi-10_gSM-1p0_gDM-1p0_13TeV-powheg/RunIISpring15DR74-Asympt25ns_MCRUN2_74_V9-v1/MINIAODSIM
/DMS_NNPDF30_Pseudoscalar_Mphi-5000_Mchi-50_gSM-1p0_gDM-1p0_13TeV-powheg/RunIISpring15DR74-Asympt25ns_MCRUN2_74_V9-v1/MINIAODSIM
/DMS_NNPDF30_Pseudoscalar_Mphi-5000_Mchi-100_gSM-1p0_gDM-1p0_13TeV-powheg/RunIISpring15DR74-Asympt25ns_MCRUN2_74_V9-v1/MINIAODSIM
/DMS_NNPDF30_Pseudoscalar_Mphi-5000_Mchi-150_gSM-1p0_gDM-1p0_13TeV-powheg/RunIISpring15DR74-Asympt25ns_MCRUN2_74_V9-v1/MINIAODSIM
/DMS_NNPDF30_Pseudoscalar_Mphi-5000_Mchi-500_gSM-1p0_gDM-1p0_13TeV-powheg/RunIISpring15DR74-Asympt25ns_MCRUN2_74_V9-v1/MINIAODSIM
/DMS_NNPDF30_Pseudoscalar_Mphi-5000_Mchi-1000_gSM-1p0_gDM-1p0_13TeV-powheg/RunIISpring15DR74-Asympt25ns_MCRUN2_74_V9-v1/MINIAODSIM
/DMS_NNPDF30_Pseudoscalar_Mphi-10000_Mchi-1_gSM-1p0_gDM-1p0_13TeV-powheg/RunIISpring15DR74-Asympt25ns_MCRUN2_74_V9-v1/MINIAODSIM
/DMS_NNPDF30_Pseudoscalar_Mphi-10000_Mchi-10_gSM-1p0_gDM-1p0_13TeV-powheg/RunIISpring15DR74-Asympt25ns_MCRUN2_74_V9-v1/MINIAODSIM
/DMS_NNPDF30_Pseudoscalar_Mphi-10000_Mchi-50_gSM-1p0_gDM-1p0_13TeV-powheg/RunIISpring15DR74-Asympt25ns_MCRUN2_74_V9-v1/MINIAODSIM
/DMS_NNPDF30_Pseudoscalar_Mphi-10000_Mchi-100_gSM-1p0_gDM-1p0_13TeV-powheg/RunIISpring15DR74-Asympt25ns_MCRUN2_74_V9-v1/MINIAODSIM
/DMS_NNPDF30_Pseudoscalar_Mphi-10000_Mchi-150_gSM-1p0_gDM-1p0_13TeV-powheg/RunIISpring15DR74-Asympt25ns_MCRUN2_74_V9-v1/MINIAODSIM
/DMS_NNPDF30_Pseudoscalar_Mphi-10000_Mchi-500_gSM-1p0_gDM-1p0_13TeV-powheg/RunIISpring15DR74-Asympt25ns_MCRUN2_74_V9-v1/MINIAODSIM
/DMS_NNPDF30_Pseudoscalar_Mphi-10000_Mchi-1000_gSM-1p0_gDM-1p0_13TeV-powheg/RunIISpring15DR74-Asympt25ns_MCRUN2_74_V9-v1/MINIAODSIM

DRAFT

Table 12: Simulated signal samples: DM $b\bar{b}$ Scalar

Data set
/BBbarDMJets_scalar_Mchi-1_Mphi-10_TuneCUETP8M1_13TeV-madgraphMLM-pythia8/RunIISpring15DR74-Asympt25ns_MCRUN2_74_V9-v1/MINIAODSIM
/BBbarDMJets_scalar_Mchi-1_Mphi-20_TuneCUETP8M1_13TeV-madgraphMLM-pythia8/RunIISpring15DR74-Asympt25ns_MCRUN2_74_V9-v1/MINIAODSIM
/BBbarDMJets_scalar_Mchi-1_Mphi-50_TuneCUETP8M1_13TeV-madgraphMLM-pythia8/RunIISpring15DR74-Asympt25ns_MCRUN2_74_V9-v1/MINIAODSIM
/BBbarDMJets_scalar_Mchi-1_Mphi-100_TuneCUETP8M1_13TeV-madgraphMLM-pythia8/RunIISpring15DR74-Asympt25ns_MCRUN2_74_V9-v1/MINIAODSIM
/BBbarDMJets_scalar_Mchi-1_Mphi-200_TuneCUETP8M1_13TeV-madgraphMLM-pythia8/RunIISpring15DR74-Asympt25ns_MCRUN2_74_V9-v1/MINIAODSIM
/BBbarDMJets_scalar_Mchi-1_Mphi-300_TuneCUETP8M1_13TeV-madgraphMLM-pythia8/RunIISpring15DR74-Asympt25ns_MCRUN2_74_V9-v1/MINIAODSIM
/BBbarDMJets_scalar_Mchi-1_Mphi-500_TuneCUETP8M1_13TeV-madgraphMLM-pythia8/RunIISpring15DR74-Asympt25ns_MCRUN2_74_V9-v1/MINIAODSIM
/BBbarDMJets_scalar_Mchi-1_Mphi-1000_TuneCUETP8M1_13TeV-madgraphMLM-pythia8/RunIISpring15DR74-Asympt25ns_MCRUN2_74_V9-v1/MINIAODSIM
/BBbarDMJets_scalar_Mchi-1_Mphi-10000_TuneCUETP8M1_13TeV-madgraphMLM-pythia8/RunIISpring15DR74-Asympt25ns_MCRUN2_74_V9-v1/MINIAODSIM
/BBbarDMJets_scalar_Mchi-10_Mphi-10_TuneCUETP8M1_13TeV-madgraphMLM-pythia8/RunIISpring15DR74-Asympt25ns_MCRUN2_74_V9-v1/MINIAODSIM
/BBbarDMJets_scalar_Mchi-10_Mphi-15_TuneCUETP8M1_13TeV-madgraphMLM-pythia8/RunIISpring15DR74-Asympt25ns_MCRUN2_74_V9-v1/MINIAODSIM
/BBbarDMJets_scalar_Mchi-10_Mphi-50_TuneCUETP8M1_13TeV-madgraphMLM-pythia8/RunIISpring15DR74-Asympt25ns_MCRUN2_74_V9-v1/MINIAODSIM
/BBbarDMJets_scalar_Mchi-10_Mphi-100_TuneCUETP8M1_13TeV-madgraphMLM-pythia8/RunIISpring15DR74-Asympt25ns_MCRUN2_74_V9-v1/MINIAODSIM
/BBbarDMJets_scalar_Mchi-10_Mphi-10000_TuneCUETP8M1_13TeV-madgraphMLM-pythia8/RunIISpring15DR74-Asympt25ns_MCRUN2_74_V9-v1/MINIAODSIM
/BBbarDMJets_scalar_Mchi-50_Mphi-10_TuneCUETP8M1_13TeV-madgraphMLM-pythia8/RunIISpring15DR74-Asympt25ns_MCRUN2_74_V9-v1/MINIAODSIM
/BBbarDMJets_scalar_Mchi-50_Mphi-50_TuneCUETP8M1_13TeV-madgraphMLM-pythia8/RunIISpring15DR74-Asympt25ns_MCRUN2_74_V9-v1/MINIAODSIM
/BBbarDMJets_scalar_Mchi-50_Mphi-95_TuneCUETP8M1_13TeV-madgraphMLM-pythia8/RunIISpring15DR74-Asympt25ns_MCRUN2_74_V9-v1/MINIAODSIM
/BBbarDMJets_scalar_Mchi-150_Mphi-200_TuneCUETP8M1_13TeV-madgraphMLM-pythia8/RunIISpring15DR74-Asympt25ns_MCRUN2_74_V9-v1/MINIAODSIM
/BBbarDMJets_scalar_Mchi-150_Mphi-295_TuneCUETP8M1_13TeV-madgraphMLM-pythia8/RunIISpring15DR74-Asympt25ns_MCRUN2_74_V9-v1/MINIAODSIM
/BBbarDMJets_scalar_Mchi-150_Mphi-500_TuneCUETP8M1_13TeV-madgraphMLM-pythia8/RunIISpring15DR74-Asympt25ns_MCRUN2_74_V9-v1/MINIAODSIM
/BBbarDMJets_scalar_Mchi-150_Mphi-1000_TuneCUETP8M1_13TeV-madgraphMLM-pythia8/RunIISpring15DR74-Asympt25ns_MCRUN2_74_V9-v1/MINIAODSIM
/BBbarDMJets_scalar_Mchi-150_Mphi-10000_TuneCUETP8M1_13TeV-madgraphMLM-pythia8/RunIISpring15DR74-Asympt25ns_MCRUN2_74_V9-v1/MINIAODSIM
/BBbarDMJets_scalar_Mchi-500_Mphi-10_TuneCUETP8M1_13TeV-madgraphMLM-pythia8/RunIISpring15DR74-Asympt25ns_MCRUN2_74_V9-v1/MINIAODSIM
/BBbarDMJets_scalar_Mchi-500_Mphi-500_TuneCUETP8M1_13TeV-madgraphMLM-pythia8/RunIISpring15DR74-Asympt25ns_MCRUN2_74_V9-v1/MINIAODSIM
/BBbarDMJets_scalar_Mchi-500_Mphi-995_TuneCUETP8M1_13TeV-madgraphMLM-pythia8/RunIISpring15DR74-Asympt25ns_MCRUN2_74_V9-v1/MINIAODSIM
/BBbarDMJets_scalar_Mchi-500_Mphi-10000_TuneCUETP8M1_13TeV-madgraphMLM-pythia8/RunIISpring15DR74-Asympt25ns_MCRUN2_74_V9-v1/MINIAODSIM
/BBbarDMJets_scalar_Mchi-1000_Mphi-10_TuneCUETP8M1_13TeV-madgraphMLM-pythia8/RunIISpring15DR74-Asympt25ns_MCRUN2_74_V9-v1/MINIAODSIM
/BBbarDMJets_scalar_Mchi-1000_Mphi-1000_TuneCUETP8M1_13TeV-madgraphMLM-pythia8/RunIISpring15DR74-Asympt25ns_MCRUN2_74_V9-v1/MINIAODSIM
/BBbarDMJets_scalar_Mchi-1000_Mphi-10000_TuneCUETP8M1_13TeV-madgraphMLM-pythia8/RunIISpring15DR74-Asympt25ns_MCRUN2_74_V9-v1/MINIAODSIM

DRAFT

Table 13: Simulated signal samples: DM $b\bar{b}$ Pseudoscalar

Data set
/BBbarDMJets_pseudoscalar_Mchi-1_Mphi-10_TuneCUETP8M1_13TeV-madgraphMLM-pythia8/RunIISpring15DR74-Asympt25ns_MCRUN2_74_V9-v1/MINIAODSIM
/BBbarDMJets_pseudoscalar_Mchi-1_Mphi-20_TuneCUETP8M1_13TeV-madgraphMLM-pythia8/RunIISpring15DR74-Asympt25ns_MCRUN2_74_V9-v1/MINIAODSIM
/BBbarDMJets_pseudoscalar_Mchi-1_Mphi-50_TuneCUETP8M1_13TeV-madgraphMLM-pythia8/RunIISpring15DR74-Asympt25ns_MCRUN2_74_V9-v1/MINIAODSIM
/BBbarDMJets_pseudoscalar_Mchi-1_Mphi-100_TuneCUETP8M1_13TeV-madgraphMLM-pythia8/RunIISpring15DR74-Asympt25ns_MCRUN2_74_V9-v1/MINIAODSIM
/BBbarDMJets_pseudoscalar_Mchi-1_Mphi-200_TuneCUETP8M1_13TeV-madgraphMLM-pythia8/RunIISpring15DR74-Asympt25ns_MCRUN2_74_V9-v1/MINIAODSIM
/BBbarDMJets_pseudoscalar_Mchi-1_Mphi-300_TuneCUETP8M1_13TeV-madgraphMLM-pythia8/RunIISpring15DR74-Asympt25ns_MCRUN2_74_V9-v1/MINIAODSIM
/BBbarDMJets_pseudoscalar_Mchi-1_Mphi-500_TuneCUETP8M1_13TeV-madgraphMLM-pythia8/RunIISpring15DR74-Asympt25ns_MCRUN2_74_V9-v1/MINIAODSIM
/BBbarDMJets_pseudoscalar_Mchi-1_Mphi-1000_TuneCUETP8M1_13TeV-madgraphMLM-pythia8/RunIISpring15DR74-Asympt25ns_MCRUN2_74_V9-v1/MINIAODSIM
/BBbarDMJets_pseudoscalar_Mchi-1_Mphi-10000_TuneCUETP8M1_13TeV-madgraphMLM-pythia8/RunIISpring15DR74-Asympt25ns_MCRUN2_74_V9-v1/MINIAODSIM
/BBbarDMJets_pseudoscalar_Mchi-10_Mphi-10_TuneCUETP8M1_13TeV-madgraphMLM-pythia8/RunIISpring15DR74-Asympt25ns_MCRUN2_74_V9-v1/MINIAODSIM
/BBbarDMJets_pseudoscalar_Mchi-10_Mphi-15_TuneCUETP8M1_13TeV-madgraphMLM-pythia8/RunIISpring15DR74-Asympt25ns_MCRUN2_74_V9-v1/MINIAODSIM
/BBbarDMJets_pseudoscalar_Mchi-10_Mphi-50_TuneCUETP8M1_13TeV-madgraphMLM-pythia8/RunIISpring15DR74-Asympt25ns_MCRUN2_74_V9-v1/MINIAODSIM
/BBbarDMJets_pseudoscalar_Mchi-10_Mphi-100_TuneCUETP8M1_13TeV-madgraphMLM-pythia8/RunIISpring15DR74-Asympt25ns_MCRUN2_74_V9-v1/MINIAODSIM
/BBbarDMJets_pseudoscalar_Mchi-10_Mphi-10000_TuneCUETP8M1_13TeV-madgraphMLM-pythia8/RunIISpring15DR74-Asympt25ns_MCRUN2_74_V9-v1/MINIAODSIM
/BBbarDMJets_pseudoscalar_Mchi-50_Mphi-10_TuneCUETP8M1_13TeV-madgraphMLM-pythia8/RunIISpring15DR74-Asympt25ns_MCRUN2_74_V9-v1/MINIAODSIM
/BBbarDMJets_pseudoscalar_Mchi-50_Mphi-50_TuneCUETP8M1_13TeV-madgraphMLM-pythia8/RunIISpring15DR74-Asympt25ns_MCRUN2_74_V9-v1/MINIAODSIM
/BBbarDMJets_pseudoscalar_Mchi-50_Mphi-95_TuneCUETP8M1_13TeV-madgraphMLM-pythia8/RunIISpring15DR74-Asympt25ns_MCRUN2_74_V9-v1/MINIAODSIM
/BBbarDMJets_pseudoscalar_Mchi-50_Mphi-200_TuneCUETP8M1_13TeV-madgraphMLM-pythia8/RunIISpring15DR74-Asympt25ns_MCRUN2_74_V9-v1/MINIAODSIM
/BBbarDMJets_pseudoscalar_Mchi-150_Mphi-200_TuneCUETP8M1_13TeV-madgraphMLM-pythia8/RunIISpring15DR74-Asympt25ns_MCRUN2_74_V9-v1/MINIAODSIM
/BBbarDMJets_pseudoscalar_Mchi-150_Mphi-295_TuneCUETP8M1_13TeV-madgraphMLM-pythia8/RunIISpring15DR74-Asympt25ns_MCRUN2_74_V9-v1/MINIAODSIM
/BBbarDMJets_pseudoscalar_Mchi-150_Mphi-500_TuneCUETP8M1_13TeV-madgraphMLM-pythia8/RunIISpring15DR74-Asympt25ns_MCRUN2_74_V9-v1/MINIAODSIM
/BBbarDMJets_pseudoscalar_Mchi-150_Mphi-1000_TuneCUETP8M1_13TeV-madgraphMLM-pythia8/RunIISpring15DR74-Asympt25ns_MCRUN2_74_V9-v1/MINIAODSIM
/BBbarDMJets_pseudoscalar_Mchi-150_Mphi-10000_TuneCUETP8M1_13TeV-madgraphMLM-pythia8/RunIISpring15DR74-Asympt25ns_MCRUN2_74_V9-v1/MINIAODSIM
/BBbarDMJets_pseudoscalar_Mchi-500_Mphi-10_TuneCUETP8M1_13TeV-madgraphMLM-pythia8/RunIISpring15DR74-Asympt25ns_MCRUN2_74_V9-v1/MINIAODSIM
/BBbarDMJets_pseudoscalar_Mchi-500_Mphi-500_TuneCUETP8M1_13TeV-madgraphMLM-pythia8/RunIISpring15DR74-Asympt25ns_MCRUN2_74_V9-v1/MINIAODSIM
/BBbarDMJets_pseudoscalar_Mchi-500_Mphi-995_TuneCUETP8M1_13TeV-madgraphMLM-pythia8/RunIISpring15DR74-Asympt25ns_MCRUN2_74_V9-v1/MINIAODSIM
/BBbarDMJets_pseudoscalar_Mchi-500_Mphi-10000_TuneCUETP8M1_13TeV-madgraphMLM-pythia8/RunIISpring15DR74-Asympt25ns_MCRUN2_74_V9-v1/MINIAODSIM
/BBbarDMJets_pseudoscalar_Mchi-1000_Mphi-10_TuneCUETP8M1_13TeV-madgraphMLM-pythia8/RunIISpring15DR74-Asympt25ns_MCRUN2_74_V9-v1/MINIAODSIM
/BBbarDMJets_pseudoscalar_Mchi-1000_Mphi-1000_TuneCUETP8M1_13TeV-madgraphMLM-pythia8/RunIISpring15DR74-Asympt25ns_MCRUN2_74_V9-v1/MINIAODSIM
/BBbarDMJets_pseudoscalar_Mchi-1000_Mphi-10000_TuneCUETP8M1_13TeV-madgraphMLM-pythia8/RunIISpring15DR74-Asympt25ns_MCRUN2_74_V9-v1/MINIAODSIM

Table 14: Simulated signal samples: DM $t\bar{t}$ Scalar

Data set
/TTbarDMJets_scalar_Mchi-1_Mphi-10_TuneCUETP8M1_13TeV-madgraphMLM-pythia8/RunIISpring15DR74-Asympt25ns_MCRUN2_74_V9-v1/MINIAODSIM
/TTbarDMJets_scalar_Mchi-1_Mphi-20_TuneCUETP8M1_13TeV-madgraphMLM-pythia8/RunIISpring15DR74-Asympt25ns_MCRUN2_74_V9-v1/MINIAODSIM
/TTbarDMJets_scalar_Mchi-1_Mphi-50_TuneCUETP8M1_13TeV-madgraphMLM-pythia8/RunIISpring15DR74-Asympt25ns_MCRUN2_74_V9-v1/MINIAODSIM
/TTbarDMJets_scalar_Mchi-1_Mphi-100_TuneCUETP8M1_13TeV-madgraphMLM-pythia8/RunIISpring15DR74-Asympt25ns_MCRUN2_74_V9-v1/MINIAODSIM
/TTbarDMJets_scalar_Mchi-1_Mphi-200_TuneCUETP8M1_13TeV-madgraphMLM-pythia8/RunIISpring15DR74-Asympt25ns_MCRUN2_74_V9-v1/MINIAODSIM
/TTbarDMJets_scalar_Mchi-1_Mphi-300_TuneCUETP8M1_13TeV-madgraphMLM-pythia8/RunIISpring15DR74-Asympt25ns_MCRUN2_74_V9-v1/MINIAODSIM
/TTbarDMJets_scalar_Mchi-1_Mphi-500_TuneCUETP8M1_13TeV-madgraphMLM-pythia8/RunIISpring15DR74-Asympt25ns_MCRUN2_74_V9-v1/MINIAODSIM
/TTbarDMJets_scalar_Mchi-1_Mphi-1000_TuneCUETP8M1_13TeV-madgraphMLM-pythia8/RunIISpring15DR74-Asympt25ns_MCRUN2_74_V9-v2/MINIAODSIM
/TTbarDMJets_scalar_Mchi-10_Mphi-10_TuneCUETP8M1_13TeV-madgraphMLM-pythia8/RunIISpring15DR74-Asympt25ns_MCRUN2_74_V9-v1/MINIAODSIM
/TTbarDMJets_scalar_Mchi-10_Mphi-50_TuneCUETP8M1_13TeV-madgraphMLM-pythia8/RunIISpring15DR74-Asympt25ns_MCRUN2_74_V9-v1/MINIAODSIM
/TTbarDMJets_scalar_Mchi-10_Mphi-100_TuneCUETP8M1_13TeV-madgraphMLM-pythia8/RunIISpring15DR74-Asympt25ns_MCRUN2_74_V9-v1/MINIAODSIM
/TTbarDMJets_scalar_Mchi-50_Mphi-50_TuneCUETP8M1_13TeV-madgraphMLM-pythia8/RunIISpring15DR74-Asympt25ns_MCRUN2_74_V9-v1/MINIAODSIM
/TTbarDMJets_scalar_Mchi-50_Mphi-200_TuneCUETP8M1_13TeV-madgraphMLM-pythia8/RunIISpring15DR74-Asympt25ns_MCRUN2_74_V9-v1/MINIAODSIM
/TTbarDMJets_scalar_Mchi-50_Mphi-300_TuneCUETP8M1_13TeV-madgraphMLM-pythia8/RunIISpring15DR74-Asympt25ns_MCRUN2_74_V9-v1/MINIAODSIM
/TTbarDMJets_scalar_Mchi-150_Mphi-200_TuneCUETP8M1_13TeV-madgraphMLM-pythia8/RunIISpring15DR74-Asympt25ns_MCRUN2_74_V9-v1/MINIAODSIM
/TTbarDMJets_scalar_Mchi-150_Mphi-500_TuneCUETP8M1_13TeV-madgraphMLM-pythia8/RunIISpring15DR74-Asympt25ns_MCRUN2_74_V9-v3/MINIAODSIM
/TTbarDMJets_scalar_Mchi-150_Mphi-1000_TuneCUETP8M1_13TeV-madgraphMLM-pythia8/RunIISpring15DR74-Asympt25ns_MCRUN2_74_V9-v3/MINIAODSIM
/TTbarDMJets_scalar_Mchi-500_Mphi-500_TuneCUETP8M1_13TeV-madgraphMLM-pythia8/RunIISpring15DR74-Asympt25ns_MCRUN2_74_V9-v1/MINIAODSIM

DRAFT

Table 15: Simulated signal samples: DM $t\bar{t}$ Pseudoscalar

Data set
/TTbarDMJets_pseudoscalar_Mchi-1_Mphi-10_TuneCUETP8M1_13TeV-madgraphMLM-pythia8/RunIISpring15DR74-Asympt25ns_MCRUN2_74_V9-v1/MINIAODSIM
/TTbarDMJets_pseudoscalar_Mchi-1_Mphi-20_TuneCUETP8M1_13TeV-madgraphMLM-pythia8/RunIISpring15DR74-Asympt25ns_MCRUN2_74_V9-v1/MINIAODSIM
/TTbarDMJets_pseudoscalar_Mchi-1_Mphi-50_TuneCUETP8M1_13TeV-madgraphMLM-pythia8/RunIISpring15DR74-Asympt25ns_MCRUN2_74_V9-v1/MINIAODSIM
/TTbarDMJets_pseudoscalar_Mchi-1_Mphi-100_TuneCUETP8M1_13TeV-madgraphMLM-pythia8/RunIISpring15DR74-Asympt25ns_MCRUN2_74_V9-v1/MINIAODSIM
/TTbarDMJets_pseudoscalar_Mchi-1_Mphi-200_TuneCUETP8M1_13TeV-madgraphMLM-pythia8/RunIISpring15DR74-Asympt25ns_MCRUN2_74_V9-v1/MINIAODSIM
/TTbarDMJets_pseudoscalar_Mchi-1_Mphi-300_TuneCUETP8M1_13TeV-madgraphMLM-pythia8/RunIISpring15DR74-Asympt25ns_MCRUN2_74_V9-v1/MINIAODSIM
/TTbarDMJets_pseudoscalar_Mchi-1_Mphi-500_TuneCUETP8M1_13TeV-madgraphMLM-pythia8/RunIISpring15DR74-Asympt25ns_MCRUN2_74_V9-v1/MINIAODSIM
/TTbarDMJets_pseudoscalar_Mchi-10_Mphi-10_TuneCUETP8M1_13TeV-madgraphMLM-pythia8/RunIISpring15DR74-Asympt25ns_MCRUN2_74_V9-v1/MINIAODSIM
/TTbarDMJets_pseudoscalar_Mchi-10_Mphi-50_TuneCUETP8M1_13TeV-madgraphMLM-pythia8/RunIISpring15DR74-Asympt25ns_MCRUN2_74_V9-v1/MINIAODSIM
/TTbarDMJets_pseudoscalar_Mchi-10_Mphi-100_TuneCUETP8M1_13TeV-madgraphMLM-pythia8/RunIISpring15DR74-Asympt25ns_MCRUN2_74_V9-v1/MINIAODSIM
/TTbarDMJets_pseudoscalar_Mchi-50_Mphi-50_TuneCUETP8M1_13TeV-madgraphMLM-pythia8/RunIISpring15DR74-Asympt25ns_MCRUN2_74_V9-v1/MINIAODSIM
/TTbarDMJets_pseudoscalar_Mchi-50_Mphi-200_TuneCUETP8M1_13TeV-madgraphMLM-pythia8/RunIISpring15DR74-Asympt25ns_MCRUN2_74_V9-v1/MINIAODSIM
/TTbarDMJets_pseudoscalar_Mchi-50_Mphi-300_TuneCUETP8M1_13TeV-madgraphMLM-pythia8/RunIISpring15DR74-Asympt25ns_MCRUN2_74_V9-v1/MINIAODSIM
/TTbarDMJets_pseudoscalar_Mchi-150_Mphi-200_TuneCUETP8M1_13TeV-madgraphMLM-pythia8/RunIISpring15DR74-Asympt25ns_MCRUN2_74_V9-v1/MINIAODSIM
/TTbarDMJets_pseudoscalar_Mchi-150_Mphi-500_TuneCUETP8M1_13TeV-madgraphMLM-pythia8/RunIISpring15DR74-Asympt25ns_MCRUN2_74_V9-v1/MINIAODSIM
/TTbarDMJets_pseudoscalar_Mchi-150_Mphi-1000_TuneCUETP8M1_13TeV-madgraphMLM-pythia8/RunIISpring15DR74-Asympt25ns_MCRUN2_74_V9-v1/MINIAODSIM
/TTbarDMJets_pseudoscalar_Mchi-500_Mphi-500_TuneCUETP8M1_13TeV-madgraphMLM-pythia8/RunIISpring15DR74-Asympt25ns_MCRUN2_74_V9-v1/MINIAODSIM

DRAFT

4.3 Pileup reweighting

The distribution of the numbers of the pileup interactions in the simulated events is different from that in the data; the simulated events contain, on average, a larger number of pileup interactions than the data. We reweight simulated events to reproduce for this difference. This procedure is called *pileup reweighting*.

In analyses in CMS, the pileup reweighting is, in general, done in the method recommended by the physics validation group [14]. However, since, at the time of writing, no official recommendation is available we currently use a private reweighting. Once available we will update to use the recommended method.

The reweighting factors used in this version of the note is a function of the number of the reconstructed vertices derived by comparing the data and simulated events. Events passing the trigger path `HLT_ZeroBias` are used for this derivation. The condition of this trigger path is a bunch crossing. Therefore, the events virtually contain only pileup interactions. For the simulated event sample, we use the so-called neutrino guns, listed in Table 16. This sample also virtually contain only pileup interactions. In contrast, the events in the signal and control regions each has, in addition to the pileup interactions, the main interaction that produces high-p_T jets, muons, electrons, photons, or missing transverse momentum as described in Sec. 7.

Table 16: Simulated sample used in deriving pileup reweighting factors

Data set
`/SingleNeutrino/RunIISpring15DR74-Asympt25nsRaw_MCRUN2_74_V9-v2/MINIAODSIM`

The reweighting factors are derived as follows. First, we create the distributions of the numbers of the reconstructed vertices for the data and simulated sample. In creating these distributions, we add one to the number of the reconstructed vertices. This is because these events do not have the vertex for the main interaction while the events in the signal and control regions do.

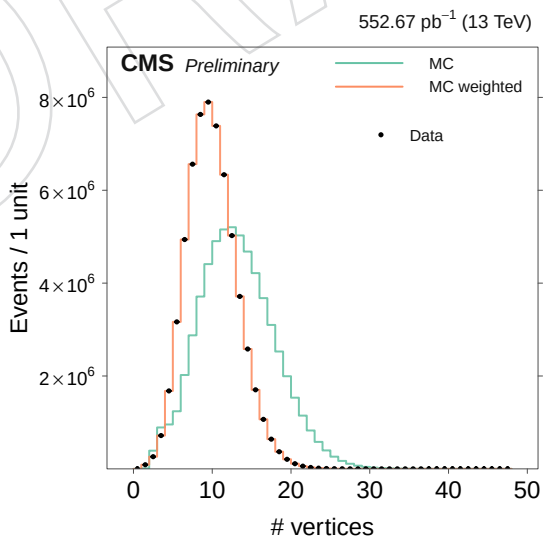

Figure 1: The distributions of the number of the reconstructed vertices in the data, the simulated events, and the reweighted simulated events. One is added to the the number of the reconstructed vertices.

DRAFT

Second, we smooth each distribution with the smoothing spline. Third, we take the ratio of the two distributions, i.e., the data over the simulated sample. The ratio is a function of the number of reconstructed vertices. The ratio becomes reweighting factors after normalised. The reweighting factors are normalised so as to preserve the number of the generated events.

Figure 1 shows the distributions of the number of the reconstructed vertices in the data, the simulated events, and the reweighted simulated events. In the figure, one is added to the the number of the reconstructed vertices. The figure demonstrates that the reweighted simulated events have the distribution of the number of the reconstructed vertices nearly identical to that in the data.

4.4 Cross sections for SM samples

Several MC samples of individual SM processes are binned according to a generator level quantity, such as the partonic H_{T} or bosonic p_{T}. This analysis chooses to use samples binned in partonic H_{T}, for the set of MC samples (W+jets, DY+jets, QCD, γ+jets, $Z \to \nu\nu$+jets) and $\hat{P}_T$ for only the QCD sample. These binned samples are provided with LO cross sections. The k-factors required to go from LO to NNLO cross section are typically determined using corresponding inclusive samples applied to each H_{T} binned sample. Further studies can provide additional corrections to the cross sections, which can prove important to the closure test procedures described in Section 12.1. As can be seen in Section 8, residual cross section corrections are measured using data in sidebands designed to enriched specific processes.

Following an inclusive selection, the distribution of the MC samples with respect to the binning variable H_T^{parton} are shown in Fig. 2, with also the $\hat{P}_T$ distribution for QCD.

As stated above, the distributions shown in Fig. 2 follow an inclusive selection, whereby there is no requirement on each event. This direct translation from MC allows to merge the binned generator level variable, and exhibits a smooth shape with respect to the cross sections in question.

A more in depth, data-driven investigation of the cross sections is shown in Sec. 8. Of which, an important point to note is that the corrections to the cross sections, derived with the data sidebands are only relevant for data/MC comparison plots and the suite of closure tests defined in Section 12.1.

DRAFT

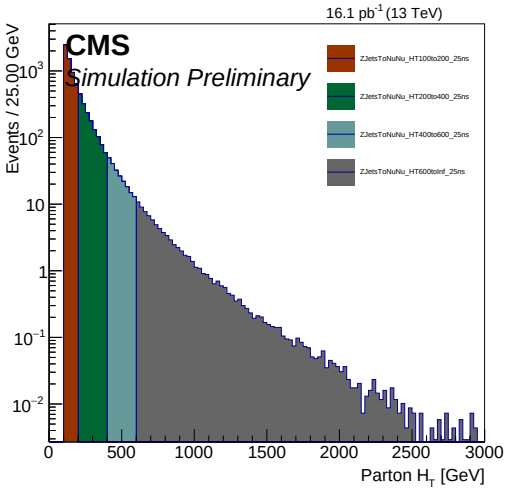

(a) $Z \to \nu\nu$ +jets

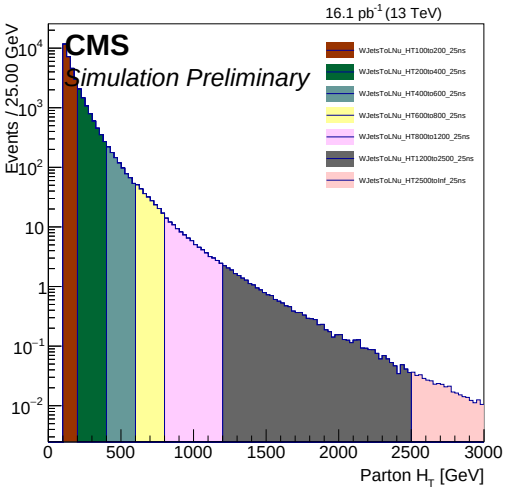

(b) $W \to l\nu$ + jets

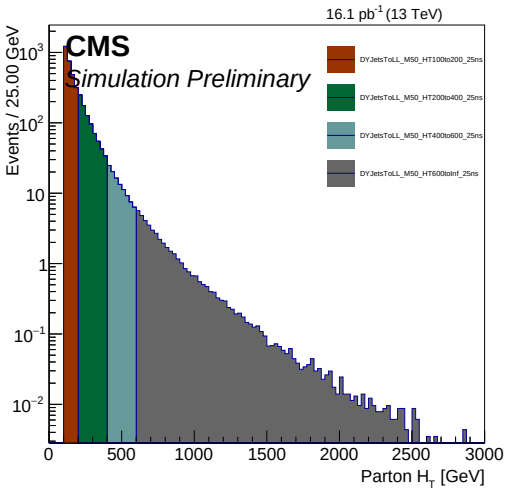

(c) $DY \to ll$ + jets

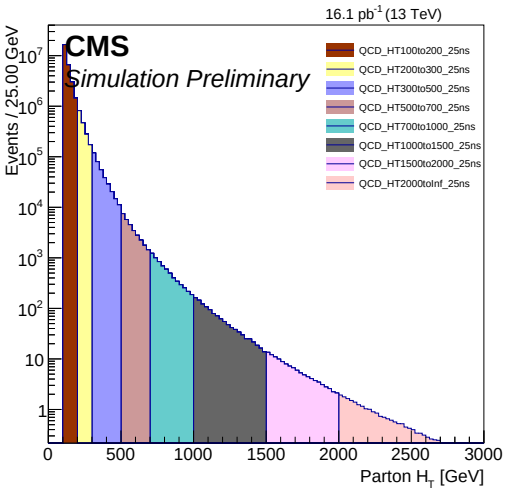

(d) QCD

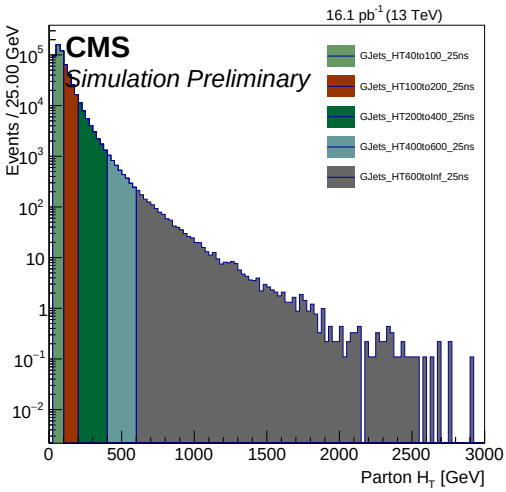

(e) γ+jets

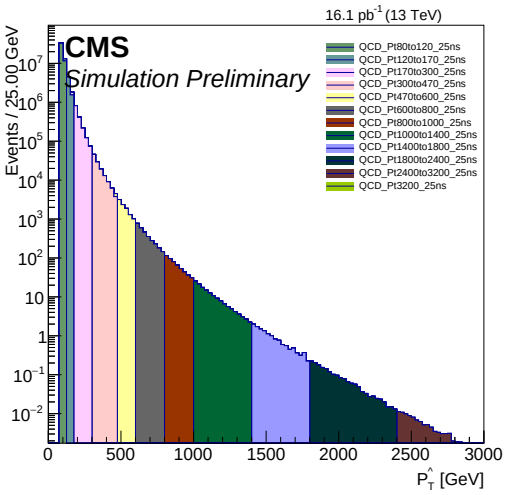

(f) QCD $\hat{P_T}$

Figure 2: Generator-level H_T^{parton} distributions for SM process, $Z \to \nu\nu$ + jets, W+jets, DY+jets, QCD, γ+jets, and $\hat{P_T}$ for QCD.

5 Trigger strategy

5.1 Hadronic signal region

In Run 2 the RA1 analysis retains the low-thresholds of Run 1 with developments to the trigger selection, maintaining sensitivity to signatures of new physics with hadronic energies as low as $H_T = 200$ GeV. This in part is achieved by a migration to PF-based jet reconstruction within the HLT which, in conjunction with a reduction of clustering radius parameter $\Delta R = 0.4$, provides improvements in jet energy resolution in high-pileup conditions and mitigates the effects of pileup contamination within the jet cone.

The RA1 analysis utilises a range of triggers for the selection of events in the hadronic signal region to provide coverage over a wide range of event topologies. A guiding principle of the analysis is to be as inclusive as possible by probing low thresholds, necessitating operation in or near the trigger turn-on. Events in the hadronic monojet signal region are selected with the use of a single H_T^{miss}-E_T^{miss} cross-trigger, `HLT_PFMETNoMu90_JetIdCleaned_PFMHTNoMu90_IDTight`, which is cross-cleaned of muons in the computation of event variables in the HLT.

The hadronic multijet signal region is selected by a suite of H_T-α_T cross-triggers with a requirement on the average p_T of the leading two jets, $p_T^{\langle j1,j2 \rangle}$, labelled: `HLT_PFHTXXX_PFDijetYYY_AlphaT0pZZ`. The use of a dijet average threshold provides an improved suppression of QCD multijet events within the trigger, enabling looser α_T thresholds to be utilised whilst maintaining acceptance to events exhibiting asymmetric jet topologies such as monojet-like signatures of compressed spectrum and DM models. It was found that a dijet average threshold of 90 GeV ensured the optimum performance when balancing efficiency and rate, with both the H_T and α_T thresholds across all jet toplogies. The dijet average requirement does however lead to a loss in efficiency for asymmetric jet events where the sub-leading jet is soft. This loss in efficiency is mitigated by taking the disjunction of the `HLT_PFHTXXX_PFDijetYYY_AlphaT0pZZ` and the monojet triggers which provides a recovery of efficiency in the turn-on and close to the plateau for the low-H_T asymmetric jet selection. The H_T-α_T triggers seed all signal multijet offline bins in the range for $H_T > 200$ GeV. Above $H_T > 800$ an additional pure H_T trigger, `HLT_PFHT800`, is also utilised which has no explicit dependence on α_T or dijet average threshold.

These triggers form the primary signal selection menu for the analysis, in addition a set of secondary triggers with higher thresholds were in operation to provide redundancy for higher luminosity scenarios. In Run 2 however the primary triggers sufficiently suppressed trigger rates such that the use of secondary triggers in the analysis are not required.

The Level-1 seeds for the H_T-α_T HLT paths are given by the disjunction of the lowest unprescaled Level-1 hadronic scalar energy and missing energy sum seeds (`HTTXXX_OR_ETMYYY`) for the given run scenario. A loose calorimeter trigger prefilter is utilised to reduce the pass-through rate prior to track-based reconstruction, ensuring the PF-based filters meet timing requirements. The calorimeter prefilter utilises loose H_T and dijet average p_T requirements in addition to a new variable α_T', defined as α_T in the limit $\Delta H_T \to 0$, which better correlates α_T between calorimeter and PF-based reconstruction. The monojet and `HLT_HT800` triggers use the `ETM50` and `HTT175` seeds respectively with loose H_T^{miss} and H_T prefilters to suppress pass-through rate.

The thresholds of the signal triggers are shown in Table 17. The choice of threshold for the H_T-α_T triggers were tuned to maintain acceptance for a range of signal topologies whilst effectively suppressing QCD multijet events to maintain acceptable trigger rates.

An important goal of the analysis is to have good acceptance to compressed SUSY and general

DRAFT

Table 17: Trigger thresholds of the Level-1, calorimeter prefilter and final PF-trigger decision for the primary HLT paths for the hadronic signal region in the $\mathcal{L} = 7 \times 10^{33}\,\mathrm{cm}^{-2}\mathrm{s}^{-1}$ scenario. Higher threshold Level-1 H_T and $E_\mathrm{T}^\mathrm{miss}$ seeds are utilised for the higher luminosity scenario.

HLT path	L1 seed	HLT calo-prefilter (H_T, α_T', $p_\mathrm{T}^{\langle j1,j2\rangle}$, $E_\mathrm{T}^\mathrm{miss}$)	HLT PF-filter (H_T, α_T, $p_\mathrm{T}^{\langle j1,j2\rangle}$, $E_\mathrm{T}^\mathrm{miss}$)
HLT_PFHT200_PFDijetAve90_AlphaT0p57	HTT125 OR ETM50	150, 0.540, 70, -	200, 0.570, 90, -
HLT_PFHT250_PFDijetAve90_AlphaT0p55	HTT125 OR ETM50	200, 0.535, 70, -	250, 0.550, 90, -
HLT_PFHT300_PFDijetAve90_AlphaT0p53	HTT125 OR ETM50	250, 0.525, 70, -	300, 0.530, 90, -
HLT_PFHT350_PFDijetAve90_AlphaT0p52	HTT125 OR ETM50	300, 0.520, 70, -	350, 0.520, 90, -
HLT_PFHT400_PFDijetAve90_AlphaT0p51	HTT125 OR ETM50	370, 0.510, 70, -	400, 0.510, 90, -
HLT_PFHT800	HTT175	650, -, -, -	800, -, -, -, -
HLT_PFMETNoMu90_PFMHTNoMu90_IDTight	ETM50	-, -, -, -, 65	-, -, -, -, 90

DM models. It is therefore critical that we operate in the trigger turn on regions for the lower thresholds. We have already successfully exercised this approach with the Run 1 analysis and will repeat this mode or operating during Run 2. As in Run 1, multiple efficiency measurements are employed, which are performed with data and propagated through to the analysis with cross checks in simulation. A summary of estimates of a selection of signal models in simulation is presented in Appendix B.

The efficiency of the signal triggers are measured in data using electron and muon samples selected by the unprescaled `HLT_Ele23_eta2p1_WPLoose_Gsf` and `HLT_IsoMu20` reference triggers with a signal selection. Biases in these measurements can be introduced due to the contamination in the computation of event variables and different treatments between trigger and offline reconstructions, the degree of which varies with H_T and n_jet.

The monojet trigger performs a cross-cleaning of muons online, enabling its efficiency to measured in an unbiased manner using a muon sample. Electrons however cannot be disentangled and to remain consisent with the trigger must be measured with offline cross-cleaning disabled. A comparison of the estimate of the monojet trigger efficiency using muon and electron samples is shown in Fig. 3. With consistent cross-cleaning of the muon online and offline the monojet trigger is measured to be fully efficienct by H_T = 300 consistent with measurements in simulation. Measured in an electron sample with no cross-cleaning however the trigger is measured to have an inefficiency which increases with H_T. The bias leptons introduce when no cross-cleaning is appled is dominant for low-H_T resulting in the disagreement between samples, this however becomes less important at high H_T and n_jet. With a proper of cross-cleaning of muons online a muon sample is thought to provide a faster turn-on.

The multijet triggers do not have the muon cross-cleaning applied online so their efficiency measurement in data is primarily performed with the use of an electron sample. To remain consistent with the reconstruction of electrons in the trigger, no cross-cleaning of electrons from jets are performed offline, with the electron being included in the computation of event-level jet energy sums, such as H_T, $\not{H}_\mathrm{T}$ and α_T. The turn-on for the individual H_T-α_T triggers are shown in Appendix C

The trigger efficiency of the multijet triggers in the $H_\mathrm{T}^\mathrm{miss}$ dimension after a full signal selection is shown in Fig. 114 which is shown to be close to or at the plateau when taking the disjunction of the triggers for H_T ¡ 800 GeV. The efficiency without a proper cross-cleaning is predicted to be exceed that measured with electron bias. A full efficiency is therefore assumed for these triggers with a systematic to this estimate assigned equal to the inefficiency estimated by the respective reference trigger.

DRAFT

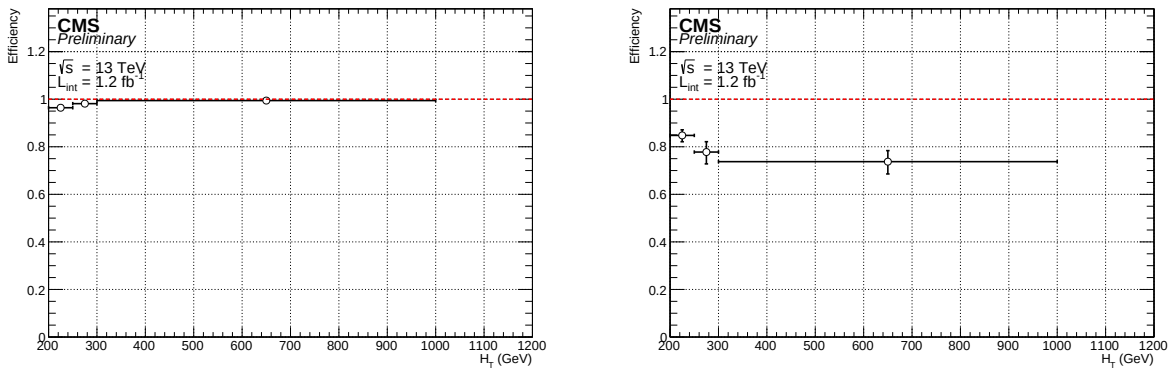

(a) Muon sample

(b) Electron sample

Figure 3: Trigger efficiency of the monojet trigger measured in muon and electron samples.

triggers for $H_T < 800$ GeV. Full efficiency is therefore assumed for these triggers with a systematic to this estimate assigned equal to the inefficiency estimated by the respective reference trigger. For $H_T > 800$ GeV, where the bias of electrons is a smaller effect, the trigger efficiency is measured for the disjunction of the H_T-α_T and `HLT_HT800` triggers, inclusively on jet multiplicity, and a correction applied which is shown in Fig. 5.

DRAFT

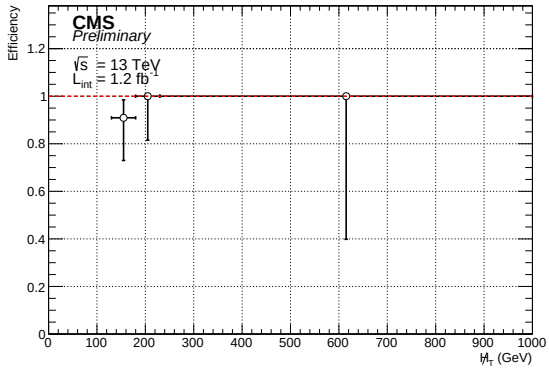

(a) $200 < H_T < 250$

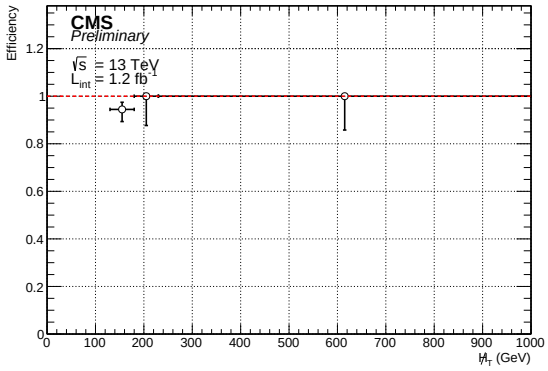

(b) $250 < H_T < 300$

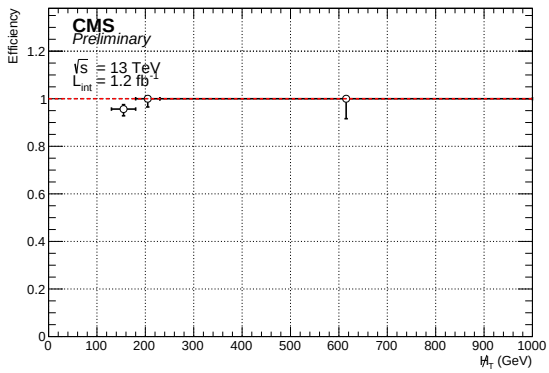

(c) $300 < H_T < 350$

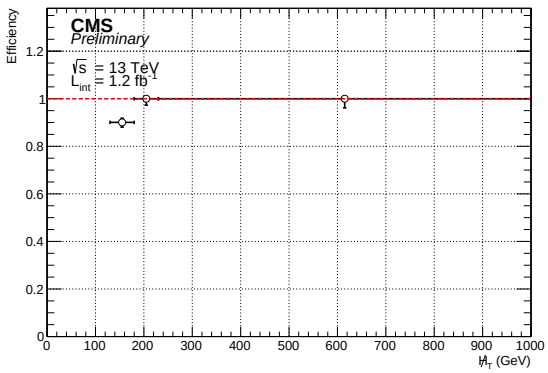

(d) $350 < H_T < 400$

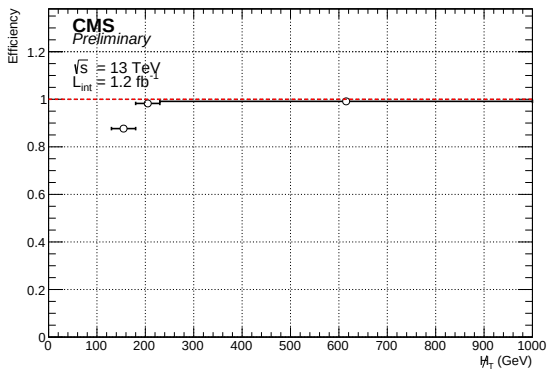

(e) $400 < H_T < 600$

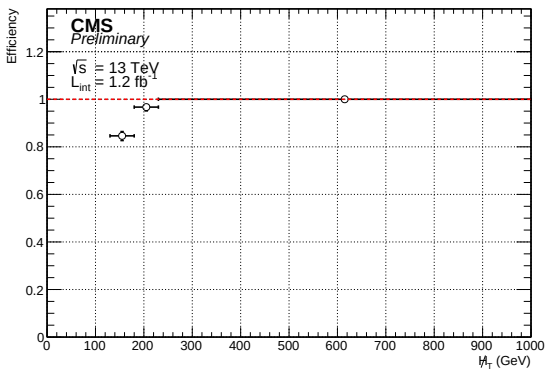

(f) $600 < H_T < 800$

Figure 4: Signal trigger efficiency in the H_T^{miss} dimension measured with an electron sample.

5.2 Control samples

Prescaled H_T triggers, `HLT_PFHTXXX`, and a prescaled H_T-α_T cross-trigger, are utilised in the selection of events for the hadronic control region. Shown in Table 18 these triggers share the same Level-1 seeds and H_T threshold of the signal cross-triggers and are similarly each mapped to a unique offline bin. The efficiency of these triggers are similarly measured from an electron reference trigger in addition to an independent measurement with the `HLT_Physics`

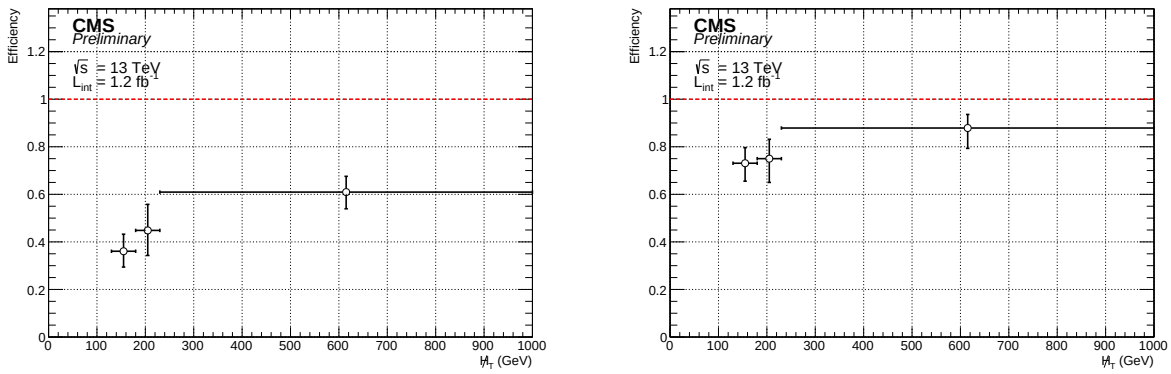

(a) $800 < H_T < 850$

(b) $850 < H_T < 900$

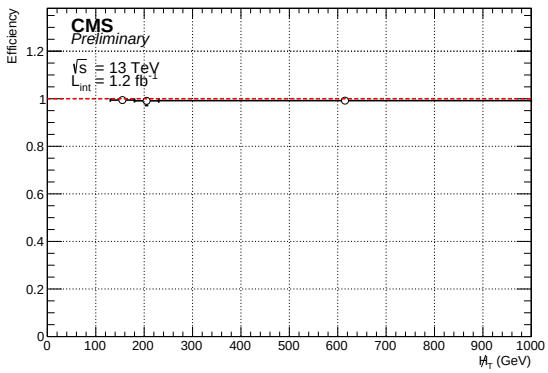

(c) $H_T > 900$

Figure 5: Signal trigger efficiency in the H_T^{miss} dimension measured with an electron sample.

minimum bias trigger.

Table 18: Hadronic control triggers.

HLT path	Prescale
HLT_PFHT200	3060
HLT_PFHT250	2040
HLT_PFHT300	1020
HLT_PFHT350	180
HLT_PFHT400	120
HLT_PFHT200_PFAlphaT0p51	175

The non-hadronic control regions are seeded by the lowest-threshold unprescaled triggers available in the given run scenario. In the high-luminosity scenario The μ + jets and $\mu\mu$ + jets control samples are selected with the HLT_IsoMu20 trigger, and the γ + jets control sample by the HLT_Photon175 trigger.

The efficiency of the control triggers is measured with data-driven methods (provided by the relevant POG). The tag and probe method is used in the measurement of efficiencies of the muon and electron triggers and a loose photon reference trigger is utilised in the measurement of the photon trigger efficiency. For the results in this note for the muon control regions the emulated trigger bit in MC is used to simulate the trigger. An offline p_T requirement of 200 GeV

DRAFT

is made on the photon to ensure it is in the efficiency plateau of the trigger.

DRAFT

6 Physics objects

The definitions of the physics objects used in this analysis follow the recommendations of the various Physics Object Groups (POGs). During data taking these recommendations are subject to change and will be be updated if necessary.

6.1 Jets

Jets are defined as sets of particle-flow (PF) candidates clustered by the anti-k_T jet clustering algorithm [15] with a distance parameter of 0.4 (PFJets). Charged Hadron Subtraction (CHS) is applied, i.e., charged hadrons that can be traced back to pileup vertices are not clustered. The four-momenta of jets are initially defined as the four-vector sum of the four-momenta of the constituent particle-flow candidates and then scaled by the jet energy correction factors designated as L1FastJet, L2Relative, and L3Absolute [16].

It should be noted that the early L1 FastJet corrections require improvements at this stage, and as a result can impact the L2 and L3 corrections. The "loose" working point Jet-Id selection criteria was chosen.

6.2 b-tagged jets

Jets originating from bottom quarks are identified through vertices that are displaced with respect to the primary interaction [17]. The algorithm used to tag b-jets is the Combined Secondary Vertex tagger V2, using the "medium" working point, which is achieved by requiring a cut of > 0.89 on the algorithm discriminator variable. This results in a gluon/light-quark mis-tag rate of $\sim$1 % (where "light" means u, d and s quarks) with a b-tag signal efficiency of about 80 %.

6.3 Muons

Muons are identified according to the "medium" working point definition of the recommended identification algorithm, which provides $\sim$ 98 % efficiency. Muons are also required to be well isolated, i.e. with a low activity in the vicinity of their track.

In the hadronic signal region, a PF-based relative isolation is used with a variable cone size, which is referred to as "mini-isolation". This isolation algorithm helps in recovering some efficiency in the lepton selection for boosted topology of top quark decays, in which the muon's track may be found close to the jet activity due to the boost of the parent top. Therefore, the cone size used for the calculation of the lepton isolation is reduced as a function of the lepton p_{T}, as follows: $R = 0.2$ for $p_{\mathrm{T}\ell} \leq 50\,\mathrm{GeV}$, $0.05 < R < 0.2$ for $50\,\mathrm{GeV} < p_{\mathrm{T}\ell} < 200\,\mathrm{GeV}$ and $R = 0.05$ for $p_{\mathrm{T}\ell} > 200\,\mathrm{GeV}$.

In the μ + jets and $\mu\mu$ + jets samples, to have better QCD background control, the standard PF-based relative isolation is used, with a cone size of 0.4.

The transverse momenta of PF neutral and charged candidates within a cone around the lepton are summed. The relative combined isolation I^{rel}_{comb} is then defined as the ratio of this scalar sum to the transverse momentum of the lepton candidate. The neutral hadron and photon contribution to the isolation is corrected by subtracting the expected neutral contribution from PU collisions, $\Delta\beta = 1/2 \sum_{\mathrm{PU}}^{\mathrm{chhad}} p_{\mathrm{T}}$. The factor 1/2 takes into account the neutral to charged ratio as measured in [18].

Muons are defined as isolated when they have $I^{mini}_{Iso} < 0.2$ within R for mini-isolation, and $I^{rel}_{comb} < 0.12$.

DRAFT

Muons are vetoed in the definition of the hadronic signal region, as described in Section 7.1, while control regions with one muon ("μ + jets") or two muons ("$\mu\mu$ + jets") are defined for the purpose of the background estimation, as described in Sec. 7.7.

6.4 Photons

Photons are identified according to the "tight" working point definition ($\sim$ 71 % efficiency) of the simple cut-based photon identification algorithm [19] and required to be well isolated. A PF-based isolation is used with a cone size $\Delta R < 0.3$ and ρ x A_{eff} corrections are applied to remove the effects of pileup [20]. Table 19 summarises the identification and isolation selection used.

Photons are vetoed in the definition of the hadronic signal region, as described in Sec. 7.1, while a control region with one photon ("γ + jets") is defined for the purpose of the background estimation, as described in Sec. 7.11.

Table 19: Photon identification ("tight" working point).

Categories	Barrel	EndCap
Conversion safe electron veto	Yes	Yes
Single Tower H/E	0.05	0.05
$\sigma_{i\eta i\eta}$	0.01	0.0267
PF charged hadron isolation	0.91	0.65
PF neutral hadron isolation	$0.33 + e^{0.0044\times p_{\mathrm{T}}^{\gamma}+0.5809}$	$0.93 + e^{0.0040\times p_{\mathrm{T}}^{\gamma}+0.9402}$
PF photon isolation	$0.61 + 0.0043 \times p_{\mathrm{T}}^{\gamma}$	$0.54 + 0.0041 \times p_{\mathrm{T}}^{\gamma}$

6.5 Electrons

Electrons are identified according to the "loose" working point definition ($\sim$ 90 % efficiency) of the cut-based identification [21] for the purpose of the electron veto in the signal region, while the "tight" working point ($\sim$ 70 % efficiency) is used for the selection of electron in the corresponding control regions.

Electrons are also require required to be well isolated. Similar to muons, in the hadronic signal regions, a PF-based isolation [20] is used with a cone size determined by the mini isolation algorithm (see Sec. 6.3) and $\Delta\beta$ corrections are applied to remove the effects of pileup.

Table 20 summarises the identification and isolation selection used for the PHYS14 exercise. In the future it is intended to move to a ρ x A_{eff} pileup correction method as recommended by the electron POG.

Electrons are vetoed in the definition of the hadronic signal region, as described in Sec. 7.1.

6.6 Single isolated tracks

A single isolated track (SIT) can be used to identify W bosons through their leptonic decays: $\mathrm{W} \to \mu\nu$, $\mathrm{W} \to e\nu$, and $\mathrm{W} \to \tau(\to l)\,\nu$. Single prong decays of the tau lepton can also be identified: $\mathrm{W} \to \tau\,(\to \mathrm{h}^{\pm} + \mathrm{n}\pi^{0})\,\nu$. A single isolated track comprises a charged PF candidate with $p_{\mathrm{T}} > 10\,\mathrm{GeV}$, $\Delta z(\mathrm{track}, \mathrm{PV}) < 0.05\,\mathrm{cm}$ and with a relative isolation smaller than 0.1, where the isolation is determined from the sum of the p_{T} of the charged PF candidates within $\Delta R < 0.3$.

SIT are vetoed in the definition of the hadronic signal region, as described in Sec. 7.1.

DRAFT

Table 20: Electron identification ("tight" working point).

Categories	Barrel	EndCap
$\Delta\eta_{In}$	0.00926	0.00724
$\Delta\phi_{In}$	0.0336	0.0918
$\sigma_{i\eta i\eta}$	0.0101	0.0279
H/E	0.0597	0.0615
d0 (vtx)	0.0111	0.0351
dZ (vtx)	0.0466	0.417
$\lvert(1/E_{\mathrm{ECAL}} - 1/p_{\mathrm{trk}})\rvert$	0.012	0.00999
Mini-Iso PF relative isolation	0.1	0.1
Rel-Iso PF relative isolation	0.0354	0.0646
Missing hits	2	1

6.7 Missing transverse momentum

Missing transverse momentum ($E_{\mathrm{T}}^{\mathrm{miss}}$) is defined as the opposite of the vector sum of the transverse momentum of all particle-flow candidates in the event. The Type-I $E_{\mathrm{T}}^{\mathrm{miss}}$ correction [22] is applied, i.e., the transverse momentum of the particle-flow candidates clustered as jets are replaced with the transverse momentum of the jets that are scaled by the jet energy correction factors.

The $E_{\mathrm{T}}^{\mathrm{miss}}$ is used in the definition of the transverse mass, M_T, which is in turn used as part of the selection criteria that define the single muon control sample (Sec. 7.7), and to define a cleaning filter applied after the α_T requirement, as described in Sec. 7.

DRAFT

7 Event selection for signal and control regions

This section first outlines the set of "pre-selection" requirements that are common to all signal and control regions, before defining the selection criteria that are specific to each region.

7.1 Pre-selection

Removing instrumental sources of "fake" $E_{\mathbf{T}}^{\mathrm{miss}}$.

A number of beam- and detector-related effects can induce significant $E_{\mathrm{T}}^{\mathrm{miss}}$. Examples include beam halo, reconstruction failures, spurious detector noise, or event misreconstruction due to detector inefficiencies. These events, with large, non-physical values of $E_{\mathrm{T}}^{\mathrm{miss}}$, are rejected with high efficiency by applying a range of dedicated vetoes. All "MET filters" recommended by the JetMET POG and SUSY PAG are applied by default in this analysis and listed in Table 21.

Jet requirements.

Jets considered in the analysis are required to satisfy $p_{\mathrm{T}} > 40\,\mathrm{GeV}$ and $|\eta| < 3.0$. Events containing jets in the forward region that satisfy the requirements $p_{\mathrm{T}} > 40\,\mathrm{GeV}$ and $|\eta| > 3.0$ are rejected in order to control background contributions from SM processes, without introducing a significant reduction in signal acceptance. The jets that are selected are used in the calculation of all jet-based event-level variables, such as H_{T}, $H_{\mathrm{T}}^{\mathrm{miss}}$, and α_{T}.

Raised p_{T} thresholds and tighter η requirements on the lead jets are also required. The lead jet is required to satisfy $p_{\mathrm{T}} > 100\,\mathrm{GeV}$ and $|\eta| < 2.5$. This helps to ensure high trigger efficiencies, but also helps to improve the S/B for a wide range of models with respect to SM processes, such as V + jets production. Events are then classified based on the second leading jet. In the case that a second leading jet satisfies $p_{\mathrm{T}} > 100\,\mathrm{GeV}$ events are assigned to a "symmetric" n_{jet} category. If the second jet satisfies $40 < p_{\mathrm{T}} < 100\,\mathrm{GeV}$ events are assigned to an "asymmetric" n_{jet} category. Finally, if there is no second leading jet with $p_{\mathrm{T}} > 40\,\mathrm{GeV}$, events are assigned to the "mono-jet" category. The asymmetric and mono-jet categories have been added to the analysis to help improve acceptance to a range of DM models and compressed SUSY.

Event categorisation according to $n_{\mathbf{jet}}$ and n_{b}.

Events in the hadronic signal and all control regions (described below) are categorised identically and according to the number of jets (n_{jet}) reconstructed in each event and the number of jets identified as originating from bottom quarks (n_{b}) in each event. As a baseline, the resulting sub-samples comprise events containing exactly one, two, three, four, or at least five jets. These are further split into "monojet" (only in the $n_{\mathrm{jet}} = 1$ case), "symmetric" or "asymmetric" n_{jet} categories according to the second leading jet p_{T}, as defined above.

Events are also categorised according to the the number of b-tagged jets ("b-jets"). As a baseline, the sub-samples are defined by requiring exactly zero, one, two, or at least three b-tagged jets. By construction, $n_{\mathrm{b}} \leq n_{\mathrm{jet}}$. Events containing three or more b-tags typically implies either an additional source of b-jets beyond those from the $\mathrm{t\bar{t}}$ process (e.g. via gluon splitting) or at least one mistag of a jet from a light-flavoured parton. The number of b-tagged jets is currently taken directly from simulation.

H_{T},$H_{\mathrm{T}}^{\mathrm{miss}}$ requirements and binning.

Events are required to have significant hadronic activity by requiring $H_{\mathrm{T}} > 200\,\mathrm{GeV}$. Despite an increase in both multijet production cross sections and pileup in Run 2, the lowest H_{T} threshold is kept at the same value of the Run 1 analysis [4] in order to maintain acceptance to DM models or compressed SUSY. Events in all samples are binned identically, according to the H_{T}

DRAFT

variable. The choice of binning in H_T is driven primarily by the trigger strategy employed by the analysis, as described in Section 5, and can be summarised as follows: 50 GeV bins in the range $200 < H_T < 400$ GeV, 100 GeV bins in the range $400 < H_T < 600$ GeV, a 200 GeV bin $600 < H_T < 800$ GeV and a final inclusive bin $H_T > 800$ GeV.

Events are also required to have appreciable missing hadronic energy by requiring $H_T^{miss} > 130$ GeV. This ensures that all events used within the analysis have a degree of missing energy similar to that required in the signal region via an α_T cut. This is outlined in Sec. 7.3.

The lower threshold of the last (inclusive) H_T bin is not forced to 800 GeV, it is instead determined independently for each (n_{jet},n_b) event category and is chosen to always align with one of the "default" boundaries defined above. The metric for choosing the final bin threshold is based on the number of events in the corresponding event category and H_T bin of the data control samples. This ensures that all bins in the data control samples are sufficiently populated to ensure a statistically significant prediction in each of the corresponding signal region bins. Currently, this is achieved by requiring at least 10 predicted events in each H_T and n_{jet} category of the control regions along with the requirement that there is at least one observed event per $n_b$category. If this is not the case, events from high H_T bins are combined into a single inclusive bin that satisfies this metric. This metric ensures that there are sufficient events in the control samples to probe for potential systematic effects with closure tests between simulation and data, as described in Sec. 12.

Table 21: Summary of the pre-selection criteria.

Selection	Requirement
"MET filters"	Primary Vertex, CSC Beam Halo, HBHE Noise and Isolation, ECAL Endcap SC Noise
Jet acceptance	$p_T > 40$ GeV, $\|\eta\| < 3$
Lead jet acceptance	$p_T > 100$ GeV, $\|\eta\| < 2.5$
Second jet acceptance	$p_T > 100$ GeV OR $40 < p_T < 100$ GeV
Loosest H_T requirement	$H_T > 200$ GeV
Loosest H_T^{miss} requirement	> 130 GeV
Baseline H_T binning	200–250, 250–300, 300–350, 350–400, 400–500, 500–600, 600–800, >800 GeV
Baseline n_{jet} multiplicities	1 (mono-jet), 2, 3, 4, ≥5 (both symmetric and asymmetric)
Baseline $n_b$multiplicities	0, 1, 2, ≥ 3 ($n_b \leq n_{jet}$)

Summary of pre-selection requirements.

Table 21 summarises the pre-selection requirements and default categorisation and binning scheme. The threshold of the final H_T bin per (n_{jet},n_b) category is summarised in Table 22. An identical scheme is used for the signal region and all control regions. No extrapolation is performed in the variables n_{jet}, n_b, and H_T in this analysis. For each of the signal and control regions, thirty event categories are considered, each with up to seven bins in H_T, assuming an integrated luminosity of 1.28fb^{-1}.

Table 22: Threshold (GeV) of the final H_T bin as a function of event category (n_{jet},n_b), which is always aligned with respect to one of the baseline boundaries (motivated primarily by the trigger) of 200, 250, 300, 350, 400, 600, 800 GeV.

n_{jet}	2			3				4				≥ 5			
n_b	0	1	2	0	1	2	3	0	1	2	≥ 3	0	1	2	≥ 3
Symmetric	800	800	800	800	800	800	500	800	800	800	800	800	800	800	800
Asymmetric	600	600	600	600	600	600	400	600	600	600	500	600	600	600	500

DRAFT

7.2 Lepton and photon vetoes

To select a sample of events in the hadronic final state and to suppress SM processes with genuine $E_{\mathrm{T}}^{\mathrm{miss}}$ from neutrinos, events containing an isolated electron with $p_{\mathrm{T}} > 10\,\mathrm{GeV}$ and $|\eta| < 2.5$ or an isolated muon with $p_{\mathrm{T}} > 10\,\mathrm{GeV}$ and $|\eta| < 2.5$ are vetoed. Further, to reduce the "lost leptons" backgrounds from $\mathrm{W}+$jets and $\mathrm{t\bar{t}}$, events containing single isolated tracks with $p_{\mathrm{T}} > 10\,\mathrm{GeV}$ and $|\eta| < 2.5$, as defined in Sec. 6, are vetoed as part of the signal region selection criteria. In the case of the single and di-lepton control samples, a further requirement is made such that events are not vetoed due to the presence of a track from the well identified leptons, by requiring $\Delta R(\mathrm{track}, \mathrm{lepton}) > 0.02$.

Finally, to select a purely hadronic topology and to allow for a orthogonal control region, events are vetoed in which an isolated photon with $p_{\mathrm{T}} > 25\,\mathrm{GeV}$ and $|\eta| < 2.5$ is identified.

7.3 The hadronic signal region

The lepton and photon vetoes are applied to select hadronic final states. All pre-selection criteria are also applied. Following these selections, the multijet background from QCD is still several orders of magnitude larger than the typical signal expected from SUSY.

H_{T}-dependent α_{T} requirements.

Background events from multijet production populate the region $\alpha_{\mathrm{T}} \lesssim 0.5$ and therefore can be rejected with very high efficiency by requiring an appropriate cut on α_{T}. In the Run 1 analyses, a minimum requirement of $\alpha_{\mathrm{T}} > 0.55$ was imposed, with a raised threshold (as high as 0.65) used at low H_{T} to control against a potential increase in contamination from multijet production due to worsening resolution and jet p_{T} threshold effects. (The latter effect refers to "fake" $H_{\mathrm{T}}^{\mathrm{miss}}$ arising from the rare occurrence of multiple soft jets below threshold that are relatively collinear.) The minimum threshold of 0.55 was motivated primarily by the control of the multijet background and considered conservative for mid to high regions in H_{T}, while maintaining good signal acceptance. However, improving jet resolutions and a reduced jet threshold effect relative to an increasing H_{T} scale means that looser α_{T} thresholds can be used at higher values of H_{T}.

A useful approximate conversion between α_{T} and $H_{\mathrm{T}}^{\mathrm{miss}}$ can be obtained by calculating α_{T}, as described by Eq. 4, while forcing $\Delta H_{\mathrm{T}} = 0\,\mathrm{GeV}$,. Hence, using this metric, the dependence of the α_{T} requirement as a function of the H_{T} bin can be determined such that the effective requirement on $H_{\mathrm{T}}^{\mathrm{miss}}$ is comparable, i.e. roughly constant, across all H_{T} bins. The values typically fall in the range $\sim 110 < H_{\mathrm{T}}^{\mathrm{miss}} <\sim 160\,\mathrm{GeV}$. This approximate levelling of the "effective" $H_{\mathrm{T}}^{\mathrm{miss}}$ threshold implies increasingly tighter requirements against instrumental effects versus H_{T}, while maximising signal acceptance. Table 23 summarises the expected α_{T} thresholds and corresponding "effective" $H_{\mathrm{T}}^{\mathrm{miss}}$ thresholds for each H_{T} bin. The α_{T} threshold is dependent only on H_{T} and not on n_{jet} nor n_{b}that are used to define the event categories.

Table 23: α_{T} and corresponding "effective" $H_{\mathrm{T}}^{\mathrm{miss}}$ (GeV) thresholds versus lower bound of H_{T} bin. For all H_{T} bins satisfying $H_{\mathrm{T}} > 800\,\mathrm{GeV}$, the direct requirement of $H_{\mathrm{T}}^{\mathrm{miss}} > 130\,\mathrm{GeV}$ is imposed rather than a requirement on α_{T}. No α_{T} requirement is imposed in the monojet bins.

H_{T}	200	250	300	350	400	500	600
α_{T} threshold	0.65	0.60	0.55	0.53	0.52	0.52	0.52
"Effective" $H_{\mathrm{T}}^{\mathrm{miss}}$	$\sim$128	$\sim$138	$\sim$125	$\sim$123	$\sim$110	$\sim$138	$\sim$162

For Run 2, all signal region bins satisfying $H_{\mathrm{T}} > 800\,\mathrm{GeV}$ are seeded by the single-object `HLT_HT800` trigger, which is expected to be unprescaled. For these high H_{T} bins, no α_{T} thresh-

old is required, which removes the inefficiencies of this variable for high jet multiplicity events. Instead, the following $H_{\mathrm{T}}^{\mathrm{miss}} > 130\,\mathrm{GeV}$ requirement helps to control the multijet background along with the imposition of $\Delta\phi^*_{\mathrm{min}} > 0.5$ (described below).

$\Delta\phi^*_{\mathrm{min}}$ requirement.

Further, an additional powerful variable $\Delta\phi^*_{\mathrm{min}}$ is used to suppress multijet contamination due to both instrumental effects and semi-leptonic heavy-flavour decays with genuine $E_{\mathrm{T}}^{\mathrm{miss}}$ in the final state. The variable is determined as follows. The jet-based estimate of the missing transverse energy, $\vec{H}_{\mathrm{T}}^{\mathrm{miss}}$, is recomputed while ignoring one of the reconstructed jets (the "test" jet). The difference in the azimuthal angle between the recomputed $\vec{H}_{\mathrm{T}}^{\mathrm{miss}}$ and the "test" jet is then determined. This process is repeated for each jet in the event and the minimum of all the azimuthal differences, $\Delta\phi^*_{\mathrm{min}}$, is determined. For monojet events, the calculation is performed using all jets with $p_{\mathrm{T}} > 20\,\mathrm{GeV}$. The "test" jet whose subtraction from the calculation $\vec{H}_{\mathrm{T}}^{\mathrm{miss}}$ yields this minimum value, is identified as the jet that is most likely to have given rise to the missing transverse energy in the event. Events with significant $H_{\mathrm{T}}^{\mathrm{miss}}$ due to instrumental effects or heavy flavour decays populate the region $\Delta\phi^*_{\mathrm{min}} \approx 0$ and so candidate signal event are accepted only if they satisfy $\Delta\phi^*_{\mathrm{min}} > 0.5$. The use of the $\Delta\phi^*_{\mathrm{min}}$ and α_{T} variables provide an extremely powerful rejection factor against contamination from multijet events and allow to maintain low jet p_{T}, H_{T}, and $H_{\mathrm{T}}^{\mathrm{miss}}$ thresholds, which in turn maximises signal acceptance for a large range of DM and SUSY models with final states characterised by the presence of significant $E_{\mathrm{T}}^{\mathrm{miss}}$.

$H_{\mathrm{T}}^{\mathrm{miss}}/E_{\mathrm{T}}^{\mathrm{miss}}$ cleaning filter.

To protect against multiple jets failing the E_{T} threshold or falling out of detector acceptance, the jet-based estimate of the missing transverse energy, $H_{\mathrm{T}}^{\mathrm{miss}}$, is compared to the missing transverse energy variable, $E_{\mathrm{T}}^{\mathrm{miss}}$, and events with $R_{\mathrm{miss}} = H_{\mathrm{T}}^{\mathrm{miss}}/E_{\mathrm{T}}^{\mathrm{miss}} > 1.25$ are rejected.

Detector dead cell control.

Masked regions in the ECAL (which amount to about 1% of the ECAL channel count) or HCAL, or by missing instrumentation in the barrel-endcap gap, could cause severe energy losses. A data-driven method is developed to identify dead cells. The procedure is carried out on events that pass a loose selection of one good primary vertex, $n_{\mathrm{jet}} > 1$ and $H_{\mathrm{T}} > 150\,\mathrm{GeV}$. For each identified jet with $p_{\mathrm{T}} > 20\,\mathrm{GeV}$ in data, the azimuthal angle ($\Delta\phi_{jet}$) between the jet and the recomputed $\vec{H}_{\mathrm{T}}^{\mathrm{miss}}$ is determined, in the same way as in the procedure to compute the $\Delta\phi^*_{\mathrm{min}}$ variable. The positions of all jets which give $\Delta\phi^*_{\mathrm{min}} < 0.3$ are plotted in an $\eta - \phi$ map. Subsequently, the positions of all jets with $p_{\mathrm{T}} > 20\,\mathrm{GeV}$ are plotted in a second $\eta - \phi$ map. These two maps are then divided to form a 2D ratio map, taking the first map as the numerator and second as the denominator. Jets pointing to dead cells are likely to give $\Delta\phi^*_{\mathrm{min}} < 0.3$, so the location of dead cells in η and ϕ have higher values in this 2D ratio map.

Figure 6 is the 2D ratio map made with unblinded signal region with luminosity of 149.49 pb^{-1}. In the lower left region of the plot, two areas with significant instrumental effects are clear. To ensure these effects are filtered out by all cleaning cuts within the analysis, an $\eta - \phi$ map of all jets with $p_{\mathrm{T}} > 20\,\mathrm{GeV}$ and $\Delta\phi^*_{\mathrm{min}} < 0.3$ are plotted after the signal region selection (as described in Sec. 7.3), shown in Fig. 7. The areas with significant instrumental effects visible in Fig. 6 do not appear to remain in Fig. 7. This implies the current suite of cleaning cuts is enough to remove any localised detector effects.

Beam halo.

DRAFT

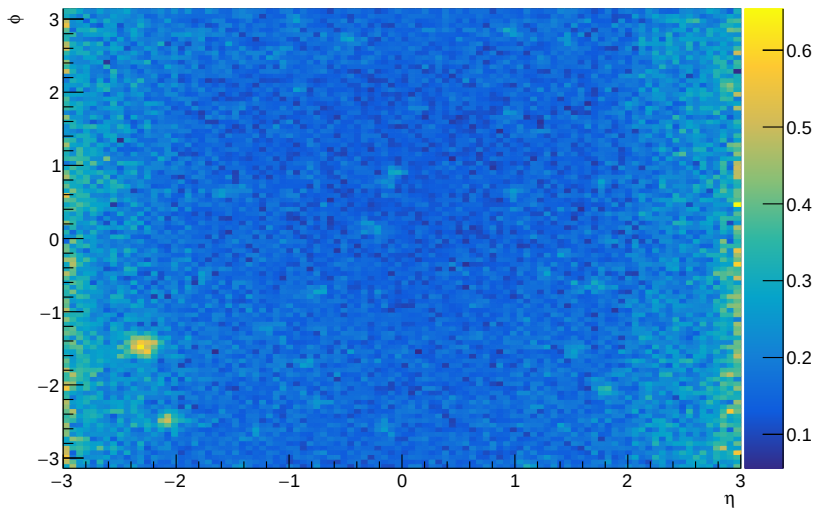

Figure 6: The 2D ratio of jets ($p_T > 20\,\text{GeV}$) with $\Delta\phi^*_{\text{min}} < 0.3$ plotted in the $\eta - \phi$ plane, divided by all jets that satisfy $p_T > 20\,\text{GeV}$. Made with 149.49 pb^{-1} of events that pass a loose selection of one good primary vertex, $n_{\text{jet}} > 1$ and $H_T > 150\,\text{GeV}$.

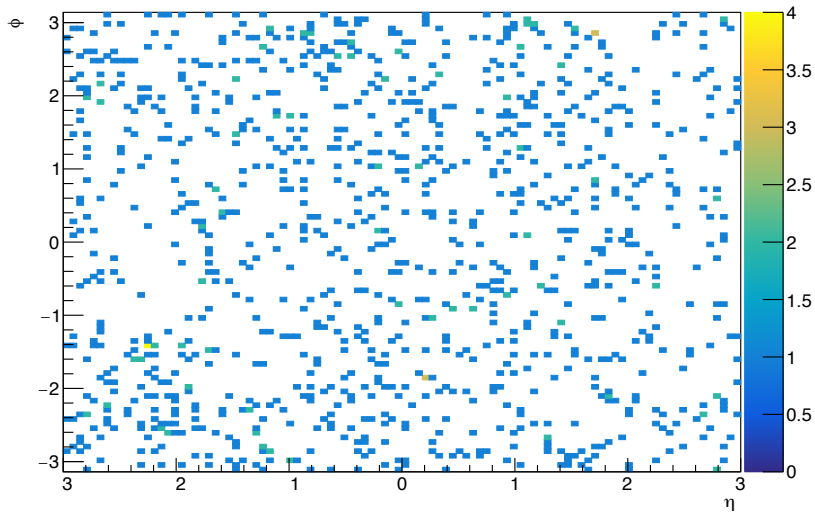

Figure 7: Jets ($p_T > 20\,\text{GeV}$) with $\Delta\phi^*_{\text{min}} < 0.3$ plotted in the $\eta - \phi$ plane. Made with 1.26fb^{-1} of events that pass the full signal region selection.

The CSC beam halo filter has been found to be less efficient during the early Run 2 data-taking period compared to the previous run.

Beam halo events manifest themselves as single energy deposits in the calorimeters, which introduces large amounts of "fake" E_T^{miss}. This effect is especially prominent in the signal region monojet category, particularly at ϕ coordinates of 0 and π because of the tendency of halo particles to lie within the plane of the LHC ring. This is evident in Fig. 8.

Such spurious events are suppressed by requiring at least 10% of the leading jet's energy to

originate from charged hadrons, $CHF > 0.1$. The effectiveness of this selection is demonstrated in Fig. 8.

Beyond the filter available in the data ntuples, the JetMET POG have provided lists of events that should fail the CSC beam halo and bad ECAL super cluster filters. These extra events are vetoed and the efficiency of events in the signal region (Sec. 7.3) and single muon control region (Sec. 7.7) that pass this veto for each analysis bin are plotted in Fig. 9. In the vast majority of bins the extra filters are 100% efficient, with a few bins with an inefficiency at the $2-3\%$ level. This confirms that the CHF cut is already effectively removing spurious events that are present due to beam halo effects.

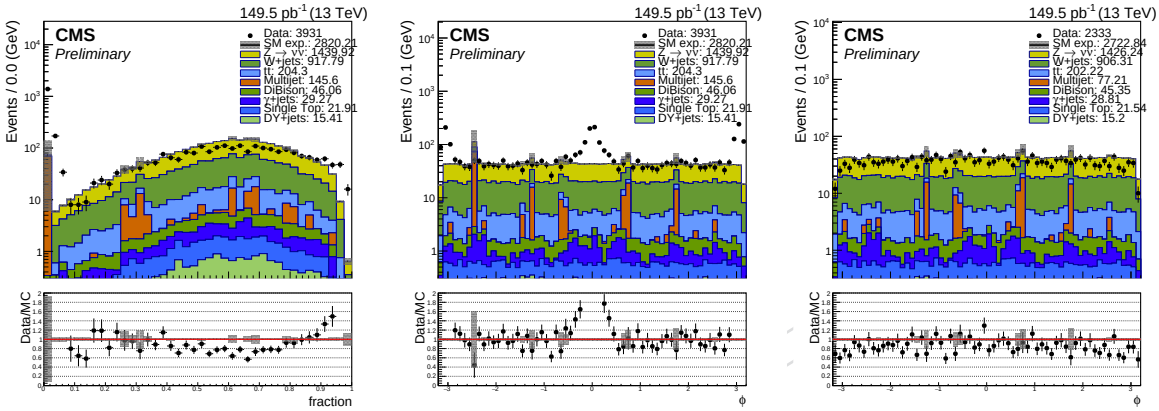

Figure 8: Distributions in the signal region of the lead jet charged hadron energy fraction (CHF) (Left), lead jet ϕ direction (Centre), and lead jet ϕ direction after applying a requirement of CHF > 0.1. The large excess in data at charged hadron fractions close to zero and $\phi = 0, \pi$ is consistent with beam halo effects, and is effectively suppressed by the aforementioned selection.

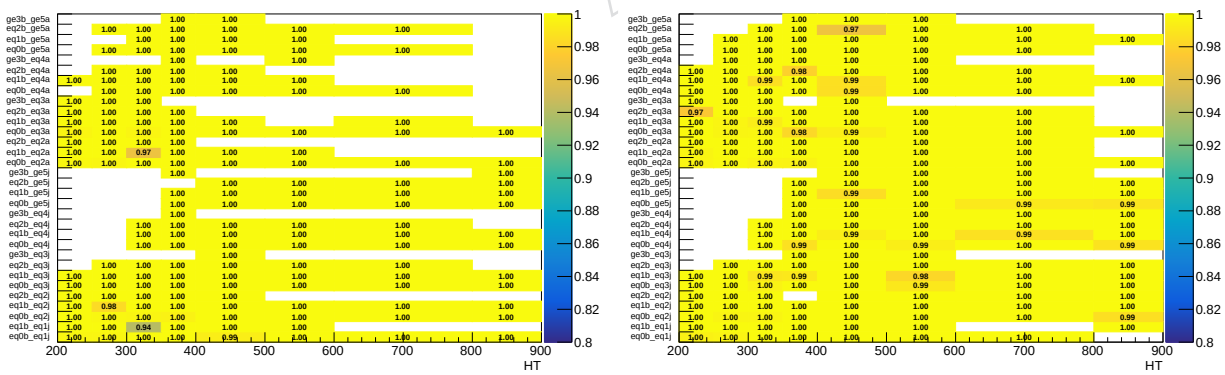

(a) Signal region selection (b) Single muon control region selection

Figure 9: Efficiencies of the CSC beam halo and bad ECAL super cluster filters applied on 1.26fb^{-1} of data passing the single muon and signal region selections.

Summary of signal region selection.

The requirements that define the hadronic signal region are summarised in Table 24.

Table 24: Summary of the signal region selection criteria, applied in addition to the preselection summarised in Table 21.

Selection	Requirement
α_T	>0.52–0.65 (H_T-dependent) for region $200 < H_T < 800$ GeV
$\Delta\phi^*_{min}$	> 0.5
H_T^{miss}/E_T^{miss}	< 1.25
"Dead ECAL filter"	(see text)
"Beam Halo Filter"	CHF(leading jet) > 0.1

7.4 Adding the H_T^{miss} dimension

As described above, and as used in Run 1, the analysis takes advantage of three discriminating variables, n_{jet}, n_b, and H_T, to provide sensitivity to a large range of SUSY (and DM) models. No extrapolation in these variables is performed, with predictions of SM background yields in the (n_{jet},n_b,H_T) bins of the signal region based on both observed counts and transfer factors derived from simulated yields in the corresponding (n_{jet},n_b,H_T) bins of the control samples. Each prediction is statistically and systematically independent.

In Run 1, for each (n_{jet},n_b,H_T) bin in the signal region, an extrapolation in the variable α_T was necessary to obtain background predictions based on the muon control samples, which did not impose any α_T requirement. No extrapolation in α_T was performed for the photon control sample, which used the same α_T requirements as the signal region. The α_T requirements used in Run 1 for the signal region correspond loosely to H_T^{miss} thresholds in the range $\sim$130 to $\sim$500 GeV depending on the H_T bin. Uncertainties in this extrapolation were determined through closure tests with respect to data, including one dedicated to the α_T extrapolation, plus additional cross checks.

In Run 2, we additionally bin event counts in the signal region according to the variable H_T^{miss} in order to provide further discriminating power between any potential signal and the SM background counts. Hence, while no extrapolation is performed in n_{jet}, n_b, nor H_T, the analysis relies on information obtained from simulation to extrapolate from counts (integrated over H_T^{miss}) in the control samples to a predicted distribution in H_T^{miss} for each corresponding (n_{jet},n_b,H_T) bin in the signal region.

The H_T^{miss} dimension is included in the likelihood model using templates determined per (n_{jet},n_b,H_T) bin from simulation. An associated normalisation nuisance is determined from closure tests between simulation and data, as described in Sec. 12. Alternative templates are used to encode the systematic uncertainty in the H_T^{miss} distribution obtained from simulation.

The templates use H_T^{miss} bins of 50 GeV in width. A metric is used to determine the threshold of the final H_T^{miss} bin used by the templates. This metric is currently based on requiring a minimum number of both observed counts in the *data control samples* and (unweighted) simulated events with H_T^{miss} values higher than the final bin threshold. While the counts in the (n_{jet} ,n_b ,H_T) bins of each data control sample are not be binned according to H_T^{miss} (as in the signal region), the former requirement ensures that there are sufficient events in each (n_{jet} ,n_b ,H_T) bin of the control samples to probe for potential systematic effects *across all bins in* H_T^{miss} using closure tests between simulation and data, as described in Sec. 12. Hence, a data-driven validation for potential biases and on the systematic uncertainty in the H_T^{miss} template is possible. The latter requirement minimises the statistical uncertainties associated with the finite number of simulated events for the various SM background processes. Both requirement are based on counts according to n_{jet} and $n_b$but inclusive with respect to n_b.

DRAFT

7.5 The hadronic control region

A hadronic control region that is enriched in multijet events and disjoint with respect to the signal region is obtained by applying both the pre-selection criteria and lepton/photon vetoes, as defined above, and inverting the (H_T-dependent) α_T and/or H_T^{miss}/E_T^{miss} requirements. The sample of events populating this control region are used primarily to estimate any residual background contamination from QCD multijet events, described in Sec. 10.

7.6 Commonalities between the data control regions

There are five control regions with leptons or photons in the final state: μ + jets, $\mu\mu$ + jets, and γ + jets. The full pre-selection is applied as part of the definition of each of these control regions. The cuts on event-level jet-based quantities are identical to those applied in the hadronic search region and the same n_{jet}, n_b, and H_T binning is used. The lepton(s) or photon is not considered in the calculation of the event-level variables.

The selection criteria of the various control regions are defined such that the background composition and event kinematics of the control regions mirror as closely as possible those for the signal region. This is done in order to minimise the reliance on the simulation to model correctly the backgrounds and event kinematics in the control and signal samples.

Two exceptions are made. First, no $\Delta\phi^*_{min}$ requirement is imposed as part of the selection criteria defining the control regions. Second, in the case of the four leptonic control regions, no requirement is made on α_T. This is made possible by the remaining kinematic selection criteria, which are sufficiently selective to ensure that the leptonic event samples remain rich in events from the W + jets, $t\bar{t}$ and $Z \to \ell\ell$ processes with negligible contamination from QCD multijet events. Thus, the acceptance of the leptonic control regions can be significantly increased, which simultaneously improves their predictive power and further reduces the effect of any potential signal contamination.

The lepton event samples can be used to predict components of the SM background across all H_T bins, while the γ + jets sample can only be used for the region $H_T > 400$ GeV due to the photon trigger requirements.

7.7 The μ + jets control sample

The selection criteria for the μ + jets sample are chosen to identify W bosons decaying to a muon and a neutrino in the phase-space of the signal. In order to select events containing W bosons, exactly one tight isolated muon within an acceptance of $p_T > 30$ GeV and $|\eta| < 2.1$ is required (due to the trigger), and the transverse mass of the W candidate must satisfy $30 < M_T(\mu, \not{E}_T^{PF}) < 125$ GeV (to suppress QCD multijet and potential signal events). Events are vetoed if $\Delta R(\mu, \text{jet}_i) < 0.5$ running over all jets i. The single isolated track veto, described in Sections 6 and 7.2, is also applied, which considers all single isolated tracks in the event except that associated with the identified, isolated muon. Finally, the cleaning cut H_T^{miss}/E_T^{miss} is also applied, as done in the signal region, where the E_T^{miss} is adjusted to account for the transverse momentum of the identified, isolated muon.

7.8 The $\mu\mu$ + jets control sample

The selection criteria are identical to those for the μ + jets sample, with the following exceptions that are tuned to identify Z bosons decaying to two muons in the kinematic phase space of the signal region. In order to select an event sample containing Z bosons, exactly two tight isolated muons within an acceptance of $p_T > 30$ GeV and $|\eta| < 2.1$ are required (due to the trigger). The

DRAFT

invariant mass of the two muons must satisfy $m_Z - 25 < M_{\mu_1\mu_2} < m_Z + 25$ and they must have opposite charge. Events are vetoed if $\Delta R(\mu_i, \text{jet}_j) < 0.5$ is satisfied, running over all muons i and all jets j. The single isolated track veto is also applied considering all single isolated tracks in the event except those associated with the two identified, isolated muons. Finally, the cleaning cut $H_\text{T}^\text{miss}/E_\text{T}^\text{miss}$ is also applied, as done in the signal region, where the E_T^miss is adjusted to account for the transverse momenta of the two identified, isolated muons.

7.9 The e + jets control sample

The selection criteria that define the e + jets control sample mirror those of the μ + jets sample, i.e., they are tuned to identify W boson decaying to an electron and a neutrino in the kinematic phase space of the signal region.

Electrons are required to satisfy the Tight working point and satisfy the requirements $p_\text{T} > 30\,\text{GeV}$ and $|\eta| < 2.1$. The tightening of the Loose working point defined in Sec. 6.5 was found to greatly reduce multijet contamination without a large reduction in statistics within the electron control samples. The transverse mass of the W candidate must satisfy $30 < M_\text{T}(e, \not{E}_\text{T}^\text{PF}) < 125\,\text{GeV}$.

7.10 The ee + jets control sample

The selection criteria that define the ee + jets control sample mirror those of the $\mu\mu$ + jets sample. They are tuned to identify Z boson decaying to a pair of electrons in the kinematic phase space of the signal region.

Both electrons need to satisfy Tight working point and the requirements $p_\text{T} > 30\,\text{GeV}$ and $|\eta| < 2.1$. The invariant mass of the two electrons must satisfy $m_Z - 25 < M_{e_1e_2} < m_Z + 25$ and they must have opposite charge.

7.11 The γ + jets control sample

The γ + jets sample is defined by requiring exactly one photon satisfying tight isolation criteria and within an acceptance of $p_\text{T} > 200\,\text{GeV}$ (limited by trigger requirements) and $|\eta| < 1.45$. Furthermore, events are vetoed if $\Delta R(\gamma, \text{jet}_i) < 1.0$ is satisfied, running over all jets i. One important difference with respect to the leptonic control samples is the application of the H_T-dependent α_T requirements imposed as part of the signal region definition. This is done primarily to ensure that the photon control sample and signal region are subject to identical kinematic requirements and the photon carries sufficient transverse energy so that the mass of the Z boson becomes a negligible effect when using the γ + jets sample to predict the kinematic distributions of the $\text{Z} \to \nu\bar{\nu}$ background. The cleaning cut $H_\text{T}^\text{miss}/E_\text{T}^\text{miss}$ is also applied, as done in the signal region, where the E_T^miss is adjusted to account for the transverse energy of the identified, isolated photon. As stated above, the γ + jets sample can only be used to predict background components in the region $H_\text{T} > 400\,\text{GeV}$ due to trigger requirements.

DRAFT

8 Corrections to cross section for SM samples

The cross sections for the most relevant SM background are summarised in Table 25.

Table 25: Cross sections for the main SM backgrounds.

Sample	Cross section (pb)	Accuracy	K-factor
W+jets, $100 < H_T < 200$ GeV	1347 ± 2	LO	1.21
W+jets, $200 < H_T < 400$ GeV	360 ± 1	LO	1.21
W+jets, $400 < H_T < 600$ GeV	48.9 ± 0.17	LO	1.21
W+jets, $600 < H_T < 800$ GeV	12.8 ± 0.4	LO	1.21
W+jets, $800 < H_T < 1200$ GeV	5.26 ± 0.19	LO	1.21
W+jets, $1200 < H_T < 2500$ GeV	1.33 ± 0.05	LO	1.21
W+jets, $H_T > 2500$ GeV	0.0309 ± 0.0011	LO	1.21
DY+jets, $100 < H_T < 200$ GeV	139 ± 4	LO	1.23
DY+jets, $200 < H_T < 400$ GeV	42.8 ± 1.4	LO	1.23
DY+jets, $400 < H_T < 600$ GeV	5.5 ± 0.2	LO	1.23
DY+jets, $H_T > 600$ GeV	2.2 ± 0.8	LO	1.23
γ+jets, $40 < H_T < 100$ GeV	20730 ± 66	LO	-
γ+jets, $100 < H_T < 200$ GeV	9226 ± 36	LO	-
γ+jets, $200 < H_T < 400$ GeV	2281 ± 47	LO	-
γ+jets, $400 < H_T < 600$ GeV	273 ± 9	LO	-
γ+jets, $H_T > 600$ GeV	94.5 ± 3.2	LO	-
$Z \to \nu\nu$+jets, $100 < H_T < 200$ GeV	280.47	LO	1.23
$Z \to \nu\nu$+jets, $200 < H_T < 400$ GeV	78.36	LO	1.23
$Z \to \nu\nu$+jets, $400 < H_T < 600$ GeV	10.94	LO	1.23
$Z \to \nu\nu$+jets, $H_T > 600$ GeV	4.20	LO	1.23
TTJets	831.76^{+20}_{-30}	NNLO	-

In the high-H_T, high-$\not{E}_T$ corner of the phase space used in this search, the normalisations of the MC samples do not necessarily agree with the observation. Moreover, the cross section is known only to a limited number of perturbative orders and additional corrections could be in principle sizeable.

Nonetheless, the analysis strategy for the background predictions is built in such a way to be mildly, if not negligibly, dependent on these corrections. The backgrounds are in fact estimated from control regions in data, and the effect of cross section corrections on the transfer factors is expected to largely cancel out, because the background composition is very similar between the signal region and the control regions used to estimate each background.

However, the effect could be sizeable for the closure test procedure described in Sec. 12.1, because in this case much more "extreme" translations are done. For instance, the test carried on in the single muon control sample, where events with no b-tags are used to predict events with 1 b-tag maps a W-enriched sample to a $t\bar{t}$-enriched one and is sensitive to the relative corrections of W with respect to $t\bar{t}$. For this reason it's important to measure any residual cross section corrections. This is done using sidebands in data enriched in a specific process, as described in the following.

8.1 Correction to the γ+jets sample

The situation is somehow different for γ+jets with respect to the other processes. Infact the cross section for this process is known only at LO and no k-factor has been calculated yet for 13 TeV, so a worse agreement is expected for the yields in the single photon control region. The observation confirms indeed this hypothesis, with the simulation underestimating the yields by $\sim 20\%$.

A correction is derived using a sideband in data, by selecting events in the region $350 < H_T < 400$ GeV. The data yields are corrected for the small QCD contamination (taken from MC) and

DRAFT

divided by the expected number of events in the simulation. The sideband is shown in Fig. 10 (left). The correction factor to be applied to the GJets sample found with this procedure is 1.30 ± 0.08, which is in fair agreement with the $k-$factor used in the 8 TeV analysis (~ 1.21).

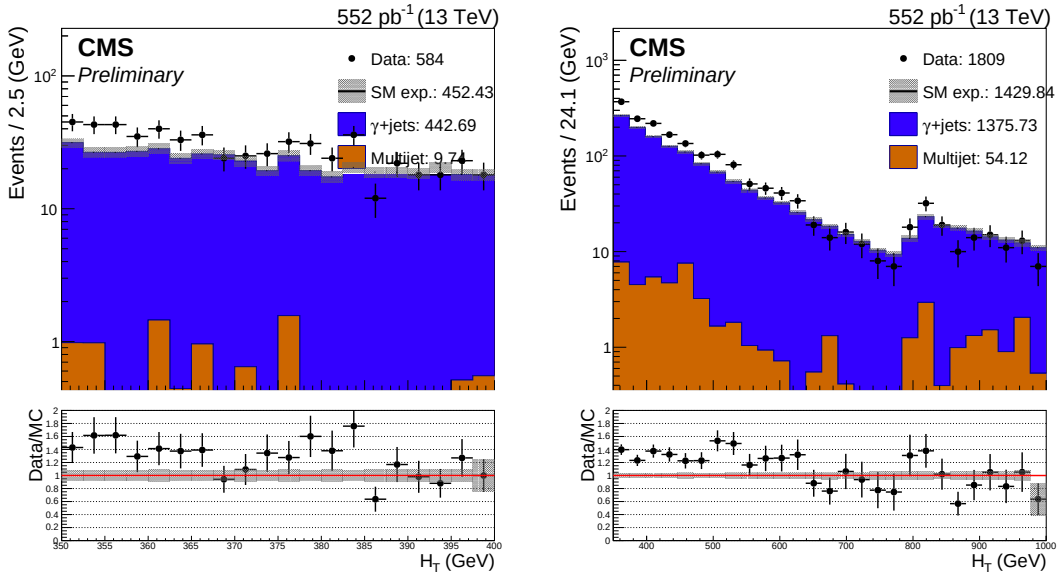

Figure 10: The single photon events compared to the MC expectation in the sideband $350 < H_T < 400$ GeV (left) and in the full H_T range (right)

8.2 Correction to the W+jets, $t\bar{t}$+jets and Z+jets samples

For the W+jets, $t\bar{t}$+jets and Z+jets samples we expect smaller corrections, because the cross section is known with better accuracy, either by complete calculation or via k-factors applied to the LO cross section. For this reason, the use of a sideband in H_T is not optimal in this case, since it is more sensitive to the modelling of the H_T shape in the LO MC samples (we plan to cross-check with NLO samples in the future). The low-H_T sideband is suboptimal in particular for $t\bar{t}$, because it selects events with a rare topology for this kind of process, which comes with larger jet multiplicities and thus large value of H_T.
Instead, the $H_T^{miss}/E_T^{miss} > 1.25$ sideband is used, with the following selection:

- $\mathrm{W+jets}$: single muon, $n_{jet} = 2, 3$, $n_b = 0$
- $\mathrm{Z+jets}$: double muon, $n_{jet} = 2, 3$, $n_b = 0$
- $\mathrm{t\bar{t}+jets}$: single muon, $n_{jet} \geq 2$, $n_b \geq 2$

These selections give a purity of 78%, 96% and 92% respectively for $\mathrm{W+jets}$, $\mathrm{Z+jets}$ and $\mathrm{t\bar{t}+jets}$. All contaminations are estimated from MC.
The H_T^{miss}/E_T^{miss} distributions for these three selection are shown in Fig. 11.
These distributions are not very well modelled by the simulation, pointing to possible reconstruction effects not yet understood in this first stage of data commissioning. The $\mathrm{t\bar{t}+jets}$ enriched distribution (right) also confirms the effect of missing b-tag scale factors, whose effect is also seen in the $n_b$distribution.

Given these features of the MC modelling, no conclusive correction is derived from the following studies. However, a preliminary investigation on the H_T dependence of MC corrections is presented, with the aim of repeating it in the near future, where a better understanding of the detector will be available.

DRAFT

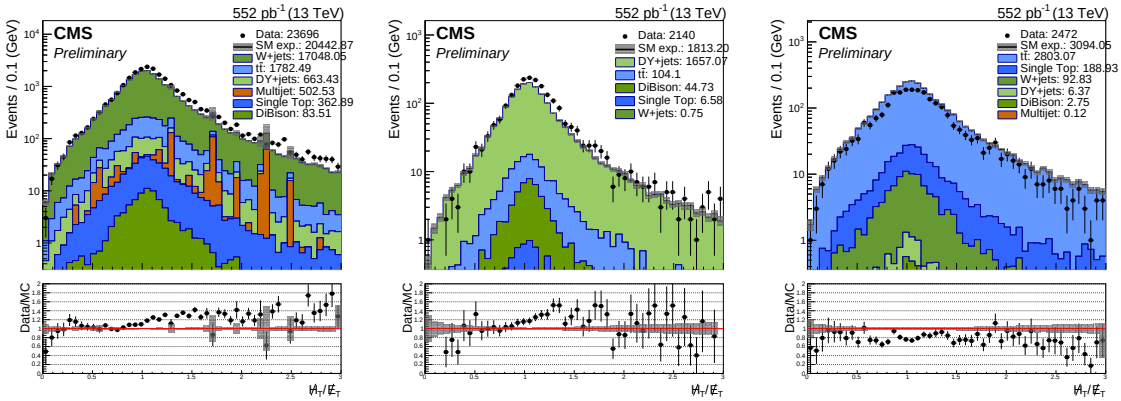

Figure 11: The "N-1" distribution of H_T^{miss}/E_T^{miss} for the W + jets (left), Z + jets (center) and $t\bar{t}$ + jets (right) selection.

In Fig. 12, the correction factor derived from the H_T^{miss}/E_T^{miss} sideband is extracted in coarse bins in H_T for the 3 processes. Since the analysis is sensitive to relative corrections rather than absolute ones, the 3 ratios of correction factors are showed in Fig. 13. They are compatible with flat within the statistical uncertainties. Therefore any H_T dependence approximately cancels out in the ratio of transfer factors, thus any correction would have a negligible impact.
For an inclusive correction, as stated previously, a better understanding of detector effects is required and thus this study is postponed.

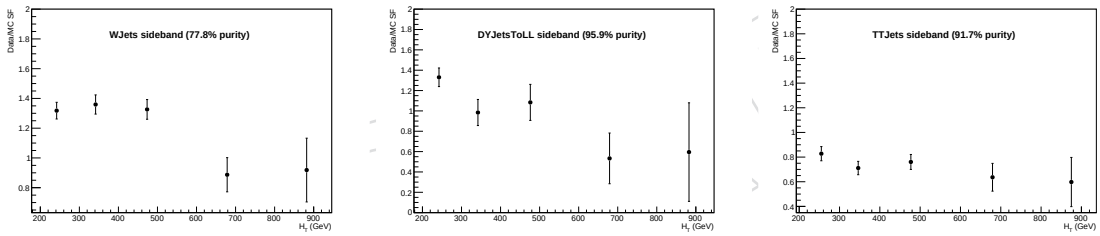

Figure 12: The correction factor as a function of H_T for the W + jets (left), Z + jets (center) and $t\bar{t}$ + jets (right) selection.

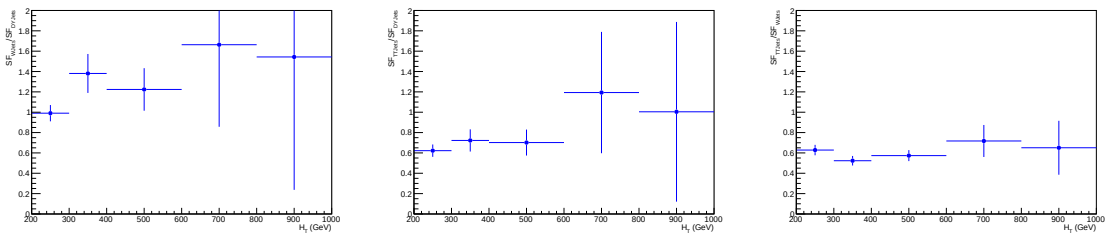

Figure 13: The ratio of correction factors as a function of H_T: W + jets/Z + jets (left), $t\bar{t}$ + jets/Z + jets (center) and $t\bar{t}$ + jets/W + jets (right).

9 Characterisation of the signal and control regions

The event selection criteria for the signal and control regions are detailed in Sec. 7. A selection of relevant data/MC comparison plots are presented here. The distributions are shown separetely according three n_{jet} categories: symmetric, asymmetric, and monojet. The distributions are intended to provide a qualitative understanding of the simulation modelling for key variables. However, the analysis is not sensitive due the reliance on simulation via ratios only (i.e. transfer factors) and the one-to-one mapping of (n_{jet}, n_{b}, H_{T}) binning between the control and signal regions. The simulated distributions are normalized to an integrated luminosity of 1280.2 fb^{-1} (the data/MC scale factors are also shown in all plots).

In addition to distributions, the binned yields in the μ + jets, $\mu\mu$ + jets, and γ + jets control samples can be found in Tables 26-28, 29-31, and 32-34, respectively, which correspond to an integrated luminosity of 1.28 fb^{-1}. (Projected yields for 3fb^{-1} are found in App. H.) Finally, Tables 35, 36 and 37 summarise the expected yields, as determined from simulation, in the signal region for an integrated luminosity of 1.28 fb^{-1}.

DRAFT

9.1 Yields and distributions for the μ + jets control sample

Table 26: Yields in the μ + jets control region for 1.26fb^{-1} for symmetric categories. The letter "a" in jet e.g. "2a" indicates the asymmetric jet bins. All entries are non-zero but are truncated to one decimal place.

H_T (GeV) (n_{jet}, n_b)	200-250	250-300	300-350	350-400	400-500	500-600	600-800	800-∞
(2, 0)	271	410	397	301	368	180	136	74
(2, 1)	44	46	37	37	40	29	20	12
(2, 2)	1	1	1	–	5	2	3	1
(3, 0)	1	103	253	230	406	216	180	104
(3, 1)	1	46	99	107	143	57	51	15
(3, 2)	–	14	39	34	34	18	11	3
(3, ≥ 3)	–	–	–	2	2	1	–	–
(4, 0)	–	–	26	77	203	163	166	84
(4, 1)	–	–	27	70	157	92	78	38
(4, 2)	–	–	4	37	68	32	37	18
(4, ≥ 3)	–	–	–	2	5	4	1	1
(≥ 5, 0)	–	–	–	6	56	70	111	91
(≥ 5, 1)	–	–	–	6	67	83	108	91
(≥ 5, 2)	–	–	–	5	33	52	61	35
(≥ 5, ≥ 3)	–	–	–	–	3	3	8	3

Table 27: Yields in the μ + jets control region for 1.26fb^{-1} for asymmetric categories. The letter "a" in jet e.g. "2a" indicates the asymmetric jet bins. All entries are non-zero but are truncated to one decimal place.

H_T (GeV) (n_{jet}, n_b)	200-250	250-300	300-350	350-400	400-500	500-600	600-800	800-∞
(2a, 0)	2726	1352	607	259	221	51	14	–
(2a, 1)	388	213	74	34	22	6	1	–
(2a, 2)	31	10	8	6	4	1	1	–
(3a, 0)	603	803	449	232	170	42	15	–
(3a, 1)	250	352	143	57	43	10	4	–
(3a, 2)	76	87	45	27	11	3	2	–
(3a, ≥ 3)	1	4	2	–	1	–	–	–
(4a, 0)	6	102	170	119	73	20	6	–
(4a, 1)	6	58	148	91	76	13	6	–
(4a, 2)	2	36	64	48	28	3	4	–
(4a, ≥ 3)	–	2	4	3	3	1	–	–
(≥ 5a, 0)	–	–	10	37	57	15	7	–
(≥ 5a, 1)	–	–	14	39	65	27	6	–
(≥ 5a, 2)	–	–	8	17	30	14	2	–
(≥ 5a, ≥ 3)	–	–	–	2	2	1	–	–

Table 28: Yields in the μ + jets control region for 1.26fb^{-1} for monojet categories. The letter "a" in jet e.g. "2a" indicates the asymmetric jet bins. All entries are non-zero but are truncated to one decimal place.

H_T (GeV) (n_{jet}, n_b)	200-250	250-300	300-350	350-400	400-500	500-600	600-800	800-∞
(1, 0)	2466	899	360	165	148	53	20	–
(1, 1)	120	46	15	7	6	1	0	–

DRAFT

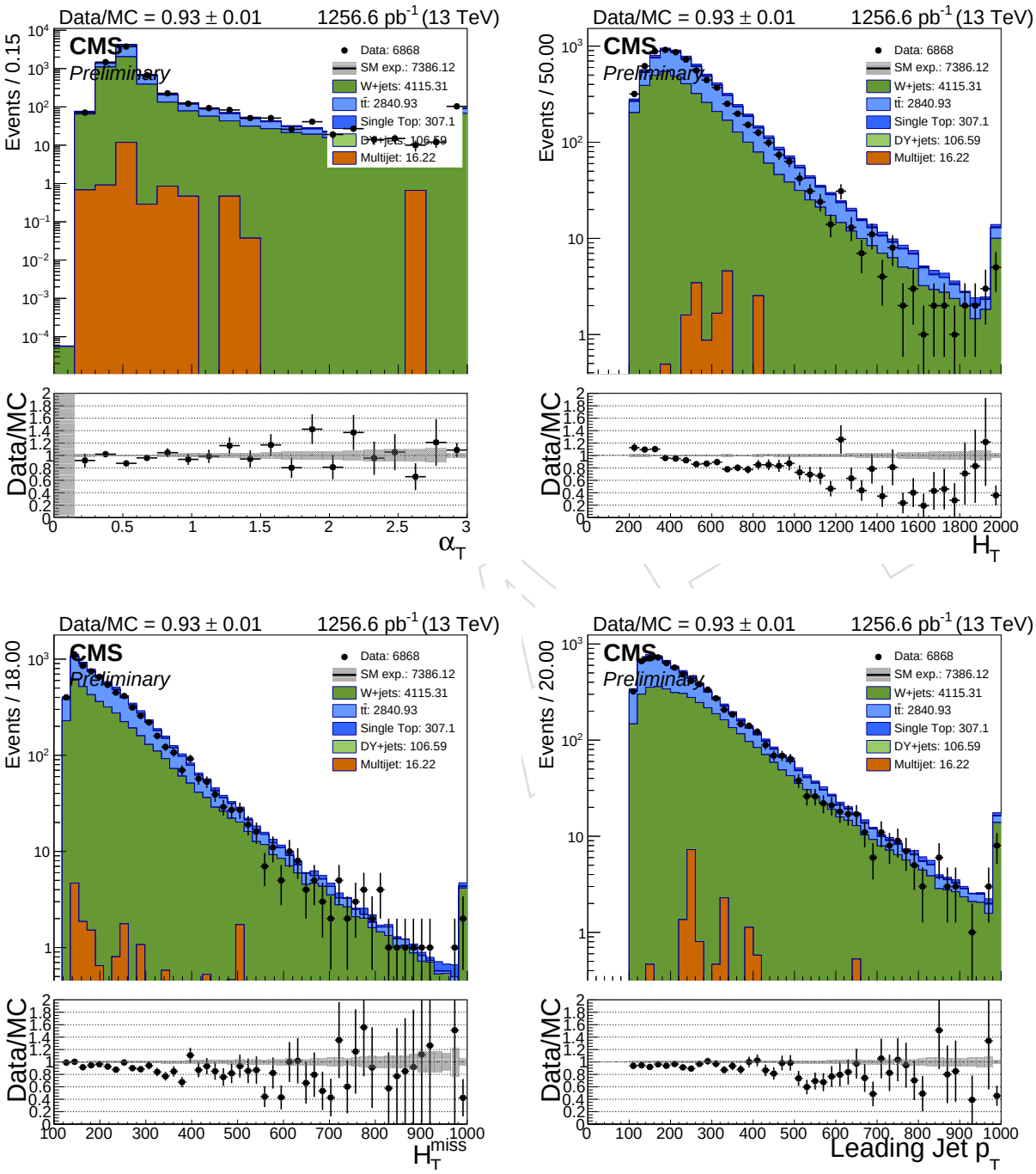

Figure 14: Key analysis variables for single muon control region (symmetric n_{jet} bins)

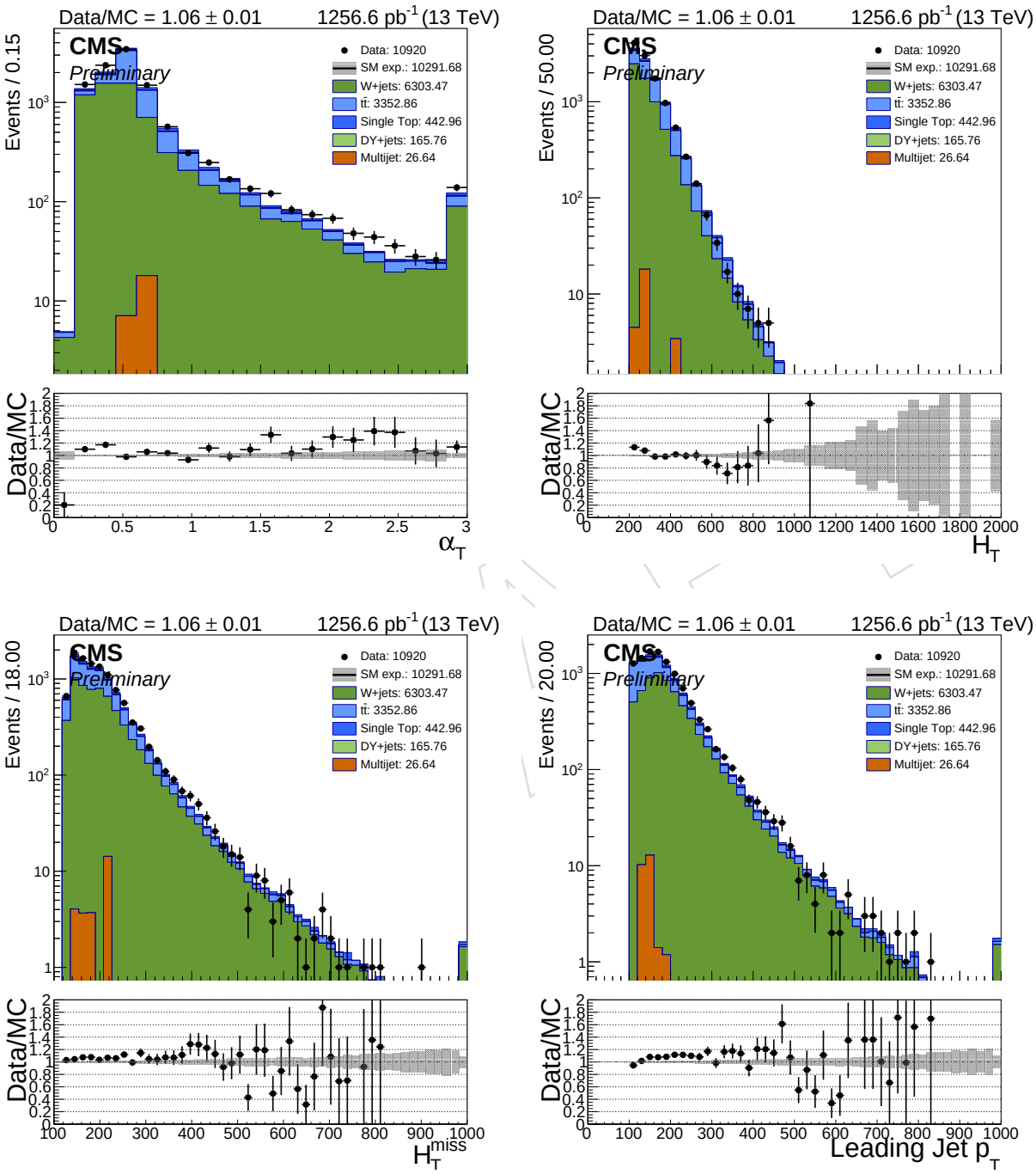

Figure 15: Key analysis variables for single muon control region (asymmetric n_{jet} bins)

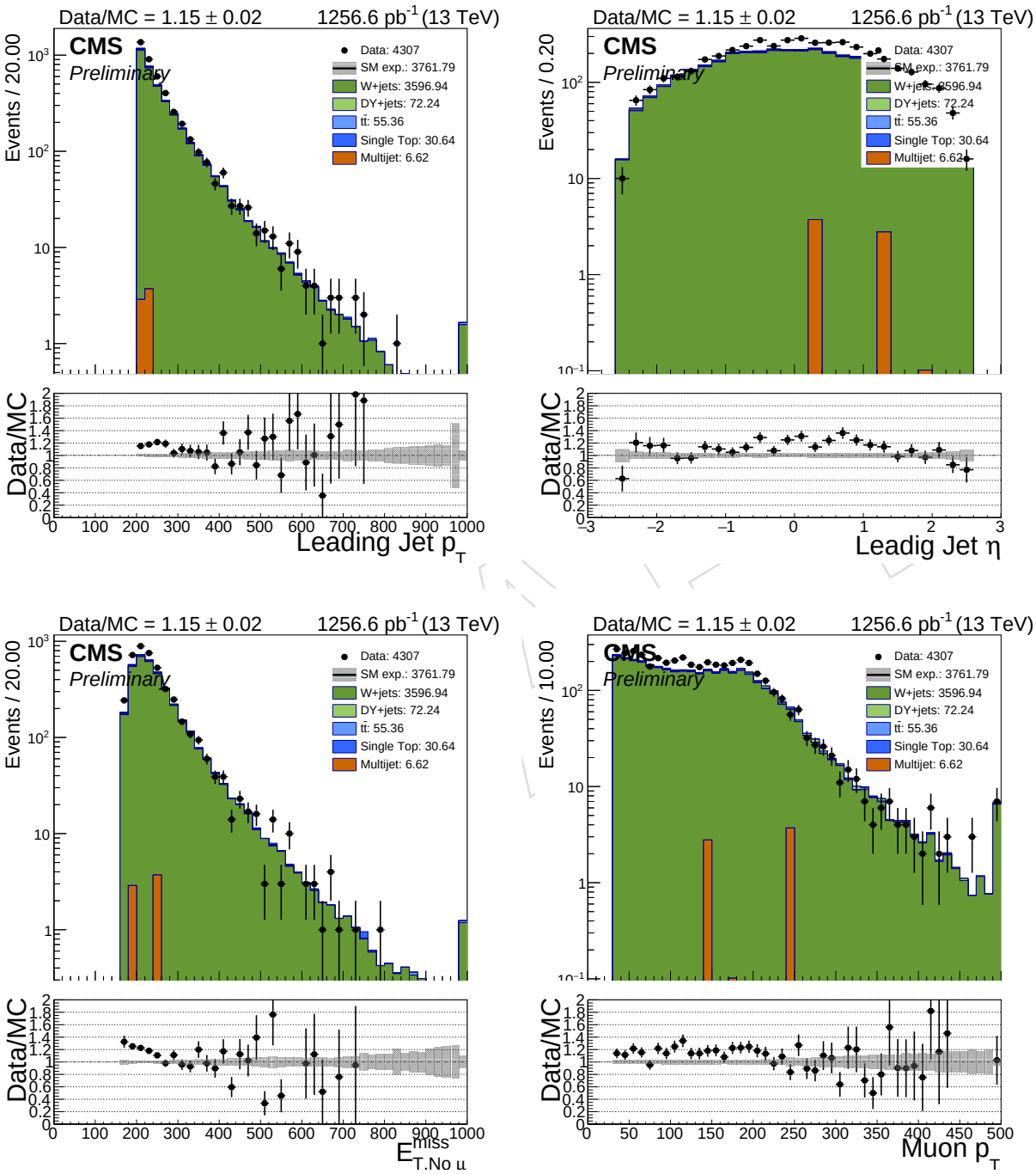

Figure 16: Key analysis variables for single muon control region (monojet bins)

9.2 Yields and distributions for the $\mu\mu$ + jets control sample

Table 29: Yields in the $\mu\mu$ + jets control region for 1.26fb^{-1} for symmetric categories. The letter "a" in jet e.g. "2a" indicates the asymmetric jet bins. All entries are non-zero but are truncated to one decimal place.

H_T (GeV) (n_{jet}, n_b)	200-250	250-300	300-350	350-400	400-500	500-600	600-800	800-∞
(2, 0)	37	45	41	23	33	25	12	6
(2, 1)	3	5	8	2	5	1	1	1
(2, 2)	0	0	0	–	0	0	0	0
(3, 0)	0	8	25	27	30	23	10	10
(3, 1)	0	2	3	4	1	1	4	2
(3, 2)	–	1	2	0	0	0	1	0
(3, ≥ 3)	–	–	–	0	0	0	–	–
(4, 0)	–	–	3	1	13	11	16	10
(4, 1)	–	–	1	1	2	0	3	4
(4, 2)	–	–	0	0	0	0	0	1
(4, ≥ 3)	–	–	–	0	0	0	0	0
(≥ 5, 0)	–	–	–	0	2	4	5	10
(≥ 5, 1)	–	–	–	0	1	4	2	2
(≥ 5, 2)	–	–	–	0	0	0	1	2
(≥ 5, ≥ 3)	–	–	–	–	1	0	0	0

Table 30: Yields in the $\mu\mu$ + jets control region for 1.26fb^{-1} for asymmetric categories. The letter "a" in jet e.g. "2a" indicates the asymmetric jet bins. All entries are non-zero but are truncated to one decimal place.

H_T (GeV) (n_{jet}, n_b)	200-250	250-300	300-350	350-400	400-500	500-600	600-800	800-∞
(2a, 0)	268	151	59	33	21	6	2	–
(2a, 1)	26	15	7	2	1	1	0	–
(2a, 2)	1	2	3	0	1	0	0	–
(3a, 0)	46	70	32	21	11	6	0	–
(3a, 1)	5	8	4	2	5	1	0	–
(3a, 2)	5	2	1	0	0	0	0	–
(3a, ≥ 3)	0	0	0	–	0	–	–	–
(4a, 0)	1	13	16	9	6	2	1	–
(4a, 1)	0	4	2	2	1	0	0	–
(4a, 2)	0	0	1	0	0	1	0	–
(4a, ≥ 3)	–	0	0	0	1	0	–	–
(≥ 5a, 0)	–	–	1	3	3	2	0	–
(≥ 5a, 1)	–	–	0	1	1	0	1	–
(≥ 5a, 2)	–	–	0	0	0	0	0	–
(≥ 5a, ≥ 3)	–	–	–	0	0	0	–	–

Table 31: Yields in the $\mu\mu$ + jets control region for 1.26fb^{-1} for monojet categories. The letter "a" in jet e.g. "2a" indicates the asymmetric jet bins. All entries are non-zero but are truncated to one decimal place.

H_T (GeV) (n_{jet}, n_b)	200-250	250-300	300-350	350-400	400-500	500-600	600-800	800-∞
(1, 0)	325	119	59	26	21	9	4	–
(1, 1)	10	7	5	0	0	0	0	–

DRAFT

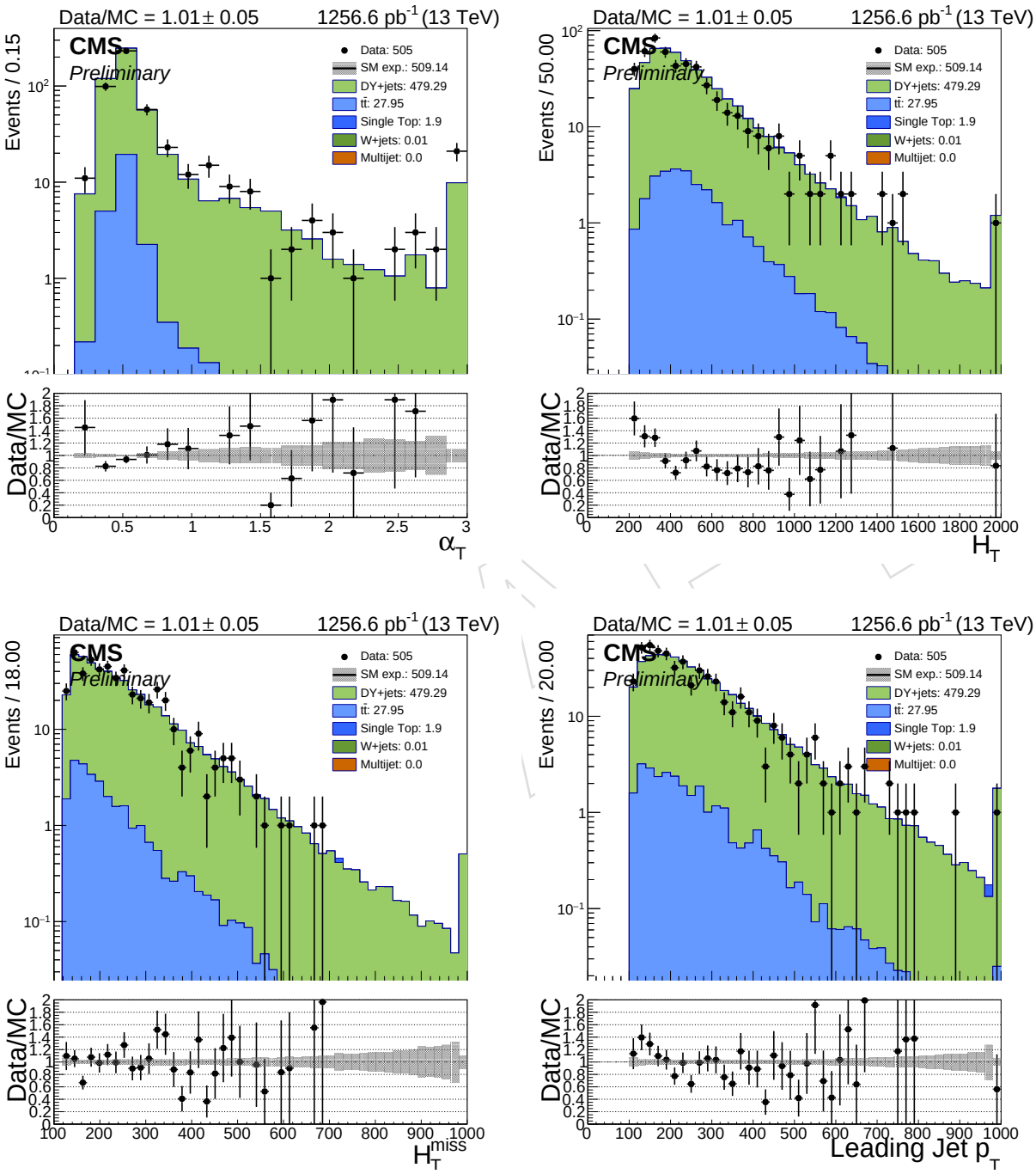

Figure 17: Key analysis variables for double muon control region (symmetric n_{jet} bins)

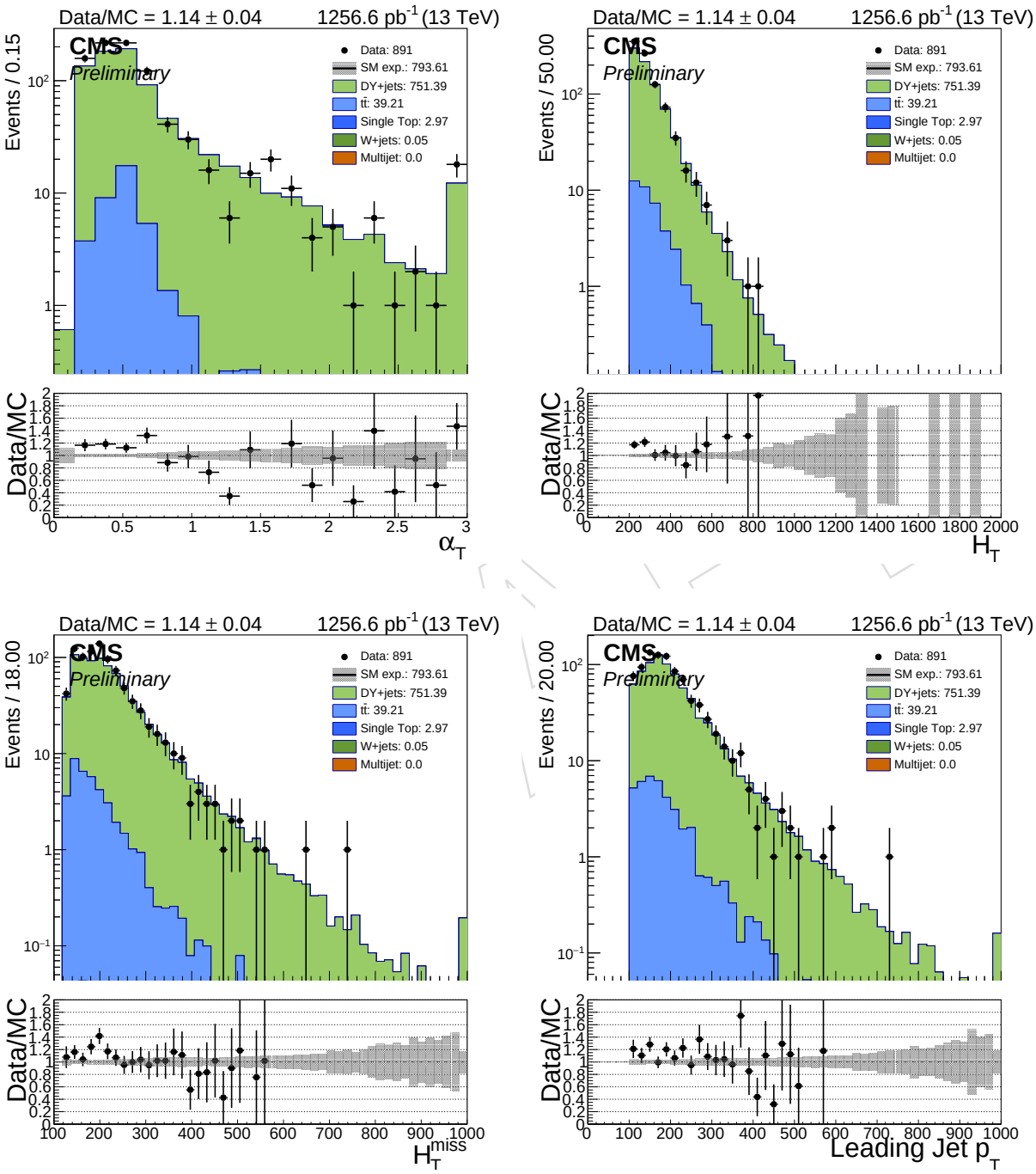

Figure 18: Key analysis variables for double muon control region (asymmetric n_{jet} bins)

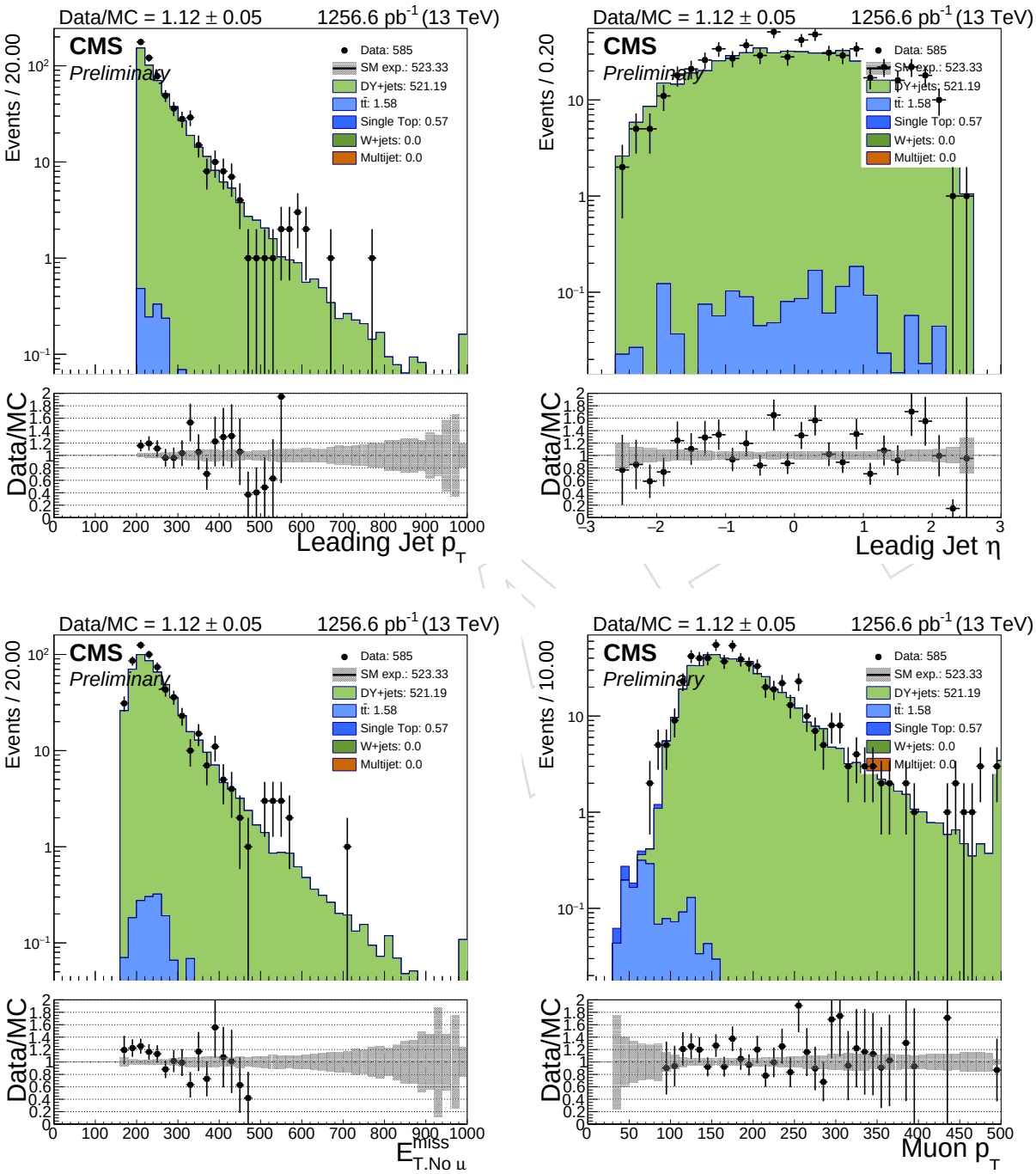

Figure 19: Key analysis variables for double muon control region (monojet bins)

9.3 Yields and distributions for the photon + jets control sample

Table 32: Yields in the γ + jets control region for 1.26fb^{-1} for symmetric categories. The letter "a" in jet e.g. "2a" indicates the asymmetric jet bins. All entries are non-zero but are truncated to one decimal place.

H_T (GeV) (n_{jet}, n_b)	400-500	500-600	600-800	800-∞
(2, 0)	189	65	37	76
(2, 1)	9	1	0	7
(2, 2)	0	0	0	0
(3, 0)	272	122	69	132
(3, 1)	23	13	8	24
(3, 2)	4	0	2	1
(3, ≥ 3)	1	0	–	–
(4, 0)	132	92	73	83
(4, 1)	20	16	6	22
(4, 2)	2	1	1	2
(4, ≥ 3)	0	0	1	0
(≥ 5, 0)	26	40	49	63
(≥ 5, 1)	3	5	9	15
(≥ 5, 2)	2	3	1	4
(≥ 5, ≥ 3)	0	0	0	0

Table 33: Yields in the γ + jets control region for 1.26fb^{-1} for asymmetric categories. The letter "a" in jet e.g. "2a" indicates the asymmetric jet bins. All entries are non-zero but are truncated to one decimal place.

H_T (GeV) (n_{jet}, n_b)	400-500	500-600	600-800	800-∞
(2a, 0)	96	28	11	–
(2a, 1)	6	1	1	–
(2a, 2)	0	0	0	–
(3a, 0)	61	7	5	–
(3a, 1)	4	2	2	–
(3a, 2)	0	0	0	–
(3a, ≥ 3)	0	–	–	–
(4a, 0)	65	9	2	–
(4a, 1)	9	2	0	–
(4a, 2)	0	0	0	–
(4a, ≥ 3)	0	0	–	–
(≥ 5a, 0)	32	7	3	–
(≥ 5a, 1)	8	2	0	–
(≥ 5a, 2)	2	0	0	–
(≥ 5a, ≥ 3)	0	0	–	–

Table 34: Yields in the γ + jets control region for 1.26fb^{-1} for monojet categories. The letter "a" in jet e.g. "2a" indicates the asymmetric jet bins. All entries are non-zero but are truncated to one decimal place.

H_T (GeV) (n_{jet}, n_b)	400-500	500-600	600-800	800-∞
(1, 0)	347	116	43	–
(1, 1)	14	3	0	–

DRAFT

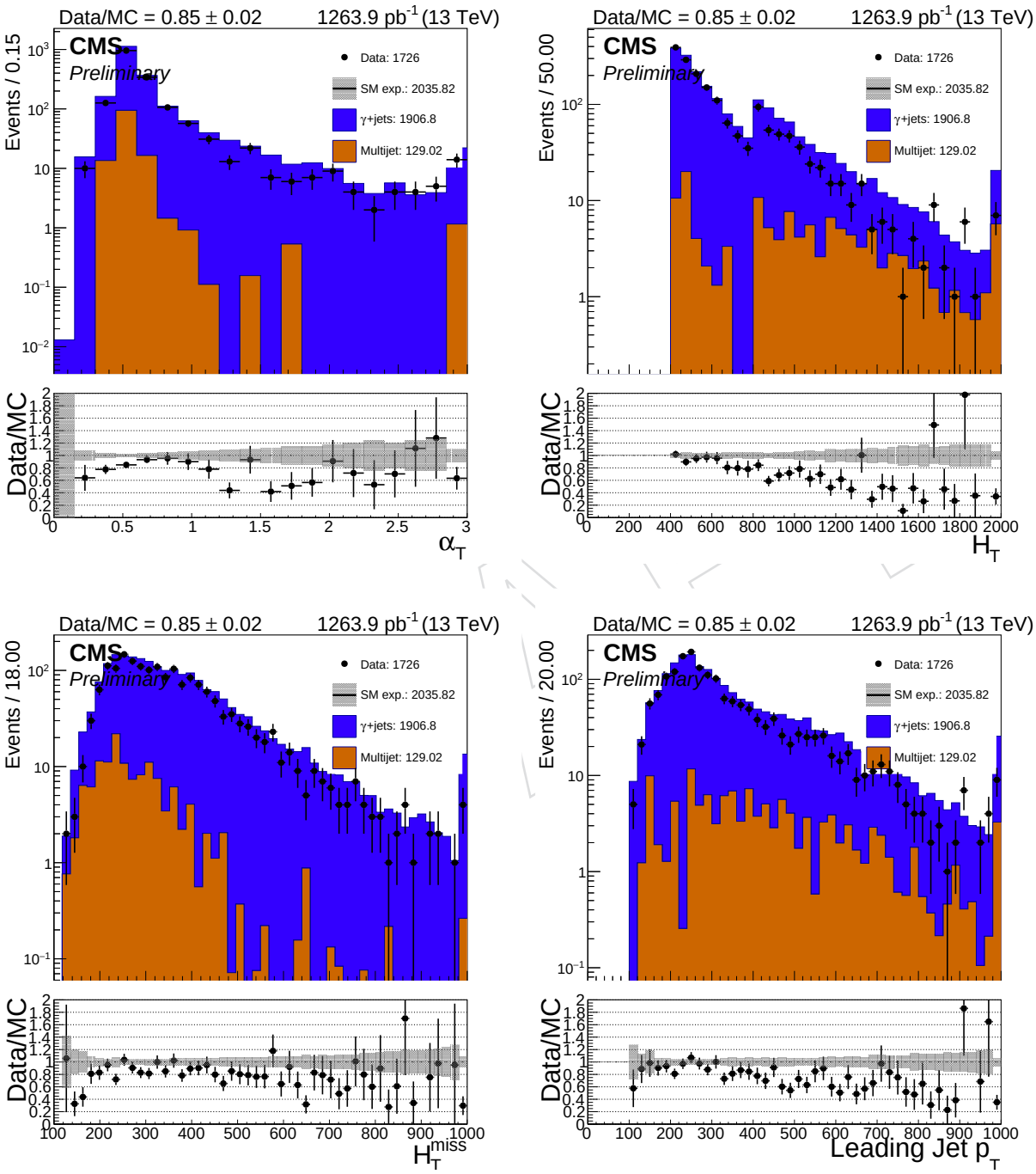

Figure 20: Key analysis variables for single photon control region (symmetric n_{jet} bins)

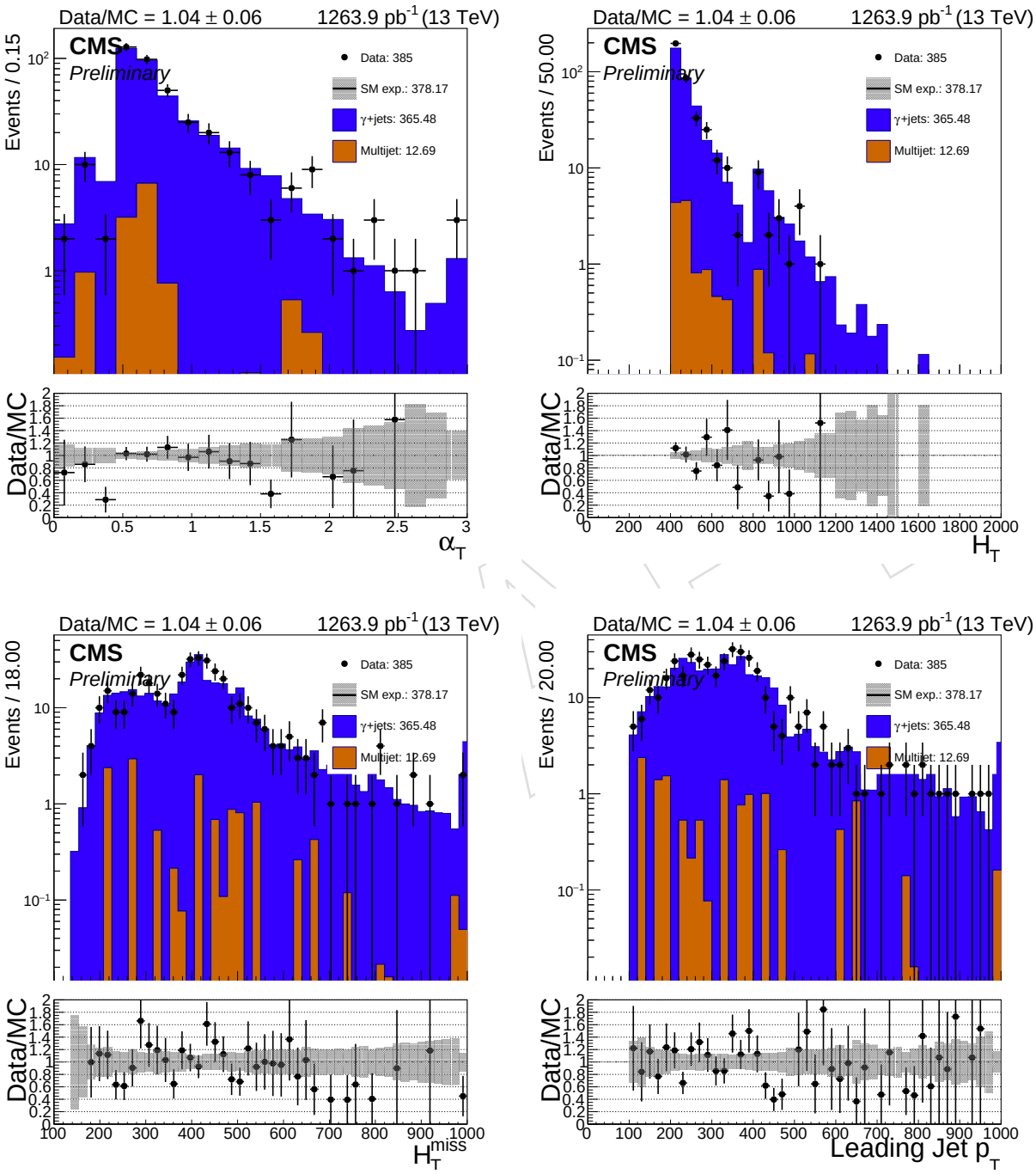

Figure 21: Key analysis variables for single photon control region (asymmetric n_{jet} bins)

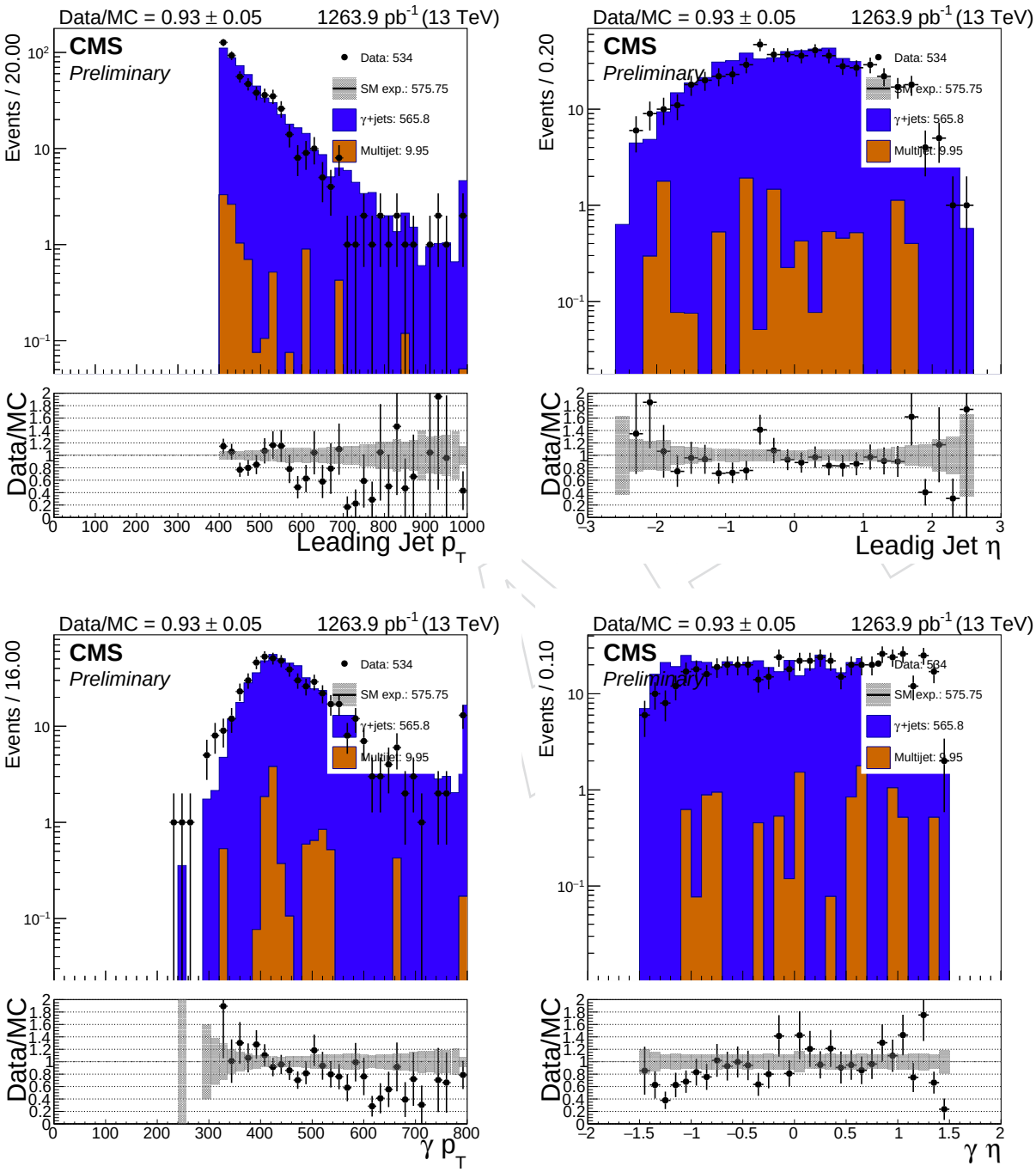

Figure 22: Key analysis variables for single photon control region (monojet bins)

9.4 Expected yields and distributions in the signal region

In the absence of multijet events from QCD, the remaining significant backgrounds in the signal region are expected to stem from SM processes with genuine $E_{\mathrm{T}}^{\mathrm{miss}}$ in the final state. For the low jet multiplicity categories, the largest backgrounds with genuine $E_{\mathrm{T}}^{\mathrm{miss}}$ are from the associated production of W or Z bosons with jets, followed by either the weak decays $\mathrm{Z} \to \nu\bar{\nu}$ or $\mathrm{W} \to \tau\nu$, where the τ decays hadronically and is identified as a jet, or by leptonic decays that are outside acceptance or not rejected by the dedicated electron or muon vetoes. For the higher jet multiplicity categories, top quark production followed by semileptonic weak top quark decay becomes dominant. The relative contribution from $\mathrm{t\bar{t}}$ depends on the jet multiplicity with increase importance for large jet multiplicities.

Tables 35, 36 and 37 summarise the expected yields, as determined from simulation, in the signal region for an integrated luminosity of 1.28 fb^{-1}. In addition to the total expected yield (SM) per (n_{jet}, n_{b}, H_{T}) bin, the $\mathrm{t\bar{t}W}$ and $\mathrm{Z} \to \nu\bar{\nu}$ contributions are also shown (the former of which contains all residual contributions from sub-dominant processes such as e.g. diboson production). These numbers are indicative only.

DRAFT

Table 35: MC yields in the signal region for 1.26fb^{-1} for symmetric categories. The letter "a" in jet e.g. "2a" indicates the asymmetric jet bins. All entries are non-zero but are truncated to one decimal place.

H_T (GeV)	(n_{jet}, n_b)	200-250	250-300	300-350	350-400	400-500	500-600	600-800	800-∞
SM	(2, 0)	$458.4^{+6.8}_{-6.8}$	$495.0^{+6.7}_{-6.7}$	$331.0^{+5.3}_{-5.3}$	$199.5^{+3.6}_{-3.6}$	$183.1^{+2.8}_{-2.8}$	$63.8^{+1.4}_{-1.4}$	$31.4^{+0.7}_{-0.7}$	$34.5^{+0.6}_{-0.6}$
Ttw	(2, 0)	$220.2^{+5.9}_{-5.9}$	$221.5^{+5.9}_{-5.9}$	$139.6^{+4.5}_{-4.5}$	$77.0^{+3.0}_{-3.0}$	$64.9^{+2.2}_{-2.2}$	$20.1^{+1.0}_{-1.0}$	$9.4^{+0.4}_{-0.4}$	$10.1^{+0.4}_{-0.4}$
Zinv	(2, 0)	$238.2^{+3.3}_{-3.3}$	$273.5^{+3.3}_{-3.3}$	$191.4^{+2.7}_{-2.7}$	$122.5^{+2.0}_{-2.0}$	$118.1^{+1.8}_{-1.8}$	$43.7^{+1.0}_{-1.0}$	$22.1^{+0.5}_{-0.5}$	$24.4^{+0.5}_{-0.5}$
SM	(2, 1)	$50.0^{+1.9}_{-1.9}$	$45.8^{+1.7}_{-1.7}$	$31.6^{+1.4}_{-1.4}$	$17.6^{+1.0}_{-1.0}$	$15.6^{+0.8}_{-0.8}$	$5.3^{+0.4}_{-0.4}$	$3.1^{+0.2}_{-0.2}$	$3.6^{+0.2}_{-0.2}$
Ttw	(2, 1)	$33.1^{+1.6}_{-1.6}$	$27.4^{+1.5}_{-1.5}$	$16.1^{+1.2}_{-1.2}$	$7.4^{+0.8}_{-0.8}$	$6.4^{+0.6}_{-0.6}$	$1.9^{+0.3}_{-0.3}$	$0.7^{+0.1}_{-0.1}$	$1.1^{+0.2}_{-0.2}$
Zinv	(2, 1)	$16.8^{+0.9}_{-0.9}$	$18.3^{+0.8}_{-0.8}$	$15.5^{+0.7}_{-0.7}$	$10.2^{+0.6}_{-0.6}$	$9.2^{+0.5}_{-0.5}$	$3.5^{+0.3}_{-0.3}$	$2.4^{+0.2}_{-0.2}$	$2.4^{+0.1}_{-0.1}$
SM	(2, 2)	$3.2^{+0.4}_{-0.4}$	$3.3^{+0.4}_{-0.4}$	$2.1^{+0.3}_{-0.3}$	–	$0.9^{+0.2}_{-0.2}$	$0.6^{+0.2}_{-0.2}$	$0.2^{+0.0}_{-0.0}$	$0.1^{+0.0}_{-0.0}$
Ttw	(2, 2)	$1.7^{+0.3}_{-0.3}$	$1.5^{+0.3}_{-0.3}$	$1.1^{+0.3}_{-0.3}$	–	$0.4^{+0.1}_{-0.1}$	$0.3^{+0.1}_{-0.1}$	$0.0^{+0.0}_{-0.0}$	$0.0^{+0.0}_{-0.0}$
Zinv	(2, 2)	$1.5^{+0.2}_{-0.2}$	$1.8^{+0.3}_{-0.3}$	$1.1^{+0.2}_{-0.2}$	–	$0.5^{+0.1}_{-0.1}$	$0.3^{+0.1}_{-0.1}$	$0.1^{+0.0}_{-0.0}$	$0.1^{+0.0}_{-0.0}$
SM	(3, 0)	$0.6^{+0.2}_{-0.2}$	$87.6^{+2.7}_{-2.7}$	$242.9^{+4.6}_{-4.6}$	$247.9^{+4.3}_{-4.3}$	$293.6^{+3.8}_{-3.8}$	$108.6^{+1.9}_{-1.9}$	$61.8^{+0.9}_{-0.9}$	$49.4^{+0.7}_{-0.7}$
Ttw	(3, 0)	$0.4^{+0.1}_{-0.1}$	$42.4^{+2.4}_{-2.4}$	$117.9^{+4.0}_{-4.0}$	$118.4^{+3.8}_{-3.8}$	$127.4^{+3.1}_{-3.1}$	$40.9^{+1.4}_{-1.4}$	$19.3^{+0.6}_{-0.6}$	$14.7^{+0.5}_{-0.5}$
Zinv	(3, 0)	$0.2^{+0.1}_{-0.1}$	$45.2^{+1.3}_{-1.3}$	$125.1^{+2.2}_{-2.2}$	$129.5^{+2.1}_{-2.1}$	$166.2^{+2.1}_{-2.1}$	$67.7^{+1.2}_{-1.2}$	$42.5^{+0.7}_{-0.7}$	$34.7^{+0.6}_{-0.6}$
SM	(3, 1)	$0.2^{+0.1}_{-0.1}$	$19.8^{+1.0}_{-1.0}$	$49.3^{+1.6}_{-1.6}$	$49.2^{+1.6}_{-1.6}$	$50.5^{+1.5}_{-1.5}$	$16.3^{+0.8}_{-0.8}$	$8.6^{+0.4}_{-0.4}$	$6.8^{+0.3}_{-0.3}$
Ttw	(3, 1)	$0.2^{+0.1}_{-0.1}$	$15.5^{+0.9}_{-0.9}$	$36.4^{+1.5}_{-1.5}$	$35.3^{+1.5}_{-1.5}$	$30.7^{+1.3}_{-1.3}$	$8.2^{+0.6}_{-0.6}$	$3.4^{+0.3}_{-0.3}$	$2.2^{+0.2}_{-0.2}$
Zinv	(3, 1)	$0.0^{+0.0}_{-0.0}$	$4.3^{+0.4}_{-0.4}$	$12.9^{+0.7}_{-0.7}$	$13.9^{+0.7}_{-0.7}$	$19.8^{+0.8}_{-0.8}$	$8.1^{+0.4}_{-0.4}$	$5.2^{+0.2}_{-0.2}$	$4.6^{+0.2}_{-0.2}$
SM	(3, 2)	–	$3.5^{+0.4}_{-0.4}$	$10.4^{+0.7}_{-0.7}$	$10.4^{+0.7}_{-0.7}$	$8.6^{+0.5}_{-0.5}$	$2.5^{+0.3}_{-0.3}$	$0.9^{+0.1}_{-0.1}$	$0.6^{+0.1}_{-0.1}$
Ttw	(3, 2)	–	$2.8^{+0.4}_{-0.4}$	$8.7^{+0.6}_{-0.6}$	$8.9^{+0.7}_{-0.7}$	$6.7^{+0.5}_{-0.5}$	$1.6^{+0.2}_{-0.2}$	$0.3^{+0.1}_{-0.1}$	$0.2^{+0.0}_{-0.0}$
Zinv	(3, 2)	–	$0.6^{+0.2}_{-0.2}$	$1.7^{+0.2}_{-0.2}$	$1.5^{+0.2}_{-0.2}$	$1.9^{+0.2}_{-0.2}$	$0.9^{+0.1}_{-0.1}$	$0.6^{+0.1}_{-0.1}$	$0.4^{+0.1}_{-0.1}$
SM	$(3, \geq 3)$	–	–	–	$0.6^{+0.2}_{-0.2}$	$0.2^{+0.1}_{-0.1}$	$0.1^{+0.0}_{-0.0}$	–	–
Ttw	$(3, \geq 3)$	–	–	–	$0.5^{+0.2}_{-0.2}$	$0.2^{+0.1}_{-0.1}$	$0.1^{+0.0}_{-0.0}$	–	–
Zinv	$(3, \geq 3)$	–	–	–	$0.1^{+0.1}_{-0.1}$	$0.0^{+0.0}_{-0.0}$	$0.0^{+0.0}_{-0.0}$	–	–
SM	(4, 0)	–	–	$36.4^{+1.8}_{-1.8}$	$107.0^{+2.8}_{-2.8}$	$205.4^{+3.3}_{-3.3}$	$99.3^{+1.9}_{-1.9}$	$64.2^{+1.1}_{-1.1}$	$42.1^{+0.6}_{-0.6}$
Ttw	(4, 0)	–	–	$20.7^{+1.6}_{-1.6}$	$57.8^{+2.5}_{-2.5}$	$104.7^{+2.8}_{-2.8}$	$41.8^{+1.5}_{-1.5}$	$23.9^{+0.8}_{-0.8}$	$13.4^{+0.4}_{-0.4}$
Zinv	(4, 0)	–	–	$15.7^{+0.8}_{-0.8}$	$49.3^{+1.3}_{-1.3}$	$100.7^{+1.7}_{-1.7}$	$57.5^{+1.2}_{-1.2}$	$40.3^{+0.7}_{-0.7}$	$28.6^{+0.5}_{-0.5}$
SM	(4, 1)	–	–	$14.2^{+0.8}_{-0.8}$	$41.5^{+1.4}_{-1.4}$	$64.0^{+1.6}_{-1.6}$	$24.7^{+1.0}_{-1.0}$	$13.9^{+0.6}_{-0.6}$	$8.6^{+0.3}_{-0.3}$
Ttw	(4, 1)	–	–	$11.9^{+0.8}_{-0.8}$	$34.7^{+1.3}_{-1.3}$	$49.4^{+1.4}_{-1.4}$	$15.4^{+0.8}_{-0.8}$	$7.0^{+0.5}_{-0.5}$	$3.4^{+0.2}_{-0.2}$
Zinv	(4, 1)	–	–	$2.3^{+0.3}_{-0.3}$	$6.8^{+0.5}_{-0.5}$	$14.6^{+0.6}_{-0.6}$	$9.3^{+0.5}_{-0.5}$	$6.9^{+0.3}_{-0.3}$	$5.2^{+0.2}_{-0.2}$
SM	(4, 2)	–	–	$5.3^{+0.4}_{-0.4}$	$14.4^{+0.8}_{-0.8}$	$24.0^{+0.9}_{-0.9}$	$7.8^{+0.5}_{-0.5}$	$2.8^{+0.3}_{-0.3}$	$1.5^{+0.2}_{-0.2}$
Ttw	(4, 2)	–	–	$4.8^{+0.4}_{-0.4}$	$13.6^{+0.8}_{-0.8}$	$21.2^{+0.9}_{-0.9}$	$6.3^{+0.5}_{-0.5}$	$1.9^{+0.3}_{-0.3}$	$0.7^{+0.1}_{-0.1}$
Zinv	(4, 2)	–	–	$0.6^{+0.2}_{-0.2}$	$0.8^{+0.2}_{-0.2}$	$2.9^{+0.3}_{-0.3}$	$1.5^{+0.2}_{-0.2}$	$1.0^{+0.1}_{-0.1}$	$0.7^{+0.1}_{-0.1}$
SM	$(4, \geq 3)$	–	–	–	$1.0^{+0.2}_{-0.2}$	$2.1^{+0.3}_{-0.3}$	$0.6^{+0.2}_{-0.2}$	$0.1^{+0.0}_{-0.0}$	$0.0^{+0.0}_{-0.0}$
Ttw	$(4, \geq 3)$	–	–	–	$0.9^{+0.2}_{-0.2}$	$1.9^{+0.3}_{-0.3}$	$0.5^{+0.1}_{-0.1}$	$0.1^{+0.0}_{-0.0}$	$0.0^{+0.0}_{-0.0}$
Zinv	$(4, \geq 3)$	–	–	–	$0.1^{+0.1}_{-0.1}$	$0.2^{+0.1}_{-0.1}$	$0.1^{+0.1}_{-0.1}$	$0.0^{+0.0}_{-0.0}$	$0.0^{+0.0}_{-0.0}$
SM	$(\geq 5, 0)$	–	–	–	$5.2^{+0.6}_{-0.6}$	$55.5^{+1.7}_{-1.7}$	$53.1^{+1.5}_{-1.5}$	$51.4^{+1.1}_{-1.1}$	$38.8^{+0.7}_{-0.7}$
Ttw	$(\geq 5, 0)$	–	–	–	$3.2^{+0.5}_{-0.5}$	$32.4^{+1.5}_{-1.5}$	$27.5^{+1.2}_{-1.2}$	$24.2^{+0.9}_{-0.9}$	$14.8^{+0.5}_{-0.5}$
Zinv	$(\geq 5, 0)$	–	–	–	$2.0^{+0.2}_{-0.2}$	$23.1^{+0.8}_{-0.8}$	$25.6^{+0.8}_{-0.8}$	$27.2^{+0.6}_{-0.6}$	$24.0^{+0.5}_{-0.5}$
SM	$(\geq 5, 1)$	–	–	–	$3.0^{+0.3}_{-0.3}$	$35.5^{+1.2}_{-1.2}$	$28.3^{+1.0}_{-1.0}$	$22.2^{+0.8}_{-0.8}$	$14.1^{+0.5}_{-0.5}$
Ttw	$(\geq 5, 1)$	–	–	–	$2.6^{+0.3}_{-0.3}$	$31.2^{+1.1}_{-1.1}$	$24.0^{+1.0}_{-1.0}$	$16.4^{+0.8}_{-0.8}$	$9.0^{+0.4}_{-0.4}$
Zinv	$(\geq 5, 1)$	–	–	–	$0.3^{+0.1}_{-0.1}$	$4.3^{+0.3}_{-0.3}$	$4.4^{+0.3}_{-0.3}$	$5.8^{+0.3}_{-0.3}$	$5.1^{+0.2}_{-0.2}$
SM	$(\geq 5, 2)$	–	–	–	$1.3^{+0.2}_{-0.2}$	$17.6^{+0.8}_{-0.8}$	$13.8^{+0.7}_{-0.7}$	$7.9^{+0.5}_{-0.5}$	$5.0^{+0.3}_{-0.3}$
Ttw	$(\geq 5, 2)$	–	–	–	$1.2^{+0.2}_{-0.2}$	$16.8^{+0.8}_{-0.8}$	$12.7^{+0.7}_{-0.7}$	$6.8^{+0.5}_{-0.5}$	$4.0^{+0.3}_{-0.3}$
Zinv	$(\geq 5, 2)$	–	–	–	$0.1^{+0.1}_{-0.1}$	$0.8^{+0.1}_{-0.1}$	$1.1^{+0.2}_{-0.2}$	$1.1^{+0.1}_{-0.1}$	$1.1^{+0.1}_{-0.1}$
SM	$(\geq 5, \geq 3)$	–	–	–	–	$1.6^{+0.2}_{-0.2}$	$1.7^{+0.2}_{-0.2}$	$1.4^{+0.2}_{-0.2}$	$0.7^{+0.1}_{-0.1}$
Ttw	$(\geq 5, \geq 3)$	–	–	–	–	$1.6^{+0.2}_{-0.2}$	$1.6^{+0.2}_{-0.2}$	$1.2^{+0.2}_{-0.2}$	$0.5^{+0.1}_{-0.1}$
Zinv	$(\geq 5, \geq 3)$	–	–	–	–	$0.0^{+0.0}_{-0.0}$	$0.0^{+0.0}_{-0.0}$	$0.2^{+0.1}_{-0.1}$	$0.1^{+0.0}_{-0.0}$

DRAFT

Table 36: MC yields in the signal region for 1.26fb^{-1} for asymmetric categories. The letter "a" in jet e.g. "2a" indicates the asymmetric jet bins. All entries are non-zero but are truncated to one decimal place.

H_T (GeV)	(n_{jet}, n_b)	200-250	250-300	300-350	350-400	400-500	500-600	600-800	800-∞
SM	(2a, 0)	$2349.9^{+16.0}_{-16.0}$	$694.8^{+7.7}_{-7.7}$	$271.1^{+4.7}_{-4.7}$	$111.7^{+2.7}_{-2.7}$	$73.5^{+1.8}_{-1.8}$	$19.1^{+0.8}_{-0.8}$	$7.7^{+0.4}_{-0.4}$	–
Ttw	(2a, 0)	$1102.8^{+13.7}_{-13.7}$	$290.7^{+6.6}_{-6.6}$	$106.9^{+4.0}_{-4.0}$	$38.8^{+2.2}_{-2.2}$	$22.2^{+1.3}_{-1.3}$	$5.8^{+0.6}_{-0.6}$	$1.9^{+0.3}_{-0.3}$	–
Zinv	(2a, 0)	$1247.1^{+8.2}_{-8.2}$	$404.1^{+3.9}_{-3.9}$	$164.2^{+2.5}_{-2.5}$	$72.9^{+1.6}_{-1.6}$	$51.3^{+1.2}_{-1.2}$	$13.3^{+0.5}_{-0.5}$	$5.9^{+0.3}_{-0.3}$	–
SM	(2a, 1)	$224.0^{+4.0}_{-4.0}$	$62.6^{+2.0}_{-2.0}$	$22.2^{+1.2}_{-1.2}$	$9.0^{+0.6}_{-0.6}$	$6.1^{+0.5}_{-0.5}$	$1.6^{+0.3}_{-0.3}$	$0.7^{+0.1}_{-0.1}$	–
Ttw	(2a, 1)	$137.6^{+3.5}_{-3.5}$	$34.6^{+1.8}_{-1.8}$	$10.5^{+1.0}_{-1.0}$	$3.1^{+0.5}_{-0.5}$	$2.2^{+0.4}_{-0.4}$	$0.4^{+0.2}_{-0.2}$	$0.2^{+0.1}_{-0.1}$	–
Zinv	(2a, 1)	$86.5^{+2.0}_{-2.0}$	$28.0^{+1.0}_{-1.0}$	$11.7^{+0.6}_{-0.6}$	$6.0^{+0.4}_{-0.4}$	$3.8^{+0.3}_{-0.3}$	$1.1^{+0.2}_{-0.2}$	$0.5^{+0.1}_{-0.1}$	–
SM	(2a, 2)	$17.5^{+1.1}_{-1.1}$	$4.5^{+0.5}_{-0.5}$	$1.8^{+0.4}_{-0.4}$	$0.9^{+0.3}_{-0.3}$	$0.4^{+0.1}_{-0.1}$	$0.0^{+0.0}_{-0.0}$	$0.0^{+0.0}_{-0.0}$	–
Ttw	(2a, 2)	$9.4^{+0.9}_{-0.9}$	$2.3^{+0.4}_{-0.4}$	$0.9^{+0.3}_{-0.3}$	$0.7^{+0.3}_{-0.3}$	$0.2^{+0.1}_{-0.1}$	$0.0^{+0.0}_{-0.0}$	$0.0^{+0.0}_{-0.0}$	–
Zinv	(2a, 2)	$8.0^{+0.6}_{-0.6}$	$2.1^{+0.3}_{-0.3}$	$0.9^{+0.2}_{-0.2}$	$0.3^{+0.1}_{-0.1}$	$0.2^{+0.1}_{-0.1}$	$0.0^{+0.0}_{-0.0}$	$0.0^{+0.0}_{-0.0}$	–
SM	(3a, 0)	$640.5^{+8.0}_{-8.0}$	$638.6^{+7.7}_{-7.7}$	$325.0^{+5.3}_{-5.3}$	$108.3^{+2.7}_{-2.7}$	$50.8^{+1.6}_{-1.6}$	$10.2^{+0.6}_{-0.6}$	$3.6^{+0.2}_{-0.2}$	–
Ttw	(3a, 0)	$335.2^{+7.0}_{-7.0}$	$324.3^{+6.9}_{-6.9}$	$159.1^{+4.7}_{-4.7}$	$45.2^{+2.2}_{-2.2}$	$18.5^{+1.2}_{-1.2}$	$3.3^{+0.4}_{-0.4}$	$0.9^{+0.2}_{-0.2}$	–
Zinv	(3a, 0)	$305.3^{+3.8}_{-3.8}$	$314.4^{+3.5}_{-3.5}$	$165.9^{+2.5}_{-2.5}$	$63.1^{+1.5}_{-1.5}$	$32.4^{+1.0}_{-1.0}$	$6.9^{+0.4}_{-0.4}$	$2.8^{+0.2}_{-0.2}$	–
SM	(3a, 1)	$150.6^{+3.0}_{-3.0}$	$148.0^{+2.9}_{-2.9}$	$69.8^{+2.0}_{-2.0}$	$20.8^{+1.1}_{-1.1}$	$7.8^{+0.6}_{-0.6}$	$1.2^{+0.2}_{-0.2}$	$0.4^{+0.1}_{-0.1}$	–
Ttw	(3a, 1)	$121.5^{+2.8}_{-2.8}$	$116.5^{+2.7}_{-2.7}$	$52.3^{+1.8}_{-1.8}$	$13.9^{+1.0}_{-1.0}$	$4.3^{+0.5}_{-0.5}$	$0.7^{+0.2}_{-0.2}$	$0.1^{+0.0}_{-0.0}$	–
Zinv	(3a, 1)	$29.0^{+1.1}_{-1.1}$	$31.5^{+1.1}_{-1.1}$	$17.5^{+0.8}_{-0.8}$	$6.9^{+0.5}_{-0.5}$	$3.5^{+0.3}_{-0.3}$	$0.5^{+0.1}_{-0.1}$	$0.3^{+0.0}_{-0.0}$	–
SM	(3a, 2)	$24.2^{+1.0}_{-1.0}$	$26.7^{+1.1}_{-1.1}$	$18.9^{+1.0}_{-1.0}$	$4.2^{+0.4}_{-0.4}$	$1.3^{+0.2}_{-0.2}$	$0.2^{+0.1}_{-0.1}$	$0.0^{+0.0}_{-0.0}$	–
Ttw	(3a, 2)	$20.7^{+0.9}_{-0.9}$	$22.4^{+1.0}_{-1.0}$	$15.9^{+0.9}_{-0.9}$	$3.6^{+0.4}_{-0.4}$	$0.7^{+0.2}_{-0.2}$	$0.1^{+0.1}_{-0.1}$	$0.0^{+0.0}_{-0.0}$	–
Zinv	(3a, 2)	$3.4^{+0.4}_{-0.4}$	$4.3^{+0.4}_{-0.4}$	$3.0^{+0.3}_{-0.3}$	$0.6^{+0.1}_{-0.1}$	$0.6^{+0.1}_{-0.1}$	$0.1^{+0.0}_{-0.0}$	$0.0^{+0.0}_{-0.0}$	–
SM	(3a, ≥ 3)	$0.4^{+0.1}_{-0.1}$	$0.8^{+0.2}_{-0.2}$	$0.4^{+0.1}_{-0.1}$	–	$0.0^{+0.0}_{-0.0}$	–	–	–
Ttw	(3a, ≥ 3)	$0.4^{+0.1}_{-0.1}$	$0.6^{+0.1}_{-0.1}$	$0.4^{+0.1}_{-0.1}$	–	$0.0^{+0.0}_{-0.0}$	–	–	–
Zinv	(3a, ≥ 3)	$0.0^{+0.0}_{-0.0}$	$0.2^{+0.1}_{-0.1}$	$0.0^{+0.0}_{-0.0}$	–	$0.0^{+0.0}_{-0.0}$	–	–	–
SM	(4a, 0)	$1.8^{+0.4}_{-0.4}$	$72.9^{+2.5}_{-2.5}$	$184.3^{+3.9}_{-3.9}$	$122.3^{+3.0}_{-3.0}$	$69.5^{+1.9}_{-1.9}$	$9.4^{+0.6}_{-0.6}$	$1.9^{+0.2}_{-0.2}$	–
Ttw	(4a, 0)	$0.6^{+0.3}_{-0.3}$	$41.8^{+2.3}_{-2.3}$	$100.8^{+3.5}_{-3.5}$	$66.9^{+2.7}_{-2.7}$	$32.2^{+1.6}_{-1.6}$	$3.4^{+0.5}_{-0.5}$	$0.4^{+0.1}_{-0.1}$	–
Zinv	(4a, 0)	$1.2^{+0.3}_{-0.3}$	$31.1^{+1.1}_{-1.1}$	$83.4^{+1.8}_{-1.8}$	$55.4^{+1.4}_{-1.4}$	$37.3^{+1.0}_{-1.0}$	$6.0^{+0.4}_{-0.4}$	$1.4^{+0.1}_{-0.1}$	–
SM	(4a, 1)	$0.6^{+0.1}_{-0.1}$	$25.7^{+1.1}_{-1.1}$	$77.9^{+2.2}_{-2.2}$	$46.7^{+1.5}_{-1.5}$	$23.3^{+1.0}_{-1.0}$	$1.9^{+0.3}_{-0.3}$	$0.3^{+0.0}_{-0.0}$	–
Ttw	(4a, 1)	$0.4^{+0.1}_{-0.1}$	$20.7^{+1.0}_{-1.0}$	$66.9^{+2.1}_{-2.1}$	$38.8^{+1.4}_{-1.4}$	$17.7^{+0.9}_{-0.9}$	$1.1^{+0.2}_{-0.2}$	$0.1^{+0.0}_{-0.0}$	–
Zinv	(4a, 1)	$0.1^{+0.1}_{-0.1}$	$5.1^{+0.4}_{-0.4}$	$11.0^{+0.6}_{-0.6}$	$7.9^{+0.5}_{-0.5}$	$5.7^{+0.4}_{-0.4}$	$0.7^{+0.1}_{-0.1}$	$0.2^{+0.0}_{-0.0}$	–
SM	(4a, 2)	$0.2^{+0.1}_{-0.1}$	$7.7^{+0.6}_{-0.6}$	$28.4^{+1.0}_{-1.0}$	$18.3^{+0.8}_{-0.8}$	$7.6^{+0.5}_{-0.5}$	$0.5^{+0.1}_{-0.1}$	$0.0^{+0.0}_{-0.0}$	–
Ttw	(4a, 2)	$0.2^{+0.1}_{-0.1}$	$6.6^{+0.5}_{-0.5}$	$26.4^{+1.0}_{-1.0}$	$17.2^{+0.8}_{-0.8}$	$6.7^{+0.5}_{-0.5}$	$0.4^{+0.1}_{-0.1}$	$0.0^{+0.0}_{-0.0}$	–
Zinv	(4a, 2)	$0.0^{+0.0}_{-0.0}$	$1.2^{+0.3}_{-0.3}$	$1.9^{+0.3}_{-0.3}$	$1.1^{+0.2}_{-0.2}$	$0.9^{+0.2}_{-0.2}$	$0.1^{+0.0}_{-0.0}$	$0.0^{+0.0}_{-0.0}$	–
SM	(4a, ≥ 3)	–	$0.7^{+0.2}_{-0.2}$	$1.8^{+0.2}_{-0.2}$	$0.9^{+0.2}_{-0.2}$	$0.5^{+0.1}_{-0.1}$	$0.1^{+0.0}_{-0.0}$	–	–
Ttw	(4a, ≥ 3)	–	$0.6^{+0.2}_{-0.2}$	$1.7^{+0.2}_{-0.2}$	$0.8^{+0.2}_{-0.2}$	$0.5^{+0.1}_{-0.1}$	$0.1^{+0.0}_{-0.0}$	–	–
Zinv	(4a, ≥ 3)	–	$0.1^{+0.0}_{-0.0}$	$0.1^{+0.1}_{-0.1}$	$0.1^{+0.0}_{-0.0}$	$0.0^{+0.0}_{-0.0}$	$0.0^{+0.0}_{-0.0}$	–	–
SM	(≥ 5a, 0)	–	–	$18.0^{+1.1}_{-1.1}$	$43.4^{+1.8}_{-1.8}$	$56.8^{+1.9}_{-1.9}$	$9.9^{+0.6}_{-0.6}$	$2.9^{+0.3}_{-0.3}$	–
Ttw	(≥ 5a, 0)	–	–	$11.3^{+1.0}_{-1.0}$	$27.1^{+1.6}_{-1.6}$	$36.3^{+1.8}_{-1.8}$	$5.5^{+0.6}_{-0.6}$	$1.4^{+0.3}_{-0.3}$	–
Zinv	(≥ 5a, 0)	–	–	$6.7^{+0.5}_{-0.5}$	$16.3^{+0.8}_{-0.8}$	$20.5^{+0.8}_{-0.8}$	$4.4^{+0.3}_{-0.3}$	$1.5^{+0.2}_{-0.2}$	–
SM	(≥ 5a, 1)	–	–	$11.5^{+0.7}_{-0.7}$	$28.1^{+1.0}_{-1.0}$	$37.3^{+1.2}_{-1.2}$	$7.2^{+0.5}_{-0.5}$	$1.1^{+0.2}_{-0.2}$	–
Ttw	(≥ 5a, 1)	–	–	$10.5^{+0.6}_{-0.6}$	$25.4^{+1.0}_{-1.0}$	$34.0^{+1.2}_{-1.2}$	$6.4^{+0.5}_{-0.5}$	$0.8^{+0.2}_{-0.2}$	–
Zinv	(≥ 5a, 1)	–	–	$1.0^{+0.2}_{-0.2}$	$2.7^{+0.3}_{-0.3}$	$3.2^{+0.3}_{-0.3}$	$0.9^{+0.1}_{-0.1}$	$0.3^{+0.1}_{-0.1}$	–
SM	(≥ 5a, 2)	–	–	$4.9^{+0.5}_{-0.5}$	$14.9^{+0.7}_{-0.7}$	$20.6^{+0.8}_{-0.8}$	$3.6^{+0.4}_{-0.4}$	$0.4^{+0.1}_{-0.1}$	–
Ttw	(≥ 5a, 2)	–	–	$4.6^{+0.5}_{-0.5}$	$14.4^{+0.7}_{-0.7}$	$19.6^{+0.8}_{-0.8}$	$3.2^{+0.3}_{-0.3}$	$0.4^{+0.1}_{-0.1}$	–
Zinv	(≥ 5a, 2)	–	–	$0.2^{+0.1}_{-0.1}$	$0.5^{+0.1}_{-0.1}$	$1.0^{+0.2}_{-0.2}$	$0.3^{+0.1}_{-0.1}$	$0.0^{+0.0}_{-0.0}$	–
SM	(≥ 5a, ≥ 3)	–	–	–	$1.5^{+0.2}_{-0.2}$	$2.4^{+0.3}_{-0.3}$	$0.6^{+0.1}_{-0.1}$	–	–
Ttw	(≥ 5a, ≥ 3)	–	–	–	$1.5^{+0.2}_{-0.2}$	$2.3^{+0.3}_{-0.3}$	$0.5^{+0.1}_{-0.1}$	–	–
Zinv	(≥ 5a, ≥ 3)	–	–	–	$0.0^{+0.0}_{-0.0}$	$0.1^{+0.1}_{-0.1}$	$0.1^{+0.1}_{-0.1}$	–	–

DRAFT

Table 37: MC yields in the signal region for 1.26fb^{-1} for monojet categories. The letter "a" in jet e.g. "2a" indicates the asymmetric jet bins. All entries are non-zero but are truncated to one decimal place.

H_T (GeV)	(n_{jet}, n_b)	200-250	250-300	300-350	350-400	400-500	500-600	600-800	800-∞
SM	(1, 0)	$3655.7^{+20.3}_{-20.3}$	$1221.7^{+10.1}_{-10.1}$	$487.2^{+6.0}_{-6.0}$	$207.5^{+3.5}_{-3.5}$	$155.0^{+2.6}_{-2.6}$	$46.0^{+1.2}_{-1.2}$	$20.4^{+0.5}_{-0.5}$	–
Ttw	(1, 0)	$1415.0^{+16.9}_{-16.9}$	$420.3^{+8.4}_{-8.4}$	$145.4^{+4.8}_{-4.8}$	$52.0^{+2.6}_{-2.6}$	$38.5^{+1.8}_{-1.8}$	$9.3^{+0.7}_{-0.7}$	$3.5^{+0.3}_{-0.3}$	–
Zinv	(1, 0)	$2240.8^{+11.2}_{-11.2}$	$801.4^{+5.6}_{-5.6}$	$341.8^{+3.6}_{-3.6}$	$155.5^{+2.3}_{-2.3}$	$116.5^{+1.8}_{-1.8}$	$36.8^{+0.9}_{-0.9}$	$16.9^{+0.5}_{-0.5}$	–
SM	(1, 1)	$127.8^{+3.3}_{-3.3}$	$46.1^{+1.8}_{-1.8}$	$20.8^{+1.3}_{-1.3}$	$8.2^{+0.6}_{-0.6}$	$7.4^{+0.6}_{-0.6}$	$1.9^{+0.2}_{-0.2}$	$1.1^{+0.1}_{-0.1}$	–
Ttw	(1, 1)	$39.0^{+2.5}_{-2.5}$	$12.2^{+1.3}_{-1.3}$	$6.0^{+1.0}_{-1.0}$	$1.6^{+0.4}_{-0.4}$	$2.0^{+0.4}_{-0.4}$	$0.5^{+0.2}_{-0.2}$	$0.3^{+0.1}_{-0.1}$	–
Zinv	(1, 1)	$88.8^{+2.1}_{-2.1}$	$34.0^{+1.2}_{-1.2}$	$14.8^{+0.7}_{-0.7}$	$6.7^{+0.5}_{-0.5}$	$5.4^{+0.4}_{-0.4}$	$1.4^{+0.2}_{-0.2}$	$0.8^{+0.1}_{-0.1}$	–

DRAFT

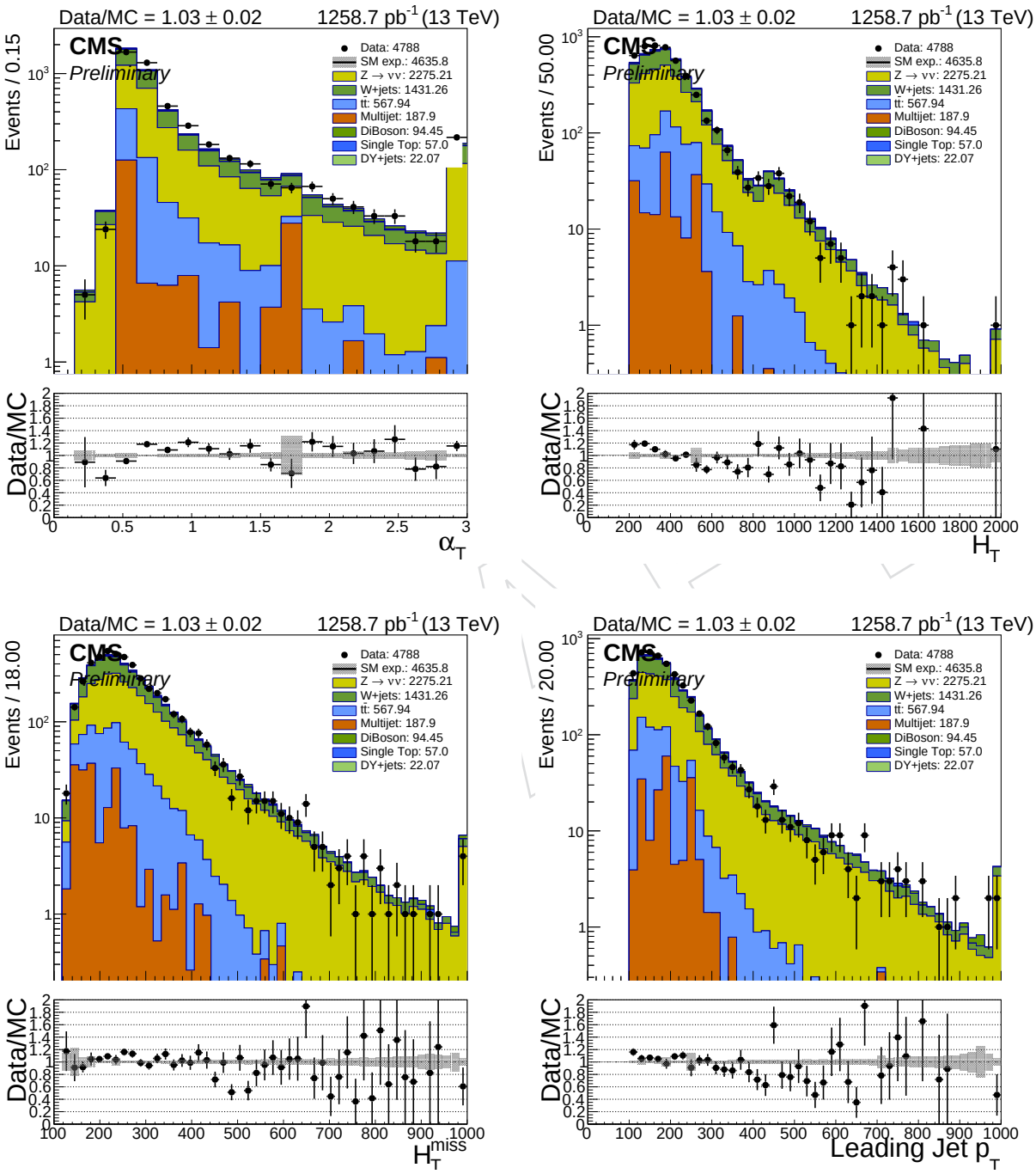

Figure 23: Key analysis variables for hadronic signal region (symmetric n_{jet} bins)

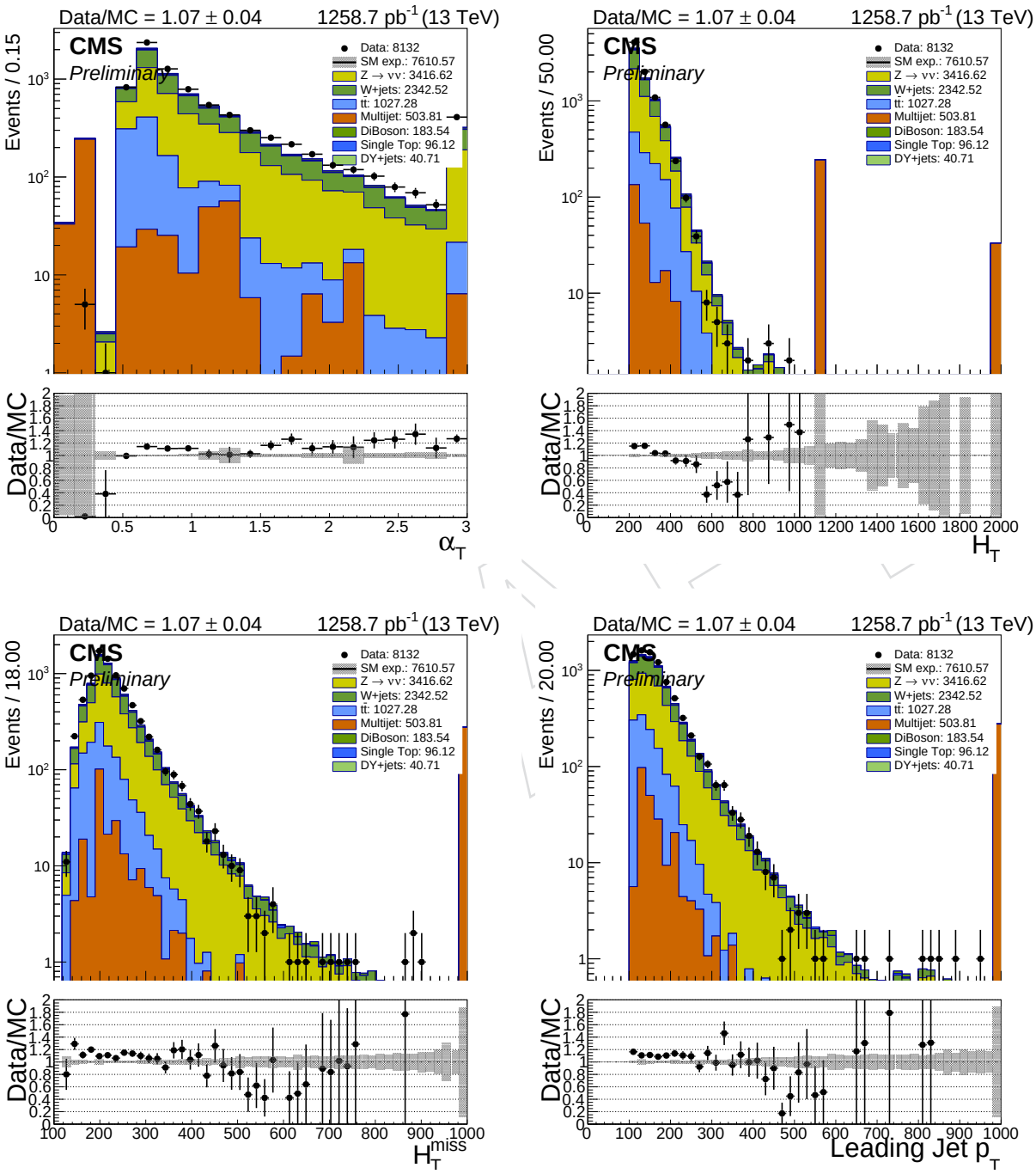

Figure 24: Key analysis variables for hadronic signal region (asymmetric n_{jet} bins)

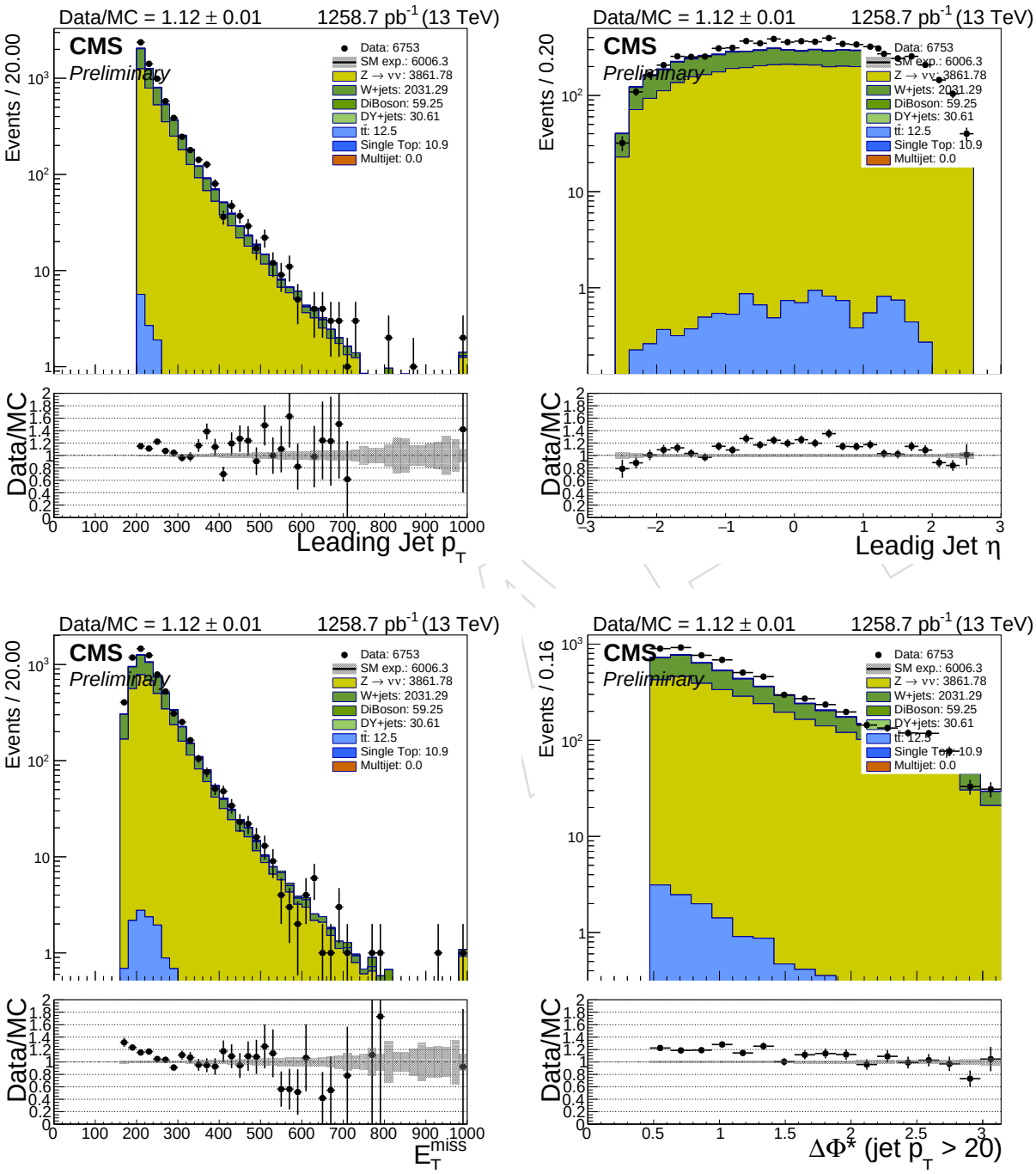

Figure 25: Key analysis variables for hadronic signal region (monojet bins)

10 Estimation for QCD multijet events

One of the major challenges for searches of new physics in the jets + $E_{\mathrm{T}}^{\mathrm{miss}}$ final state is the control of background events from QCD multijet production. The difficulties in the determination of precise estimates for this background stem from the large cross sections expected in the high-energy, high-luminosity hadron collider environment at the LHC, which are further compounded by the lack of precise theoretical predictions for the cross sections and kinematic properties of multijet events. Hence, without special consideration and treatment, significant uncertainties on large background expectations can overwhelm any potential sensitivity to new physics signatures.

With regards to QCD multijet production, the approach of this search is to favour the suppression of the multijet background to a negligible level over the goal of high efficiency for any given signal model. A conservative uncertainty on a negligible contribution is preferred over a procedure that attempts to accurately estimate a non-negligible contribution from multijet events. The level of contamination should be sufficiently small (i.e. sub-percent level) such that the associated uncertainty, even if large, will be sub-dominant with respect to the uncertainties on the remaining SM backgrounds with genuine $E_{\mathrm{T}}^{\mathrm{miss}}$ such as $\mathrm{W}+\mathrm{jets}$, $\mathrm{Z} \to \nu\bar{\nu}$, and $\mathrm{t\bar{t}}$, henceforth labelled as non-multijet processes.

Any contamination from QCD multijet events is controlled primarily through the α_{T} and $\Delta\phi^{*}_{\mathrm{min}}$ variables. The α_{T} variable is able to distiguish with high efficiency the sources of "fake" $E_{\mathrm{T}}^{\mathrm{miss}}$, such as jet energy mismeasurement, from those with "genuine" $E_{\mathrm{T}}^{\mathrm{miss}}$, such as neutrinos. The $\Delta\phi^{*}_{\mathrm{min}}$ variable is also very efficient at identifying jets that suffer under-measurements, as well as over-measurements, in (otherwise balanced) multijet events. The variable is also particularly suited to identifying multijet events that exhibit significant $E_{\mathrm{T}}^{\mathrm{miss}}$ due to the production of neutrinos (collinear with a jet axis) in semileptonic heavy-flavour decays. Both variables are individually capable of reducing the yields from multijet events by several orders of magnitude, and combined provide an extremely robust method to reject multijet events.

In Run 1, the α_{T} and $\Delta\phi^{*}_{\mathrm{min}}$ thresholds required to control multijet contamination to the required level were determined by a dedicated data-driven method, which relied on multijet-enriched sidebands in the variables α_{T}, $\Delta\phi^{*}_{\mathrm{min}}$, and $H_{\mathrm{T}}^{\mathrm{miss}}/E_{\mathrm{T}}^{\mathrm{miss}}$. The $H_{\mathrm{T}}^{\mathrm{miss}}/E_{\mathrm{T}}^{\mathrm{miss}}$ variable, discussed in Sec. 7, is used to filter QCD multijet events that contain soft jets below threshold contributing significantly to $H_{\mathrm{T}}^{\mathrm{miss}}$. The method relied on extrapolating the exponential modelling of the number of multijet events passing and failing a requirement on the variable $H_{\mathrm{T}}^{\mathrm{miss}}/E_{\mathrm{T}}^{\mathrm{miss}}$, i.e. the pass/fail ratio $\mathcal{R}$, as a function of α_{T} for a given signal region bin (defined in terms of n_{jet}, n_{b}, and H_{T}). In essence, the approach employed was an ABCD method that accounted for the correlation between the variables $\mathcal{R}$ and α_{T}, followed by an additional requirement on $\Delta\phi^{*}_{\mathrm{min}}$ determined and validated in a data control sideband.

For this search, we employ a simpler approach that relies on the determination of the ratio $\mathcal{R}$ per (n_{jet},H_{T}) bin from simulation. The ratio is determined following the application of the α_{T} and $\Delta\phi^{*}_{\mathrm{min}}$ requirements, which in the former case are H_{T}-dependent. For the region $H_{\mathrm{T}} > 800\,\mathrm{GeV}$, the requirement $H_{\mathrm{T}}^{\mathrm{miss}} > 130\,\mathrm{GeV}$ is made in place of any on α_{T}. No α_{T} nor $H_{\mathrm{T}}^{\mathrm{miss}}$ requirements are imposed for events in the monojet category.[1] The requirements on α_{T}, $H_{\mathrm{T}}^{\mathrm{miss}}$, and $\Delta\phi^{*}_{\mathrm{min}}$ as a function of H_{T} are summarised in Sec. 7. Each ratio $\mathcal{R}$ is then used as a multiplier on data counts per (n_{jet},H_{T}) bin obtained in the $H_{\mathrm{T}}^{\mathrm{miss}}/E_{\mathrm{T}}^{\mathrm{miss}}$ data sideband. The data counts are corrected for contributions from V+jets and $\mathrm{t\bar{t}}$ (and other residual contributions from non-

[1] For events in the monojet bin, an implicit requirement of $H_{\mathrm{T}}^{\mathrm{miss}} > 200\,\mathrm{GeV}$ is indeed made given that $H_{\mathrm{T}}^{\mathrm{miss}} = H_{\mathrm{T}}$ for monojet events. No α_{T} calculation can be made given the absence of a second jet.

DRAFT

multijet processes) in order to obtain an estimate of the number of QCD multijet events, $\mathcal{Q}$ in each sideband bin. The product of these (corrected) counts and the ratio, $\mathcal{Q} \times r H_T^{miss} / E_T^{miss}$, provides an estimate of the level of QCD multijet events in each (n_{jet},H_T) bin of the signal region. The estimate is currently made inclusively with respect to the n_b and H_T^{miss} for each (n_{jet},H_T) bin. The method is outlined in more detail below.

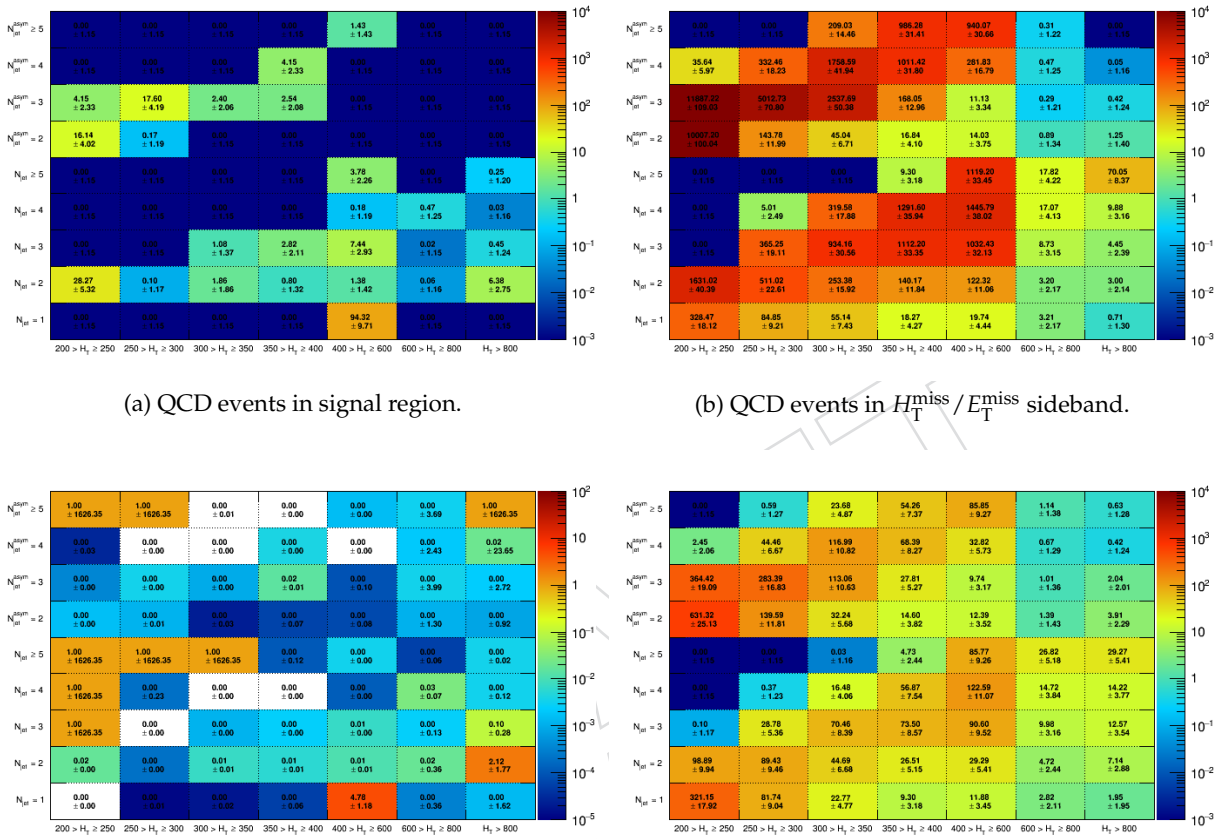

(a) QCD events in signal region.

(b) QCD events in H_T^{miss} / E_T^{miss} sideband.

(c) Ratio $\mathcal{R}$ for QCD events.

(d) EWK events in H_T^{miss} / E_T^{miss} sideband.

Figure 26: Expected number of QCD multijet events determined from simulation, binned according to n_{jet} and H_T, that (a) satify and (b) fail the requirement $H_T^{miss} / E_T^{miss} < 1.25$. Also shown in (c) is the ratio $\mathcal{R}$ for QCD multijets, again determined from simulation. Finally, (d) shows the expected number of EWK events (V+jets and $t\bar{t}$, plus other residual non-multijet backgrounds) that fail the $H_T^{miss} / E_T^{miss} < 1.25$ requirement, again determined from simulation and binned according to n_{jet} and H_T.

The number of counts from multijet events satisfying and failing the requirement $H_T^{miss} / E_T^{miss} < 1.25$, i.e. the pass/fail ratio $\mathcal{R}$, is determined from simulation per (n_{jet},H_T) bin. The pass and fail counts and the ratios are summarised in Fig. 26a, 26b, and 26c. Figure 26d shows the expected counts from non-multijet backgrounds in the H_T^{miss} / E_T^{miss} sideband, as determined from simulation.

The data counts in the H_T^{miss} / E_T^{miss} sideband are collected with the `HLT_HTxxx_AlphaT0pyy` and `HLT_HT800` signal triggers described in Sec. 5. Events satisfy the full signal region requirements plus the inverted H_T^{miss} / E_T^{miss} requirement and are binned according to n_{jet} and H_T. Any contribution from non-multijet backgrounds (V+jets, $t\bar{t}$, etc.) in each bin is estimated from sim-

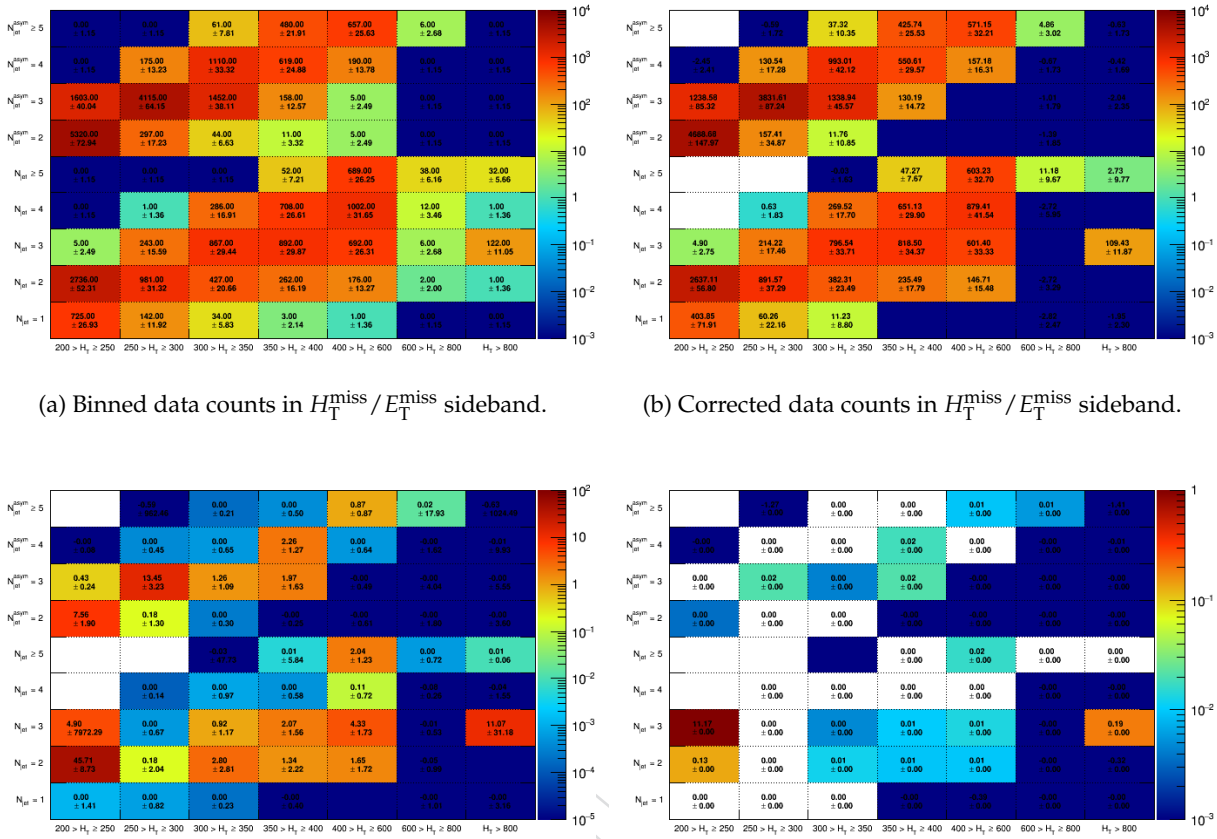

(a) Binned data counts in H_T^{miss}/E_T^{miss} sideband.

(b) Corrected data counts in H_T^{miss}/E_T^{miss} sideband.

(c) QCD multijet predictions in the signal region.

(d) Ratio of predicted multijet and non-multijet yields.

Figure 27: Expected number of QCD multijet events determined from simulation, binned according to n_{jet} and H_T that (a) fail and (b) satisfy the $H_T^{miss}/E_T^{miss} < 1.25$ requirement. Also shown in (c) is the ratio $\mathcal{R}$ for QCD multijets, again determined from simulation. Finally, (d) shows the expected number of EWK events (V+jets and $t\bar{t}$ plus other residual non-multijet backgrounds) that the fail the $H_T^{miss}/E_T^{miss} < 1.25$ requirement, again determined from simulation and binned according to n_{jet} and H_T.

ulation[2] and subtracted from the data counts. Any remaining counts, $\mathcal{Q}$, are assumed to arise from multijet production. Figure 27a shows the observed counts in the H_T^{miss}/E_T^{miss} sideband, and Fig. 27b shows the counts after subtracting the expected contributions from non-multijet processes. Figure 27c shows the predicted counts for the multijet contribution in the signal region bins, which are obtained from the products of $\mathcal{R}$ and $\mathcal{Q}$, summarised in Figs. 26c and 27b. Finally, Fig. 27d shows the ratios of predicted multijet counts with respect to the expected EWK counts, in order to quantify the (predicted) relative contamination from multijet events in the signal region bins.

The predictions summarised in Fig. 27d support the expectation based on experience with 8 TeV data that the H_T-dependent α_T thresholds defined in Table 24 and the requirement of $\Delta\phi^*_{min} > 0.5$ are sufficient to reduce the multijet contamination in all bins of the signal region to the sub-percent with respect to the total non-multijet background. With this level of suppression, it is expected that the uncertainty associated with the residual multijet contamination

[2] In the future, the counts from non-multijet backgrounds will be estimated from the muon data control samples and transfer factors determined from simulation (using the method described in Sec. 11).

to be sub-dominant with respect to, and fully aborbed by, the systematic uncertainties on the non-multijet backgrounds, which are expected to be at the level of $\sim$10% or larger.

DRAFT

11 Background estimation for processes with genuine $E_{\mathrm{T}}^{\mathrm{miss}}$

11.1 Overview of SM background processes

Once all the signal region selection requirements have been imposed, the contribution from QCD multijet events is expected to be negligible, as demonstrated in Appendix A. In the absence of multijet events, the background counts in the signal region arise from SM processes with significant $E_{\mathrm{T}}^{\mathrm{miss}}$ in the final state. In events with low statistics of jets and b-quark jets, the largest backgrounds with genuine $E_{\mathrm{T}}^{\mathrm{miss}}$ are from the associated production of W or Z bosons with jets, followed by either the weak decays $\mathrm{Z} \to \nu\bar{\nu}$ or $\mathrm{W} \to \tau\nu$, where the τ decays hadronically and is identified as a jet; or by leptonic decays that are not rejected by the dedicated electron or muon vetoes. The veto of events containing isolated tracks is efficient at further suppressing these backgrounds as well as the single-prong hadronic decay of the tau lepton. At higher jet and b-quark jet multiplicities, top quark production followed by semileptonic weak top quark decay becomes important. Residual contributions from processes such as single-top-quark, $\mathrm{t\bar{t}V}$ or $\mathrm{t\bar{t}H}$, diboson, and Drell-Yan production are also expected. These SM processes are collectively referred to as the non-multijet backgrounds.

The simulated samples are normalised using the most accurate cross section calculations currently available, usually with next-to-next-to-leading-order (NNLO) accuracy. To model the effects of pileup, the simulated events are generated with a nominal distribution of pp interactions per bunch crossing, which are then reweighted to match the pileup distribution as measured in data.

11.2 The "transfer factor" method

The method used to estimate the aforementioned SM background contributions in the hadronic signal region relies on the use of a transfer factor (TF) determined from MC samples to transform the observed yield in a given H_{T}, jet (n_{jet}) and b-tag (n_{b}) multiplicity bin of a control sample, $N_{\mathrm{obs}}^{\mathrm{control}}(n_{\mathrm{jet}}, n_{\mathrm{b}}, H_{\mathrm{T}})$, into a predicted yield for the corresponding bin of the hadronic signal region, $N_{\mathrm{pred}}^{\mathrm{signal}}(n_{\mathrm{jet}}, n_{\mathrm{b}}, H_{\mathrm{T}})$. The choice of n_{jet} and n_{b} event categorisation and H_{T} binning in the control samples is identical to that for the signal region, as defined in Sec. 7.

Each transfer factor is simply a ratio of the yields obtained from MC simulation for the same bin of the signal region and a given control sample:

$$\mathrm{TF} = \frac{N_{\mathrm{MC}}^{\mathrm{signal}}(n_{\mathrm{jet}}, n_{\mathrm{b}}, H_{\mathrm{T}})}{N_{\mathrm{MC}}^{\mathrm{control}}(n_{\mathrm{jet}}, n_{\mathrm{b}}, H_{\mathrm{T}})} \tag{5}$$

In this way, predictions of background counts from SM processes can be made based on the various control samples:

$$N_{\mathrm{pred}}^{\mathrm{signal}}(n_{\mathrm{jet}}, n_{\mathrm{b}}, H_{\mathrm{T}}) = \frac{N_{\mathrm{MC}}^{\mathrm{signal}}(n_{\mathrm{jet}}, n_{\mathrm{b}}, H_{\mathrm{T}})}{N_{\mathrm{MC}}^{\mathrm{control}}(n_{\mathrm{jet}}, n_{\mathrm{b}}, H_{\mathrm{T}})} \times N_{\mathrm{obs}}^{\mathrm{control}}(n_{\mathrm{jet}}, n_{\mathrm{b}}, H_{\mathrm{T}}) \tag{6}$$

When constructing the transfer factors, the MC expectations for the following SM processes are considered: W + jets (N_{W}), $\mathrm{t\bar{t}}$ + jets ($N_{\mathrm{t\bar{t}}}$), $\mathrm{Z} \to \nu\bar{\nu}$ + jets ($N_{\mathrm{Z}\to\nu\bar{\nu}}$), DY + jets ($N_{\mathrm{DY}}$), γ + jets (N_{γ}), single top + jets production via the s, t, and tW-channels (N_{top}), $WW+$ jets, WZ + jets, and $ZZ+$jets ($N_{\mathrm{di-boson}}$), and $\mathrm{t\bar{t}V}$ or $\mathrm{t\bar{t}H}$ ($N_{\mathrm{t\bar{t}X}}$). Details on the MC samples used are given in Sec. 4. All MC samples are normalised to the integrated luminosity of the appopriate data sample.

DRAFT

The selection criteria for the data control samples closely resemble those for the signal region, differing mainly through the use of a lepton or photon object *tag* (that is ignored in the calculation of jet-based kinematic variables such as H_{T}, $H_{\mathrm{T}}^{\mathrm{miss}}$, α_{T}, etc.) and minimal additional kinematic requirements (e.g. invariant or transerve mass windows) to obtain W, Z, and $\mathrm{t\bar{t}}$-enriched event samples. The same selection criteria are designed to suppress signal contamination in the control samples so that unbiased data-driven estimates for the SM backgrounds in the signal region can be made. More detail on the selection criteria can be found in Sec. 7.

The transfer factors account for differences in cross sections and branching ratios, acceptance and reconstruction efficiencies, and/or kinematic requirements between the signal and control regions. Any dependence on n_{jet}, n_{b}, or H_{T} is largely attributable to differences in acceptance due to the presence or otherwise of α_{T} or $H_{\mathrm{T}}^{\mathrm{miss}}$ requirements.

Many systematic effects are expected to cancel largely in the transfer factor. However, a systematic uncertainty is assigned to each transfer factor to account for theoretical uncertainties and effects such as the mismodelling of kinematics (e.g. acceptances) and instrumental effects (e.g. reconstruction efficiencies).

In the end, a fitting procedure that provides the final result is defined formally by the likelihood model described in Sec. 14. In summary, the observation in each bin (defined in terms of the variables n_{jet}, n_{b}, and H_{T}) of the signal sample is modelled as Poisson-distributed about the sum of a SM expectation (and a potential signal contribution). The components of this SM expectation are related to the expected yields in the control samples via transfer factors derived from simulation. The observations in each bin (again defined by n_{jet}, n_{b}, and H_{T}) of the control samples are similarly modelled as Poisson-distributed about the expectated yields for each control sample. In this way, for a given bin, the observed yields in the signal and control samples are connected via the transfer factors derived from simulation.

The transfer factors are shown in Tables 42, 43, 38, 39, 44, 45, 40, and 41. The procedure to determine the systematic uncertainties associated with these transfer factors is described in Sec. 12.

The transfer factors are shown in tables below.

Table 38: Transfer factors from the μ + jets control region to the Z_{inv} background for symmetric categories. The letter "a" in jet e.g. "2a" indicates the asymmetric jet bins. All entries are non-zero but are truncated to one decimal place.

H_{T} (GeV) (n_{jet}, n_{b})	200-250	250-300	300-350	350-400	400-500	500-600	600-800	800-∞
(2, 0)	$1.02^{+0.03}_{-0.03}$	$0.80^{+0.02}_{-0.02}$	$0.60^{+0.02}_{-0.02}$	$0.44^{+0.01}_{-0.01}$	$0.33^{+0.01}_{-0.01}$	$0.25^{+0.01}_{-0.01}$	$0.15^{+0.00}_{-0.00}$	$0.32^{+0.01}_{-0.01}$
(2, 1)	$0.36^{+0.02}_{-0.02}$	$0.35^{+0.02}_{-0.02}$	$0.36^{+0.02}_{-0.02}$	$0.31^{+0.02}_{-0.02}$	$0.20^{+0.01}_{-0.01}$	$0.16^{+0.01}_{-0.01}$	$0.12^{+0.01}_{-0.01}$	$0.27^{+0.02}_{-0.02}$
(2, 2)	$0.49^{+0.11}_{-0.11}$	$0.43^{+0.08}_{-0.08}$	$0.36^{+0.08}_{-0.08}$	–	$0.12^{+0.03}_{-0.03}$	$0.13^{+0.04}_{-0.04}$	$0.07^{+0.02}_{-0.02}$	$0.07^{+0.03}_{-0.03}$
(3, 0)	$0.28^{+0.15}_{-0.15}$	$0.43^{+0.02}_{-0.02}$	$0.58^{+0.02}_{-0.02}$	$0.52^{+0.01}_{-0.01}$	$0.45^{+0.01}_{-0.01}$	$0.30^{+0.01}_{-0.01}$	$0.21^{+0.00}_{-0.00}$	$0.29^{+0.01}_{-0.01}$
(3, 1)	$0.03^{+0.04}_{-0.04}$	$0.08^{+0.01}_{-0.01}$	$0.11^{+0.01}_{-0.01}$	$0.12^{+0.01}_{-0.01}$	$0.13^{+0.01}_{-0.01}$	$0.12^{+0.01}_{-0.01}$	$0.09^{+0.00}_{-0.00}$	$0.17^{+0.01}_{-0.01}$
(3, 2)	–	$0.05^{+0.01}_{-0.01}$	$0.05^{+0.01}_{-0.01}$	$0.04^{+0.01}_{-0.01}$	$0.04^{+0.00}_{-0.00}$	$0.04^{+0.01}_{-0.01}$	$0.03^{+0.01}_{-0.01}$	$0.06^{+0.01}_{-0.01}$
(3, ≥ 3)	–	–	–	$0.07^{+0.05}_{-0.05}$	$0.01^{+0.00}_{-0.00}$	$0.01^{+0.01}_{-0.01}$	–	–
(4, 0)	–	–	$0.52^{+0.04}_{-0.04}$	$0.55^{+0.02}_{-0.02}$	$0.44^{+0.01}_{-0.01}$	$0.35^{+0.01}_{-0.01}$	$0.24^{+0.00}_{-0.00}$	$0.26^{+0.01}_{-0.01}$
(4, 1)	–	–	$0.08^{+0.01}_{-0.01}$	$0.08^{+0.01}_{-0.01}$	$0.08^{+0.00}_{-0.00}$	$0.08^{+0.00}_{-0.00}$	$0.07^{+0.00}_{-0.00}$	$0.11^{+0.01}_{-0.01}$
(4, 2)	–	–	$0.04^{+0.01}_{-0.01}$	$0.02^{+0.00}_{-0.00}$	$0.03^{+0.00}_{-0.00}$	$0.03^{+0.00}_{-0.00}$	$0.02^{+0.00}_{-0.00}$	$0.04^{+0.01}_{-0.01}$
(4, ≥ 3)	–	–	–	$0.04^{+0.03}_{-0.03}$	$0.03^{+0.01}_{-0.01}$	$0.02^{+0.01}_{-0.01}$	$0.01^{+0.01}_{-0.01}$	$0.01^{+0.01}_{-0.01}$
(≥ 5, 0)	–	–	–	$0.32^{+0.05}_{-0.05}$	$0.36^{+0.02}_{-0.02}$	$0.28^{+0.01}_{-0.01}$	$0.20^{+0.01}_{-0.01}$	$0.20^{+0.00}_{-0.00}$
(≥ 5, 1)	–	–	–	$0.04^{+0.01}_{-0.01}$	$0.05^{+0.00}_{-0.00}$	$0.04^{+0.00}_{-0.00}$	$0.03^{+0.00}_{-0.00}$	$0.04^{+0.00}_{-0.00}$
(≥ 5, 2)	–	–	–	$0.01^{+0.01}_{-0.01}$	$0.02^{+0.00}_{-0.00}$	$0.01^{+0.00}_{-0.00}$	$0.01^{+0.00}_{-0.00}$	$0.01^{+0.00}_{-0.00}$
(≥ 5, ≥ 3)	–	–	–	–	$0.01^{+0.00}_{-0.00}$	$0.00^{+0.00}_{-0.00}$	$0.01^{+0.00}_{-0.00}$	$0.01^{+0.00}_{-0.00}$

DRAFT

Table 39: Transfer factors from the μ + jets control region to the Z_{inv} background for asymmetric categories. The letter “a” in jet e.g. “2a” indicates the asymmetric jet bins. All entries are non-zero but are truncated to one decimal place.

H_T (GeV) (n_{jet}, n_b)	200-250	250-300	300-350	350-400	400-500	500-600	600-800	800-∞
(2a, 0)	$0.55^{+0.01}_{-0.01}$	$0.34^{+0.01}_{-0.01}$	$0.30^{+0.01}_{-0.01}$	$0.30^{+0.01}_{-0.01}$	$0.30^{+0.01}_{-0.01}$	$0.28^{+0.01}_{-0.01}$	$0.25^{+0.01}_{-0.01}$	–
(2a, 1)	$0.22^{+0.01}_{-0.01}$	$0.18^{+0.01}_{-0.01}$	$0.16^{+0.01}_{-0.01}$	$0.21^{+0.02}_{-0.02}$	$0.18^{+0.02}_{-0.02}$	$0.20^{+0.03}_{-0.03}$	$0.19^{+0.03}_{-0.03}$	–
(2a, 2)	$0.21^{+0.02}_{-0.02}$	$0.12^{+0.02}_{-0.02}$	$0.12^{+0.03}_{-0.03}$	$0.07^{+0.02}_{-0.02}$	$0.09^{+0.04}_{-0.04}$	$0.07^{+0.05}_{-0.05}$	$0.07^{+0.06}_{-0.06}$	–
(3a, 0)	$0.57^{+0.01}_{-0.01}$	$0.44^{+0.01}_{-0.01}$	$0.42^{+0.01}_{-0.01}$	$0.32^{+0.01}_{-0.01}$	$0.23^{+0.01}_{-0.01}$	$0.19^{+0.01}_{-0.01}$	$0.18^{+0.01}_{-0.01}$	–
(3a, 1)	$0.10^{+0.00}_{-0.00}$	$0.09^{+0.00}_{-0.00}$	$0.10^{+0.00}_{-0.00}$	$0.10^{+0.01}_{-0.01}$	$0.08^{+0.01}_{-0.01}$	$0.04^{+0.01}_{-0.01}$	$0.06^{+0.01}_{-0.01}$	–
(3a, 2)	$0.04^{+0.00}_{-0.00}$	$0.04^{+0.00}_{-0.00}$	$0.05^{+0.01}_{-0.01}$	$0.03^{+0.01}_{-0.01}$	$0.05^{+0.01}_{-0.01}$	$0.04^{+0.02}_{-0.02}$	$0.03^{+0.01}_{-0.01}$	–
(3a, $\geq$ 3)	$0.02^{+0.01}_{-0.01}$	$0.04^{+0.02}_{-0.02}$	–	–	–	–	–	–
(4a, 0)	$0.16^{+0.04}_{-0.04}$	$0.28^{+0.01}_{-0.01}$	$0.43^{+0.01}_{-0.01}$	$0.42^{+0.02}_{-0.02}$	$0.39^{+0.01}_{-0.01}$	$0.24^{+0.02}_{-0.02}$	$0.15^{+0.02}_{-0.02}$	–
(4a, 1)	$0.02^{+0.01}_{-0.01}$	$0.05^{+0.00}_{-0.00}$	$0.06^{+0.00}_{-0.00}$	$0.07^{+0.01}_{-0.01}$	$0.09^{+0.01}_{-0.01}$	$0.05^{+0.01}_{-0.01}$	$0.04^{+0.01}_{-0.01}$	–
(4a, 2)	–	$0.03^{+0.01}_{-0.01}$	$0.02^{+0.00}_{-0.00}$	$0.02^{+0.00}_{-0.00}$	$0.03^{+0.00}_{-0.00}$	$0.02^{+0.01}_{-0.01}$	$0.00^{+0.00}_{-0.00}$	–
(4a, $\geq$ 3)	–	$0.02^{+0.01}_{-0.01}$	$0.02^{+0.01}_{-0.01}$	$0.02^{+0.01}_{-0.01}$	–	–	–	–
($\geq$ 5a, 0)	–	–	$0.40^{+0.04}_{-0.04}$	$0.38^{+0.02}_{-0.02}$	$0.32^{+0.02}_{-0.02}$	$0.22^{+0.02}_{-0.02}$	$0.21^{+0.03}_{-0.03}$	–
($\geq$ 5a, 1)	–	–	$0.05^{+0.01}_{-0.01}$	$0.05^{+0.01}_{-0.01}$	$0.04^{+0.00}_{-0.00}$	$0.03^{+0.01}_{-0.01}$	$0.02^{+0.01}_{-0.01}$	–
($\geq$ 5a, 2)	–	–	$0.02^{+0.01}_{-0.01}$	$0.02^{+0.00}_{-0.00}$	$0.02^{+0.00}_{-0.00}$	$0.02^{+0.00}_{-0.00}$	$0.01^{+0.00}_{-0.00}$	–
($\geq$ 5a, $\geq$ 3)	–	–	–	$0.00^{+0.00}_{-0.00}$	$0.02^{+0.01}_{-0.01}$	$0.03^{+0.02}_{-0.02}$	–	–

Table 40: Transfer factors from the γ + jets control region to the Z_{inv} background for symmetric categories. The letter “a” in jet e.g. “2a” indicates the asymmetric jet bins. All entries are non-zero but are truncated to one decimal place.

H_T (GeV) (n_{jet}, n_b)	400-500	500-600	600-800	800-∞
(2, 0)	$0.71^{+0.03}_{-0.03}$	$0.62^{+0.04}_{-0.04}$	$0.47^{+0.03}_{-0.03}$	$0.23^{+0.01}_{-0.01}$
(2, 1)	$0.68^{+0.11}_{-0.11}$	$0.57^{+0.13}_{-0.13}$	$0.75^{+0.14}_{-0.14}$	$0.23^{+0.03}_{-0.03}$
(2, 2)	$0.51^{+0.32}_{-0.32}$	$0.92^{+0.70}_{-0.70}$	$0.93^{+0.92}_{-0.92}$	$0.21^{+0.14}_{-0.14}$
(3, 0)	$0.63^{+0.02}_{-0.02}$	$0.58^{+0.03}_{-0.03}$	$0.59^{+0.02}_{-0.02}$	$0.22^{+0.01}_{-0.01}$
(3, 1)	$0.75^{+0.09}_{-0.09}$	$0.62^{+0.09}_{-0.09}$	$0.84^{+0.11}_{-0.11}$	$0.23^{+0.02}_{-0.02}$
(3, 2)	$0.85^{+0.30}_{-0.30}$	$0.82^{+0.35}_{-0.35}$	$0.71^{+0.27}_{-0.27}$	$0.20^{+0.06}_{-0.06}$
(3, $\geq$ 3)	–	–	–	–
(4, 0)	$0.72^{+0.04}_{-0.04}$	$0.63^{+0.04}_{-0.04}$	$0.51^{+0.02}_{-0.02}$	$0.23^{+0.01}_{-0.01}$
(4, 1)	$0.69^{+0.10}_{-0.10}$	$0.69^{+0.10}_{-0.10}$	$0.66^{+0.08}_{-0.08}$	$0.26^{+0.02}_{-0.02}$
(4, 2)	$0.59^{+0.16}_{-0.16}$	$0.71^{+0.27}_{-0.27}$	$0.43^{+0.12}_{-0.12}$	$0.22^{+0.05}_{-0.05}$
(4, $\geq$ 3)	$6.56^{+7.24}_{-7.24}$	$0.57^{+0.65}_{-0.65}$	$0.52^{+0.60}_{-0.60}$	–
($\geq$ 5, 0)	$0.77^{+0.10}_{-0.10}$	$0.64^{+0.06}_{-0.06}$	$0.50^{+0.03}_{-0.03}$	$0.25^{+0.01}_{-0.01}$
($\geq$ 5, 1)	$0.79^{+0.20}_{-0.20}$	$0.44^{+0.08}_{-0.08}$	$0.42^{+0.05}_{-0.05}$	$0.21^{+0.02}_{-0.02}$
($\geq$ 5, 2)	$0.91^{+0.47}_{-0.47}$	$0.65^{+0.25}_{-0.25}$	$0.40^{+0.13}_{-0.13}$	$0.24^{+0.04}_{-0.04}$
($\geq$ 5, $\geq$ 3)	–	–	$2.36^{+2.05}_{-2.05}$	$0.43^{+0.23}_{-0.23}$

DRAFT

Table 41: Transfer factors from the γ + jets control region to the Z_{inv} background for asymmetric categories. The letter "a" in jet e.g. "2a" indicates the asymmetric jet bins. All entries are non-zero but are truncated to one decimal place.

H_T (GeV) (n_{jet}, n_b)	400-500	500-600	600-800	800-∞
(2a, 0)	$0.62^{+0.04}_{-0.04}$	$0.56^{+0.06}_{-0.06}$	$0.43^{+0.05}_{-0.05}$	–
(2a, 1)	$0.84^{+0.20}_{-0.20}$	$0.60^{+0.22}_{-0.22}$	$1.27^{+0.46}_{-0.46}$	–
(2a, 2)	–	–	–	–
(3a, 0)	$0.63^{+0.05}_{-0.05}$	$0.59^{+0.09}_{-0.09}$	$0.64^{+0.11}_{-0.11}$	–
(3a, 1)	$0.51^{+0.12}_{-0.12}$	$0.32^{+0.13}_{-0.13}$	$0.32^{+0.13}_{-0.13}$	–
(3a, 2)	$0.58^{+0.37}_{-0.37}$	$0.49^{+0.54}_{-0.54}$	$0.44^{+0.50}_{-0.50}$	–
(3a, $\geq$ 3)	–	–	–	–
(4a, 0)	$0.65^{+0.05}_{-0.05}$	$0.58^{+0.10}_{-0.10}$	$0.49^{+0.12}_{-0.12}$	–
(4a, 1)	$0.74^{+0.15}_{-0.15}$	$0.30^{+0.11}_{-0.11}$	$0.46^{+0.26}_{-0.26}$	–
(4a, 2)	$0.70^{+0.36}_{-0.36}$	–	–	–
(4a, $\geq$ 3)	–	–	–	–
($\geq$ 5a, 0)	$0.60^{+0.07}_{-0.07}$	$0.60^{+0.12}_{-0.12}$	$0.51^{+0.14}_{-0.14}$	–
($\geq$ 5a, 1)	$0.90^{+0.29}_{-0.29}$	$0.40^{+0.15}_{-0.15}$	$0.56^{+0.29}_{-0.29}$	–
($\geq$ 5a, 2)	$0.71^{+0.44}_{-0.44}$	$3.83^{+3.60}_{-3.60}$	–	–
($\geq$ 5a, $\geq$ 3)	–	–	–	–

Table 42: Transfer factors from the μ + jets control region to the $t\bar{t}/W$ background for symmetric categories. The letter "a" in jet e.g. "2a" indicates the asymmetric jet bins. All entries are non-zero but are truncated to one decimal place.

H_T (GeV) (n_{jet}, n_b)	200-250	250-300	300-350	350-400	400-500	500-600	600-800	800-∞
(2, 0)	$0.94^{+0.03}_{-0.03}$	$0.64^{+0.02}_{-0.02}$	$0.44^{+0.02}_{-0.02}$	$0.27^{+0.01}_{-0.01}$	$0.18^{+0.01}_{-0.01}$	$0.12^{+0.01}_{-0.01}$	$0.06^{+0.00}_{-0.00}$	$0.13^{+0.01}_{-0.01}$
(2, 1)	$0.71^{+0.04}_{-0.04}$	$0.52^{+0.03}_{-0.03}$	$0.37^{+0.03}_{-0.03}$	$0.22^{+0.03}_{-0.03}$	$0.14^{+0.01}_{-0.01}$	$0.08^{+0.01}_{-0.01}$	$0.04^{+0.01}_{-0.01}$	$0.13^{+0.02}_{-0.02}$
(2, 2)	$0.54^{+0.12}_{-0.12}$	$0.36^{+0.09}_{-0.09}$	$0.36^{+0.10}_{-0.10}$	–	$0.09^{+0.03}_{-0.03}$	$0.15^{+0.06}_{-0.06}$	$0.01^{+0.01}_{-0.01}$	$0.03^{+0.02}_{-0.02}$
(3, 0)	$0.43^{+0.22}_{-0.22}$	$0.40^{+0.03}_{-0.03}$	$0.54^{+0.02}_{-0.02}$	$0.47^{+0.02}_{-0.02}$	$0.34^{+0.01}_{-0.01}$	$0.18^{+0.01}_{-0.01}$	$0.09^{+0.00}_{-0.00}$	$0.12^{+0.00}_{-0.00}$
(3, 1)	$0.21^{+0.12}_{-0.12}$	$0.30^{+0.02}_{-0.02}$	$0.32^{+0.01}_{-0.01}$	$0.31^{+0.01}_{-0.01}$	$0.21^{+0.01}_{-0.01}$	$0.12^{+0.01}_{-0.01}$	$0.06^{+0.00}_{-0.00}$	$0.08^{+0.01}_{-0.01}$
(3, 2)	–	$0.20^{+0.03}_{-0.03}$	$0.24^{+0.02}_{-0.02}$	$0.22^{+0.02}_{-0.02}$	$0.13^{+0.01}_{-0.01}$	$0.07^{+0.01}_{-0.01}$	$0.02^{+0.01}_{-0.01}$	$0.03^{+0.01}_{-0.01}$
(3, $\geq$ 3)	–	–	–	$0.42^{+0.17}_{-0.17}$	$0.07^{+0.03}_{-0.03}$	$0.05^{+0.04}_{-0.04}$	–	–
(4, 0)	–	–	$0.68^{+0.07}_{-0.07}$	$0.65^{+0.03}_{-0.03}$	$0.46^{+0.01}_{-0.01}$	$0.25^{+0.01}_{-0.01}$	$0.14^{+0.00}_{-0.00}$	$0.12^{+0.00}_{-0.00}$
(4, 1)	–	–	$0.43^{+0.03}_{-0.03}$	$0.42^{+0.02}_{-0.02}$	$0.26^{+0.01}_{-0.01}$	$0.13^{+0.01}_{-0.01}$	$0.08^{+0.01}_{-0.01}$	$0.07^{+0.01}_{-0.01}$
(4, 2)	–	–	$0.36^{+0.04}_{-0.04}$	$0.32^{+0.02}_{-0.02}$	$0.23^{+0.01}_{-0.01}$	$0.11^{+0.01}_{-0.01}$	$0.04^{+0.01}_{-0.01}$	$0.04^{+0.01}_{-0.01}$
(4, $\geq$ 3)	–	–	–	$0.26^{+0.06}_{-0.06}$	$0.27^{+0.04}_{-0.04}$	$0.10^{+0.03}_{-0.03}$	$0.02^{+0.01}_{-0.01}$	$0.02^{+0.01}_{-0.01}$
($\geq$ 5, 0)	–	–	–	$0.53^{+0.10}_{-0.10}$	$0.51^{+0.03}_{-0.03}$	$0.30^{+0.01}_{-0.01}$	$0.18^{+0.01}_{-0.01}$	$0.12^{+0.00}_{-0.00}$
($\geq$ 5, 1)	–	–	–	$0.30^{+0.04}_{-0.04}$	$0.35^{+0.01}_{-0.01}$	$0.19^{+0.01}_{-0.01}$	$0.10^{+0.00}_{-0.00}$	$0.07^{+0.00}_{-0.00}$
($\geq$ 5, 2)	–	–	–	$0.26^{+0.05}_{-0.05}$	$0.33^{+0.02}_{-0.02}$	$0.16^{+0.01}_{-0.01}$	$0.06^{+0.00}_{-0.00}$	$0.05^{+0.00}_{-0.00}$
($\geq$ 5, $\geq$ 3)	–	–	–	–	$0.24^{+0.04}_{-0.04}$	$0.17^{+0.03}_{-0.03}$	$0.08^{+0.01}_{-0.01}$	$0.04^{+0.01}_{-0.01}$

DRAFT

Table 43: Transfer factors from the μ + jets control region to the $t\bar{t}/W$ background for asymmetric categories. The letter “a” in jet e.g. “2a” indicates the asymmetric jet bins. All entries are non-zero but are truncated to one decimal place.

H_T (GeV) (n_{jet}, n_b)	200-250	250-300	300-350	350-400	400-500	500-600	600-800	800-∞
(2a, 0)	$0.49^{+0.01}_{-0.01}$	$0.25^{+0.01}_{-0.01}$	$0.19^{+0.01}_{-0.01}$	$0.16^{+0.01}_{-0.01}$	$0.13^{+0.01}_{-0.01}$	$0.12^{+0.01}_{-0.01}$	$0.08^{+0.01}_{-0.01}$	–
(2a, 1)	$0.34^{+0.01}_{-0.01}$	$0.22^{+0.01}_{-0.01}$	$0.14^{+0.01}_{-0.01}$	$0.11^{+0.02}_{-0.02}$	$0.11^{+0.02}_{-0.02}$	$0.08^{+0.04}_{-0.04}$	$0.09^{+0.03}_{-0.03}$	–
(2a, 2)	$0.24^{+0.03}_{-0.03}$	$0.13^{+0.03}_{-0.03}$	$0.12^{+0.04}_{-0.04}$	$0.19^{+0.09}_{-0.09}$	$0.07^{+0.04}_{-0.04}$	–	$0.08^{+0.06}_{-0.06}$	–
(3a, 0)	$0.63^{+0.02}_{-0.02}$	$0.45^{+0.01}_{-0.01}$	$0.40^{+0.01}_{-0.01}$	$0.23^{+0.01}_{-0.01}$	$0.13^{+0.01}_{-0.01}$	$0.09^{+0.01}_{-0.01}$	$0.06^{+0.01}_{-0.01}$	–
(3a, 1)	$0.41^{+0.01}_{-0.01}$	$0.32^{+0.01}_{-0.01}$	$0.28^{+0.01}_{-0.01}$	$0.20^{+0.01}_{-0.01}$	$0.10^{+0.01}_{-0.01}$	$0.07^{+0.02}_{-0.02}$	$0.02^{+0.01}_{-0.01}$	–
(3a, 2)	$0.26^{+0.01}_{-0.01}$	$0.21^{+0.01}_{-0.01}$	$0.27^{+0.02}_{-0.02}$	$0.17^{+0.02}_{-0.02}$	$0.07^{+0.02}_{-0.02}$	$0.05^{+0.03}_{-0.03}$	–	–
(3a, ≥ 3)	$0.16^{+0.05}_{-0.05}$	$0.15^{+0.04}_{-0.04}$	$0.19^{+0.06}_{-0.06}$	–	$0.01^{+0.01}_{-0.01}$	–	–	–
(4a, 0)	$0.09^{+0.04}_{-0.04}$	$0.38^{+0.02}_{-0.02}$	$0.53^{+0.02}_{-0.02}$	$0.51^{+0.03}_{-0.03}$	$0.33^{+0.02}_{-0.02}$	$0.14^{+0.02}_{-0.02}$	$0.05^{+0.01}_{-0.01}$	–
(4a, 1)	$0.08^{+0.02}_{-0.02}$	$0.20^{+0.01}_{-0.01}$	$0.37^{+0.01}_{-0.01}$	$0.36^{+0.01}_{-0.01}$	$0.27^{+0.02}_{-0.02}$	$0.09^{+0.02}_{-0.02}$	$0.02^{+0.01}_{-0.01}$	–
(4a, 2)	$0.09^{+0.04}_{-0.04}$	$0.15^{+0.01}_{-0.01}$	$0.32^{+0.01}_{-0.01}$	$0.31^{+0.02}_{-0.02}$	$0.21^{+0.02}_{-0.02}$	$0.07^{+0.02}_{-0.02}$	$0.01^{+0.01}_{-0.01}$	–
(4a, ≥ 3)	–	$0.21^{+0.06}_{-0.06}$	$0.32^{+0.05}_{-0.05}$	$0.22^{+0.05}_{-0.05}$	$0.23^{+0.06}_{-0.06}$	$0.23^{+0.19}_{-0.19}$	–	–
(≥ 5a, 0)	–	–	$0.67^{+0.08}_{-0.08}$	$0.63^{+0.05}_{-0.05}$	$0.57^{+0.03}_{-0.03}$	$0.27^{+0.03}_{-0.03}$	$0.19^{+0.04}_{-0.04}$	–
(≥ 5a, 1)	–	–	$0.52^{+0.04}_{-0.04}$	$0.46^{+0.02}_{-0.02}$	$0.37^{+0.01}_{-0.01}$	$0.22^{+0.02}_{-0.02}$	$0.08^{+0.02}_{-0.02}$	–
(≥ 5a, 2)	–	–	$0.37^{+0.04}_{-0.04}$	$0.46^{+0.03}_{-0.03}$	$0.38^{+0.02}_{-0.02}$	$0.17^{+0.02}_{-0.02}$	$0.08^{+0.02}_{-0.02}$	–
(≥ 5a, ≥ 3)	–	–	–	$0.41^{+0.07}_{-0.07}$	$0.37^{+0.05}_{-0.05}$	$0.23^{+0.06}_{-0.06}$	–	–

Table 44: Transfer factors from the $\mu\mu$ + jets control region to the Z_{inv} background for symmetric categories. The letter “a” in jet e.g. “2a” indicates the asymmetric jet bins. All entries are non-zero but are truncated to one decimal place.

H_T (GeV) (n_{jet}, n_b)	200-250	250-300	300-350	350-400	400-500	500-600	600-800	800-∞
(2, 0)	$9.90^{+0.68}_{-0.68}$	$7.80^{+0.44}_{-0.44}$	$5.05^{+0.27}_{-0.27}$	$4.15^{+0.21}_{-0.21}$	$3.06^{+0.09}_{-0.09}$	$2.16^{+0.07}_{-0.07}$	$1.31^{+0.04}_{-0.04}$	$2.71^{+0.09}_{-0.09}$
(2, 1)	$7.16^{+1.53}_{-1.53}$	$4.77^{+0.83}_{-0.83}$	$3.58^{+0.60}_{-0.60}$	$2.98^{+0.47}_{-0.47}$	$2.37^{+0.19}_{-0.19}$	$2.15^{+0.24}_{-0.24}$	$1.53^{+0.15}_{-0.15}$	$2.69^{+0.26}_{-0.26}$
(2, 2)	$10.32^{+5.34}_{-5.34}$	$3.33^{+1.49}_{-1.49}$	$7.27^{+3.60}_{-3.60}$	–	$2.34^{+0.87}_{-0.87}$	$3.46^{+1.51}_{-1.51}$	$1.41^{+0.54}_{-0.54}$	$3.10^{+1.89}_{-1.89}$
(3, 0)	$4.98^{+4.53}_{-4.53}$	$6.05^{+0.77}_{-0.77}$	$6.76^{+0.50}_{-0.50}$	$5.94^{+0.33}_{-0.33}$	$4.76^{+0.14}_{-0.14}$	$3.07^{+0.09}_{-0.09}$	$2.00^{+0.05}_{-0.05}$	$2.52^{+0.07}_{-0.07}$
(3, 1)	–	$4.45^{+1.07}_{-1.07}$	$3.74^{+0.60}_{-0.60}$	$4.66^{+0.61}_{-0.61}$	$3.30^{+0.27}_{-0.27}$	$2.22^{+0.18}_{-0.18}$	$1.58^{+0.11}_{-0.11}$	$2.24^{+0.17}_{-0.17}$
(3, 2)	–	$1.17^{+0.49}_{-0.49}$	$2.46^{+0.72}_{-0.72}$	$1.71^{+0.43}_{-0.43}$	$1.71^{+0.32}_{-0.32}$	$1.42^{+0.33}_{-0.33}$	$0.94^{+0.20}_{-0.20}$	$1.69^{+0.49}_{-0.49}$
(3, ≥ 3)	–	–	–	$0.76^{+0.74}_{-0.74}$	$0.23^{+0.22}_{-0.22}$	$4.24^{+5.21}_{-5.21}$	–	–
(4, 0)	–	–	$5.24^{+1.03}_{-1.03}$	$7.61^{+0.91}_{-0.91}$	$6.13^{+0.26}_{-0.26}$	$4.15^{+0.16}_{-0.16}$	$2.69^{+0.08}_{-0.08}$	$2.52^{+0.09}_{-0.09}$
(4, 1)	–	–	$9.05^{+4.45}_{-4.45}$	$6.41^{+1.09}_{-1.09}$	$3.46^{+0.35}_{-0.35}$	$2.75^{+0.25}_{-0.25}$	$1.96^{+0.15}_{-0.15}$	$2.19^{+0.16}_{-0.16}$
(4, 2)	–	–	$5.02^{+2.97}_{-2.97}$	$1.49^{+0.57}_{-0.57}$	$2.66^{+0.50}_{-0.50}$	$2.11^{+0.48}_{-0.48}$	$1.12^{+0.25}_{-0.25}$	$1.55^{+0.28}_{-0.28}$
(4, ≥ 3)	–	–	–	$3.59^{+3.91}_{-3.91}$	$2.82^{+1.99}_{-1.99}$	$2.49^{+1.86}_{-1.86}$	$1.33^{+0.94}_{-0.94}$	$0.36^{+0.23}_{-0.23}$
(≥ 5, 0)	–	–	–	$17.39^{+6.00}_{-6.00}$	$6.71^{+0.84}_{-0.84}$	$5.37^{+0.35}_{-0.35}$	$3.23^{+0.14}_{-0.14}$	$2.54^{+0.08}_{-0.08}$
(≥ 5, 1)	–	–	–	$4.12^{+2.82}_{-2.82}$	$3.58^{+0.70}_{-0.70}$	$2.65^{+0.49}_{-0.49}$	$2.34^{+0.22}_{-0.22}$	$1.68^{+0.11}_{-0.11}$
(≥ 5, 2)	–	–	–	$1.73^{+2.20}_{-2.20}$	$1.53^{+0.45}_{-0.45}$	$1.43^{+0.34}_{-0.34}$	$1.28^{+0.26}_{-0.26}$	$1.02^{+0.14}_{-0.14}$
(≥ 5, ≥ 3)	–	–	–	–	$0.43^{+0.37}_{-0.37}$	$0.88^{+0.67}_{-0.67}$	$2.78^{+1.34}_{-1.34}$	$1.04^{+0.45}_{-0.45}$

DRAFT

Table 45: Transfer factors from the $\mu\mu$ + jets control region to the Z_{inv} background for asymmetric categories. The letter "a" in jet e.g. "2a" indicates the asymmetric jet bins. All entries are non-zero but are truncated to one decimal place.

H_{T} (GeV) (n_{jet}, n_{b})	200-250	250-300	300-350	350-400	400-500	500-600	600-800	800-∞
(2a, 0)	$5.38^{+0.12}_{-0.12}$	$3.15^{+0.10}_{-0.10}$	$2.50^{+0.10}_{-0.10}$	$2.25^{+0.12}_{-0.12}$	$2.42^{+0.10}_{-0.10}$	$1.92^{+0.12}_{-0.12}$	$1.68^{+0.12}_{-0.12}$	–
(2a, 1)	$3.46^{+0.22}_{-0.22}$	$2.10^{+0.20}_{-0.20}$	$1.69^{+0.22}_{-0.22}$	$2.45^{+0.43}_{-0.43}$	$2.08^{+0.27}_{-0.27}$	$1.58^{+0.38}_{-0.38}$	$1.02^{+0.46}_{-0.46}$	–
(2a, 2)	$2.22^{+0.35}_{-0.35}$	$1.00^{+0.23}_{-0.23}$	$3.60^{+1.34}_{-1.34}$	$6.70^{+4.32}_{-4.32}$	$1.77^{+1.07}_{-1.07}$	$1.33^{+1.23}_{-1.23}$	$1.12^{+1.02}_{-1.02}$	–
(3a, 0)	$7.15^{+0.37}_{-0.37}$	$5.09^{+0.22}_{-0.22}$	$5.18^{+0.30}_{-0.30}$	$3.38^{+0.22}_{-0.22}$	$2.02^{+0.10}_{-0.10}$	$1.52^{+0.13}_{-0.13}$	$1.31^{+0.12}_{-0.12}$	–
(3a, 1)	$3.93^{+0.47}_{-0.47}$	$3.35^{+0.33}_{-0.33}$	$2.83^{+0.34}_{-0.34}$	$1.97^{+0.30}_{-0.30}$	$1.44^{+0.20}_{-0.20}$	$0.73^{+0.17}_{-0.17}$	$0.85^{+0.21}_{-0.21}$	–
(3a, 2)	$2.02^{+0.44}_{-0.44}$	$1.89^{+0.36}_{-0.36}$	$1.94^{+0.44}_{-0.44}$	$1.05^{+0.33}_{-0.33}$	$0.98^{+0.31}_{-0.31}$	$0.71^{+0.42}_{-0.42}$	$0.57^{+0.50}_{-0.50}$	–
(3a, $\geq$ 3)	$0.57^{+0.56}_{-0.56}$	$0.84^{+0.88}_{-0.88}$	–	–	–	–	–	–
(4a, 0)	$2.53^{+1.57}_{-1.57}$	$4.95^{+0.65}_{-0.65}$	$6.75^{+0.63}_{-0.63}$	$5.95^{+0.53}_{-0.53}$	$5.11^{+0.37}_{-0.37}$	$2.15^{+0.25}_{-0.25}$	$1.51^{+0.20}_{-0.20}$	–
(4a, 1)	$0.73^{+0.81}_{-0.81}$	$3.89^{+0.99}_{-0.99}$	$3.98^{+0.71}_{-0.71}$	$4.09^{+0.75}_{-0.75}$	$3.16^{+0.49}_{-0.49}$	$1.59^{+0.41}_{-0.41}$	$0.78^{+0.27}_{-0.27}$	–
(4a, 2)	–	$4.93^{+2.12}_{-2.12}$	$2.54^{+0.70}_{-0.70}$	$1.61^{+0.52}_{-0.52}$	$1.94^{+0.57}_{-0.57}$	$0.34^{+0.19}_{-0.19}$	$0.14^{+0.13}_{-0.13}$	–
(4a, $\geq$ 3)	–	$52.32^{+64.24}_{-64.24}$	$1.26^{+1.02}_{-1.02}$	–	–	–	–	–
($\geq$ 5a, 0)	–	–	$10.24^{+4.41}_{-4.41}$	$7.91^{+1.70}_{-1.70}$	$7.50^{+0.96}_{-0.96}$	$4.08^{+0.53}_{-0.53}$	$3.02^{+0.51}_{-0.51}$	–
($\geq$ 5a, 1)	–	–	$7.18^{+3.72}_{-3.72}$	$3.29^{+1.12}_{-1.12}$	$2.16^{+0.48}_{-0.48}$	$2.45^{+0.73}_{-0.73}$	$1.56^{+0.62}_{-0.62}$	–
($\geq$ 5a, 2)	–	–	$18.63^{+18.22}_{-18.22}$	$1.81^{+1.08}_{-1.08}$	$3.86^{+1.40}_{-1.40}$	$1.36^{+0.69}_{-0.69}$	$0.55^{+0.38}_{-0.38}$	–
($\geq$ 5a, $\geq$ 3)	–	–	–	–	$2.66^{+2.07}_{-2.07}$	$10.88^{+11.66}_{-11.66}$	–	–

DRAFT

11.3 Adding the H_T^{miss} dimension

The aforementioned description of the TFs provide an estimate of the total SM background as a function of the (n_{jet},n_b,H_T) bin that is integrated over H_T^{miss}. However, the analysis takes advantage of H_T^{miss} distribution obtained from simulation. This information is propagated to the likelihood model via an H_T^{miss} template per (n_{jet},n_b,H_T) bin, which is equivalent to dicing the numerator of the TF according to H_T^{miss}, i.e. $N_{MC}^{signal}(n_{jet}, n_b, H_T, H_T^{miss})$. In this regard, the TFs described above provide an estimate of the normalisation for each H_T^{miss} template.

11.4 Data control samples used in the method

To estimate the contributions from these backgrounds, three data control regions are used, which are binned identically to the signal region: μ + jets, $\mu\mu$ + jets and γ + jets. Their definitions are provided in Sec. 7. The e + jets and ee + jets control regions are not used now, but are investigated to be used analagously to the μ + jets and $\mu\mu$ + jets regions in the future. The selection criteria for these control regions are defined such that any potential contamination from new physics processes or QCD multijets is negligible.

In previous versions of this analysis, the $\mu\mu$ + jets and γ + jets control samples are used to predict the $Z \to \nu\bar{\nu}$ +jets background. We plan to extend this approach by relying on all (and not just a sub-set of) relevant control samples to predict the two dominant components of the total SM background (W + jets and $t\bar{t}$, or $Z \to \nu\bar{\nu}$ + jets). Specifically, we are using the μ + jets sample to predict the W + jets and $t\bar{t}$ backgrounds (across all $n_b$bins) and up to three samples comprising $Z(\to \mu\mu)$ + jets, γ + jets and $W(\to \mu\nu)$ + jets to predict the $Z \to \nu\bar{\nu}$ + jets background for events containing exactly zero or one b-tagged jets. Any correlations are appropriately handled by the likelihood model (via the `Combine` tool).

The predictions of the $Z \to \nu\bar{\nu}$ + jets background based on the $Z(\to \mu\mu)$ + jets control samples exhibits significantly larger statistical uncertainties at high n_{jet}, n_b, H_T, or H_T^{miss} due to lower event counts arising from the lower Z cross section (w.r.t. γ + jets and W + jets). Regardless, these samples are included in the likelihood fit to provide additional confidence in the control of the $Z \to \nu\bar{\nu}$ + jets background.

Concerning the use of W-enriched samples to predict the $Z \to \nu\bar{\nu}$ +jets background, we have studied this approach in detail with the 8 TeV dataset. Based on the outcome of these studies, we have decided to proceed with this approach, as part of the baseline likelihood description. Studies were based on closure tests with 8 TeV data (as described in Sec. 12.1). Closure tests are a critial tool to determine which samples can be used to predict the SM background components. In particular, we have studied the effect of new closure tests designed to test the W-enriched to Z-enriched extrapolation, specifically μ + jets to γ + jets, μ + jets to $\mu\mu$ + jets and μ^+ to μ^- closure tests. This study is detailed in Appendix F. If further studies of the closure tests with 13 TeV data suggest that using the μ + jets control region to predict the $Z \to \nu\bar{\nu}$ background is not feasible, we will revert back to the approach used in Run I analysis (i.e. relying solely on the $Z \to \ell\ell$ and γ + jets samples). Early investigations suggest there are not any major problems. Most importantly, we retain full flexibility in our approach and the control samples used to predict the various background components.

Currently, the projected sensitivity, as described in the current version of this note, is based on predictions of SM background components made from control regions as follows. For events containing exactly zero or one b-tagged jets, the μ + jets (enriched in $W(\to e\nu)$ + jets), γ + jets and $\mu\mu$ + jets control samples are used to estimate the irreducible $Z \to \nu\bar{\nu}$ + jets background, while the μ + jets control sample is used to estimate all remaining SM processes (predominately

DRAFT

W + jets and $t\bar{t}$). For events containing two or more b-tagged jets, the μ + jets sample is used to predict the total SM background (dominated by $t\bar{t}$).

DRAFT

12 Systematic uncertainties in the transfer factors

This section addresses the estimation of systematic uncertainties in the estimation of event counts from non-multijet backgrounds. This analysis aims to rely as much as possible on the data control samples to check for sources of bias in the transfer factors described in Sec. 11.2 and derive the associated systematic uncertainties. The strategies that are employed to ascertain the presence of biases or otherwise, and the procedures used to derive systematic uncertainties, are described below.

Two types of systematic uncertainty are considered separately. First, we consider "normalisation" uncertainties in the predictions of background counts in each (n_{jet}, n_{b}, H_{T}) bin, integrated over $H_{\mathrm{T}}^{\mathrm{miss}}$, of the signal region. Second, systematic uncertainties associated with the $H_{\mathrm{T}}^{\mathrm{miss}}$ templates obtained from simulation for each individual (n_{jet}, n_{b}, H_{T}) bin are determined from multiple data control samples. The determination and validation of the $H_{\mathrm{T}}^{\mathrm{miss}}$ templates and their associated uncertainties are described fully in Sec. 13.

This chapter covers in detail the normalisation systematic uncertainties associated with predictions per (n_{jet}, n_{b}, H_{T}) bins. The use of ensembles of "closure tests" to derive systematic uncertainties are described in detail in Secs. 12.1 and 12.3. The definition of ensembles geared towards the specific background processes is provided in Sec. 12.4. The observed level of closure in data and the resulting systematic uncertainties, based on control samples corresponding to 1.28 fb^{-1} of integrated luminosity, is covered in Sec. **??**. Additional contributions to the total normalisation systematics that are based on dedicated ensembles to cover the α_{T} extrapolation made in the search are described in Sec. 12.7. Further dedicated ensembles that provide additional cross checks are covered in Sec. 12.8. Finally, Sec. 12.9 outlines simulation-based studies of the effects of potential sources of bias on the transfer factors.

12.1 Definition of a closure test

The background estimates determined in each (n_{jet}, n_{b}, H_{T}) bin rely on transfer factors to extrapolate data counts in control region bins to predictions in the corresponding signal region bins, as described in Sec. 11.2. Since the transfer factors are obtained from simulation, an appropriate systematic uncertainty is assigned to each transfer factor to account for limitations in the simulation modelling of event kinematics and instrumental effects. The next sections describe how the systematic uncertainties are determined from closure tests in data.

The sensitivity of the transfer factors to potential limitations in the simulation modelling is established through sets of closure tests, which confront data yields measured in one data control (sub-)sample against the predictions determined from another data control (sub-)sample as a function of H_{T}. i.e., an extrapolation is made from one control (sub-)sample to another (rather than to the signal region) in bins of H_{T} via transfer factors determined from simulation. A large ensemble (i.e. hundreds) of closure tests are performed between a number of control (sub-)samples to identify any potential sources of bias in the transfer factors.

The level of statistical consistency between the predicted and observed yields of each closure test in the ensemble is inspected. The level of agreement between the predicted and observed yields is expressed as the ratio $(N_{\mathrm{obs}} - N_{\mathrm{pred}})/N_{\mathrm{pred}}$ while considering only the statistical uncertainties on N_{pred} and N_{obs}. Therefore, the level of closure is defined by the statistical significance of a deviation in the ratio from zero. A "set" of closure tests includes statistically independent tests determined as a function of H_{T} (according to the H_{T} binning used in the control and signal regions). In this way, a set of closure tests allows one to establish the presence of significant biases or dependence on H_{T}. Importantly, if statistically significant biases

DRAFT

are observed, further studies are required to understand and correct for these biases.

Under the assumption of closure for each test of the ensemble, systematic uncertainties on the transfer factors are derived for each (n_{jet}, n_{b}) category and H_{T} bin. The treatment for estimating the systematic uncertainties on the transfer factors is described in Sec. 12.3.

12.2 Definition of the "core" closure tests

The core closure tests rely on the μ + jets, $\mu\mu$ + jets, and γ + jets control samples, as defined in Secs. 7.7, 7.8, and 7.11. (The e + jets and ee + jets control samples are not currently used.)

The μ + jets $\rightarrow$ γ + jets tests deal with the consistency of the prediction of $\mathrm{W}(\rightarrow \mathrm{e}\nu) +$ jets with γ + jets, even in the presence of contamination from $\mathrm{t\bar{t}}$. This is important for understanding the consistency of the $\mathrm{Z} \rightarrow \nu\bar{\nu}$ + jets background predictions from both $\mathrm{W}(\rightarrow \mathrm{e}\nu) +$ jets and γ + jets events along with the associated assumptions (such as the negligible effect of the vector boson mass on kinematic distributions from the V + jets and γ + jets samples under sufficient boost). Similarly, the $\mu + jets \rightarrow \mu\mu + jets$ tests also addresses the modelling of vector boson production, also in the presence of contamination from $\mathrm{t\bar{t}}$). Finally, the $\mu\mu + jets \rightarrow \gamma + jets$ tests deal with the consistency between the $\mathrm{Z} \rightarrow ee$ + jets and γ + jets samples, which is a further check on the validity of using the γ + jets process to predict the $\mathrm{Z} \rightarrow \nu\bar{\nu}$ + jets process. The muon trigger and reconstruction efficiencies are also indirectly probed, given that different numbers of muons are required in each of the two sub-samples.

Additionally, to test the prediction of $\mathrm{Z} \rightarrow \nu\bar{\nu}$ + jets processes with the W-enriched μ + jets control sample, we introduce the $\mu^+ \rightarrow \mu^-$ closure test, as mentioned in Sec. 11. The production mechanism of W from pp collisions means high p_T W bosons are predominantly left handed [23]. For high p_T bosons, this implies that W^+ decays to the left handed neutrino along its direction of motion while the lepton is pointing backward. The opposite behaviour is expected for the W^-. The lepton is therefore more boosted (and the neutrino less boosted) in W^+ decays than W^- decays. This leads to a larger number of W^+ decays in the single lepton control regions (which relies on the lepton p_T for acceptance) than in the signal region (which relies on the neutrino p_T for acceptance). The new closure test checks if this leads to a bias in the prediction of the $\mathrm{Z} \rightarrow \nu\bar{\nu}$ + jets background.

The control of the $\mathrm{Z} \rightarrow \nu\bar{\nu}$ + jets background, established via the tests described above, is also validated with the full Run 1 data set at $\sqrt{s} = 8\,\mathrm{TeV}$, as described in Appendix F.

The 0 b-tag $\rightarrow$ 1 b-tag and 1 b-tag $\rightarrow$ 2 b-tag tests probe the sensitivity of the transfer factors to the relative admixture of events from the W + jets and $\mathrm{t\bar{t}}$ processes by varying the number of b-tagged jets within the μ + jets sample. These tests are conservative, as the admixture changes little between the μ + jets sample and the signal region (as there is no extrapolation in n_{b}), whereas the closure tests use sub-samples with different n_{b}bins and therefore different admixtures of W + jets and $\mathrm{t\bar{t}}$ events. e.g., the former uses a W-enriched sub-sample (selected by requiring zero b-jets) to predict yields in a $\mathrm{t\bar{t}}$-enriched sub-sample (selected by requiring one b-jet).

The aformentioned two b-tag related tests also probe the modelling of the reconstruction of b-quark jets, although this is addressed more precisely by dedicated studies involving varying the uncertainties in b-tag scale factors, as the one performed in the previous analysis, see for instance [5]. Until the formula method is applied, the b-tag SFs will be applied and their uncertainties propagated through to the transfer factors. These variations will be taken as an additional contriubtion to the total normalisation systematic uncertainties per (n_{jet}, n_{b}, H_{T}) bin. However, based on the behaviour observed during Run 1, these are a sub-dominant contribu-

tion to the total systematic uncertainties.

The $n_{\text{jet}} = 2 \rightarrow n_{\text{jet}} = 3$ and $n_{\text{jet}} = 4 \rightarrow n_{\text{jet}} \geq 5$ tests are an agressive test of the simulation modelling of jet multiplicities in the μ + jets, $\mu\mu$ + jets and γ + jets samples, which is checked due to the exclusive binning in jet multiplicity. The different n_{jet} requirements also lead to different admixture of W + jets and $\text{t}\bar{\text{t}}$ in the case of the μ + jets sample.

The TT→TL closure tests are designed to test the effects of the extrapolation in the lepton definition used for the veto in the signal region (see Sec. 7.2) and the selection in the muon control regions (see Sec. 7.7 and 7.8). Two di-muon samples are defined that pass the $\mu\mu$ + jets control region selection, minus the single isolated track veto and M_{ll} requirement. One sample is required to have two muons that pass the tight criteria defined for the muon control region (TT), the other sample is required to have one muon that passes this tight criteria and one muon that passes the loose criteria defined for the signal region veto (TL). The TT sample is then used to predict the TL sample for these closure tests.

Finally, closure tests that probe the modelling of the α_{T} and $\Delta\phi^{*}_{\text{min}}$ extrapolations in the analysis are also performed. In both cases, the test checks if events with genuine $E_{\text{T}}^{\text{miss}}$ found in the core of the variable distribution below some threshold value can be used to predict the events in the tail (above the same threshold value).

The aforementioned closure tests are not the only ones considered or checked, i.e., the list above is not exhaustive. However, they are a representative set that cover the main potential sources of bias in the transfer factors derived from simulation.

12.3 Systematic uncertainties from ensembles of closure tests

Each set of closure tests should demonstrate in data, within the statistical precision of each test, that there are no significant biases or dependencies on n_{jet} nor H_{T} inherent in the transfer factors obtained from simulation. Once it is established that no significant bias or trend is observed for any set of closure tests, the systematic uncertainties associated with the transfer factors are determined from ensembles of closure tests. The statistical precision of the closure tests are considered when determining the systematic uncertainties that are assigned to the transfer factors, as it is only the statistical uncertainties associated with the tests that limit our knowledge of whether closure is actually achieved or otherwise. Ensembles comprising several tests are considered in bins of (n_{jet},H_{T}) to derive a systematic uncertainty for that bin.

The systematic uncertainties in the transfer factors are considered as a "normalisation" uncertainty in the SM background predictions, which are determined per (n_{jet}, n_{b}) category per H_{T} bin and are assumed to be fully uncorrelated between the different (n_{jet}, n_{b}) categories and H_{T} bins. Further details or the likelihood model are provided in Section 14. The systematic uncertainty is estimated by taking the quadrature sum of the weighted mean and (square root of) weighted sample variance for the closure tests within the given H_{T} bin.

In order to find "expected systematics", N_{obs} and N_{pred} are determined from the same sample of simulated events (that guarantees closure) with statistical uncertainties errors are taken from the unweighted and weighted counts, respectively. The expected systematic uncertainty is then taken as the weighted mean of the error on the ensemble of closure tests. This is an estimator of the expected variance, assuming no bias is found in data.

We note the behaviour of the magnitude of the systematic uncertainties on the integrated luminosity, which reduce with increasing luminosity. This is a reflection of the fully statistical nature of the "systematic" in the absence of bias.

DRAFT

12.4 Closure test ensembles for specific backgrounds

Several versions of this search have derived a single set of process-independent systematic uncertainties as a function of (n_{jet}, n_{b}, H_{T}) based on a single ensemble of a core set of closure tests.

During the Early Analysis review, an alternative approach was advised, which involves splitting the closure tests into different ensembles, each specific to a particular process or effect and containing only the most relevant closure tests. This allows for the independent derivation of systematic errors that is specific to a background process.

Table **??** summarises lists of closure tests ensembles used to derive normalisation systematic uncertainties for: the total SM background in the monojet category (over the full H_{T} range); the $\text{t}\bar{\text{t}}\text{W}$ background components for the symmetric and asymmetric n_{jet} bins (over the full H_{T} range); and the $\text{Z} \to \nu\bar{\nu}$ background components for the symmetric and asymmetric n_{jet} bins for the two regions $H_{\text{T}} < 400\,\text{GeV}$ and $H_{\text{T}} > 400\,\text{GeV}$.

12.5 Closure tests based on 1.28 fb^{-1}

The core set of closure tests used by this search are shown in Figs. 28, 29, 30, 31, 32, and 33, identifiable by the legends. The closure tests ensembles are defined according to Sec. 12.4 and per n_{jet} category.

In the case of the tests designed to probe the $\text{Z} \to \nu\bar{\nu}$ background prediction, different ensembles are defined for events with values below and above the threshold $H_{\text{T}} = 400\,\text{GeV}$. Figures. 28, 30, and 31 show the results of the closure tests performed on events in the "symmetric" jet category and in Figs. 29, 32 and 33 the results of the closure tests performed on events in the "asymmetric" jet category. For events in the "mono-jet" category, the closure tests that rely on more than one jet (such as the $1b - tag \to \geq 2b - tag$ tests) are removed. The results of these tests are in shown in Fig 34.

Prior to deriving uncertainties, each individual set of closure tests (as a function of H_{T}) have been inspected for closure. Zero and first order polynomial fits are performed along the H_{T} dimension for each set of closure tests per jet category. The fits are inspected for any indication of bias averaged over H_{T} as well as any H_{T}-dependant bias. In the case of the closure tests presented in this section, all tests demonstrate an acceptable level of closure given the current understanding of the detector performance. One visible bias is due to the lack of b-tag scale factors. Simulated events will be reweighted when these scale factors become available, but for now we notice a slight deficit in the number of b-tags observed than predicted. This is manifest in the $0b - tag \to 1b - tag$ and $1b - tag \to \geq 2b - tag$ closure tests, that exhibit consistently negative values. We expect this to improve with the application of the scale factors.

DRAFT

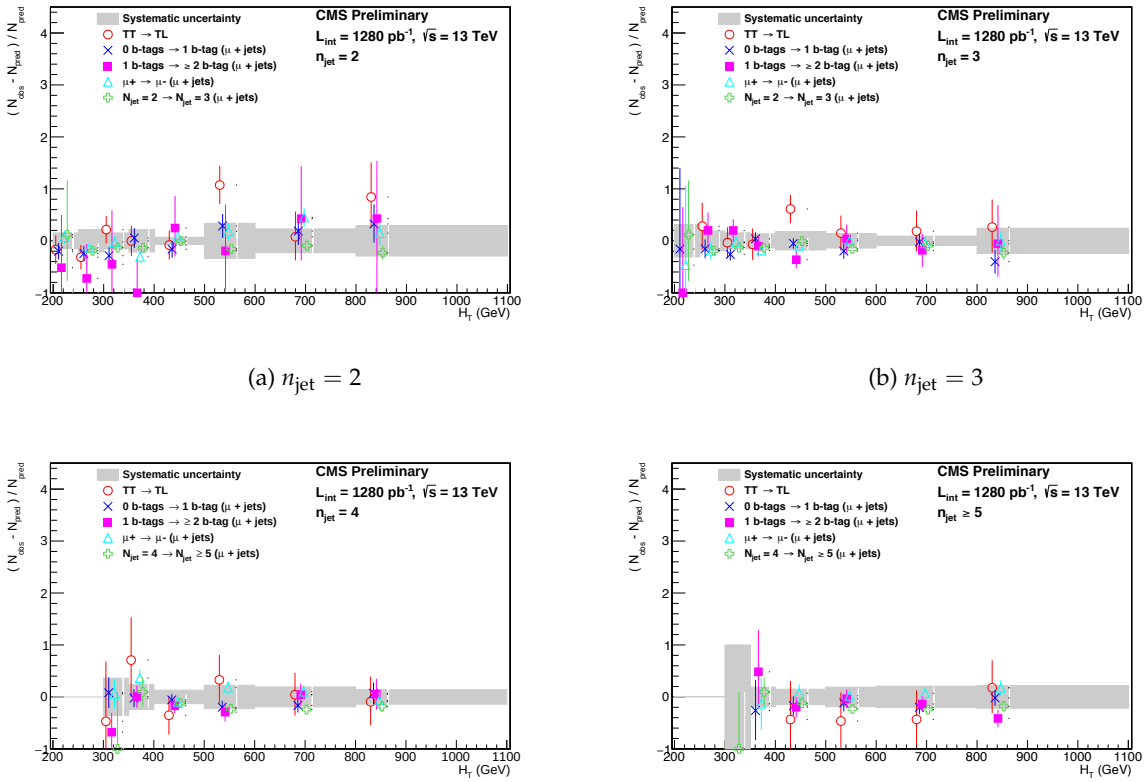

(a) $n_{\text{jet}} = 2$

(b) $n_{\text{jet}} = 3$

(c) $n_{\text{jet}} = 4$

(d) $n_{\text{jet}} \geq 5$

Figure 28: Sets of closure tests (open symbols) designed to probe the W and $t\bar{t}$ + jets background, overlaid on top of the systematic uncertainty estimates used for each of the seven H_{T} bins (shaded bands) carried out with 1.28fb^{-1} of 13 TeV data. All events fit into the "symmetric" jet category.

DRAFT

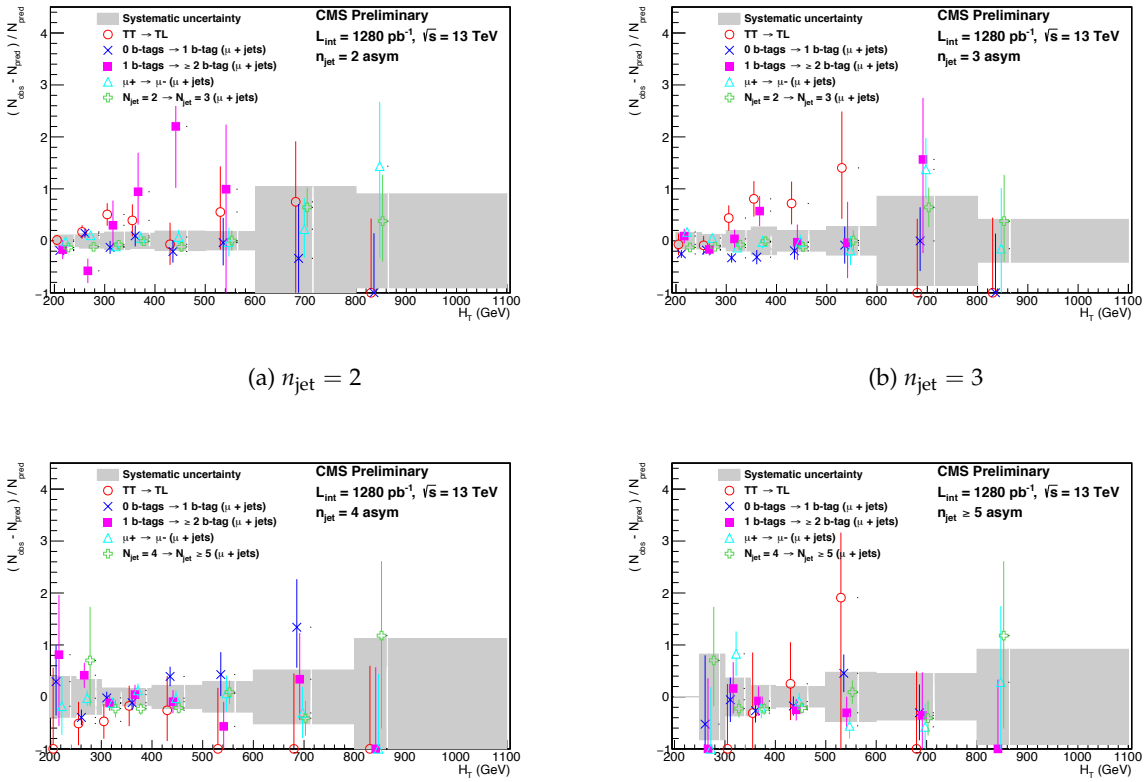

(a) $n_{\text{jet}} = 2$

(b) $n_{\text{jet}} = 3$

(c) $n_{\text{jet}} = 4$

(d) $n_{\text{jet}} \geq 5$

Figure 29: Sets of closure tests (open symbols) designed to probe the W and $t\bar{t}$ + jets background, overlaid on top of the systematic uncertainty estimates used for each of the seven H_T bins (shaded bands) carried out with 1.28fb^{-1} of 13 TeV data. All events fit into the "asymmetric" jet category.

DRAFT

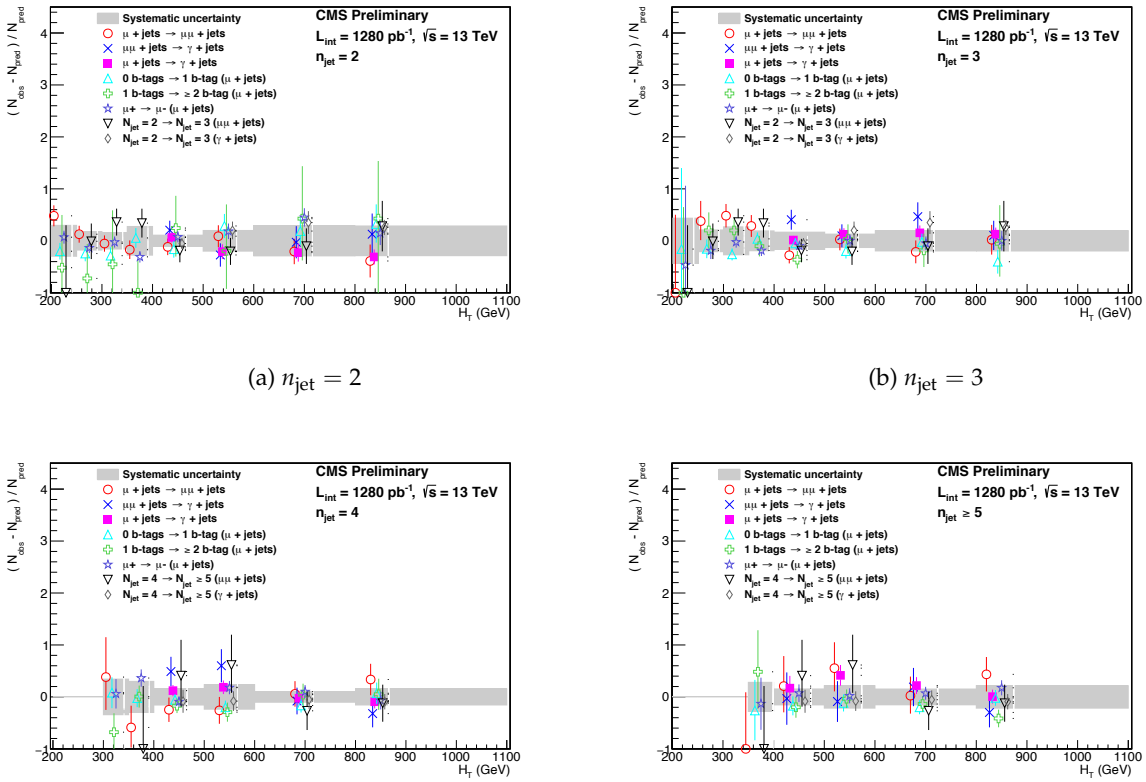

(a) $n_{\text{jet}} = 2$

(b) $n_{\text{jet}} = 3$

(c) $n_{\text{jet}} = 4$

(d) $n_{\text{jet}} \geq 5$

Figure 30: Sets of closure tests (open symbols) designed to probe the $Z \to \nu\bar{\nu}$ + jets background, overlaid on top of the systematic uncertainty estimates for each of the seven H_{T} bins (shaded bands) carried out with 1.28fb^{-1} of 13 TeV data. **Only systematics in these plots with $H_{\text{T}} <$ 400 GeV are used in the analysis.** All events fit into the "symmetric" jet category.

DRAFT

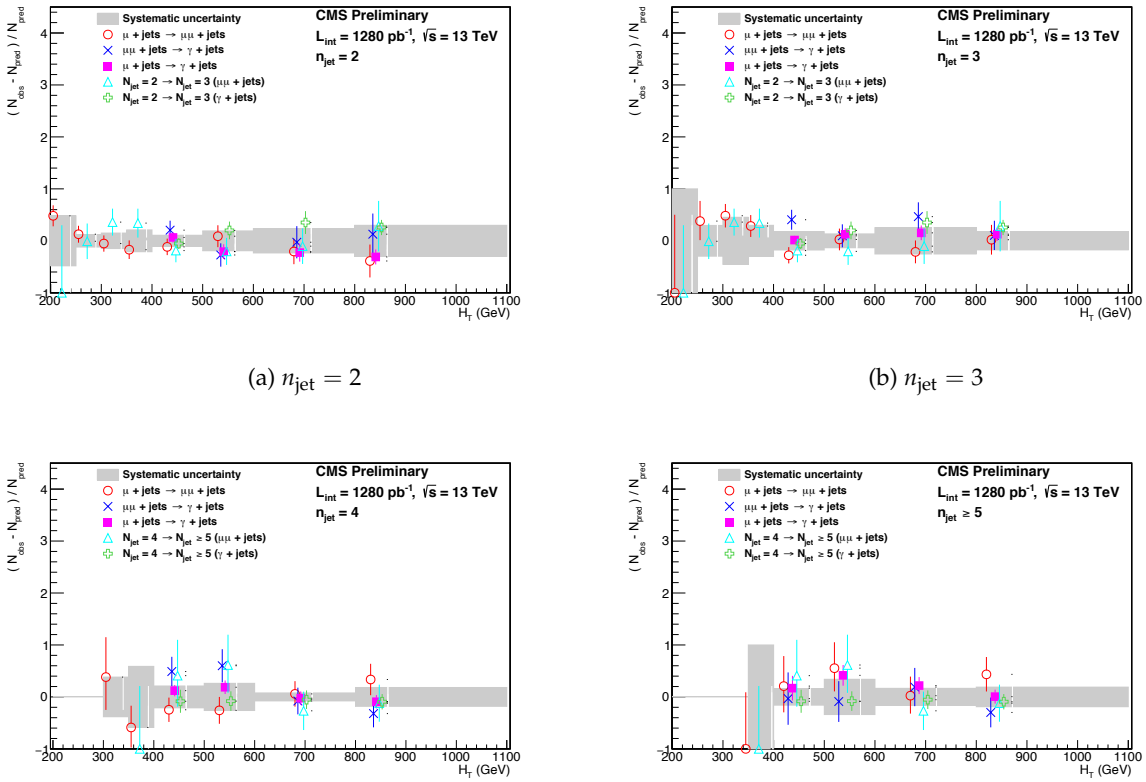

(a) $n_{\text{jet}} = 2$

(b) $n_{\text{jet}} = 3$

(c) $n_{\text{jet}} = 4$

(d) $n_{\text{jet}} \geq 5$

Figure 31: Sets of closure tests (open symbols) designed to probe the $Z \to \nu\bar{\nu}$ + jets background, overlaid on top of the systematic uncertainty estimates for each of the seven H_{T} bins (shaded bands) carried out with 1.28fb^{-1} of 13 TeV data. **Only systematics in these plots with $H_{\text{T}} >$ 400 GeV are used in the analysis.** All events fit into the "symmetric" jet category.

DRAFT

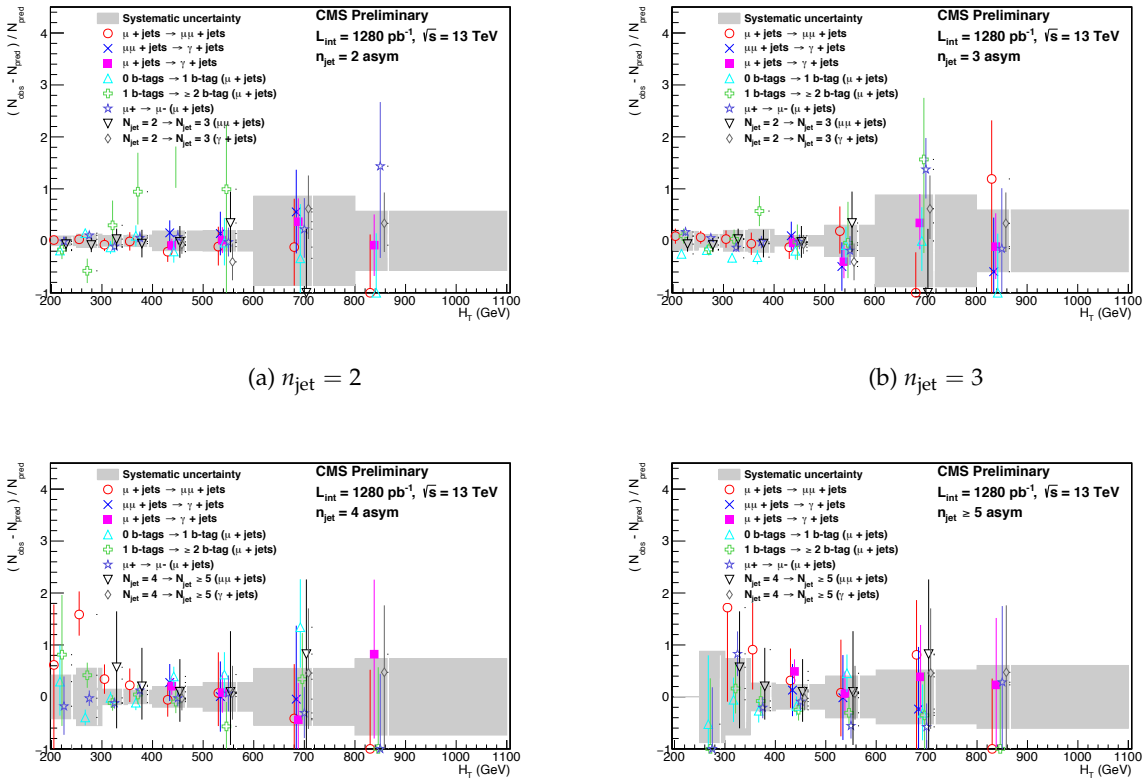

(a) $n_{\text{jet}} = 2$

(b) $n_{\text{jet}} = 3$

(c) $n_{\text{jet}} = 4$

(d) $n_{\text{jet}} \geq 5$

Figure 32: Sets of closure tests (open symbols) designed to probe the $Z \to \nu\bar{\nu}$ + jets background, overlaid on top of the systematic uncertainty estimates for each of the seven H_T bins (shaded bands) carried out with 1.28fb^{-1} of 13 TeV data. **Only systematics in these plots with $H_T <$ 400 GeV are used in the analysis.** All events fit into the "asymmetric" jet category.

DRAFT

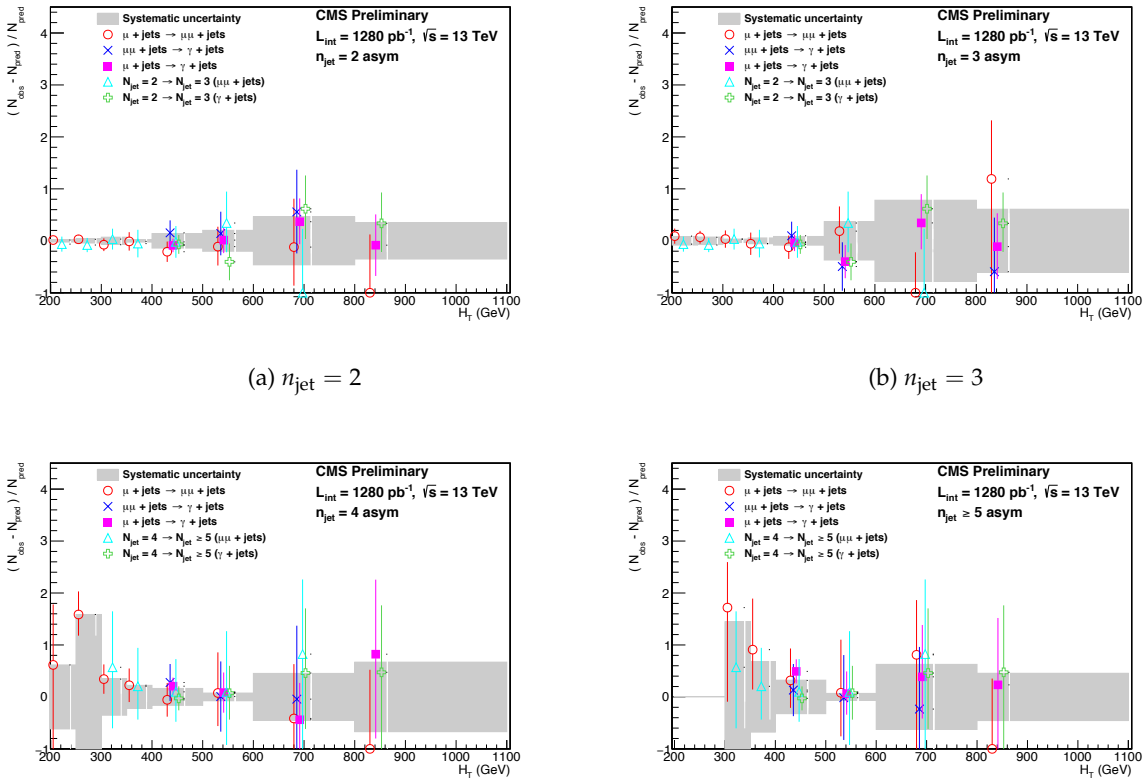

(a) $n_{\text{jet}} = 2$

(b) $n_{\text{jet}} = 3$

(c) $n_{\text{jet}} = 4$

(d) $n_{\text{jet}} \geq 5$

Figure 33: Sets of closure tests (open symbols) designed to probe the $Z \to \nu\bar{\nu}$ + jets background, overlaid on top of the systematic uncertainty estimates for each of the seven H_T bins (shaded bands) carried out with 1.28fb^{-1} of 13 TeV data. **Only systematics in these plots with $H_T >$ 400 GeV are used in the analysis.** All events fit into the "asymmetric" jet category.

DRAFT

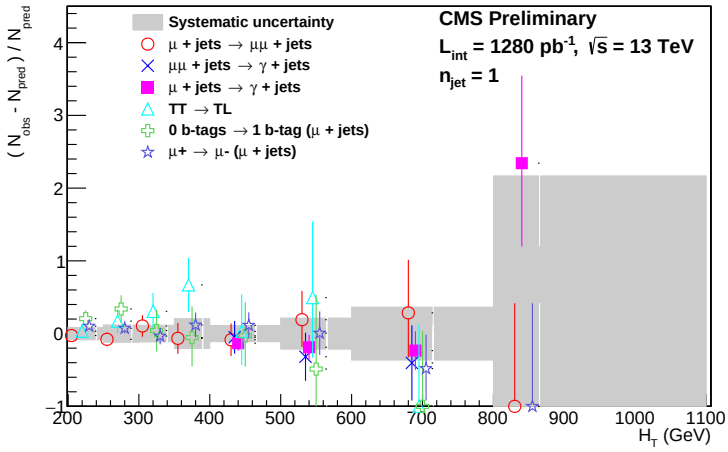

(a) $n_{\text{jet}} = 1$

Figure 34: Sets of closure tests (open symbols) overlaid on top of the systematic uncertainty estimates used for each of the seven H_{T} bins (shaded bands) carried out with 1.28fb^{-1} of 13 TeV data. All events fit into the "mono-jet" jet category.

DRAFT

12.6 Normalisation systematic uncertainties based on 1.28 fb^{-1}

Normalisation systematics are derived from the closure test ensembles, described above, based on the current data set, which are summarised in Table 46. In the kinematically restricted bins, such as those with a high jet multiplicity and low value of H_T, the limited statistics leads to large systematic errors. These bins are not used in the analysis. In the bins populated with a reasonable number of events, the systematic errors determined from the closure tests vary from 10 to 40%.

Table 46: Systematic uncertainties (percent) in the predictions of the $t\bar{t}W$ and $Z \to \nu\bar{\nu}$ (the latter in parentheses) background components as a function of n_{jet}, n_b, and H_T, as determined from ensembles of closure tests based on multiple data control samples. The data control samples correspond to an integrated luminosity of 1.26 fb^{-1}.

Category	H_T bin							
(n_{jet},n_b)	200	250	300	350	400	500	600	800
Monojet:								
(1,0)	9 (9)	12 (12)	11 (11)	21 (21)	11 (11)	21 (21)	36 (36)	-
(1,1)	9 (9)	12 (12)	11 (11)	21 (21)	11 (11)	21 (21)	36 (36)	-
Symmetric:								
(2,0)	15 (30)	21 (18)	15 (16)	22 (28)	7 (11)	34 (19)	23 (23)	29 (30)
(2,1)	15 (30)	21 (18)	15 (16)	22 (28)	7 (11)	34 (19)	23 (23)	29 (30)
(2,2)	15 (30)	21 (18)	15 (16)	22 (28)	7 (11)	34 (19)	23 (23)	29 (30)
(3,0)	31 (44)	19 (21)	15 (27)	14 (19)	18 (18)	14 (13)	9 (25)	24 (17)
(3,1)	31 (44)	19 (21)	15 (27)	14 (19)	18 (18)	14 (13)	9 (25)	24 (17)
(3,2)	31 (44)	19 (21)	15 (27)	14 (19)	18 (18)	14 (13)	9 (25)	24 (17)
(3,3)	31 (44)	19 (21)	15 (27)	14 (19)	18 (18)	14 (13)	9 (25)	24 (17)
(4,0)	-	-	36 (34)	24 (30)	13 (21)	22 (27)	19 (8)	14 (18)
(4,1)	-	-	36 (34)	24 (30)	13 (21)	22 (27)	19 (8)	14 (18)
(4,2)	-	-	36 (34)	24 (30)	13 (21)	22 (27)	19 (8)	14 (18)
(4,≥3)	-	-	36 (34)	24 (30)	13 (21)	22 (27)	19 (8)	14 (18)
(5,0)	-	-	-	19 (28)	15 (16)	19 (34)	21 (17)	22 (19)
(5,1)	-	-	-	19 (28)	15 (16)	19 (34)	21 (17)	22 (19)
(5,2)	-	-	-	19 (28)	15 (16)	19 (34)	21 (17)	22 (19)
(5,≥3)	-	-	-	19 (28)	15 (16)	19 (34)	21 (17)	22 (19)
Asymmetric:								
(2,0)	11 (9)	14 (13)	17 (10)	14 (11)	19 (14)	17 (20)	105 (46)	91 (35)
(2,1)	11 (9)	14 (13)	17 (10)	14 (11)	19 (14)	17 (20)	105 (46)	91 (35)
(2,2)	11 (9)	14 (13)	17 (10)	14 (11)	19 (14)	17 (20)	105 (46)	91 (35)
(3,0)	16 (18)	12 (12)	19 (20)	27 (22)	20 (8)	28 (37)	86 (78)	41 (61)
(3,1)	16 (18)	12 (12)	19 (20)	27 (22)	20 (8)	28 (37)	86 (78)	41 (61)
(3,2)	16 (18)	12 (12)	19 (20)	27 (22)	20 (8)	28 (37)	86 (78)	41 (61)
(3,3)	16 (18)	12 (12)	19 (20)	27 (22)	20 (8)	28 (37)	86 (78)	41 (61)
(4,0)	-	34 (55)	17 (15)	16 (13)	22 (16)	29 (7)	52 (43)	112 (67)
(4,1)	-	34 (55)	17 (15)	16 (13)	22 (16)	29 (7)	52 (43)	112 (67)
(4,2)	-	34 (55)	17 (15)	16 (13)	22 (16)	29 (7)	52 (43)	112 (67)
(4,≥3)	-	34 (55)	17 (15)	16 (13)	22 (16)	29 (7)	52 (43)	112 (67)
(5,0)	-	-	36 (73)	22 (27)	19 (32)	47 (7)	45 (53)	92 (45)
(5,1)	-	-	36 (73)	22 (27)	19 (32)	47 (7)	45 (53)	92 (45)
(5,2)	-	-	36 (73)	22 (27)	19 (32)	47 (7)	45 (53)	92 (45)
(5,≥3)	-	-	36 (73)	22 (27)	19 (32)	47 (7)	45 (53)	92 (45)

DRAFT

12.7 Dedicated closure test ensemble and systematic for α_T modelling

The closure tests in Fig. 35 probe the modelling of the α_T distribution (following the application of the $H_T^{miss} > 130$ GeV requirement in the control and signal regions) in genuine E_T^{miss} events as a function of H_T. This is important to verify the approach of using μ + jets and $\mu\mu$ + jets samples without an α_T requirement to make background predictions in the signal region. The tests confront data yields in a μ + jets ($\mu\mu$ + jets) samples with an α_T requirement against predictions determined in a μ + jets ($\mu\mu$ + jets) sample with the α_T requirement inverted. As usual, corresponding expectations from simulation are obtained to construct the transfer factors required to make the predictions.

These closure tests are not considered in the ensembles presented in Sec. 12.5 (as was normally the case for previous iterations of the analysis) and instead added as a new separate ensemble from which an additional contribution to the total systematic uncertainty per (n_{jet}, n_b, H_T) bin is derived. These contributions are assumed be be fully correlated across n_b(and uncorrelated as a function of n_{jet} and H_T). The magnitude of these contributions are presented in Table 47. For $H_T < 800$ GeV these numbers are derived from the α_T closure tests. However, as there is no α_T requirement for $H_T > 800$ GeV, the $\Delta\phi*$ closure tests in Sec. 12.8 are used to derive the systematic in this case.

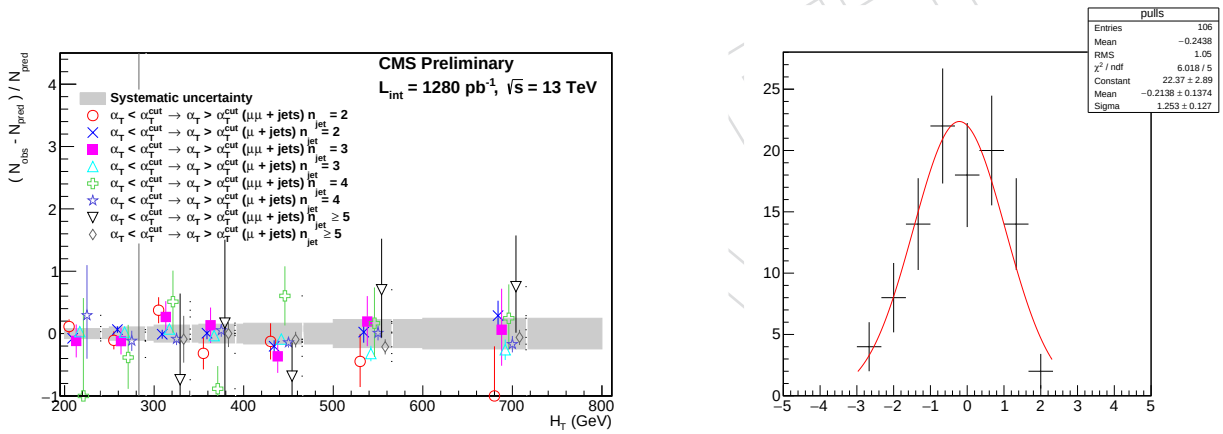

(a) (b)

Figure 35: Closure tests probing the α_T extrapolation for each n_{jet} category (open symbols) overlaid on top of the systematic uncertainty estimates used for each of the seven H_T bins (shaded bands) carried out with 1.28fb^{-1} of 13 TeV data. Also shown are the pulls for each closure test.

Table 47: Systematic uncertainties (percent) in the predictions of the $t\bar{t}W$ and $Z \rightarrow \nu\bar{\nu}$ (the latter in parentheses) background components as a function of H_T due to the extrapolation in the α_T ($\Delta\phi^*_{min}$) variable in the region $H_T > 800$ GeV ($H_T > 800$ GeV), as determined from ensembles of closure tests in multiple data control samples. The data control samples correspond to an integrated luminosity of 1.26 fb^{-1}.

H_T bin (GeV)							
200	250	300	350	400	500	600	800
8 (8)	11 (11)	14 (14)	15 (15)	17 (17)	23 (23)	25 (25)	23 (23)

12.8 Additional ensembles as cross checks

Along with the closure tests used to derive the systematics, additional tests are carried out to cross check other potential instances of mismodelling. If any of these tests demonstrate a source of bias, further investigation into this effect is carried out.

The closure tests in Fig. 36 probe the modelling of the $\Delta\phi*$ distribution in genuine $E_{\mathrm{T}}^{\mathrm{miss}}$ events as a function of H_{T}. This is important to verify the approach of using μ + jets and $\mu\mu$ + jets samples without an $\Delta\phi*$ requirement to make background predictions in the signal region. The tests confront data yields in a μ + jets ($\mu\mu$ + jets) samples with an $\Delta\phi*$ requirement against predictions determined in a μ + jets ($\mu\mu$ + jets) sample with the $\Delta\phi*$ requirement inverted.

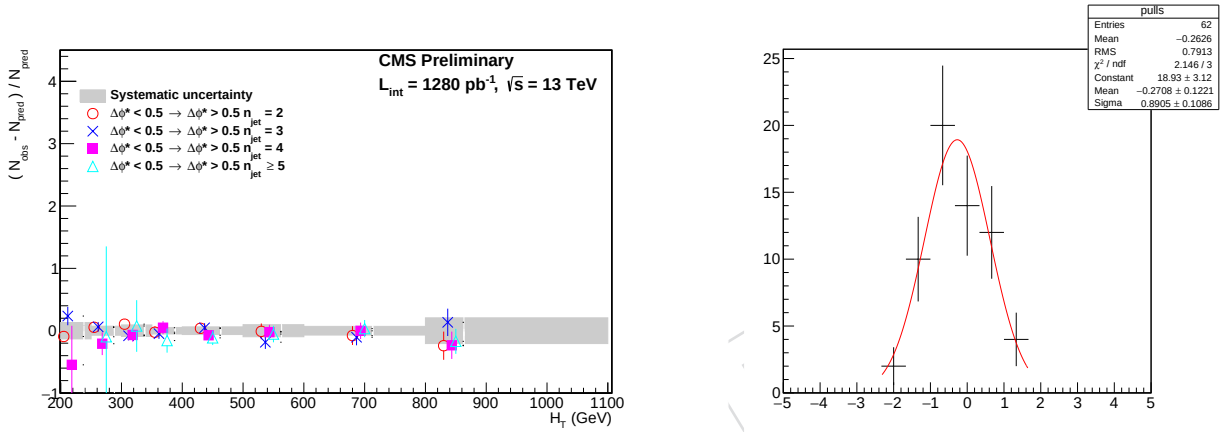

(a) Closure tests (b) Pulls of closure tests

Figure 36: Closure tests probing the $\Delta\phi*$ extrapolation for each n_{jet} category (open symbols) and their pulls fit with a gaussian. Made with the μ + jets control sample, carried out with $1.28\mathrm{fb}^{-1}$ of 13 TeV data.

The closure tests in Fig. 37 probe the effects of the extrapolation in the lepton definition used for the veto in the signal region, as described in Sec. 12.5. These tests are included in the systematic calculation for the W and $\mathrm{t\bar{t}}$ + jets backgrounds, but can be seen in isolation here.

12.9 Simulation-based studies of normalisation systematic uncertainties

As described in Secs. 11 and 12.1, the non-multijet background yields per $(n_{\mathrm{jet}}, n_{\mathrm{b}}, H_{\mathrm{T}})$ bin are estimated through the use of control regions and appropriate MC-based transfer factors. This approach aims to minimise the sensitivity to simulation mismodelling, as many systematic biases are expected to cancel to a large extent in the ratios defining the transfer factors. Systematic uncertainties on the transfer factors accounting for residual biases are derived from the data-driven closure tests.

We still consider a wide range of systematic effects arising from uncertainties in jet energy scales, b-tag scale factors, parton distribution functions, lepton and photon identification, etc. These are all expected to be sub-dominant with respect to the systematic uncertainties derived from the closure tests, and we check that this is the case.

The procedure to determine the effect of these sources of systematic uncertainties is to construct the transfer factors when varying in turn each source by their up and down one sigma uncertainties, and express this as a percentage difference relative to the nominal transfer factors.

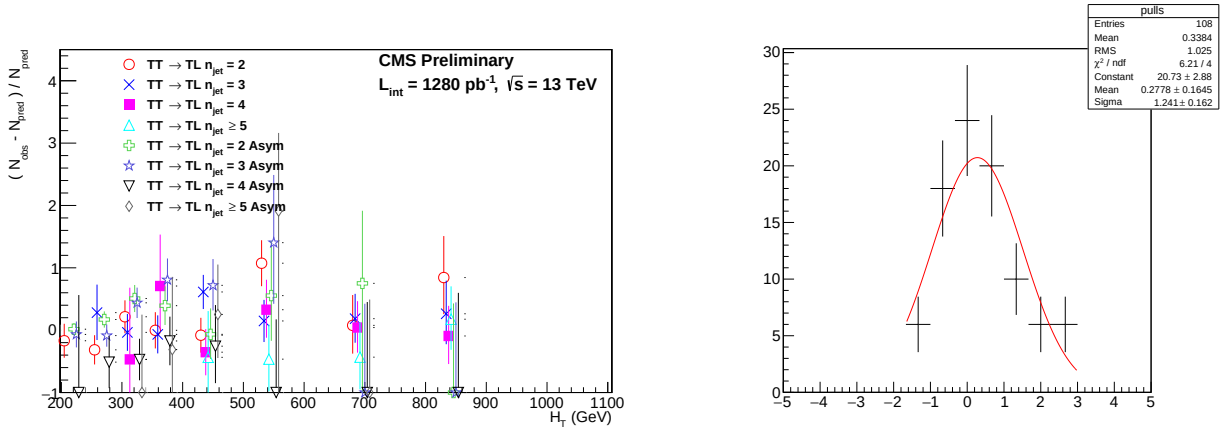

(a) Closure tests (b) Pulls of closure tests

Figure 37: Closure tests probing the effect of lost leptons in the analysis for each n_{jet} category (open symbols) and their pulls fit with a gaussian. Carried out with 1.28fb^{-1} of 13 TeV data. Events with two muons that pass the control region (tight) muon criteria are used to predict events with one tight muon and one muon that passes the signal region veto criteria (loose)

These sources of systematic uncertainty can affect both the experimental acceptance of the signal and control regions, as well as event migration between analysis bins. The aim in this case is to assess the relative changes in the transfer factors across bins as the variations are performed and the overall integrated yields are fixed.

As a preliminary study, the effect of varying the jet energy scale in the μ + jets and $\mu\mu$ + jets control regions is investigated. The energies of jets used in the analysis are corrected as a function of their p_{T} and η via the procedure recommended by the JetMET POG. These corrections have an associated uncertainty, which can propagate through the analysis. As the analysis is designed such that bins with the same value of H_{T} and jet multiplicity in the control regions are used to predict the background in the signal region, we expect to be protected against many of the effects caused by these jet energy scale uncertainties. However, the jet energy scale can still have an effect, due to jets moving in and out acceptance (above and below 40 GeV).

Full selection, as described in Sec. 7, is required. If any control region bin has fewer than 1 predicted events at 1280pb^{-1} it is left out of the study. Pseudo transfer factors are calculated in each analysis bin, defined as the number of events in a signal region after passing the signal region α_{T} cut in a particular bin divided by the total number of events in that bin. This is carried out using the jet energy corrections with their nominal, most likely, value and with their minus one sigma, lower bound, value. The relative change in these two transfer factors is then calculated. For the μ + jets control region, these values are shown in Fig. 38. For the $\mu\mu$ + jets control region, these values are shown in Fig. 39.

Overall, the effect of varying the jet energy scale down appears to be small. With variations in the pseudo transfer factors being typically less than 10%. Any larger effects are likely due to statistical fluctuations in bins with a small number of events.

A check has also been performed on the systematic effect on the background prediction due to QCD contamination in the control samples, which has been found to be at the percent level for the μ + jets and γ + jets control regions. Applying an aribtrarily large variation of $\pm$100% on

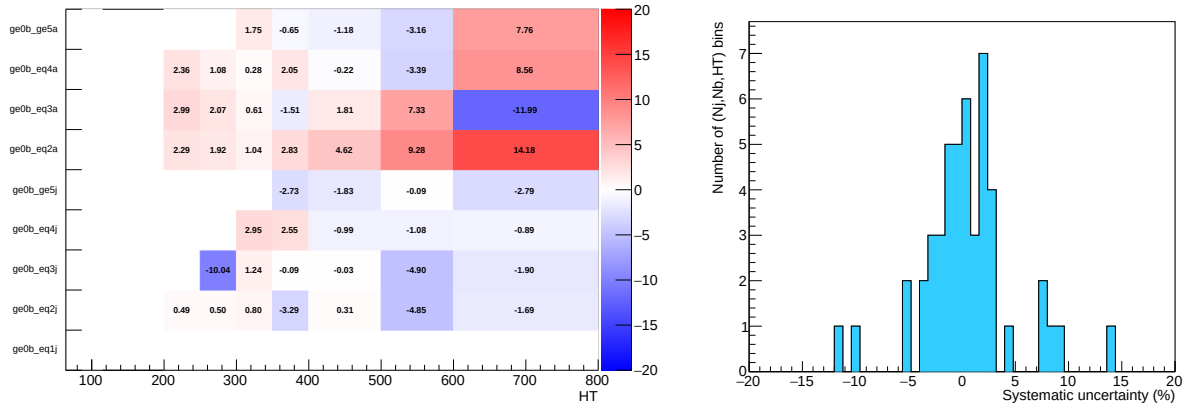

(a) The relative change in transfer factors per H_T bin and jet category

(b) The relative change in transfer factors for every analysis bin with an α_T cut, inclusive on b-tags

Figure 38: The change in pseudo transfer factors when calculating them with nominal jet energy corrections and the minus one sigma level jet energy corrections in the μ + jets control sample.

DRAFT

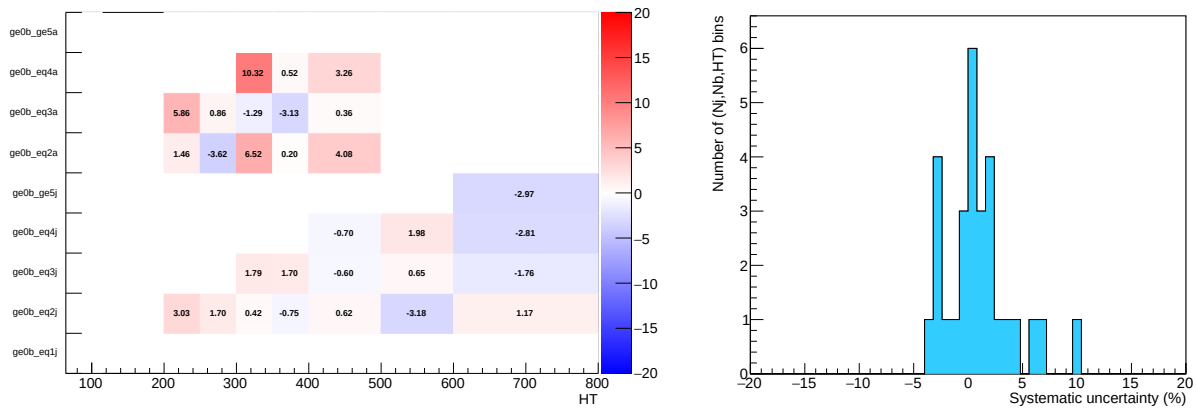

(a) The relative change in transfer factors per H_T bin and jet category

(b) The relative change in transfer factors for every analysis bin with an α_T cut, inclusive on b-tags

Figure 39: The change in pseudo transfer factors when calculating them with nominal jet energy corrections and the minus one sigma level jet energy corrections in the $\mu\mu$ + jets control sample.

the number of Monte Carlo QCD events leads to a systematic variation on the transfer factors of at most 5% in the majority of bins.

These preliminary studies suggest that the jet energy scale and QCD uncertainties are small and should be covered by the systematics derived from the closure tests in Sec. 12.5. The closure tests are therefore a conservative estimate to which it can be established, based on data, that there is no significant bias in the background predictions.

DRAFT

13 Systematic uncertainties in the $H_{\mathrm{T}}^{\mathrm{miss}}$ dimension

The estimate of the number of events per (n_{jet}, n_{b}, H_{T}) bin, integrated over $H_{\mathrm{T}}^{\mathrm{miss}}$, is derived from data control samples, with the associated systematic uncertainty determined from closure tests described in Sec. 12.3. This section describes the method used to assess the systematic uncertainties in the distribution of events according to $H_{\mathrm{T}}^{\mathrm{miss}}$. A data driven approach is utilised under the hypothesis of zero bias in the data and MC agreement. The level of closure in the control regions is used to derive alternative templates accounting for systematic uncertainties.

When looking at the $H_{\mathrm{T}}^{\mathrm{miss}}$ dimension inclusively in H_{T} there are large theoretical uncertainties that originate from mixing events at different scales. These uncertainties can be mitigated if the events are binned according to a variable, such as H_{T}, which is strongly correlated with the scale of the event. After this categorisation is applied, the uncertainty in the distribution of the $H_{\mathrm{T}}^{\mathrm{miss}}$ variable (as well as any other MET-like variable) is expected to be mainly affected by the MC modelling of the particle decays and, to a lesser extent, by jet reconstruction effects, such as jet energy scale and resolution. This approach, which will be often referred to as *scale anchoring* in the following, is used in this analysis. The distribution in $H_{\mathrm{T}}^{\mathrm{miss}}$ is measured in data using the control regions and compared to MC to determine the validity of the zero bias hypothesis after scale anchoring.

In Sec. 13.1 the 8 TeV data is used used to validate the scale anchoring approach. In Sec. 13.2 the procedure used to extract the systematic uncertainties in the $H_{\mathrm{T}}^{\mathrm{miss}}$ dimension is described and results shown with 8 TeV data. In Sec. 13.3 the validation is repeated with 13 TeV data and in Sec. 13.4 the results of a bias injection test described. Finally, in Sec. 13.5 the expected systematics for 3fb^{-1} in Run 2 are be shown.

13.1 Validation with 8 TeV Data

In previous versions of this analysis three control regions were used: μ + jets, $\mu\mu$ + jets and γ + jets. To parameterise the data/MC agreement orthogonal polynomials are used such that odd and even powers are decorrelated [24]. The nth order orthogonal polynomial which is fitted to the data/MC distribution is defined in Eq. 7.

$$f_n(x) = \sum_{k=0}^{k=n} (p_k) \times (\bar{x} - x)^k \tag{7}$$

where $\bar{x}$ is the weighted mean of the distribution and $p_k = 0$ implies the kth order is negligible. In Fig. 40 the data/MC distribution against $H_{\mathrm{T}}^{\mathrm{miss}}$ for the control region selection (detailed in [5]) is shown inclusive in H_{T} and categories. By fitting a first order orthogonal polynomial it can be seen that there is a large linear bias. This bias in the data/MC agreement is expected as events at different scales are mixed. The first order orthogonal polynomial is used to measure the level of bias remaining when the $H_{\mathrm{T}}^{\mathrm{miss}}$ dimension is binned in H_{T}. This allows the normalisation parameter to be decorrelated from the parameter which controls the distribution in $H_{\mathrm{T}}^{\mathrm{miss}}$. The normalisation in each H_{T} bin and its systematics is then defined following the data-drived method used in Run 1, see Sec, 13.2 for details.

By anchoring the scale using binning in the H_{T} dimension the remaining bias should be negligible. In Figs. 41 and 42 example fits of an orthogonal linear function to the data/MC ratio are shown for the three control regions. Comparing to the inclusive distribution the linear component can be seen to be compatible with the null hypothesis, i.e. no bias. In order to formalise this assertion the pull of the linear component from zero is calculated. This pull distribution is

DRAFT

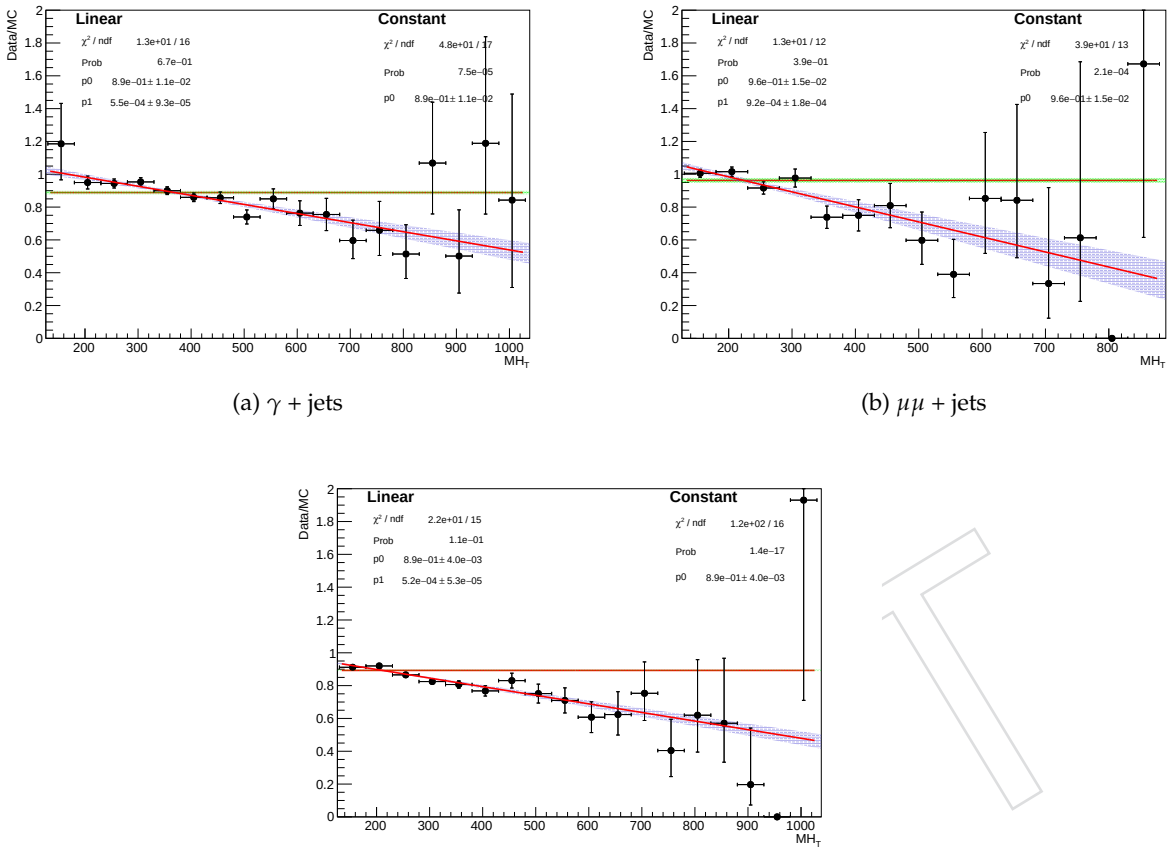

(a) γ + jets

(b) $\mu\mu$ + jets

(c) μ + jets

Figure 40: The data/MC distribution against H_T^{miss} for an inclusive selection on category and H_T showing the results of a linear fit. A large bias is observed.

shown for each of the three control regions in in Fig. 43 and can be seen in each case to have mean and sigma consistent with zero and one respectively. This confirms that the linear component is compatible with zero ($p_1 = 0$), i.e. no significant bias is observed, and the uncertainty on the parameter is correctly estimated by the fit. Fig. 44 shows the distribution of the pulls in category and H_T bins. Those anchored by H_T are consistent with zero (including inclusive jet categories) while the fits inclusive in H_T show very large pulls. This shows, as expected, the H_T anchoring is critical for removing bias in the H_T^{miss} dimension. The linear fits to the data/MC ratio additionally show a p-value following a uniform distribution between 0 and 1 as shown in Fig. 45.

13.2 Deriving systematics on the H_T^{miss} imension

The systematic in the H_T^{miss} dimension is extracted from the hypothesis of no bias. This is done by using the control regions to determine the statistical precision to which this hypothesis can be confirmed. This information is then used to derive the systematic uncertainty, as described in the following.

Each background in the signal region ($t\bar{t}$/W and Z_{inv}) is predicted using several control regions. In order to determine the uncertainty in the H_T^{miss} dimension a combined linear fit is made over all relevant control regions of the linear function. A requirement of at least 10 events and a non-trivial number of degrees of freedom is made to ensure a reasonable fit. Where this

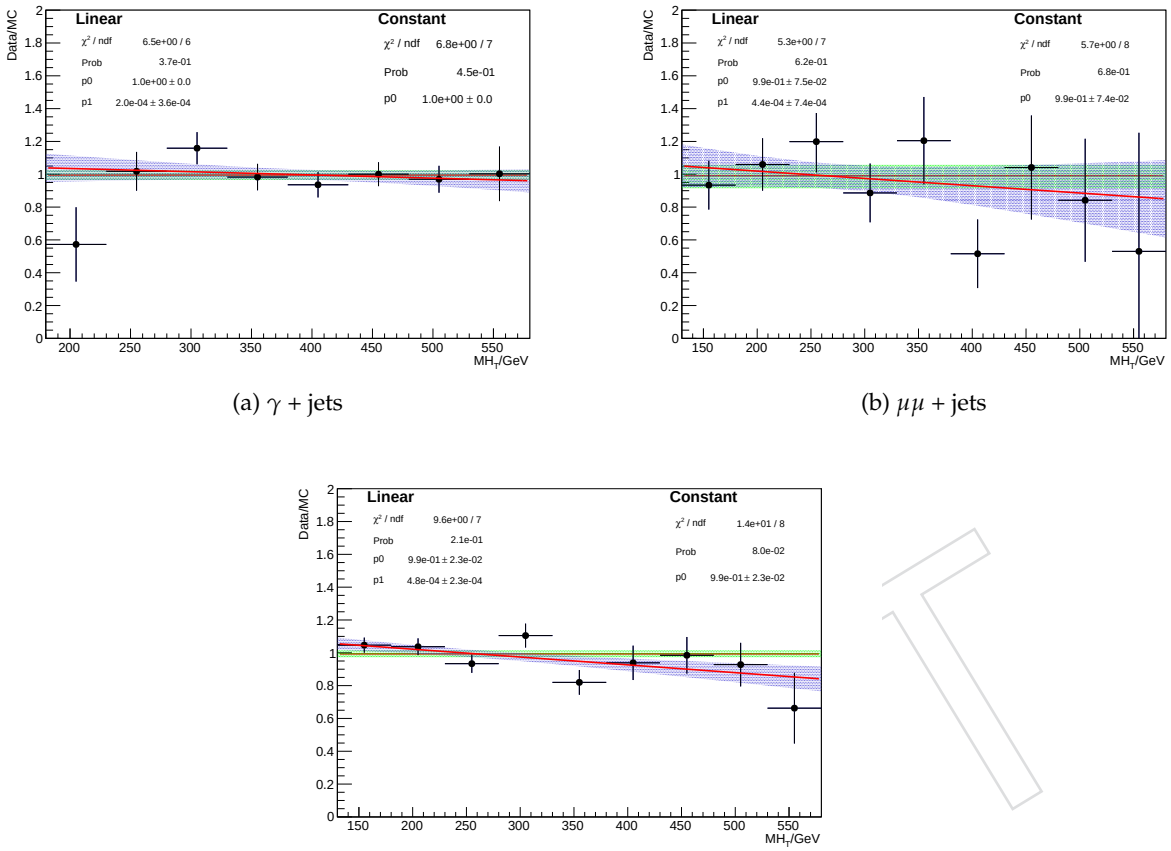

(a) γ + jets

(b) $\mu\mu$ + jets

(c) μ + jets

Figure 41: The data/MC distribution against H_T^{miss} for the 0b, $\leq$ 3j category and H_T 475-575 GeV bin. The large bias in the linear component seen in Fig. 40 is mitigated.

requiement is not satisfied the H_T^{miss} distribution is not used in the signal region. An H_T^{miss} requirement of 130 GeV is made to ensure a similar phase space to the signal region (this maps the minimum H_T^{miss} due to the α_T requirements in the signal region). The uncertainty on the linear parameter from the fit is then used to define the up and down one sigma variations of the nominal template. As a conservative estimate, the best fit value of the parameter is added in quadrature to its uncertainty in order to derive the overall variation.

The result of this procedure is shown in Fig. 46 for different H_T bins and categories, using the data from the 8 TeV signal region. Here the template variations for both relevant backgrounds are combined to show the overall uncertainty on the H_T^{miss} dimension. The scatter of the points around one is compatible with statistical fluctuations as no signal has been observed in this data sample.

An additional validation is carried out by comparing expected and observed uncertainties on the linear parameter defining the template variations. The expected uncertainties are derived by using a linear fit to the MC/MC ratio where the numerator have uncertainties given by the Poisson uncertainty on the number of predicted counts while the uncertainty on the denominator comes from the statistical uncertainty on the MC prediction. The relative uncertainties on $1 + p_1$ derived from this approach for $t\bar{t}$/W and Z_{inv} are shown in Fig. 47 and Fig. 48 and compared to those observed. These show good agreement which provides additional motivation for the zero bias hypothesis as well as validating the method for deriving expected uncertain-

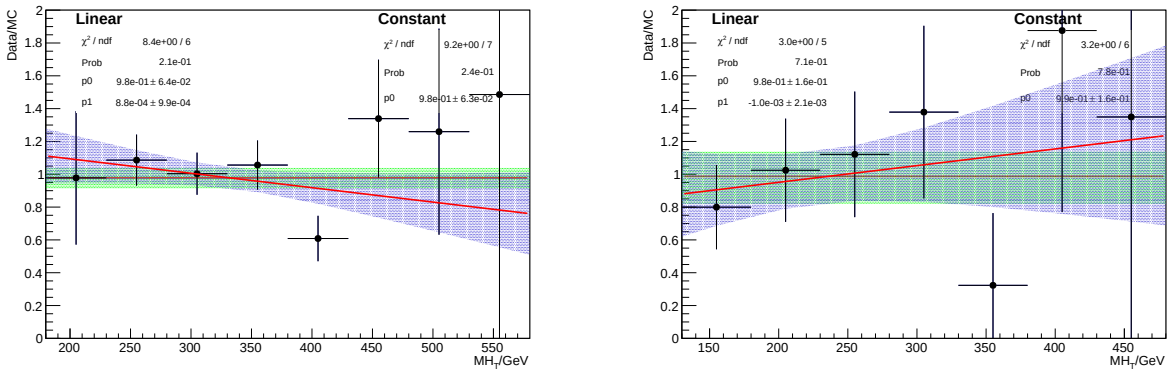

(a) γ + jets

(b) $\mu\mu$ + jets

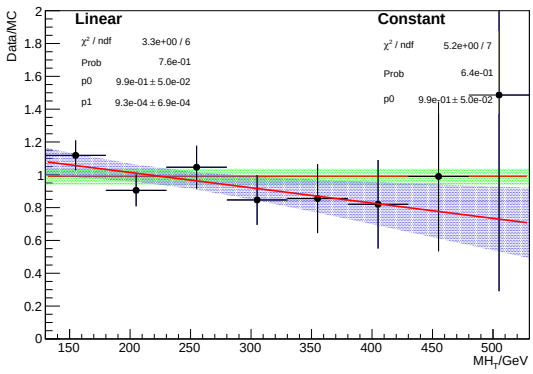

(c) μ + jets

Figure 42: The data/MC distribution against H_T^{miss} for the 0b, $\geq$ 4j category and H_T 475-575 GeV bin. The large bias in the linear component seen in Fig. 40 is mitigated.

ties.

An H_T^{miss} cut of 130 GeV is sufficient to ensure the signal and control regions share a similar phase space, however, it is instructive to repeat the validation using indential α_T requirements in the control regions (γ + jets always has these requirements). This will largely reduce the statistics of the control region due to the agressive nature of the α_T variable which is designed to remove QCD. In Figure 49, the pull of the linear parameter for the μ + jets control region with an α_T cut is shown. This is compatible with the no bias hypothesis as observed with the H_T^{miss} cut.

13.3 Validation with 13 TeV ata

The scale anchoring approach has been validated with 1.28fb^{-1} of data collected at 13 TeV. In Fig. 50 the pulls of the linear parameter for the combined fit over the control regions used for the $t\bar{t}$/W prediction (μ + jets) and for Z_{inv} (μ + jets, $\mu\mu$ + jets, γ + jets) are shown to be consistent with no bias. In Fig. 51 the french flag plot of the pulls also shows no regions with consistent bias for either background. Finally, figure Fig. 47 and Fig. 47 show the observed systematics agree well with those expected as was observed in the full 8 TeV dataset. These validations are continually updated as additional data becomes available. As a gauge of the effect of the template variations the uncertainty parameter can be translate to an uncertainty on the last bin. This is typically of the order of 10% depending on the category and is shown in Fig. 52.

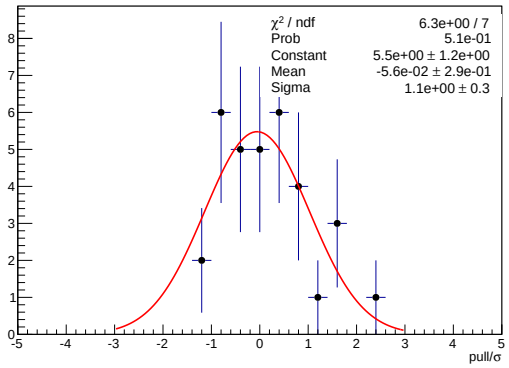

(a) γ + jets

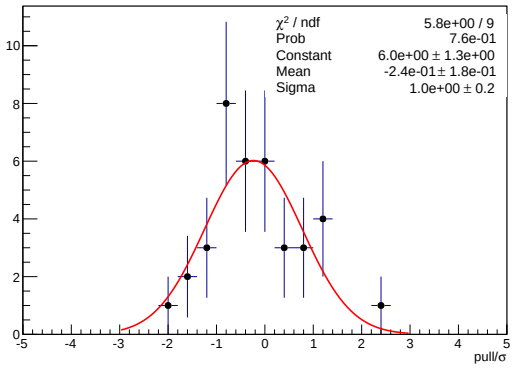

(b) $\mu\mu$ + jets

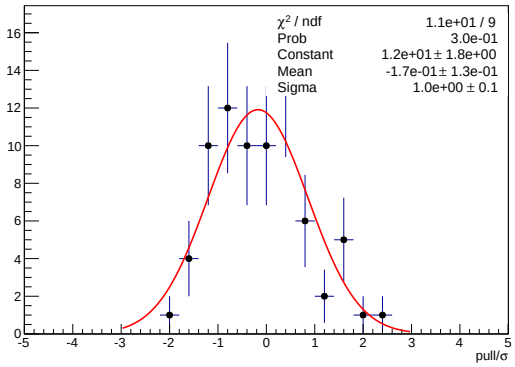

(c) μ + jets

Figure 43: The pull distribution of the linear parameter from the flat hypothesis showing no significant bias.

13.4 Bias injection test

To understand the effect of a bias which effects only very high H_T^{miss} bins on the validation procedure a bias injection test is carried out. The prediction in the final bin only is varied and the effect on the overall pull studied. The results are shown for the symmetric jet categories only as for asymmetric categories the final H_T^{miss} bin dominates the fit. This is an extreme test of the ability to probe bias using the linear fit. Fig. 53 displays the results of this test showing the pull distribution is sensitive to such a bias. In Fig. 54 the change in predicted systematic is shown for the case of halving the prediction in the last bin. This shows an overall substantial increase in the systematics predicted.

13.5 Expected systematic uncertainties for the 13 TeV nalysis

Using the method described in Sec. 13.2 the expected uncertainties from 13 TeV MC for both $t\bar{t}/W$ and Z_{inv} using all relevant control regions are shown in Fig. 55 for 3fb^{-1}. Depending on the category and H_T bin, uncertainties between 1 and 10% are found on the linear parameter. An example of the overall uncertainties on the H_T^{miss} templates is shown in Figure 56. The alternative templates derived with this method are folded into the likelihood described in Section 14 to account for systematic uncertainties in the H_T^{miss} dimension.

DRAFT

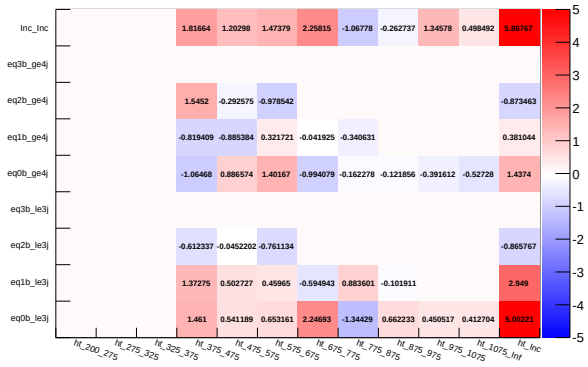

(a) γ + jets

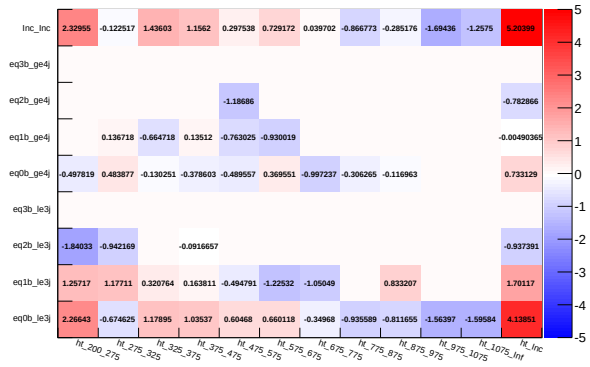

(b) $\mu\mu$ + jets

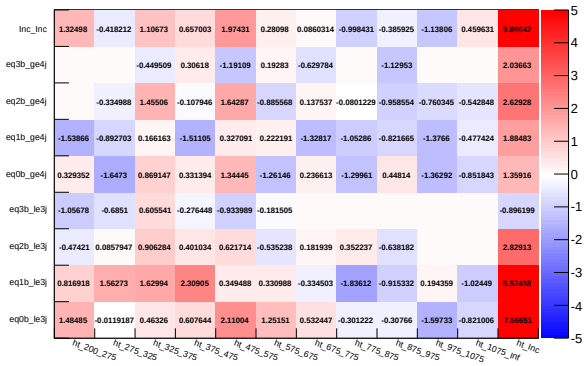

(c) μ + jets

Figure 44: The pull distribution of the linear parameter from the flat hypothesis across all H_T bins and categories. There are no significant pulls for the H_T binned fits while the H_T inclusive case shows very large pulls as expected. Due to trigger requirements the γ + jets control sample may only be used for $H_T > 375$ GeV.

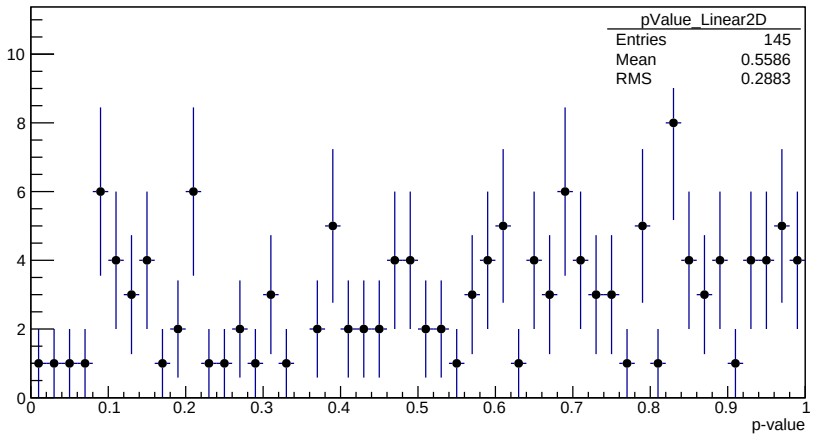

Figure 45: The distributions of the p-value for the linear fit.

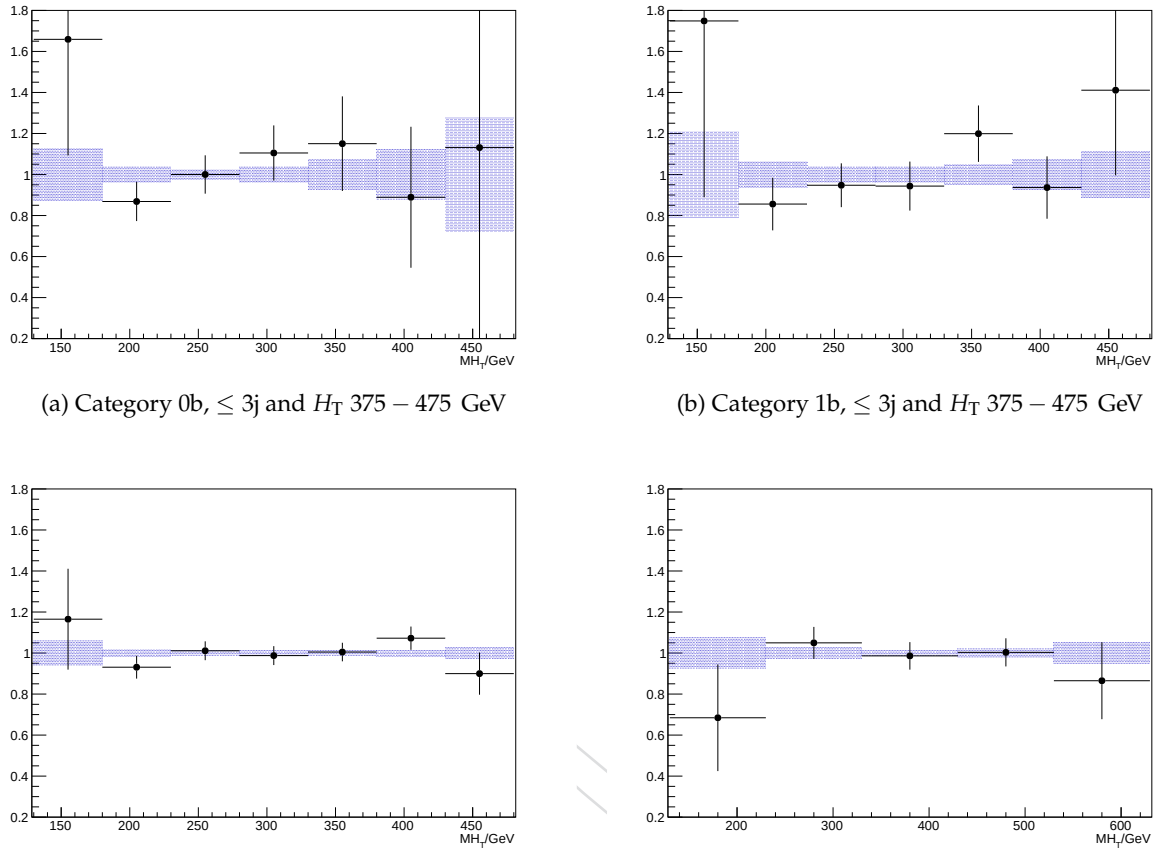

(a) Category 0b, $\leq$ 3j and H_T 375 – 475 GeV

(b) Category 1b, $\leq$ 3j and H_T 375 – 475 GeV

(c) Category 0b, $\geq$ 4j and H_T 375 – 475 GeV

(d) Category 0b, $\leq$ 3j and H_T 475 – 575 GeV

Figure 46: Signal data/MC shown with template variations predicted from the control regions.

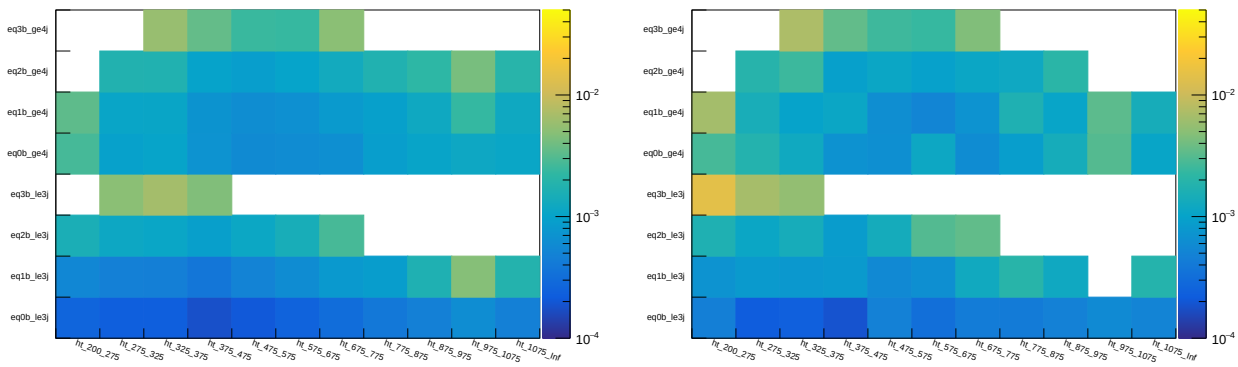

(a) Expected uncertainties

(b) Observed uncertainties

Figure 47: Expected relative uncertainties shown for $t\bar{t}$/W in Fig. 47a are consistent with observed relative uncertainties shown in Fig. 47b.

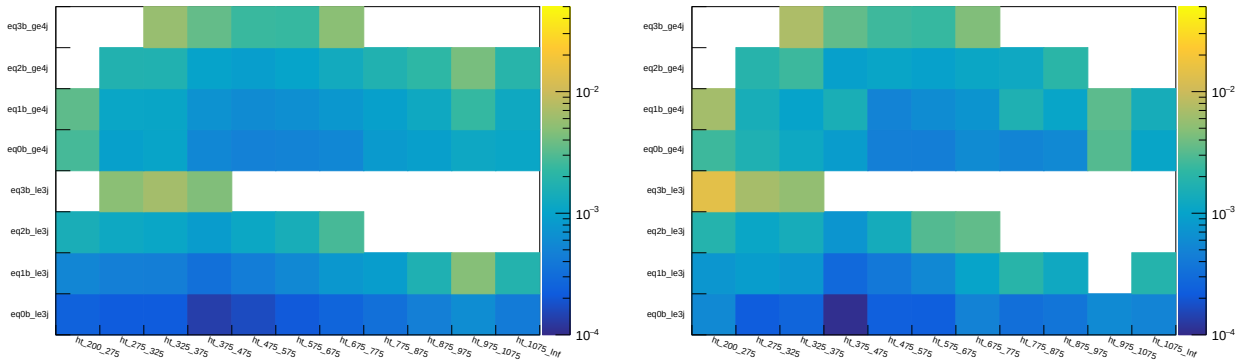

(a) Expected uncertainties (b) Observed uncertainties

Figure 48: Expected relative uncertainties shown for Z_{inv} in Fig. 48a are consistent with observed relative uncertainties shown in Fig. 48b.

DRAFT

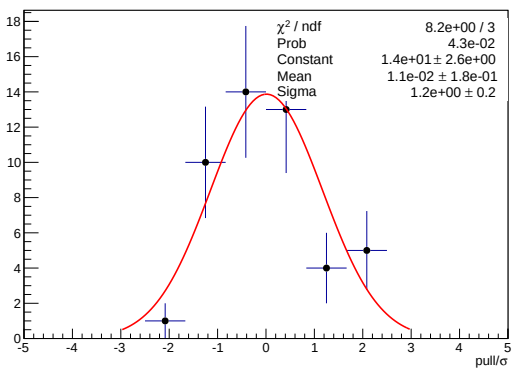

Figure 49: Pull distribution for the μ + jets control region with signal region α_{T} requirements showing no overall bias

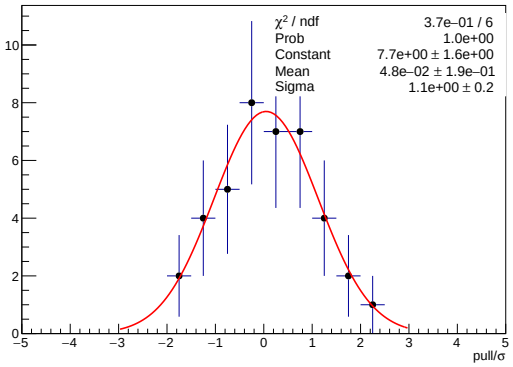

(a) γ + jets

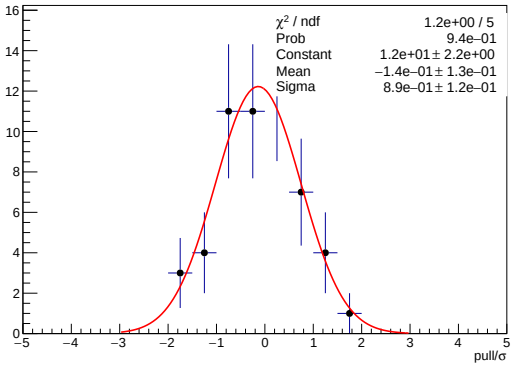

(b) $\mu\mu$ + jets

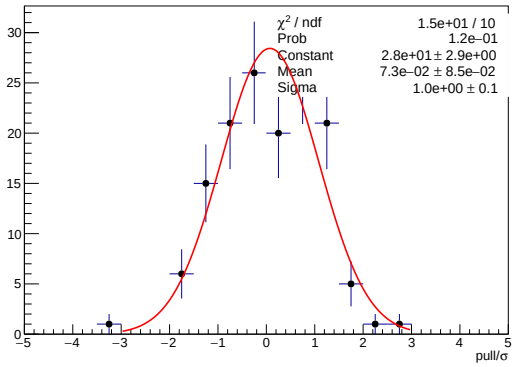

(c) μ + jets

Figure 50: The pull distribution of the linear parameter from the flat hypothesis showing no significant bias for any control region.

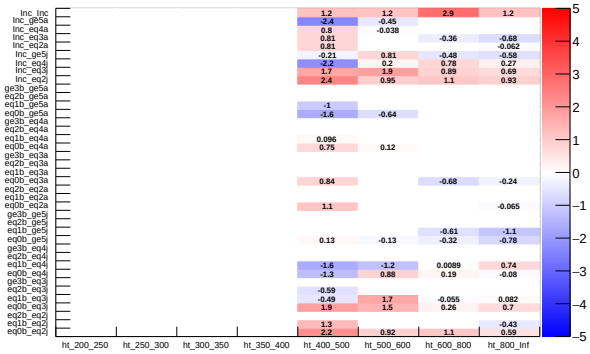

(a) γ + jets

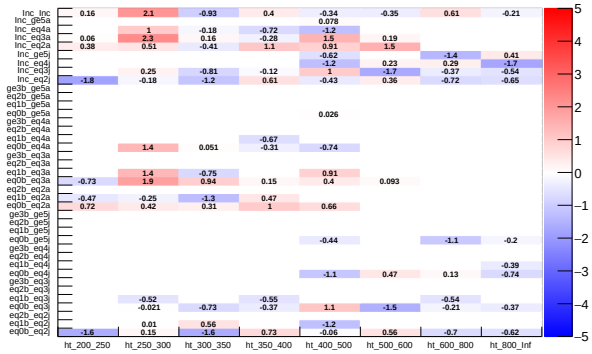

(b) $\mu\mu$ + jets

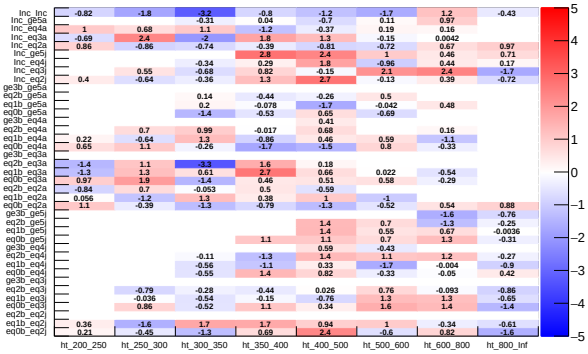

(c) μ + jets

Figure 51: The pull distribution of the linear parameter from the flat hypothesis across all H_{T} bins and categories. There are no significant pulls for the H_{T} binned fits while the H_{T} inclusive case shows very large pulls as expected. Due to trigger requirements the γ + jets control sample may only be used for $H_{\mathrm{T}} > 400\,\mathrm{GeV}$.

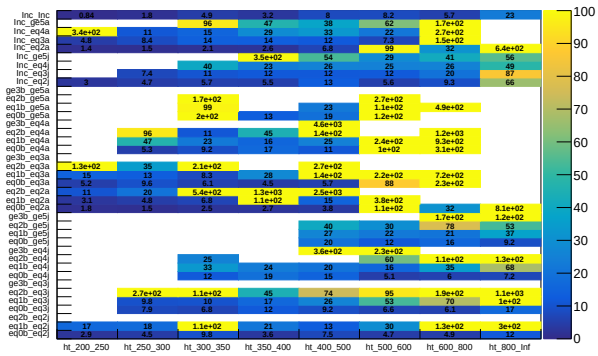

Figure 52: Expected uncertanties on the final bin over all categories and H_{T} bins for $3\mathrm{fb}^{-1}$.

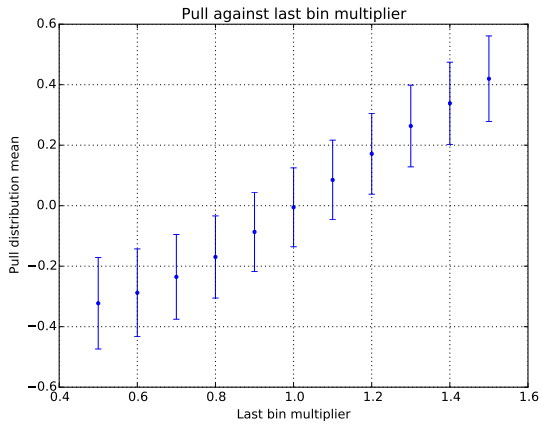

Figure 53: Mean pull against last bin multiplier for the μ + jets control region showing the linear polynomial is sensitive to a bias effecting the final bin only.

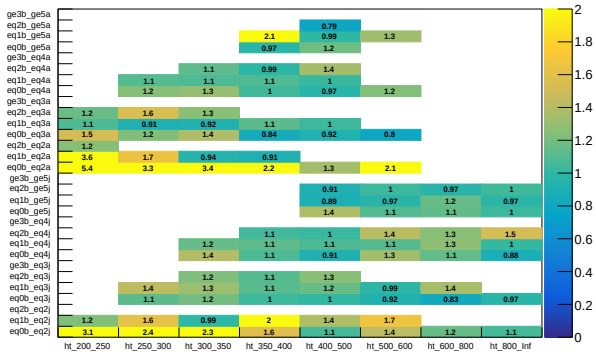

Figure 54: Change in systematic parameter when the prediction in the last bin is halved

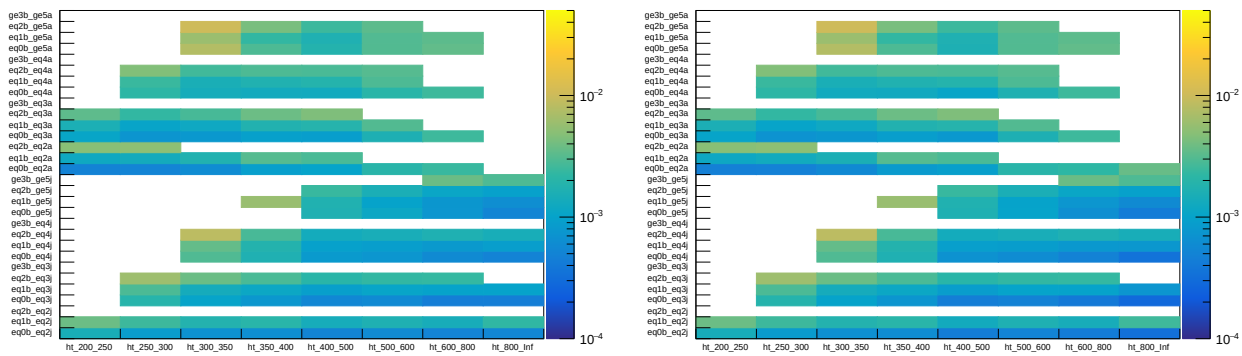

(a) $t\bar{t}/W$ (b) Z_{inv}

Figure 55: Expected relative uncertainties on the template shown for Z_{inv} in Figure 55b and $t\bar{t}/W$ in Fig. 55a are around 1 to 10%.

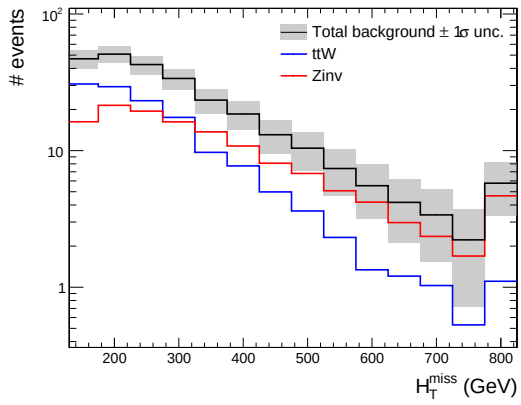

Figure 56: Example template for 0b,$\geq$ 5j and $H_T > 800$ GeV showing the uncertainties from both components of the background on the total background prediction.

Draft

14 Likelihood model

Consider a given category of event as defined by n_{jet}, n_{b} and H_{T}, which are in the following identified with $H_{\text{T}}^{\text{cat}}$. In each category, the signal is extracted using the discriminating variable $H_{\text{T}}^{\text{miss}}$. Histogram templates of the $H_{\text{T}}^{\text{miss}}$ distribution are built for the signal and the background processes using the MC samples described in Sec. 4. The binning of the templates is chosen taking into account both the limited statistics in the simulation and the control of the background in data.

A minimum of 10 unweighted events is required in each bin of the MC histogram template, in order to make the MC statistics uncertainty subdominant with respect to the other systematic sources.

Furthermore, we require at least 10 events in the highest bin in the relevant control regions. This requirement allows to perform a statistically meaningful closure test in data up to the highest values of $H_{\text{T}}^{\text{miss}}$.

Finally, a minimum bin width constraint of 50 GeV is applied, in order to reduce the bin-by-bin migration due to the finite $H_{\text{T}}^{\text{miss}}$ resolution.

The binning of the $H_{\text{T}}^{\text{miss}}$ templates for all the $H_{\text{T}}^{\text{cat}}$ is given in Appendix G.

For each category $H_{\text{T}}^{\text{cat}}$ and $H_{\text{T}}^{\text{miss}}$ bin, i, in the signal region, let $n_{\text{had},i}^{H_{\text{T}}^{\text{cat}}}$ be the number of observed events, $b_{\text{had},i}^{H_{\text{T}}^{\text{cat}}}$ the number of predicted background events and $s_{\text{had},i}^{H_{\text{T}}^{\text{cat}}}$ the expected number of signal events.

The likelihood function for the hadronic signal region is, in each $H_{\text{T}}^{\text{cat}}$:

$$\mathcal{L}_{\text{had}}^{H_{\text{T}}^{\text{cat}}} = \prod_i \text{Poisson}(n_{\text{had},i}^{H_{\text{T}}^{\text{cat}}} | \, b_{\text{had},i}^{H_{\text{T}}^{\text{cat}}} + s_{\text{had},i}^{H_{\text{T}}^{\text{cat}}}) \tag{8}$$

The control regions are not split in the $H_{\text{T}}^{\text{miss}}$ dimension, and their information is only used to constrain the normalisation of the background processes in the signal region, as described in Sec. 11. Their likelihood is therefore written as:

$$\mathcal{L}_{\text{CR,j}}^{H_{\text{T}}^{\text{cat}}} = \text{Pois}(n_{\text{CR,j}}^{H_{\text{T}}^{\text{cat}}} | \, b_{\text{CR,j}}^{H_{\text{T}}^{\text{cat}}} + s_{\text{CR,j}}^{H_{\text{T}}^{\text{cat}}}) \tag{9}$$

In Eq. 9, $n_{\text{CR,j}}^{H_{\text{T}}^{\text{cat}}}$ is the number of observed events, $b_{\text{CR,j}}^{H_{\text{T}}^{\text{cat}}}$ the number of predicted background events and $s_{\text{CR,j}}^{H_{\text{T}}^{\text{cat}}}$ the expected number of signal events in the control region j.

Eq. 9 applies to all the control region used for the background estimation, as defined in Sec. 7.

Notice that the signal contribution $s_{\text{CR,j}}^{H_{\text{T}}^{\text{cat}}}$ in Eq. 9, as estimated from MC, is in general negligible. Where the signal contamination is sizeable, it is included in the likelihood as an additional process contributing to the event yield in that particular bin.

The prediction of the background yields in the signal region and in the corresponding control samples are connected by means of transfer factors, as explained in Sec. 11. This connection is implemented by introducing a log-uniform nuisance parameter, which is correlated between the signal region and the control region, separately for each background process ($Z_{\text{inv.}}$, $\text{t}\bar{\text{t}}/\text{W}$) [3]. This binds the background yields in the signal and control region to float together, taking into account the statistical uncertainty associated with the counts in the control samples.

[3] In the following we use Z_{inv} to indicate the $Z \to \text{inv}$ process and $\text{t}\bar{\text{t}}/\text{W}$ to indicate the sum of the yields of the $t\bar{t}$ and $W+\text{jets}$ processes.

DRAFT

The systematic uncertainties affecting the transfer factors, described in Sec. 12.1, are incorporated in the likelihood by means of log-normal nuisance parameters, which are taken as uncorrelated between each of the $H_{\mathrm{T}}^{\mathrm{cat}}$ bins. The uncertainty on the signal efficiency times acceptance, described in Sec. 16.4, is taken as correlated across all the $H_{\mathrm{T}}^{\mathrm{cat}}$ bins. The uncertainty that encapsulates the potential for bin migration within the $H_{\mathrm{T}}^{\mathrm{miss}}$ distribution of events is implemented providing alternative templates corresponding to up/down variation of each source, separately for each $H_{\mathrm{T}}^{\mathrm{cat}}$ bin. The procedure to assess the alternative templates is described in detail in Sec. 13.
The uncertainty due to the limited statistics in the MC samples used to populate the template histograms is incorporated as additional nuisance parameters, one per template bin, taken as uncorrelated across the histogram bins.

The total likelihood is the product over all the $H_{\mathrm{T}}^{\mathrm{cat}}$ bins and all the control regions, and can be written as:

$$\mathcal{L} = \prod_{H_{\mathrm{T}}^{\mathrm{cat}}} \mathcal{L}_{\mathrm{had}}^{H_{\mathrm{T}}^{\mathrm{cat}}} \times \prod_{\mathrm{j}} \mathcal{L}_{\mathrm{CR,j}}^{H_{\mathrm{T}}^{\mathrm{cat}}} \tag{10}$$

The fit is carried on in two steps. In the first, the background prediction for the signal region $b_{\mathrm{had},i}^{H_{\mathrm{T}}^{\mathrm{cat}}}$ are extracted from a likelihood fit using the control regions only in Eq. 9. In the second step, the fit is done using the full likelihood (Eq. 10) and all the correlations between the backgrounds in control regions and signal region are taken into account, together with the statistical uncertainty associated to the finite number of events in the control region.
The likelihood is profiled against all nuisance parameters in order to derive expected exclusion limits and sensitivity. These are shown in Sec. 16.

DRAFT

15 Results

In this section the main results concerning the fit are summarised.

Tables 48- 50 summarise the predicted and observed yields in the signal region for "symmetric" and "asymmetric" topologies respectively, corresponding to an integrated luminosity of 1.26 fb^{-1}. The predicted yields are based on a fit to multiple data control samples to obtain predictions in (n_{jet},n_{b},H_{T}). The observed counts in the signal region are not considered in this fit. The uncertainties reflect all statistical and (pre-fit) systematic sources added in quadrature. The $\mathrm{t\bar{t}W}$ and $\mathrm{Z} \to \nu\bar{\nu}$ components are also shown (the former of which contains all residual contributions from sub-dominant processes such as e.g. diboson production). This table summarises our best knowledge of the SM background rates in the signal region while not considering counts in the signal region itself.

Table 48: Predictions and Data in the signal region for 1.26fb^{-1} for monojet categories. The letter "a" in jet e.g. "2a" indicates the asymmetric jet bins. All entries are non-zero but are truncated to one decimal place.

H_{T} (GeV)	(n_{jet}, n_{b})	200-250	250-300	300-350	350-400	400-500	500-600	600-800	800-∞
Data	(1, 0)	4199	1347	493	251	159	54	18	–
SM	(1, 0)	$4202.6^{+424.5}_{-424.3}$	$1379.4^{+176.4}_{-176.2}$	$522.8^{+84.2}_{-83.9}$	$208.4^{+42.6}_{-42.3}$	$158.9^{+29.4}_{-29.4}$	$50.2^{+14.1}_{-14.0}$	$15.3^{+7.9}_{-7.8}$	–
Ttw	(1, 0)	$1626.6^{+190.5}_{-190.4}$	$474.6^{+74.8}_{-74.7}$	$156.0^{+28.4}_{-28.3}$	$52.2^{+12.6}_{-12.6}$	$39.5^{+8.0}_{-8.0}$	$10.1^{+3.2}_{-3.2}$	$2.6^{+1.6}_{-1.6}$	–
Zinv	(1, 0)	$2576.0^{+300.4}_{-300.2}$	$904.9^{+141.6}_{-141.4}$	$366.8^{+65.9}_{-65.6}$	$156.2^{+37.1}_{-36.8}$	$119.4^{+23.7}_{-23.6}$	$40.1^{+12.3}_{-12.3}$	$12.6^{+7.5}_{-7.4}$	–
Data	(1, 1)	139	46	17	13	7	5	0	–
SM	(1, 1)	$159.6^{+20.0}_{-19.6}$	$67.6^{+12.0}_{-11.4}$	$24.3^{+6.2}_{-5.5}$	$5.9^{+2.6}_{-2.0}$	$6.8^{+1.9}_{-1.7}$	$1.2^{+0.7}_{-0.5}$	$0.2^{+0.3}_{-0.1}$	–
Ttw	(1, 1)	$48.8^{+7.8}_{-7.6}$	$17.8^{+4.2}_{-4.0}$	$7.0^{+2.4}_{-2.2}$	$1.1^{+0.6}_{-0.5}$	$1.8^{+0.7}_{-0.6}$	$0.3^{+0.2}_{-0.2}$	$0.1^{+0.1}_{-0.0}$	–
Zinv	(1, 1)	$110.9^{+16.5}_{-16.0}$	$49.8^{+10.7}_{-10.1}$	$17.3^{+5.3}_{-4.6}$	$4.8^{+2.4}_{-1.9}$	$5.0^{+1.6}_{-1.4}$	$0.9^{+0.6}_{-0.4}$	$0.2^{+0.3}_{-0.1}$	–

Tables 51- 53 summarises the post-fit (background-only fit) predicted backgrounds and the observed yields in the signal region corresponding to an integrated luminosity of 1.26 fb^{-1}.

In Figures 57- 80 the fit in the $\not{H}_{\mathrm{T}}$ dimension is shown for all the analysis bins where the $\not{H}_{\mathrm{T}}$ templates are used.

In Figures 81- 88 the pull of the nuisance parameters with respect to the pre-fit value is shown, grouped into different type of nuisances and split between "asymmetric" and "symmetric" topologies.

DRAFT

Figure 57: Post-fit $\not{H}_{\mathrm{T}}$ templates for the bin $n_{\mathrm{jet}}^{\mathrm{asym}} = 2$, $n_{\mathrm{b}} = 0$

.

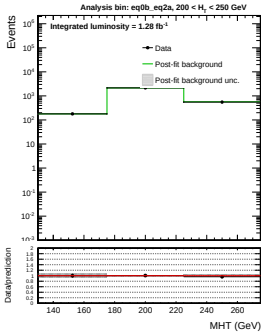

(a) $n_{\mathrm{jet}}^{\mathrm{asym}} = 2$, $n_{\mathrm{b}} = 0$, $200 < H_{\mathrm{T}} < 250$ GeV

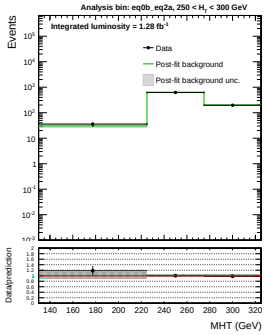

(b) $n_{\mathrm{jet}}^{\mathrm{asym}} = 2$, $n_{\mathrm{b}} = 0$, $250 < H_{\mathrm{T}} < 300$ GeV

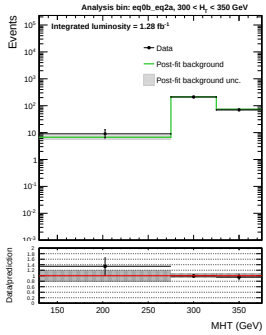

(c) $n_{\mathrm{jet}}^{\mathrm{asym}} = 2$, $n_{\mathrm{b}} = 0$, $300 < H_{\mathrm{T}} < 350$ GeV

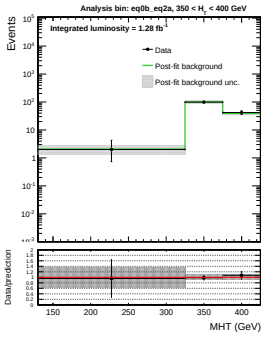

(d) $n_{\mathrm{jet}}^{\mathrm{asym}} = 2$, $n_{\mathrm{b}} = 0$, $350 < H_{\mathrm{T}} < 400$ GeV

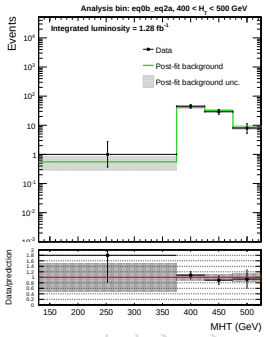

(e) $n_{\mathrm{jet}}^{\mathrm{asym}} = 2$, $n_{\mathrm{b}} = 0$, $400 < H_{\mathrm{T}} < 500$ GeV

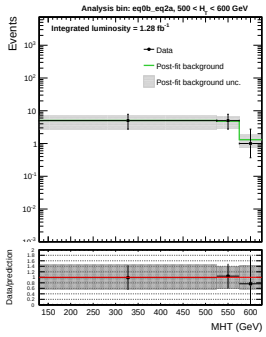

(f) $n_{\mathrm{jet}}^{\mathrm{asym}} = 2$, $n_{\mathrm{b}} = 0$, $500 < H_{\mathrm{T}} < 600$ GeV

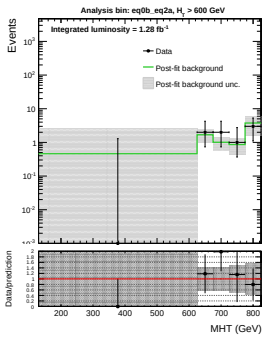

(g) $n_{\mathrm{jet}}^{\mathrm{asym}} = 2$, $n_{\mathrm{b}} = 0$, $H_{\mathrm{T}} > 600$ GeV

DRAFT

Figure 58: Post-fit $\not{H}_T$ templates for the bin $n_{\text{jet}}^{\text{sym}} = 2$, $n_b = 0$

.

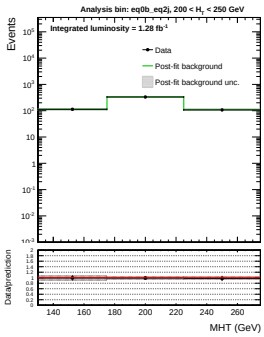

(a) $n_{\text{jet}}^{\text{sym}} = 2$, $n_b = 0$, $200 < H_T < 250$ GeV

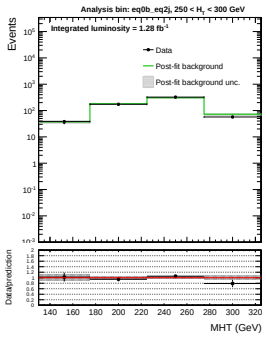

(b) $n_{\text{jet}}^{\text{sym}} = 2$, $n_b = 0$, $250 < H_T < 300$ GeV

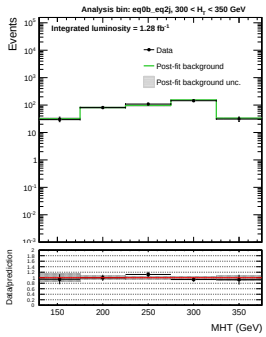

(c) $n_{\text{jet}}^{\text{sym}} = 2$, $n_b = 0$, $300 < H_T < 350$ GeV

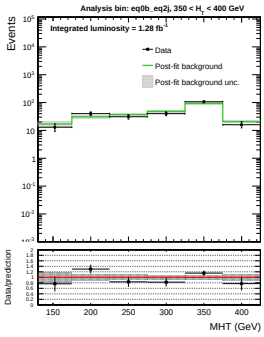

(d) $n_{\text{jet}}^{\text{sym}} = 2$, $n_b = 0$, $350 < H_T < 400$ GeV

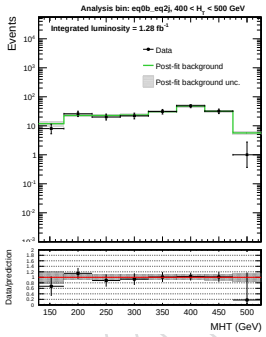

(e) $n_{\text{jet}}^{\text{sym}} = 2$, $n_b = 0$, $400 < H_T < 500$ GeV

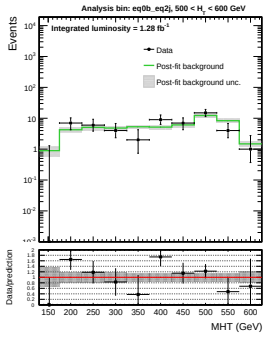

(f) $n_{\text{jet}}^{\text{sym}} = 2$, $n_b = 0$, $500 < H_T < 600$ GeV

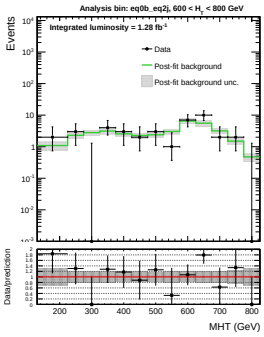

(g) $n_{\text{jet}}^{\text{sym}} = 2$, $n_b = 0$, $600 < H_T < 800$ GeV

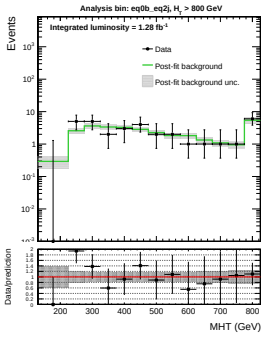

(h) $n_{\text{jet}}^{\text{sym}} = 2$, $n_b = 0$, $H_T > 800$ GeV

Figure 59: Post-fit $\not{H}_{\mathrm{T}}$ templates for the bin $n_{\mathrm{jet}}^{\mathrm{asym}} = 3$, $n_{\mathrm{b}} = 0$

.

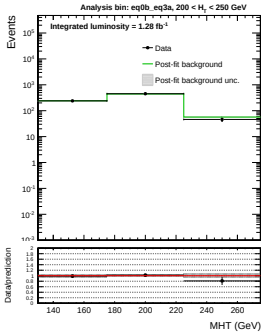

(a) $n_{\mathrm{jet}}^{\mathrm{asym}} = 3$, $n_{\mathrm{b}} = 0$, $200 < H_{\mathrm{T}} < 250$ GeV

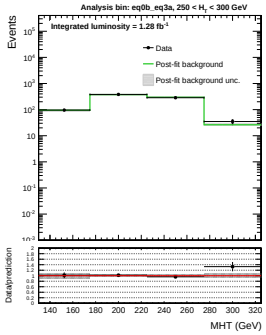

(b) $n_{\mathrm{jet}}^{\mathrm{asym}} = 3$, $n_{\mathrm{b}} = 0$, $250 < H_{\mathrm{T}} < 300$ GeV

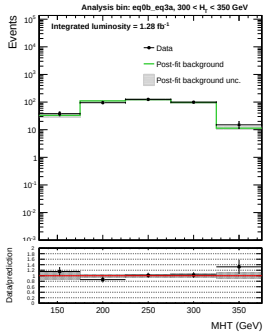

(c) $n_{\mathrm{jet}}^{\mathrm{asym}} = 3$, $n_{\mathrm{b}} = 0$, $300 < H_{\mathrm{T}} < 350$ GeV

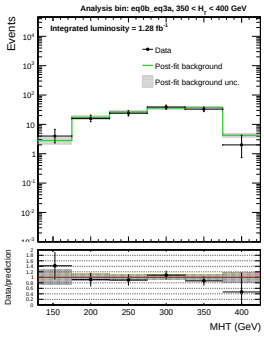

(d) $n_{\mathrm{jet}}^{\mathrm{asym}} = 3$, $n_{\mathrm{b}} = 0$, $350 < H_{\mathrm{T}} < 400$ GeV

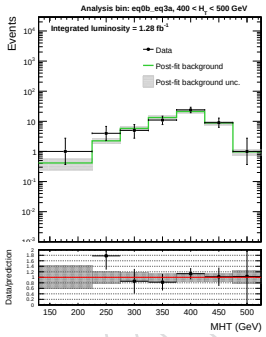

(e) $n_{\mathrm{jet}}^{\mathrm{asym}} = 3$, $n_{\mathrm{b}} = 0$, $400 < H_{\mathrm{T}} < 500$ GeV

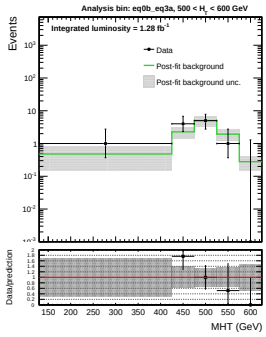

(f) $n_{\mathrm{jet}}^{\mathrm{asym}} = 3$, $n_{\mathrm{b}} = 0$, $500 < H_{\mathrm{T}} < 600$ GeV

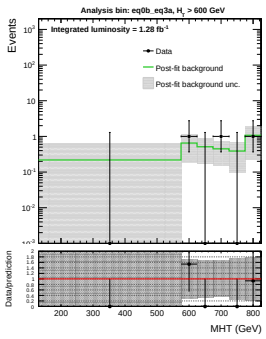

(g) $n_{\mathrm{jet}}^{\mathrm{asym}} = 3$, $n_{\mathrm{b}} = 0$, $H_{\mathrm{T}} > 600$ GeV

DRAFT

Figure 60: Post-fit $\not{H}_{\mathrm{T}}$ templates for the bin $n_{\mathrm{jet}}^{\mathrm{sym}} = 3$, $n_{\mathrm{b}} = 0$

.

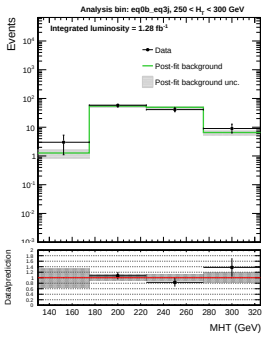

(a) $n_{\mathrm{jet}}^{\mathrm{sym}} = 3$, $n_{\mathrm{b}} = 0$, $250 < H_{\mathrm{T}} < 300$ GeV

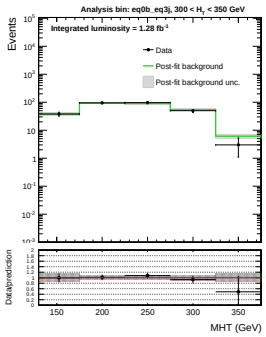

(b) $n_{\mathrm{jet}}^{\mathrm{sym}} = 3$, $n_{\mathrm{b}} = 0$, $300 < H_{\mathrm{T}} < 350$ GeV

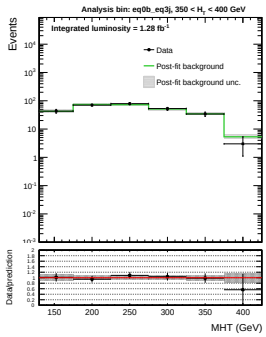

(c) $n_{\mathrm{jet}}^{\mathrm{sym}} = 3$, $n_{\mathrm{b}} = 0$, $350 < H_{\mathrm{T}} < 400$ GeV

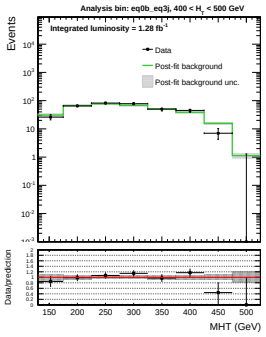

(d) $n_{\mathrm{jet}}^{\mathrm{sym}} = 3$, $n_{\mathrm{b}} = 0$, $400 < H_{\mathrm{T}} < 500$ GeV

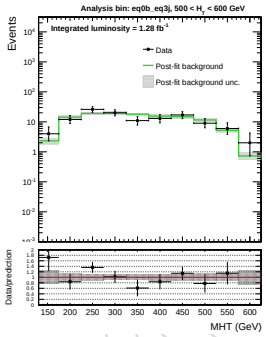

(e) $n_{\mathrm{jet}}^{\mathrm{sym}} = 3$, $n_{\mathrm{b}} = 0$, $500 < H_{\mathrm{T}} < 600$ GeV

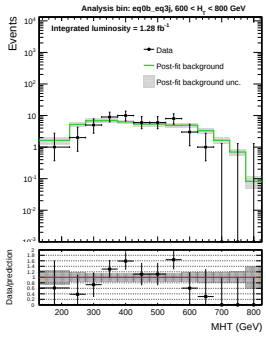

(f) $n_{\mathrm{jet}}^{\mathrm{sym}} = 3$, $n_{\mathrm{b}} = 0$, $600 < H_{\mathrm{T}} < 800$ GeV

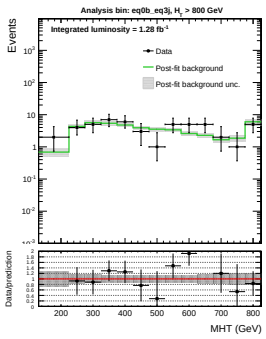

(g) $n_{\mathrm{jet}}^{\mathrm{sym}} = 3$, $n_{\mathrm{b}} = 0$, $H_{\mathrm{T}} > 800$ GeV

DRAFT

Figure 61: Post-fit $\not{H}_{\mathrm{T}}$ templates for the bin $n_{\mathrm{jet}}^{\mathrm{asym}} = 4$, $n_{\mathrm{b}} = 0$

.

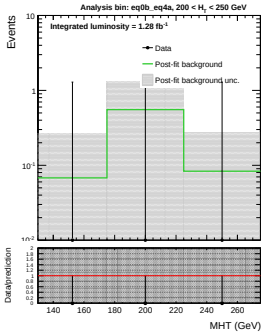

(a) $n_{\mathrm{jet}}^{\mathrm{asym}} = 4$, $n_{\mathrm{b}} = 0$, $200 < H_{\mathrm{T}} < 250$ GeV

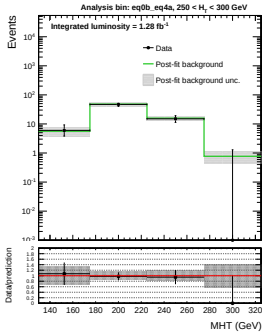

(b) $n_{\mathrm{jet}}^{\mathrm{asym}} = 4$, $n_{\mathrm{b}} = 0$, $250 < H_{\mathrm{T}} < 300$ GeV

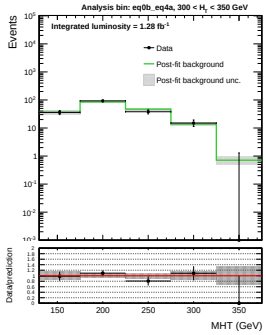

(c) $n_{\mathrm{jet}}^{\mathrm{asym}} = 4$, $n_{\mathrm{b}} = 0$, $300 < H_{\mathrm{T}} < 350$ GeV

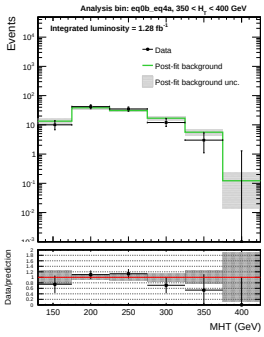

(d) $n_{\mathrm{jet}}^{\mathrm{asym}} = 4$, $n_{\mathrm{b}} = 0$, $350 < H_{\mathrm{T}} < 400$ GeV

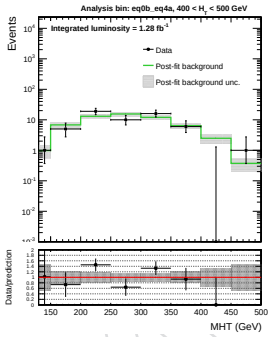

(e) $n_{\mathrm{jet}}^{\mathrm{asym}} = 4$, $n_{\mathrm{b}} = 0$, $400 < H_{\mathrm{T}} < 500$ GeV

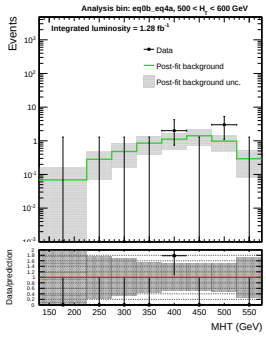

(f) $n_{\mathrm{jet}}^{\mathrm{asym}} = 4$, $n_{\mathrm{b}} = 0$, $500 < H_{\mathrm{T}} < 600$ GeV

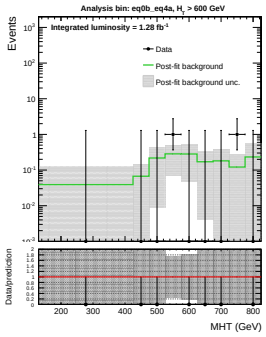

(g) $n_{\mathrm{jet}}^{\mathrm{asym}} = 4$, $n_{\mathrm{b}} = 0$, $H_{\mathrm{T}} > 600$ GeV

DRAFT

Figure 62: Post-fit $\not{H}_{\mathrm{T}}$ templates for the bin $n_{\mathrm{jet}}^{\mathrm{sym}} = 4$, $n_{\mathrm{b}} = 0$

.

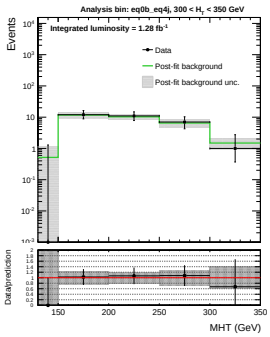

(a) $n_{\mathrm{jet}}^{\mathrm{sym}} = 4$, $n_{\mathrm{b}} = 0$, $300 < H_{\mathrm{T}} < 350$ GeV

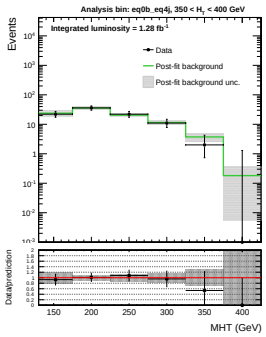

(b) $n_{\mathrm{jet}}^{\mathrm{sym}} = 4$, $n_{\mathrm{b}} = 0$, $350 < H_{\mathrm{T}} < 400$ GeV

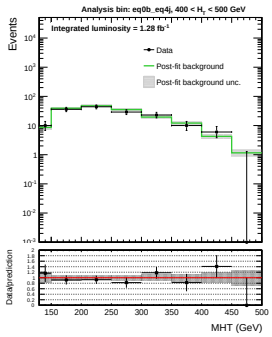

(c) $n_{\mathrm{jet}}^{\mathrm{sym}} = 4$, $n_{\mathrm{b}} = 0$, $400 < H_{\mathrm{T}} < 500$ GeV

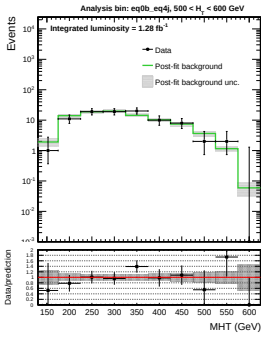

(d) $n_{\mathrm{jet}}^{\mathrm{sym}} = 4$, $n_{\mathrm{b}} = 0$, $500 < H_{\mathrm{T}} < 600$ GeV

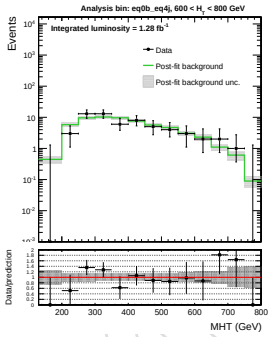

(e) $n_{\mathrm{jet}}^{\mathrm{sym}} = 4$, $n_{\mathrm{b}} = 0$, $600 < H_{\mathrm{T}} < 800$ GeV

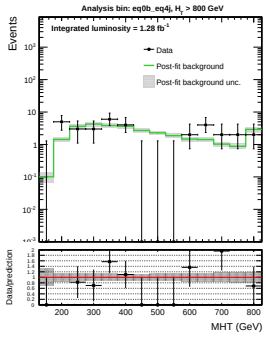

(f) $n_{\mathrm{jet}}^{\mathrm{sym}} = 4$, $n_{\mathrm{b}} = 0$, $H_{\mathrm{T}} > 800$ GeV

DRAFT

Figure 63: Post-fit $\not{H}_{\mathrm{T}}$ templates for the bin $n_{\mathrm{jet}}^{\mathrm{asym}} = 5$, $n_{\mathrm{b}} = 0$

.

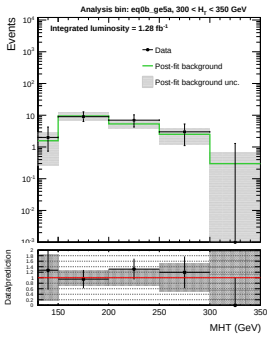

(a) $n_{\mathrm{jet}}^{\mathrm{asym}} = 5$, $n_{\mathrm{b}} = 0$, $300 < H_{\mathrm{T}} < 350$ GeV

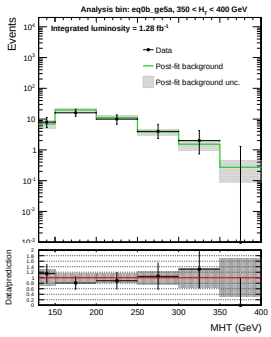

(b) $n_{\mathrm{jet}}^{\mathrm{asym}} = 5$, $n_{\mathrm{b}} = 0$, $350 < H_{\mathrm{T}} < 400$ GeV

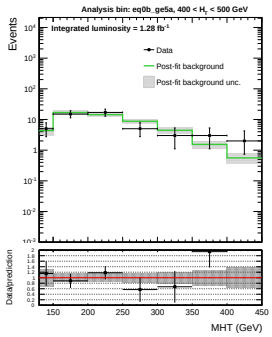

(c) $n_{\mathrm{jet}}^{\mathrm{asym}} = 5$, $n_{\mathrm{b}} = 0$, $400 < H_{\mathrm{T}} < 500$ GeV

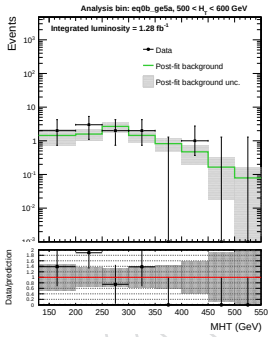

(d) $n_{\mathrm{jet}}^{\mathrm{asym}} = 5$, $n_{\mathrm{b}} = 0$, $500 < H_{\mathrm{T}} < 600$ GeV

DRAFT

Figure 64: Post-fit $\not{H}_{\mathrm{T}}$ templates for the bin $n_{\mathrm{jet}}^{\mathrm{sym}} = 5$, $n_{\mathrm{b}} = 0$

.

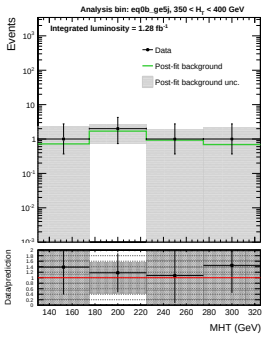

(a) $n_{\mathrm{jet}}^{\mathrm{sym}} = 5$, $n_{\mathrm{b}} = 0$, $350 < H_{\mathrm{T}} < 400$ GeV

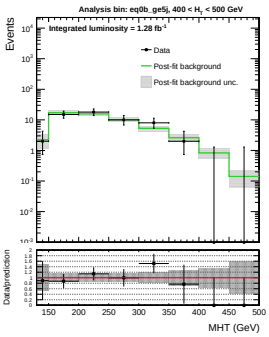

(b) $n_{\mathrm{jet}}^{\mathrm{sym}} = 5$, $n_{\mathrm{b}} = 0$, $400 < H_{\mathrm{T}} < 500$ GeV

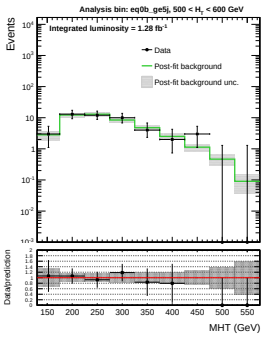

(c) $n_{\mathrm{jet}}^{\mathrm{sym}} = 5$, $n_{\mathrm{b}} = 0$, $500 < H_{\mathrm{T}} < 600$ GeV

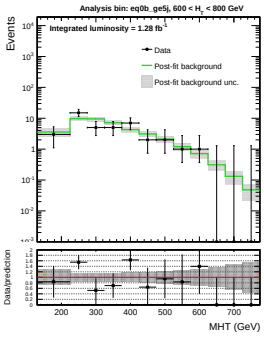

(d) $n_{\mathrm{jet}}^{\mathrm{sym}} = 5$, $n_{\mathrm{b}} = 0$, $600 < H_{\mathrm{T}} < 800$ GeV

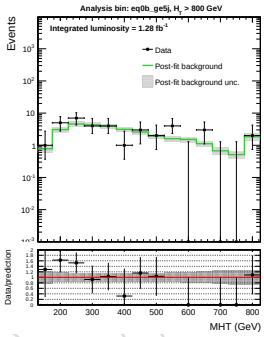

(e) $n_{\mathrm{jet}}^{\mathrm{sym}} = 5$, $n_{\mathrm{b}} = 0$, $H_{\mathrm{T}} > 800$ GeV

DRAFT

Figure 65: Post-fit $\not{H}_{\mathrm{T}}$ templates for the bin $n_{\mathrm{jet}}^{\mathrm{asym}} = 2$, $n_{\mathrm{b}} = 1$

.

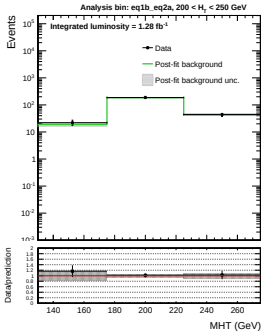

(a) $n_{\mathrm{jet}}^{\mathrm{asym}} = 2$, $n_{\mathrm{b}} = 1$, $200 < H_{\mathrm{T}} < 250$ GeV

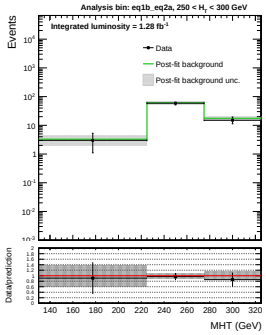

(b) $n_{\mathrm{jet}}^{\mathrm{asym}} = 2$, $n_{\mathrm{b}} = 1$, $250 < H_{\mathrm{T}} < 300$ GeV

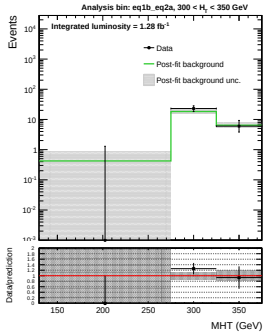

(c) $n_{\mathrm{jet}}^{\mathrm{asym}} = 2$, $n_{\mathrm{b}} = 1$, $300 < H_{\mathrm{T}} < 350$ GeV

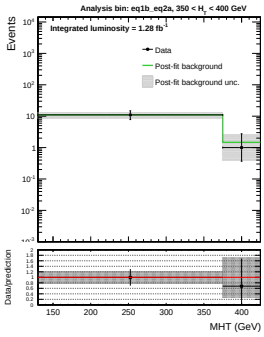

(d) $n_{\mathrm{jet}}^{\mathrm{asym}} = 2$, $n_{\mathrm{b}} = 1$, $350 < H_{\mathrm{T}} < 400$ GeV

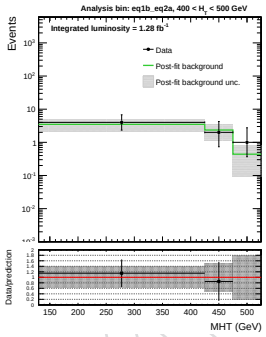

(e) $n_{\mathrm{jet}}^{\mathrm{asym}} = 2$, $n_{\mathrm{b}} = 1$, $400 < H_{\mathrm{T}} < 500$ GeV

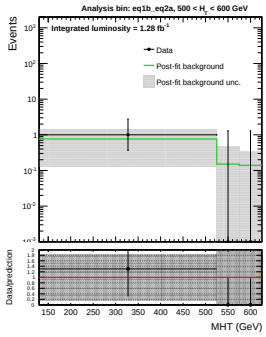

(f) $n_{\mathrm{jet}}^{\mathrm{asym}} = 2$, $n_{\mathrm{b}} = 1$, $500 < H_{\mathrm{T}} < 600$ GeV

DRAFT

Figure 66: Post-fit $\not{H}_{\mathrm{T}}$ templates for the bin $n_{\mathrm{jet}}^{\mathrm{sym}} = 2$, $n_{\mathrm{b}} = 1$

.

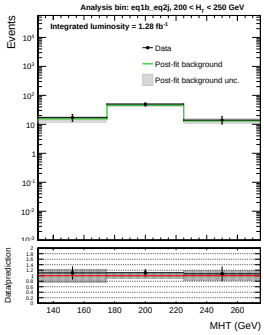

(a) $n_{\mathrm{jet}}^{\mathrm{sym}} = 2$, $n_{\mathrm{b}} = 1$, $200 < H_{\mathrm{T}} < 250$ GeV

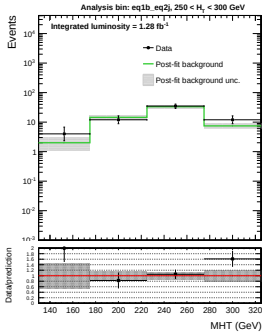

(b) $n_{\mathrm{jet}}^{\mathrm{sym}} = 2$, $n_{\mathrm{b}} = 1$, $250 < H_{\mathrm{T}} < 300$ GeV

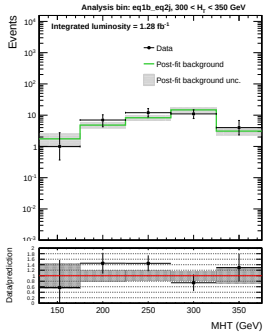

(c) $n_{\mathrm{jet}}^{\mathrm{sym}} = 2$, $n_{\mathrm{b}} = 1$, $300 < H_{\mathrm{T}} < 350$ GeV

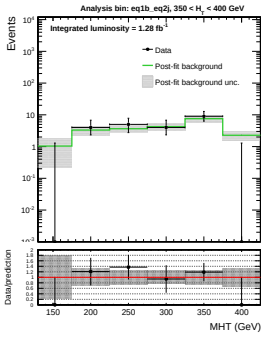

(d) $n_{\mathrm{jet}}^{\mathrm{sym}} = 2$, $n_{\mathrm{b}} = 1$, $350 < H_{\mathrm{T}} < 400$ GeV

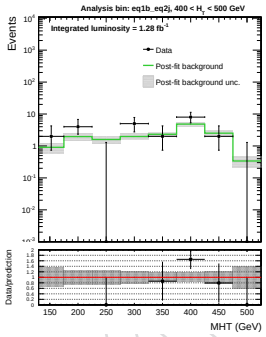

(e) $n_{\mathrm{jet}}^{\mathrm{sym}} = 2$, $n_{\mathrm{b}} = 1$, $400 < H_{\mathrm{T}} < 500$ GeV

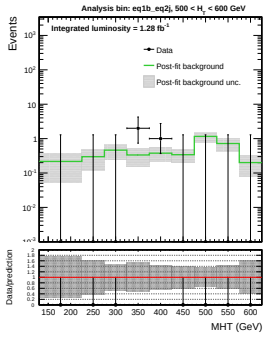

(f) $n_{\mathrm{jet}}^{\mathrm{sym}} = 2$, $n_{\mathrm{b}} = 1$, $500 < H_{\mathrm{T}} < 600$ GeV

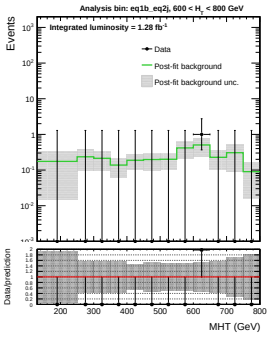

(g) $n_{\mathrm{jet}}^{\mathrm{sym}} = 2$, $n_{\mathrm{b}} = 1$, $600 < H_{\mathrm{T}} < 800$ GeV

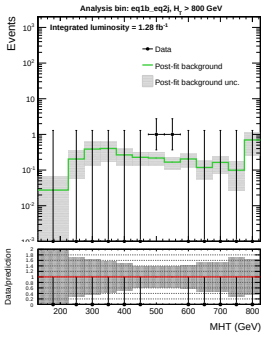

(h) $n_{\mathrm{jet}}^{\mathrm{sym}} = 2$, $n_{\mathrm{b}} = 1$, $H_{\mathrm{T}} > 800$ GeV

Figure 67: Post-fit $\not{H}_{\mathrm{T}}$ templates for the bin $n_{\mathrm{jet}}^{\mathrm{asym}} = 3$, $n_{\mathrm{b}} = 1$

.

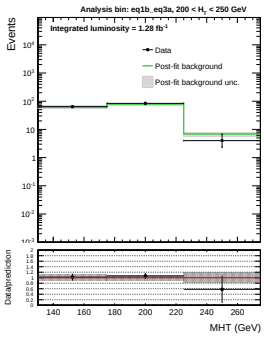

(a) $n_{\mathrm{jet}}^{\mathrm{asym}} = 3$, $n_{\mathrm{b}} = 1$, $200 < H_{\mathrm{T}} < 250$ GeV

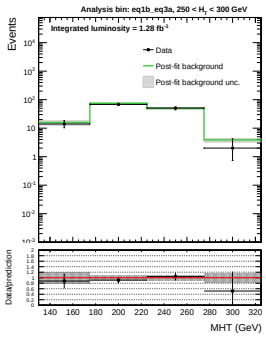

(b) $n_{\mathrm{jet}}^{\mathrm{asym}} = 3$, $n_{\mathrm{b}} = 1$, $250 < H_{\mathrm{T}} < 300$ GeV

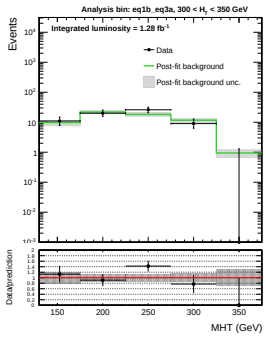

(c) $n_{\mathrm{jet}}^{\mathrm{asym}} = 3$, $n_{\mathrm{b}} = 1$, $300 < H_{\mathrm{T}} < 350$ GeV

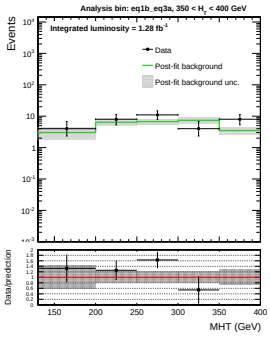

(d) $n_{\mathrm{jet}}^{\mathrm{asym}} = 3$, $n_{\mathrm{b}} = 1$, $350 < H_{\mathrm{T}} < 400$ GeV

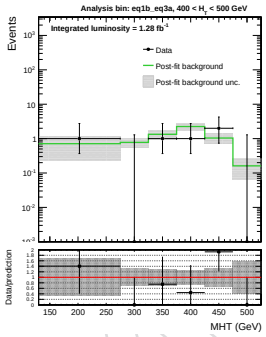

(e) $n_{\mathrm{jet}}^{\mathrm{asym}} = 3$, $n_{\mathrm{b}} = 1$, $400 < H_{\mathrm{T}} < 500$ GeV

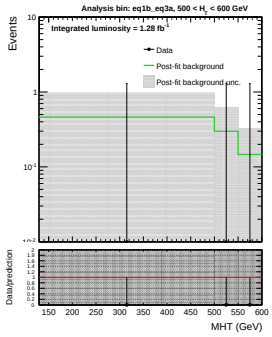

(f) $n_{\mathrm{jet}}^{\mathrm{asym}} = 3$, $n_{\mathrm{b}} = 1$, $500 < H_{\mathrm{T}} < 600$ GeV

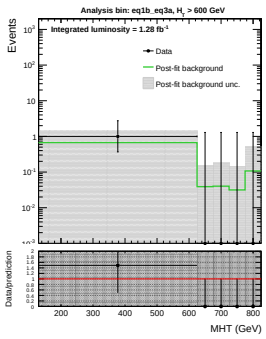

(g) $n_{\mathrm{jet}}^{\mathrm{asym}} = 3$, $n_{\mathrm{b}} = 1$, $H_{\mathrm{T}} > 600$ GeV

DRAFT

Figure 68: Post-fit $\not{H}_T$ templates for the bin $n_{\text{jet}}^{\text{sym}} = 3$, $n_b = 1$

.

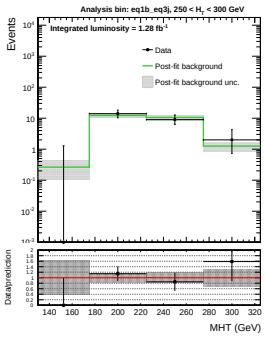

(a) $n_{\text{jet}}^{\text{sym}} = 3$, $n_b = 1$, $250 < H_T < 300$ GeV

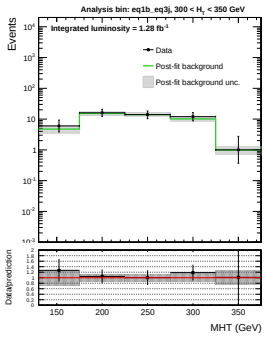

(b) $n_{\text{jet}}^{\text{sym}} = 3$, $n_b = 1$, $300 < H_T < 350$ GeV

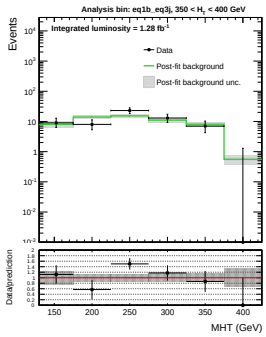

(c) $n_{\text{jet}}^{\text{sym}} = 3$, $n_b = 1$, $350 < H_T < 400$ GeV

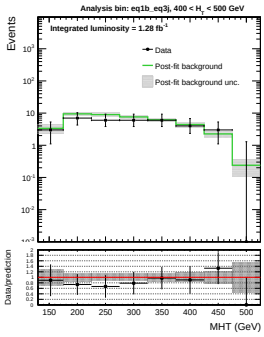

(d) $n_{\text{jet}}^{\text{sym}} = 3$, $n_b = 1$, $400 < H_T < 500$ GeV

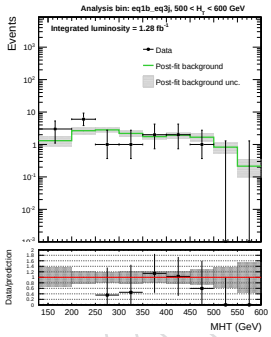

(e) $n_{\text{jet}}^{\text{sym}} = 3$, $n_b = 1$, $500 < H_T < 600$ GeV

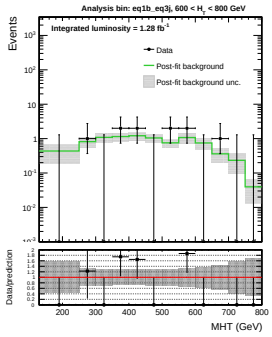

(f) $n_{\text{jet}}^{\text{sym}} = 3$, $n_b = 1$, $600 < H_T < 800$ GeV

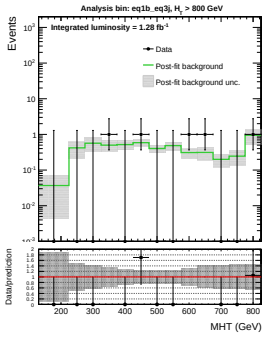

(g) $n_{\text{jet}}^{\text{sym}} = 3$, $n_b = 1$, $H_T > 800$ GeV

DRAFT

Figure 69: Post-fit $\not{H}_{\mathrm{T}}$ templates for the bin $n_{\mathrm{jet}}^{\mathrm{asym}} = 4$, $n_{\mathrm{b}} = 1$

.

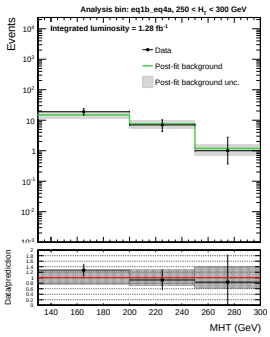

(a) $n_{\mathrm{jet}}^{\mathrm{asym}} = 4$, $n_{\mathrm{b}} = 1$, $250 < H_{\mathrm{T}} < 300$ GeV

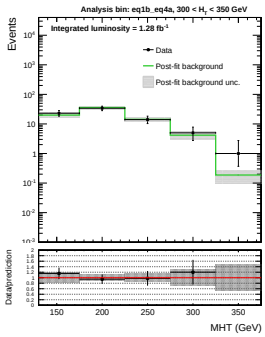

(b) $n_{\mathrm{jet}}^{\mathrm{asym}} = 4$, $n_{\mathrm{b}} = 1$, $300 < H_{\mathrm{T}} < 350$ GeV

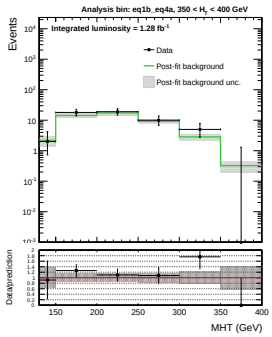

(c) $n_{\mathrm{jet}}^{\mathrm{asym}} = 4$, $n_{\mathrm{b}} = 1$, $350 < H_{\mathrm{T}} < 400$ GeV

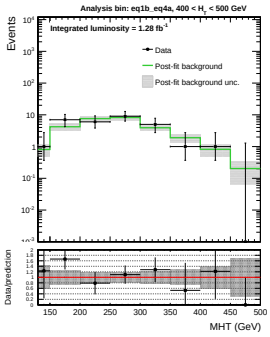

(d) $n_{\mathrm{jet}}^{\mathrm{asym}} = 4$, $n_{\mathrm{b}} = 1$, $400 < H_{\mathrm{T}} < 500$ GeV

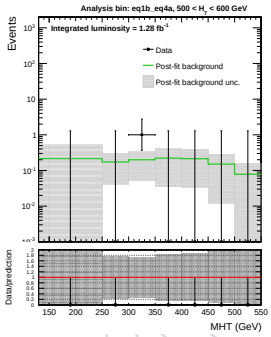

(e) $n_{\mathrm{jet}}^{\mathrm{asym}} = 4$, $n_{\mathrm{b}} = 1$, $500 < H_{\mathrm{T}} < 600$ GeV

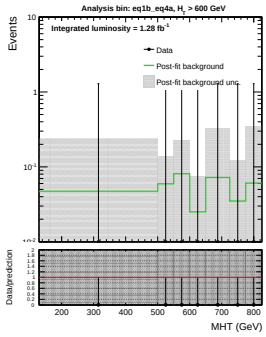

(f) $n_{\mathrm{jet}}^{\mathrm{asym}} = 4$, $n_{\mathrm{b}} = 1$, $H_{\mathrm{T}} > 600$ GeV

DRAFT

Figure 70: Post-fit $\not{H}_{\mathrm{T}}$ templates for the bin $n_{\mathrm{jet}}^{\mathrm{sym}} = 4$, $n_{\mathrm{b}} = 1$

.

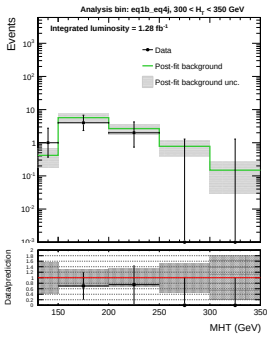

(a) $n_{\mathrm{jet}}^{\mathrm{sym}} = 4$, $n_{\mathrm{b}} = 1$, $300 < H_{\mathrm{T}} < 350$ GeV

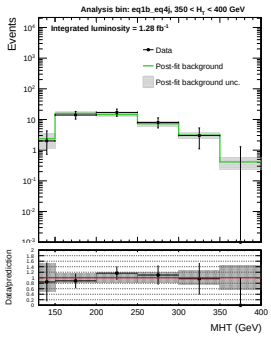

(b) $n_{\mathrm{jet}}^{\mathrm{sym}} = 4$, $n_{\mathrm{b}} = 1$, $350 < H_{\mathrm{T}} < 400$ GeV

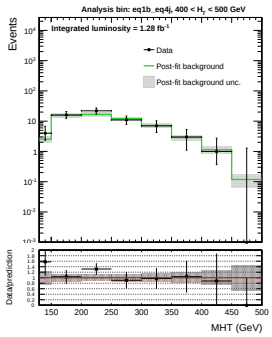

(c) $n_{\mathrm{jet}}^{\mathrm{sym}} = 4$, $n_{\mathrm{b}} = 1$, $400 < H_{\mathrm{T}} < 500$ GeV

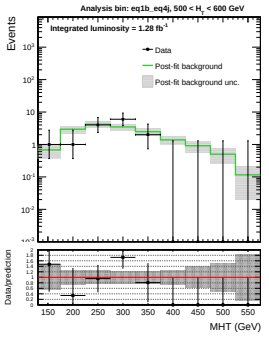

(d) $n_{\mathrm{jet}}^{\mathrm{sym}} = 4$, $n_{\mathrm{b}} = 1$, $500 < H_{\mathrm{T}} < 600$ GeV

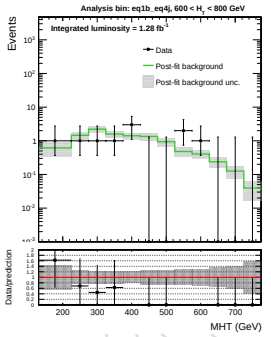

(e) $n_{\mathrm{jet}}^{\mathrm{sym}} = 4$, $n_{\mathrm{b}} = 1$, $600 < H_{\mathrm{T}} < 800$ GeV

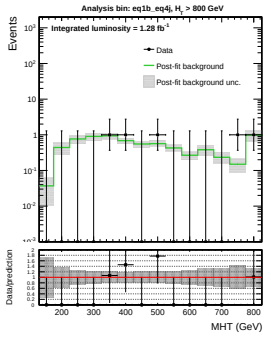

(f) $n_{\mathrm{jet}}^{\mathrm{sym}} = 4$, $n_{\mathrm{b}} = 1$, $H_{\mathrm{T}} > 800$ GeV

DRAFT

Figure 71: Post-fit $\not{H}_{\mathrm{T}}$ templates for the bin $n_{\mathrm{jet}}^{\mathrm{asym}} = 5$, $n_{\mathrm{b}} = 1$

.

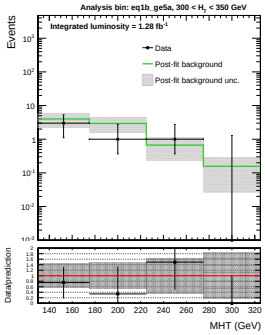

(a) $n_{\mathrm{jet}}^{\mathrm{asym}} = 5$, $n_{\mathrm{b}} = 1$, $300 < H_{\mathrm{T}} < 350$ GeV

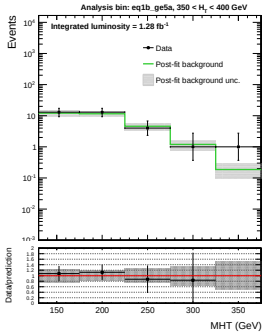

(b) $n_{\mathrm{jet}}^{\mathrm{asym}} = 5$, $n_{\mathrm{b}} = 1$, $350 < H_{\mathrm{T}} < 400$ GeV

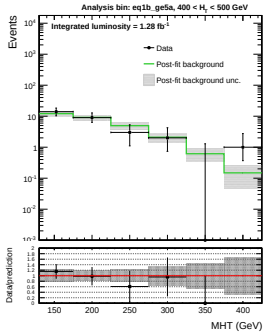

(c) $n_{\mathrm{jet}}^{\mathrm{asym}} = 5$, $n_{\mathrm{b}} = 1$, $400 < H_{\mathrm{T}} < 500$ GeV

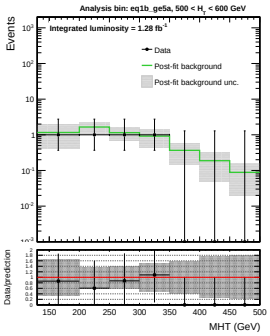

(d) $n_{\mathrm{jet}}^{\mathrm{asym}} = 5$, $n_{\mathrm{b}} = 1$, $500 < H_{\mathrm{T}} < 600$ GeV

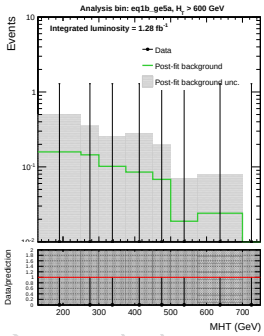

(e) $n_{\mathrm{jet}}^{\mathrm{asym}} = 5$, $n_{\mathrm{b}} = 1$, $H_{\mathrm{T}} > 600$ GeV

DRAFT

Figure 72: Post-fit $\not{H}_{\mathrm{T}}$ templates for the bin $n_{\mathrm{jet}}^{\mathrm{sym}} = 5$, $n_{\mathrm{b}} = 1$

.

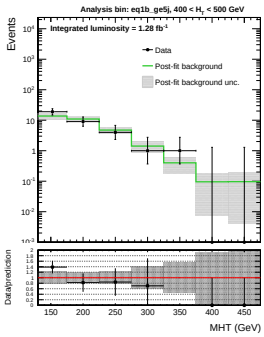

(a) $n_{\mathrm{jet}}^{\mathrm{sym}} = 5$, $n_{\mathrm{b}} = 1$, $400 < H_{\mathrm{T}} < 500$ GeV

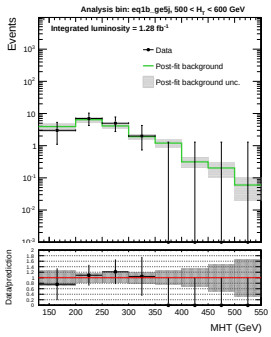

(b) $n_{\mathrm{jet}}^{\mathrm{sym}} = 5$, $n_{\mathrm{b}} = 1$, $500 < H_{\mathrm{T}} < 600$ GeV

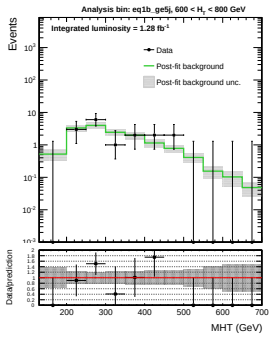

(c) $n_{\mathrm{jet}}^{\mathrm{sym}} = 5$, $n_{\mathrm{b}} = 1$, $600 < H_{\mathrm{T}} < 800$ GeV

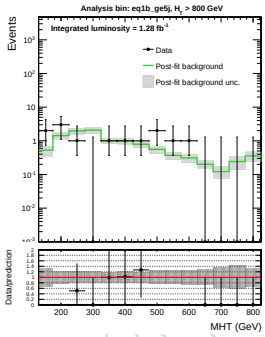

(d) $n_{\mathrm{jet}}^{\mathrm{sym}} = 5$, $n_{\mathrm{b}} = 1$, $H_{\mathrm{T}} > 800$ GeV

DRAFT

Figure 73: Post-fit $\not{H}_{\mathrm{T}}$ templates for the bin $n_{\mathrm{jet}}^{\mathrm{asym}} = 2$, $n_{\mathrm{b}} = 2$

.

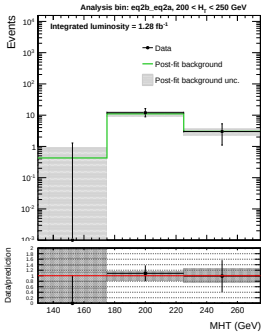

(a) $n_{\mathrm{jet}}^{\mathrm{asym}} = 2$, $n_{\mathrm{b}} = 2$, $200 < H_{\mathrm{T}} < 250$ GeV

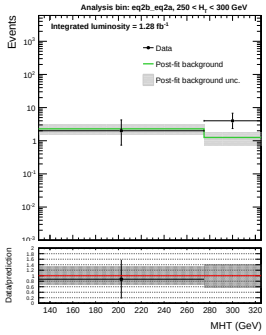

(b) $n_{\mathrm{jet}}^{\mathrm{asym}} = 2$, $n_{\mathrm{b}} = 2$, $250 < H_{\mathrm{T}} < 300$ GeV

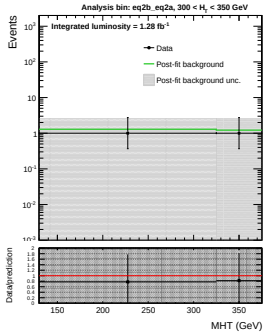

(c) $n_{\mathrm{jet}}^{\mathrm{asym}} = 2$, $n_{\mathrm{b}} = 2$, $300 < H_{\mathrm{T}} < 350$ GeV

DRAFT

Figure 74: Post-fit $\not{H}_T$ templates for the bin $n_{jet}^{asym} = 3$, $n_b = 2$

.

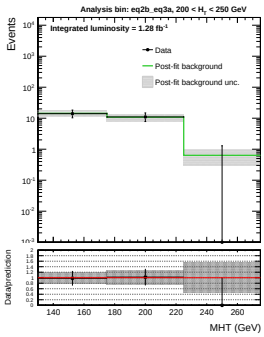

(a) $n_{jet}^{asym} = 3$, $n_b = 2$, $200 < H_T < 250$ GeV

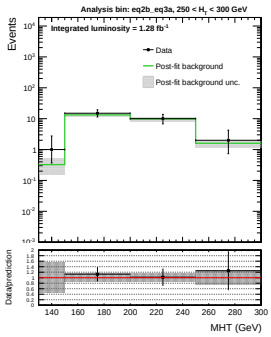

(b) $n_{jet}^{asym} = 3$, $n_b = 2$, $250 < H_T < 300$ GeV

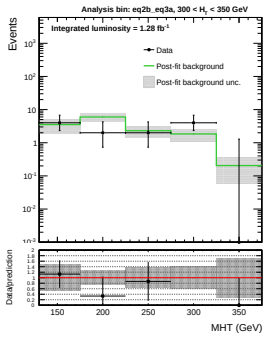

(c) $n_{jet}^{asym} = 3$, $n_b = 2$, $300 < H_T < 350$ GeV

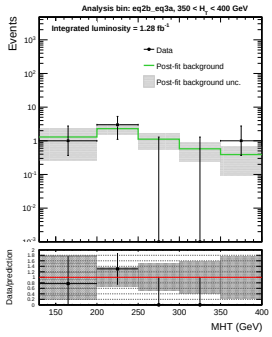

(d) $n_{jet}^{asym} = 3$, $n_b = 2$, $350 < H_T < 400$ GeV

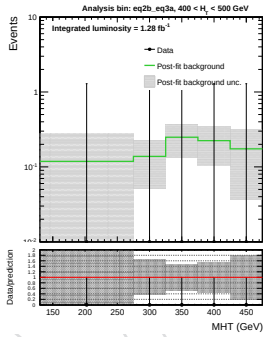

(e) $n_{jet}^{asym} = 3$, $n_b = 2$, $400 < H_T < 500$ GeV

DRAFT

Figure 75: Post-fit $\not{H}_{\mathrm{T}}$ templates for the bin $n_{\mathrm{jet}}^{\mathrm{sym}} = 3$, $n_{\mathrm{b}} = 2$

.

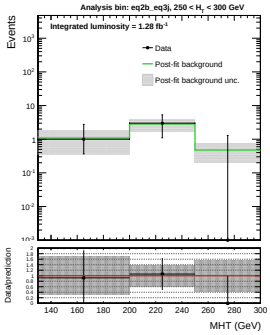

(a) $n_{\mathrm{jet}}^{\mathrm{sym}} = 3$, $n_{\mathrm{b}} = 2$, $250 < H_{\mathrm{T}} < 300$ GeV

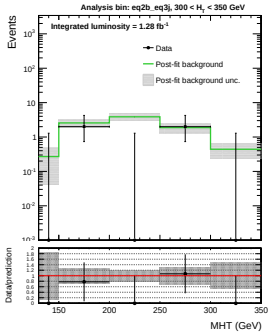

(b) $n_{\mathrm{jet}}^{\mathrm{sym}} = 3$, $n_{\mathrm{b}} = 2$, $300 < H_{\mathrm{T}} < 350$ GeV

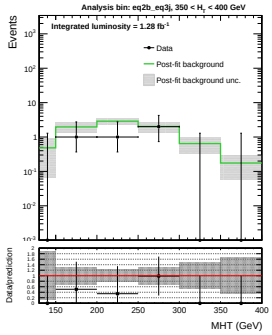

(c) $n_{\mathrm{jet}}^{\mathrm{sym}} = 3$, $n_{\mathrm{b}} = 2$, $350 < H_{\mathrm{T}} < 400$ GeV

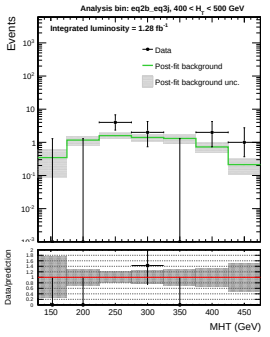

(d) $n_{\mathrm{jet}}^{\mathrm{sym}} = 3$, $n_{\mathrm{b}} = 2$, $400 < H_{\mathrm{T}} < 500$ GeV

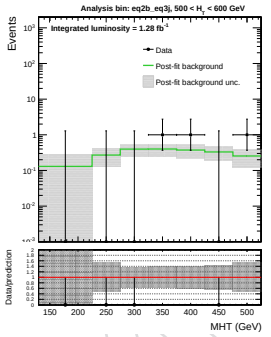

(e) $n_{\mathrm{jet}}^{\mathrm{sym}} = 3$, $n_{\mathrm{b}} = 2$, $500 < H_{\mathrm{T}} < 600$ GeV

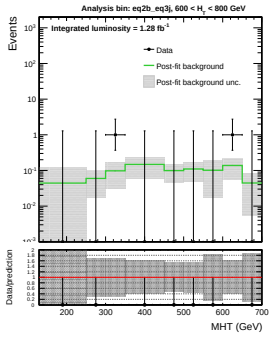

(f) $n_{\mathrm{jet}}^{\mathrm{sym}} = 3$, $n_{\mathrm{b}} = 2$, $600 < H_{\mathrm{T}} < 800$ GeV

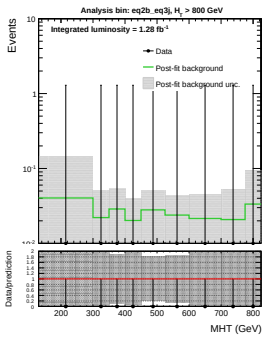

(g) $n_{\mathrm{jet}}^{\mathrm{sym}} = 3$, $n_{\mathrm{b}} = 2$, $H_{\mathrm{T}} > 800$ GeV

DRAFT

Figure 76: Post-fit $\not{H}_{\mathrm{T}}$ templates for the bin $n_{\mathrm{jet}}^{\mathrm{asym}} = 4$, $n_{\mathrm{b}} = 2$

.

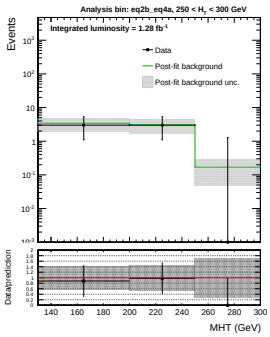

(a) $n_{\mathrm{jet}}^{\mathrm{asym}} = 4$, $n_{\mathrm{b}} = 2$, $250 < H_{\mathrm{T}} < 300$ GeV

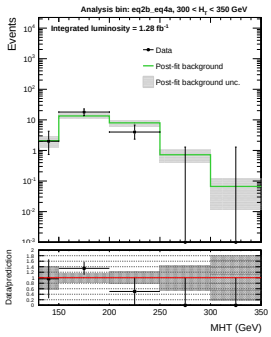

(b) $n_{\mathrm{jet}}^{\mathrm{asym}} = 4$, $n_{\mathrm{b}} = 2$, $300 < H_{\mathrm{T}} < 350$ GeV

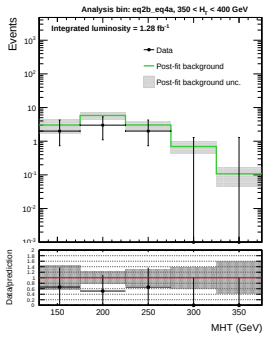

(c) $n_{\mathrm{jet}}^{\mathrm{asym}} = 4$, $n_{\mathrm{b}} = 2$, $350 < H_{\mathrm{T}} < 400$ GeV

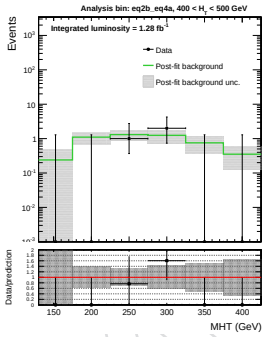

(d) $n_{\mathrm{jet}}^{\mathrm{asym}} = 4$, $n_{\mathrm{b}} = 2$, $400 < H_{\mathrm{T}} < 500$ GeV

DRAFT

Figure 77: Post-fit $\not{H}_{\mathrm{T}}$ templates for the bin $n_{\mathrm{jet}}^{\mathrm{sym}} = 4$, $n_{\mathrm{b}} = 2$

.

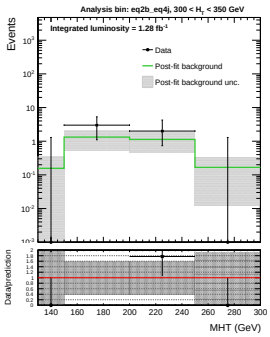

(a) $n_{\mathrm{jet}}^{\mathrm{sym}} = 4$, $n_{\mathrm{b}} = 2$, $300 < H_{\mathrm{T}} < 350$ GeV

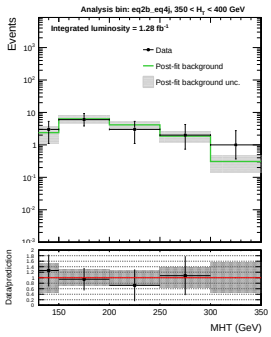

(b) $n_{\mathrm{jet}}^{\mathrm{sym}} = 4$, $n_{\mathrm{b}} = 2$, $350 < H_{\mathrm{T}} < 400$ GeV

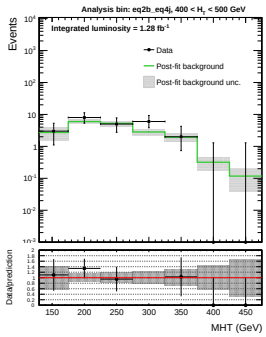

(c) $n_{\mathrm{jet}}^{\mathrm{sym}} = 4$, $n_{\mathrm{b}} = 2$, $400 < H_{\mathrm{T}} < 500$ GeV

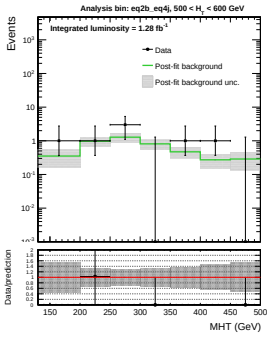

(d) $n_{\mathrm{jet}}^{\mathrm{sym}} = 4$, $n_{\mathrm{b}} = 2$, $500 < H_{\mathrm{T}} < 600$ GeV

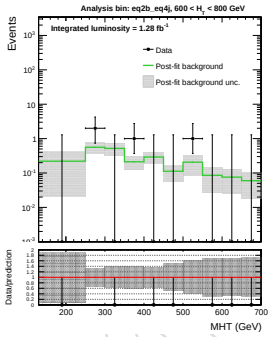

(e) $n_{\mathrm{jet}}^{\mathrm{sym}} = 4$, $n_{\mathrm{b}} = 2$, $600 < H_{\mathrm{T}} < 800$ GeV

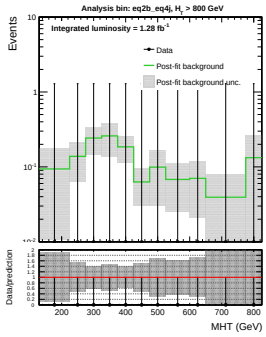

(f) $n_{\mathrm{jet}}^{\mathrm{sym}} = 4$, $n_{\mathrm{b}} = 2$, $H_{\mathrm{T}} > 800$ GeV

DRAFT

Figure 78: Post-fit $\not{H}_{\mathrm{T}}$ templates for the bin $n_{\mathrm{jet}}^{\mathrm{asym}} = 5$, $n_{\mathrm{b}} = 2$

.

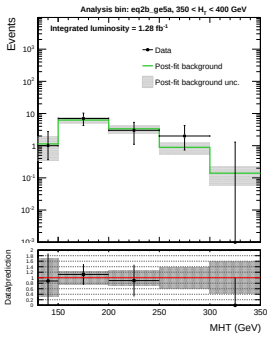

(a) $n_{\mathrm{jet}}^{\mathrm{asym}} = 5$, $n_{\mathrm{b}} = 2$, $350 < H_{\mathrm{T}} < 400$ GeV

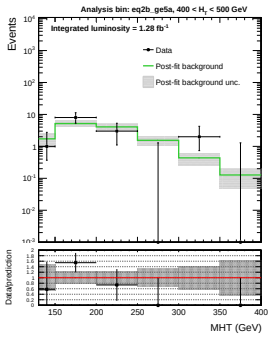

(b) $n_{\mathrm{jet}}^{\mathrm{asym}} = 5$, $n_{\mathrm{b}} = 2$, $400 < H_{\mathrm{T}} < 500$ GeV

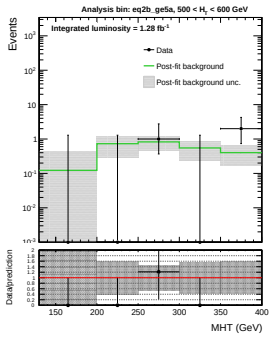

(c) $n_{\mathrm{jet}}^{\mathrm{asym}} = 5$, $n_{\mathrm{b}} = 2$, $500 < H_{\mathrm{T}} < 600$ GeV

DRAFT

Figure 79: Post-fit $\not{H}_{\mathrm{T}}$ templates for the bin $n_{\mathrm{jet}}^{\mathrm{sym}} = 5$, $n_{\mathrm{b}} = 2$

.

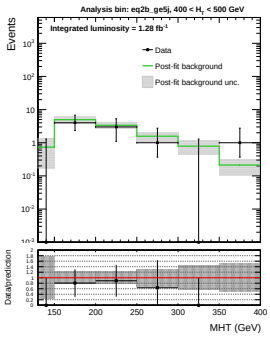

(a) $n_{\mathrm{jet}}^{\mathrm{sym}} = 5$, $n_{\mathrm{b}} = 2$, $400 < H_{\mathrm{T}} < 500$ GeV

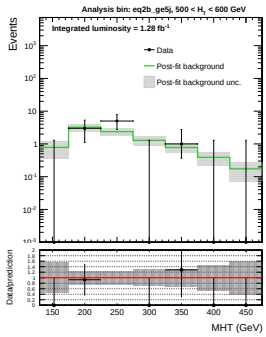

(b) $n_{\mathrm{jet}}^{\mathrm{sym}} = 5$, $n_{\mathrm{b}} = 2$, $500 < H_{\mathrm{T}} < 600$ GeV

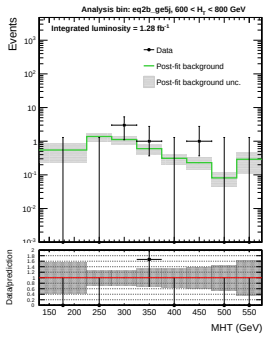

(c) $n_{\mathrm{jet}}^{\mathrm{sym}} = 5$, $n_{\mathrm{b}} = 2$, $600 < H_{\mathrm{T}} < 800$ GeV

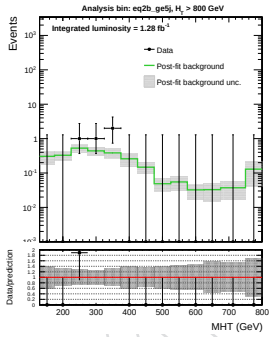

(d) $n_{\mathrm{jet}}^{\mathrm{sym}} = 5$, $n_{\mathrm{b}} = 2$, $H_{\mathrm{T}} > 800$ GeV

DRAFT

Figure 80: Post-fit $\not{H}_{\mathrm{T}}$ templates for the bin $n_{\mathrm{jet}}^{\mathrm{sym}} = 5$, $n_{\mathrm{b}} \geq 3$

.

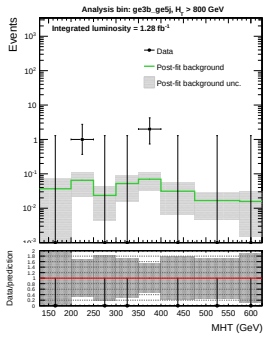

(a) $n_{\mathrm{jet}}^{\mathrm{sym}} = 5$, $n_{\mathrm{b}} = 3$, $H_{\mathrm{T}} >$ 800 GeV

DRAFT

Table 49: Predictions and Data in the signal region for 1.26fb^{-1} for symmetric categories. The letter "a" in jet e.g. "2a" indicates the asymmetric jet bins. All entries are non-zero but are truncated to one decimal place.

H_T (GeV)	(n_{jet}, n_b)	200-250	250-300	300-350	350-400	400-500	500-600	600-800	800-∞
Data	(2, 0)	552	592	395	247	189	55	39	33
SM	(2, 0)	$546.7^{+95.1}_{-94.9}$	$594.8^{+96.6}_{-96.4}$	$407.0^{+71.6}_{-71.5}$	$208.4^{+51.4}_{-51.3}$	$193.2^{+34.9}_{-34.9}$	$65.1^{+17.8}_{-17.8}$	$27.7^{+8.4}_{-8.4}$	$28.1^{+8.7}_{-8.7}$
Ttw	(2, 0)	$262.7^{+50.7}_{-50.4}$	$266.2^{+60.3}_{-60.2}$	$171.7^{+36.4}_{-36.4}$	$80.4^{+21.1}_{-21.0}$	$68.6^{+12.6}_{-12.6}$	$20.5^{+8.1}_{-8.0}$	$8.2^{+2.8}_{-2.8}$	$8.2^{+3.0}_{-3.0}$
Zinv	(2, 0)	$284.1^{+74.4}_{-74.2}$	$328.6^{+67.5}_{-67.4}$	$235.3^{+49.4}_{-49.3}$	$127.9^{+43.0}_{-43.0}$	$124.7^{+24.9}_{-24.9}$	$44.6^{+13.1}_{-13.0}$	$19.4^{+6.8}_{-6.8}$	$19.9^{+7.1}_{-7.1}$
Data	(2, 1)	81	63	35	22	23	3	1	2
SM	(2, 1)	$47.9^{+9.5}_{-9.1}$	$41.1^{+8.2}_{-7.9}$	$29.9^{+6.3}_{-6.0}$	$18.7^{+5.1}_{-5.0}$	$13.3^{+2.8}_{-2.7}$	$5.5^{+1.7}_{-1.7}$	$2.7^{+1.0}_{-1.0}$	$3.5^{+1.3}_{-1.2}$
Ttw	(2, 1)	$31.8^{+7.8}_{-7.4}$	$24.7^{+6.7}_{-6.4}$	$15.2^{+4.1}_{-3.9}$	$7.9^{+2.5}_{-2.4}$	$5.5^{+1.4}_{-1.3}$	$1.9^{+0.9}_{-0.9}$	$0.6^{+0.3}_{-0.3}$	$1.1^{+0.5}_{-0.5}$
Zinv	(2, 1)	$16.1^{+4.9}_{-4.7}$	$16.5^{+4.2}_{-4.0}$	$14.6^{+3.9}_{-3.7}$	$10.8^{+4.1}_{-4.0}$	$7.8^{+2.0}_{-1.9}$	$3.6^{+1.3}_{-1.2}$	$2.1^{+0.9}_{-0.8}$	$2.4^{+1.0}_{-1.0}$
Data	(2, 2)	2	3	2	–	2	0	0	0
SM	(2, 2)	$1.0^{+1.2}_{-0.5}$	$0.7^{+0.9}_{-0.3}$	$0.7^{+0.8}_{-0.3}$	–	$0.8^{+0.4}_{-0.3}$	$0.5^{+0.4}_{-0.2}$	$0.2^{+0.2}_{-0.1}$	$0.1^{+0.1}_{-0.0}$
Ttw	(2, 2)	$0.5^{+0.9}_{-0.3}$	$0.3^{+0.5}_{-0.2}$	$0.3^{+0.6}_{-0.2}$	–	$0.3^{+0.2}_{-0.2}$	$0.3^{+0.3}_{-0.2}$	$0.0^{+0.0}_{-0.0}$	$0.0^{+0.0}_{-0.0}$
Zinv	(2, 2)	$0.5^{+0.8}_{-0.3}$	$0.4^{+0.7}_{-0.3}$	$0.3^{+0.6}_{-0.2}$	–	$0.5^{+0.3}_{-0.2}$	$0.2^{+0.2}_{-0.1}$	$0.2^{+0.2}_{-0.1}$	$0.1^{+0.1}_{-0.0}$
Data	(3, 0)	1	111	283	282	353	120	51	51
SM	(3, 0)	$0.7^{+0.9}_{-0.4}$	$86.3^{+14.0}_{-13.8}$	$286.5^{+53.9}_{-53.8}$	$234.8^{+44.0}_{-43.9}$	$310.2^{+63.5}_{-63.5}$	$108.7^{+25.7}_{-25.7}$	$53.9^{+17.3}_{-17.3}$	$41.9^{+11.1}_{-11.1}$
Ttw	(3, 0)	$0.4^{+0.7}_{-0.3}$	$41.8^{+9.3}_{-9.2}$	$139.0^{+29.1}_{-29.0}$	$112.1^{+22.7}_{-22.5}$	$134.7^{+33.0}_{-32.9}$	$41.0^{+10.5}_{-10.5}$	$16.8^{+4.4}_{-4.4}$	$12.4^{+4.0}_{-4.0}$
Zinv	(3, 0)	$0.3^{+0.5}_{-0.2}$	$44.5^{+9.3}_{-9.1}$	$147.5^{+37.0}_{-36.8}$	$122.7^{+31.0}_{-30.9}$	$175.6^{+41.7}_{-41.7}$	$67.8^{+17.5}_{-17.4}$	$37.1^{+14.6}_{-14.6}$	$29.5^{+8.4}_{-8.4}$
Data	(3, 1)	2	25	49	60	35	16	10	5
SM	(3, 1)	$0.2^{+0.4}_{-0.2}$	$18.3^{+3.9}_{-3.7}$	$42.5^{+8.4}_{-8.3}$	$46.8^{+9.0}_{-8.9}$	$47.0^{+10.1}_{-10.1}$	$13.3^{+3.4}_{-3.3}$	$8.0^{+2.6}_{-2.5}$	$5.6^{+1.6}_{-1.6}$
Ttw	(3, 1)	$0.2^{+0.4}_{-0.2}$	$14.3^{+3.6}_{-3.4}$	$31.3^{+7.1}_{-7.0}$	$33.6^{+7.3}_{-7.2}$	$28.5^{+7.3}_{-7.3}$	$6.7^{+1.9}_{-1.9}$	$3.2^{+0.9}_{-0.9}$	$1.8^{+0.7}_{-0.6}$
Zinv	(3, 1)	$0.0^{+0.1}_{-0.0}$	$4.0^{+1.0}_{-1.0}$	$11.1^{+3.0}_{-2.9}$	$13.2^{+3.5}_{-3.5}$	$18.4^{+4.6}_{-4.6}$	$6.6^{+1.9}_{-1.8}$	$4.9^{+2.0}_{-2.0}$	$3.8^{+1.3}_{-1.2}$
Data	(3, 2)	–	4	4	4	9	3	2	0
SM	(3, 2)	–	$3.5^{+1.1}_{-1.0}$	$11.4^{+2.8}_{-2.6}$	$8.6^{+2.1}_{-2.0}$	$5.9^{+1.6}_{-1.5}$	$1.8^{+0.6}_{-0.5}$	$0.7^{+0.3}_{-0.3}$	$0.3^{+0.1}_{-0.1}$
Ttw	(3, 2)	–	$2.9^{+1.1}_{-0.9}$	$9.6^{+2.6}_{-2.4}$	$7.3^{+2.0}_{-1.9}$	$4.6^{+1.4}_{-1.3}$	$1.1^{+0.4}_{-0.4}$	$0.3^{+0.1}_{-0.1}$	$0.1^{+0.1}_{-0.0}$
Zinv	(3, 2)	–	$0.7^{+0.3}_{-0.2}$	$1.9^{+0.6}_{-0.6}$	$1.3^{+0.4}_{-0.4}$	$1.3^{+0.4}_{-0.4}$	$0.7^{+0.3}_{-0.2}$	$0.4^{+0.2}_{-0.2}$	$0.2^{+0.1}_{-0.1}$
Data	(3, ≥ 3)	–	–	–	0	1	0	–	–
SM	(3, ≥ 3)	–	–	–	$0.9^{+0.9}_{-0.5}$	$0.2^{+0.2}_{-0.1}$	$0.0^{+0.1}_{-0.0}$	–	–
Ttw	(3, ≥ 3)	–	–	–	$0.8^{+0.8}_{-0.5}$	$0.1^{+0.2}_{-0.1}$	$0.0^{+0.1}_{-0.0}$	–	–
Zinv	(3, ≥ 3)	–	–	–	$0.1^{+0.2}_{-0.1}$	$0.0^{+0.0}_{-0.0}$	$0.0^{+0.0}_{-0.0}$	–	–
Data	(4, 0)	–	–	31	93	158	92	60	33
SM	(4, 0)	–	–	$31.5^{+11.0}_{-10.7}$	$87.0^{+22.4}_{-22.1}$	$185.1^{+35.5}_{-35.4}$	$97.9^{+28.3}_{-28.3}$	$62.5^{+15.8}_{-15.8}$	$30.5^{+7.9}_{-7.9}$
Ttw	(4, 0)	–	–	$17.9^{+8.4}_{-8.1}$	$46.9^{+14.6}_{-14.4}$	$94.4^{+19.7}_{-19.6}$	$41.2^{+12.8}_{-12.8}$	$23.3^{+7.2}_{-7.2}$	$9.8^{+2.8}_{-2.7}$
Zinv	(4, 0)	–	–	$13.6^{+6.4}_{-6.2}$	$40.0^{+14.9}_{-14.8}$	$90.7^{+20.8}_{-20.8}$	$56.7^{+20.7}_{-20.7}$	$39.2^{+10.0}_{-10.0}$	$20.8^{+6.0}_{-6.0}$
Data	(4, 1)	–	–	7	44	64	14	10	5
SM	(4, 1)	–	–	$14.3^{+5.8}_{-5.6}$	$35.4^{+9.8}_{-9.7}$	$53.3^{+10.6}_{-10.5}$	$20.1^{+5.7}_{-5.7}$	$11.3^{+3.1}_{-3.0}$	$7.8^{+2.1}_{-2.1}$
Ttw	(4, 1)	–	–	$12.0^{+5.6}_{-5.4}$	$29.6^{+9.3}_{-9.1}$	$41.2^{+8.9}_{-8.8}$	$12.5^{+4.0}_{-4.0}$	$5.7^{+1.9}_{-1.9}$	$3.1^{+1.0}_{-0.9}$
Zinv	(4, 1)	–	–	$2.3^{+1.1}_{-1.1}$	$5.8^{+2.2}_{-2.2}$	$12.1^{+2.9}_{-2.9}$	$7.6^{+2.9}_{-2.8}$	$5.6^{+1.5}_{-1.5}$	$4.7^{+1.5}_{-1.4}$
Data	(4, 2)	–	–	5	15	24	7	4	0
SM	(4, 2)	–	–	$1.6^{+1.1}_{-0.8}$	$12.5^{+4.1}_{-3.9}$	$17.0^{+3.8}_{-3.7}$	$4.2^{+1.4}_{-1.3}$	$2.2^{+0.7}_{-0.7}$	$1.5^{+0.5}_{-0.5}$
Ttw	(4, 2)	–	–	$1.4^{+1.1}_{-0.8}$	$11.8^{+4.0}_{-3.9}$	$15.0^{+3.6}_{-3.5}$	$3.4^{+1.2}_{-1.2}$	$1.5^{+0.6}_{-0.5}$	$0.8^{+0.3}_{-0.3}$
Zinv	(4, 2)	–	–	$0.2^{+0.1}_{-0.1}$	$0.7^{+0.3}_{-0.3}$	$2.0^{+0.6}_{-0.5}$	$0.8^{+0.4}_{-0.3}$	$0.8^{+0.2}_{-0.2}$	$0.8^{+0.3}_{-0.3}$
Data	(4, ≥ 3)	–	–	–	3	0	0	0	0
SM	(4, ≥ 3)	–	–	–	$0.6^{+0.6}_{-0.3}$	$1.5^{+0.8}_{-0.6}$	$0.5^{+0.3}_{-0.2}$	$0.1^{+0.1}_{-0.0}$	$0.0^{+0.0}_{-0.0}$
Ttw	(4, ≥ 3)	–	–	–	$0.5^{+0.6}_{-0.3}$	$1.3^{+0.8}_{-0.6}$	$0.4^{+0.3}_{-0.2}$	$0.0^{+0.0}_{-0.0}$	$0.0^{+0.0}_{-0.0}$
Zinv	(4, ≥ 3)	–	–	–	$0.1^{+0.1}_{-0.1}$	$0.1^{+0.1}_{-0.1}$	$0.1^{+0.1}_{-0.1}$	$0.0^{+0.0}_{-0.0}$	$0.0^{+0.0}_{-0.0}$
Data	(≥ 5, 0)	–	–	–	5	55	47	41	36
SM	(≥ 5, 0)	–	–	–	$5.0^{+2.2}_{-1.7}$	$47.9^{+9.5}_{-9.3}$	$44.0^{+12.9}_{-12.8}$	$42.6^{+11.7}_{-11.6}$	$28.1^{+7.9}_{-7.9}$
Ttw	(≥ 5, 0)	–	–	–	$3.1^{+1.8}_{-1.3}$	$28.0^{+6.5}_{-6.3}$	$22.8^{+6.7}_{-6.6}$	$20.0^{+6.5}_{-6.5}$	$10.7^{+3.6}_{-3.5}$
Zinv	(≥ 5, 0)	–	–	–	$1.9^{+1.2}_{-0.9}$	$19.9^{+4.4}_{-4.3}$	$21.2^{+8.9}_{-8.9}$	$22.6^{+6.8}_{-6.8}$	$17.4^{+5.6}_{-5.6}$
Data	(≥ 5, 1)	–	–	–	1	34	17	16	13
SM	(≥ 5, 1)	–	–	–	$2.0^{+1.0}_{-0.8}$	$26.6^{+5.9}_{-5.8}$	$19.3^{+5.4}_{-5.4}$	$14.4^{+4.2}_{-4.2}$	$10.2^{+3.0}_{-2.9}$
Ttw	(≥ 5, 1)	–	–	–	$1.8^{+1.0}_{-0.7}$	$23.4^{+5.5}_{-5.4}$	$16.3^{+4.9}_{-4.8}$	$10.6^{+3.5}_{-3.5}$	$6.5^{+2.2}_{-2.2}$
Zinv	(≥ 5, 1)	–	–	–	$0.2^{+0.1}_{-0.1}$	$3.2^{+0.8}_{-0.8}$	$3.0^{+1.3}_{-1.3}$	$3.8^{+1.2}_{-1.2}$	$3.7^{+1.2}_{-1.2}$
Data	(≥ 5, 2)	–	–	–	0	9	9	5	4
SM	(≥ 5, 2)	–	–	–	$1.4^{+0.8}_{-0.6}$	$11.7^{+3.1}_{-2.9}$	$9.3^{+2.8}_{-2.7}$	$4.5^{+1.4}_{-1.4}$	$2.5^{+0.8}_{-0.8}$
Ttw	(≥ 5, 2)	–	–	–	$1.3^{+0.8}_{-0.6}$	$11.1^{+3.0}_{-2.8}$	$8.6^{+2.7}_{-2.6}$	$3.9^{+1.3}_{-1.3}$	$2.0^{+0.7}_{-0.7}$
Zinv	(≥ 5, 2)	–	–	–	$0.1^{+0.1}_{-0.1}$	$0.5^{+0.2}_{-0.2}$	$0.7^{+0.3}_{-0.3}$	$0.6^{+0.2}_{-0.2}$	$0.5^{+0.2}_{-0.2}$
Data	(≥ 5, ≥ 3)	–	–	–	–	0	0	0	3
SM	(≥ 5, ≥ 3)	–	–	–	–	$1.0^{+0.7}_{-0.4}$	$0.5^{+0.4}_{-0.3}$	$0.8^{+0.4}_{-0.3}$	$0.2^{+0.1}_{-0.1}$
Ttw	(≥ 5, ≥ 3)	–	–	–	–	$1.0^{+0.7}_{-0.4}$	$0.5^{+0.4}_{-0.3}$	$0.7^{+0.4}_{-0.3}$	$0.1^{+0.1}_{-0.1}$
Zinv	(≥ 5, ≥ 3)	–	–	–	–	$0.0^{+0.0}_{-0.0}$	$0.0^{+0.0}_{-0.0}$	$0.1^{+0.1}_{-0.1}$	$0.0^{+0.0}_{-0.0}$

DRAFT

Table 50: Predictions and Data in the signal region for 1.26fb^{-1} for asymmetric categories. The letter "a" in jet e.g. "2a" indicates the asymmetric jet bins. All entries are non-zero but are truncated to one decimal place.

H_T (GeV)	(n_{jet}, n_b)	200-250	250-300	300-350	350-400	400-500	500-600	600-800	800-∞
Data	(2a, 0)	2887	857	290	143	83	11	4	–
SM	(2a, 0)	$2811.3^{+309.8}_{-309.7}$	$795.9^{+102.0}_{-101.9}$	$291.8^{+48.3}_{-48.3}$	$117.9^{+19.2}_{-19.1}$	$90.8^{+18.2}_{-18.2}$	$20.6^{+5.9}_{-5.9}$	$5.3^{+3.4}_{-3.4}$	–
Ttw	(2a, 0)	$1319.3^{+185.1}_{-185.0}$	$333.0^{+54.3}_{-54.3}$	$115.1^{+26.1}_{-26.1}$	$40.9^{+8.6}_{-8.6}$	$27.5^{+6.0}_{-6.0}$	$6.3^{+2.0}_{-2.0}$	$1.3^{+2.6}_{-2.6}$	–
Zinv	(2a, 0)	$1492.0^{+191.1}_{-191.0}$	$462.9^{+74.0}_{-74.0}$	$176.8^{+31.1}_{-31.0}$	$77.0^{+13.7}_{-13.6}$	$63.3^{+14.4}_{-14.4}$	$14.3^{+4.8}_{-4.7}$	$4.0^{+2.1}_{-2.1}$	–
Data	(2a, 1)	254	77	29	12	7	1	0	–
SM	(2a, 1)	$217.2^{+26.0}_{-25.9}$	$82.6^{+11.5}_{-11.4}$	$22.3^{+4.3}_{-4.2}$	$10.5^{+2.3}_{-2.1}$	$6.4^{+1.6}_{-1.5}$	$1.5^{+0.7}_{-0.6}$	$0.3^{+0.3}_{-0.2}$	–
Ttw	(2a, 1)	$133.4^{+19.9}_{-19.8}$	$45.6^{+8.2}_{-8.2}$	$10.6^{+2.8}_{-2.8}$	$3.6^{+1.1}_{-1.0}$	$2.3^{+0.8}_{-0.8}$	$0.4^{+0.3}_{-0.3}$	$0.1^{+0.2}_{-0.2}$	–
Zinv	(2a, 1)	$83.8^{+11.6}_{-11.5}$	$37.0^{+6.5}_{-6.4}$	$11.8^{+2.5}_{-2.4}$	$6.9^{+1.8}_{-1.6}$	$4.0^{+1.2}_{-1.2}$	$1.1^{+0.6}_{-0.5}$	$0.2^{+0.2}_{-0.1}$	–
Data	(2a, 2)	15	6	2	1	0	0	0	–
SM	(2a, 2)	$13.3^{+2.5}_{-2.3}$	$2.7^{+0.8}_{-0.7}$	$2.5^{+0.9}_{-0.8}$	$1.6^{+0.8}_{-0.7}$	$0.8^{+0.4}_{-0.4}$	$0.1^{+0.1}_{-0.1}$	$0.1^{+0.1}_{-0.1}$	–
Ttw	(2a, 2)	$7.2^{+1.8}_{-1.7}$	$1.4^{+0.6}_{-0.5}$	$1.3^{+0.7}_{-0.6}$	$1.1^{+0.8}_{-0.7}$	$0.3^{+0.3}_{-0.2}$	$0.0^{+0.0}_{-0.0}$	$0.0^{+0.1}_{-0.1}$	–
Zinv	(2a, 2)	$6.1^{+1.5}_{-1.3}$	$1.3^{+0.5}_{-0.4}$	$1.3^{+0.6}_{-0.5}$	$0.4^{+0.3}_{-0.2}$	$0.4^{+0.3}_{-0.2}$	$0.1^{+0.1}_{-0.1}$	$0.0^{+0.1}_{-0.0}$	–
Data	(3a, 0)	739	798	372	118	55	11	1	–
SM	(3a, 0)	$720.3^{+104.8}_{-104.6}$	$718.0^{+77.6}_{-77.5}$	$364.1^{+69.8}_{-69.7}$	$126.8^{+26.6}_{-26.5}$	$58.6^{+12.9}_{-12.9}$	$10.9^{+4.0}_{-3.9}$	$3.3^{+2.2}_{-2.1}$	–
Ttw	(3a, 0)	$377.0^{+67.8}_{-67.7}$	$364.5^{+48.3}_{-48.2}$	$178.2^{+42.2}_{-42.1}$	$53.0^{+14.7}_{-14.6}$	$21.3^{+6.2}_{-6.2}$	$3.5^{+1.5}_{-1.5}$	$0.8^{+0.7}_{-0.7}$	–
Zinv	(3a, 0)	$343.3^{+68.7}_{-68.6}$	$353.4^{+45.3}_{-45.2}$	$185.9^{+44.5}_{-44.4}$	$73.8^{+19.0}_{-18.9}$	$37.3^{+9.4}_{-9.3}$	$7.3^{+3.3}_{-3.3}$	$2.5^{+2.0}_{-2.0}$	–
Data	(3a, 1)	152	135	66	35	5	0	1	–
SM	(3a, 1)	$127.2^{+20.7}_{-20.6}$	$143.8^{+17.6}_{-17.5}$	$53.9^{+11.4}_{-11.3}$	$16.6^{+4.0}_{-3.9}$	$7.6^{+1.9}_{-1.9}$	$1.2^{+0.5}_{-0.5}$	$0.4^{+0.3}_{-0.3}$	–
Ttw	(3a, 1)	$102.7^{+19.2}_{-19.1}$	$113.2^{+15.7}_{-15.6}$	$40.4^{+10.0}_{-9.9}$	$11.1^{+3.4}_{-3.3}$	$4.2^{+1.4}_{-1.4}$	$0.7^{+0.4}_{-0.4}$	$0.1^{+0.1}_{-0.1}$	–
Zinv	(3a, 1)	$24.5^{+5.1}_{-5.1}$	$30.6^{+4.2}_{-4.2}$	$13.5^{+3.4}_{-3.4}$	$5.5^{+1.6}_{-1.6}$	$3.5^{+1.0}_{-1.0}$	$0.5^{+0.3}_{-0.2}$	$0.3^{+0.3}_{-0.3}$	–
Data	(3a, 2)	25	28	12	5	0	0	0	–
SM	(3a, 2)	$23.9^{+4.6}_{-4.5}$	$22.1^{+3.4}_{-3.3}$	$14.2^{+3.6}_{-3.5}$	$5.0^{+1.6}_{-1.5}$	$1.2^{+0.4}_{-0.4}$	$0.2^{+0.2}_{-0.1}$	$0.0^{+0.1}_{-0.0}$	–
Ttw	(3a, 2)	$20.5^{+4.4}_{-4.3}$	$18.5^{+3.2}_{-3.1}$	$11.9^{+3.4}_{-3.3}$	$4.3^{+1.5}_{-1.4}$	$0.7^{+0.3}_{-0.3}$	$0.1^{+0.1}_{-0.1}$	$0.0^{+0.0}_{-0.0}$	–
Zinv	(3a, 2)	$3.4^{+0.9}_{-0.8}$	$3.6^{+0.7}_{-0.7}$	$2.3^{+0.7}_{-0.7}$	$0.7^{+0.3}_{-0.3}$	$0.5^{+0.2}_{-0.2}$	$0.1^{+0.1}_{-0.1}$	$0.0^{+0.1}_{-0.0}$	–
Data	(3a, ≥ 3)	2	1	1	–	0	–	–	–
SM	(3a, ≥ 3)	$0.2^{+0.3}_{-0.1}$	$0.7^{+0.4}_{-0.3}$	$0.4^{+0.4}_{-0.2}$	–	$0.0^{+0.0}_{-0.0}$	–	–	–
Ttw	(3a, ≥ 3)	$0.2^{+0.3}_{-0.1}$	$0.6^{+0.4}_{-0.3}$	$0.4^{+0.4}_{-0.2}$	–	$0.0^{+0.0}_{-0.0}$	–	–	–
Zinv	(3a, ≥ 3)	$0.0^{+0.0}_{-0.0}$	$0.1^{+0.1}_{-0.1}$	$0.0^{+0.0}_{-0.0}$	–	$0.0^{+0.0}_{-0.0}$	–	–	–
Data	(4a, 0)	0	68	182	102	58	5	2	–
SM	(4a, 0)	$1.7^{+0.8}_{-0.7}$	$72.6^{+24.1}_{-24.1}$	$167.8^{+30.4}_{-30.2}$	$111.8^{+19.6}_{-19.4}$	$61.9^{+14.5}_{-14.4}$	$7.6^{+2.1}_{-2.1}$	$1.2^{+0.7}_{-0.6}$	–
Ttw	(4a, 0)	$0.6^{+0.4}_{-0.4}$	$41.6^{+15.1}_{-15.0}$	$91.8^{+20.5}_{-20.3}$	$61.2^{+13.4}_{-13.2}$	$28.7^{+9.5}_{-9.4}$	$2.8^{+1.1}_{-1.0}$	$0.3^{+0.2}_{-0.2}$	–
Zinv	(4a, 0)	$1.1^{+0.7}_{-0.6}$	$31.0^{+18.4}_{-18.4}$	$76.0^{+16.4}_{-16.2}$	$50.6^{+10.0}_{-9.9}$	$33.3^{+8.5}_{-8.4}$	$4.8^{+1.5}_{-1.4}$	$0.9^{+0.6}_{-0.6}$	–
Data	(4a, 1)	1	27	77	54	30	1	0	–
SM	(4a, 1)	$0.6^{+0.3}_{-0.3}$	$15.6^{+5.1}_{-5.0}$	$63.4^{+13.1}_{-13.0}$	$39.2^{+7.9}_{-7.8}$	$27.0^{+7.6}_{-7.5}$	$1.7^{+0.6}_{-0.6}$	$0.3^{+0.2}_{-0.2}$	–
Ttw	(4a, 1)	$0.4^{+0.3}_{-0.2}$	$12.5^{+4.7}_{-4.6}$	$54.4^{+12.3}_{-12.2}$	$32.6^{+7.3}_{-7.2}$	$20.4^{+6.9}_{-6.8}$	$1.1^{+0.5}_{-0.5}$	$0.1^{+0.1}_{-0.1}$	–
Zinv	(4a, 1)	$0.1^{+0.1}_{-0.1}$	$3.1^{+1.9}_{-1.9}$	$9.0^{+2.0}_{-2.0}$	$6.7^{+1.4}_{-1.4}$	$6.6^{+1.8}_{-1.8}$	$0.7^{+0.3}_{-0.3}$	$0.2^{+0.1}_{-0.1}$	–
Data	(4a, 2)	0	6	24	7	3	0	0	–
SM	(4a, 2)	$0.2^{+0.2}_{-0.1}$	$6.1^{+2.2}_{-2.1}$	$21.8^{+5.2}_{-5.0}$	$15.8^{+3.8}_{-3.6}$	$6.4^{+2.2}_{-2.1}$	$0.3^{+0.2}_{-0.2}$	$0.1^{+0.1}_{-0.1}$	–
Ttw	(4a, 2)	$0.2^{+0.2}_{-0.1}$	$5.2^{+2.1}_{-2.0}$	$20.3^{+5.0}_{-4.9}$	$14.9^{+3.7}_{-3.6}$	$5.7^{+2.2}_{-2.1}$	$0.3^{+0.2}_{-0.2}$	$0.1^{+0.1}_{-0.1}$	–
Zinv	(4a, 2)	$0.0^{+0.0}_{-0.0}$	$0.9^{+0.6}_{-0.6}$	$1.5^{+0.4}_{-0.4}$	$0.9^{+0.3}_{-0.3}$	$0.7^{+0.3}_{-0.3}$	$0.1^{+0.1}_{-0.0}$	$0.0^{+0.0}_{-0.0}$	–
Data	(4a, ≥ 3)	–	0	0	2	0	1	–	–
SM	(4a, ≥ 3)	–	$0.5^{+0.5}_{-0.3}$	$1.3^{+0.9}_{-0.6}$	$0.7^{+0.5}_{-0.3}$	$0.9^{+0.7}_{-0.5}$	$0.1^{+0.2}_{-0.1}$	–	–
Ttw	(4a, ≥ 3)	–	$0.4^{+0.5}_{-0.3}$	$1.2^{+0.9}_{-0.6}$	$0.7^{+0.5}_{-0.3}$	$0.9^{+0.7}_{-0.5}$	$0.1^{+0.2}_{-0.1}$	–	–
Zinv	(4a, ≥ 3)	–	$0.0^{+0.0}_{-0.0}$	$0.1^{+0.1}_{-0.1}$	$0.0^{+0.1}_{-0.0}$	$0.0^{+0.0}_{-0.0}$	$0.0^{+0.0}_{-0.0}$	–	–
Data	(≥ 5a, 0)	–	–	21	40	50	10	2	–
SM	(≥ 5a, 0)	–	–	$11.3^{+4.1}_{-3.6}$	$38.7^{+9.0}_{-8.6}$	$51.9^{+13.0}_{-12.9}$	$8.2^{+2.9}_{-2.8}$	$2.6^{+1.5}_{-1.4}$	–
Ttw	(≥ 5a, 0)	–	–	$7.1^{+3.3}_{-2.8}$	$24.2^{+6.9}_{-6.5}$	$33.2^{+9.3}_{-9.2}$	$4.5^{+2.2}_{-2.1}$	$1.2^{+0.8}_{-0.7}$	–
Zinv	(≥ 5a, 0)	–	–	$4.2^{+2.2}_{-2.0}$	$14.6^{+4.7}_{-4.5}$	$18.7^{+7.1}_{-7.1}$	$3.7^{+1.4}_{-1.4}$	$1.3^{+1.2}_{-1.1}$	–
Data	(≥ 5a, 1)	–	–	5	32	29	4	0	–
SM	(≥ 5a, 1)	–	–	$8.0^{+3.1}_{-2.7}$	$20.3^{+5.3}_{-5.0}$	$28.7^{+7.7}_{-7.6}$	$6.8^{+2.8}_{-2.8}$	$0.8^{+0.5}_{-0.4}$	–
Ttw	(≥ 5a, 1)	–	–	$7.3^{+3.0}_{-2.7}$	$18.3^{+5.1}_{-4.9}$	$26.2^{+7.4}_{-7.3}$	$5.9^{+2.8}_{-2.7}$	$0.6^{+0.4}_{-0.4}$	–
Zinv	(≥ 5a, 1)	–	–	$0.7^{+0.4}_{-0.3}$	$2.0^{+0.7}_{-0.6}$	$2.5^{+1.0}_{-1.0}$	$0.8^{+0.3}_{-0.3}$	$0.2^{+0.2}_{-0.2}$	–
Data	(≥ 5a, 2)	–	–	6	13	14	3	1	–
SM	(≥ 5a, 2)	–	–	$3.1^{+1.5}_{-1.2}$	$8.1^{+2.8}_{-2.4}$	$12.2^{+3.8}_{-3.6}$	$2.6^{+1.3}_{-1.2}$	$0.1^{+0.2}_{-0.1}$	–
Ttw	(≥ 5a, 2)	–	–	$2.9^{+1.5}_{-1.2}$	$7.8^{+2.8}_{-2.4}$	$11.6^{+3.7}_{-3.5}$	$2.4^{+1.3}_{-1.2}$	$0.1^{+0.2}_{-0.1}$	–
Zinv	(≥ 5a, 2)	–	–	$0.1^{+0.1}_{-0.1}$	$0.3^{+0.1}_{-0.1}$	$0.6^{+0.3}_{-0.3}$	$0.2^{+0.1}_{-0.1}$	$0.0^{+0.0}_{-0.0}$	–
Data	(≥ 5a, ≥ 3)	–	–	–	1	1	0	–	–
SM	(≥ 5a, ≥ 3)	–	–	–	$0.8^{+0.9}_{-0.5}$	$0.8^{+0.8}_{-0.4}$	$0.2^{+0.3}_{-0.1}$	–	–
Ttw	(≥ 5a, ≥ 3)	–	–	–	$0.8^{+0.9}_{-0.5}$	$0.7^{+0.8}_{-0.4}$	$0.2^{+0.3}_{-0.1}$	–	–
Zinv	(≥ 5a, ≥ 3)	–	–	–	$0.0^{+0.0}_{-0.0}$	$0.0^{+0.1}_{-0.0}$	$0.0^{+0.0}_{-0.0}$	–	–

DRAFT

Table 51: Predictions and Data in the signal region for 1.26fb^{-1} for monojet categories. The letter "a" in jet e.g. "2a" indicates the asymmetric jet bins. All entries are non-zero but are truncated to one decimal place.

H_T (GeV)	(n_{jet}, n_b)	200-250	250-300	300-350	350-400	400-500	500-600	600-800	800-∞
Data	(1, 0)	4199	1347	493	251	159	54	23	–
SM	(1, 0)	$4199.2^{+70.1}_{-70.1}$	$1349.4^{+37.3}_{-37.3}$	$498.5^{+19.6}_{-19.6}$	$244.0^{+14.2}_{-14.2}$	$158.9^{+9.4}_{-9.4}$	$52.5^{+5.9}_{-5.9}$	$22.0^{+4.4}_{-4.4}$	–
Ttw	(1, 0)	$1625.6^{+113.8}_{-113.8}$	$467.6^{+53.2}_{-53.2}$	$151.2^{+15.8}_{-15.8}$	$56.5^{+9.8}_{-9.8}$	$39.5^{+3.9}_{-3.9}$	$10.3^{+2.4}_{-2.4}$	$3.7^{+1.9}_{-1.9}$	–
Zinv	(1, 0)	$2573.6^{+114.1}_{-114.1}$	$881.8^{+61.5}_{-61.5}$	$347.3^{+21.1}_{-21.1}$	$187.5^{+15.4}_{-15.4}$	$119.5^{+9.3}_{-9.3}$	$42.2^{+5.8}_{-5.8}$	$18.3^{+4.2}_{-4.2}$	–
Data	(1, 1)	139	46	17	13	7	5	0	–
SM	(1, 1)	$146.6^{+10.6}_{-10.6}$	$53.8^{+6.3}_{-6.3}$	$20.1^{+3.4}_{-3.4}$	$9.5^{+2.3}_{-2.3}$	$6.9^{+1.3}_{-1.3}$	$2.1^{+1.0}_{-1.0}$	$0.2^{+0.4}_{-0.4}$	–
Ttw	(1, 1)	$45.3^{+4.1}_{-4.1}$	$14.7^{+2.5}_{-2.5}$	$5.9^{+1.2}_{-1.2}$	$1.7^{+0.5}_{-0.5}$	$1.8^{+0.4}_{-0.4}$	$0.5^{+0.2}_{-0.2}$	$0.0^{+0.1}_{-0.1}$	–
Zinv	(1, 1)	$101.3^{+8.5}_{-8.5}$	$39.0^{+5.0}_{-5.0}$	$14.2^{+2.5}_{-2.5}$	$7.7^{+2.0}_{-2.0}$	$5.0^{+1.0}_{-1.0}$	$1.6^{+0.8}_{-0.8}$	$0.1^{+0.4}_{-0.4}$	–

DRAFT

Table 52: Predictions and Data in the signal region for 1.26fb^{-1} for symmetric categories. The letter "a" in jet e.g. "2a" indicates the asymmetric jet bins. All entries are non-zero but are truncated to one decimal place.

H_T (GeV)	(n_{jet}, n_b)	200-250	250-300	300-350	350-400	400-500	500-600	600-800	800-∞
Data	(2, 0)	552	592	395	247	189	55	39	33
SM	(2, 0)	$559.6^{+25.3}_{-25.3}$	$599.0^{+27.4}_{-27.4}$	$398.0^{+19.7}_{-19.7}$	$246.9^{+18.0}_{-18.0}$	$196.5^{+12.9}_{-12.9}$	$53.6^{+7.4}_{-7.4}$	$36.8^{+5.6}_{-5.6}$	$30.7^{+4.8}_{-4.8}$
Ttw	(2, 0)	$281.6^{+36.0}_{-36.0}$	$268.3^{+38.2}_{-38.2}$	$168.8^{+22.6}_{-22.6}$	$95.2^{+21.2}_{-21.2}$	$71.5^{+7.2}_{-7.2}$	$17.0^{+5.1}_{-5.1}$	$10.6^{+2.7}_{-2.7}$	$8.6^{+2.3}_{-2.3}$
Zinv	(2, 0)	$278.1^{+35.6}_{-35.6}$	$330.7^{+37.2}_{-37.2}$	$229.2^{+23.4}_{-23.4}$	$151.7^{+22.3}_{-22.3}$	$125.0^{+10.0}_{-10.0}$	$36.7^{+6.3}_{-6.3}$	$26.2^{+4.7}_{-4.7}$	$22.1^{+4.6}_{-4.6}$
Data	(2, 1)	81	63	35	22	23	3	1	2
SM	(2, 1)	$73.7^{+7.0}_{-7.0}$	$57.2^{+6.2}_{-6.2}$	$32.7^{+4.6}_{-4.6}$	$22.0^{+4.0}_{-4.0}$	$16.5^{+2.4}_{-2.4}$	$4.1^{+1.3}_{-1.3}$	$2.9^{+1.0}_{-1.0}$	$3.2^{+0.9}_{-0.9}$
Ttw	(2, 1)	$48.7^{+6.3}_{-6.3}$	$35.1^{+5.4}_{-5.4}$	$16.7^{+3.0}_{-3.0}$	$9.3^{+2.1}_{-2.1}$	$6.6^{+1.0}_{-1.0}$	$1.4^{+0.6}_{-0.6}$	$0.7^{+0.3}_{-0.3}$	$1.0^{+0.4}_{-0.4}$
Zinv	(2, 1)	$25.0^{+5.4}_{-5.4}$	$22.1^{+4.2}_{-4.2}$	$16.1^{+2.7}_{-2.7}$	$12.8^{+3.2}_{-3.2}$	$9.8^{+1.6}_{-1.6}$	$2.7^{+0.8}_{-0.8}$	$2.2^{+0.8}_{-0.8}$	$2.1^{+0.7}_{-0.7}$
Data	(2, 2)	2	3	2	–	2	0	0	0
SM	(2, 2)	$1.6^{+1.2}_{-1.2}$	$1.8^{+1.3}_{-1.3}$	$1.2^{+0.8}_{-0.8}$	–	$1.0^{+0.4}_{-0.4}$	$0.3^{+0.3}_{-0.3}$	$0.2^{+0.2}_{-0.2}$	$0.1^{+0.2}_{-0.2}$
Ttw	(2, 2)	$0.8^{+0.7}_{-0.7}$	$0.8^{+0.5}_{-0.5}$	$0.6^{+0.4}_{-0.4}$	–	$0.4^{+0.2}_{-0.2}$	$0.2^{+0.2}_{-0.2}$	$0.0^{+0.0}_{-0.0}$	$0.0^{+0.0}_{-0.0}$
Zinv	(2, 2)	$0.8^{+0.6}_{-0.6}$	$1.0^{+0.8}_{-0.8}$	$0.6^{+0.4}_{-0.4}$	–	$0.6^{+0.3}_{-0.3}$	$0.1^{+0.2}_{-0.2}$	$0.2^{+0.2}_{-0.2}$	$0.0^{+0.1}_{-0.1}$
Data	(3, 0)	1	111	283	282	353	120	51	51
SM	(3, 0)	$1.4^{+1.9}_{-1.9}$	$111.2^{+10.7}_{-10.7}$	$282.0^{+16.7}_{-16.7}$	$280.0^{+16.0}_{-16.0}$	$348.4^{+20.3}_{-20.3}$	$121.4^{+9.7}_{-9.7}$	$53.1^{+6.3}_{-6.3}$	$46.1^{+4.6}_{-4.6}$
Ttw	(3, 0)	$0.9^{+1.2}_{-1.2}$	$53.9^{+7.6}_{-7.6}$	$136.3^{+18.6}_{-18.6}$	$132.2^{+17.8}_{-17.8}$	$150.4^{+23.3}_{-23.3}$	$45.9^{+7.0}_{-7.0}$	$17.7^{+3.5}_{-3.5}$	$13.5^{+2.9}_{-2.9}$
Zinv	(3, 0)	$0.5^{+0.8}_{-0.8}$	$57.3^{+8.6}_{-8.6}$	$145.7^{+19.1}_{-19.1}$	$147.8^{+18.3}_{-18.3}$	$198.0^{+24.3}_{-24.3}$	$75.4^{+7.9}_{-7.9}$	$35.4^{+5.5}_{-5.5}$	$32.6^{+4.4}_{-4.4}$
Data	(3, 1)	2	25	49	60	35	16	10	5
SM	(3, 1)	$1.4^{+1.4}_{-1.4}$	$24.3^{+4.0}_{-4.0}$	$45.0^{+5.0}_{-5.0}$	$57.1^{+6.0}_{-6.0}$	$42.5^{+6.0}_{-6.0}$	$15.3^{+2.5}_{-2.5}$	$9.0^{+2.1}_{-2.1}$	$5.5^{+1.1}_{-1.1}$
Ttw	(3, 1)	$1.2^{+1.2}_{-1.2}$	$19.1^{+3.5}_{-3.5}$	$33.4^{+4.3}_{-4.3}$	$41.1^{+5.1}_{-5.1}$	$25.3^{+4.5}_{-4.5}$	$7.7^{+1.4}_{-1.4}$	$3.4^{+0.8}_{-0.8}$	$1.8^{+0.4}_{-0.4}$
Zinv	(3, 1)	$0.2^{+0.2}_{-0.2}$	$5.3^{+1.0}_{-1.0}$	$11.6^{+2.4}_{-2.4}$	$16.0^{+3.2}_{-3.2}$	$17.2^{+3.3}_{-3.3}$	$7.6^{+1.4}_{-1.4}$	$5.5^{+1.6}_{-1.6}$	$3.7^{+0.8}_{-0.8}$
Data	(3, 2)	–	4	4	4	9	3	2	0
SM	(3, 2)	–	$4.4^{+1.2}_{-1.2}$	$9.0^{+1.9}_{-1.9}$	$8.2^{+1.7}_{-1.7}$	$6.8^{+1.4}_{-1.4}$	$2.1^{+0.6}_{-0.6}$	$0.9^{+0.3}_{-0.3}$	$0.2^{+0.2}_{-0.2}$
Ttw	(3, 2)	–	$3.6^{+1.0}_{-1.0}$	$7.5^{+1.7}_{-1.7}$	$6.9^{+1.4}_{-1.4}$	$5.3^{+1.1}_{-1.1}$	$1.3^{+0.4}_{-0.4}$	$0.3^{+0.1}_{-0.1}$	$0.1^{+0.0}_{-0.0}$
Zinv	(3, 2)	–	$0.8^{+0.3}_{-0.3}$	$1.5^{+0.4}_{-0.4}$	$1.3^{+0.4}_{-0.4}$	$1.5^{+0.4}_{-0.4}$	$0.8^{+0.2}_{-0.2}$	$0.5^{+0.2}_{-0.2}$	$0.2^{+0.1}_{-0.1}$
Data	(3, ≥ 3)	–	–	–	0	1	0	–	–
SM	(3, ≥ 3)	–	–	–	$0.7^{+0.8}_{-0.8}$	$0.2^{+0.2}_{-0.2}$	$0.1^{+0.1}_{-0.1}$	–	–
Ttw	(3, ≥ 3)	–	–	–	$0.6^{+0.7}_{-0.7}$	$0.2^{+0.2}_{-0.2}$	$0.0^{+0.1}_{-0.1}$	–	–
Zinv	(3, ≥ 3)	–	–	–	$0.1^{+0.1}_{-0.1}$	$0.0^{+0.0}_{-0.0}$	$0.0^{+0.0}_{-0.0}$	–	–
Data	(4, 0)	–	–	31	93	158	92	60	33
SM	(4, 0)	–	–	$30.5^{+5.7}_{-5.7}$	$95.1^{+9.7}_{-9.7}$	$167.5^{+11.0}_{-11.0}$	$91.4^{+9.8}_{-9.8}$	$60.7^{+7.8}_{-7.8}$	$31.4^{+3.7}_{-3.7}$
Ttw	(4, 0)	–	–	$17.4^{+4.5}_{-4.5}$	$51.8^{+9.4}_{-9.4}$	$86.5^{+9.6}_{-9.6}$	$38.2^{+7.4}_{-7.4}$	$22.5^{+4.2}_{-4.2}$	$9.9^{+1.6}_{-1.6}$
Zinv	(4, 0)	–	–	$13.1^{+4.4}_{-4.4}$	$43.3^{+9.2}_{-9.2}$	$81.0^{+9.1}_{-9.1}$	$53.2^{+9.1}_{-9.1}$	$38.2^{+5.5}_{-5.5}$	$21.5^{+3.2}_{-3.2}$
Data	(4, 1)	–	–	7	44	64	14	10	5
SM	(4, 1)	–	–	$9.7^{+3.1}_{-3.1}$	$43.5^{+6.0}_{-6.0}$	$58.2^{+5.9}_{-5.9}$	$16.8^{+3.4}_{-3.4}$	$10.9^{+2.2}_{-2.2}$	$7.3^{+1.0}_{-1.0}$
Ttw	(4, 1)	–	–	$7.9^{+2.8}_{-2.8}$	$36.4^{+5.6}_{-5.6}$	$45.3^{+5.1}_{-5.1}$	$10.4^{+2.3}_{-2.3}$	$5.5^{+1.4}_{-1.4}$	$2.9^{+0.5}_{-0.5}$
Zinv	(4, 1)	–	–	$1.8^{+0.9}_{-0.9}$	$7.1^{+2.2}_{-2.2}$	$12.9^{+2.2}_{-2.2}$	$6.3^{+1.8}_{-1.8}$	$5.4^{+1.1}_{-1.1}$	$4.4^{+0.8}_{-0.8}$
Data	(4, 2)	–	–	5	15	24	7	4	0
SM	(4, 2)	–	–	$2.8^{+1.4}_{-1.4}$	$15.0^{+3.0}_{-3.0}$	$19.2^{+2.7}_{-2.7}$	$4.5^{+1.2}_{-1.2}$	$2.3^{+0.6}_{-0.6}$	$1.4^{+0.3}_{-0.3}$
Ttw	(4, 2)	–	–	$2.5^{+1.3}_{-1.3}$	$14.2^{+2.9}_{-2.9}$	$17.0^{+2.5}_{-2.5}$	$3.6^{+1.0}_{-1.0}$	$1.6^{+0.4}_{-0.4}$	$0.7^{+0.2}_{-0.2}$
Zinv	(4, 2)	–	–	$0.2^{+0.2}_{-0.2}$	$0.9^{+0.3}_{-0.3}$	$2.2^{+0.4}_{-0.4}$	$0.8^{+0.3}_{-0.3}$	$0.8^{+0.2}_{-0.2}$	$0.7^{+0.2}_{-0.2}$
Data	(4, ≥ 3)	–	–	–	3	0	0	0	0
SM	(4, ≥ 3)	–	–	–	$1.4^{+0.9}_{-0.9}$	$1.1^{+0.7}_{-0.7}$	$0.4^{+0.3}_{-0.3}$	$0.1^{+0.1}_{-0.1}$	$0.0^{+0.0}_{-0.0}$
Ttw	(4, ≥ 3)	–	–	–	$1.2^{+0.8}_{-0.8}$	$1.0^{+0.6}_{-0.6}$	$0.3^{+0.2}_{-0.2}$	$0.0^{+0.0}_{-0.0}$	$0.0^{+0.0}_{-0.0}$
Zinv	(4, ≥ 3)	–	–	–	$0.2^{+0.2}_{-0.2}$	$0.1^{+0.1}_{-0.1}$	$0.1^{+0.1}_{-0.1}$	$0.0^{+0.0}_{-0.0}$	$0.0^{+0.0}_{-0.0}$
Data	(≥ 5, 0)	–	–	–	5	55	47	41	36
SM	(≥ 5, 0)	–	–	–	$4.0^{+2.0}_{-2.0}$	$54.1^{+6.8}_{-6.8}$	$45.4^{+6.6}_{-6.6}$	$41.8^{+5.6}_{-5.6}$	$31.6^{+3.8}_{-3.8}$
Ttw	(≥ 5, 0)	–	–	–	$2.5^{+1.3}_{-1.3}$	$31.6^{+4.6}_{-4.6}$	$22.9^{+4.9}_{-4.9}$	$19.6^{+3.6}_{-3.6}$	$11.8^{+2.5}_{-2.5}$
Zinv	(≥ 5, 0)	–	–	–	$1.5^{+0.8}_{-0.8}$	$22.5^{+3.2}_{-3.2}$	$22.5^{+5.1}_{-5.1}$	$22.2^{+3.9}_{-3.9}$	$19.8^{+3.4}_{-3.4}$
Data	(≥ 5, 1)	–	–	–	1	34	17	16	13
SM	(≥ 5, 1)	–	–	–	$1.3^{+0.9}_{-0.9}$	$31.4^{+4.5}_{-4.5}$	$18.1^{+3.1}_{-3.1}$	$14.9^{+3.0}_{-3.0}$	$10.9^{+1.8}_{-1.8}$
Ttw	(≥ 5, 1)	–	–	–	$1.2^{+0.8}_{-0.8}$	$27.6^{+4.1}_{-4.1}$	$15.3^{+2.8}_{-2.8}$	$11.1^{+2.6}_{-2.6}$	$7.1^{+1.5}_{-1.5}$
Zinv	(≥ 5, 1)	–	–	–	$0.1^{+0.1}_{-0.1}$	$3.8^{+0.7}_{-0.7}$	$2.8^{+0.9}_{-0.9}$	$3.8^{+0.8}_{-0.8}$	$3.8^{+0.8}_{-0.8}$
Data	(≥ 5, 2)	–	–	–	0	9	9	5	4
SM	(≥ 5, 2)	–	–	–	$0.8^{+0.6}_{-0.6}$	$11.7^{+2.5}_{-2.5}$	$9.0^{+1.9}_{-1.9}$	$4.6^{+1.2}_{-1.2}$	$2.7^{+0.6}_{-0.6}$
Ttw	(≥ 5, 2)	–	–	–	$0.7^{+0.5}_{-0.5}$	$11.1^{+2.4}_{-2.4}$	$8.3^{+1.8}_{-1.8}$	$4.0^{+1.1}_{-1.1}$	$2.2^{+0.6}_{-0.6}$
Zinv	(≥ 5, 2)	–	–	–	$0.0^{+0.0}_{-0.0}$	$0.6^{+0.1}_{-0.1}$	$0.7^{+0.3}_{-0.3}$	$0.6^{+0.2}_{-0.2}$	$0.6^{+0.1}_{-0.1}$
Data	(≥ 5, ≥ 3)	–	–	–	–	0	0	0	3
SM	(≥ 5, ≥ 3)	–	–	–	–	$0.9^{+0.5}_{-0.5}$	$0.4^{+0.3}_{-0.3}$	$0.7^{+0.4}_{-0.4}$	$0.3^{+0.1}_{-0.1}$
Ttw	(≥ 5, ≥ 3)	–	–	–	–	$0.8^{+0.5}_{-0.5}$	$0.4^{+0.3}_{-0.3}$	$0.6^{+0.3}_{-0.3}$	$0.3^{+0.1}_{-0.1}$
Zinv	(≥ 5, ≥ 3)	–	–	–	–	$0.0^{+0.0}_{-0.0}$	$0.0^{+0.0}_{-0.0}$	$0.1^{+0.0}_{-0.0}$	$0.1^{+0.0}_{-0.0}$

DRAFT

Table 53: Predictions and Data in the signal region for 1.26fb^{-1} for asymmetric categories. The letter "a" in jet e.g. "2a" indicates the asymmetric jet bins. All entries are non-zero but are truncated to one decimal place.

H_T (GeV)	(n_{jet}, n_b)	200-250	250-300	300-350	350-400	400-500	500-600	600-800	800-∞
Data	(2a, 0)	2887	857	290	143	83	11	8	–
SM	(2a, 0)	$2894.8^{+53.6}_{-53.6}$	$854.8^{+28.8}_{-28.8}$	$293.3^{+16.3}_{-16.3}$	$141.9^{+11.4}_{-11.4}$	$83.3^{+9.1}_{-9.1}$	$11.3^{+3.3}_{-3.3}$	$7.7^{+3.1}_{-3.1}$	–
Ttw	(2a, 0)	$1356.9^{+104.0}_{-104.0}$	$356.3^{+36.6}_{-36.6}$	$114.7^{+16.0}_{-16.0}$	$49.3^{+6.9}_{-6.9}$	$25.3^{+4.4}_{-4.4}$	$3.5^{+1.3}_{-1.3}$	$1.6^{+0.9}_{-0.9}$	–
Zinv	(2a, 0)	$1537.8^{+97.3}_{-97.3}$	$498.5^{+38.5}_{-38.5}$	$178.6^{+16.0}_{-16.0}$	$92.7^{+9.5}_{-9.5}$	$58.1^{+7.0}_{-7.0}$	$7.9^{+2.3}_{-2.3}$	$6.1^{+2.5}_{-2.5}$	–
Data	(2a, 1)	254	77	29	12	7	1	0	–
SM	(2a, 1)	$246.7^{+12.6}_{-12.6}$	$81.7^{+6.3}_{-6.3}$	$25.2^{+3.3}_{-3.3}$	$12.4^{+2.5}_{-2.5}$	$6.1^{+1.3}_{-1.3}$	$0.9^{+0.5}_{-0.5}$	$0.3^{+0.4}_{-0.4}$	–
Ttw	(2a, 1)	$152.9^{+11.3}_{-11.3}$	$45.0^{+5.5}_{-5.5}$	$12.1^{+2.3}_{-2.3}$	$4.2^{+0.9}_{-0.9}$	$2.2^{+0.5}_{-0.5}$	$0.2^{+0.1}_{-0.1}$	$0.1^{+0.1}_{-0.1}$	–
Zinv	(2a, 1)	$93.8^{+9.1}_{-9.1}$	$36.7^{+4.4}_{-4.4}$	$13.1^{+1.8}_{-1.8}$	$8.1^{+1.7}_{-1.7}$	$3.8^{+0.9}_{-0.9}$	$0.6^{+0.4}_{-0.4}$	$0.2^{+0.3}_{-0.3}$	–
Data	(2a, 2)	15	6	2	1	0	0	0	–
SM	(2a, 2)	$14.5^{+2.5}_{-2.5}$	$3.5^{+0.9}_{-0.9}$	$2.5^{+0.9}_{-0.9}$	$1.7^{+0.7}_{-0.7}$	$0.6^{+0.3}_{-0.3}$	$0.0^{+0.3}_{-0.3}$	$0.1^{+0.2}_{-0.2}$	–
Ttw	(2a, 2)	$7.8^{+1.4}_{-1.4}$	$1.9^{+0.5}_{-0.5}$	$1.3^{+0.5}_{-0.5}$	$1.2^{+0.6}_{-0.6}$	$0.3^{+0.1}_{-0.1}$	$0.0^{+0.0}_{-0.0}$	$0.0^{+0.1}_{-0.1}$	–
Zinv	(2a, 2)	$6.7^{+1.2}_{-1.2}$	$1.7^{+0.4}_{-0.4}$	$1.3^{+0.5}_{-0.5}$	$0.5^{+0.2}_{-0.2}$	$0.3^{+0.2}_{-0.2}$	$0.0^{+0.3}_{-0.3}$	$0.0^{+0.1}_{-0.1}$	–
Data	(3a, 0)	739	798	372	118	55	11	3	–
SM	(3a, 0)	$743.4^{+26.9}_{-26.9}$	$792.7^{+27.2}_{-27.2}$	$374.0^{+19.0}_{-19.0}$	$125.3^{+10.4}_{-10.4}$	$52.9^{+6.9}_{-6.9}$	$10.0^{+3.5}_{-3.5}$	$3.4^{+2.0}_{-2.0}$	–
Ttw	(3a, 0)	$391.3^{+43.1}_{-43.1}$	$403.5^{+27.6}_{-27.6}$	$183.4^{+25.6}_{-25.6}$	$53.0^{+9.5}_{-9.5}$	$19.1^{+4.3}_{-4.3}$	$3.1^{+1.5}_{-1.5}$	$0.8^{+1.2}_{-1.2}$	–
Zinv	(3a, 0)	$352.1^{+40.9}_{-40.9}$	$389.2^{+26.3}_{-26.3}$	$190.5^{+25.2}_{-25.2}$	$72.3^{+10.0}_{-10.0}$	$33.7^{+5.6}_{-5.6}$	$6.8^{+2.7}_{-2.7}$	$2.6^{+1.4}_{-1.4}$	–
Data	(3a, 1)	152	135	66	35	5	0	1	–
SM	(3a, 1)	$148.4^{+10.7}_{-10.7}$	$143.4^{+9.8}_{-9.8}$	$62.6^{+7.1}_{-7.1}$	$27.0^{+4.7}_{-4.7}$	$6.3^{+1.6}_{-1.6}$	$0.9^{+0.6}_{-0.6}$	$0.7^{+0.8}_{-0.8}$	–
Ttw	(3a, 1)	$120.7^{+10.2}_{-10.2}$	$111.8^{+8.6}_{-8.6}$	$47.5^{+6.2}_{-6.2}$	$18.9^{+4.1}_{-4.1}$	$3.4^{+1.0}_{-1.0}$	$0.5^{+0.4}_{-0.4}$	$0.2^{+0.3}_{-0.3}$	–
Zinv	(3a, 1)	$27.7^{+5.9}_{-5.9}$	$31.7^{+3.3}_{-3.3}$	$15.1^{+3.3}_{-3.3}$	$8.1^{+1.9}_{-1.9}$	$2.9^{+0.8}_{-0.8}$	$0.4^{+0.3}_{-0.3}$	$0.5^{+0.6}_{-0.6}$	–
Data	(3a, 2)	25	28	12	5	0	0	0	–
SM	(3a, 2)	$25.7^{+3.5}_{-3.5}$	$25.0^{+2.9}_{-2.9}$	$13.9^{+2.4}_{-2.4}$	$5.7^{+1.6}_{-1.6}$	$0.9^{+0.4}_{-0.4}$	$0.2^{+0.2}_{-0.2}$	$0.0^{+0.1}_{-0.1}$	–
Ttw	(3a, 2)	$22.0^{+3.2}_{-3.2}$	$21.0^{+2.6}_{-2.6}$	$11.6^{+2.2}_{-2.2}$	$4.9^{+1.4}_{-1.4}$	$0.5^{+0.2}_{-0.2}$	$0.1^{+0.1}_{-0.1}$	$0.0^{+0.0}_{-0.0}$	–
Zinv	(3a, 2)	$3.7^{+0.7}_{-0.7}$	$4.0^{+0.5}_{-0.5}$	$2.3^{+0.6}_{-0.6}$	$0.8^{+0.3}_{-0.3}$	$0.4^{+0.2}_{-0.2}$	$0.1^{+0.1}_{-0.1}$	$0.0^{+0.1}_{-0.1}$	–
Data	(3a, ≥ 3)	2	1	1	–	0	–	–	–
SM	(3a, ≥ 3)	$0.5^{+0.3}_{-0.3}$	$0.8^{+0.4}_{-0.4}$	$0.5^{+0.4}_{-0.4}$	–	$0.0^{+0.0}_{-0.0}$	–	–	–
Ttw	(3a, ≥ 3)	$0.4^{+0.3}_{-0.3}$	$0.6^{+0.3}_{-0.3}$	$0.5^{+0.4}_{-0.4}$	–	$0.0^{+0.0}_{-0.0}$	–	–	–
Zinv	(3a, ≥ 3)	$0.0^{+0.0}_{-0.0}$	$0.2^{+0.1}_{-0.1}$	$0.0^{+0.0}_{-0.0}$	–	$0.0^{+0.0}_{-0.0}$	–	–	–
Data	(4a, 0)	0	68	182	102	58	5	2	–
SM	(4a, 0)	$0.7^{+1.1}_{-1.1}$	$70.3^{+10.0}_{-10.0}$	$183.2^{+12.4}_{-12.4}$	$105.1^{+9.2}_{-9.2}$	$57.7^{+7.3}_{-7.3}$	$5.5^{+2.4}_{-2.4}$	$1.6^{+1.7}_{-1.7}$	–
Ttw	(4a, 0)	$0.3^{+0.4}_{-0.4}$	$41.7^{+10.1}_{-10.1}$	$100.1^{+11.1}_{-11.1}$	$57.3^{+6.7}_{-6.7}$	$26.8^{+5.3}_{-5.3}$	$2.0^{+1.0}_{-1.0}$	$0.4^{+0.5}_{-0.5}$	–
Zinv	(4a, 0)	$0.5^{+0.7}_{-0.7}$	$28.6^{+9.8}_{-9.8}$	$83.1^{+10.3}_{-10.3}$	$47.9^{+6.4}_{-6.4}$	$30.9^{+5.4}_{-5.4}$	$3.5^{+1.5}_{-1.5}$	$1.2^{+1.3}_{-1.3}$	–
Data	(4a, 1)	1	27	77	54	30	1	0	–
SM	(4a, 1)	$0.3^{+0.7}_{-0.7}$	$23.6^{+4.8}_{-4.8}$	$74.6^{+7.2}_{-7.2}$	$46.3^{+5.7}_{-5.7}$	$27.7^{+4.6}_{-4.6}$	$1.3^{+0.7}_{-0.7}$	$0.4^{+0.6}_{-0.6}$	–
Ttw	(4a, 1)	$0.2^{+0.6}_{-0.6}$	$19.4^{+4.1}_{-4.1}$	$64.4^{+6.6}_{-6.6}$	$39.0^{+5.1}_{-5.1}$	$21.4^{+4.1}_{-4.1}$	$0.8^{+0.4}_{-0.4}$	$0.1^{+0.2}_{-0.2}$	–
Zinv	(4a, 1)	$0.1^{+0.2}_{-0.2}$	$4.2^{+2.3}_{-2.3}$	$10.2^{+1.8}_{-1.8}$	$7.2^{+1.3}_{-1.3}$	$6.3^{+1.4}_{-1.4}$	$0.5^{+0.3}_{-0.3}$	$0.2^{+0.4}_{-0.4}$	–
Data	(4a, 2)	0	6	24	7	3	0	0	–
SM	(4a, 2)	$0.1^{+0.3}_{-0.3}$	$6.7^{+2.1}_{-2.1}$	$24.2^{+3.7}_{-3.7}$	$12.7^{+2.2}_{-2.2}$	$5.0^{+1.4}_{-1.4}$	$0.2^{+0.2}_{-0.2}$	$0.1^{+0.2}_{-0.2}$	–
Ttw	(4a, 2)	$0.1^{+0.3}_{-0.3}$	$5.6^{+2.0}_{-2.0}$	$22.5^{+3.5}_{-3.5}$	$11.8^{+2.1}_{-2.1}$	$4.4^{+1.3}_{-1.3}$	$0.2^{+0.1}_{-0.1}$	$0.0^{+0.1}_{-0.1}$	–
Zinv	(4a, 2)	$0.0^{+0.0}_{-0.0}$	$1.0^{+0.6}_{-0.6}$	$1.7^{+0.4}_{-0.4}$	$0.8^{+0.2}_{-0.2}$	$0.6^{+0.2}_{-0.2}$	$0.0^{+0.0}_{-0.0}$	$0.0^{+0.1}_{-0.1}$	–
Data	(4a, ≥ 3)	–	0	0	2	0	1	–	–
SM	(4a, ≥ 3)	–	$0.4^{+0.4}_{-0.4}$	$1.1^{+0.7}_{-0.7}$	$0.9^{+0.5}_{-0.5}$	$0.6^{+0.5}_{-0.5}$	$0.2^{+0.2}_{-0.2}$	–	–
Ttw	(4a, ≥ 3)	–	$0.4^{+0.4}_{-0.4}$	$1.0^{+0.6}_{-0.6}$	$0.9^{+0.5}_{-0.5}$	$0.6^{+0.5}_{-0.5}$	$0.2^{+0.2}_{-0.2}$	–	–
Zinv	(4a, ≥ 3)	–	$0.0^{+0.0}_{-0.0}$	$0.1^{+0.0}_{-0.0}$	$0.1^{+0.0}_{-0.0}$	$0.0^{+0.0}_{-0.0}$	$0.0^{+0.0}_{-0.0}$	–	–
Data	(≥ 5a, 0)	–	2	21	40	50	10	2	–
SM	(≥ 5a, 0)	–	$1.5^{+2.0}_{-2.0}$	$19.2^{+4.2}_{-4.2}$	$43.5^{+6.2}_{-6.2}$	$51.0^{+6.5}_{-6.5}$	$8.7^{+2.4}_{-2.4}$	$2.3^{+1.5}_{-1.5}$	–
Ttw	(≥ 5a, 0)	–	$1.3^{+1.6}_{-1.6}$	$12.0^{+3.1}_{-3.1}$	$27.1^{+4.9}_{-4.9}$	$32.7^{+5.7}_{-5.7}$	$4.9^{+1.5}_{-1.5}$	$1.1^{+0.8}_{-0.8}$	–
Zinv	(≥ 5a, 0)	–	$0.2^{+0.7}_{-0.7}$	$7.1^{+2.5}_{-2.5}$	$16.4^{+3.6}_{-3.6}$	$18.3^{+4.4}_{-4.4}$	$3.8^{+1.4}_{-1.4}$	$1.2^{+1.0}_{-1.0}$	–
Data	(≥ 5a, 1)	–	0	5	32	29	4	0	–
SM	(≥ 5a, 1)	–	$0.4^{+1.1}_{-1.1}$	$7.8^{+2.2}_{-2.2}$	$29.6^{+4.3}_{-4.3}$	$29.1^{+4.7}_{-4.7}$	$5.5^{+2.0}_{-2.0}$	$0.6^{+0.7}_{-0.7}$	–
Ttw	(≥ 5a, 1)	–	$0.4^{+0.9}_{-0.9}$	$7.0^{+2.0}_{-2.0}$	$26.9^{+4.1}_{-4.1}$	$26.5^{+4.5}_{-4.5}$	$4.8^{+1.9}_{-1.9}$	$0.5^{+0.5}_{-0.5}$	–
Zinv	(≥ 5a, 1)	–	$0.1^{+0.3}_{-0.3}$	$0.7^{+0.4}_{-0.4}$	$2.7^{+0.7}_{-0.7}$	$2.5^{+0.7}_{-0.7}$	$0.7^{+0.3}_{-0.3}$	$0.1^{+0.3}_{-0.3}$	–
Data	(≥ 5a, 2)	–	–	6	13	14	3	1	–
SM	(≥ 5a, 2)	–	–	$5.0^{+1.9}_{-1.9}$	$11.7^{+2.8}_{-2.8}$	$13.1^{+2.7}_{-2.7}$	$2.7^{+1.1}_{-1.1}$	$0.2^{+0.3}_{-0.3}$	–
Ttw	(≥ 5a, 2)	–	–	$4.8^{+1.8}_{-1.8}$	$11.3^{+2.7}_{-2.7}$	$12.5^{+2.6}_{-2.6}$	$2.4^{+1.1}_{-1.1}$	$0.2^{+0.3}_{-0.3}$	–
Zinv	(≥ 5a, 2)	–	–	$0.2^{+0.1}_{-0.1}$	$0.4^{+0.1}_{-0.1}$	$0.6^{+0.2}_{-0.2}$	$0.2^{+0.1}_{-0.1}$	$0.0^{+0.0}_{-0.0}$	–
Data	(≥ 5a, ≥ 3)	–	–	–	1	1	0	–	–
SM	(≥ 5a, ≥ 3)	–	–	–	$1.0^{+0.8}_{-0.8}$	$0.9^{+0.8}_{-0.8}$	$0.2^{+0.4}_{-0.4}$	–	–
Ttw	(≥ 5a, ≥ 3)	–	–	–	$1.0^{+0.8}_{-0.8}$	$0.8^{+0.7}_{-0.7}$	$0.2^{+0.3}_{-0.3}$	–	–
Zinv	(≥ 5a, ≥ 3)	–	–	–	$0.0^{+0.0}_{-0.0}$	$0.0^{+0.0}_{-0.0}$	$0.0^{+0.0}_{-0.0}$	–	–

DRAFT

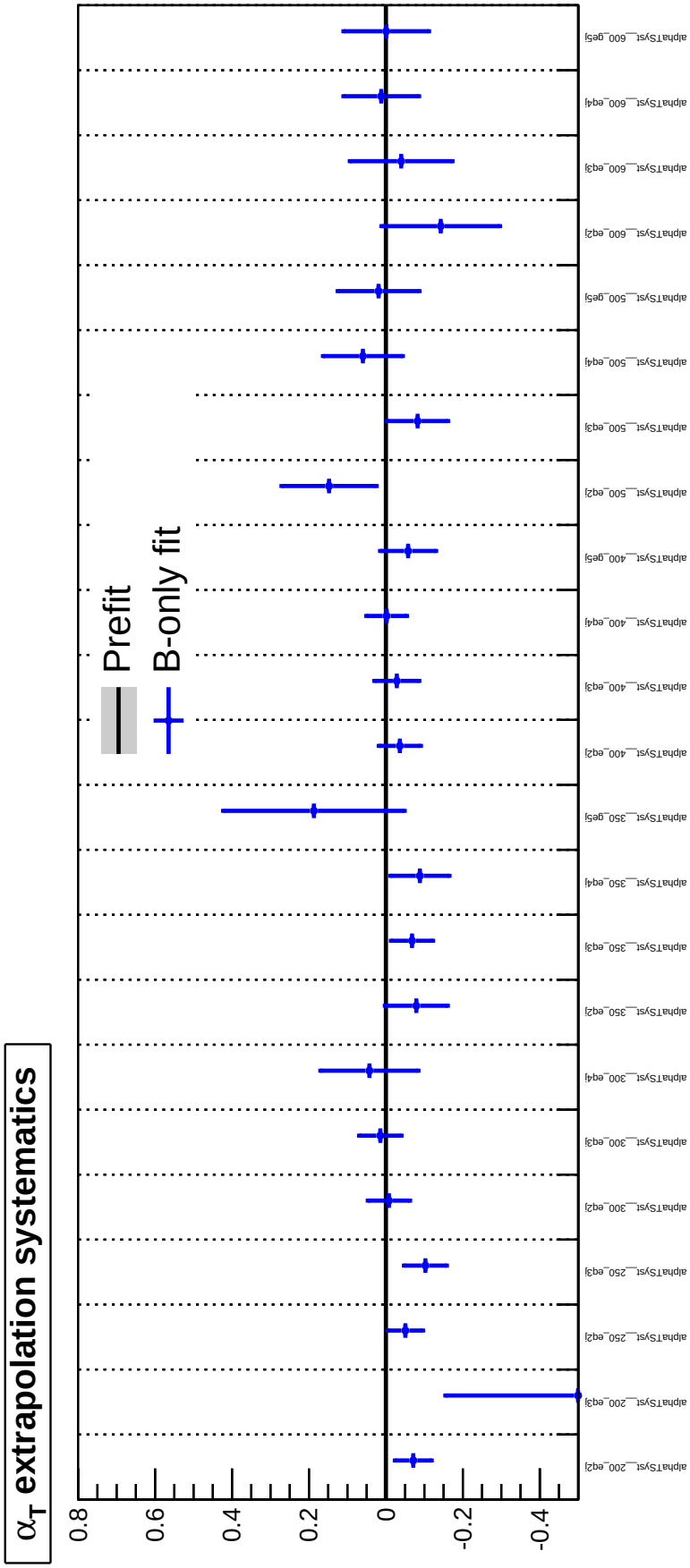

Figure 81: Pulls on the "α_T extrapolation" nuisance parameters for the "symmetric" topologies.

Figure 82: Pulls on the "α_T extrapolation" nuisance parameters for the "asymmetric" topologies.

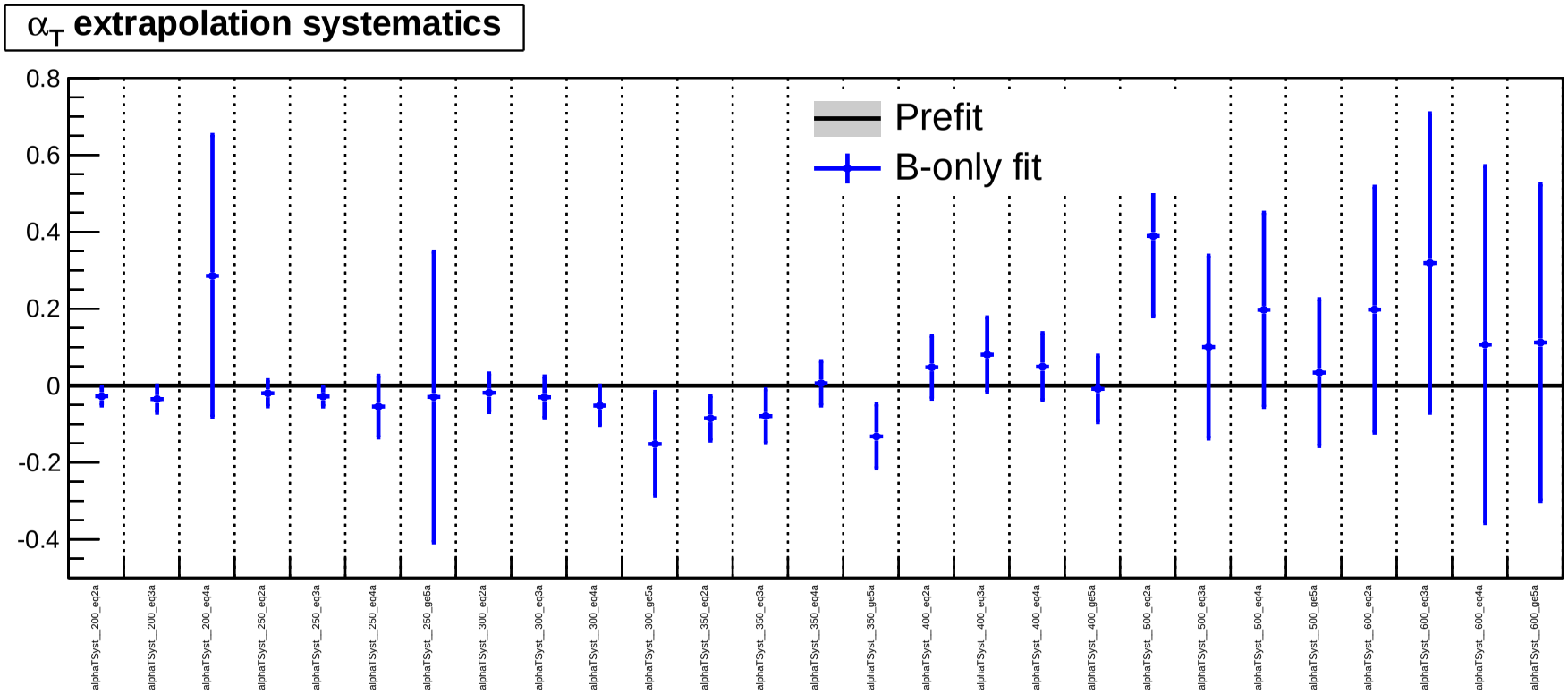

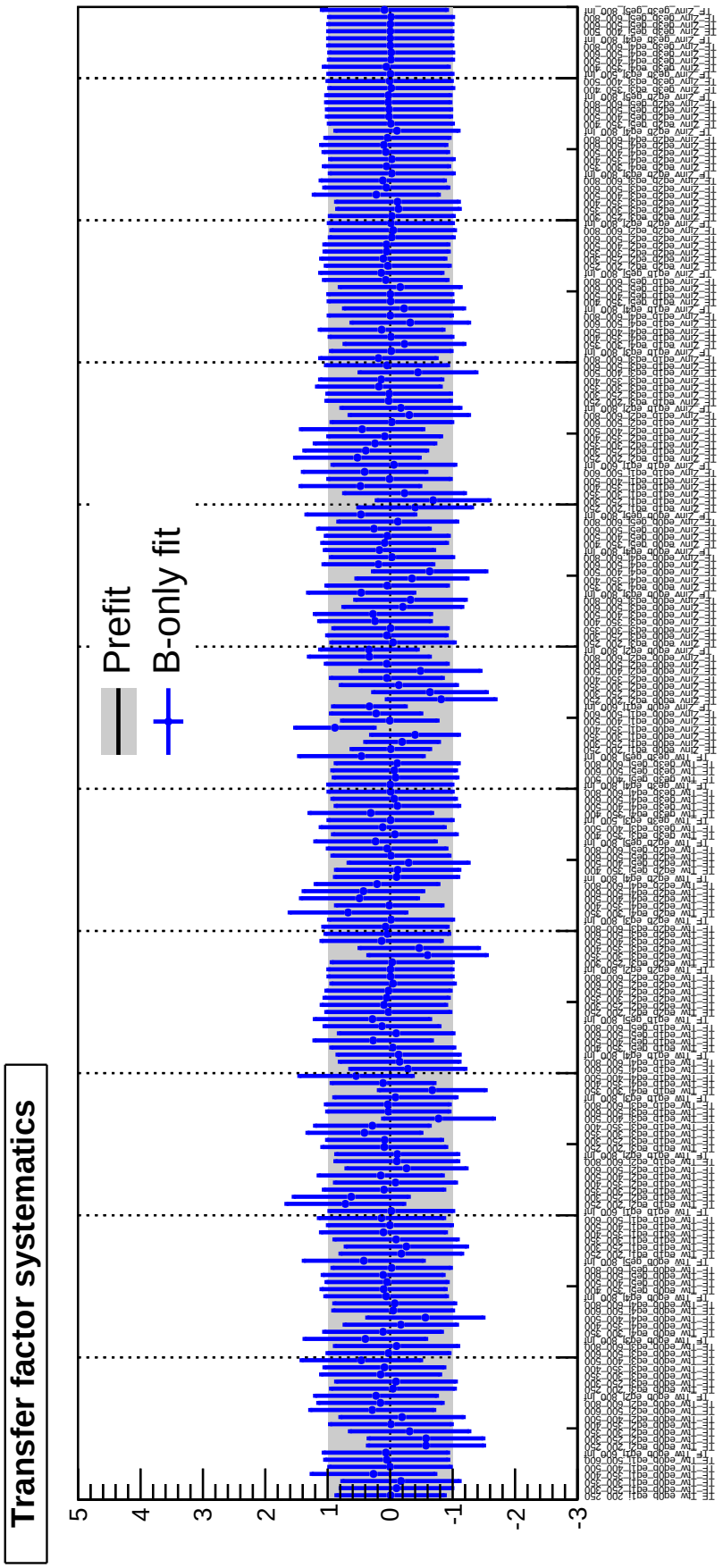

Figure 83: Pulls on the "transfer factors systematic" nuisance parameters for the "symmetric" topologies.

Figure 84: Pulls on the “transfer factors systematic” nuisance parameters for the “asymmetric” topologies.

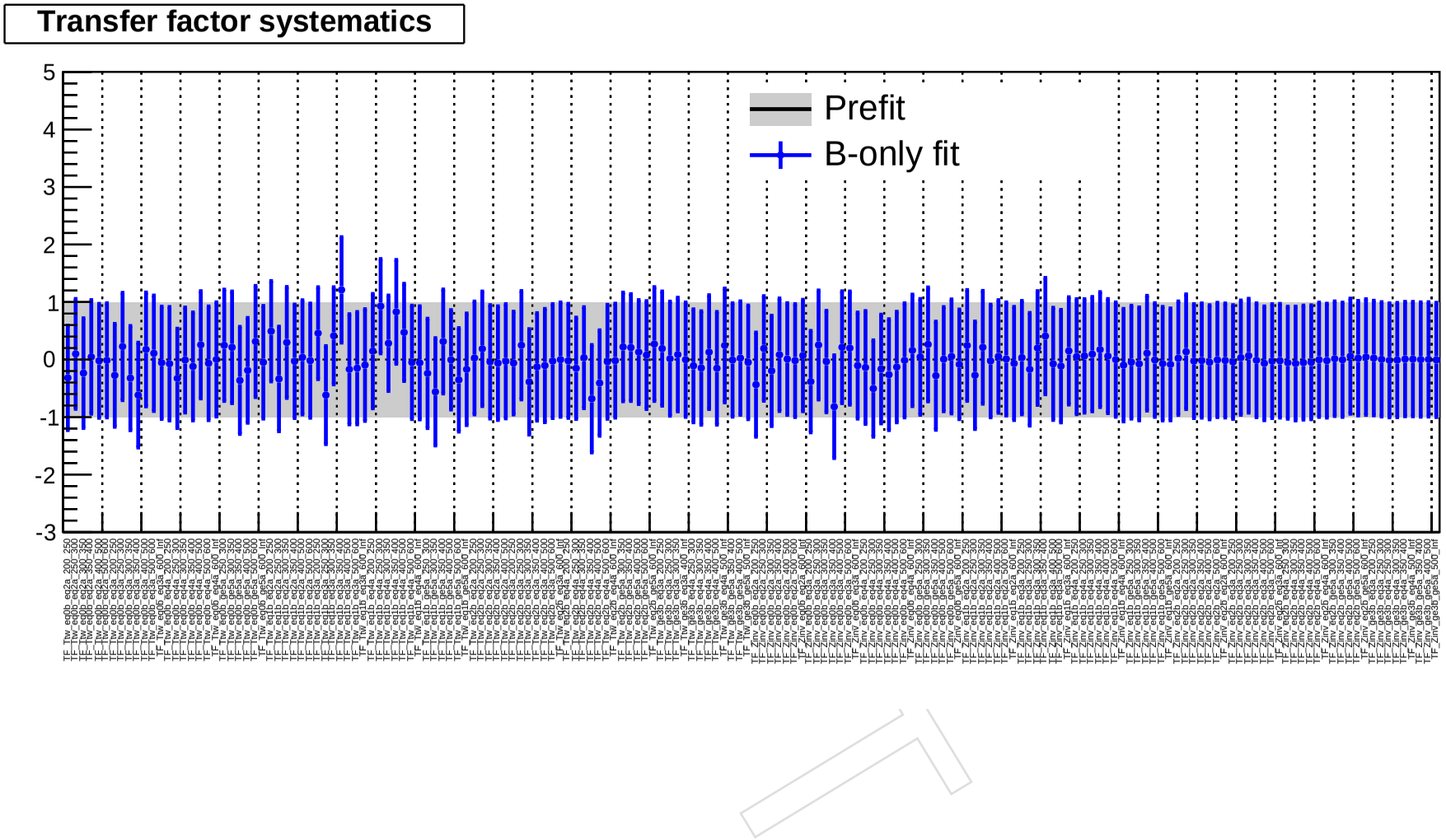

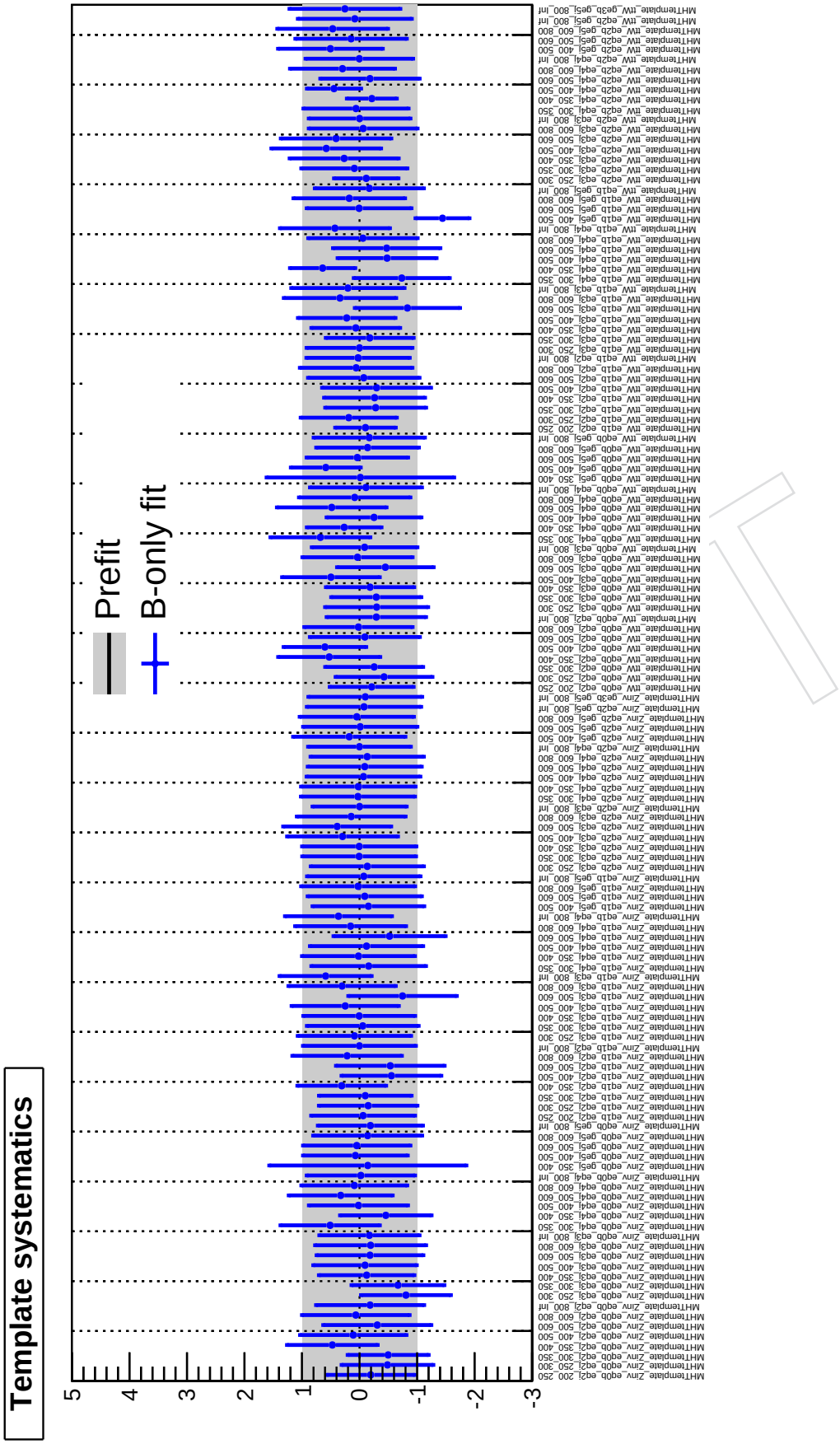

Figure 85: Pulls on the "template systematic" nuisance parameters for the "symmetric" topologies.

Figure 86: Pulls on the “template systematic” nuisance parameters for the “asymmetric” topologies.

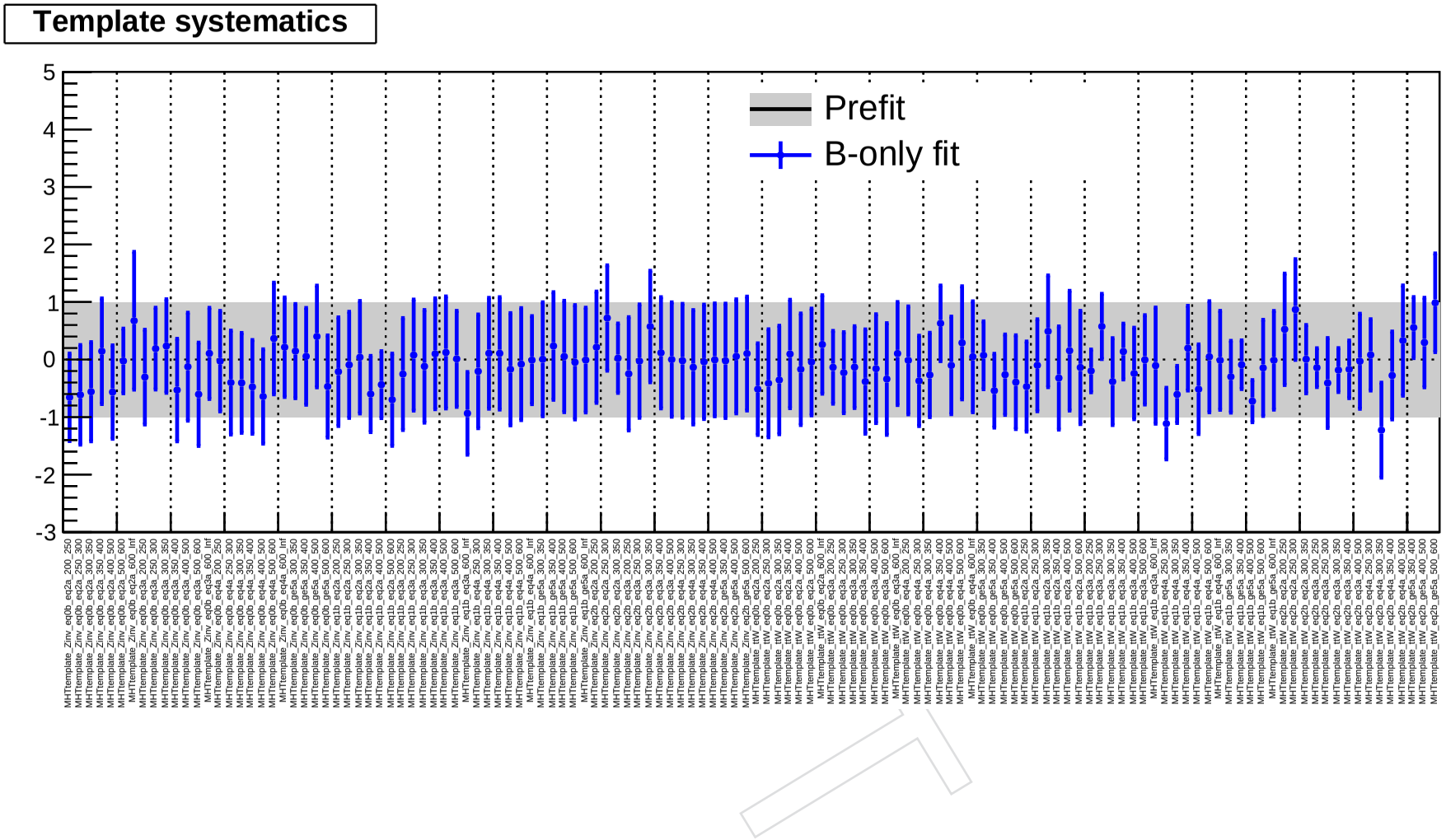

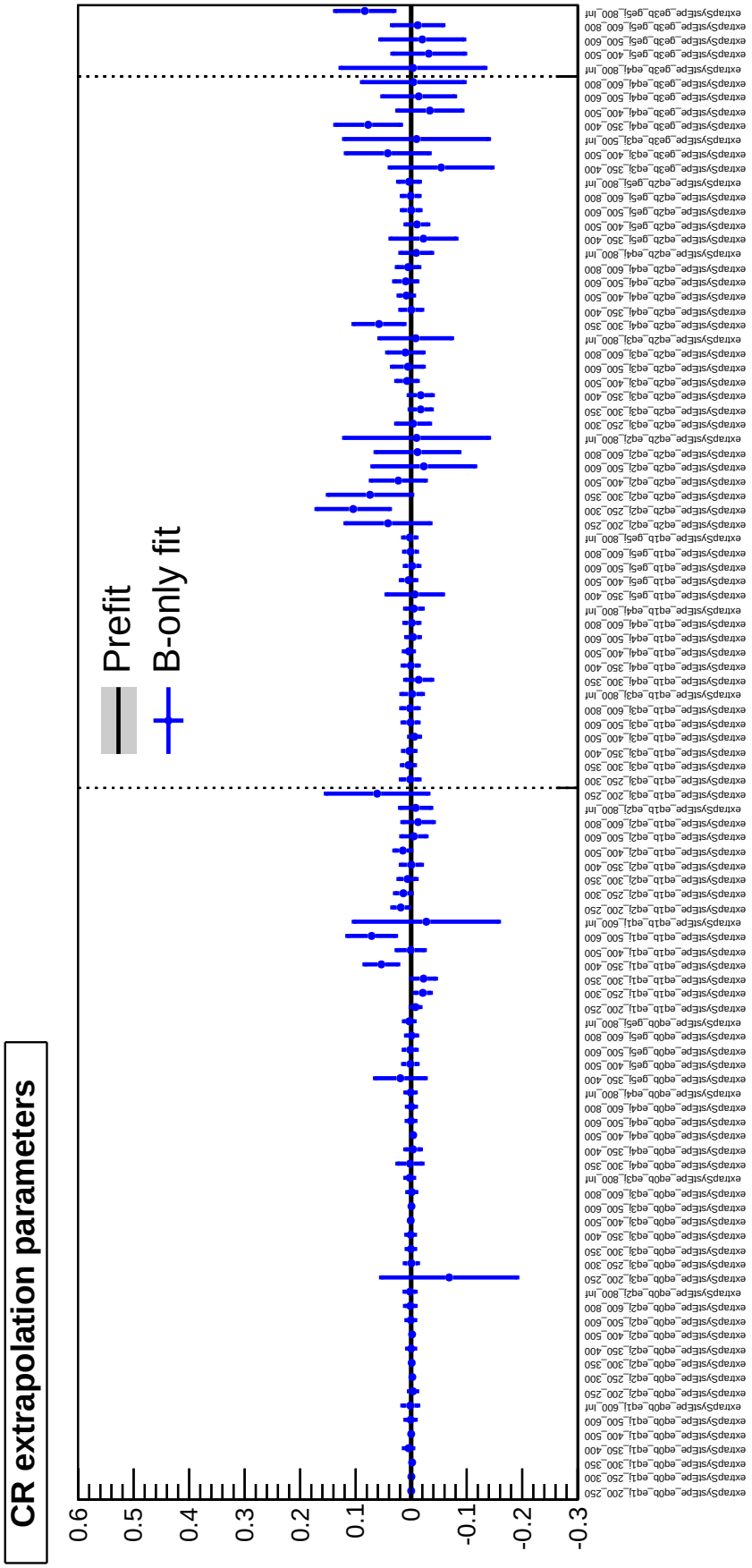

Figure 87: Pulls on the "control region extrapolation systematic" nuisance parameters for the "symmetric" topologies.

Figure 88: Pulls on the “control region extrapolation systematic” nuisance parameters for the “asymmetric” topologies.

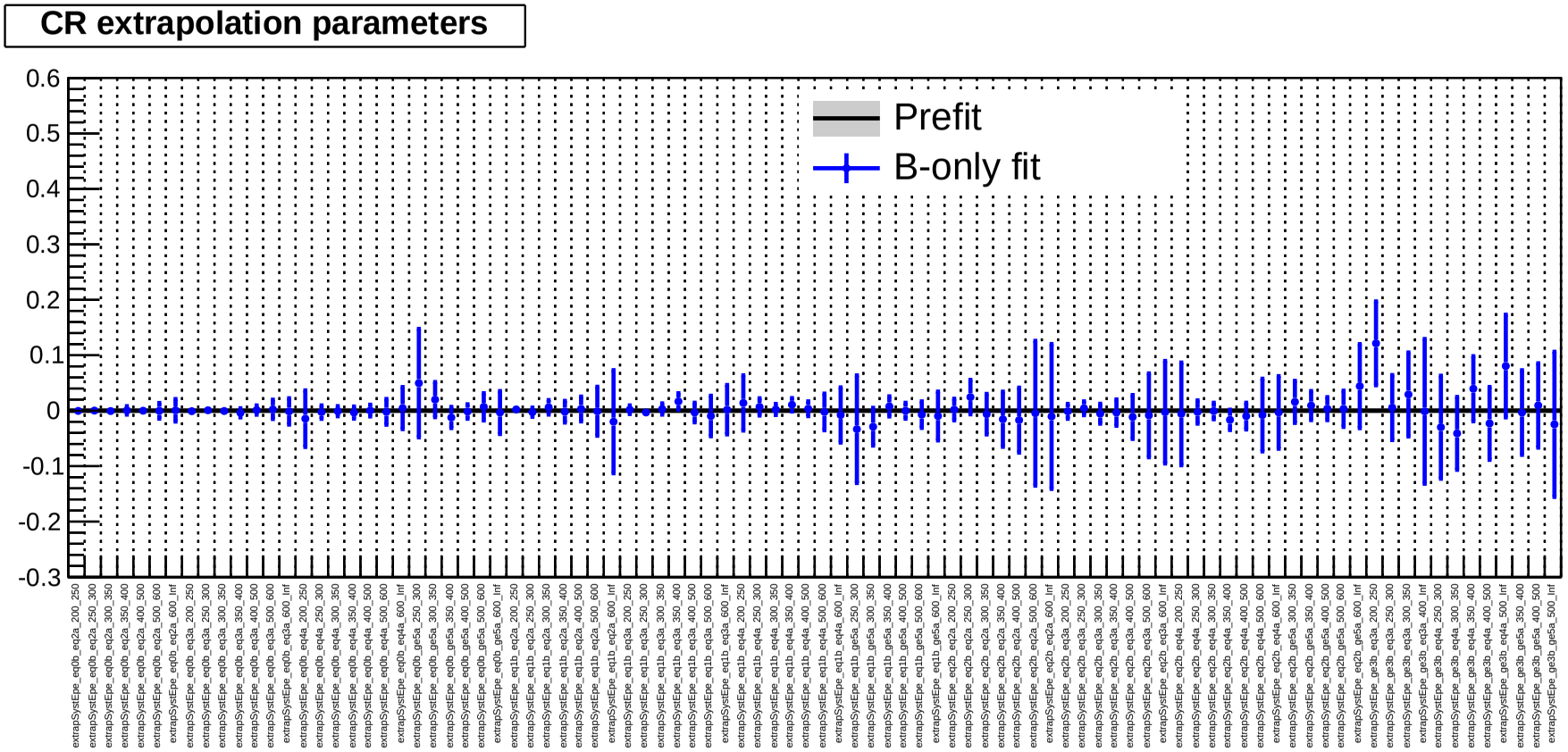

16 Interpretation in Simplified SUSY models

To interpret the results of this search, simplified models [25–27] for the production of supersymmetric particles are considered. They use only a limited set of sparticles in the production and decay and enable comprehensive studies of individual SUSY event topologies. These studies can be performed in terms of fundamental properties such as decay modes, production cross sections and sparticle masses.

16.1 Signal models

Results are presented for gluino pair production followed by decay into four b-quarks, called T1bbbb throughout the text. This is at the moment the only simplified model available: we will update with the interpretation of other models as soon as they will become available.
The signal efficiency times acceptance is determined per model per event category (n_{jet},n_{b}) per H_{T} bin. Systematic uncertainties on the signal acceptance are taken from the 2012 analysis (see Sec. 16.3).

16.2 Signal acceptance and contamination

The level of signal contamination in the control regions is expected to be negligible for most of the models that are targeted by this all-hadronic search. The requirement of one muon, two muons or one photon in the μ+jets, $\mu\mu$+jets and γ+jets respectively ensures that the control regions are depleted by any hadronic signature of the signal. The only partial exception is the gluino pair production and stop pair production followed by decay into top quarks, named `T1tttt` and `T2tt` respectively. In this case, when tops undergo a leptonic decay there may be a residual signal contamination in the muon control region.
Since the relevant signal samples are not yet available for the Spring15 campaign, the results shown in this section refer to the PHYS14 exercise. They will be updated as soon as possible with the new MC samples.

Figure 89 characterises the level of signal contamination in the μ + jets control sample for the benchmark model `T2tt` ($m_{Stop} = 850$ GeV, $m_{LSP} = 100$ GeV) relative to the signal acceptance in the signal region. Figures 89 (a) and (b) show the expected signal yield counts as a function of event category and H_{T} bin in the signal and μ + jets control regions, respectively.

Figure 89 (c) shows the ratio of these expected yields (signal region with respect to the μ + jets control region). The ratio is typically small, at the percent level for the most sensitive categories (i.e. with four or more jets and one or two b-tagged jets).

In addition, the event counts from SM background processes in the μ + jets control sample are significantly higher than in the signal region, as no α_{T} requirement is made for the μ + jets sample. Therefore, the S/B ratios for the signal region relative to the μ + jets sample are larger by many factors, typically $\gg$10. Figure 89 (d) shows the ratio of $\text{S/B}_{\text{signal}}$ over $\text{S/B}_{\text{-+jets}}$ as a function of the event category and H_{T} bin.

Figure 90 characterises the level of signal contamination in the μ + jets control sample for the benchmark model `T1tttt` ($m_{Gluino} = 1500$ GeV, $m_{LSP} = 100$ GeV). A larger level of contamination is expected for this model (with respect to `T2tt`), due to the presence of four W bosons produced in the decay of the gluino-pair system (via off-shell top squarks). The ratio of yields in the signal and μ + jets control regions is at the level of $\sim$10–20% for the most sensitive categories (i.e. with four or more jets, two or more b-tagged jets, and at high H_{T}). The ratio of S/B values for the signal region relative to the μ + jets sample is still large, typically $\gg$10.

DRAFT

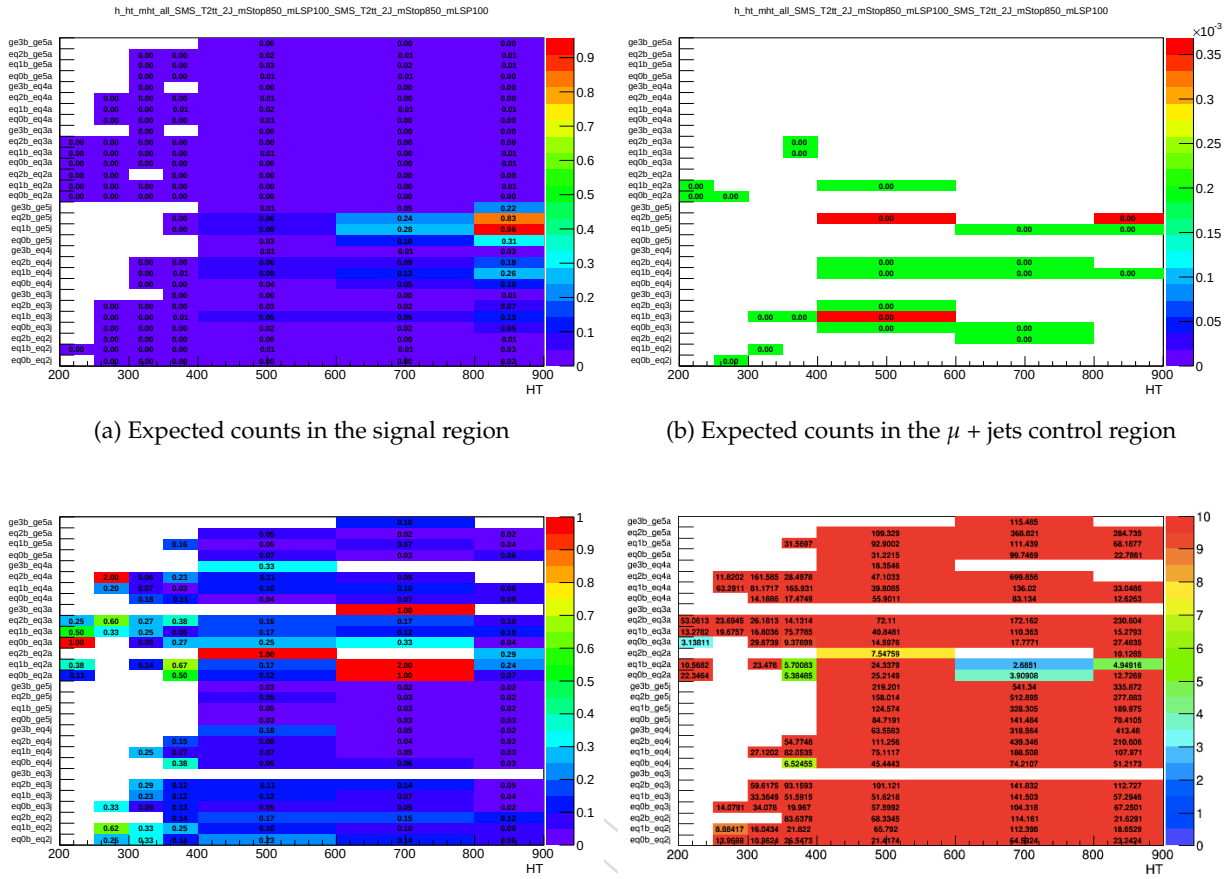

(a) Expected counts in the signal region

(b) Expected counts in the μ + jets control region

(c) Ratio of signal acceptance (μ + jets control region w.r.t. signal region)

(d) Ratio of S/B values (signal region w.r.t. μ + jets)

Figure 89: Characterisation of signal acceptance and contamination in the signal and μ + jets control regions, respectively, for the benchmark model `T2tt` (850,100).

For both models (and in general), the level of contamination for the $\mu\mu$ + jets sample is smaller still due to the requirement of a second muon. The contamination for the γ + jets sample is expected to be zero for the models under consideration.

Finally, the potential for signal contamination in all control samples is fully accounted for in the likelihood model used to extract information on sensitivity to any given signal model.

16.3 Systematic uncertainties on signal efficiency times acceptance

For these results the same systematic uncertainty on the signal yield as in the previous Run 1 analysis is assumed [5]. The following sources of uncertainty were considered: luminosity, parton distribution functions, jet energy scale, initial state radiation, efficiencies of the $H_{\mathrm{T}}^{\mathrm{miss}}/E_{\mathrm{T}}^{\mathrm{miss}}$ filter and "dead ECAL" filter. Each contribution is considered to be independent and all contributions are summed in quadrature.

The uncertainty applied is 30% for all the mass point in the vicinity of the "diagonal", i.e. where $m_{Gluino} - m_{LSP} < m_{top}$, and 15% for all the other points. The systematic is taken as fully correlated across all the bins (see Sec. 14). The uncorrelated approach has been checked to give very similar results.

No uncertainty for the signal $\not{H}_{\mathrm{T}}$ template is considered in these results, but dedicated studies

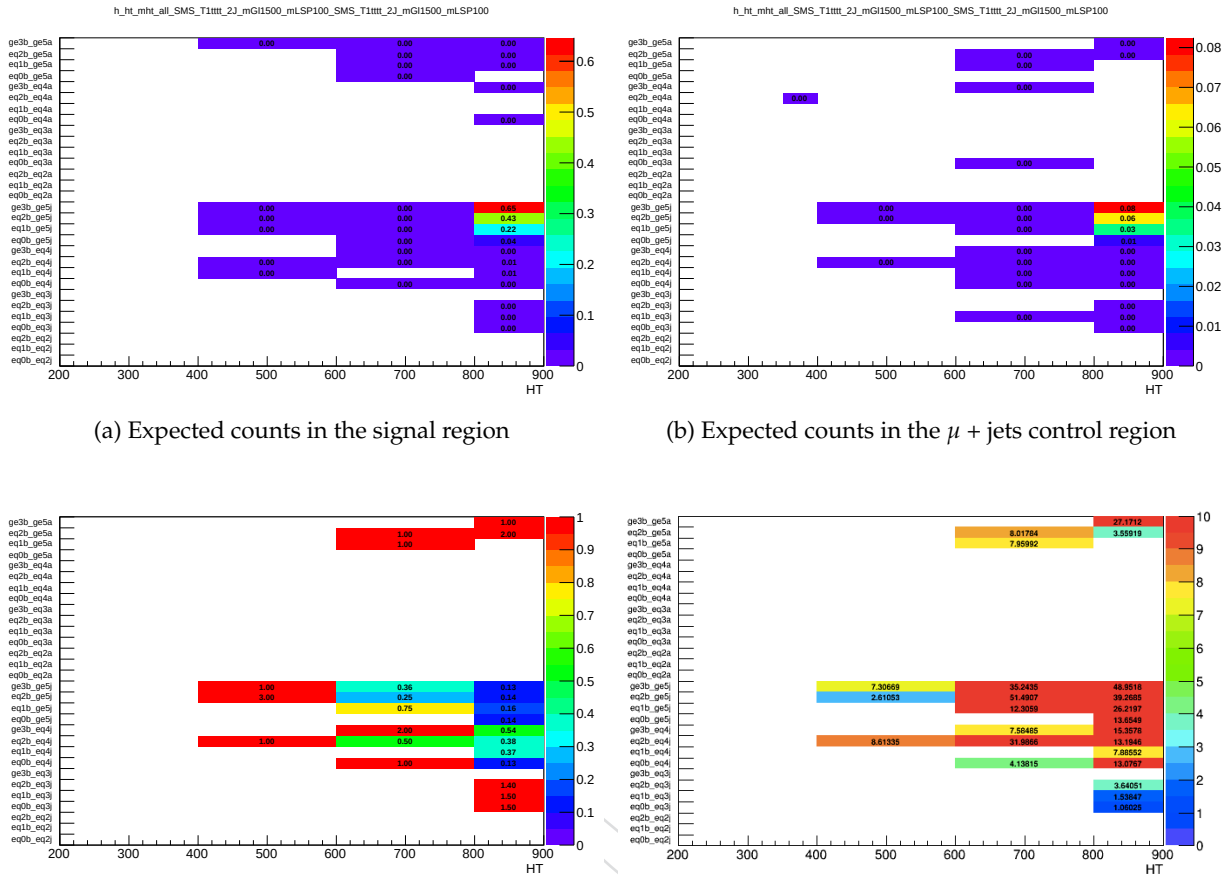

(a) Expected counts in the signal region

(b) Expected counts in the μ + jets control region

(c) Ratio of signal acceptance (signal region w.r.t. μ + jets)

(d) Ratio of S/B values (signal region w.r.t. μ + jets)

Figure 90: Characterisation of signal acceptance and contamination in the signal and μ + jets control regions, respectively, for the benchmark model `T1tttt` (1500,100).

will be carried on in the future about this.

16.4 Expected exclusion limits and discovery significance

In order to extract the signal contribution in the fit, the distribution of events according to the $H_{\mathrm{T}}^{\mathrm{miss}}$ variable, encoded as template histograms, is used as described in Sec. 7.4 and 14.
Upper limits on the cross section and discovery significance are computed using the asymptotic formulae and the pre-fit Asimov datasets [28]. The upper limits are computed using the CL_s criterion [29].
All the statistical results are produced using the *combine* tool, provided within the HiggsAnalysis-CombinedLimit package [30].

In Figure 91 and 92 the expected upper limits on the cross section and the signal strength $\mu = \sigma/\sigma_{\mathrm{theory}}$ are shown for 1.26 fb^{-1} of integrated luminosity, in the (m_{Gluino}, m_{LSP}) plane, for the `T1bbbb` model. The exclusion contour is also shown together with $\pm 1\sigma$ uncertainty (dashed lines) from the expected limit.

Figure 91: 95% C.L. expected (solid black line) oberved (solid red line) upper limit on the cross section for the `T1bbbb` model.

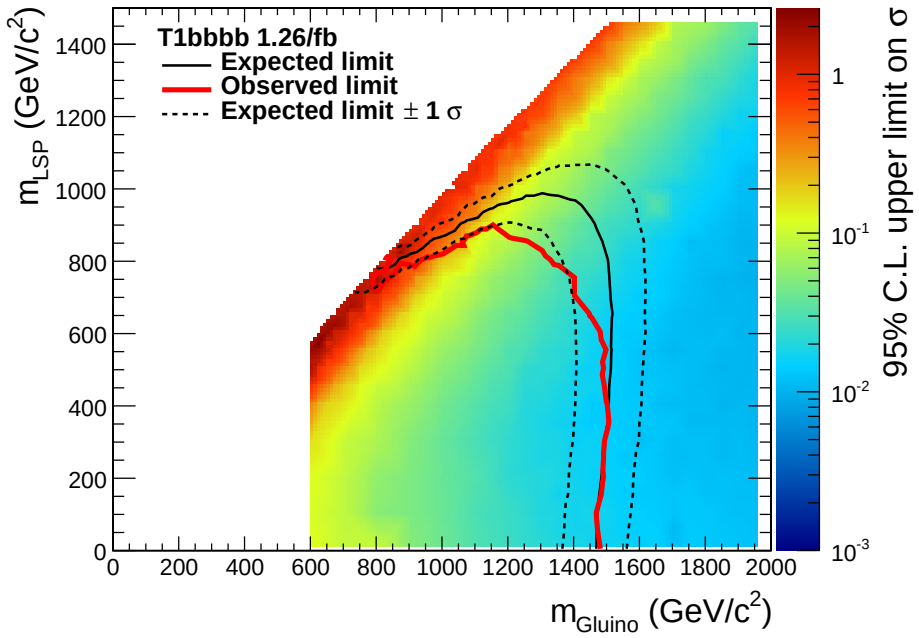

Figure 92: 95% C.L. expected (solid black line) oberved (solid red line) upper limit on the signal strength for the `T1bbbb` model.

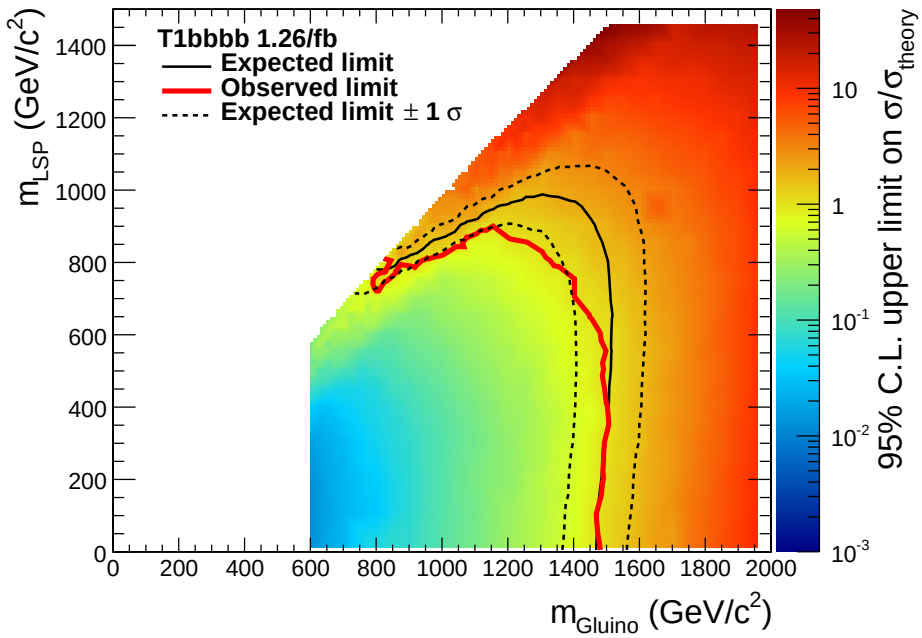

17 Interpretation in Dark Matter models

In Run 1, the results of the α_T analysis were interpreted in the context of supersymmetric simplified models. For Run 2, significant effort has been invested in extending the analysis strategy to include searches for the production of dark matter, namely the inclusion of the asymmetric and monojet categories.

The generic signature of dark matter pair production in colliders is missing transverse momentum from the dark matter along with recoiling energetic visible particles that are used to trigger the event. First analyses used contact operators [31] in effective field theories (EFTs) with various coupling structures to interpret dark matter searches. Experimental limits using monojet final states have been published using 7 and 8 TeV LHC data [9, 32] for a variety of operators.

The lack of predictive information and severe validity constraints of EFTs have lead to the development of improved minimal simplified dark matter (MSDM) models. These models enable the comparison between different experimental searches in a relatively model-independent way [33].

The α_T analysis is sensitive to DM production in association with both light (g, u, d, c, s) and heavy flavoured (b, t) jets. In this section we present the expected sensitivity of the analysis to these topologies with 2 fb^{-1} of 13 TeV data. The simplified models considered in the interpretations are those recommended by the ATLAS-CMS DM Forum for early LHC Run 2 searches. We have utilised all available Spring15 samples of the corresponding models that were available at the time of writing. These samples populate key regions of the M_Φ-m_χ mass plane, and correspond roughly to those shown in Tab. 54.

m_{DM}	m_Φ									
1	10	20	50	100	200	300	500	1000	2000	10000
10	10	15	50	100						10000
50	10		50	95	200	300				10000
150	10				200	295	500	1000		10000
500	10						500	995		10000
1000	10							1000	1995	10000

Table 54: Benchmark dark matter and mediator masses. The parameter space follows the DM Forum recommendations [7]. Points are chosen roughly equidistant on a logarithmic scale. Points on the on-shell diagonal are always chosen to be 5 GeV away from the threshold to avoid numerical instabilities in the event generation.

17.1 Light flavour models

The light flavour simplified models consist of a DM particle χ of mass m_χ that is a Dirac fermion, and a spin-1 (vector or axial-vector) or spin-0 (scalar or pseudoscalar) mediating particle Φ of mass M_Φ in an s-channel. The couplings of the mediator with the standard model and dark matter particles are given by g_{SM} and g_{DM}, respectively. The recommendations by the DM Forum on the choice of couplings is $g_{SM} = 1$,$g_{DM} = 1$ for (pseudo)scalar models, and $g_{SM} = 0.25$,$g_{DM} = 1$ for (axial-)vector models. Assuming that no additional visible or invisible particles contribute to the decay of the mediator, we impose the minimal width determined by the choice of couplings. An example Feynman diagram is shown in Fig. 93.

Assuming 2 fb^{-1} of data we list the cross sections, yields and selection efficiencies for the four light jet models in Tables 55-58. The signal selection efficiencies are around $\sim$ 1% for mass

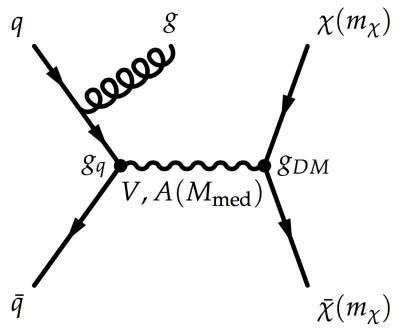

Figure 93: Representative Feynman diagram showing the pair production of Dark Matter particles in association with a parton from the initial state via a vector or axial-vector mediator. The cross section and kinematics depend upon the mediator and Dark Matter masses, and the mediator couplings to Dark Matter and quarks respectively: (m_Φ, m_{DM}, g_{DM}, g_{SM}). [7]

points near the expected exclusion region, and are correspondingly larger (smaller) for higher (lower) mass points. The asymmetric and monojet categories are seen to almost double the acceptance to these models compared to the Run 1 symmetric categories alone, justifying the inclusion of these selections into the analysis.

DRAFT

m_ϕ	m_χ	σ [pb]	Yield (sym)	Yield (asy)	Yield (mon)	Efficiency [%]
10000	100	2.51e-03	0.07	0.02	0.04	1.38
10000	150	2.24e-03	0.07	0.02	0.04	1.56
10000	50	2.84e-03	0.06	0.02	0.03	1.10
1000	100	4.11e+01	1107.27	279.91	565.94	1.35
1000	150	4.02e+01	1147.46	287.23	603.26	1.43
1000	50	4.57e+01	1272.87	302.50	699.23	1.39
100	100	1.19e+03	8588.02	2411.80	4604.37	0.36
100	10	9.79e+04	87537.01	29383.31	40665.66	0.04
100	50	2.96e+04	45100.19	13667.83	25859.11	0.08
2000	100	2.70e+00	115.24	31.42	57.52	2.14
200	100	3.71e+03	19511.17	4393.45	11959.69	0.26
200	10	1.25e+04	48534.78	13502.52	25570.36	0.19
200	150	4.18e+02	5561.86	1298.57	3156.65	0.67
200	1	1.31e+04	56454.39	17681.43	28950.18	0.22
200	50	1.09e+04	44088.03	11850.36	24632.48	0.20
20	1	6.38e+06	72483.61	0.00	0.00	0.00
300	100	2.44e+03	19720.73	4445.89	11576.49	0.40
300	10	3.54e+03	29071.13	6856.89	16700.41	0.41
300	150	9.46e+02	8744.02	2265.54	4810.24	0.46
300	50	3.27e+03	26866.17	6843.17	14620.56	0.41
500	100	4.86e+02	7380.17	1893.05	4192.51	0.76
500	10	5.88e+02	9061.43	2347.71	4872.11	0.77
500	150	3.98e+02	6360.90	1761.40	3418.34	0.80
500	1	5.91e+02	10385.84	2800.08	5636.24	0.88
500	50	5.42e+02	8462.85	2268.04	4672.87	0.78
50	10	6.10e+05	47859.40	28684.06	14400.69	0.00
50	1	6.61e+05	121202.87	34849.16	61463.90	0.01
50	50	1.01e+04	28974.34	8068.27	14747.42	0.14

Table 55: Cross section, yields at 2 fb^{-1} (split according to symmetric, asymmetric, and monojet categories), and total selection efficiency for the vector light jet samples.

DRAFT

m_ϕ	m_χ	σ [pb]	Yield (sym)	Yield (asy)	Yield (mon)	Efficiency [%]
10000	10	2.91e-03	0.07	0.02	0.04	1.17
10000	1	2.88e-03	0.07	0.02	0.04	1.26
10000	50	2.54e-03	0.08	0.02	0.04	1.49
1000	10	4.83e+01	1178.17	289.85	629.83	1.22
1000	1	4.95e+01	1142.25	289.22	594.70	1.15
1000	50	4.46e+01	1131.30	264.21	618.53	1.27
100	100	4.11e+02	4384.24	1050.68	2357.71	0.53
100	1	1.00e+05	101995.59	36805.44	52340.20	0.05
100	50	8.00e+03	23369.91	7118.13	12993.94	0.15
2000	100	2.46e+00	79.13	21.02	41.54	1.61
2000	150	2.10e+00	74.72	19.70	37.32	1.78
2000	1	3.06e+00	92.42	22.76	49.06	1.51
200	10	1.23e+04	51056.48	11985.12	29218.46	0.21
200	1	1.31e+04	52831.74	14467.39	30866.86	0.20
200	50	7.21e+03	35890.11	9161.42	19359.67	0.25
20	10	4.58e+05	93914.10	12513.71	53173.72	0.01
20	1	6.44e+06	103204.94	34447.50	68757.44	0.00
300	100	1.22e+03	13105.43	3878.97	7016.05	0.54
300	10	3.59e+03	27848.92	6970.75	15647.50	0.39
300	150	2.49e+02	3286.71	842.69	1723.61	0.66
300	1	3.68e+03	26982.67	6253.03	15556.70	0.37
300	50	2.68e+03	25546.89	6264.67	14470.72	0.48
500	100	3.83e+02	6791.40	1719.08	3706.41	0.89
500	10	6.32e+02	8883.82	2245.14	5025.72	0.70
500	150	2.41e+02	4093.84	1057.36	2238.78	0.85
500	1	6.37e+02	8864.53	2393.54	4694.17	0.70
500	50	5.32e+02	7954.51	2031.11	4428.90	0.75
50	10	4.70e+05	111414.74	29186.42	71315.44	0.01
50	1	6.79e+05	116310.63	15959.55	31470.40	0.01
50	50	3.74e+03	13222.86	4101.89	7254.64	0.18

Table 56: Cross section, yields at 2 fb^{-1} (split according to symmetric, asymmetric, and monojet categories), and total selection efficiency for the axial-vector light jet samples.

m_ϕ	m_χ	σ [pb]	Yield (sym)	Yield (asy)	Yield (mon)	Efficiency [%]
10000	1000	6.76e-09	0.00	0.00	0.00	2.37
10000	10	2.34e-06	0.00	0.00	0.00	0.77
10000	150	1.34e-06	0.00	0.00	0.00	0.96
10000	1	2.36e-06	0.00	0.00	0.00	0.74
10000	500	1.08e-07	0.00	0.00	0.00	1.86
10000	50	2.18e-06	0.00	0.00	0.00	0.80
1000	1000	1.62e-06	0.00	0.00	0.00	2.26
1000	100	1.84e-01	4.12	1.31	1.63	1.12
1000	10	1.93e-01	4.26	1.34	1.64	1.10
1000	150	1.68e-01	3.64	1.15	1.40	1.08
1000	1	1.97e-01	4.32	1.37	1.75	1.09
1000	500	2.58e-03	0.07	0.02	0.03	1.34
1000	50	1.94e-01	4.32	1.32	1.68	1.12
100	100	3.30e-01	3.11	1.06	1.35	0.47
100	10	1.14e+02	294.71	96.97	135.89	0.13
100	1	1.14e+02	278.07	84.60	127.56	0.12
100	50	2.04e+00	10.42	3.64	4.41	0.26
10	10	9.95e+00	22.29	7.23	11.13	0.11
10	1	1.16e+03	288.78	78.95	144.23	0.01
2000	1000	1.99e-05	0.00	0.00	0.00	2.09
2000	100	2.92e-03	0.09	0.03	0.03	1.47
2000	10	3.26e-03	0.09	0.03	0.03	1.37
2000	150	2.61e-03	0.08	0.02	0.03	1.50
2000	1	3.27e-03	0.09	0.03	0.03	1.37
2000	500	1.16e-03	0.04	0.01	0.02	1.92
2000	50	3.17e-03	0.09	0.03	0.03	1.38
200	100	8.18e-01	6.41	2.17	2.82	0.39
200	10	3.95e+01	224.49	80.00	96.19	0.28
200	150	1.70e-01	1.74	0.56	0.74	0.51
200	1	3.18e+01	184.12	52.35	83.96	0.29
200	50	3.95e+01	230.66	77.79	99.61	0.29
20	10	1.21e+01	18.21	4.73	8.66	0.08
20	1	7.18e+02	356.47	114.30	161.44	0.02
300	100	2.32e+01	184.25	62.45	80.01	0.40
300	10	2.32e+01	182.25	68.25	69.57	0.39
300	150	4.86e-01	4.67	1.60	1.86	0.48
300	1	2.32e+01	177.75	61.74	76.83	0.38
300	50	2.32e+01	182.55	61.69	81.21	0.39
5000	1000	3.29e-07	0.00	0.00	0.00	2.51
5000	100	3.02e-05	0.00	0.00	0.00	0.92
5000	10	3.94e-05	0.00	0.00	0.00	0.88
5000	150	2.24e-05	0.00	0.00	0.00	1.04
5000	1	3.94e-05	0.00	0.00	0.00	0.83
5000	500	2.41e-06	0.00	0.00	0.00	1.88
5000	50	3.72e-05	0.00	0.00	0.00	0.85
500	100	6.69e+00	75.12	25.53	29.27	0.56
500	10	7.47e+00	80.43	26.31	35.17	0.54
500	150	5.56e+00	62.20	19.33	25.65	0.56
500	1	7.47e+00	85.57	28.03	35.46	0.57
500	500	3.02e-04	0.01	0.00	0.00	1.50
500	50	7.31e+00	81.16	26.37	33.22	0.56
50	10	2.87e+02	313.26	93.83	148.50	0.05
50	1	2.87e+02	323.54	111.81	157.05	0.06

Table 57: Cross section, yields at 2 fb^{-1} (split according to symmetric, asymmetric, and monojet categories), and total selection efficiency for the scalar light jet samples.

DRAFT

m_ϕ	m_χ	σ [pb]	Yield (sym)	Yield (asy)	Yield (mon)	Efficiency [%]
10000	1000	2.10e-08	0.00	0.00	0.00	2.24
10000	100	3.96e-06	0.00	0.00	0.00	0.72
10000	10	4.67e-06	0.00	0.00	0.00	0.64
10000	150	3.22e-06	0.00	0.00	0.00	0.74
10000	1	4.63e-06	0.00	0.00	0.00	0.66
10000	500	1.08e-07	0.00	0.00	0.00	1.66
10000	50	2.18e-06	0.00	0.00	0.00	0.71
1000	1000	7.80e-06	0.00	0.00	0.00	2.15
1000	100	1.84e-01	3.94	1.27	1.54	1.07
1000	10	1.93e-01	4.06	1.25	1.67	1.05
1000	150	1.68e-01	3.83	1.16	1.54	1.14
1000	1	2.63e-01	5.53	1.78	1.99	1.05
1000	500	2.96e-02	0.78	0.24	0.30	1.32
1000	50	2.60e-01	5.72	1.74	2.23	1.10
100	100	1.62e+00	12.88	4.11	5.70	0.40
100	10	2.62e+02	676.41	213.23	330.76	0.13
100	50	1.42e+01	57.23	19.60	25.49	0.20
10	10	3.38e+01	52.31	14.44	27.99	0.08
10	1	2.60e+03	827.02	266.30	472.02	0.02
2000	1000	2.28e-04	0.01	0.00	0.00	2.08
2000	10	3.26e-03	0.07	0.02	0.03	1.13
2000	150	4.11e-03	0.11	0.03	0.04	1.33
2000	1	4.73e-03	0.11	0.03	0.04	1.19
2000	500	1.82e-03	0.07	0.02	0.02	1.89
2000	50	4.97e-03	0.12	0.04	0.05	1.23
200	100	8.18e+00	53.78	15.53	26.28	0.33
200	10	9.75e+01	552.80	211.74	227.97	0.28
200	150	1.11e+00	10.14	3.38	4.21	0.46
200	1	9.73e+01	536.96	169.39	233.85	0.28
200	50	9.72e+01	553.89	189.81	249.17	0.28
20	10	4.58e+01	53.54	18.58	22.37	0.06
20	1	1.63e+03	823.78	289.11	320.64	0.03
300	100	5.89e+01	449.12	144.04	201.64	0.38
300	10	7.13e+01	533.38	181.83	236.09	0.37
300	150	7.94e+00	62.63	19.97	29.00	0.39
300	50	7.00e+01	547.25	177.13	230.49	0.39
5000	1000	7.22e-07	0.00	0.00	0.00	2.36
5000	100	6.52e-05	0.00	0.00	0.00	0.82
5000	10	7.49e-05	0.00	0.00	0.00	0.72
5000	150	5.19e-05	0.00	0.00	0.00	0.81
5000	1	7.72e-05	0.00	0.00	0.00	0.71
5000	500	5.43e-06	0.00	0.00	0.00	1.79
5000	50	7.26e-05	0.00	0.00	0.00	0.73
500	100	1.07e+01	124.52	40.85	51.93	0.58
500	10	1.12e+01	132.84	42.34	55.86	0.59
500	150	9.58e+00	119.05	38.76	49.58	0.62
500	1	1.12e+01	135.25	43.16	54.49	0.60
500	500	1.26e-03	0.04	0.01	0.01	1.41
500	50	1.10e+01	123.75	42.31	51.14	0.56
50	10	6.47e+02	763.59	232.39	335.07	0.06
50	1	6.44e+02	747.59	190.96	360.59	0.06
50	50	4.15e+00	22.18	6.97	10.22	0.27

Table 58: Cross section, yields at 2 fb^{-1} (split according to symmetric, asymmetric, and monojet categories), and total selection efficiency for the pseudo-scalar light jet samples.

DRAFT

17.1.1 Projected sensitivities

The expected 95% CL signal strength limits at an integrated luminosity of 2 fb^{-1} for the available samples of the four light jet simplified dark matter models are presented in Tables 59-62.

Figures 94 and 95 show the corresponding interpolated axial-vector and pseudoscalar expected exclusion contours in the M_{Φ}-m_{χ} mass plane.

Tables 63-66 summarise the most sensitive (n_{jet},n_{b},H_{T},$H_{\mathrm{T}}^{\mathrm{miss}}$) signal region bins for a representative mass point (near the exclusion boundary) of each light jet model. As expected, the sensitivity for these models mostly lies at low jet multiplicities, low-medium H_{T}, and at $H_{\mathrm{T}}^{\mathrm{miss}}$ values close to the upper bound of the relevant H_{T} bin Note that the $H_{\mathrm{T}}^{\mathrm{miss}}$ dimension is not utilised within the monojet category. Also note that, for convenience, all signal models have been normalised to a cross section of 10 pb in these tables.

DRAFT

Table 59: 95% CL upper limits on the signal strength at 2 fb^{-1} for the light jet vector samples

m_{DM} (GeV) \ M_{Med} (GeV)	20	50	100	200	300	500	1000	2000	10000
150				0.05	0.03	0.04	0.21		3.43e+03
100			0.02	0.01	0.01	0.04	0.24	2.11	3.53e+03
50		0.01	0.00	0.00	0.01	0.03	0.21		4.19e+03
10		0.00	0.00	0.00	0.01	0.03			
1	0.00	0.00		0.00		0.02			

Table 60: 95% CL upper limits on the signal strength at 2 fb^{-1} for the light jet axial-vector samples

m_{DM} (GeV) \ M_{Med} (GeV)	20	50	100	200	300	500	1000	2000	10000
150					0.07	0.06		3.42	
100			0.06		0.02	0.04		3.06	
50		0.01	0.01	0.01	0.01	0.03	0.23		3.34e+03
10	0.00	0.00		0.00	0.01	0.03	0.21		3.51e+03
1	0.00	0.00	0.00	0.00	0.01	0.03	0.21	2.64	3.30e+03

DRAFT

Table 61: 95% CL upper limits on the signal strength at 2 fb^{-1} for the light jet scalar samples

m_{DM} (GeV) \ M_{Med} (GeV)	10	20	50	100	200	300	500	1000	2000	5000	10000
1000								2.78e+06	2.36e+05	1.22e+07	6.10e+08
500							2.47e+04	3.26e+03	4.71e+03	2.26e+06	5.45e+07
150					135.70	45.48	3.55	59.73	2.83e+03	4.83e+05	8.25e+06
100				68.91	29.33	1.06	2.90	55.46	2.58e+03	3.89e+05	
50				18.76	0.73	1.14	2.53	54.65	2.40e+03	2.74e+05	6.28e+06
10	3.88	7.64	0.43	0.61	0.85	1.11	2.63	49.11	2.29e+03	3.04e+05	5.55e+06
1	0.46	0.31	0.54	0.59	1.04	1.19	2.56	52.82	2.45e+03	3.26e+05	6.08e+06

Table 62: 95% CL upper limits on the signal strength at 2 fb^{-1} for the light jet pseudo-scalar samples

m_{DM} (GeV) \ M_{Med} (GeV)	10	20	50	100	200	300	500	1000	2000	5000	10000
1000								5.94e+05	2.10e+04	5.82e+06	2.07e+08
500							6.05e+03	283.29	3.06e+03	1.09e+06	6.17e+07
150					20.13	3.45	1.85	57.64	2.00e+03	2.46e+05	4.52e+06
100				15.59	4.03	0.49	1.76	56.73		2.03e+05	3.80e+06
50			9.59	2.99	0.33	0.37	1.79	40.73	1.71e+03	1.38e+05	7.27e+06
10	2.90	2.80	0.18	0.25	0.36	0.38	1.68	55.98	2.88e+03	2.12e+05	3.56e+06
1	0.15	0.13	0.19		0.38		1.70	39.95	1.81e+03	2.03e+05	3.80e+06

DRAFT

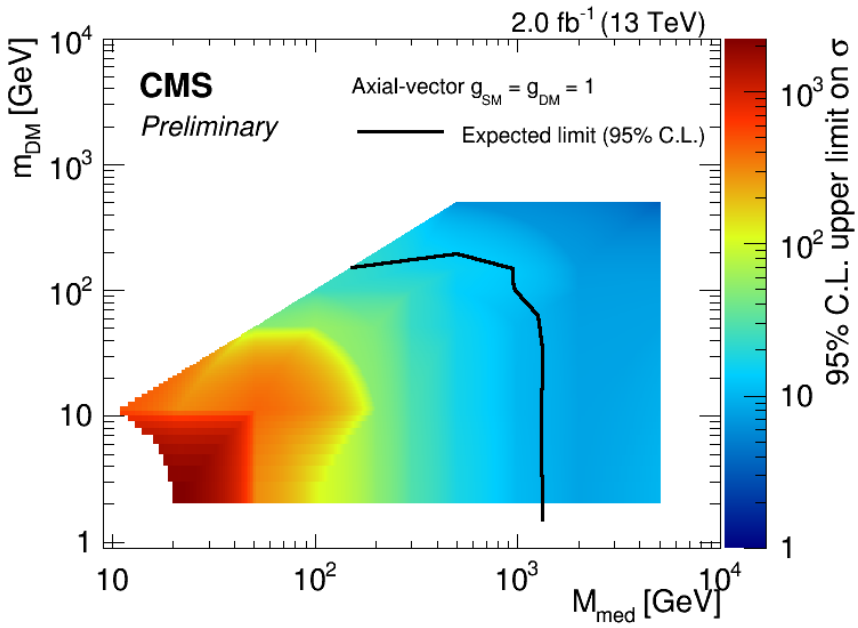

Figure 94: Expected 95% CL upper limit on the cross section, and exclusion contour for the axial-vector light flavour model with unity couplings at 2 fb^{-1}.

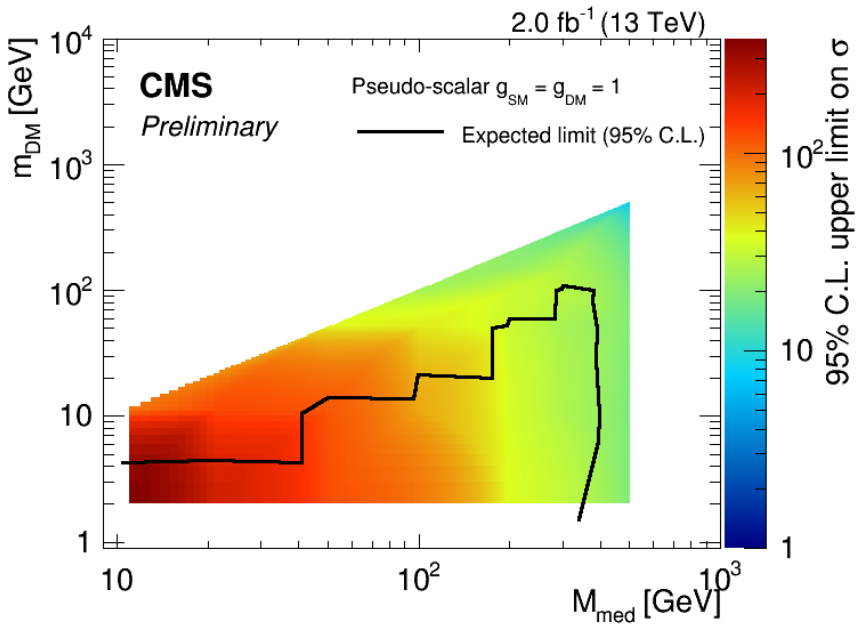

Figure 95: Expected 95% CL upper limit on the cross section, and exclusion contour for the pseudoscalar light flavour model with unity couplings at 2 fb^{-1}.

Table 63: Background and signal yields, and signal significance for a vector light jet model point

Vector Mphi-1000 Mchi-50 gSM-1p0 gDM-1p0	bgTtw	bgZinv	Signal	Significance
htBin 250-300 cat eq1j eq0b mht 0	36.75	205.88	31.90	0.42
htBin 300-350 cat eq1j eq0b mht 0	16.52	118.02	18.35	0.42
htBin 250-300 cat eq2a eq0b mht 250	15.77	51.84	8.99	0.38
htBin 250-300 cat eq3a eq0b mht 225	7.59	23.80	3.84	0.33
htBin 250-300 cat eq3j eq0b mht 0	2.80	7.88	1.59	0.29

DRAFT

Table 64: Background and signal yields, and signal significance for an axial-vector light jet model point

Axial Mphi-1000 Mchi-50 gSM-1p0 gDM-1p0	bgTtw	bgZinv	Signal	Significance
htBin 300-350 cat eq1j eq0b mht 0	16.52	118.02	15.93	0.37
htBin 250-300 cat eq1j eq0b mht 0	36.75	205.88	28.19	0.37
htBin 250-300 cat eq2j eq0b mht 200	11.97	37.94	5.28	0.31
htBin 200-250 cat eq1j eq0b mht 0	102.20	480.39	46.04	0.26
htBin 200-250 cat eq2a eq0b mht 225	13.86	42.53	5.41	0.25

Table 65: Background and signal yields, and signal significance for a scalar light jet model point

Scalar Mphi-100 Mchi-10 gSM-1p0 gDM-1p0	bgTtw	bgZinv	Signal	Significance
htBin 200-250 cat eq2a eq0b mht 225	13.86	42.53	1.08	0.03
htBin 200-250 cat eq2a eq0b mht 175	48.97	128.23	1.90	0.03
htBin 200-250 cat eq2a eq1b mht 225	1.89	3.02	0.18	0.03
htBin 200-250 cat eq1j eq0b mht 0	102.20	480.39	6.39	0.03
htBin 350-400 cat ge5a eq0b mht 0	2.01	5.92	0.09	0.02

DRAFT

Table 66: Background and signal yields, and signal significance for a pseudoscalar light jet model point

Pseudoscalar Mphi-100 Mchi-10 gSM-1p0 gDM-1p0	bgTtw	bgZinv	Signal	Significance
htBin 200-250 cat eq3a eq0b mht 175	12.68	33.18	1.18	0.07
htBin 250-300 cat eq3a eq0b mht 225	7.59	23.80	0.63	0.06
htBin 200-250 cat eq1j eq0b mht 0	102.20	480.39	7.66	0.04
htBin 200-250 cat eq2a eq2b mht 175	1.07	0.87	0.09	0.04
htBin 200-250 cat eq2a eq0b mht 225	13.86	42.53	0.63	0.03

17.2 Heavy flavour models

Owing to the principal of Minimal Flavor Violation (MFV), top and bottom quarks can play important roles in the phenomenology of dark matter. Scalar and pseudoscalar models predict not only the 'monojet' processes described in Sec. 17.1 but also the production of dark matter in association with top (or bottom) pairs. This results in signatures with relatively large jet multiplicities, in particular for DM+$t\bar{t}$ production. The α_{T} analysis is well suited to searching for such signatures. An example Feynman diagram for the pair production of dark matter particles in association with pairs of heavy quarks is shown in Fig. 96.

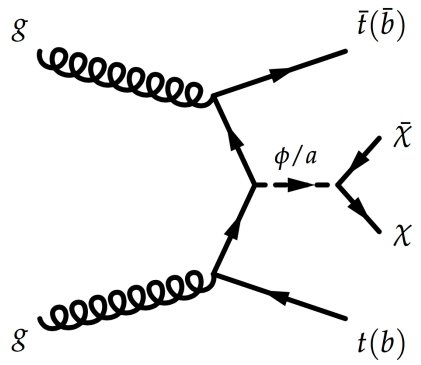

Figure 96: Feynman diagram of the pair production of Dark Matter particles in association with $t\bar{t}$ or $b\bar{b}$. [7]

The cross sections, signal yields and efficiencies for scalar and pseudoscalar DM+$t\bar{t}$ models expected with 2 fb^{-1} of data are shown in Tables 67 and 68. The selection efficiencies for these models are around $\sim$ 10%, and the improvement provided by the new asymmetric and monojet categories is again evident.

DRAFT

m_ϕ	m_χ	σ [pb]	Yield (sym)	Yield (asy)	Yield (mon)	Efficiency [%]
100	10	6.73e-01	36.36	8.16	17.63	2.70
10	10	9.49e-02	2.38	0.55	1.22	1.25
50	10	2.94e+00	72.01	18.32	36.53	1.22
200	150	1.30e-04	0.03	0.01	0.02	13.16
500	150	3.75e-03	1.02	0.15	0.48	13.55
1000	1	3.69e-04	0.12	0.02	0.06	15.79
100	1	6.72e-01	35.88	7.42	18.04	2.67
10	1	1.96e+01	146.33	43.66	65.49	0.37
200	1	9.33e-02	13.54	2.34	6.68	7.26
20	1	1.05e+01	116.24	34.16	54.99	0.55
300	1	2.95e-02	6.33	1.02	3.09	10.72
500	1	5.18e-03	1.38	0.23	0.66	13.34
50	1	2.94e+00	69.98	16.63	33.60	1.19
500	500	9.89e-07	0.00	0.00	0.00	17.51
200	50	9.22e-02	13.73	2.45	6.47	7.44
300	50	2.90e-02	6.49	1.04	3.13	11.19
50	50	2.33e-03	0.29	0.06	0.14	6.29

Table 67: Cross section, yields at 2 fb^{-1} (split according to symmetric, asymmetric, and monojet categories), and total selection efficiency for the scalar DM+$t\bar{t}$ samples.

m_ϕ	m_χ	σ [pb]	Yield (sym)	Yield (asy)	Yield (mon)	Efficiency [%]
100	10	1.90e-01	26.97	5.48	12.82	7.09
10	10	1.50e-02	1.88	0.39	0.94	6.28
50	10	3.03e-01	34.57	8.15	16.40	5.70
200	150	4.12e-04	0.10	0.02	0.05	12.39
500	150	4.61e-03	1.22	0.21	0.60	13.18
100	1	1.91e-01	27.59	6.00	12.71	7.23
10	1	4.41e-01	37.69	7.87	18.60	4.27
200	1	8.36e-02	15.86	3.26	7.69	9.48
20	1	3.99e-01	36.36	8.59	17.64	4.55
300	1	4.00e-02	8.74	1.63	4.21	10.93
500	1	5.41e-03	1.39	0.24	0.66	12.87
50	1	3.03e-01	35.23	7.97	17.00	5.81
500	500	3.27e-06	0.00	0.00	0.00	17.14
200	50	8.38e-02	15.95	3.33	7.67	9.51
300	50	3.99e-02	8.60	1.61	4.19	10.78
50	50	2.98e-03	0.54	0.10	0.26	9.04

Table 68: Cross section, yields at 2 fb^{-1} (split according to symmetric, asymmetric, and monojet categories), and total selection efficiency for the pseudo-scalar DM+$t\bar{t}$ samples.

DRAFT

17.2.1 Projected sensitivities

The expected 95% CL signal strength limits for simplified DM+$t\bar{t}$ models with scalar and pseudo-scalar couplings are calculated for 2 fb^{-1}. These are shown in Tables 69 and 70. At this integrated luminosity, the sensitivity approaches scalar mediator masses of up to 100 GeV and DM masses of about 10 GeV, whereas it is insufficient to significantly exclude the pseudoscalar model, which has generally smaller cross sections.

Figure 97 shows the interpolated scalar expected exclusion contour in the M_Φ-m_χ mass plane.

Tables 71 and 72 summarise the most sensitive (n_{jet},n_{b},H_{T},$H_{\text{T}}^{\text{miss}}$) signal region bins for a representative mass point (near the exclusion boundary) of each DM+$t\bar{t}$ model. As expected, the sensitivity for these models mostly lies at large jet and b-jet multiplicities, medium-high H_{T}, and at $H_{\text{T}}^{\text{miss}}$ values closer to the lower bound of the relevant H_{T} bin. Note that, for convenience, all signal models have been normalised to a cross section of 10 pb in these tables.

DRAFT

Table 69: 95% CL upper limits on the signal strength at 2 fb^{-1} for the scalar DM+$t\bar{t}$ samples

m_{DM} (GeV) \ M_{Med} (GeV)	10	20	50	100	200	300	500	1000
500							9.38e+04	
150					1.16e+03		40.32	
50			153.05		3.33	6.90		
10	16.01		0.53	1.17				
1	0.25	0.33	0.54	1.29	3.40	7.12	31.11	331.08

Table 70: 95% CL upper limits on the signal strength at 2 fb^{-1} for the pseudo-scalar DM+$t\bar{t}$ samples

m_{DM} (GeV) \ M_{Med} (GeV)	10	20	50	100	200	300	500
500							2.83e+04
150					414.40		32.83
50			80.31		2.74	5.02	
10	23.13		1.27	1.67			
1	1.16	1.21	1.24	1.56	2.75	4.76	29.80

DRAFT

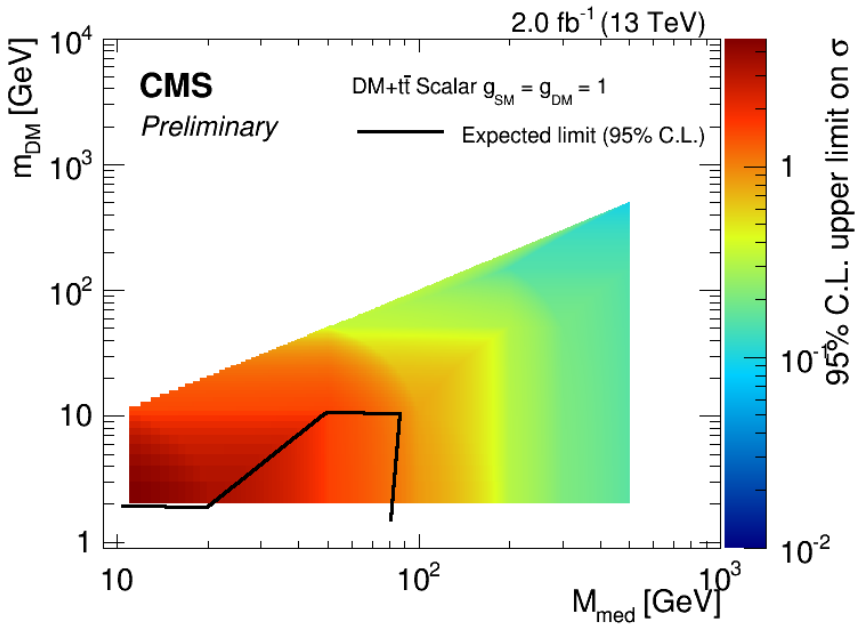

Figure 97: Expected 95% CL upper limit on the cross section, and exclusion contour for the scalar DM+$t\bar{t}$ model with unity couplings at 2 fb^{-1}.

Table 71: Background and signal yields, and signal significance for a scalar DM+$t\bar{t}$ model point

TTbarDMJets scalar Mchi-10 Mphi-100 25ns mht	bgTtw	bgZinv	Signal	Significance
htBin 400-500 cat ge5a eq2b mht 0	0.65	0.69	11.76	7.88
htBin 400-500 cat ge5a eq1b mht 150	1.77	2.77	15.81	6.12
htBin 300-350 cat eq4a eq1b mht 175	2.53	2.24	13.79	5.10
htBin 400-500 cat ge5j eq1b mht 150	1.69	3.89	14.60	5.00
htBin 350-400 cat ge5a eq2b mht 0	0.53	0.23	6.89	4.67

DRAFT

Table 72: Background and signal yields, and signal significance for a pseudoscalar DM+$t\bar{t}$ jet model point

TTbarDMJets pseudoscalar Mchi-10 Mphi-100 25ns mht	bgTtw	bgZinv	Signal	Significance
htBin 500-600 cat ge5j eq2b mht 225	0.39	1.03	28.23	18.36
htBin 350-400 cat ge5a eq1b mht 0	1.23	1.12	30.25	16.90
htBin 400-500 cat ge5a eq1b mht 150	1.77	2.77	42.35	16.42
htBin 400-500 cat ge5a eq2b mht 0	0.65	0.69	23.80	15.98
htBin 400-500 cat ge5j eq2b mht 150	0.69	0.67	24.60	15.88

18 Summary

We report on the prospects for a missing energy plus jet search that is sensitive to models of Supersymmetry and Dark Matter. The analysis follows an inclusive approach designed to capture a wide scope of possible final states, use of robust methods to be insensitive to multijet production, instrumental effects and MC mis-modelling. Thus making it ideal for early data discoveries. The Run 1 analysis has been improved in several areas, including an increase in the acceptance of the signal region and an optimisation of the signal event categorisation. By relaxing the minimal jet multiplicity to a single jet and adding a orthogonal jet selection with a lower p_{T} requirement on the second leading jet. This leads to significantly improved acceptance to compressed SUSY and Dark Matter models.

Candidate signal events are binned according to the number of reconstructed jets, the number of jets identified to originate from bottom quarks, and the scalar and vector sums of the transverse energy of jets. The sum of standard model backgrounds per bin is estimated from a simultaneous binned likelihood fit to event yields in the signal region and μ + jets, $\mu\mu$ + jets, and γ + jets control samples. The analysis relies heavily on methods and cross-checks derived from the data control samples to demonstrate control of the SM background predictions.

Preliminary projections are presented for SUSY and DM simplified models using currently recoreded $\sqrt{s} = 13$ TeV data and projections assuming 3fb^{-1} of data.

DRAFT

References

[1] CMS Collaboration, "Search for Supersymmetry in pp Collisions at 7 TeV in Events with Jets and Missing Transverse Energy", *Phys.Lett.* **B698** (2011) 196–218, doi:10.1016/j.physletb.2011.03.021, arXiv:1101.1628.

[2] CMS Collaboration, "Search for Supersymmetry at the LHC in Events with Jets and Missing Transverse Energy", *Phys.Rev.Lett.* **107** (2011) 221804, doi:10.1103/PhysRevLett.107.221804, arXiv:1109.2352.

[3] CMS Collaboration, "Search for supersymmetry in final states with missing transverse energy and 0, 1, 2, or at least 3 b-quark jets in 7 TeV pp collisions using the variable alphaT", *JHEP* **1301** (2013) 077, doi:10.1007/JHEP01(2013)077, arXiv:1210.8115.

[4] CMS Collaboration, "Search for supersymmetry in hadronic final states with missing transverse energy using the variables α_T and b-quark multiplicity in pp collisions at $\sqrt{s} = 8$ TeV", *Eur.Phys.J.* **C73** (2013), no. 9, 2568, doi:10.1140/epjc/s10052-013-2568-6, arXiv:1303.2985.

[5] M. Baber et al., "Search for compressed supersymmetric scenarios in final states with jets and missing transerve momentum in $\sqrt{s} = 8$ TeV pp collisions with the α_{T} variable", CMS Note 2013/366, SUS-14-006, 2013.

[6] J. Olsen, "Introduction and Goals of PHYS14". https://indico.cern.ch/event/356534/contribution/0, December, 2014.

[7] D. Abercrombie et al., "Dark Matter Benchmark Models for Early LHC Run-2 Searches: Report of the ATLAS/CMS Dark Matter Forum", arXiv:1507.00966.

[8] CMS Collaboration, "Search for New Physics with a Mono-Jet and Missing Transverse Energy in *pp* Collisions at $\sqrt{s} = 7$ TeV", *Phys.Rev.Lett.* **107** (2011) 201804, doi:10.1103/PhysRevLett.107.201804, arXiv:1106.4775.

[9] CMS Collaboration, "Search for dark matter and large extra dimensions in monojet events in *pp* collisions at $\sqrt{s} = 7$ TeV", *JHEP* **1209** (2012) 094, doi:10.1007/JHEP09(2012)094, arXiv:1206.5663.

[10] CMS Collaboration, "Search for dark matter, extra dimensions, and unparticles in monojet events in proton-proton collisions at $\sqrt{s} = 8$ TeV", *Eur.Phys.J.* **C75** (2015), no. 5, 235, doi:10.1140/epjc/s10052-015-3451-4, arXiv:1408.3583.

[11] L. Randall and D. Tucker-Smith, "Dijet Searches for Supersymmetry at the LHC", *Phys.Rev.Lett.* **101** (2008) 221803, doi:10.1103/PhysRevLett.101.221803, arXiv:0806.1049.

[12] CMS Collaboration, "SUSY searches with dijet events", Technical Report CMS-PAS-SUS-08-005, CERN, Oct, 2008.

[13] CMS Collaboration, "Search strategy for exclusive multi-jet events from supersymmetry at CMS", Technical Report CMS-PAS-SUS-09-001, CERN, Jul, 2009.

[14] CMS Collaboration, "Pileup Information". https://twiki.cern.ch/twiki/bin/viewauth/CMS/PdmVPileUpDescription.

DRAFT

[15] M. Cacciari, G. P. Salam, and G. Soyez, "The Anti-k(t) jet clustering algorithm", *JHEP* **0804** (2008) 063, doi:10.1088/1126-6708/2008/04/063, arXiv:0802.1189.

[16] CMS Collaboration, "Determination of Jet Energy Calibration and Transverse Momentum Resolution in CMS", *JINST* **6** (2011) P11002, doi:10.1088/1748-0221/6/11/P11002, arXiv:1107.4277.

[17] CMS Collaboration, "Identification of b-quark jets with the CMS experiment", *JINST* **8** (2013) P04013, doi:10.1088/1748-0221/8/04/P04013, arXiv:1211.4462.

[18] CMS Collaboration, "Commissioning of the Particle-Flow reconstruction in Minimum-Bias and Jet Events from pp Collisions at 7 TeV", CMS Physics Analysis Summary CMS-PAS-PFT-10-002, 2010.

[19] CMS Collaboration, "Egamma cut-based photon ID for Run 2". https://twiki.cern.ch/twiki/bin/viewauth/CMS/CutBasedPhotonIdentificationRun2.

[20] CMS Collaboration, "Egamma Particle Flow Based Isolation". https://twiki.cern.ch/twiki/bin/view/CMS/EgammaPFBasedIsolation.

[21] CMS Collaboration, "Egamma cut-based electron ID for Run 2". https://twiki.cern.ch/twiki/bin/viewauth/CMS/CutBasedElectronIdentificationRun2.

[22] CMS Collaboration, "Performance of the CMS missing transverse momentum reconstruction in pp data at $\sqrt{s}$ = 8 TeV", *JINST* **10** (2015), no. 02, P02006, doi:10.1088/1748-0221/10/02/P02006, arXiv:1411.0511.

[23] Z. Bern et al., "Left-Handed W Bosons at the LHC", *Phys. Rev.* **D84** (2011) 034008, doi:10.1103/PhysRevD.84.034008, arXiv:1103.5445.

[24] J. Cohen, P. Cohen, S. G. West, and L. S. Aiken, "Applied multiple regression/correlation analysis for the behavioral sciences". Routledge, 2013.

[25] J. Alwall, P. Schuster, and N. Toro, "Simplified Models for a First Characterization of New Physics at the LHC", *Phys. Rev.* **D79** (2009) 075020, doi:10.1103/PhysRevD.79.075020, arXiv:0810.3921.

[26] J. Alwall, M.-P. Le, M. Lisanti, and J. G. Wacker, "Model-Independent Jets plus Missing Energy Searches", *Phys.Rev.* **D79** (2009) 015005, doi:10.1103/PhysRevD.79.015005, arXiv:0809.3264.

[27] LHC New Physics Working Group Collaboration, "Simplified Models for LHC New Physics Searches", *J.Phys.* **G39** (2012) 105005, doi:10.1088/0954-3899/39/10/105005, arXiv:1105.2838.

[28] G. Cowan, K. Cranmer, E. Gross, and O. Vitells, "Asymptotic formulae for likelihood-based tests of new physics", *Eur.Phys.J.* **C71** (2011) 1554, doi:10.1140/epjc/s10052-011-1554-0, 10.1140/epjc/s10052-013-2501-z, arXiv:1007.1727.

[29] A. L. Read, "Presentation of search results: The CL(s) technique", *J.Phys.* **G28** (2002) 2693–2704, doi:10.1088/0954-3899/28/10/313.

[30] "Higgs Combination Sattistics Tool". https://twiki.cern.ch/twiki/bin/viewauth/CMS/SWGuideHiggsAnalysisCombinedLimit.

DRAFT

[31] J. Goodman et al., "Constraints on Dark Matter from Colliders", *Phys. Rev.* **D82** (2010) 116010, doi:10.1103/PhysRevD.82.116010, arXiv:1008.1783.

[32] ATLAS Collaboration, "Search for dark matter candidates and large extra dimensions in events with a jet and missing transverse momentum with the ATLAS detector", *JHEP* **1304** (2013) 075, doi:10.1007/JHEP04(2013)075, arXiv:1210.4491.

[33] O. Buchmueller, M. J. Dolan, S. A. Malik, and C. McCabe, "Characterising dark matter searches at colliders and direct detection experiments: Vector mediators", *JHEP* **1501** (2015) 037, doi:10.1007/JHEP01(2015)037, arXiv:1407.8257.

DRAFT

A Kinematic distributions for the signal region

This appendix shows distributions of events in the signal region in each H_T bin in each symmetric and asymmetric n_{jet} bin for each process as functions of 7 different variables, i.e., α_T, H_T^{miss}, $\Delta\phi^*_{min}$, E_T^{miss}, the lead jet p_T, the second hardest jet p_T, and n_b.

These distributions are shown in 14 figures from Figs. 98-111. The distributions of each variable are shown in two figures: one for symmetric n_{jet} bins and the other for asymmetric n_{jet} bins. Each figure contains 28 panels, each shows the distribution in the specific H_T bin and n_{jet} bin for all processes. These panels are arranged in 4 columns, for 4 different n_{jet} bins, and 7 rows, for 7 different H_T bins, and share the axes. [4]

In these figures, the event selection for the signal region described in Section 7 and summarised in tables 21, 23, and 24 are applied. As described in Section 7.1, the events in the symmetric n_{jet} bins have the second hardest jet with p_T greater than 100 GeV. The events in the asymmetric n_{jet} bins have the second hardest jet with p_T between 40 and 100 GeV.

From these figures, e.g. the $n_b$distributions in Figs. 110 and 111, it can be seen that many H_T and n_{jet} bins do not contain a multijet event. However, some bins do contain many multijet events. For example, in Fig. 111, the bin for $350 < H_T < 400$ GeV and $n_{jet} = 3$ (the panel in the 4th row from the top and the 2nd column from the left) has many multijet events at $n_b = 0$. The origin of these multijet events will be clearer in distributions shown in very fine bins of a histogram. For example, the panel in the same position in Fig. 103 shows the distribution of the same set of events in very fine bins of $\Delta\phi^*_{min}$. There, all multijet events are in a single bin of $\Delta\phi^*_{min}$. These multijet events correspond to one MC event, weighed by a large cross section of QCD. In Figures 102 and 103, nearly all entries from multijet events are very tall and contained in isolated bins $\Delta\phi^*_{min}$, which indicates that these multijet events correspond a small number of MC events.

Event filters and calibrations in the event reconstruction were still actively developed when MC samples used in this note were generated. We expect that many of these multijet events still we find in the signal region will be removed when these filters or calibrations are well tuned for Run 2 data.

On the other hand, as can be seen in Figure 102, many multijet events reside in slightly above the cut applied on $\Delta\phi^*_{min}$ in the highest H_T and high n_{jet} bins. If these multijet events persist after the filters and calibrations are tuned, they can be removed by raising the value of $\Delta\phi^*_{min}$ cut.

[4] This type of data visualisation is called *Trellis Graphics* (`http://ect.bell-labs.com/sl/project/trellis/wwww.html`), which was originally developed at the Bell Labs in 1990s. Trellis Graphics is particularly useful for examining multivariate categorical data e.g. to find patters or correlations.

DRAFT

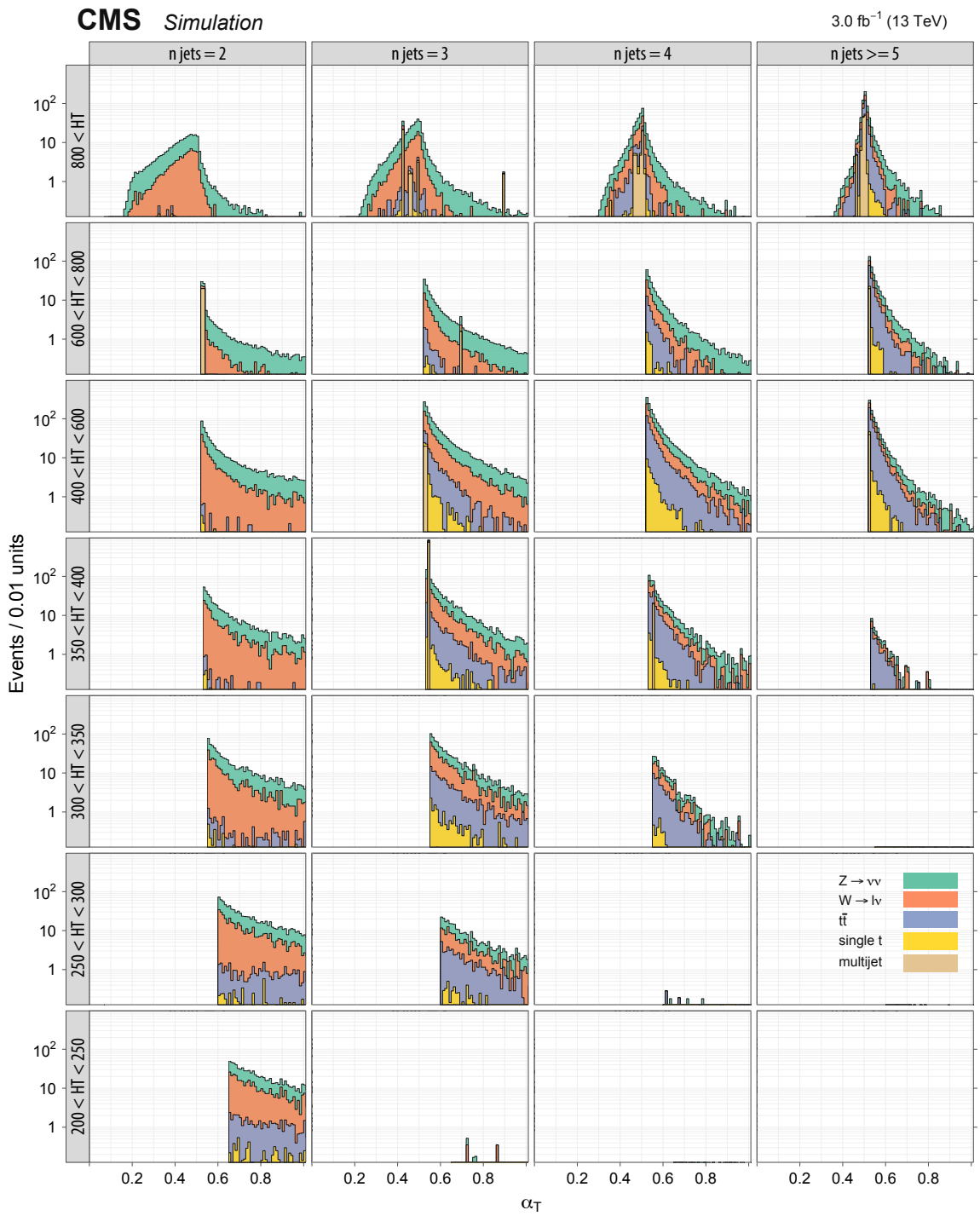

Figure 98: **The α_T distributions, symmetric n_{jet} bins:** The α_T distributions of the events in the signal region in each H_T bin in each symmetric n_{jet} bin for each process. Panels in different rows show events in different H_T bins. Panels in different columns show events in different symmetric n_{jet} bins. Different processes are shown in different colors (or gray scales).

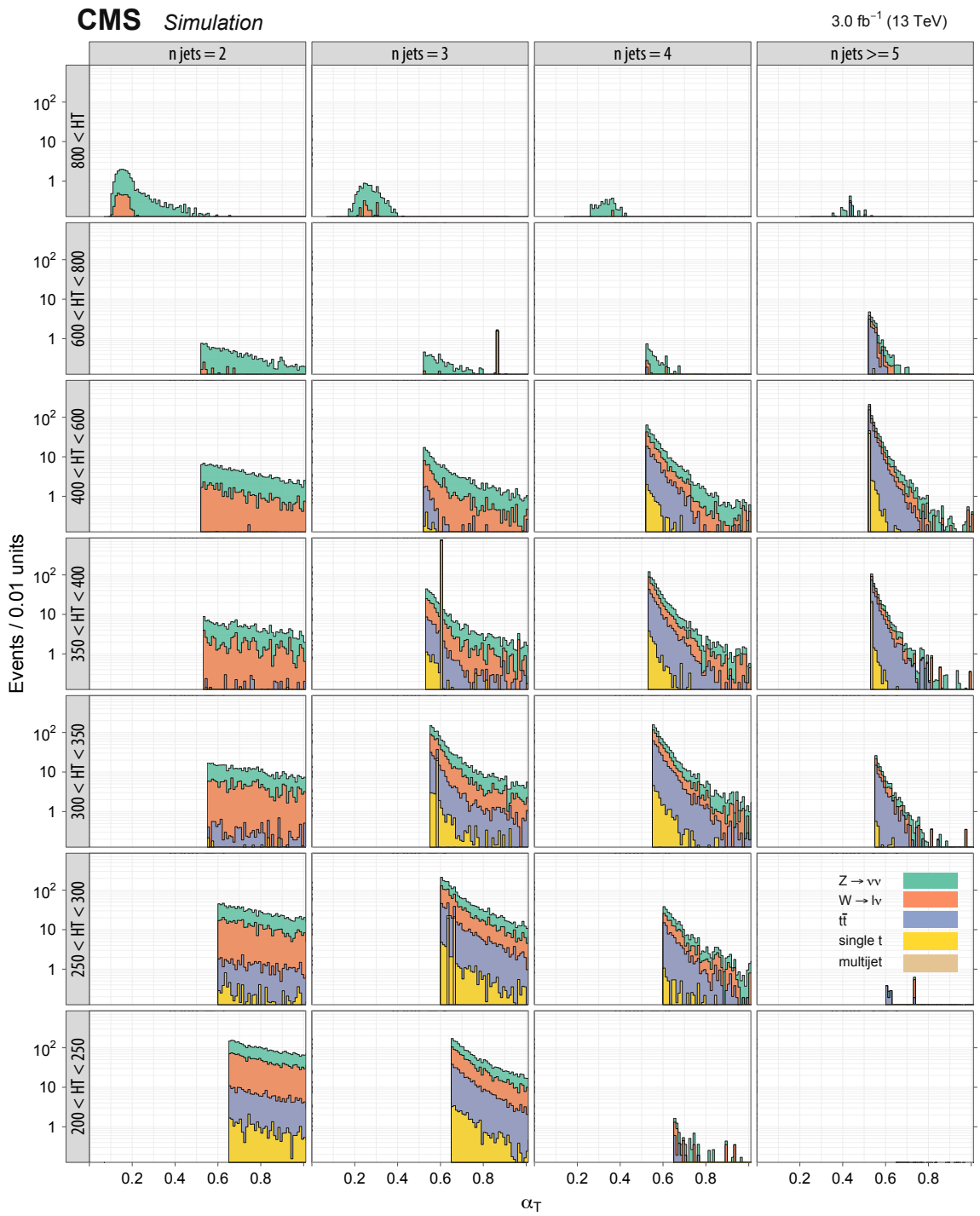

Figure 99: **The α_T distributions, asymmetric n_{jet} bins:** The α_T distributions of the events in the signal region in each H_T bin in each asymmetric n_{jet} bin for each process. Panels in different rows show events in different H_T bins. Panels in different columns show events in different asymmetric n_{jet} bins. Different processes are shown in different colors (or gray scales).

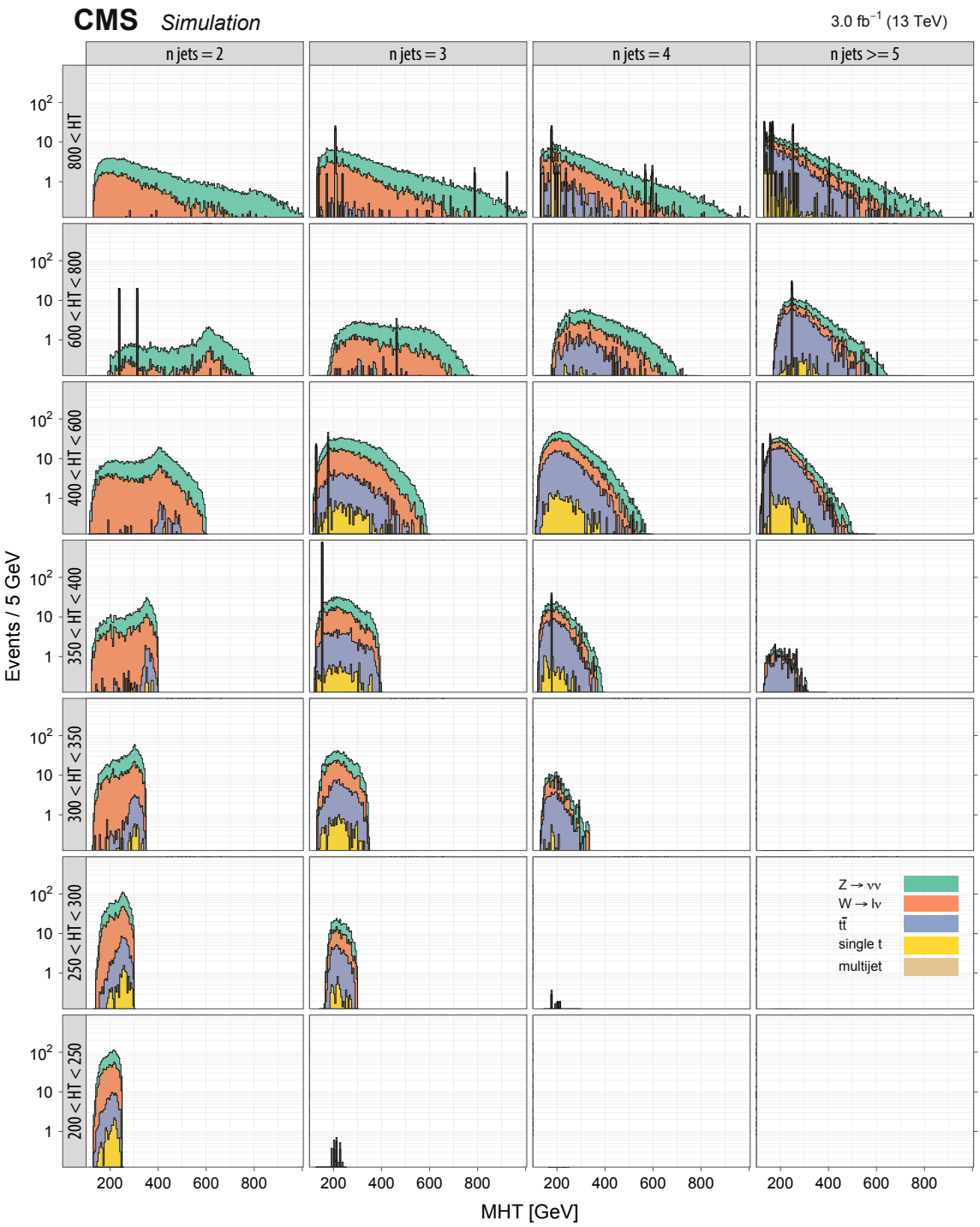

Figure 100: **The H_T^{miss} distributions, symmetric n_{jet} bins:** The H_T^{miss} distributions of the events in the signal region in each H_T bin in each symmetric n_{jet} bin for each process. Panels in different rows show events in different H_T bins. Panels in different columns show events in different symmetric n_{jet} bins. Different processes are shown in different colors (or gray scales).

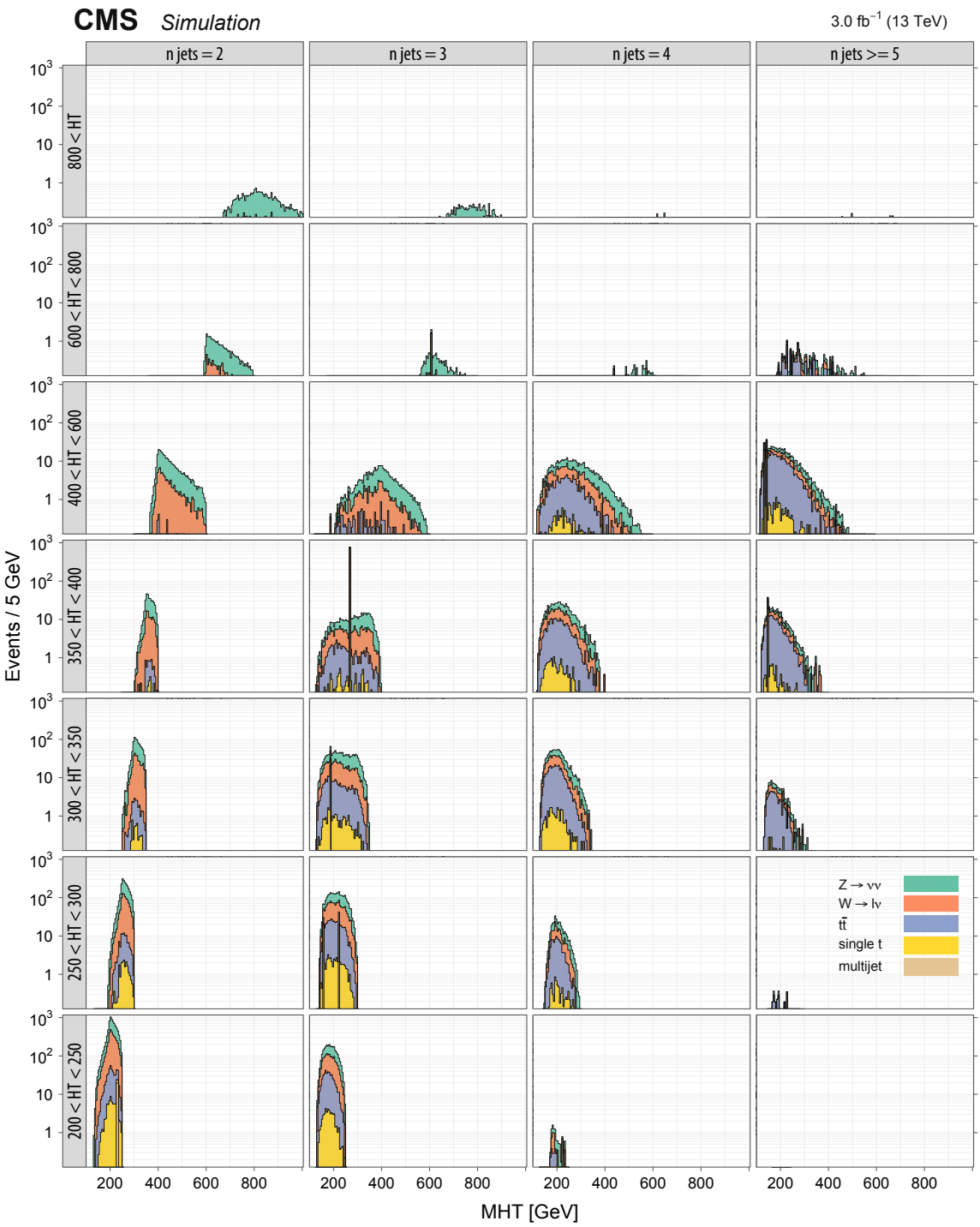

Figure 101: **The H_T^{miss} distributions, asymmetric n_{jet} bins:** The H_T^{miss} distributions of the events in the signal region in each H_T bin in each asymmetric n_{jet} bin for each process. Panels in different rows show events in different H_T bins. Panels in different columns show events in different asymmetric n_{jet} bins. Different processes are shown in different colors (or gray scales).

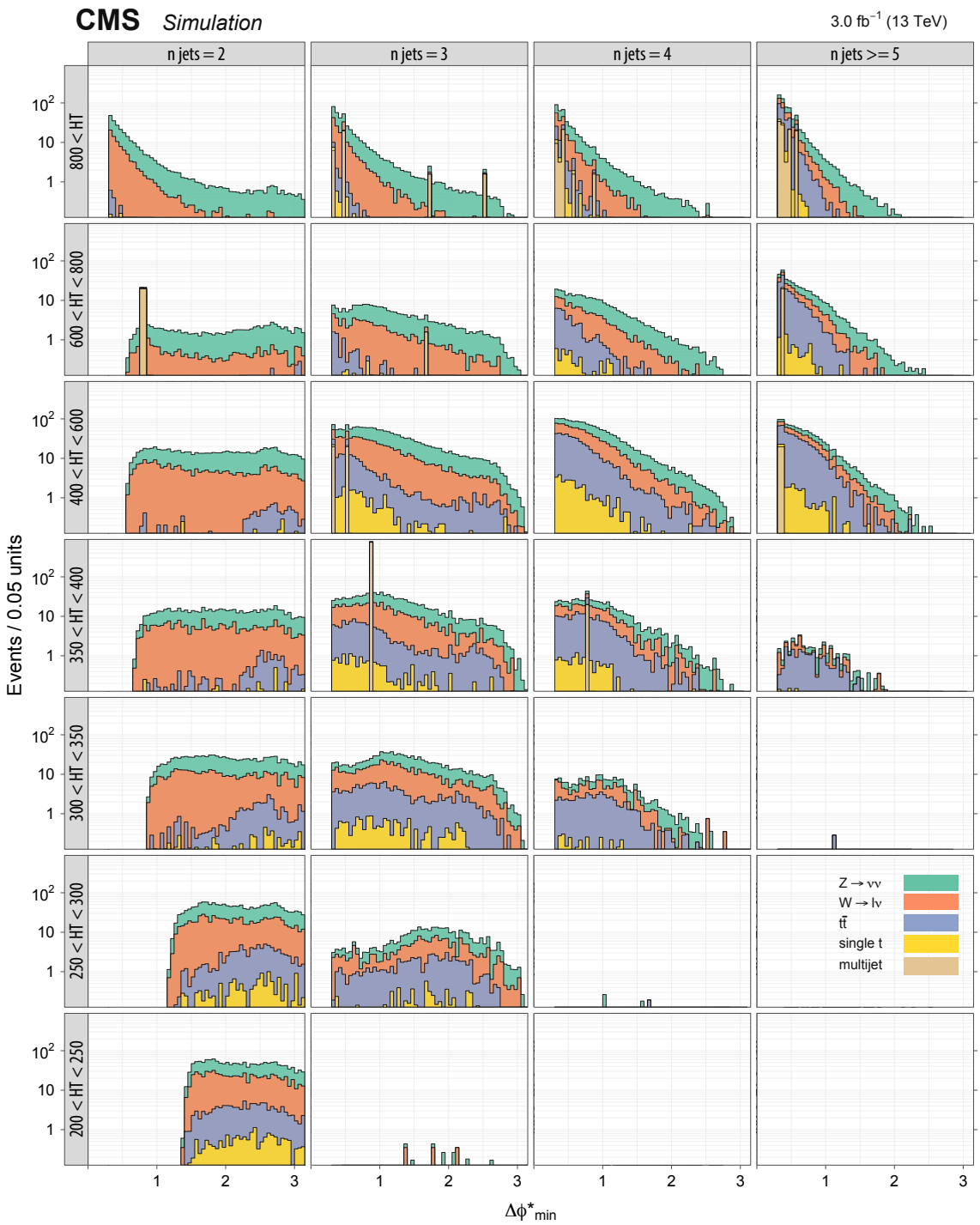

Figure 102: **The $\Delta\phi^*_{\mathrm{min}}$ distributions, symmetric n_{jet} bins:** The $\Delta\phi^*_{\mathrm{min}}$ distributions of the events in the signal region in each H_{T} bin in each symmetric n_{jet} bin for each process. Panels in different rows show events in different H_{T} bins. Panels in different columns show events in different symmetric n_{jet} bins. Different processes are shown in different colors (or gray scales).

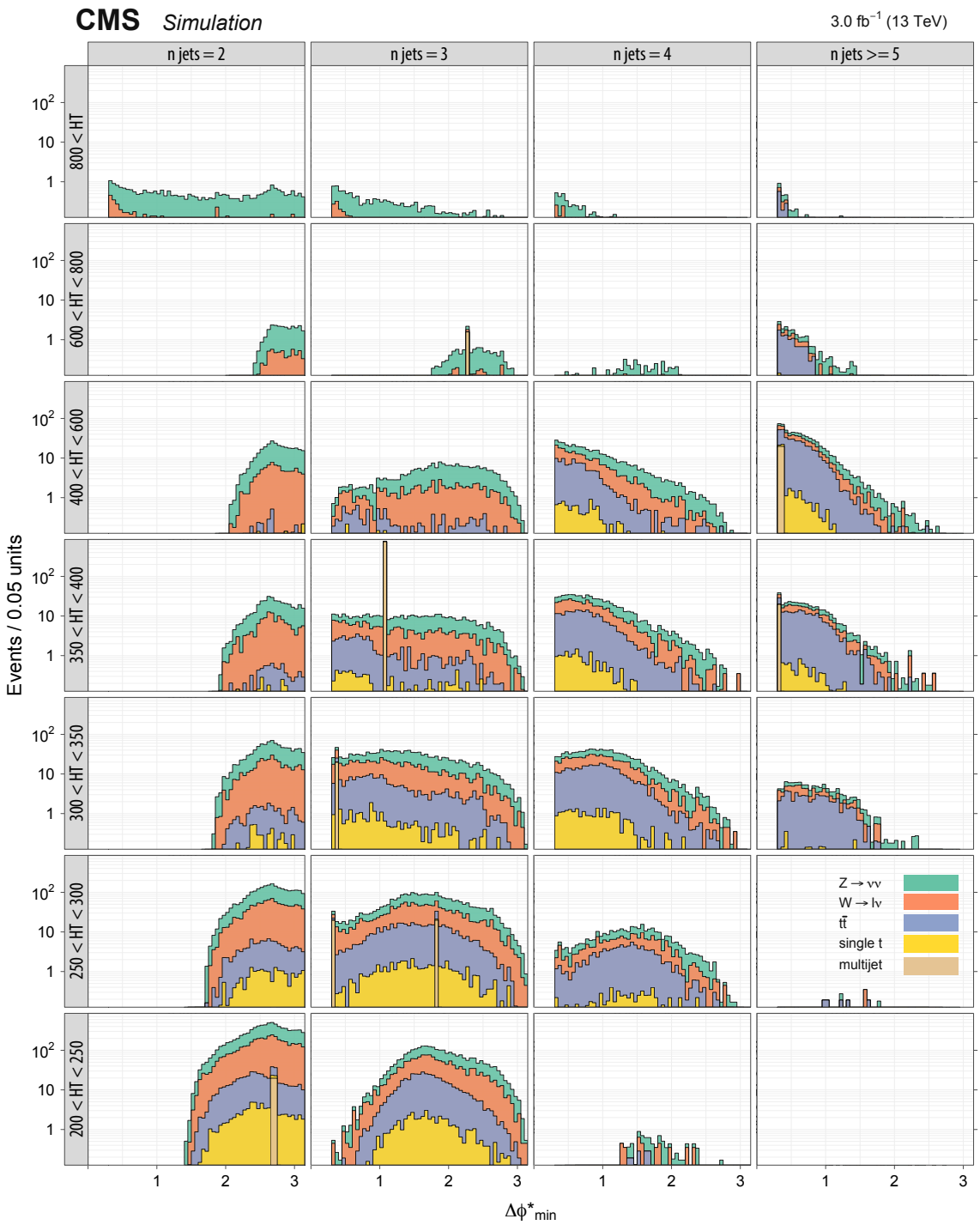

Figure 103: **The $\Delta\phi^*_{\mathrm{min}}$ distributions, asymmetric n_{jet} bins:** The $\Delta\phi^*_{\mathrm{min}}$ distributions of the events in the signal region in each H_{T} bin in each asymmetric n_{jet} bin for each process. Panels in different rows show events in different H_{T} bins. Panels in different columns show events in different asymmetric n_{jet} bins. Different processes are shown in different colors (or gray scales).

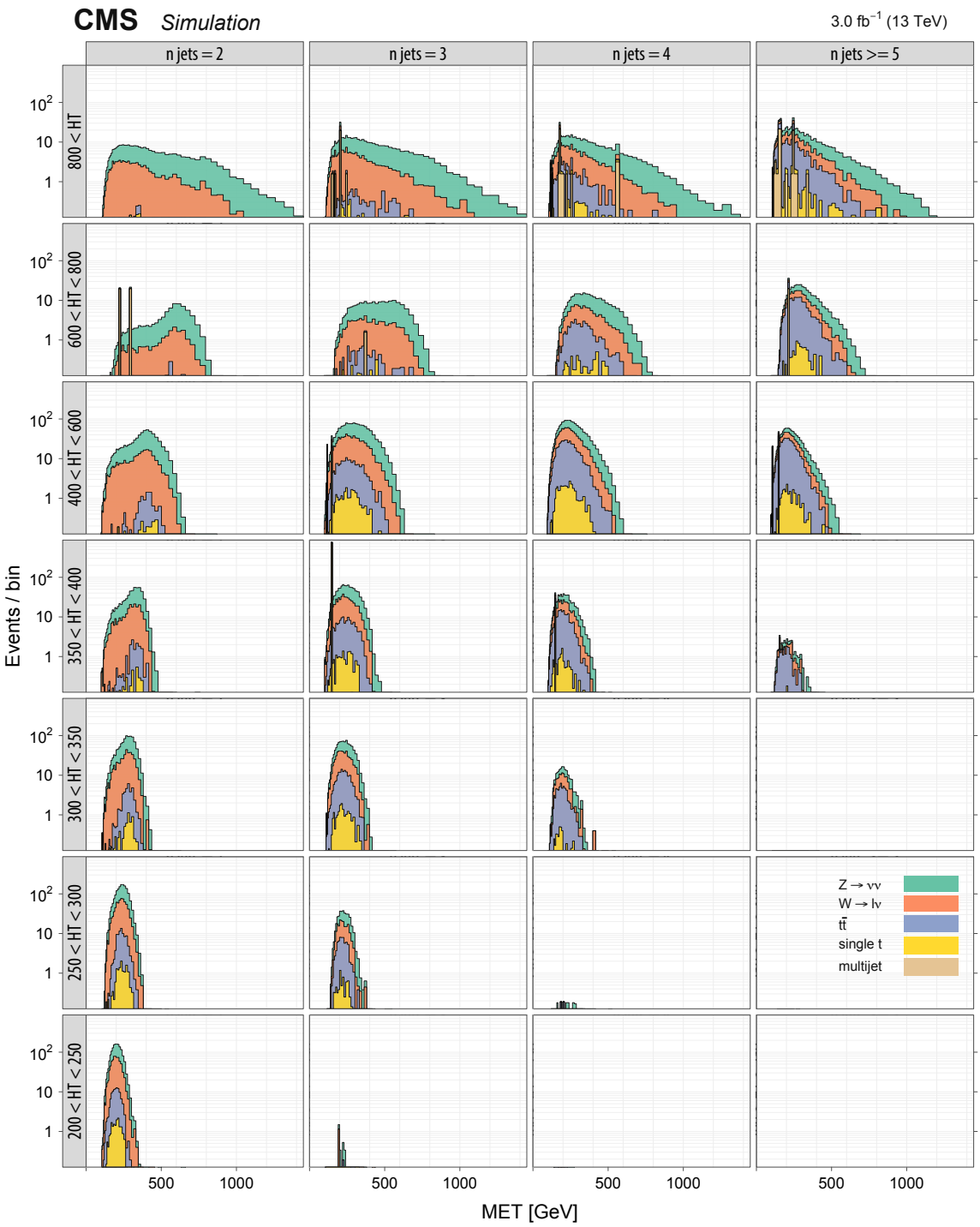

Figure 104: **The E_T^{miss} distributions, symmetric n_{jet} bins:** The E_T^{miss} distributions of the events in the signal region in each H_T bin in each symmetric n_{jet} bin for each process. Panels in different rows show events in different H_T bins. Panels in different columns show events in different symmetric n_{jet} bins. Different processes are shown in different colors (or gray scales).

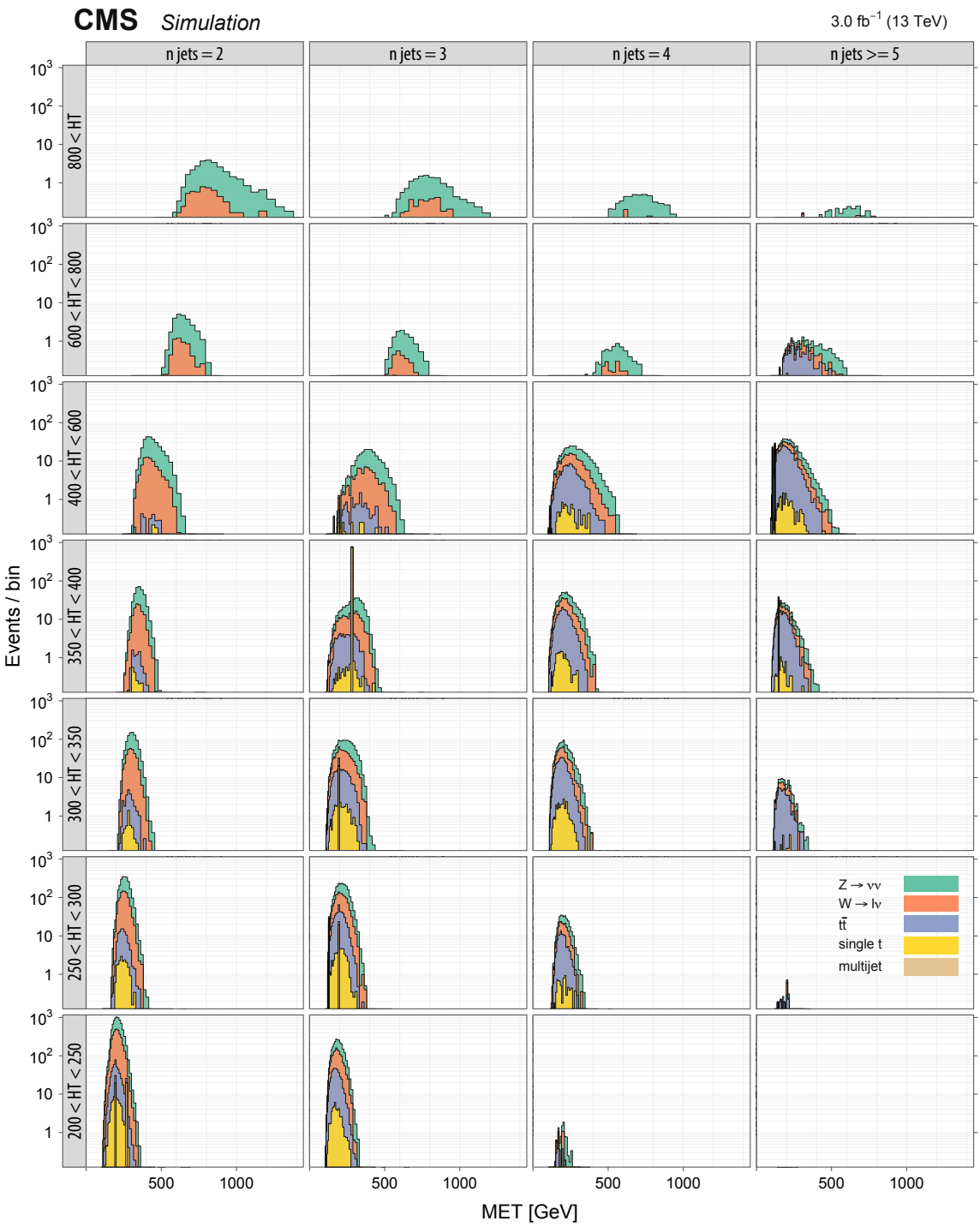

Figure 105: **The E_T^{miss} distributions, asymmetric n_{jet} bins:** The E_T^{miss} distributions of the events in the signal region in each H_T bin in each asymmetric n_{jet} bin for each process. Panels in different rows show events in different H_T bins. Panels in different columns show events in different asymmetric n_{jet} bins. Different processes are shown in different colors (or gray scales).

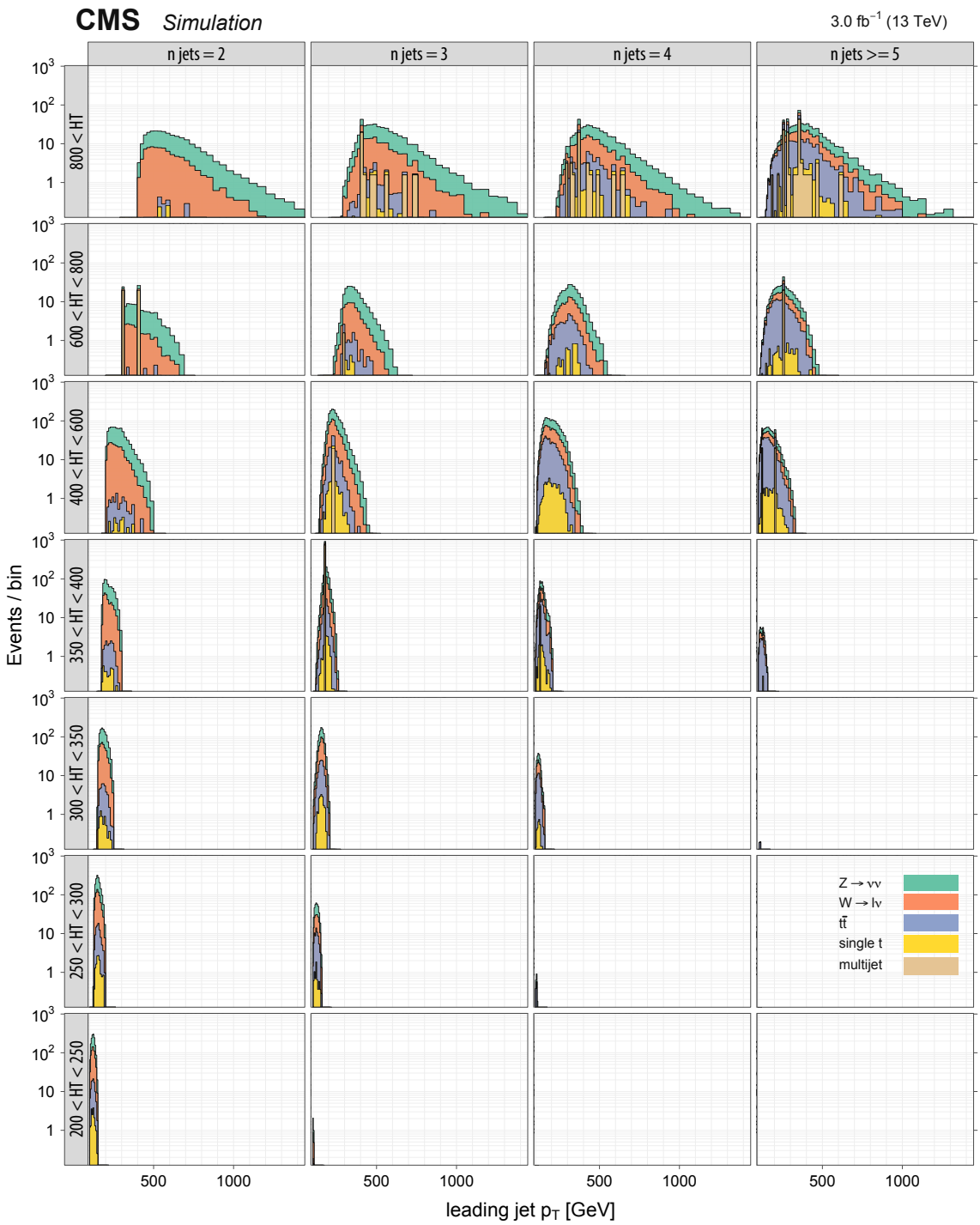

Figure 106: **The lead jet p_T distributions, symmetric n_{jet} bins:** The lead jet p_T distributions of the events in the signal region in each H_T bin in each symmetric n_{jet} bin for each process. Panels in different rows show events in different H_T bins. Panels in different columns show events in different symmetric n_{jet} bins. Different processes are shown in different colors (or gray scales).

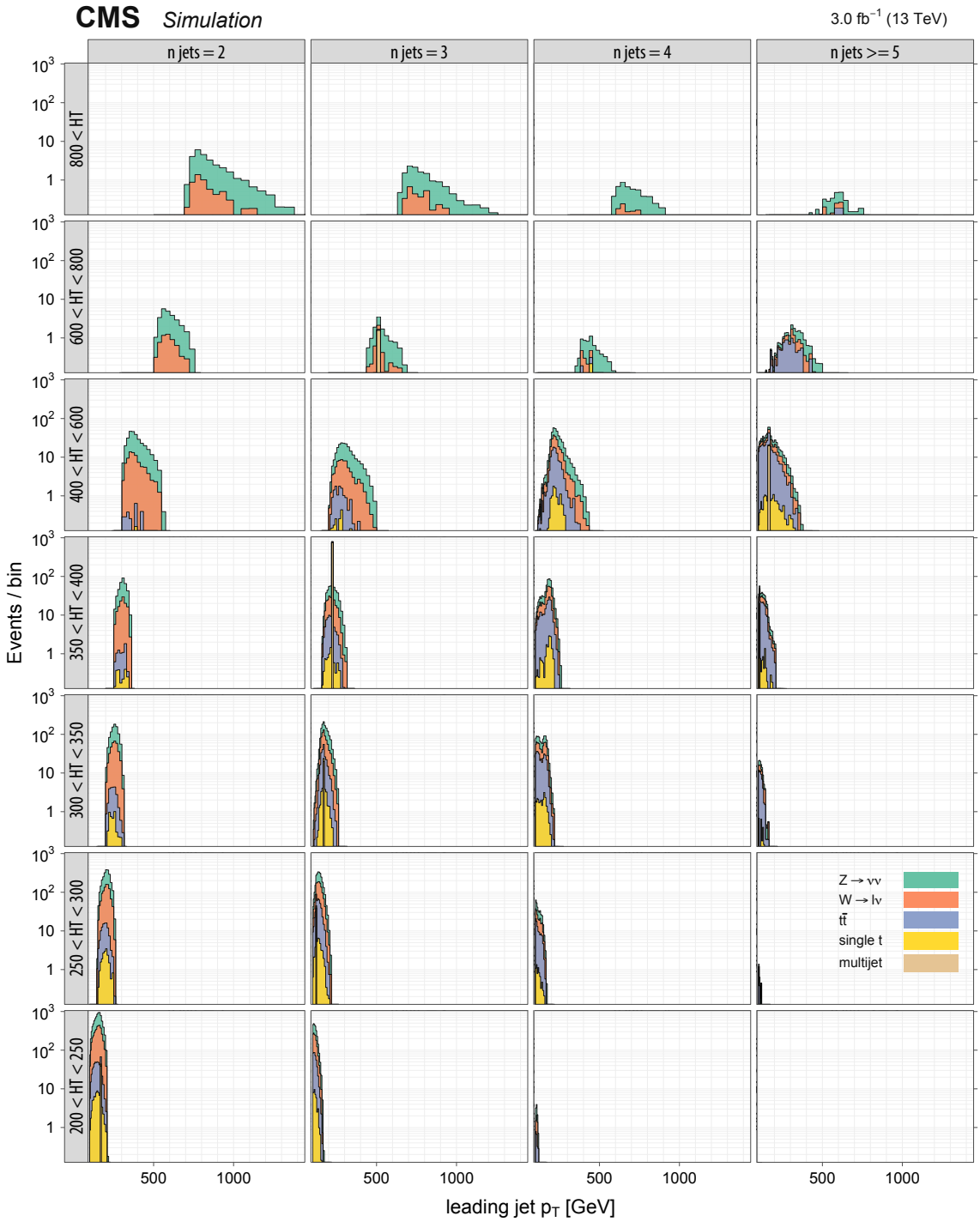

Figure 107: **The lead jet p_T distributions, symmetric n_{jet} bins:** The lead jet p_T distributions of the events in the signal region in each H_T bin in each asymmetric n_{jet} bin for each process. Panels in different rows show events in different H_T bins. Panels in different columns show events in different asymmetric n_{jet} bins. Different processes are shown in different colors (or gray scales).

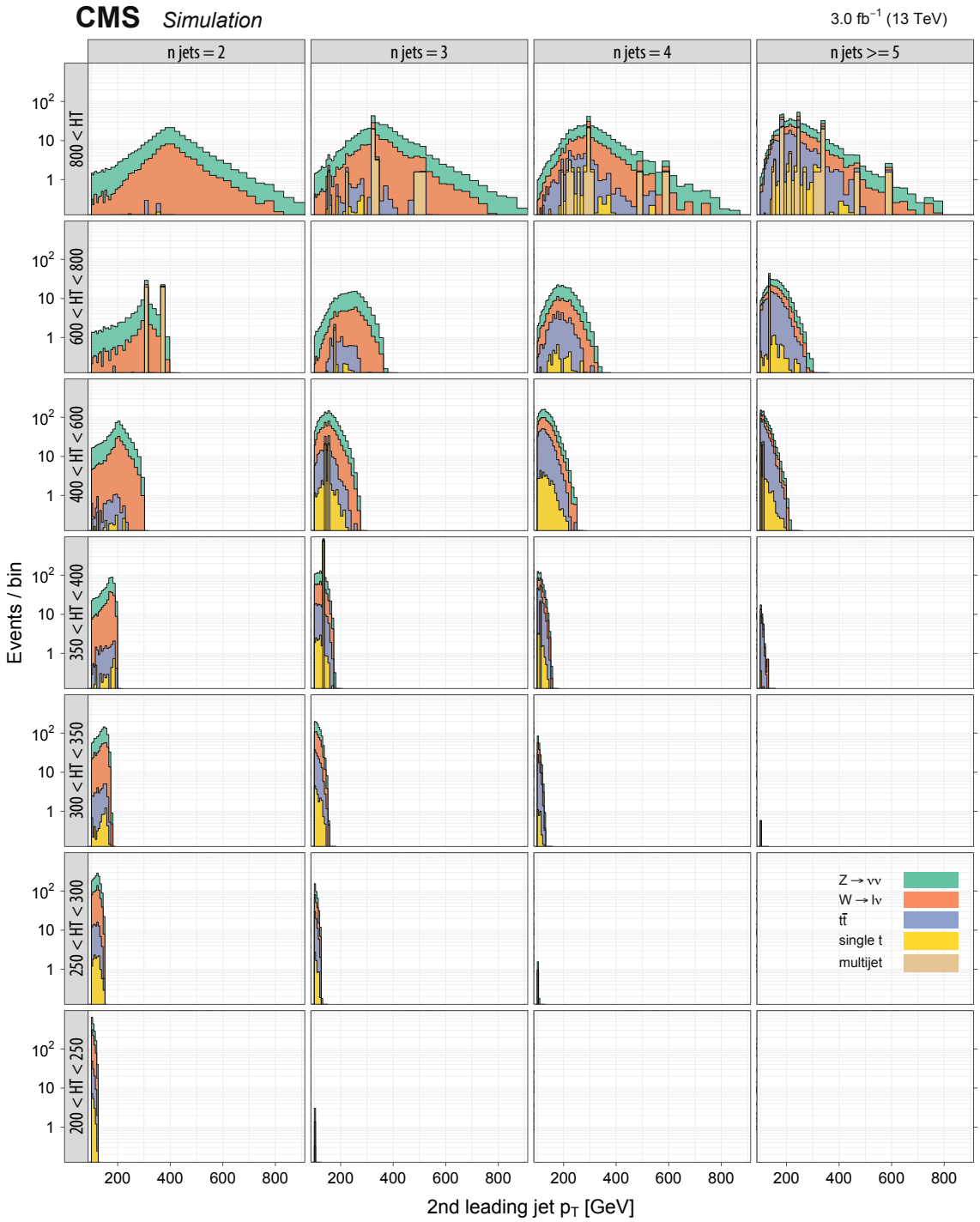

Figure 108: **The second hardest jet p_T distributions, symmetric n_{jet} bins:** The second hardest jet p_T distributions of the events in the signal region in each H_T bin in each symmetric n_{jet} bin for each process. Panels in different rows show events in different H_T bins. Panels in different columns show events in different symmetric n_{jet} bins. Different processes are shown in different colors (or gray scales).

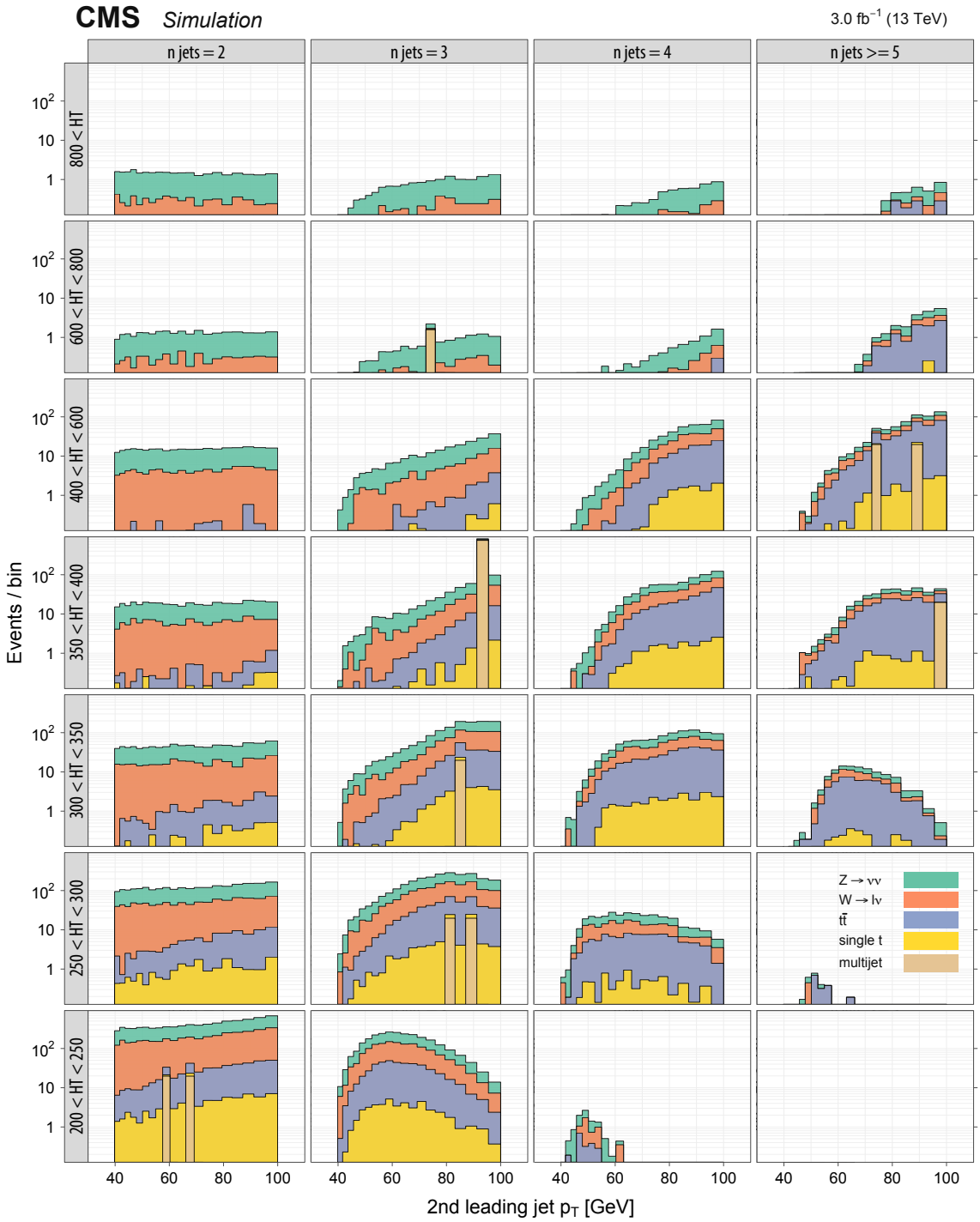

Figure 109: **The second hardest jet p_T distributions, asymmetric n_{jet} bins:** The second hardest jet p_T distributions of the events in the signal region in each H_T bin in each asymmetric n_{jet} bin for each process. Panels in different rows show events in different H_T bins. Panels in different columns show events in different asymmetric n_{jet} bins. Different processes are shown in different colors (or gray scales).

Figure 110: **The $n_b$distributions, symmetric n_{jet} bins:** The n_b distributions of the events in the signal region in each H_T bin in each symmetric n_{jet} bin for each process. Panels in different rows show events in different H_T bins. Panels in different columns show events in different symmetric n_{jet} bins. Different processes are shown in different colors (or gray scales).

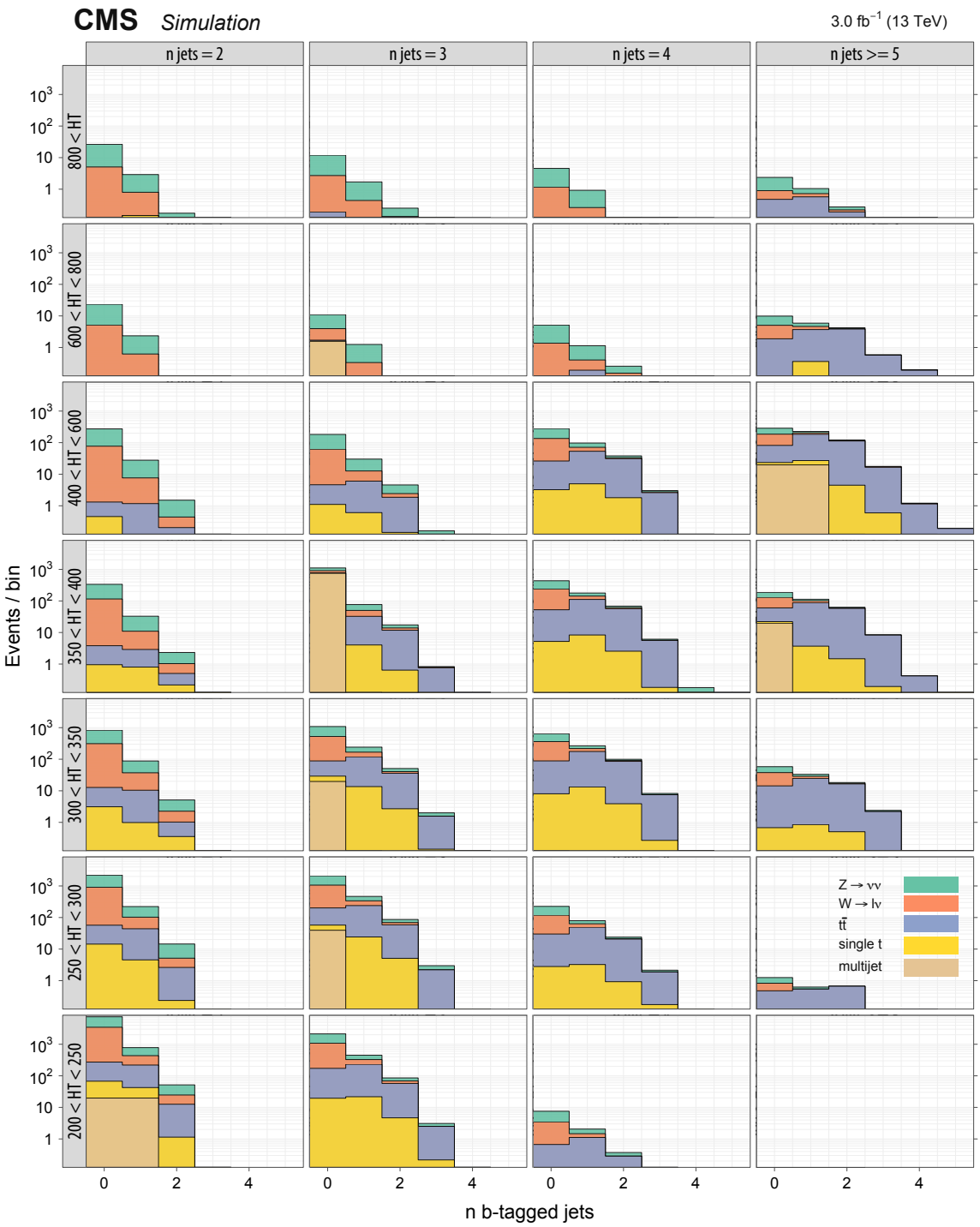

Figure 111: **The n_b distributions, asymmetric n_{jet} bins:** The n_b distributions of the events in the signal region in each H_T bin in each asymmetric n_{jet} bin for each process. Panels in different rows show events in different H_T bins. Panels in different columns show events in different asymmetric n_{jet} bins. Different processes are shown in different colors (or gray scales).

B Trigger efficiency measurements of signal models

These plots are to be updated to reflect the current trigger strategy

Based on simulation studies, the signal triggers demonstrate high efficiencies for a range of benchmark signal models and SM processes with genuine $E_{\mathrm{T}}^{\mathrm{miss}}$. The trigger efficiency for two benchmark signal models, `T2tt` (425,325) and `T1tttt` (1200,800), are shown in Figs. 112 for the low and high jet multiplicity analysis bins, respectively, which illustrate a "representative" performance for each of the respective models.

The use of a dijet average threshold is fully efficient for the categories with "symmetric" p_{T} selection requirements on the leading two jets, as illustrated in Fig. 113. In the case of the "asymmetric" scenario, when the second leading jet satisfied $40 < p_{\mathrm{T}} < 100\,\mathrm{GeV}$, some inefficiencies are observed due to this challenging class of event, where both the leading and second jet are relatively soft and the H_{T} is low. The figure shows the efficiencies for the lowest H_{T} bin, $200 < H_{\mathrm{T}} < 250\,\mathrm{GeV}$, which improve significantly for the higher H_{T} bins in the region $H_{\mathrm{T}} < 250\,\mathrm{GeV}$.

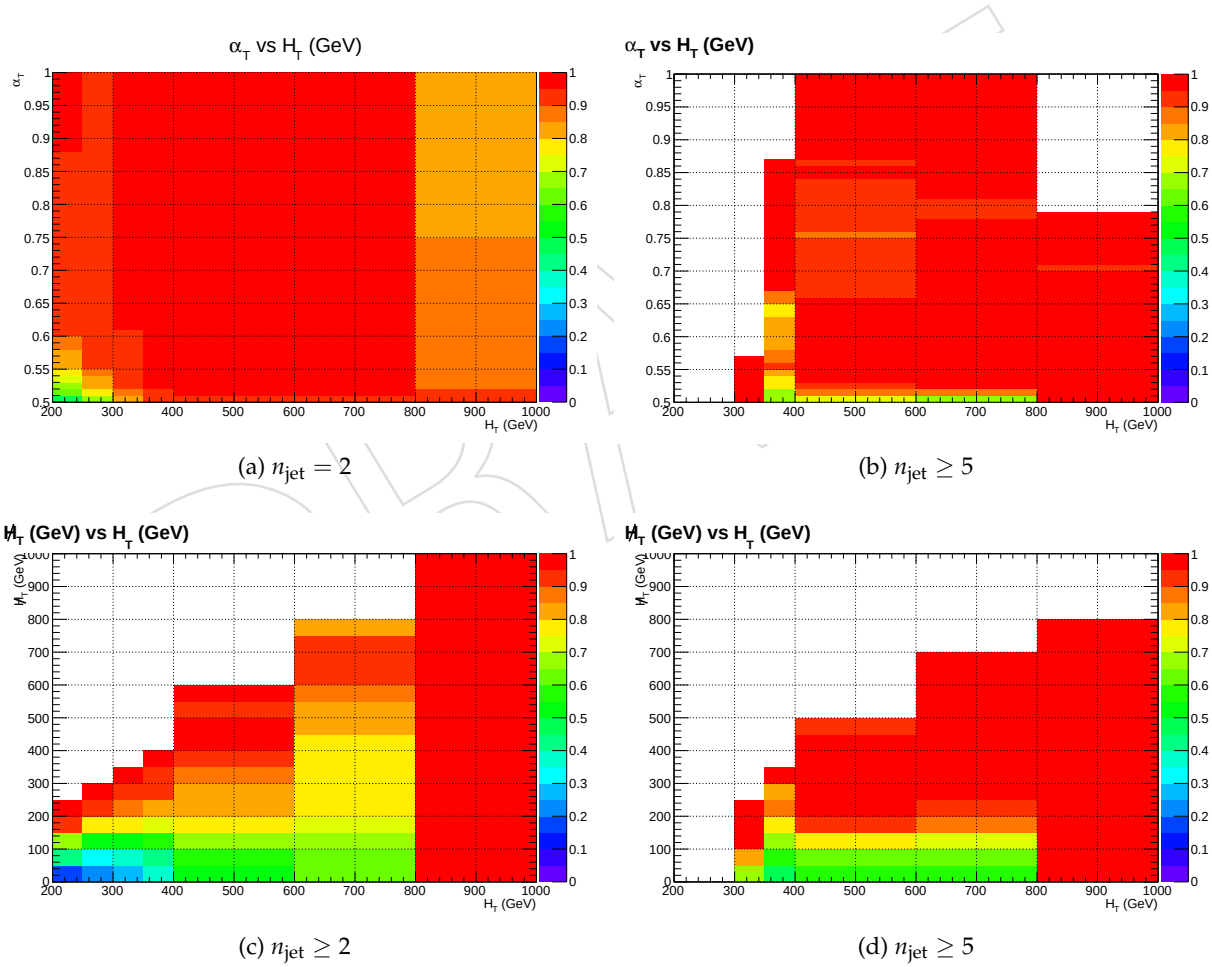

(a) $n_{\mathrm{jet}} = 2$

(b) $n_{\mathrm{jet}} \geq 5$

(c) $n_{\mathrm{jet}} \geq 2$

(d) $n_{\mathrm{jet}} \geq 5$

Figure 112: Cumulative trigger efficiency for the T2tt(425,325) and T1tttt(1200,800) simplified models after signal selection in the α_{T}-H_{T} and $H_{\mathrm{T}}^{\mathrm{miss}}$-$H_{\mathrm{T}}$ planes for representative analysis jet multiplicity bins.

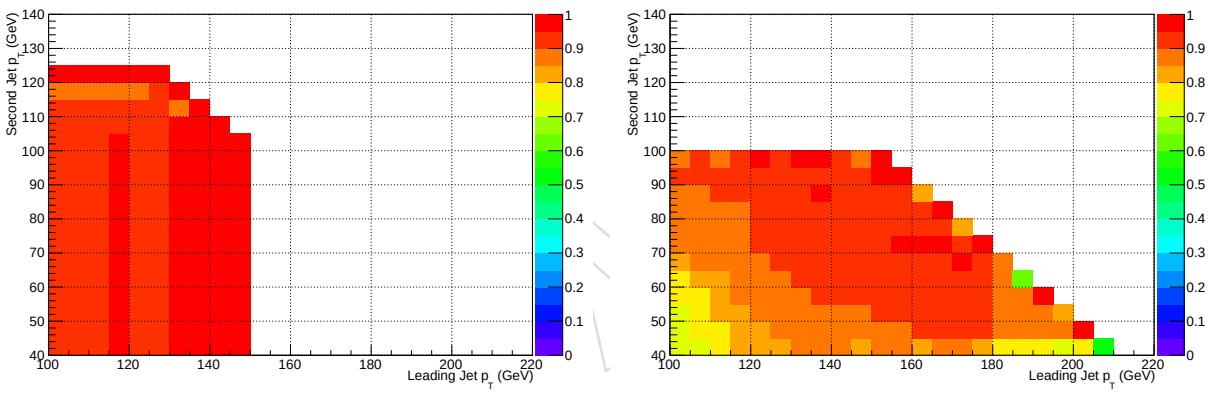

(a) Symmetric-n_{jet} requirement

(b) Asymmetric-n_{jet} requirement

Figure 113: Cumulative trigger efficiency for the T2tt(425,325) simplified model after signal selection as a function of leading and second jet threshold for the symmetric and asymmetric selection requirements for the lowest-H_{T} bin.

C Trigger efficiency measurements of α_T triggers

Illustrative α_T turn-ons of the individual H_T-α_T triggers with an offline H_T selection applied using the `HLT_Ele23_eta2p1_WPLoose_Gsf` reference trigger.

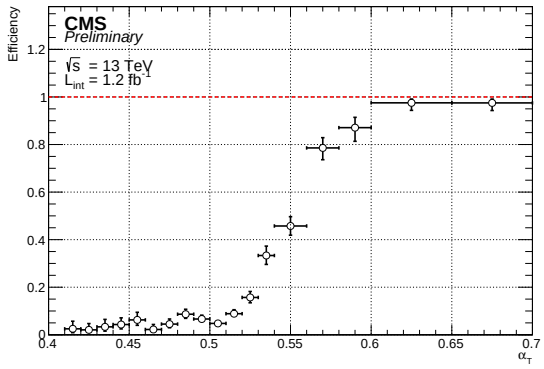

(a) HLT_PFHT200_DiPFJetAve90_PFAlphaT0p57 ($H_T > 300$ GeV)

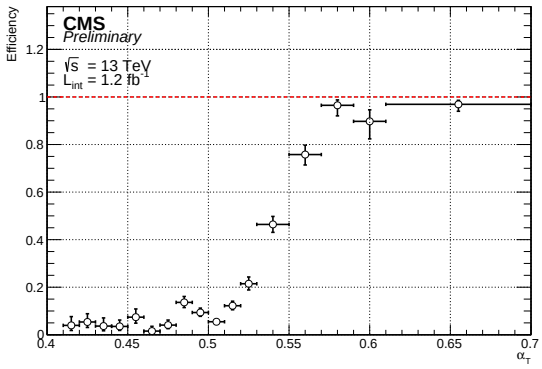

(b) HLT_PFHT250_DiPFJetAve90_PFAlphaT0p55 ($H_T > 350$ GeV)

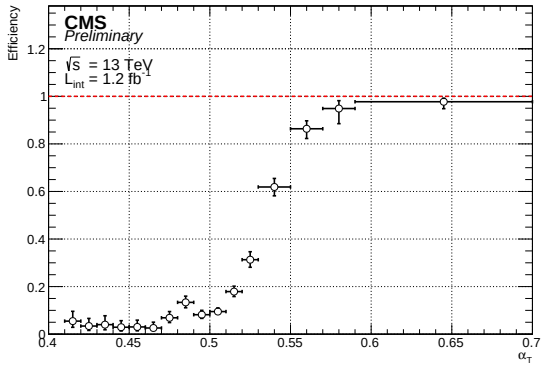

(c) HLT_PFHT300_DiPFJetAve90_PFAlphaT0p53 ($H_T > 400$ GeV)

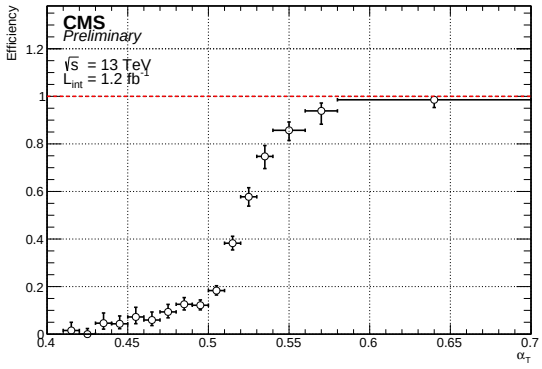

(d) HLT_PFHT350_DiPFJetAve90_PFAlphaT0p52 ($H_T > 450$ GeV)

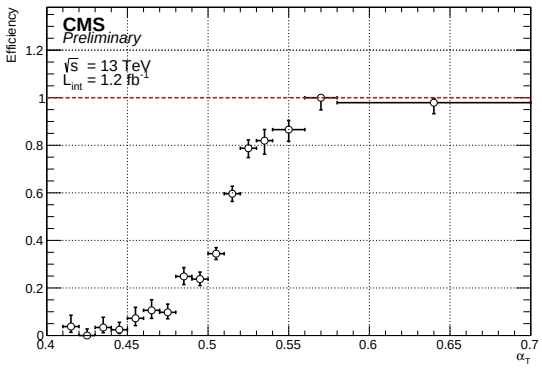

(e) HLT_PFHT400_DiPFJetAve90_PFAlphaT0p51 ($H_T > 500$ GeV)

Figure 114: The trigger efficiency measured in the data as a function of α_T for the H_T-α_T triggers used to seed the analysis bins in the signal region. The offline H_T is also specified.

D Low-H_T Level-1 seeds

Some models of new physics, such as supersymmetric compressed spectrum models, are challenging to select at the trigger level due to low-hadronic energy visible in the final state. Sensitivity to such models require low trigger thresholds which is difficult to achieve without incurring a large increase in the Level-1 trigger rate. New Level-1 seeds which enable low thresholds to be utilised by actively vetoing QCD event topologies have been studied and are shown to have higher efficiencies for such models than can be achieved with the current Level-1 menu.

The $\Delta\phi(j_1^{L1}, j_2^{L1})$ seed exploits the typical dijet topologies exhibited in QCD dijet production by vetoing events where the azimuthal separation of the leading jets exceeds eight calorimeter regions, corresponding to a veto of: $\Delta\phi(j_1^{L1}, j_2^{L1}) \geq 160°$, where a jet threshold of $p_T > 32$ GeV is imposed on the second jet. This enables a much lower threshold on the H_T-leg to be achieved, with a small increase in other thresholds in the menu, enabling for example the rate neutral trigger: `L1_DoubleJetC32_WdPhi7_HTT125` to be utilised.

An alternate H_T^{miss}/H_T 'reduced-MHT' seed exploits the correlation in missing hadronic energy and visible hadronic energy typical of decays with genuine E_T^{miss} and the decorrelation of these quantities for QCD with fake-E_T^{miss} by requiring a minimum H_T^{miss}/H_T ratio. This again enables triggers with a significant reduction in the threshold on the H_T-leg, for example with the rate neutral trigger: `L1_HTT125_rHTM0p3`.

The logical disjunction of these two seeds can further improve signal efficiency whilst maintaining an effective suppression of QCD events by increasing acceptance to additional topologies. ISR-dominated final states for instance typically have large H_T^{miss}/H_T but may fail the $\Delta\phi(j_1^{L1}, j_2^{L1})$ selection, where as events with high jet multiplicities typically have high $\Delta\phi(j_1^{L1}, j_2^{L1})$ but may fail the H_T^{miss}/H_T threshold due to the breakdown in H_T^{miss}/H_T at high jet multiplicities. Combined these seeds allow even smaller thresholds to be used on the H_T-leg without loss of efficiency to ISR-dominated or high jet multiplicity events, for example with the trigger: `L1_HTT110_rHTM0p6_rHTM0p0_WdPhi6`.

The new trigger seeds is implemented in the trigger hardware by repurposing the bits currently utilised for H_T^{miss} and $\phi(H_T^{miss})$ trigger primitives with the new H_T^{miss}/H_T and $\Delta\phi(j_1^{L1}, j_2^{L1})$ primitives respectively. These changes have been discussed with trigger experts and are deemed to be relatively simple to implement in the calorimeter trigger firmware and has little impact on the operation global trigger. The latest version of the Level-1 trigger emulator currently has the `L1_DoubleJetC32_WdPhi7_HTT125`, `L1_HTT125_rHTM0p3` and `L1_HTT110_rHTM0p6_rHTM0p0_WdPhi6` low-H_T trigger primitives implemented, enabling a wider study within the collaboration.

The performance after the full offline selection of the low-H_T Level-1 seeds was studied for a range of signal models in the lowest H_T and n_{jet} analysis bins which are predominantly populated by compressed models. Performance was measured relative to the current PU40bx25 Level-1 hadronic menu, `HTT175 OR DoubleJetC100 OR QuadJetC60 OR ETM70`, with the rate equivalent low-H_T menues defined as: Low-H_T seed `OR HTT200 OR DoubleJetC120 OR QuadJetC60 OR ETM70`. The efficiencies of the proposed menues for $n_{jet} = 2$ and $n_{jet} = 3$, shown in Table 73 and Table 74 respectively, show significant improvements in trigger efficiency utilising the low-H_T seeds with respect to the current hadronic menu and similar performance to what could be obtained by reducing the E_T^{miss} threshold without the additional 3 kHz Level-1 trigger rate this would incur.

It is important to note that the new L1 seeds discussed in this section are currently only potential alternatives to the existing L1 `ETM` and `HTT` seeds. Their inclusive may require some rate

DRAFT

balancing within the existing menus at the expense of other seeds. Studies have considered the re-allocation of rate (∼5 kHz) from the `DoubleJetC` seed. The inclusion of these new seeds may be a beneficial strategy to employ if the thresholds on the `ETM` and `HTT` seeds are to be raised due to increasing instantaneous luminosity and/or pileup conditions later in the run of 2015.

Table 73: Trigger efficiency for $n_{\text{jet}} = 2$, $200 < H_{\text{T}} \leq 300$ analysis bin and corresponding rate of the current Level-1 hadronic menu and proposed low-H_{T} trigger menues for a range of compressed signal models.

Signal model	Hadronic menu	$\Delta\phi(j_1^{L1}, j_2^{L1})$	$H_{\text{T}}^{\text{miss}}/H_{\text{T}}$	$\Delta\phi(j_1^{L1}, j_2^{L1})$ `OR` $H_{\text{T}}^{\text{miss}}/H_{\text{T}}$	Hadronic menu `OR ETM60`
T2cc(250, 210)	0.60	0.86	0.91	0.94	0.95
T2qq(400, 400)	0.63	0.82	0.88	0.95	0.94
T2tt(300, 200)	0.53	0.91	0.95	0.99	0.96
Menu rate (kHz)	15	15	15	15	19

Table 74: Trigger efficiency for $n_{\text{jet}} = 3$, $200 < H_{\text{T}} \leq 300$ analysis bin and corresponding rate of the current Level-1 hadronic menu and proposed low-H_{T} trigger menues for a range of compressed signal models.

Signal model	Hadronic menu	$\Delta\phi(j_1^{L1}, j_2^{L1})$	$H_{\text{T}}^{\text{miss}}/H_{\text{T}}$	$\Delta\phi(j_1^{L1}, j_2^{L1})$ `OR` $H_{\text{T}}^{\text{miss}}/H_{\text{T}}$	Hadronic menu `OR ETM60`
T2cc(250, 210)	0.45	0.74	0.74	0.83	0.94
T2qq(400, 400)	0.46	0.88	0.88	0.93	0.92
T2tt(300, 200)	0.41	0.76	0.83	0.84	0.86
Menu rate (kHz)	15	15	15	15	19

DRAFT

E Nuisance Parameters Fit

A maximum likelihood fit to the asimov dataset is performed for all signal models. The results for the most sensitive category for a sample signal model (T1bbbb 1500,100) and for a 10, 25, 50, and 100% template variation in the final bin are shown in Fig. 115. The nuisances on the transfer factors (as well as the signal acceptance) agree well with their pre-fit values. This is expected as these nuisances are uncorrelated and derived from the statistical precision of control samples, which should be higher than that in the signal region. For an uncertainty of greater than 10% on the last bin the width of the template systematic is reduced by the fit. The information in the signal region is sufficient in this case to constrain the template variation.

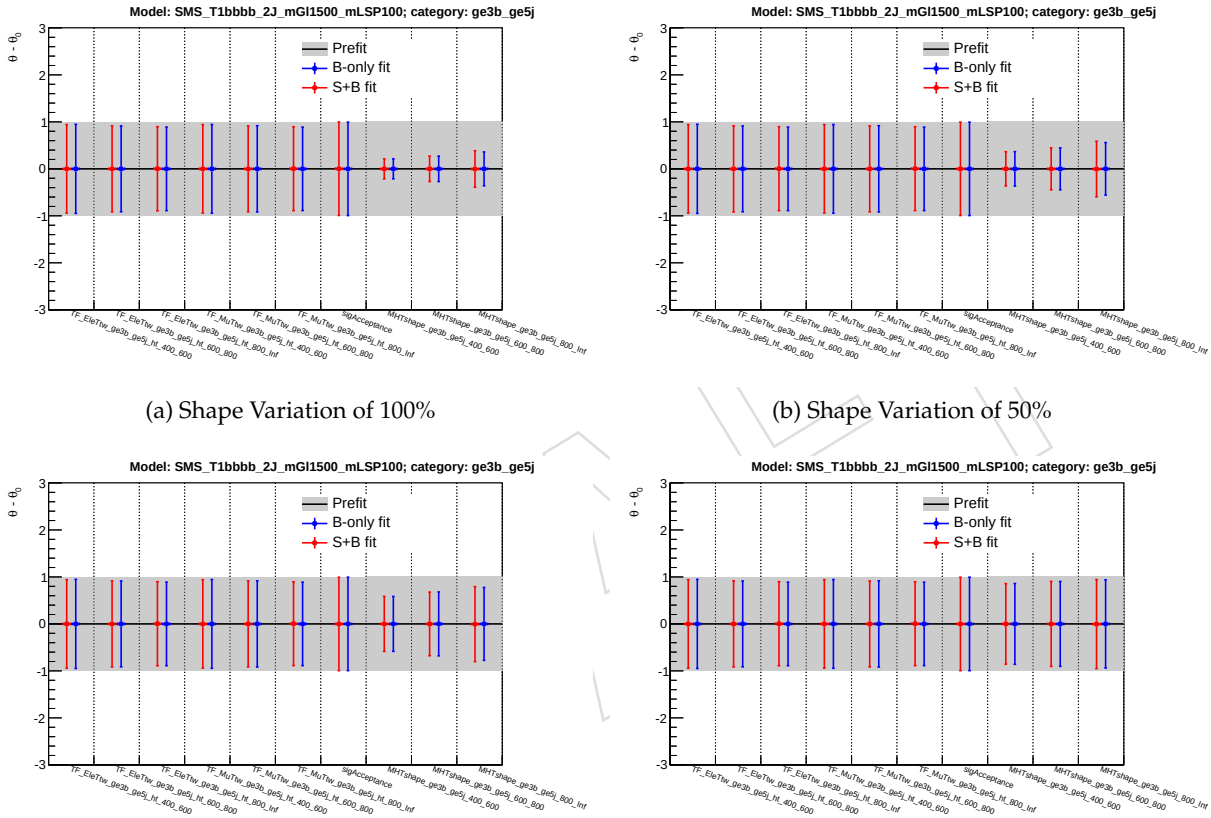

(a) Shape Variation of 100%

(b) Shape Variation of 50%

(c) Shape Variation of 25%

(d) Shape Variation of 10%

Figure 115: Effect of the fit on the nuisances for the most sensitive category of T1bbbb 1500, 100. The only substantial difference between pre and post fit is seen in the shape

F Control of Z_{inv} background

An accurate prediction of the Z_{inv} background is a crucial part of the analysis. Up to five control samples may be used to predict the Z_{inv} background: μ + jets, $\mu\mu$ + jets, e + jets, ee + jets and γ + jets. In previous versions of this analysis only the $\mathrm{Z}(\rightarrow \mu\mu) +$ jets and γ + jets to predict the Z_{inv} background. The single lepton control samples also provide $\mathrm{W} +$ jets enriched samples to predict Z_{inv} with significantly higher statistical power. Several closure tests are used to probe the systematcs related to the predictions of the Z_{inv} background and are described below.

The closure tests are described in full in Sec. 12.1, Those relevant for the Z_{inv} prediction are the $\mu\mu$ + jets to γ + jets which probes the photon prediction, the μ + jets to $\mu\mu$ + jets which probes the prediction from W and the μ + jets to γ + jets which probes vector boson prediction using the photon sample. In addition to these, a test to probe the effect of W polarisation on experimental acceptance, μ^+ + jets to μ^- + jets, is described below. Using data from 8 TeV, these closure tests are shown in Fig. 116. This shows that the predictions of Z_{inv} from all control samples are consistent within statistical uncertainty with no bias or trend.

The production mechanism of W from pp collisions means high p_T W bosons are predominantly left handed [23]. For high p_T bosons, this implies that W^+ will decay to the left handed neutrino along its direction of motion while the lepton will be backward. The opposite behaviour is expected for the W^-. The lepton will therefore be more boosted (and the neutrino less boosted) in W^+ decays than W^- decays. This leads to a larger number of W^+ decays in the single lepton control regions (which relies on the lepton p_T for acceptance) than in the signal region (which relies on the neutrino p_T for acceptance). In order to understand if this leads to a bias in the prediction of the W and unpolarised Z_{inv} background in the signal region when using a single lepton control region a closure test from μ^+ + jets to μ^- + jets will be added (shown in Fig. 116.

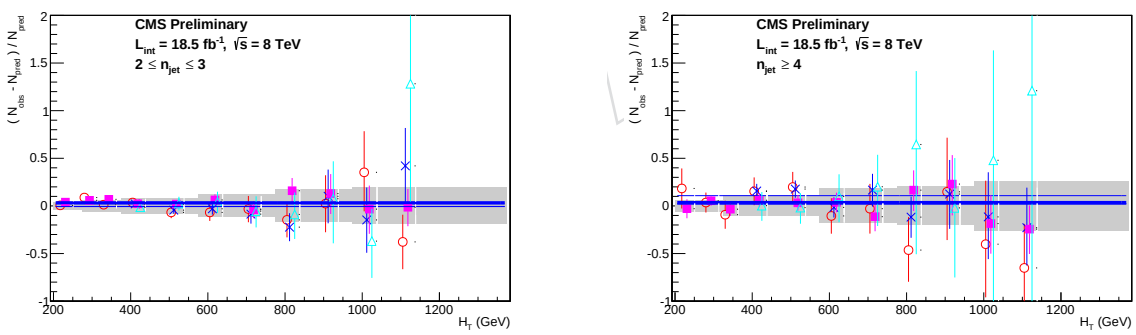

(a) Closure tests for ≤ 3 jets

(b) Closure tests for ≥ 4 jets

Figure 116: Closure tests that probe the effects of W polarisation on experimental acceptance. The red circles correspond to the μ + jets to $\mu\mu$ + jets closure test, the blue crosses correspond to the μ + jets to γ + jets closure test, the pink squares correspond to the μ^+ + jets to μ^- + jets closure test and the turquoise triangles correspond to the $\mu\mu$ + jets to γ + jets closure test.

G H_T^{miss} templates

In Section 14 the use of templates in the H_T^{miss} variable to extract the signal is described, and the criteria for the choice of the binning are outlined. For each bin, the following two requirements must be fulfilled:

- Each bin must contain at least 10 unweighted events. This criterium makes the MC statistical uncertainty sub-dominant with respect to the other sources of systematic uncertainty.
- The square root of the weighted variance of the statistical error in the last H_T^{miss} bin, computed with the single-muon and single-electron control regions, must account for less than 30%. This requirement allows to perform a meaningful closure test in data up to the highest bin in the H_T^{miss} variable.

In Tables 75-104 the binning of the H_T^{miss} templates are given for each jet category and each H_T bin. The last bin is up to the H_T boundary for the bins $H_T < 800$ GeV and is open in the bin $H_T > 800$ GeV.

DRAFT

Table 75: Binning of the H_T^{miss} templates, for the category $n_b = 0, n_{jet} \geq 5$.

Jet category	H_T bin	H_T^{miss} binning
$n_b = 0, n_{jet} \geq 5$	$350 < H_T < 400$ GeV	[130.0, 200.0, 250.0, 300.0] GeV
$n_b = 0, n_{jet} \geq 5$	$400 < H_T < 600$ GeV	[130.0, 150.0, 200.0, 250.0, 300.0, 350.0, 400.0, 450.0, 500.0] GeV
$n_b = 0, n_{jet} \geq 5$	$600 < H_T < 800$ GeV	[130.0, 225.0, 275.0, 325.0, 375.0, 425.0, 475.0, 525.0, 575.0, 625.0, 675.0] GeV
$n_b = 0, n_{jet} \geq 5$	$H_T > 800$ GeV	[130.0, 175.0, 225.0, 275.0, 325.0, 375.0, 425.0, 475.0, 525.0, 575.0,
		625.0, 675.0, 725.0, 775.0, 825.0, 875.0, 950.0, 1050.0, 1100.0] GeV

Table 76: Binning of the H_T^{miss} templates, for the category $n_b = 1, n_{jet} \geq 5$.

Jet category	H_T bin	H_T^{miss} binning
$n_b = 1, n_{jet} \geq 5$	$350 < H_T < 400$ GeV	[130.0] GeV
$n_b = 1, n_{jet} \geq 5$	$400 < H_T < 600$ GeV	[130.0, 175.0, 225.0, 275.0, 325.0, 375.0, 425.0, 475.0] GeV
$n_b = 1, n_{jet} \geq 5$	$600 < H_T < 800$ GeV	[130.0, 225.0, 275.0, 325.0, 375.0, 425.0, 475.0, 525.0, 575.0] GeV
$n_b = 1, n_{jet} \geq 5$	$H_T > 800$ GeV	[130.0, 150.0, 200.0, 250.0, 300.0, 350.0, 400.0, 450.0, 500.0, 550.0,
		625.0, 725.0, 800.0, 975.0, 1025.0] GeV

Table 77: Binning of the H_T^{miss} templates, for the category $n_b = 2, n_{jet} \geq 5$.

Jet category	H_T bin	H_T^{miss} binning
$n_b = 2, n_{jet} \geq 5$	$300 < H_T < 350$ GeV	[130.0] GeV
$n_b = 2, n_{jet} \geq 5$	$350 < H_T < 400$ GeV	[130.0, 175.0, 225.0, 275.0] GeV
$n_b = 2, n_{jet} \geq 5$	$400 < H_T < 600$ GeV	[130.0, 175.0, 225.0, 275.0, 325.0, 375.0, 425.0, 475.0] GeV
$n_b = 2, n_{jet} \geq 5$	$600 < H_T < 800$ GeV	[130.0, 200.0, 250.0, 300.0, 350.0, 400.0, 450.0, 500.0, 550.0, 625.0, 675.0] GeV
$n_b = 2, n_{jet} \geq 5$	$H_T > 800$ GeV	[130.0, 175.0, 225.0, 275.0, 325.0, 375.0, 425.0, 475.0, 525.0, 575.0,
		650.0, 725.0, 825.0, 875.0, 950.0, 1050.0, 1100.0] GeV

Table 78: Binning of the H_T^{miss} templates, for the category $n_b \geq 3, n_{jet} \geq 5$.

Jet category	H_T bin	H_T^{miss} binning
$n_b \geq 3, n_{jet} \geq 5$	$350 < H_T < 400$ GeV	[130.0] GeV
$n_b \geq 3, n_{jet} \geq 5$	$400 < H_T < 600$ GeV	[130.0, 175.0, 225.0, 275.0, 325.0, 375.0] GeV
$n_b \geq 3, n_{jet} \geq 5$	$600 < H_T < 800$ GeV	[130.0, 250.0, 300.0, 350.0, 400.0, 450.0] GeV
$n_b \geq 3, n_{jet} \geq 5$	$H_T > 800$ GeV	[130.0, 150.0, 200.0, 250.0, 300.0, 350.0, 400.0, 475.0, 525.0] GeV

Table 79: Binning of the H_T^{miss} templates, for the category $n_b = 0, n_{jet} = 4$.

Jet category	H_T bin	H_T^{miss} binning
$n_b = 0, n_{jet} = 4$	$250 < H_T < 300$ GeV	[130.0] GeV
$n_b = 0, n_{jet} = 4$	$300 < H_T < 350$ GeV	[130.0, 175.0, 225.0, 275.0, 325.0] GeV
$n_b = 0, n_{jet} = 4$	$350 < H_T < 400$ GeV	[130.0, 150.0, 200.0, 250.0, 300.0, 350.0, 400.0] GeV
$n_b = 0, n_{jet} = 4$	$400 < H_T < 600$ GeV	[130.0, 175.0, 225.0, 275.0, 325.0, 375.0, 425.0, 475.0, 525.0, 575.0] GeV
$n_b = 0, n_{jet} = 4$	$600 < H_T < 800$ GeV	[130.0, 225.0, 275.0, 325.0, 375.0, 425.0, 475.0, 525.0, 575.0, 625.0,
		675.0, 725.0] GeV
$n_b = 0, n_{jet} = 4$	$H_T > 800$ GeV	[130.0, 175.0, 225.0, 275.0, 325.0, 375.0, 425.0, 475.0, 525.0, 575.0,
		625.0, 675.0, 725.0, 775.0, 825.0, 875.0, 925.0, 1000.0, 1150.0, 1200.0] GeV

DRAFT

Table 80: Binning of the H_T^{miss} templates, for the category $n_b = 1, n_{jet} = 4$.

Jet category	H_T bin	H_T^{miss} binning
$n_b = 1, n_{jet} = 4$	$300 < H_T < 350$ GeV	[130.0, 200.0, 250.0, 300.0] GeV
$n_b = 1, n_{jet} = 4$	$350 < H_T < 400$ GeV	[130.0, 175.0, 225.0, 275.0, 325.0, 375.0] GeV
$n_b = 1, n_{jet} = 4$	$400 < H_T < 600$ GeV	[130.0, 175.0, 225.0, 275.0, 325.0, 375.0, 425.0, 475.0, 525.0] GeV
$n_b = 1, n_{jet} = 4$	$600 < H_T < 800$ GeV	[130.0, 225.0, 275.0, 325.0, 375.0, 425.0, 475.0, 550.0, 600.0, 650.0] GeV
$n_b = 1, n_{jet} = 4$	$H_T > 800$ GeV	[130.0, 175.0, 225.0, 275.0, 325.0, 375.0, 425.0, 475.0, 550.0, 650.0,
		700.0, 825.0, 875.0] GeV

Table 81: Binning of the H_T^{miss} templates, for the category $n_b = 2, n_{jet} = 4$.

Jet category	H_T bin	H_T^{miss} binning
$n_b = 2, n_{jet} = 4$	$250 < H_T < 300$ GeV	[130.0] GeV
$n_b = 2, n_{jet} = 4$	$300 < H_T < 350$ GeV	[130.0, 150.0, 200.0, 250.0, 300.0] GeV
$n_b = 2, n_{jet} = 4$	$350 < H_T < 400$ GeV	[130.0, 175.0, 225.0, 275.0, 325.0, 375.0] GeV
$n_b = 2, n_{jet} = 4$	$400 < H_T < 600$ GeV	[130.0, 175.0, 225.0, 275.0, 325.0, 375.0, 425.0, 475.0, 525.0] GeV
$n_b = 2, n_{jet} = 4$	$600 < H_T < 800$ GeV	[130.0, 275.0, 325.0, 375.0, 425.0, 475.0, 575.0, 675.0, 725.0] GeV
$n_b = 2, n_{jet} = 4$	$H_T > 800$ GeV	[130.0, 175.0, 225.0, 275.0, 325.0, 375.0, 425.0, 475.0, 550.0, 625.0,
		775.0, 825.0] GeV

Table 82: Binning of the H_T^{miss} templates, for the category $n_b \geq 3, n_{jet} = 4$.

Jet category	H_T bin	H_T^{miss} binning
$n_b \geq 3, n_{jet} = 4$	$300 < H_T < 350$ GeV	[130.0] GeV
$n_b \geq 3, n_{jet} = 4$	$350 < H_T < 400$ GeV	[130.0, 175.0, 225.0, 275.0] GeV
$n_b \geq 3, n_{jet} = 4$	$400 < H_T < 600$ GeV	[130.0, 175.0, 225.0, 275.0, 325.0, 375.0] GeV
$n_b \geq 3, n_{jet} = 4$	$600 < H_T < 800$ GeV	[130.0, 325.0, 375.0] GeV
$n_b \geq 3, n_{jet} = 4$	$H_T > 800$ GeV	[130.0] GeV

Table 83: Binning of the H_T^{miss} templates, for the category $n_b = 0, n_{jet} = 3$.

Jet category	H_T bin	H_T^{miss} binning
$n_b = 0, n_{jet} = 3$	$200 < H_T < 250$ GeV	[130.0] GeV
$n_b = 0, n_{jet} = 3$	$250 < H_T < 300$ GeV	[130.0, 225.0, 275.0, 325.0] GeV
$n_b = 0, n_{jet} = 3$	$300 < H_T < 350$ GeV	[130.0, 175.0, 225.0, 275.0, 325.0, 375.0] GeV
$n_b = 0, n_{jet} = 3$	$350 < H_T < 400$ GeV	[130.0, 175.0, 225.0, 275.0, 325.0, 375.0, 425.0] GeV
$n_b = 0, n_{jet} = 3$	$400 < H_T < 600$ GeV	[130.0, 150.0, 200.0, 250.0, 300.0, 350.0, 400.0, 450.0, 500.0, 550.0, 600.0] GeV
$n_b = 0, n_{jet} = 3$	$600 < H_T < 800$ GeV	[130.0, 225.0, 275.0, 325.0, 375.0, 425.0, 475.0, 525.0, 575.0, 625.0,
		675.0, 725.0, 775.0] GeV
$n_b = 0, n_{jet} = 3$	$H_T > 800$ GeV	[130.0, 175.0, 225.0, 275.0, 325.0, 375.0, 425.0, 475.0, 525.0, 575.0,
		625.0, 675.0, 725.0, 775.0, 825.0, 875.0, 925.0, 1025.0, 1075.0, 1175.0, 1225.0] GeV

DRAFT

Table 84: Binning of the H_T^{miss} templates, for the category $n_b = 1, n_{jet} = 3$.

Jet category	H_T bin	H_T^{miss} binning
$n_b = 1, n_{jet} = 3$	$250 < H_T < 300$ GeV	[130.0, 225.0, 275.0, 325.0] GeV
$n_b = 1, n_{jet} = 3$	$300 < H_T < 350$ GeV	[130.0, 175.0, 225.0, 275.0, 325.0, 375.0] GeV
$n_b = 1, n_{jet} = 3$	$350 < H_T < 400$ GeV	[130.0, 175.0, 225.0, 275.0, 325.0, 375.0, 425.0] GeV
$n_b = 1, n_{jet} = 3$	$400 < H_T < 600$ GeV	[130.0, 175.0, 225.0, 275.0, 325.0, 375.0, 425.0, 475.0, 525.0, 575.0] GeV
$n_b = 1, n_{jet} = 3$	$600 < H_T < 800$ GeV	[130.0, 225.0, 275.0, 325.0, 375.0, 425.0, 475.0, 525.0, 575.0, 625.0,
		675.0, 725.0] GeV
$n_b = 1, n_{jet} = 3$	$H_T > 800$ GeV	[130.0, 175.0, 225.0, 275.0, 325.0, 375.0, 425.0, 475.0, 525.0, 575.0,
		625.0, 700.0, 750.0, 800.0, 875.0, 925.0] GeV

Table 85: Binning of the H_T^{miss} templates, for the category $n_b = 2, n_{jet} = 3$.

Jet category	H_T bin	H_T^{miss} binning
$n_b = 2, n_{jet} = 3$	$200 < H_T < 250$ GeV	[130.0] GeV
$n_b = 2, n_{jet} = 3$	$250 < H_T < 300$ GeV	[130.0, 200.0, 250.0, 300.0] GeV
$n_b = 2, n_{jet} = 3$	$300 < H_T < 350$ GeV	[130.0, 200.0, 250.0, 300.0, 350.0] GeV
$n_b = 2, n_{jet} = 3$	$350 < H_T < 400$ GeV	[130.0, 150.0, 200.0, 250.0, 300.0, 350.0, 400.0] GeV
$n_b = 2, n_{jet} = 3$	$400 < H_T < 600$ GeV	[130.0, 150.0, 200.0, 250.0, 300.0, 350.0, 400.0, 450.0, 500.0] GeV
$n_b = 2, n_{jet} = 3$	$600 < H_T < 800$ GeV	[130.0, 325.0, 375.0, 450.0, 500.0, 550.0, 600.0, 700.0, 750.0] GeV
$n_b = 2, n_{jet} = 3$	$H_T > 800$ GeV	[130.0, 150.0, 200.0, 250.0, 300.0, 350.0, 400.0, 475.0, 525.0, 625.0,
		675.0, 725.0, 775.0, 825.0, 925.0, 1000.0, 1050.0] GeV

Table 86: Binning of the H_T^{miss} templates, for the category $n_b \geq 3, n_{jet} = 3$.

Jet category	H_T bin	H_T^{miss} binning
$n_b \geq 3, n_{jet} = 3$	$250 < H_T < 300$ GeV	[130.0] GeV
$n_b \geq 3, n_{jet} = 3$	$300 < H_T < 350$ GeV	[130.0] GeV
$n_b \geq 3, n_{jet} = 3$	$350 < H_T < 400$ GeV	[130.0, 225.0, 275.0] GeV
$n_b \geq 3, n_{jet} = 3$	$400 < H_T < 600$ GeV	[130.0, 300.0, 350.0] GeV

DRAFT

Table 87: Binning of the H_T^{miss} templates, for the category $n_b = 0, n_{jet} = 2$.

Jet category	H_T bin	H_T^{miss} binning
$n_b = 0, n_{jet} = 2$	$200 < H_T < 250$ GeV	[130.0, 175.0, 225.0, 275.0] GeV
$n_b = 0, n_{jet} = 2$	$250 < H_T < 300$ GeV	[130.0, 175.0, 225.0, 275.0, 325.0] GeV
$n_b = 0, n_{jet} = 2$	$300 < H_T < 350$ GeV	[130.0, 175.0, 225.0, 275.0, 325.0, 375.0] GeV
$n_b = 0, n_{jet} = 2$	$350 < H_T < 400$ GeV	[130.0, 175.0, 225.0, 275.0, 325.0, 375.0, 425.0] GeV
$n_b = 0, n_{jet} = 2$	$400 < H_T < 600$ GeV	[130.0, 175.0, 225.0, 275.0, 325.0, 375.0, 425.0, 475.0, 525.0, 575.0, 625.0] GeV
$n_b = 0, n_{jet} = 2$	$600 < H_T < 800$ GeV	[130.0, 200.0, 250.0, 300.0, 350.0, 400.0, 450.0, 500.0, 550.0, 600.0,
		650.0, 700.0, 750.0, 800.0] GeV
$n_b = 0, n_{jet} = 2$	$H_T > 800$ GeV	[130.0, 175.0, 225.0, 275.0, 325.0, 375.0, 425.0, 475.0, 525.0, 575.0,
		625.0, 675.0, 725.0, 775.0, 825.0, 875.0, 925.0, 975.0, 1025.0, 1150.0, 1200.0] GeV

Table 88: Binning of the H_T^{miss} templates, for the category $n_b = 1, n_{jet} = 2$.

Jet category	H_T bin	H_T^{miss} binning
$n_b = 1, n_{jet} = 2$	$200 < H_T < 250$ GeV	[130.0, 175.0, 225.0, 275.0] GeV
$n_b = 1, n_{jet} = 2$	$250 < H_T < 300$ GeV	[130.0, 225.0, 275.0, 325.0] GeV
$n_b = 1, n_{jet} = 2$	$300 < H_T < 350$ GeV	[130.0, 175.0, 225.0, 275.0, 325.0, 375.0] GeV
$n_b = 1, n_{jet} = 2$	$350 < H_T < 400$ GeV	[130.0, 175.0, 225.0, 275.0, 325.0, 375.0, 425.0] GeV
$n_b = 1, n_{jet} = 2$	$400 < H_T < 600$ GeV	[130.0, 200.0, 250.0, 300.0, 350.0, 400.0, 450.0, 500.0, 550.0, 600.0] GeV
$n_b = 1, n_{jet} = 2$	$600 < H_T < 800$ GeV	[130.0, 250.0, 300.0, 350.0, 500.0, 575.0, 625.0, 675.0] GeV
$n_b = 1, n_{jet} = 2$	$H_T > 800$ GeV	[130.0, 175.0, 225.0, 275.0, 325.0, 375.0, 425.0, 475.0, 850.0, 900.0] GeV

Table 89: Binning of the H_T^{miss} templates, for the category $n_b = 2, n_{jet} = 2$.

Jet category	H_T bin	H_T^{miss} binning
$n_b = 2, n_{jet} = 2$	$200 < H_T < 250$ GeV	[130.0, 200.0, 250.0] GeV
$n_b = 2, n_{jet} = 2$	$250 < H_T < 300$ GeV	[130.0, 225.0, 275.0, 325.0] GeV
$n_b = 2, n_{jet} = 2$	$300 < H_T < 350$ GeV	[130.0, 200.0, 250.0, 300.0, 350.0] GeV
$n_b = 2, n_{jet} = 2$	$350 < H_T < 400$ GeV	[130.0, 250.0, 300.0, 350.0, 400.0] GeV
$n_b = 2, n_{jet} = 2$	$400 < H_T < 600$ GeV	[130.0, 250.0, 300.0, 350.0, 400.0, 450.0, 500.0, 550.0, 600.0] GeV
$n_b = 2, n_{jet} = 2$	$600 < H_T < 800$ GeV	[130.0, 325.0, 450.0, 525.0, 575.0, 625.0, 675.0, 725.0, 775.0] GeV
$n_b = 2, n_{jet} = 2$	$H_T > 800$ GeV	[130.0, 200.0, 250.0, 350.0, 400.0, 775.0, 875.0, 925.0] GeV

DRAFT

Table 90: Binning of the H_T^{miss} templates, for the category $n_b = 0, n_{jet}^{asy} \geq 5$.

Jet category	H_T bin	H_T^{miss} binning
$n_b = 0, n_{jet}^{asy} \geq 5$	$250 < H_T < 300$ GeV	[130.0] GeV
$n_b = 0, n_{jet}^{asy} \geq 5$	$300 < H_T < 350$ GeV	[130.0, 175.0, 225.0, 275.0] GeV
$n_b = 0, n_{jet}^{asy} \geq 5$	$350 < H_T < 400$ GeV	[130.0, 150.0, 200.0, 250.0, 300.0, 350.0] GeV
$n_b = 0, n_{jet}^{asy} \geq 5$	$400 < H_T < 600$ GeV	[130.0, 175.0, 225.0, 275.0, 325.0, 375.0, 425.0, 475.0] GeV
$n_b = 0, n_{jet}^{asy} \geq 5$	$600 < H_T < 800$ GeV	[130.0, 275.0, 350.0, 400.0, 450.0, 500.0, 550.0] GeV
$n_b = 0, n_{jet}^{asy} \geq 5$	$H_T > 800$ GeV	[130.0] GeV

Table 91: Binning of the H_T^{miss} templates, for the category $n_b = 1, n_{jet}^{asy} \geq 5$.

Jet category	H_T bin	H_T^{miss} binning
$n_b = 1, n_{jet}^{asy} \geq 5$	$250 < H_T < 300$ GeV	[130.0] GeV
$n_b = 1, n_{jet}^{asy} \geq 5$	$300 < H_T < 350$ GeV	[130.0, 175.0, 225.0, 275.0] GeV
$n_b = 1, n_{jet}^{asy} \geq 5$	$350 < H_T < 400$ GeV	[130.0, 175.0, 225.0, 275.0, 325.0] GeV
$n_b = 1, n_{jet}^{asy} \geq 5$	$400 < H_T < 600$ GeV	[130.0, 150.0, 200.0, 250.0, 300.0, 350.0, 400.0, 450.0] GeV
$n_b = 1, n_{jet}^{asy} \geq 5$	$600 < H_T < 800$ GeV	[130.0, 325.0, 400.0, 450.0] GeV
$n_b = 1, n_{jet}^{asy} \geq 5$	$H_T > 800$ GeV	[130.0] GeV

Table 92: Binning of the H_T^{miss} templates, for the category $n_b = 2, n_{jet}^{asy} \geq 5$.

Jet category	H_T bin	H_T^{miss} binning
$n_b = 2, n_{jet}^{asy} \geq 5$	$250 < H_T < 300$ GeV	[130.0] GeV
$n_b = 2, n_{jet}^{asy} \geq 5$	$300 < H_T < 350$ GeV	[130.0, 175.0, 225.0, 275.0] GeV
$n_b = 2, n_{jet}^{asy} \geq 5$	$350 < H_T < 400$ GeV	[130.0, 150.0, 200.0, 250.0, 300.0] GeV
$n_b = 2, n_{jet}^{asy} \geq 5$	$400 < H_T < 600$ GeV	[130.0, 150.0, 200.0, 250.0, 300.0, 350.0, 400.0, 450.0] GeV
$n_b = 2, n_{jet}^{asy} \geq 5$	$600 < H_T < 800$ GeV	[130.0, 275.0, 350.0, 400.0] GeV
$n_b = 2, n_{jet}^{asy} \geq 5$	$H_T > 800$ GeV	[130.0] GeV

Table 93: Binning of the H_T^{miss} templates, for the category $n_b \geq 3, n_{jet}^{asy} \geq 5$.

Jet category	H_T bin	H_T^{miss} binning
$n_b \geq 3, n_{jet}^{asy} \geq 5$	$300 < H_T < 350$ GeV	[130.0, 200.0, 250.0] GeV
$n_b \geq 3, n_{jet}^{asy} \geq 5$	$350 < H_T < 400$ GeV	[130.0, 175.0, 225.0, 275.0] GeV
$n_b \geq 3, n_{jet}^{asy} \geq 5$	$400 < H_T < 600$ GeV	[130.0, 150.0, 200.0, 250.0, 300.0, 350.0] GeV

Table 94: Binning of the H_T^{miss} templates, for the category $n_b = 0, n_{jet}^{asy} = 4$.

Jet category	H_T bin	H_T^{miss} binning
$n_b = 0, n_{jet}^{asy} = 4$	$200 < H_T < 250$ GeV	[130.0] GeV
$n_b = 0, n_{jet}^{asy} = 4$	$250 < H_T < 300$ GeV	[130.0, 200.0, 250.0, 300.0] GeV
$n_b = 0, n_{jet}^{asy} = 4$	$300 < H_T < 350$ GeV	[130.0, 150.0, 200.0, 250.0, 300.0, 350.0] GeV
$n_b = 0, n_{jet}^{asy} = 4$	$350 < H_T < 400$ GeV	[130.0, 150.0, 200.0, 250.0, 300.0, 350.0, 400.0] GeV
$n_b = 0, n_{jet}^{asy} = 4$	$400 < H_T < 600$ GeV	[130.0, 150.0, 200.0, 250.0, 300.0, 350.0, 400.0, 450.0, 500.0, 550.0] GeV
$n_b = 0, n_{jet}^{asy} = 4$	$600 < H_T < 800$ GeV	[130.0, 500.0, 575.0, 625.0, 675.0] GeV
$n_b = 0, n_{jet}^{asy} = 4$	$H_T > 800$ GeV	[130.0, 600.0, 675.0, 775.0, 825.0, 875.0] GeV

DRAFT

Table 95: Binning of the H_T^{miss} templates, for the category $n_b = 1, n_{jet}^{asy} = 4$.

Jet category	H_T bin	H_T^{miss} binning
$n_b = 1, n_{jet}^{asy} = 4$	$200 < H_T < 250$ GeV	[130.0] GeV
$n_b = 1, n_{jet}^{asy} = 4$	$250 < H_T < 300$ GeV	[130.0, 200.0, 250.0, 300.0] GeV
$n_b = 1, n_{jet}^{asy} = 4$	$300 < H_T < 350$ GeV	[130.0, 150.0, 200.0, 250.0, 300.0, 350.0] GeV
$n_b = 1, n_{jet}^{asy} = 4$	$350 < H_T < 400$ GeV	[130.0, 175.0, 225.0, 275.0, 325.0, 375.0] GeV
$n_b = 1, n_{jet}^{asy} = 4$	$400 < H_T < 600$ GeV	[130.0, 150.0, 200.0, 250.0, 300.0, 350.0, 400.0, 450.0, 500.0] GeV
$n_b = 1, n_{jet}^{asy} = 4$	$600 < H_T < 800$ GeV	[130.0] GeV
$n_b = 1, n_{jet}^{asy} = 4$	$H_T > 800$ GeV	[130.0] GeV

Table 96: Binning of the H_T^{miss} templates, for the category $n_b = 2, n_{jet}^{asy} = 4$.

Jet category	H_T bin	H_T^{miss} binning
$n_b = 2, n_{jet}^{asy} = 4$	$200 < H_T < 250$ GeV	[130.0] GeV
$n_b = 2, n_{jet}^{asy} = 4$	$250 < H_T < 300$ GeV	[130.0, 175.0, 225.0, 275.0] GeV
$n_b = 2, n_{jet}^{asy} = 4$	$300 < H_T < 350$ GeV	[130.0, 175.0, 225.0, 275.0, 325.0] GeV
$n_b = 2, n_{jet}^{asy} = 4$	$350 < H_T < 400$ GeV	[130.0, 150.0, 200.0, 250.0, 300.0, 350.0] GeV
$n_b = 2, n_{jet}^{asy} = 4$	$400 < H_T < 600$ GeV	[130.0, 175.0, 225.0, 275.0, 325.0, 375.0, 425.0, 475.0] GeV

Table 97: Binning of the H_T^{miss} templates, for the category $n_b \geq 3, n_{jet}^{asy} = 4$.

Jet category	H_T bin	H_T^{miss} binning
$n_b \geq 3, n_{jet}^{asy} = 4$	$250 < H_T < 300$ GeV	[130.0, 200.0, 250.0] GeV
$n_b \geq 3, n_{jet}^{asy} = 4$	$300 < H_T < 350$ GeV	[130.0, 200.0, 250.0] GeV
$n_b \geq 3, n_{jet}^{asy} = 4$	$350 < H_T < 400$ GeV	[130.0, 175.0, 225.0, 275.0] GeV

Table 98: Binning of the H_T^{miss} templates, for the category $n_b = 0, n_{jet}^{asy} = 3$.

Jet category	H_T bin	H_T^{miss} binning
$n_b = 0, n_{jet}^{asy} = 3$	$200 < H_T < 250$ GeV	[130.0, 175.0, 225.0, 275.0] GeV
$n_b = 0, n_{jet}^{asy} = 3$	$250 < H_T < 300$ GeV	[130.0, 175.0, 225.0, 275.0, 325.0] GeV
$n_b = 0, n_{jet}^{asy} = 3$	$300 < H_T < 350$ GeV	[130.0, 175.0, 225.0, 275.0, 325.0, 375.0] GeV
$n_b = 0, n_{jet}^{asy} = 3$	$350 < H_T < 400$ GeV	[130.0, 175.0, 225.0, 275.0, 325.0, 375.0, 425.0] GeV
$n_b = 0, n_{jet}^{asy} = 3$	$400 < H_T < 600$ GeV	[130.0, 250.0, 300.0, 350.0, 400.0, 450.0, 500.0, 550.0, 600.0] GeV
$n_b = 0, n_{jet}^{asy} = 3$	$600 < H_T < 800$ GeV	[130.0, 600.0, 650.0, 700.0, 750.0] GeV
$n_b = 0, n_{jet}^{asy} = 3$	$H_T > 800$ GeV	[130.0, 600.0, 650.0, 700.0, 750.0, 800.0, 850.0, 900.0, 950.0, 1000.0] GeV

Table 99: Binning of the H_T^{miss} templates, for the category $n_b = 1, n_{jet}^{asy} = 3$.

Jet category	H_T bin	H_T^{miss} binning
$n_b = 1, n_{jet}^{asy} = 3$	$200 < H_T < 250$ GeV	[130.0, 175.0, 225.0, 275.0] GeV
$n_b = 1, n_{jet}^{asy} = 3$	$250 < H_T < 300$ GeV	[130.0, 175.0, 225.0, 275.0, 325.0] GeV
$n_b = 1, n_{jet}^{asy} = 3$	$300 < H_T < 350$ GeV	[130.0, 175.0, 225.0, 275.0, 325.0, 375.0] GeV
$n_b = 1, n_{jet}^{asy} = 3$	$350 < H_T < 400$ GeV	[130.0, 200.0, 250.0, 300.0, 350.0, 400.0] GeV
$n_b = 1, n_{jet}^{asy} = 3$	$400 < H_T < 600$ GeV	[130.0, 300.0, 350.0, 400.0, 450.0, 500.0, 550.0] GeV
$n_b = 1, n_{jet}^{asy} = 3$	$600 < H_T < 800$ GeV	[130.0, 625.0, 675.0] GeV
$n_b = 1, n_{jet}^{asy} = 3$	$H_T > 800$ GeV	[130.0, 800.0, 850.0] GeV

DRAFT

Table 100: Binning of the H_T^{miss} templates, for the category $n_b = 2, n_{jet}^{asy} = 3$.

Jet category	H_T bin	H_T^{miss} binning
$n_b = 2, n_{jet}^{asy} = 3$	$200 < H_T < 250$ GeV	[130.0, 175.0, 225.0, 275.0] GeV
$n_b = 2, n_{jet}^{asy} = 3$	$250 < H_T < 300$ GeV	[130.0, 175.0, 225.0, 275.0, 325.0] GeV
$n_b = 2, n_{jet}^{asy} = 3$	$300 < H_T < 350$ GeV	[130.0, 150.0, 200.0, 250.0, 300.0, 350.0] GeV
$n_b = 2, n_{jet}^{asy} = 3$	$350 < H_T < 400$ GeV	[130.0, 225.0, 275.0, 325.0, 375.0] GeV
$n_b = 2, n_{jet}^{asy} = 3$	$400 < H_T < 600$ GeV	[130.0, 325.0, 375.0, 425.0, 475.0, 525.0, 575.0] GeV

Table 101: Binning of the H_T^{miss} templates, for the category $n_b \geq 3, n_{jet}^{asy} = 3$.

Jet category	H_T bin	H_T^{miss} binning
$n_b \geq 3, n_{jet}^{asy} = 3$	$200 < H_T < 250$ GeV	[130.0, 175.0, 225.0] GeV
$n_b \geq 3, n_{jet}^{asy} = 3$	$250 < H_T < 300$ GeV	[130.0, 200.0, 250.0] GeV
$n_b \geq 3, n_{jet}^{asy} = 3$	$300 < H_T < 350$ GeV	[130.0, 200.0, 250.0] GeV

Table 102: Binning of the H_T^{miss} templates, for the category $n_b = 0, n_{jet}^{asy} = 2$.

Jet category	H_T bin	H_T^{miss} binning
$n_b = 0, n_{jet}^{asy} = 2$	$200 < H_T < 250$ GeV	[130.0, 175.0, 225.0, 275.0] GeV
$n_b = 0, n_{jet}^{asy} = 2$	$250 < H_T < 300$ GeV	[130.0, 225.0, 275.0, 325.0] GeV
$n_b = 0, n_{jet}^{asy} = 2$	$300 < H_T < 350$ GeV	[130.0, 275.0, 325.0, 375.0] GeV
$n_b = 0, n_{jet}^{asy} = 2$	$350 < H_T < 400$ GeV	[130.0, 325.0, 375.0, 425.0] GeV
$n_b = 0, n_{jet}^{asy} = 2$	$400 < H_T < 600$ GeV	[130.0, 425.0, 475.0, 525.0, 575.0, 625.0] GeV
$n_b = 0, n_{jet}^{asy} = 2$	$600 < H_T < 800$ GeV	[130.0, 650.0, 700.0, 750.0, 800.0] GeV
$n_b = 0, n_{jet}^{asy} = 2$	$H_T > 800$ GeV	[130.0, 700.0, 750.0, 800.0, 850.0, 900.0, 950.0, 1000.0, 1075.0, 1150.0, 1200.0] GeV

Table 103: Binning of the H_T^{miss} templates, for the category $n_b = 1, n_{jet}^{asy} = 2$.

Jet category	H_T bin	H_T^{miss} binning
$n_b = 1, n_{jet}^{asy} = 2$	$200 < H_T < 250$ GeV	[130.0, 175.0, 225.0, 275.0] GeV
$n_b = 1, n_{jet}^{asy} = 2$	$250 < H_T < 300$ GeV	[130.0, 225.0, 275.0, 325.0] GeV
$n_b = 1, n_{jet}^{asy} = 2$	$300 < H_T < 350$ GeV	[130.0, 325.0, 375.0] GeV
$n_b = 1, n_{jet}^{asy} = 2$	$350 < H_T < 400$ GeV	[130.0, 375.0, 425.0] GeV
$n_b = 1, n_{jet}^{asy} = 2$	$400 < H_T < 600$ GeV	[130.0, 400.0, 450.0, 500.0, 550.0, 600.0] GeV
$n_b = 1, n_{jet}^{asy} = 2$	$600 < H_T < 800$ GeV	[130.0, 625.0, 675.0, 725.0] GeV
$n_b = 1, n_{jet}^{asy} = 2$	$H_T > 800$ GeV	[130.0] GeV

Table 104: Binning of the H_T^{miss} templates, for the category $n_b = 2, n_{jet}^{asy} = 2$.

Jet category	H_T bin	H_T^{miss} binning
$n_b = 2, n_{jet}^{asy} = 2$	$200 < H_T < 250$ GeV	[130.0, 175.0, 225.0, 275.0] GeV
$n_b = 2, n_{jet}^{asy} = 2$	$250 < H_T < 300$ GeV	[130.0, 275.0, 325.0] GeV
$n_b = 2, n_{jet}^{asy} = 2$	$300 < H_T < 350$ GeV	[130.0, 325.0, 375.0] GeV
$n_b = 2, n_{jet}^{asy} = 2$	$350 < H_T < 400$ GeV	[130.0, 375.0, 425.0] GeV

DRAFT

H Yields for 3fb^{-1}

The tables below contain the predicted yields for 3fb^{-1} for the signal region and the control regions.

Table 105: Yields for the Electroweak process in the signal region for 3.0fb^{-1}. The letter "a" in jet e.g. "2a" indicates the asymmetric jet bins.

		H_T (GeV)							
n_{jet}	n_b	200-250	250-300	300-350	350-400	400-500	500-600	600-800	800-∞
1	0	7291.15 ±40.24	2438.42 ±20.04	975.06 ±12.03	413.56 ±6.92	307.19 ±5.04	90.67 ±2.39	40.27 ±1.20	9.39 ±0.79
1	1	252.78 ±6.62	90.28 ±3.54	41.28 ±2.57	16.98 ±1.34	14.50 ±1.20	3.70 ±0.78	1.90 ±0.69	0.30 ±0.67
2	0	899.02 ±13.69	969.97 ±13.33	652.84 ±10.54	398.14 ±7.34	363.80 ±5.69	126.53 ±2.86	62.69 ±1.39	85.19 ±1.46
2	1	99.89 ±4.74	91.44 ±4.22	62.33 ±3.25	35.76 ±2.28	29.90 ±1.76	11.43 ±1.09	6.57 ±0.78	8.29 ±0.77
2	2	5.32 ±1.09	5.69 ±1.00	3.86 ±0.89	2.70 ±0.82	1.89 ±0.76	0.95 ±0.69	0.31 ±0.67	0.19 ±0.66
3	0	1.42 ±0.76	175.90 ±5.79	481.02 ±9.40	487.61 ±8.71	586.13 ±7.79	217.59 ±3.89	124.73 ±1.98	120.66 ±1.73
3	1	0.55 ±0.70	44.71 ±3.37	102.19 ±4.78	103.72 ±4.77	101.44 ±4.00	30.89 ±1.81	17.15 ±1.02	16.99 ±0.95
3	2	0.00 ±0.66	8.23 ±1.55	19.52 ±2.15	23.31 ±2.40	16.46 ±1.91	3.97 ±0.86	1.98 ±0.73	1.33 ±0.68
3	≥ 3	0.00 ±0.66	0.00 ±0.66	0.11 ±0.67	0.51 ±0.69	0.31 ±0.68	0.31 ±0.68	0.07 ±0.66	0.01 ±0.66
4	0	-	1.32 ±0.75	76.70 ±4.06	215.86 ±6.18	406.89 ±7.10	196.72 ±3.97	127.62 ±2.20	102.43 ±1.61
4	1	-	0.21 ±0.67	29.14 ±2.69	78.21 ±4.32	137.53 ±5.69	49.03 ±2.86	28.43 ±1.80	19.79 ±1.17
4	2	-	0.00 ±0.66	12.84 ±1.99	29.62 ±2.81	50.91 ±3.54	14.31 ±1.77	7.21 ±1.39	3.94 ±0.84
4	≥ 3	-	0.00 ±0.66	0.20 ±0.68	1.62 ±0.79	2.45 ±0.86	1.35 ±0.75	0.59 ±0.70	0.10 ±0.66
≥ 5	0	-	-	0.00 ±0.66	10.88 ±1.52	115.00 ±4.31	109.12 ±3.61	101.33 ±2.68	92.09 ±2.03
≥ 5	1	-	-	0.00 ±0.66	7.36 ±1.46	74.56 ±4.31	62.14 ±3.80	45.39 ±2.96	35.90 ±2.40
≥ 5	2	-	-	0.00 ±0.66	3.34 ±1.13	30.88 ±2.86	25.71 ±2.59	20.95 ±2.29	12.55 ±1.70
≥ 5	≥ 3	-	-	0.00 ±0.66	0.93 ±0.75	3.87 ±1.20	3.31 ±1.11	1.44 ±0.77	1.51 ±0.78
2a	0	4622.92 ±32.17	1354.85 ±15.28	528.84 ±9.30	219.56 ±5.32	144.32 ±3.56	37.08 ±1.63	15.42 ±0.90	14.10 ±0.84
2a	1	441.43 ±9.80	121.34 ±4.81	41.02 ±2.58	17.98 ±1.50	12.72 ±1.22	2.76 ±0.75	1.31 ±0.68	1.05 ±0.68
2a	2	30.69 ±2.48	6.02 ±0.98	3.23 ±0.86	1.47 ±0.74	0.44 ±0.68	0.07 ±0.66	0.07 ±0.66	0.03 ±0.66
3a	0	1259.29 ±16.64	1259.13 ±16.02	640.12 ±10.98	212.64 ±5.50	101.48 ±3.21	20.08 ±1.36	6.90 ±0.77	6.12 ±0.75
3a	1	311.67 ±8.88	307.52 ±8.66	137.15 ±5.60	43.47 ±3.05	16.48 ±1.68	1.92 ±0.72	1.22 ±0.71	0.73 ±0.67
3a	2	49.63 ±3.52	56.27 ±3.75	35.78 ±3.07	7.23 ±1.43	1.93 ±0.76	0.40 ±0.67	0.06 ±0.66	0.03 ±0.66
3a	≥ 3	1.21 ±0.77	0.98 ±0.72	0.59 ±0.71	0.01 ±0.66	0.08 ±0.67	0.00 ±0.66	0.00 ±0.66	0.00 ±0.66
4a	0	-	147.18 ±5.58	368.00 ±8.55	240.63 ±6.56	134.45 ±3.95	19.48 ±1.40	3.72 ±0.73	2.12 ±0.69
4a	1	-	56.40 ±3.76	167.07 ±6.80	96.71 ±4.88	46.45 ±3.21	3.39 ±0.88	0.50 ±0.67	0.40 ±0.67
4a	2	-	15.08 ±2.01	53.45 ±3.71	35.20 ±3.12	15.09 ±2.06	0.83 ±0.70	0.02 ±0.66	0.05 ±0.66
4a	≥ 3	-	0.32 ±0.67	4.66 ±1.29	2.24 ±0.96	0.71 ±0.72	0.19 ±0.68	0.00 ±0.66	0.01 ±0.66
≥ 5a	0	-	-	35.71 ±2.82	84.14 ±4.12	112.10 ±4.50	19.59 ±1.60	5.37 ±0.86	0.90 ±0.68
≥ 5a	1	-	-	19.46 ±2.14	64.43 ±4.10	86.19 ±4.76	13.17 ±1.88	1.64 ±0.77	0.15 ±0.67
≥ 5a	2	-	-	12.99 ±1.97	27.10 ±2.74	45.10 ±3.57	7.65 ±1.51	0.85 ±0.72	0.04 ±0.66
≥ 5a	≥ 3	-	-	1.24 ±0.79	4.16 ±1.21	3.32 ±1.09	2.11 ±0.86	0.52 ±0.70	0.00 ±0.66

DRAFT

Table 106: Yields for the $t\bar{t}$ process in the signal region for 3.0fb^{-1}. The letter "a" in jet e.g. "2a" indicates the asymmetric jet bins.

		H_T (GeV)							
n_{jet}	n_b	200-250	250-300	300-350	350-400	400-500	500-600	600-800	800-∞
1	0	26.65 ±2.68	6.77 ±1.21	0.44 ±0.63	0.01 ±0.39	0.10 ±0.33	0.00 ±0.26	0.00 ±0.26	0.00 ±0.26
1	1	8.15 ±1.25	2.74 ±0.85	0.09 ±0.28	0.59 ±0.37	0.06 ±0.27	0.00 ±0.26	0.00 ±0.26	0.00 ±0.26
2	0	49.33 ±3.56	39.52 ±3.35	16.86 ±2.12	7.34 ±1.36	3.25 ±1.02	0.06 ±0.28	0.01 ±0.29	0.32 ±0.32
2	1	45.36 ±3.48	34.21 ±2.96	16.10 ±2.00	6.46 ±1.30	3.24 ±0.90	1.48 ±0.52	0.31 ±0.32	0.12 ±0.27
2	2	2.03 ±0.75	1.34 ±0.51	1.33 ±0.47	1.07 ±0.44	0.71 ±0.39	0.02 ±0.26	0.00 ±0.26	0.00 ±0.26
3	0	0.47 ±0.33	20.57 ±2.45	38.82 ±3.24	29.81 ±2.83	28.74 ±2.76	4.69 ±1.05	2.03 ±0.79	1.93 ±0.56
3	1	0.48 ±0.34	31.33 ±3.03	62.14 ±4.04	55.89 ±3.97	37.89 ±3.15	6.85 ±1.24	2.14 ±0.61	1.54 ±0.48
3	2	0.00 ±0.26	6.42 ±1.38	14.62 ±1.94	17.54 ±2.18	11.65 ±1.74	1.59 ±0.51	0.57 ±0.37	0.04 ±0.26
3	≥ 3	0.00 ±0.26	0.00 ±0.26	0.02 ±0.26	0.33 ±0.31	0.29 ±0.30	0.28 ±0.31	0.00 ±0.26	0.00 ±0.26
4	0	-	0.30 ±0.31	13.95 ±1.98	35.61 ±3.12	45.97 ±3.60	12.09 ±1.74	3.96 ±1.07	1.50 ±0.53
4	1	-	0.11 ±0.28	21.74 ±2.41	56.10 ±3.89	92.18 ±5.34	20.61 ±2.46	8.42 ±1.54	2.60 ±0.82
4	2	-	0.00 ±0.26	11.34 ±1.86	25.85 ±2.66	43.50 ±3.41	10.41 ±1.58	4.71 ±1.23	1.70 ±0.53
4	≥ 3	-	0.00 ±0.26	0.20 ±0.30	1.33 ±0.49	1.92 ±0.59	1.14 ±0.44	0.51 ±0.34	0.01 ±0.26
≥ 5	0	-	-	0.00 ±0.26	2.89 ±0.86	29.66 ±2.90	22.46 ±2.47	11.65 ±1.84	6.14 ±1.45
≥ 5	1	-	-	0.00 ±0.26	6.55 ±1.31	58.65 ±4.09	45.59 ±3.58	26.85 ±2.77	17.30 ±2.24
≥ 5	2	-	-	0.00 ±0.26	3.19 ±0.95	28.27 ±2.76	22.48 ±2.48	17.48 ±2.18	9.23 ±1.57
≥ 5	≥ 3	-	-	0.00 ±0.26	0.93 ±0.44	3.77 ±1.03	3.03 ±0.92	1.03 ±0.46	1.11 ±0.48
2a	0	219.15 ±7.78	47.03 ±3.59	9.33 ±1.64	3.45 ±0.90	1.52 ±0.52	0.20 ±0.30	0.51 ±0.33	0.00 ±0.26
2a	1	169.63 ±6.81	36.82 ±3.15	6.57 ±1.24	3.22 ±0.86	1.46 ±0.53	0.07 ±0.27	0.00 ±0.26	0.08 ±0.27
2a	2	8.65 ±1.52	0.79 ±0.36	0.49 ±0.35	0.11 ±0.27	0.00 ±0.26	0.00 ±0.26	0.00 ±0.26	0.00 ±0.26
3a	0	144.39 ±6.22	130.66 ±6.03	52.33 ±3.89	12.95 ±1.92	3.75 ±0.99	0.52 ±0.33	0.00 ±0.26	0.00 ±0.26
3a	1	212.44 ±7.64	201.91 ±7.52	81.21 ±4.74	21.25 ±2.43	6.15 ±1.30	0.33 ±0.30	0.54 ±0.35	0.00 ±0.26
3a	2	40.53 ±3.33	43.28 ±3.43	24.62 ±2.62	5.70 ±1.25	0.66 ±0.38	0.00 ±0.26	0.00 ±0.26	0.00 ±0.26
3a	≥ 3	1.11 ±0.46	0.66 ±0.38	0.59 ±0.36	0.00 ±0.26	0.08 ±0.27	0.00 ±0.26	0.00 ±0.26	0.00 ±0.26
4a	0	-	26.51 ±2.72	62.29 ±4.13	33.24 ±2.99	10.79 ±1.69	1.67 ±0.59	0.07 ±0.26	0.00 ±0.26
4a	1	-	41.59 ±3.42	127.64 ±6.02	69.45 ±4.40	30.06 ±2.95	1.09 ±0.54	0.00 ±0.26	0.07 ±0.26
4a	2	-	11.96 ±1.84	48.42 ±3.60	32.34 ±3.03	12.94 ±1.94	0.54 ±0.34	0.00 ±0.26	0.00 ±0.26
4a	≥ 3	-	0.21 ±0.28	4.42 ±1.14	2.12 ±0.74	0.71 ±0.38	0.19 ±0.29	0.00 ±0.26	0.00 ±0.26
$\geq$ 5a	0	-	-	10.70 ±1.78	21.73 ±2.46	27.40 ±2.71	3.17 ±0.96	0.59 ±0.36	0.00 ±0.26
$\geq$ 5a	1	-	-	16.55 ±2.00	56.42 ±3.96	73.22 ±4.56	10.14 ±1.72	0.90 ±0.46	0.06 ±0.27
$\geq$ 5a	2	-	-	12.05 ±1.85	25.70 ±2.65	42.48 ±3.49	6.96 ±1.37	0.79 ±0.39	0.00 ±0.26
$\geq$ 5a	≥ 3	-	-	1.24 ±0.50	4.03 ±1.04	3.06 ±0.90	1.95 ±0.61	0.52 ±0.35	0.00 ±0.26

DRAFT

Table 107: Yields for the W process in the signal region for 3.0fb^{-1}. The letter "a" in jet e.g. "2a" indicates the asymmetric jet bins.

		H_T (GeV)							
n_{jet}	n_b	200-250	250-300	300-350	350-400	400-500	500-600	600-800	800-∞
1	0	2723.78 ±33.30	808.48 ±16.54	284.89 ±9.58	97.93 ±5.09	71.21 ±3.46	16.37 ±1.44	6.15 ±0.68	0.96 ±0.58
1	1	63.58 ±4.85	19.51 ±2.53	10.86 ±2.06	2.60 ±0.83	3.28 ±0.85	0.84 ±0.61	0.26 ±0.57	0.02 ±0.57
2	0	365.20 ±11.45	374.98 ±11.13	246.58 ±8.83	140.95 ±5.97	121.18 ±4.27	38.38 ±2.00	17.53 ±0.88	23.53 ±0.86
2	1	19.95 ±2.64	20.05 ±2.51	14.64 ±2.07	8.54 ±1.45	8.09 ±1.12	2.82 ±0.77	1.45 ±0.59	2.12 ±0.60
2	2	0.23 ±0.60	0.70 ±0.64	0.32 ±0.60	0.19 ±0.57	0.07 ±0.57	0.33 ±0.58	0.04 ±0.57	0.04 ±0.57
3	0	0.44 ±0.63	62.97 ±4.54	187.56 ±7.66	195.06 ±7.14	218.50 ±5.88	74.08 ±2.76	36.06 ±1.14	33.26 ±0.95
3	1	0.00 ±0.57	4.48 ±1.23	14.00 ±2.17	19.95 ±2.28	23.01 ±1.95	7.69 ±1.00	4.56 ±0.64	4.10 ±0.63
3	2	0.00 ±0.57	0.46 ±0.61	1.47 ±0.76	2.73 ±0.87	0.87 ±0.62	0.48 ±0.59	0.30 ±0.57	0.30 ±0.57
3	≥ 3	0.00 ±0.57	0.00 ±0.57	0.00 ±0.57	0.00 ±0.57	0.00 ±0.57	0.00 ±0.57	0.00 ±0.57	0.00 ±0.57
4	0	-	0.70 ±0.64	30.90 ±3.16	80.85 ±4.65	156.72 ±5.10	67.40 ±2.69	41.50 ±1.28	30.69 ±0.92
4	1	-	0.00 ±0.57	2.69 ±1.01	8.26 ±1.59	15.43 ±1.47	9.42 ±1.12	6.08 ±0.67	4.75 ±0.63
4	2	-	0.00 ±0.57	0.43 ±0.61	2.06 ±0.82	1.67 ±0.72	0.88 ±0.61	0.52 ±0.58	0.48 ±0.57
4	≥ 3	-	0.00 ±0.57	0.00 ±0.57	0.00 ±0.57	0.16 ±0.57	0.00 ±0.57	0.03 ±0.57	0.06 ±0.57
≥ 5	0	-	-	0.00 ±0.57	3.95 ±1.13	38.35 ±2.72	34.42 ±2.08	34.52 ±1.47	29.17 ±0.91
≥ 5	1	-	-	0.00 ±0.57	0.17 ±0.57	6.98 ±1.15	7.51 ±1.07	6.67 ±0.83	6.57 ±0.66
≥ 5	2	-	-	0.00 ±0.57	0.00 ±0.57	0.90 ±0.64	1.10 ±0.66	1.24 ±0.61	0.86 ±0.58
≥ 5	≥ 3	-	-	0.00 ±0.57	0.00 ±0.57	0.00 ±0.57	0.20 ±0.57	0.04 ±0.57	0.07 ±0.57
2a	0	1869.70 ±26.61	487.25 ±12.58	184.72 ±7.69	67.56 ±4.20	38.33 ±2.56	9.64 ±1.13	2.96 ±0.61	2.22 ±0.60
2a	1	95.40 ±5.77	27.31 ±2.99	10.31 ±1.83	2.48 ±0.79	3.63 ±0.88	0.39 ±0.58	0.26 ±0.57	0.11 ±0.57
2a	2	6.04 ±1.53	1.01 ±0.69	0.82 ±0.66	0.83 ±0.64	0.03 ±0.57	0.00 ±0.57	0.04 ±0.57	0.00 ±0.57
3a	0	495.03 ±13.38	489.10 ±13.07	250.43 ±8.96	71.06 ±4.23	32.06 ±2.37	5.54 ±0.96	1.35 ±0.59	1.10 ±0.59
3a	1	39.85 ±3.90	41.54 ±3.69	20.05 ±2.49	8.01 ±1.55	3.24 ±0.84	0.61 ±0.59	0.17 ±0.57	0.06 ±0.57
3a	2	2.18 ±0.86	4.22 ±1.28	4.92 ±1.43	0.37 ±0.60	0.10 ±0.57	0.17 ±0.57	0.00 ±0.57	0.00 ±0.57
3a	≥ 3	0.00 ±0.57	0.00 ±0.57	0.00 ±0.57	0.00 ±0.57	0.00 ±0.57	0.00 ±0.57	0.00 ±0.57	0.00 ±0.57
4a	0	-	56.78 ±4.34	135.92 ±6.60	94.50 ±5.13	47.09 ±2.86	5.96 ±1.00	0.78 ±0.58	0.38 ±0.57
4a	1	-	4.61 ±1.28	16.96 ±2.89	11.23 ±1.80	4.87 ±0.96	0.84 ±0.61	0.15 ±0.57	0.07 ±0.57
4a	2	-	0.75 ±0.65	1.05 ±0.67	0.66 ±0.62	0.33 ±0.59	0.10 ±0.57	0.01 ±0.57	0.00 ±0.57
4a	≥ 3	-	0.00 ±0.57	0.00 ±0.57	0.00 ±0.57	0.00 ±0.57	0.00 ±0.57	0.00 ±0.57	0.00 ±0.57
≥ 5a	0	-	-	11.73 ±1.93	29.11 ±2.92	43.04 ±3.21	7.37 ±1.08	1.72 ±0.67	0.27 ±0.57
≥ 5a	1	-	-	0.88 ±0.66	2.32 ±0.83	6.38 ±1.21	1.24 ±0.67	0.22 ±0.57	0.01 ±0.57
≥ 5a	2	-	-	0.58 ±0.63	0.32 ±0.59	0.67 ±0.62	0.02 ±0.57	0.00 ±0.57	0.00 ±0.57
≥ 5a	≥ 3	-	-	0.00 ±0.57	0.13 ±0.58	0.00 ±0.57	0.02 ±0.57	0.00 ±0.57	0.00 ±0.57

DRAFT

Table 108: Yields for the Z_{inv} process in the signal region for 3.0fb^{-1}. The letter "a" in jet e.g. "2a" indicates the asymmetric jet bins.

		H_T (GeV)							
n_{jet}	n_b	200-250	250-300	300-350	350-400	400-500	500-600	600-800	800-∞
1	0	4540.72 ±22.42	1623.17 ±11.25	689.73 ±7.25	315.62 ±4.67	235.88 ±3.66	74.29 ±1.89	34.11 ±0.95	8.43 ±0.47
1	1	181.06 ±4.34	68.03 ±2.32	30.33 ±1.51	13.79 ±0.98	11.16 ±0.81	2.90 ±0.41	1.64 ±0.28	0.28 ±0.23
2	0	484.49 ±6.61	555.46 ±6.54	389.40 ±5.36	249.86 ±4.06	239.37 ±3.63	88.08 ±2.03	45.16 ±1.03	61.34 ±1.13
2	1	34.57 ±1.84	37.18 ±1.67	31.60 ±1.51	20.77 ±1.18	18.56 ±1.00	7.14 ±0.58	4.82 ±0.40	6.05 ±0.41
2	2	3.05 ±0.51	3.66 ±0.57	2.20 ±0.46	1.44 ±0.37	1.11 ±0.31	0.60 ±0.27	0.27 ±0.23	0.15 ±0.23
3	0	0.51 ±0.27	92.36 ±2.62	254.63 ±4.37	262.74 ±4.11	338.89 ±4.30	138.82 ±2.52	86.63 ±1.42	85.47 ±1.33
3	1	0.06 ±0.22	8.89 ±0.84	26.04 ±1.37	27.89 ±1.35	40.53 ±1.52	16.35 ±0.85	10.45 ±0.52	11.35 ±0.53
3	2	0.00 ±0.22	1.35 ±0.38	3.44 ±0.53	3.05 ±0.47	3.95 ±0.50	1.91 ±0.36	1.11 ±0.27	0.99 ±0.26
3	≥ 3	0.00 ±0.22	0.00 ±0.22	0.09 ±0.22	0.18 ±0.23	0.03 ±0.22	0.02 ±0.22	0.07 ±0.22	0.00 ±0.22
4	0	-	0.32 ±0.25	31.85 ±1.59	99.40 ±2.61	204.21 ±3.39	117.22 ±2.34	82.16 ±1.44	70.24 ±1.21
4	1	-	0.10 ±0.23	4.72 ±0.62	13.85 ±0.97	29.91 ±1.29	19.00 ±0.95	13.93 ±0.64	12.44 ±0.55
4	2	-	0.00 ±0.22	1.07 ±0.37	1.71 ±0.40	5.75 ±0.60	3.03 ±0.51	1.98 ±0.31	1.76 ±0.29
4	≥ 3	-	0.00 ±0.22	0.00 ±0.22	0.29 ±0.24	0.37 ±0.24	0.20 ±0.23	0.05 ±0.22	0.04 ±0.22
≥ 5	0	-	-	0.00 ±0.22	4.04 ±0.55	46.98 ±1.65	52.25 ±1.62	55.16 ±1.28	56.79 ±1.10
≥ 5	1	-	-	0.00 ±0.22	0.65 ±0.27	8.94 ±0.74	9.04 ±0.69	11.88 ±0.62	12.02 ±0.54
≥ 5	2	-	-	0.00 ±0.22	0.14 ±0.23	1.72 ±0.37	2.13 ±0.38	2.23 ±0.35	2.46 ±0.31
≥ 5	≥ 3	-	-	0.00 ±0.22	0.00 ±0.22	0.09 ±0.22	0.09 ±0.22	0.37 ±0.24	0.32 ±0.23
2a	0	2534.08 ±16.32	820.57 ±7.91	334.79 ±4.96	148.55 ±3.14	104.47 ±2.42	27.23 ±1.13	11.95 ±0.56	11.92 ±0.53
2a	1	176.41 ±4.06	57.21 ±2.06	24.14 ±1.33	12.28 ±0.93	7.63 ±0.66	2.30 ±0.39	1.05 ±0.26	0.86 ±0.26
2a	2	16.01 ±1.22	4.23 ±0.60	1.92 ±0.43	0.53 ±0.26	0.41 ±0.27	0.07 ±0.22	0.03 ±0.22	0.03 ±0.22
3a	0	619.87 ±7.70	639.37 ±7.03	337.36 ±5.01	128.63 ±2.93	65.67 ±1.92	14.01 ±0.90	5.55 ±0.43	5.02 ±0.39
3a	1	59.38 ±2.30	64.06 ±2.19	35.90 ±1.62	14.21 ±0.99	7.10 ±0.65	0.98 ±0.28	0.51 ±0.24	0.68 ±0.25
3a	2	6.92 ±0.75	8.77 ±0.83	6.25 ±0.72	1.16 ±0.32	1.16 ±0.33	0.22 ±0.23	0.06 ±0.22	0.03 ±0.22
3a	≥ 3	0.10 ±0.23	0.33 ±0.25	0.00 ±0.22	0.01 ±0.22	0.00 ±0.22	0.00 ±0.22	0.00 ±0.22	0.00 ±0.22
4a	0	-	63.89 ±2.22	169.79 ±3.54	112.89 ±2.78	76.57 ±2.13	11.86 ±0.77	2.87 ±0.35	1.80 ±0.29
4a	1	-	10.20 ±0.89	22.46 ±1.28	16.02 ±1.06	11.52 ±0.83	1.46 ±0.33	0.35 ±0.23	0.26 ±0.23
4a	2	-	2.36 ±0.49	3.99 ±0.57	2.20 ±0.42	1.82 ±0.36	0.19 ±0.23	0.00 ±0.22	0.05 ±0.22
4a	≥ 3	-	0.11 ±0.23	0.24 ±0.24	0.13 ±0.23	0.00 ±0.22	0.00 ±0.22	0.00 ±0.22	0.01 ±0.22
$\geq$ 5a	0	-	-	13.28 ±1.04	33.30 ±1.54	41.65 ±1.60	9.04 ±0.69	3.06 ±0.40	0.63 ±0.25
$\geq$ 5a	1	-	-	2.03 ±0.41	5.69 ±0.65	6.59 ±0.64	1.79 ±0.36	0.52 ±0.25	0.08 ±0.22
$\geq$ 5a	2	-	-	0.37 ±0.25	1.08 ±0.33	1.95 ±0.40	0.67 ±0.28	0.06 ±0.22	0.04 ±0.22
$\geq$ 5a	≥ 3	-	-	0.00 ±0.22	0.00 ±0.22	0.25 ±0.24	0.14 ±0.23	0.00 ±0.22	0.00 ±0.22

DRAFT

Table 109: Yields in the μ + jets control region for 3.0fb^{-1}. The letter "a" in jet e.g. "2a" indicates the asymmetric jet bins.

		H_T (GeV)							
n_{jet}	n_b	200-250	250-300	300-350	350-400	400-500	500-600	600-800	800-∞
1	0	4346.16 ±40.68	1592.60 ±22.75	692.78 ±14.96	331.48 ±9.23	266.59 ±6.55	86.63 ±3.11	42.70 ±1.31	9.47 ±0.77
1	1	176.85 ±7.95	59.85 ±4.23	28.35 ±2.91	14.05 ±1.86	11.54 ±1.41	3.23 ±0.84	2.24 ±0.71	0.43 ±0.66
2	0	471.52 ±12.57	689.05 ±14.87	637.02 ±14.00	572.29 ±11.83	718.87 ±10.28	346.85 ±5.76	297.17 ±3.08	152.20 ±1.89
2	1	95.74 ±5.20	103.58 ±5.45	84.33 ±4.91	67.27 ±4.10	92.15 ±4.28	43.38 ±2.58	36.22 ±2.01	18.80 ±1.41
2	2	4.24 ±1.12	8.31 ±1.54	4.30 ±1.13	6.44 ±1.27	9.18 ±1.66	4.03 ±1.15	3.95 ±1.06	1.12 ±0.72
3	0	1.35 ±0.77	211.79 ±8.25	443.28 ±11.52	507.10 ±11.23	767.36 ±11.31	449.96 ±7.21	413.35 ±4.43	244.60 ±2.97
3	1	1.59 ±0.81	111.05 ±5.76	237.40 ±8.29	230.05 ±7.84	284.89 ±8.26	146.74 ±5.75	121.29 ±4.77	59.26 ±3.08
3	2	0.42 ±0.69	25.55 ±2.66	75.23 ±4.63	82.77 ±5.03	107.47 ±5.43	45.02 ±3.55	31.32 ±2.82	11.28 ±1.65
3	≥ 3	0.00 ±0.66	2.93 ±1.20	2.59 ±1.03	1.27 ±0.78	5.27 ±1.42	2.20 ±0.93	0.77 ±0.70	0.63 ±0.70
4	0	-	0.65 ±0.71	60.89 ±4.20	186.92 ±7.02	467.26 ±9.81	326.71 ±6.90	351.12 ±5.68	218.97 ±3.33
4	1	-	0.83 ±0.73	61.14 ±4.16	170.46 ±6.86	385.68 ±10.19	232.47 ±7.69	195.99 ±6.87	94.58 ±4.21
4	2	-	0.48 ±0.69	25.35 ±2.71	89.53 ±5.06	198.32 ±7.46	117.77 ±5.70	84.26 ±4.68	40.10 ±3.20
4	≥ 3	-	0.00 ±0.66	2.19 ±0.86	6.35 ±1.47	15.17 ±2.10	11.30 ±1.95	7.87 ±1.61	3.83 ±1.17
≥ 5	0	-	-	0.54 ±0.70	12.14 ±1.86	130.45 ±5.53	193.91 ±6.33	276.01 ±6.44	249.37 ±5.19
≥ 5	1	-	-	1.15 ±0.77	16.62 ±2.19	190.79 ±7.46	263.29 ±8.51	334.02 ±9.32	249.03 ±7.79
≥ 5	2	-	-	0.43 ±0.69	7.76 ±1.53	112.22 ±5.61	160.15 ±6.59	221.24 ±7.85	155.55 ±6.53
≥ 5	≥ 3	-	-	0.00 ±0.66	1.41 ±0.80	13.60 ±2.03	20.49 ±2.48	29.88 ±2.92	24.79 ±2.71
2a	0	4607.64 ±40.47	2399.37 ±27.92	1123.04 ±18.56	488.82 ±10.94	341.74 ±7.30	93.38 ±3.06	47.18 ±1.43	9.45 ±0.77
2a	1	806.41 ±15.61	330.99 ±9.77	156.22 ±6.68	58.22 ±3.87	43.53 ±3.06	11.36 ±1.51	5.11 ±0.89	1.13 ±0.69
2a	2	78.48 ±4.71	37.04 ±3.18	13.35 ±1.82	5.84 ±1.24	2.42 ±0.86	0.97 ±0.76	1.00 ±0.72	0.42 ±0.69
3a	0	1095.83 ±19.39	1454.90 ±21.44	797.53 ±15.70	400.67 ±10.02	287.16 ±6.78	73.12 ±3.12	31.99 ±1.45	6.98 ±0.77
3a	1	605.88 ±13.19	781.84 ±15.02	376.38 ±10.31	145.18 ±6.15	88.67 ±4.49	19.84 ±1.98	8.42 ±1.33	0.70 ±0.67
3a	2	162.51 ±6.71	231.77 ±8.08	115.94 ±5.63	42.12 ±3.35	24.86 ±2.60	5.73 ±1.27	1.71 ±0.76	0.22 ±0.67
3a	≥ 3	6.24 ±1.46	7.89 ±1.58	3.97 ±1.17	1.00 ±0.76	1.14 ±0.74	0.48 ±0.69	0.00 ±0.66	0.00 ±0.66
4a	0	-	224.44 ±8.28	406.63 ±11.27	259.42 ±8.37	192.48 ±6.24	52.65 ±2.86	18.97 ±1.34	2.90 ±0.70
4a	1	-	210.63 ±7.62	358.86 ±10.03	226.29 ±7.95	142.79 ±6.25	24.00 ±2.40	8.29 ±1.42	1.63 ±0.75
4a	2	-	93.55 ±5.16	171.23 ±6.96	110.06 ±5.54	60.90 ±4.10	16.33 ±2.22	3.34 ±1.17	0.19 ±0.67
4a	≥ 3	-	4.68 ±1.19	12.39 ±1.90	8.96 ±1.71	2.92 ±1.07	0.74 ±0.71	0.41 ±0.69	0.00 ±0.66
$\geq$ 5a	0	-	-	30.76 ±2.99	88.61 ±5.02	131.59 ±5.72	39.65 ±2.78	17.35 ±1.83	1.22 ±0.67
$\geq$ 5a	1	-	-	46.91 ±3.69	128.31 ±6.11	179.72 ±7.03	51.34 ±3.73	21.09 ±2.41	1.75 ±0.80
$\geq$ 5a	2	-	-	20.97 ±2.39	60.20 ±4.15	111.31 ±5.67	36.34 ±3.23	9.64 ±1.69	1.28 ±0.78
$\geq$ 5a	≥ 3	-	-	2.35 ±1.08	7.69 ±1.59	7.74 ±1.57	4.73 ±1.36	1.92 ±0.85	0.01 ±0.66

DRAFT

Table 110: Yields in the $\mu\mu$ + jets control region for 3.0fb^{-1}. The letter "a" in jet e.g. "2a" indicates the asymmetric jet bins.

		H_T (GeV)							
n_{jet}	n_b	200-250	250-300	300-350	350-400	400-500	500-600	600-800	800-∞
1	0	599.66 ±11.60	239.18 ±7.05	106.11 ±4.54	53.85 ±2.85	41.95 ±1.63	13.37 ±0.66	6.67 ±0.48	1.42 ±0.40
1	1	31.70 ±2.63	12.31 ±1.57	7.05 ±1.26	2.61 ±0.59	1.71 ±0.45	0.48 ±0.39	0.34 ±0.39	0.13 ±0.38
2	0	48.82 ±3.24	72.32 ±3.84	75.61 ±3.85	63.15 ±2.90	80.98 ±1.85	43.37 ±1.05	35.96 ±0.76	20.80 ±0.70
2	1	6.05 ±1.17	8.26 ±1.35	8.72 ±1.34	7.19 ±1.09	8.89 ±0.73	4.49 ±0.61	3.69 ±0.48	1.93 ±0.41
2	2	0.20 ±0.40	0.89 ±0.48	0.54 ±0.44	1.15 ±0.48	0.31 ±0.39	0.17 ±0.38	0.21 ±0.39	0.04 ±0.38
3	0	0.11 ±0.39	15.80 ±1.83	37.11 ±2.67	48.48 ±2.59	73.53 ±1.85	47.28 ±1.10	46.05 ±0.84	30.27 ±0.71
3	1	0.00 ±0.38	1.81 ±0.60	6.58 ±1.25	6.07 ±0.91	14.39 ±1.37	7.19 ±0.63	7.00 ±0.59	4.41 ±0.45
3	2	0.00 ±0.38	0.66 ±0.45	1.32 ±0.52	2.54 ±0.66	3.03 ±0.82	1.68 ±0.55	0.69 ±0.39	0.69 ±0.43
3	≥ 3	0.00 ±0.38	0.02 ±0.38	0.00 ±0.38	0.20 ±0.40	0.05 ±0.38	0.01 ±0.38	0.00 ±0.38	0.02 ±0.38
4	0	-	0.00 ±0.38	7.00 ±1.26	13.83 ±1.57	37.36 ±1.59	29.98 ±0.99	31.95 ±0.76	24.60 ±0.67
4	1	-	0.00 ±0.38	0.73 ±0.45	2.61 ±0.63	7.84 ±1.03	7.14 ±0.92	7.17 ±0.64	4.69 ±0.45
4	2	-	0.00 ±0.38	0.00 ±0.38	1.48 ±0.56	3.21 ±0.84	1.81 ±0.54	1.54 ±0.47	0.97 ±0.44
4	≥ 3	-	0.00 ±0.38	0.00 ±0.38	0.00 ±0.38	0.06 ±0.39	0.05 ±0.38	0.06 ±0.38	0.07 ±0.38
≥ 5	0	-	-	0.00 ±0.38	0.21 ±0.39	6.81 ±0.86	10.29 ±0.68	18.66 ±0.78	20.99 ±0.65
≥ 5	1	-	-	0.00 ±0.38	0.06 ±0.39	3.22 ±0.68	4.34 ±0.87	5.04 ±0.64	6.72 ±0.83
≥ 5	2	-	-	0.00 ±0.38	0.08 ±0.39	1.20 ±0.51	0.98 ±0.45	2.07 ±0.60	2.50 ±0.62
≥ 5	≥ 3	-	-	0.00 ±0.38	0.00 ±0.38	0.00 ±0.38	0.16 ±0.40	0.66 ±0.46	0.12 ±0.39
2a	0	487.13 ±10.49	273.27 ±7.71	140.85 ±5.32	67.42 ±3.26	43.35 ±1.41	14.22 ±0.68	6.96 ±0.48	1.50 ±0.40
2a	1	54.68 ±3.52	27.00 ±2.43	16.02 ±1.90	5.57 ±0.89	3.71 ±0.51	1.99 ±0.56	0.62 ±0.39	0.13 ±0.38
2a	2	7.60 ±1.40	3.76 ±0.92	0.55 ±0.43	0.04 ±0.38	0.13 ±0.38	0.05 ±0.38	0.03 ±0.38	0.00 ±0.38
3a	0	90.58 ±4.47	130.42 ±5.37	69.60 ±3.78	39.93 ±2.42	34.70 ±1.40	9.16 ±0.59	4.84 ±0.50	0.79 ±0.39
3a	1	17.10 ±2.04	17.91 ±2.09	12.77 ±1.66	6.58 ±1.08	4.82 ±0.64	1.43 ±0.44	0.97 ±0.44	0.10 ±0.39
3a	2	4.25 ±1.01	8.23 ±1.56	4.29 ±1.13	1.14 ±0.48	1.47 ±0.55	0.13 ±0.38	0.02 ±0.38	0.00 ±0.38
3a	≥ 3	0.11 ±0.39	0.74 ±0.46	0.14 ±0.40	0.03 ±0.38	0.02 ±0.38	0.00 ±0.38	0.00 ±0.38	0.00 ±0.38
4a	0	-	13.39 ±1.63	24.68 ±2.16	19.82 ±1.69	15.93 ±1.04	5.21 ±0.53	2.41 ±0.46	0.36 ±0.39
4a	1	-	3.63 ±0.93	7.84 ±1.40	4.21 ±0.84	5.02 ±0.91	1.11 ±0.45	0.61 ±0.42	0.02 ±0.38
4a	2	-	0.56 ±0.45	1.85 ±0.62	1.12 ±0.50	2.62 ±0.86	0.79 ±0.47	0.31 ±0.42	0.45 ±0.44
4a	≥ 3	-	0.00 ±0.38	0.02 ±0.38	0.00 ±0.38	0.00 ±0.38	0.01 ±0.38	0.00 ±0.38	0.00 ±0.38
≥ 5a	0	-	-	1.99 ±0.60	4.41 ±0.98	5.27 ±0.64	2.44 ±0.46	1.03 ±0.40	0.23 ±0.39
≥ 5a	1	-	-	0.43 ±0.43	1.21 ±0.51	3.67 ±0.84	1.51 ±0.56	0.44 ±0.41	0.38 ±0.42
≥ 5a	2	-	-	0.00 ±0.38	0.61 ±0.45	0.67 ±0.45	0.36 ±0.40	0.55 ±0.44	0.00 ±0.38
≥ 5a	≥ 3	-	-	0.00 ±0.38	0.00 ±0.38	0.57 ±0.45	0.00 ±0.38	0.00 ±0.38	0.00 ±0.38

DRAFT

Table 111: Yields in the γ + jets control region for 3.0fb^{-1}. The letter "a" in jet e.g. "2a" indicates the asymmetric jet bins.

		H_T (GeV)			
n_{jet}	n_b	400-500	500-600	600-800	800-∞
1	0	550.71 ±16.32	178.61 ±8.10	93.67 ±4.12	23.91 ±2.01
1	1	22.97 ±3.15	7.33 ±1.66	4.52 ±1.08	1.27 ±0.85
2	0	260.59 ±10.97	109.70 ±6.32	71.72 ±3.61	166.92 ±5.04
2	1	21.74 ±3.15	9.19 ±1.96	4.92 ±1.10	16.55 ±1.74
2	2	1.63 ±0.94	0.50 ±0.77	0.24 ±0.74	0.46 ±0.75
3	0	407.84 ±14.07	180.73 ±8.12	112.58 ±4.34	241.25 ±5.98
3	1	40.80 ±4.24	19.85 ±2.71	9.77 ±1.36	31.79 ±2.29
3	2	3.64 ±1.36	1.86 ±0.89	1.24 ±0.84	2.95 ±0.99
3	≥ 3	0.00 ±0.73	0.00 ±0.73	0.04 ±0.73	0.19 ±0.74
4	0	219.39 ±10.06	143.80 ±7.37	124.20 ±4.95	193.89 ±5.41
4	1	32.41 ±3.88	21.32 ±2.92	16.71 ±1.76	31.18 ±2.24
4	2	7.82 ±1.93	3.41 ±1.10	3.58 ±1.01	4.71 ±1.08
4	≥ 3	0.05 ±0.73	0.28 ±0.76	0.12 ±0.73	0.00 ±0.73
≥ 5	0	47.09 ±5.57	63.76 ±5.12	84.96 ±4.29	148.69 ±4.75
≥ 5	1	8.28 ±1.85	15.79 ±2.54	21.15 ±2.32	37.90 ±2.46
≥ 5	2	1.46 ±0.91	2.67 ±1.03	4.29 ±1.14	6.95 ±1.23
≥ 5	≥ 3	0.00 ±0.73	0.00 ±0.73	0.12 ±0.73	0.50 ±0.75
2a	0	128.17 ±7.78	38.44 ±3.83	21.99 ±2.21	21.05 ±1.85
2a	1	7.35 ±1.77	2.80 ±1.01	0.66 ±0.76	1.92 ±0.90
2a	2	0.00 ±0.73	0.00 ±0.73	0.00 ±0.73	0.12 ±0.73
3a	0	81.16 ±6.37	18.57 ±2.62	6.75 ±1.22	11.16 ±1.46
3a	1	11.01 ±2.37	2.36 ±0.96	1.31 ±0.85	0.85 ±0.78
3a	2	1.54 ±0.93	0.35 ±0.77	0.09 ±0.73	0.00 ±0.73
3a	≥ 3	0.00 ±0.73	0.00 ±0.73	0.00 ±0.73	0.00 ±0.73
4a	0	90.41 ±6.86	15.41 ±2.55	4.62 ±1.14	3.65 ±1.05
4a	1	12.25 ±2.38	3.84 ±1.40	0.58 ±0.76	0.41 ±0.75
4a	2	2.04 ±1.00	0.00 ±0.73	0.00 ±0.73	0.00 ±0.73
4a	≥ 3	0.13 ±0.75	0.00 ±0.73	0.22 ±0.74	0.00 ±0.73
$\geq$ 5a	0	50.83 ±5.71	10.89 ±2.15	4.42 ±1.19	0.90 ±0.78
$\geq$ 5a	1	4.85 ±1.46	3.51 ±1.37	0.72 ±0.77	0.21 ±0.74
$\geq$ 5a	2	2.27 ±1.04	0.14 ±0.74	0.00 ±0.73	0.00 ±0.73
$\geq$ 5a	≥ 3	0.00 ±0.73	0.00 ±0.73	0.00 ±0.73	0.00 ±0.73

DRAFT

I Signal acceptance from asymmetric jet p_T thresholds

For a typical compressed model, Fig. 117 shows the second jet p_T distribution for two different H_T bins. In the low H_T case a large portion of the events are killed by requiring the second jet to have $E_T > 100\,\text{GeV}$.

We therefore add an new analysis category where the leading jet is required to fulfil momenta of jet $E_T > 100\,\text{GeV}$ and sub-leading jet $40\,\text{GeV} < E_T < 100\,\text{GeV}$. This new category results in new asymmetric jet bins split also in n_{jet}, n_b and H_T. The asymmetric jet bin results in much larger acceptance for monojet-type and ISR induced event topologies like DM signals and compresses SUSY scenarios. For the simplified model T2tt with $m_{\text{stop}} = 425\,\text{GeV}$ and $m_{\text{LSP}} = 325\,\text{GeV}$, including these bins increases signal acceptance by around a factor 3, for the DM models a factor of five is observed. The addition of the asymmetric bin can only lead in combination to improvements or constant sensitivities.

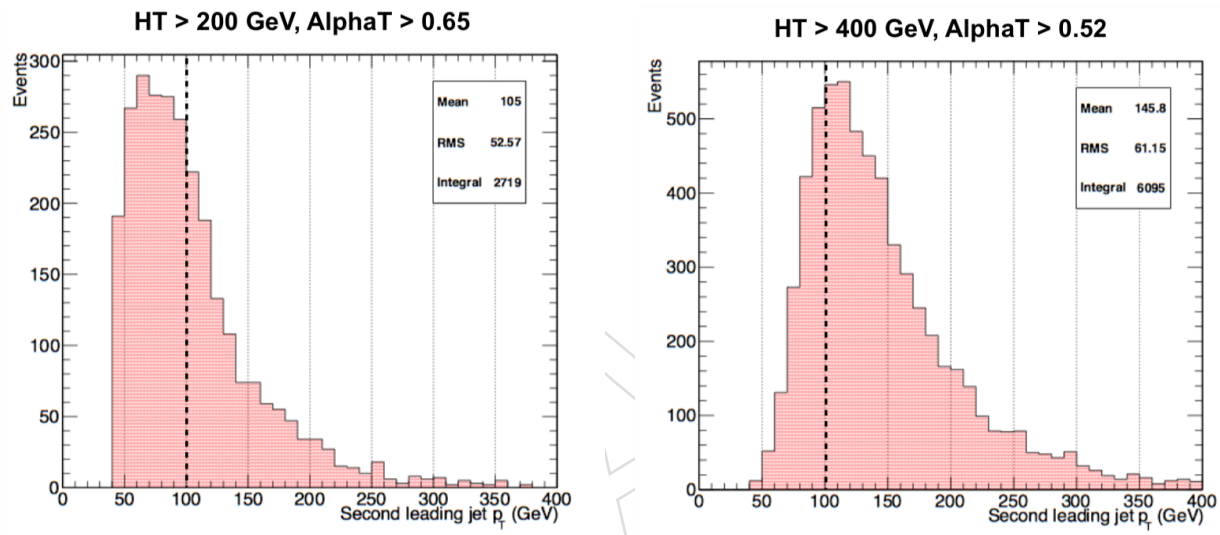

(a) Second jet p_T for $200\,\text{GeV} < H_T < 250\,\text{GeV}$, $\alpha_T > 0.65$ (b) Second jet p_T for $400\,\text{GeV} < H_T > 500\,\text{GeV}$, $\alpha_T > 0.52$

Figure 117: The second leading jet p_T for different cases of H_T after a baseline signal selection: $n_{\text{jet}} \geq 2$, lead jet $E_T > 100\,\text{GeV}$, lepton vetoes. Made with the T2tt ($m_{\text{stop}} = 425\,\text{GeV}$, $m_{\text{LSP}} = 325\,\text{GeV}$) simplified model sample.